

# Used Fuel Disposal in Crystalline Rocks: Status and FY14 Progress

## Fuel Cycle Research & Development

*Prepared for*  
**U.S. Department of Energy**  
**Used Fuel Disposition**  
**Y. Wang, E. Matteo**  
**Sandia National Laboratories**  
**J. Rutqvist, J. Davis, L. Zheng, J. Houseworth, J. Birkholzer**  
**Lawrence Berkeley National Laboratory**  
**T. Dittrich, C. W. Gable, S. Karra, N. Makedonska, S. Chu, D. Harp,**  
**S. L. Painter, P. Reimus, F. Perry**  
**Los Alamos National Laboratory**  
**P. Zhao, J. Begg, M. Zavarin, S. J. Tumey, Z. Dai, A. B. Kersting**  
**Lawrence Livermore National Laboratory**  
**J. Jerden, K. Frey, J. M. Copple, W. Ebert**  
**Argonne national laboratory**  
**September 26, 2014**  
**FCRD-UFD-2014-000060**





Sandia National Laboratories is a multi-program laboratory managed and operated by Sandia Corporation, a wholly owned subsidiary of Lockheed Martin Corporation, for the U.S. Department of Energy's National Nuclear Security Administration under contract DE-AC04-94AL85000.



#### **DISCLAIMER**

This information was prepared as an account of work sponsored by an agency of the U.S. Government. Neither the U.S. Government nor any agency thereof, nor any of their employees, makes any warranty, expressed or implied, or assumes any legal liability or responsibility for the accuracy, completeness, or usefulness, of any information, apparatus, product, or process disclosed, or represents that its use would not infringe privately owned rights. References herein to any specific commercial product, process, or service by trade name, trade mark, manufacturer, or otherwise, does not necessarily constitute or imply its endorsement, recommendation, or favoring by the U.S. Government or any agency thereof. The views and opinions of authors expressed herein do not necessarily state or reflect those of the U.S. Government or any agency thereof.



**FCT Quality Assurance Program Document**

**Appendix E  
FCT Document Cover Sheet**

Name/Title of Deliverable/Milestone Used Fuel Disposal in Crystalline Rocks: Status and FY14 Progress (M2FT-14SN0807051)  
 Work Package Title and Number Crystalline Disposal R&D  
 Work Package WBS Number FT-14SN080705  
 Responsible Work Package Manager Yifeng Wang  
 (Name/Signature)

Date Submitted 9/26/2014

Quality Rigor Level for Deliverable/Milestone	<input checked="" type="checkbox"/> QRL-3	<input type="checkbox"/> QRL-2	<input type="checkbox"/> QRL-1	<input type="checkbox"/> N/A*
			<input type="checkbox"/> Nuclear Data	

This deliverable was prepared in accordance with Sandia National Laboratories  
 (Participant/National Laboratory Name)

QA program which meets the requirements of  
 DOE Order 414.1     NQA-1-2000

**This Deliverable was subjected to:**

Technical Review

**Technical Review (TR)**

**Review Documentation Provided**

- Signed TR Report or,
- Signed TR Concurrence Sheet or,
- Signature of TR Reviewer(s) below

**Name and Signature of Reviewers**

Carlos Jove-Colon



Peer Review

**Peer Review (PR)**

**Review Documentation Provided**

- Signed PR Report or,
- Signed PR Concurrence Sheet or,
- Signature of PR Reviewer(s) below

\*Note: In some cases there may be a milestone where an item is being fabricated, maintenance is being performed on a facility, or a document is being issued through a formal document control process where it specifically calls out a formal review of the document. In these cases, documentation (e.g., inspection report, maintenance request, work planning package documentation or the documented review of the issued document through the document control process) of the completion of the activity along with the Document Cover Sheet is sufficient to demonstrate achieving the milestone. QRL for such milestones may be also be marked N/A in the work package provided the work package clearly specifies the requirement to use the Document Cover Sheet and provide supporting documentation.



## Used Fuel Disposal in Crystalline Rocks: Status and FY14 Progress

### Executive Summary

The U.S. Department of Energy Office of Nuclear Energy, Office of Fuel Cycle Technology established the Used Fuel Disposition Campaign (UFDC) in fiscal year 2010 (FY10) to conduct the research and development (R&D) activities related to storage, transportation and disposal of used nuclear fuel and high level nuclear waste. The Mission of the UFDC is

*To identify alternatives and conduct scientific research and technology development to enable storage, transportation and disposal of used nuclear fuel and wastes generated by existing and future nuclear fuel cycles.*

The work package of Crystalline Disposal R&D directly supports the following UFDC objectives:

- Develop a fundamental understanding of disposal system performance in a range of environments for potential wastes that could arise from future nuclear fuel cycle alternatives through theory, simulation, testing, and experimentation.
- Develop a computational modeling capability for the performance of storage and disposal options for a range of fuel cycle alternatives, evolving from generic models to more robust models of performance assessment.

The objective of the Crystalline Disposal R&D Work Package is to advance our understanding of long-term disposal of used fuel in crystalline rocks and to develop necessary experimental and computational capabilities to evaluate various disposal concepts in such media.

Significant progress has been made in FY14 in both experimental and modeling arenas in evaluation of used fuel disposal in crystalline rocks. The work covers a wide range of research topics identified in the R&D plan. The major accomplishments are summarized below:

- A R&D plan was developed for used fuel disposal in crystalline rocks. A total of 31 research topics (9 for system level and 22 for processes level) have been identified. The technical approach to addressing each of these topics is formulated.
- A generic reference case for crystalline disposal media has been established. The reference case specifies the emplacement concept, waste inventory, waste form, waste package, backfill/buffer properties, EBS failure scenarios, host rock properties, and biosphere. This is an important step in developing a baseline for total system model development. Three emplacement concepts were specified: waste packages containing 4 PWR assemblies emplaced in boreholes in the floors of horizontal tunnels (for comparison with the KBS-3 concept), a 12-assembly waste package emplaced in tunnels, and a 32-assembly dual purpose canister emplaced in tunnels.
- We have developed and applied THMC models to the analysis of coupled EBS processes in bentonite-backfilled repositories. We based this development on the extension of the

Barcelona Basic Model (BBM) to a dual-structure model for expansive clay, such as bentonite. The dual-structure model has been found to give results that are in better agreement with observations, in particular the rate of buffer re-saturation, by representing identifiable physical mechanisms not treated by the original BBM model. Therefore, this model improvement reduces the modeling uncertainty for THM processes in a bentonite buffer.

- We have examined the consistency of macroscopic measurements, electrical double layer (EDL)-based models, and molecular-scale simulations of clay media for adsorption and diffusion of trace levels of calcium ( $\text{Ca}^{2+}$ ), bromide ( $\text{Br}^-$ ), and tritiated water (HTO) in a loosely compacted, water-saturated Na-montmorillonite. Molecular dynamics (MD) simulations were also conducted and used to aid the interpretation of adsorption and diffusion processes in individual clay interlayer nanopores. The MD simulations allow a critical test of various transport/pore models by carefully evaluating the physical meaning of their related fitting parameters on a single set of data. These results highlight the difficulty in constraining current theories of the properties of clay barriers using transport modeling alone.
- Discrete fracture network (DFN) generation, parallel flow solutions, and particle tracking were demonstrated at application-relevant field scales using fracture parameters from a well-characterized site. We also developed and demonstrated the capability to simulate intrafracture variability within a full-scale DFN network. The ability to produce high-quality computational DFN meshes suitable for state-of-the-art parallel subsurface flow codes is a unique capability that will allow large DFNs to be considered in applications. The ability to reliably track particles on DFN control volume grids is also a unique capability.
- Refinement and extension of the DFN modeling capability was undertaken to enable representation of the tetrahedral mesh within the DFN mesh. The two realizations of the DFN with boreholes in place is an important demonstration of an advanced modeling capability combining volume and DFN meshes, and incorporating complex geometries. These simulations used the FEHM code to merge the volume and DFN meshes. FEHM has the unique capability to use define redundant computational nodes, which greatly facilitated the merging of the meshes. Comparison of simulated and measured saturation values in the BRIE borehole is underway.
- We have made significant progress in effectively demonstrating a method of interrogating and taking defensible credit for slow desorption rates to improve reactive transport predictions over long time and distance scales. We chose uranium sorption and transport in Grimsel Test Site granodiorite as a study case, but the method could be applied to any moderately sorbing radionuclide in any hydrogeologic system. Column transport data allow us interrogate slow desorption sites, while batch sorption data are not able to interrogate these slow sites. The approach we developed will help to reduce conservatism in large-scale predictions. From a practical standpoint, the three-site kinetic model developed from uranium column transport data is easy to implement in performance assessment models with little additional computational burden over a simple linear partition coefficient ( $K_d$ ) model.
- We have made significant progress in understanding colloid-facilitated radionuclide transport in nuclear waste repository environments. We demonstrated a repeat-injection

column method for evaluating and parameterizing colloid-facilitated radionuclide transport, using bentonite colloids, Am, and Grimsel Test Site granodiorite FFM as a model system. The method is designed to better interrogate the slower rates (either colloid filtration rates or radionuclide desorption rates from colloids) that have a large impact in performance assessment calculations over long time and distance scales. An increase in colloid recoveries in successive column injections would suggest a fraction of colloids that is relatively susceptible to filtration, and the colloids that remain mobile in later injections will have smaller apparent filtration rate constants that are more relevant for use in large-scale performance assessment calculations.

- A study of the dissolution of intrinsic Pu colloids in the presence of montmorillonite at different temperatures was successfully accomplished using a novel experimental setup containing a dialysis device. This device enables us to separate two solid phases, but let them interact with each other via aqueous Pu ions. Kinetics of a series processes involved in intrinsic Pu colloid dissolution was modeled using 1<sup>st</sup> order reactions to compare the rate constant of different processes. We show that the kinetic constants for dissolution were one to two orders of magnitude lower than that of diffusion of aqueous Pu species in the system. Therefore the dissolution processes was the rate-limiting step. Although the presence of clay changes neither the colloids dissolution nor diffusion rates of Pu, it can stabilize dissolved Pu species and drive intrinsic Pu colloid dissolution and the formation of more stable Pu pseudo-colloids. Temperature enhances dissolution of intrinsic Pu colloids by overcoming a moderate activation energy (28 kJ mol<sup>-1</sup>). Our thermodynamic study shows that the sorption of Pu on montmorillonite is endothermic as a positive change in enthalpy for the sorption has been obtained. The affinity of Pu for the clay increases with increasing of temperature resulting higher  $K_d$  at elevated temperature. The negative values of change of Gibbs free energy for Pu-clay sorption confirm that sorption of Pu onto clay occurs spontaneously and Pu pseudo-colloids are thermodynamically quite stable at both temperatures of 25 to 80 °C. Although the fact that intrinsic Pu colloids tend to dissolve in the presence of montmorillonite may limit the migration of intrinsic Pu colloids, the subsequent formation of thermodynamically more stable Pu pseudo-colloids can play important role in Pu transport in the environment over significant temporal and spatial scales.
- We have examined the reactivity of three different types of intrinsic Pu colloids in the presence of montmorillonite at 25 and 80°C under atmospheric conditions. Pu oxides calcined at 300 and 800 °C and intrinsic Pu colloids produced from acidic solution are quite stable under our experimental conditions. Only two out of seven experiments showed signs of intrinsic Pu colloid dissolution after 100 days. Predicted Pu concentrations calculated using dissolution rate constants obtained from intrinsic Pu colloids formed in alkaline solution are much higher than the measured Pu concentrations, suggesting that these three types of intrinsic Pu colloids are more stable, thus less reactive than the ones formed in alkaline solution. The differences in the reactivity among investigated intrinsic Pu colloids are attributed to their morphological features including crystallinity, crystal growth, aggregation and particle shapes and sizes, all of which are greatly influenced by temperatures during formation of these intrinsic Pu colloids. Intrinsic Pu colloids and/or Pu oxides formed at elevated temperatures are more stable and may play an important role in the migration of intrinsic Pu colloids away from nuclear waste repository setting.

- We have made significant progress in the development of a multiple potential model for used fuel degradation. In FY14, we added several new functionalities to the model. We added a working noble metal particle (epsilon phase) domain on fuel surface to account for the protective hydrogen effect. We also incorporated the radiolysis model subroutine into the model. We performed systematic sensitivity runs that identify and quantify the processes that affect the fuel dissolution rate.

Based on the work accomplished in FY14 and the prior years, the future work is recommended to:

- Focus on two key topics related to deep geologic disposal of used fuel in crystalline rocks: (1) better characterization and understanding of fractured media and fluid flow and transport in such media, and (2) designing effective engineered barrier systems (EBS) for waste isolation. Specific attention will be given to the development of scientifically sound thermal limits for various buffer materials.
- Explore various disposal concepts, for example, borehole disposal vs. drift emplacement, regular waste packages vs. dual purpose canisters (DPCs). Especially, the work will explore potential advantages of crystalline media for the disposal of DPCs, given the high mechanical strength of the rocks.
- Move more towards model demonstrations and applications using data obtained from international collaborations.
- Continue international collaborations, especially with Korea Atomic Research Institute (KAERI), Sweden Underground Research Lab and Czech Bedrichov Tunnel Test Facility.
- Closely coordinate with the deep borehole disposal control account. The data obtained and the tools developed in this control account may be transferable to the deep borehole disposal, or vice versa.
- Continue to work with the generic disposal system analysis control account to refine the reference case for crystalline media and help to develop a performance assessment model for the reference case.

## CONTENTS

1.0	GOALS AND OUTLINE	1
2.	REFERENCE CASE FOR GENERIC CRYSTALLINE DISPOSAL SYSTEM	5
2.1	INTRODUCTION	5
2.2	GENERIC DISPOSAL SYSTEM IN CRYSTALLINE ROCKS	7
2.3	WASTE INVENTORY	16
2.4	ENGINEERED BARRIER SYSTEM	18
2.4.1	Waste Forms	18
2.4.2	Waste Packages	20
2.4.3	Bentonite Buffer/Backfill	22
2.4.4	Seals	28
2.4.5	Radionuclide transport in EBS	29
2.5	NATURAL SYSTEM	33
2.5.1	Geologic Setting	33
2.5.2	Configuration of Generic Geologic Repository in Granite	36
2.5.3	Hydrologic Properties of Host Rock	37
2.5.4	Disturbed Rock Zone	39
2.5.5	Groundwater Chemistry and Radionuclide Transport	40
2.6	REFERENCE SCENARIOS	46
2.7	MODELING APPROACHES	47
2.8	SUMMARY	50
2.9	REFERENCES	51
3.	INVESTIGATION OF COUPLED THMC PROCESS AND REACTIVE TRANSPORT	59
3.1	INTRODUCTION	59
3.2	MODELING COUPLED THMC PROCESSES IN THE EBS	60
3.2.1	Dual-Structure Model Implementation in TOUGH-FLAC	62
3.2.2	Testing of Implementation and Validation	69
3.2.3	Application to a Generic Repository	73
3.2.4	Coupled CM coupling through dual-structure model	84
3.2.5	Conclusions	89
3.3	ION ADSORPTION AND DIFFUSION IN SMECTITE CLAY BARRIERS	90
3.3.1	Background	90
3.3.2	Experimental and modeling methods	93
3.3.3	Results	97
3.3.4	Discussion	112
3.3.5	Conclusion	113
3.4	SUMMARY	114
3.5	REFERENCES	116
4.	DEMONSTRATION OF DISCRETE FRACTURE NETWORK MODELING CAPABILITY	121

4.1	INTRODUCTION	121
4.2	APPLICATION TO THE FORSMARK SITE	123
4.3	MODELING OF BRIE EXPERIMENT	132
4.3.1	Model Development Required to Support the BRIE Modeling Effort	134
4.3.2	Scoping Calculations	134
4.3.3	Model Setup	138
4.3.4	Initial Results	143
4.4	SUMMARY	143
4.5	REFERENCES	144
5.	DESCRIBING URANIUM TRANSPORT IN A FRACTURED CRYSTALLINE ROCK USING MINI-COLUMN EXPERIMENTS	147
5.1	INTRODUCTION	147
5.2	MATERIALS AND METHODS	148
5.2.1	Groundwater	148
5.2.2	Porous Medium	152
5.2.3	Uranium and Tritiated Water	153
5.2.4	Analytical Measurements	153
5.2.5	Column Transport Experiments	153
5.2.6	Batch Adsorption/Desorption Experiments	155
5.2.7	Interpretive Modeling	156
5.3	RESULTS	157
5.3.1	Column Experimental Results	158
5.3.2	Column Experiment Interpretations	161
5.4	DISCUSSION	169
5.4.1	Comparison with Batch Experiment Results	169
5.4.2	Implications for Large-Scale Transport	175
5.5	CONCLUSIONS	178
5.6	REFERENCES	179
6.	LABORATORY INVESTIGATION OF COLLOID-FACILITATED TRANSPORT OF AMERICIUM BY BENTONITE COLLOIDS IN A GRANODIORITE SYSTEM	181
6.1	INTRODUCTION	181
6.2	MATERIALS AND METHODS	182
6.2.1	Groundwater	183
6.2.2	Porous Medium	183
6.2.3	Bentonite Colloids	184
6.2.4	Americium and Tritiated Water	186
6.2.5	Analytical Measurements	186
6.2.6	Column Transport Experiments	187
6.2.7	Interpretive Modeling	190
6.3	RESULTS	190
6.4	DISCUSSION	199
6.5	REFERENCES	200
7.	EVALUATION OF ALTERNATIVE DESCRIPTIONS OF DESORPTION OF TRI- AND TETRAVALENT SOLUTES FROM	201

	BENTONITE COLLOIDS IN TRACER TESTS AT THE GRIMSEL TEST SITE	
7.1	INTRODUCTION	201
7.2	SUMMARY OF CFM COLLOID-FACILITATED TRANSPORT TESTS	202
7.3	INTERPRETIVE MODELING APPROACH	205
7.3.1	Description of Model and Interpretive Procedure	206
7.3.2	Refinements to Evaluate Solute Desorption Processes from Colloids	211
7.3.3	Process for Selecting the Best Description of Desorption from Colloids	213
7.4	INTERPRETIVE MODELING RESULTS	214
7.5	EVALUATION OF ALTERNATIVE DESCRIPTIONS OF SOLUTE DESORPTION PROCESS FROM COLLOIDS	223
7.6	DISCUSSION	226
7.6.1	Implications for Nuclear Waste Repository Performance Assessments over Long Time and Distance Scales	226
7.6.2	Suggestions for Future CFM Colloid-Facilitated Transport Tests	231
7.7	REFERENCES	232
8.	Pu SORPTION, DESORPTION AND INTRINSIC COLLOID STABILITY UNDER GRANITIC CHEMICAL CONDITIONS	233
8.1	STABILITY OF PLUTONIUM INTRINSIC COLLOIDS IN THE PRESENCE OF CLAY AT ELEVATED TEMPERATURES: DISSOLUTION KINETICS	233
8.1.1	Introduction	233
8.1.2	Materials and Methods	234
8.1.3	Results and Discussion	238
8.1.4	Conclusions	252
8.2	STABILITY OF PLUTONIUM INTRINSIC COLLOIDS IN THE PRESENCE OF CLAY AT ELEVATED TEMPERATURES: INFLUENCE OF MORPHOLOGY ON PuO <sub>2</sub> REACTIVITY	252
8.2.1	Introduction	252
8.2.2	Material and Methods	253
8.2.3	Results and Discussion	256
8.2.4	Conclusions	265
8.3	FUTURE WORK	265
8.3.1	Stability of Intrinsic Pu Colloids across a Range of Repository Conditions	265
8.3.2	Temperature Effects on Bentonite Alteration and Sorption of Actinides	266
8.3.3	Modeling Colloid Facilitated Pu Transport at the Grimsel CFM Facility	266
8.4	REFERENCES	267
9.	MIXED POTENTIAL MODEL FOR USED FUEL DEGRADATION: APPLICATION TO CRYSTALLINE ARGILLITE ENVIRONMENTS	273

9.1	INTRODUCTION	273
9.2	CHEMICAL ENVIRONMENTS OF CRYSTALLINE AND ARGILLITE REPOSITORIES	275
9.3	MIXED POTENTIAL MODEL PROCESS OVERVIEW	277
9.4	UPDATED MPM PARAMETER DATABASE	279
9.5	ALPHA PARTICLE PENETRATION DEPTH AND DOSE RATE PROFILE USED IN MPM V2	287
9.6	INCORPORATION OF RADIOLYSIS MODEL ANALYTICAL FUNCTION INTO MPM V2	289
9.7	SENSITIVITY RESULTS MIXED POTENTIAL MODEL V2	292
9.8	CONVERSION OF MPM V2 FROM MATLAB TO FORTRAN	295
9.9	CONCLUSIONS AND FUTURE WORK	296
9.10	REFERENCES	298
10	SUMMARY	301
Appendix A	RESEARCH & DEVELOPMENT (R&D) PLAN FOR USED FUEL DISPOSAL IN CRYSTALLINE ROCKS	305
A1.0	Objectives	305
A2.0	Overview of UFDC Disposal R&D Roadmap	308
A3.0	Research Topics for Used Fuel Disposal in Crystalline Rocks	312
A4.0	Strategies for Reaching R&D Goals	326
A5.0	Summary	327
A6.0	references	333

## 1.0 GOALS AND OUTLINE

The U.S. Department of Energy Office of Nuclear Energy, Office of Fuel Cycle Technology established the Used Fuel Disposition Campaign (UFDC) in fiscal year 2010 (FY10) to conduct the research and development (R&D) activities related to storage, transportation and disposal of used nuclear fuel and high level nuclear waste. The Mission of the UFDC is

*To identify alternatives and conduct scientific research and technology development to enable storage, transportation and disposal of used nuclear fuel and wastes generated by existing and future nuclear fuel cycles.*

The work package of Crystalline Disposal R&D directly supports the following UFDC objectives:

- Develop a fundamental understanding of disposal system performance in a range of environments for potential wastes that could arise from future nuclear fuel cycle alternatives through theory, simulation, testing, and experimentation.
- Develop a computational modeling capability for the performance of storage and disposal options for a range of fuel cycle alternatives, evolving from generic models to more robust models of performance assessment.

The objective of the Crystalline Disposal R&D Work Package is to advance our understanding of long-term disposal of used fuel in crystalline rocks and to develop necessary experimental and computational capabilities to evaluate various disposal concepts in such media. FY14 work is aligned with the following considerations and project goals:

- Since this is the first time to have a separate work package for crystalline rocks, one of the main objectives for FY14 is to formulate a research plan for used fuel disposal in crystalline rocks. Crystalline rocks to be studied include granite and high-grade metamorphic rocks.
- Some of the activities of this work package were carried over from the FY13 work packages for natural system and engineered barrier system evaluation. This work package tries to maintain the continuity of those activities as the funding permits. The priority is given to the experimental work that has already started in a prior year and will have an important contribution to the evaluation of crystalline rocks as disposal media.
- This work package will focus on two key components of a deep geologic repository in crystalline rocks: (1) better characterization and understanding of fractured media and fluid flow and transport in such media, and (2) designing effective engineered barrier systems for waste isolation. Especially, the work will take into consideration the implication of the disposal of dual purpose canisters in crystalline rocks.

- The work planned for work package will fully leverage international collaborations, especially with Korea Atomic Research Institute (KAERI), Sweden Underground Research Lab and Czech Bedrichov Tunnel Test Facility.
- As a near-term goal, this work package will develop technical information that is important for waste isolation in crystalline media. This work will be coordinated with the Regional Geology control account.

The FY 14 work for the Crystalline Disposal R&D Work Package is structured into the following tasks:

- *Task 1 - Development of research plan:* The plan will summarize the status of crystalline repository study, identify the key research topic, and formulate the research strategy. This plan will serve a guideline for future work. This task will also support the revision of used fuel disposal R&D roadmap planned for FY14 for the disposal system analysis work package.
- *Task 2 - Development of used fuel degradation model:* This task will develop a preliminary model for used fuel degradation model in granitic environments. Due to the budget constraint, this activity will be jointed with the similar effort for the argillite work package. It is believed that a single model can be developed for both granite and argillite media.
- *Task 3 - Modeling of fluid flow and transport in fractured crystalline rocks:* The task will (1) demonstrate the potential application of a discrete fracture network model to actual field testing data obtained from international collaborations, (2) develop a hydro-chemical model for data interpretation for streaming potential testing to be conducted in KAERI Underground Research Tunnel (KURT), and (3) explore up-scaling techniques to link parameters and process at small-scales to those at scales relevant to performance assessment models.
- *Task 4 - Modeling of THMC behaviors in clay-based barrier materials:* The objective of this activity is to develop and apply thermal-hydrological-mechanical-chemical (THMC) modeling capabilities to assess engineering-barrier-system (EBS) responses to different temperatures and pressures, and to evaluate impacts of the interaction between EBS and host rocks. In FY14, the focus of this activity is on incorporation of impacts of chemical processes on mechanical deformation.
- *Task 5 - Experimental investigation of radionuclide interactions with natural and engineered materials:* The work will include (1) mechanistic understanding of Pu interactions with representative mineral substrates under granitic chemical conditions, (2) experiments of U and Np sorption on fracture-coating materials, and (3) experiments on uranium and iodide sorption/diffusion in compacted clay and other related materials. One objective of this work will aim to develop new buffer materials through design, for example, the materials that can withstand high thermal perturbations (e.g. caused by the emplacement of dual purpose canisters) without compromising their functionalities as engineered barriers.
- *Task 6 - International collaborations:* International collaborations are crucial for the activities proposed for this work package. These collaborations will include: Korean Atomic Energy Research Institute (KAERI) Underground Research

Tunnel (KURT) tests, Swedish Bentonite Rock Interaction Experiment (BRIE tests), Colloid Formation and Migration (CFM) tests, and Development of Coupled models and their Validation against Experiments (DECOVALEX) and Mont Terri tests.

This report summarizes work accomplished in FY14 for the Crystalline Disposal R&D Work Package. The report is outlined as follows:

- Chapter 2 provides a reference case for used fuel disposal in crystalline rocks. This reference case will be used to develop a total system performance assessment model for the evaluation of a crystalline disposal system. (Research topics addressed: S2 and S3; see Appendix A)
- Chapter 3 focuses the model development and the experimental measurements of coupled thermal-hydrologic-mechanical-chemical processes in an engineered barrier system of a crystalline repository. (P4, P10, P21 and P22)
- Chapter 4 summarizes the results of discrete fracture network (DFN) model demonstrations for fractured crystalline rocks. (P1)
- Chapters 5 and 6 summarize the study on radionuclide interaction and transport in granitic disposal environments. (P10)
- Chapter 7 evaluates the alternative descriptions of desorption of tri- and tetravalent solutes from bentonite colloids in tracer tests at the Grimsel test site. (P11)
- Chapter 8 evaluates the stability of Pu colloids in granitic disposal environments.
- Chapter 9 focuses on the development of a multiple potential model for used fuel degradation. (P10, P11)
- Appendix A provides an R&D plan for the evaluation of used fuel disposal in crystalline rocks. A set of research topics have been identified. (S3)

The reference case provided in chapter 2 and the R&D plan presented in the appendix will provide an overall framework for the integration and prioritization of all R&D activities related to the evaluation of used fuel disposal in crystalline media.

Because of the space limit of this document, some of the FY14 work is reported here. The work on international collaborations on KURT testing and DECOVALEX project has been reported in another level-2 UFDC milestone (M2FT-14LB081101 – International Collaboration Activities in Different Geologic Disposal Environments) and therefore is not reported here. The work on experimental investigation of thermal limits of buffer materials is not reported here. For this work, we are in the middle of data collection and synthesis, and a complete result will be reported in a future milestone.



## 2. REFERENCE CASE FOR GENERIC CRYSTALLINE DISPOSAL SYSTEM

### 2.1 INTRODUCTION

The Used Fuel Disposition Campaign (UFDC) of the U.S. Department of Energy (DOE) Office of Nuclear Energy (NE) is conducting research and development (R&D) on generic deep geologic disposal systems for high-activity nuclear wastes, including existing waste and waste that is expected to be generated under future fuel cycles. The term high-activity waste refers collectively to both used nuclear fuel (UNF) from nuclear reactors and high-level radioactive waste (HLW) from reprocessing of UNF, and from other sources.

Disposal system modeling activities within UFDC are developing the necessary capability to perform generic disposal system simulations for salt, crystalline rock, clay/shale, and deep borehole disposal options, with a focus on more realistic process-based modeling. A generic safety case provides preliminary evaluations of the safety of potential geologic disposal facilities, geologic media, and disposal technologies that might be evaluated in the future. Defining a reference case is a key step in developing a generic safety case. This section addresses the reference case for granite and other crystalline rocks (such as metamorphic rocks).

**Table 2-1.** Crystalline Repository Programs (Mariner et al., 2011)

<b>Country</b>	<b>Status of repository program</b>
Canada	Restarting the repository siting program; hosted multi-national research on granite in the 1980s and 1990s in the now closed Pinawa Underground Research Laboratory (URL).
Finland	Scheduled to open the nation's first HLW repository in granite in 2020 in the voluntary host municipality of Eurajoki. Opened the nearby Onkalo URL in granite in 2010.
Japan	Pursuing voluntary candidate repository sites with an expressed interest in granite. Operates URLs in clay and granite.
South Korea	Operates URL in granite
Sweden	Scheduled to open the nation's first repository for HLW in granite at Forsmark in the voluntary host community of Oesthammar in 2025. Operates a multi-national URL in granite at Äspö.
USA	Underground Research Lab (URL) in the Climax monzonite at Nevada Test Site (NST). Ended in 1987.

Several countries have studied high-level waste (HLW) disposal in crystalline rock. In particular, Sweden and Finland have performed detailed site investigation and safety assessment studies and have each submitted to the relevant regulatory authority an application for a license to construct a final repository (Table 2-1; Mariner et al., 2011). In addition, Canada, Japan and the US have operated underground research laboratories in granite. Mariner et al. (2011) summarize some of the technical issues associated with disposal of high-activity waste in crystalline rocks. Granite has its own unique attributes for deep geologic disposal of nuclear waste (Table 2-2). Because of its high mechanical strength and relatively high thermal conductivity, granite has certain advantages for emplacement and disposal of large size waste packages such as dual purpose canister (DPC). Large waste packages can be transported to the disposal drifts through an access ramp. On one hand, an EBS may be needed for a granite repository to improve waste isolation from fluid flow and transport in fractures. On the other hand, the high mechanical strength of the host rock may prevent a mechanical damage of waste packages as it occurs due to room closure in in a salt or a shale repository, thus allowing fully take credit for the engineered barrier system.

**Table 2-2.** Relative attributes of disposal media (modified from Hansen et al., 2011)

<b>Attributes</b>	<b>Salt</b>	<b>Shale</b>	<b>Granite (crystalline rock)</b>	<b>Deep boreholes</b>
<b>Thermal conductivity</b>	High	Low	Medium	Medium
<b>Permeability</b>	Low	Low	Low (unfractured) to permeable (fractured)	Low
<b>Mechanical strength</b>	Low	Low	High	High
<b>Deformation behavior</b>	Visco-plastic	Plastic to brittle	Brittle	Brittle
<b>Stability of cavity</b>	Low	Low	High	Medium at great
<b>Dissolution behavior</b>	High	Very low	Very low	Very low
<b>Chemical condition</b>	Reducing; high ionic strength; relatively simple chemical system	Reducing; complex chemical system	Reducing; relatively simple chemical system	Reducing; relative simple chemical system; moderate to high ionic strength

<b>Radionuclide retention</b>	Very low	High	Medium to high	Medium to high
<b>Thermal limit</b>	Relatively high	Relatively low (?)	No limit	No limit
<b>Available geology</b>	Wide	Wide	Wide	Wide
<b>Geologic stability</b>	High	High	High	High
<b>Engineered barrier system</b>	Minimal; waste package damage by room closure	Minimal; waste package damage by room closure	Needed. Able to fully take credit for the engineered barrier system	Borehole seal needed
<b>Human intrusion/resource exploration</b>	Relatively high	Relatively high	Low	Low
<b>Retrievability of waste</b>	Feasible	Feasible	Easily retrievable	Difficult

## 2.2 GENERIC DISPOSAL SYSTEM IN CRYSTALLINE ROCKS

A generic repository system in granite is illustrated in Figure 2-1. It consists of multiple barriers: waste forms, waste packages, engineered-barrier-system (EBS) buffer, seals/liners, disturbed rock zone (EDZ), host rock, and biosphere. The waste forms and waste packages are described with a source term that accounts for radionuclide inventory, waste form degradation, and waste package degradation. In the near and far-fields, which extend from the EBS buffer to the host rock, a complex of coupled physical and chemical processes control radionuclide release from the source term to a human accessible environment – biosphere. The reference described here is intended to provide generic specifications for a repository system in a crystalline rock, which can be used to construct a total system performance assessment (TSPA) model for the system. A TSPA model will provide a system perspective for prioritizing research and development (R&D) activities related to crystalline repository development. Given the generic nature, the generic specifications of the repository will evolve as the disposal concept matures.

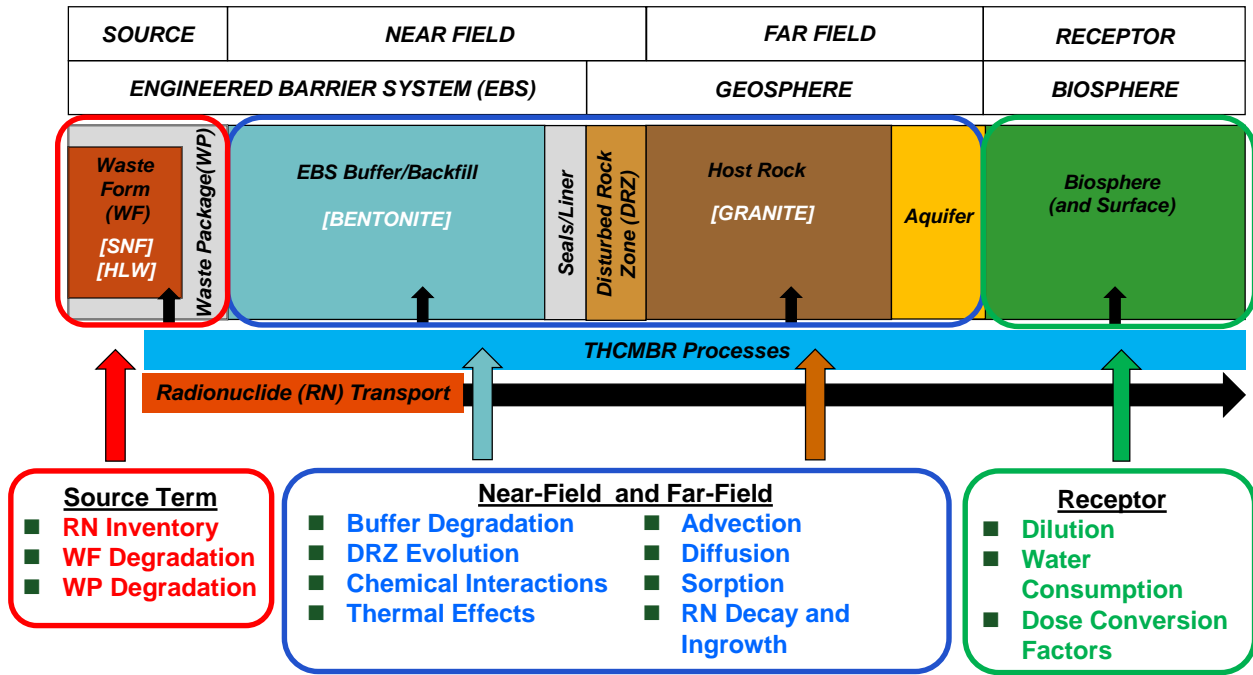


Figure 2-1. Multiple-barrier concept for a repository in crystalline rocks

**Assumptions:**

To be consistent with the reference cases for other disposal media (Freeze et al. 2013; Jove-Colon et al., 2014), the following assumptions are adopted:

- The repository will be excavated at a depth of about 600 meters within a massive igneous intrusion or a metamorphic rock.
- The horizontal repository layout consists of excavated emplacement drifts separated by the host rock, connected by a horizontal operation tunnel that can be accessed by both an access ramp and vertical shafts (Figure 2-2). The access ramp will facilitate the transportation of large waste packages to the underground.
- The repository will have a waste disposal capacity 70,000 metric tons of heavy metal (MTHM).
- Waste packages (canister/container plus disposal overpack) will be sealed permanently to avoid any risk of additional exposure during handling operations. For disposal, each waste package will be encapsulated by multilayered buffer materials (most likely bentonite clay materials).
- The repository will be able to accommodate waste packages of multiple sizes. Waste packages will be emplaced in vertical boreholes on the drift floor or directly in the drifts (especially for dual purpose canisters due to their large sizes).

Disposal drifts will then be backfilled with a mixture of clay material and crushed crystalline rocks. Multilayered backfilling is part of the EBS configuration.

- Drift spacing and waste package spacing are dictated by thermal loading, waste package size, the configuration of the EBS (e.g., backfilled vs. unbackfilled), and the thermal limit of buffer/backfill materials used for waste isolation (Hardin et al., 2013). The thermal limit of buffer/backfill materials is tentatively chosen to 200 °C. This limit is expected to be revised as more testing data are obtained from the UFDC testing programs. No thermal limit is assumed for the crystalline host rocks.
- The access ramp and shafts are used for construction, waste handling/emplacement operations, and ventilation. Drifts and access/operation shafts will be sealed at closure.
- The emplaced waste will be retrievable for a period of 50 years after waste emplacement operations are initiated.

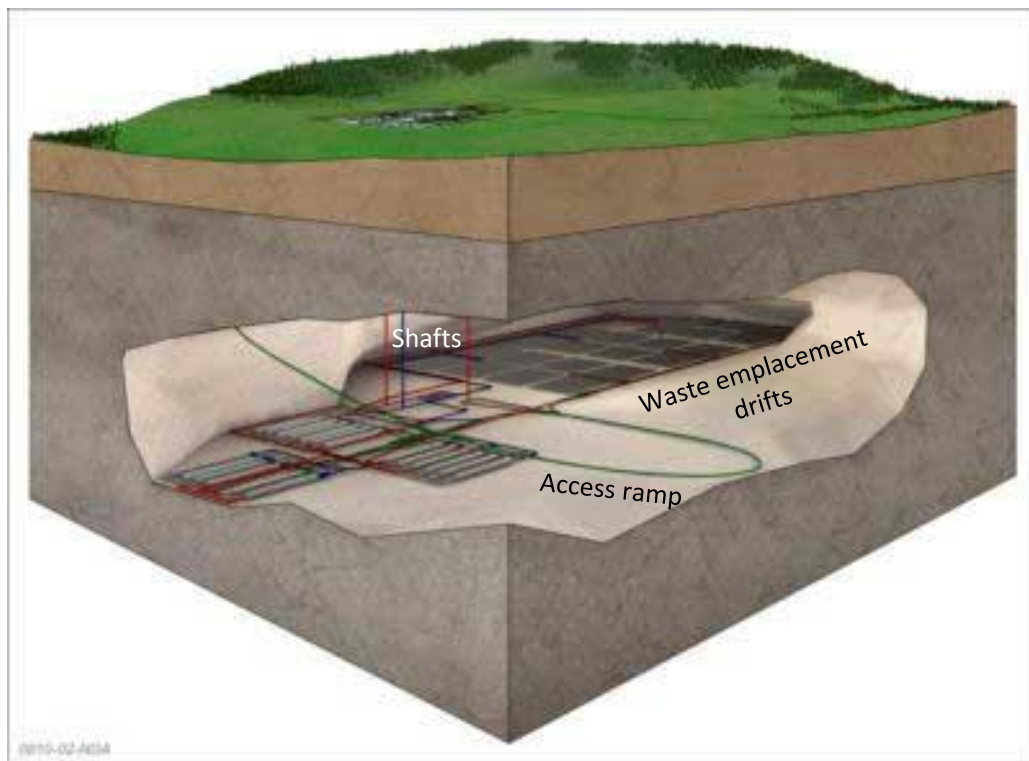


**Figure 2-2.** Physical configuration of a generic repository in granite (modified from <http://www.bbc.com/news/uk-england-cumbria-21253673>). Access ramp will be used for transport of large waste canisters such as dual purpose canisters.

## Emplacement Modes of Waste Packages

Definition of a reference case requires that an emplacement concept be specified. The KBS-3 concept (SKB, 2011) developed in Sweden is arguably the disposal system concept at the most advanced stage of development for any medium. As developed, the KBS-3 concept is tailored for relatively small waste inventories (12,000 metric tons of heavy metal for the proposed Forsmark repository in Sweden and smaller inventories in Finland). Other emplacement concepts may be suitable for crystalline rock, including axial emplacements in tunnels, emplacement in massive cavities with or without a hydraulic cage to divert water, and mined repositories with borehole arrays. However, those alternative concepts have not been explored in any detail for crystalline rock.

The KBS-3 concept and axial emplacement in tunnels are chosen for further consideration. The KBS-3 concept is chosen for a reference case because it has been studied extensively. Emplacement in tunnels (drift emplacement) is chosen to maintain consistency with salt (Freeze et al., 2013) and argillite/shale (Jove-Colon et al., 2014) reference cases. Drift emplacement is particularly useful to accommodate large waste packages such as dual purpose canisters (DPCs).

*Emplacement in tunnel boreholes:* In the KBS-3 concept (Figure 2-3), boreholes are drilled in the bottom (KBS-3V concept) or side (KBS-3H concept) of repository tunnels. Waste containers are copper shells with cast iron inserts for structural integrity. Bentonite buffer material is to be placed between the canisters and the borehole wall. The relatively small diameter (~1 m) canisters contain 4 PWR assemblies in the existing KBS-3 concept.

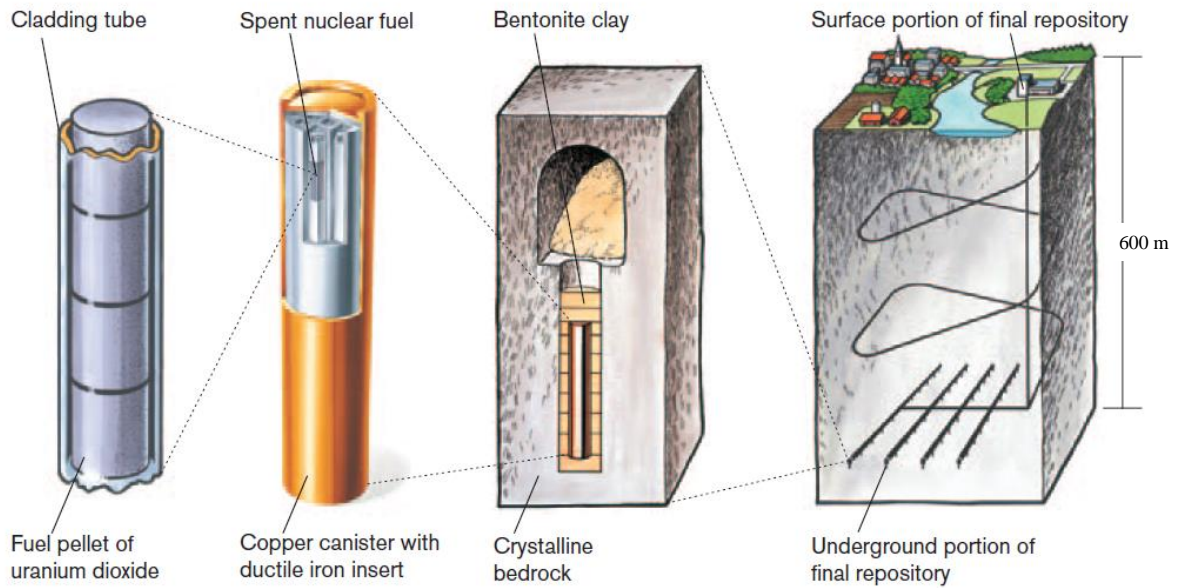


**Figure 2-3.** Emplacement in tunnel boreholes (KBS-3 concept) (modified SKB, 2011)

*Drift emplacement:* An alternative to the KBS-3 concept, which would accommodate a larger number of PWR or BWR assemblies per canister, is direct emplacement in tunnels (Figures 2-4 to 2-6). Variants of this reference case include two types of waste package: a dual-purpose canister (DPC) that contains 32 PWR (Pressurized Water Reactor) fuel assemblies (Hardin et al., 2013) and canister that contains the inventory of 12 PWR assemblies (Freeze et al., 2013).

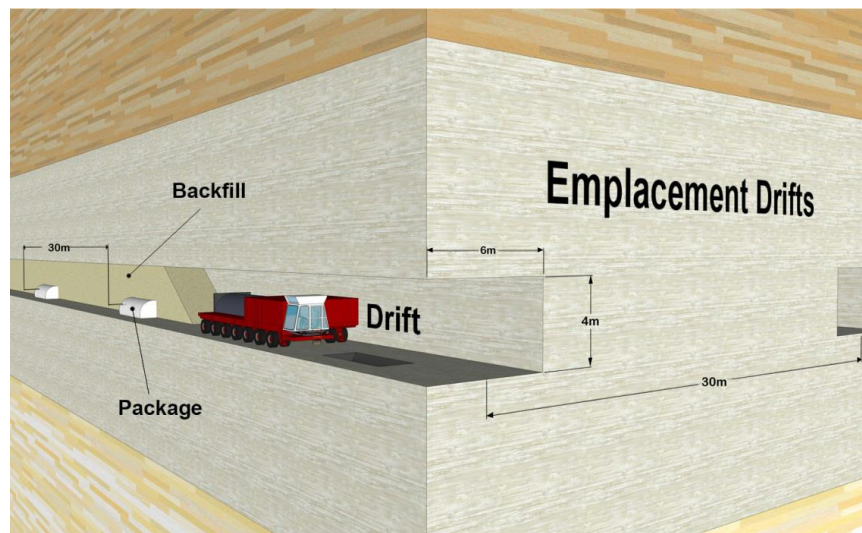


**Figure 2-4.** Emplacement in drifts with backfill

## Repository Layout

The repository layout must consider various operational, mechanical, and thermal design constraints. Liu et al. (2013) summarized the thermal constraints on EBS bentonite imposed in disposal concepts throughout the world for disposal in argillite and crystalline host-rock media. A 100°C thermal limit is imposed unanimously in all these disposal concepts despite their differences in EBS design concepts. However, the basis for a 100°C thermal limit is not backed up by rigorous scientific studies (Liu et al., 2013; Jove Colon et al. 2012). Reviews of the performance of bentonite backfill at temperatures above 100°C (e.g., Wersin et al., 2007; Pusch et al., 2010), modeling (Liu et al., 2013; Zheng et al., 2014a), and experimental studies (e.g. Pusch et al., 2003; Caporuscio et al., 2012; Cheshire et al., 2013; Cheshire et al., 2014; Wang et al., 2013) describing the mechanical and chemical changes showed little or moderate deterioration of bentonite. While further analyses of the THMC alteration of EBS bentonite at high temperatures are warranted, these modeling and experimental studies in the UFDC suggest that an crystalline repository EBS with bentonite could sustain temperatures exceeding 100°C. As mentioned above, for this reference case, the thermal limit of bentonite material is tentatively chosen to be 200 °C.

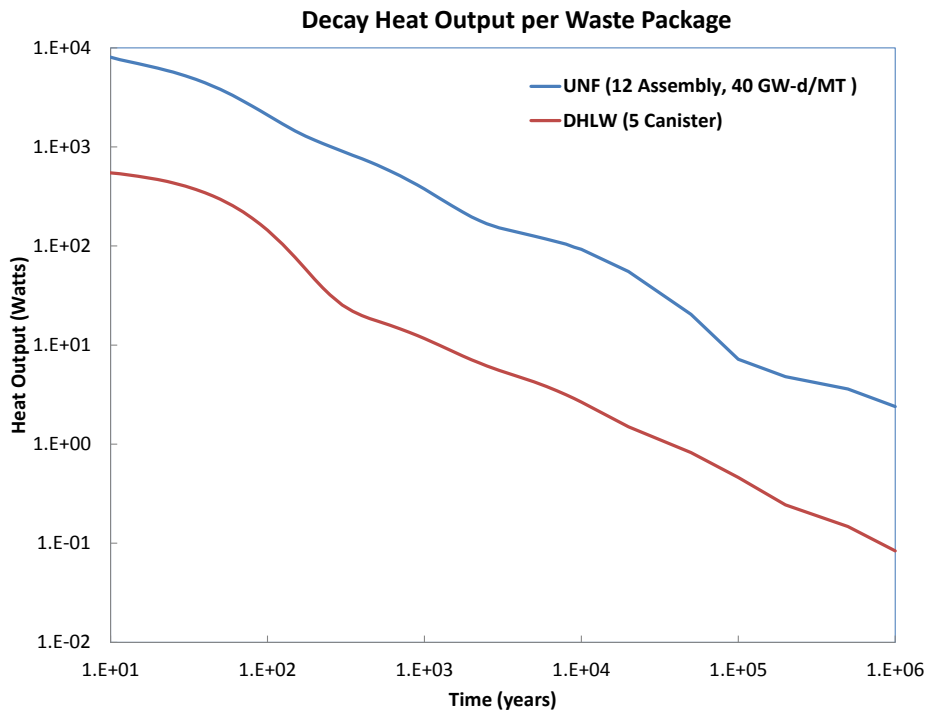


**Figure 2-5.** Heat output of used nuclear fuel (UNF) and defense high level waste (DHLW) calculated from with code ORIGEN

**Table 2-3.** Thermal conductivities of granite, clay and salt materials (Hardin et al., 2011)

Country	Material	Thermal conductivity (W/m-K)
Belgium	Clay	1.7 (parallel to bedding), 1.25 (perpendicular to bedding)
France	Clay	1.9 – 2.7 (parallel), 1.3 – 1.9 (perpendicular)
Switzerland	Clay	1.8
Sweden	Granite	3.4 – 4, 2.45 – 2.9
France	Granite	2.4 – 3.8
Finland	Granite	2.3 – 3.2
USA	Salt	3.09 at 100 °C, 3.37 at 29 °C, 4.7 at 110 °C

Typical heat outputs of used nuclear fuel (UNF) and defense high level are shown in Figure 2-5. Thermal conductivities of granite and clay materials are given in Table 2-3. For a given heat output and the size of waste packages, the detailed layout of the repository regarding drift spacing and waste package spacing can be calculated for a chosen thermal limit of buffer material. It is important to note that a generic crystalline repository will be intended to accommodate waste packages of multiple sizes. Different types of waste packages will be emplaced in different parts of the repository, with different waste package spacing and drift spacing layout. As a first-order approximation without carrying out a detail thermal dissipation calculation, the repository layouts summarized below are directly adopted from the argillite and salt reference cases (Jove-Colon et al., 2014; Freeze et al., 2013), partly based on the consideration that bentonite-based materials will be used as buffer/backfill materials in a crystalline repository, which to a large extent determine the thermal evolution around a waste package. Note that the thermal conductivity of granite is close to that of salt (Table 2-3) and also the chosen thermal limit for clay buffer material for the crystalline reference case is the same as that for salt (200 °C). It is expected that the waste package spacing and the drift spacing for a crystalline repository will be in between those for salt and argillite repositories. As an example, the repository layout for 12- and 32-PWR waste packages are discussed below.

*Layout for 12-PWR Waste Package:* The repository layout dimensions 12-PWR waste packages are given in Table 2-4. Estimated values for the repository dimensions were approximated by the UNF loading, and waste package and drift spacings consistent with the reference case for disposal in salt. Layout dimensions include a drift diameter of 4.5 m with waste package (end-to-end) and drift spacings of 5 m and 20 m, respectively. UNF storage and ventilation times of 50 years are assumed for the reference case.

*Layout for 32-PWR DPCs:* The drift layout for disposal of DPCs is given in Table 2-5 (Hardin et al., 2013). A drift of 5 m high by 7 m wide or a circular cross-section with a

diameter of 5.5 m was proposed in the report. Greenberg et al. (2013) did a series of thermal analyses for 32-PWR waste packages with a burnup of 40 GWd/MT and with different drift and waste package spacings and ventilation times. In the shale reference case, we assume a drift spacing of 70 m, waste package spacing of 20 m, and a ventilation time of 50 years.

### **Performance Objectives of Repository System**

The performance objectives of a repository system are provided in the UFDC R&D roadmap (DOE, 2011), including:

- **Containment:** Provide a high probability of substantially complete containment of short lived radionuclides for some hundreds or thousands of years, perhaps largely within the engineered barriers of the repository.
- **Limited Releases:** Delaying and limiting the rate and the consequent concentrations in which radionuclides will be released from the immediate environment in which the waste was emplaced into the surrounding geological environment and eventually transported to the biosphere. This is achieved by a combination of physical and chemical mechanisms which, among other functions, may limit the access and flux of ground water to the wastes and from the repository to the biosphere, and may limit the solubility of radionuclides, or sorb or precipitate them reversibly or permanently onto surfaces in the host geology and the EBS. In addition, the process of radioactive decay progressively reduces the amounts of radionuclides present in the disposal system (although the amounts of some important radionuclides will increase through in-growth).
- **Dispersion and Dilution:** The flux of long lived radionuclides through the geological barriers involves three-dimensional dispersion, and may take place in widely different groundwater environments. In some concepts and at some specific proposed repository sites, releases would encounter major aquifers at depth or closer to the surface, or similar large bodies of surface water. This would result in an additional, but secondary, function to limiting releases (i.e., an overall dilution of released radionuclides such that concentrations on initial return to the biosphere are lowered).
- **Defense in depth** ensured by performance of a geological disposal system dependent on multiple barriers having different safety functions.
- For the evaluation of the crystalline reference case, two performance indicators can be used. One is the mass fluxes of radionuclides across individual barriers, and another is the annual dose that a receptor could receive at a certain regulatory location. For this reference case, the receptor will be located 1.5 km away from the edge of the waste drifts (see Section of Natural System). The performance assessment (PA) calculations will be carried out for the regulatory time period of 1,000,000 years.

**Table 2-4. Repository layout for 12-PWR Waste Package**

<b>Parameters</b>	<b>Value</b>	<b>Source</b>
<b>Waste Package (WP)</b>		
WP length (m)	5	Freeze et al. (2013, table 3-3)
WP outer diameter (m)	1.29	Freeze et al. (2013, table 3-3)
Overpack thickness (alloy steel) (cm)	5	Hardin et al. (2012)
WP end-to-end spacing (in-drift) (m)	5	Jove-Colon et al. (2014)
Approx. number of WPs for 70,000 MTHM	13,398	Freeze et al. (2013, table 3-3)
<b>Emplacement Drift</b>		
Drift diameter (m)	4.5	Jove Colon et al. (2013)
Drift center-to-center spacing (m)	20	Jove-Colon et al. (2013)
Number of WPs per drift	80	Freeze et al. (2013, table 3-3)
Drift seal length (m)	10	Freeze et al. (2013, table 3-3); Bianchi et al. (2013, table 1)
Drift length, including seals (m)	805	Freeze et al. (2013, table 3-3)
Shaft access diameter (m)	5.4	Bianchi et al. 2013 Table 1
Access tunnel/ramp height (m)	5	
Access tunnel/ramp width (m)	8	
Length of access ramp (km)	2.3	Assume a 15° slope
<b>Repository</b>		
Approx. repository footprint (km <sup>2</sup> )	~ 4	Freeze et al. (2013); Jove-Colon et al. (2014)
Repository depth (m)	600	

**Table 2-5. Repository layout for 32-PWR Waste Package**

<b>Parameters</b>	<b>Value</b>	<b>Sources</b>
<b>Waste Package (WP)</b>		
WP length (m)	5	Freeze et al. (2013, table 3-3)
WP outer diameter (m) (including overpack)	1.79	Greene et al. (2013)
Overpack thickness (alloy steel) (cm)	5	Hardin et al. (2012)
WP end-to-end spacing (in-drift) (m)	10	Jove-Colon et al. (2014)
Approx. number of WPs for 70,000 MTHM	5,029	Freeze et al. (2013, table 3-3)
<b>Emplacement Drift</b>		

Drift diameter (m)	5.5	Hardin et al. (2013)
Drift center-to-center spacing (m)	70	Jove-Colon et al. (2014)
Number of WPs per drift	80	Freeze et al. 2013, Table 3-3
Drift seal length (m)	10	Freeze et al. 2013, Table 3-3; Bianchi et al. 2013 Table 1
Drift length, including seals (m)	1595	Jove-Colon et al. (2014)
Shaft access diameter (m)	5.4	Bianchi et al. 2013 Table 1
Access tunnel/ramp height (m)	5	
Access tunnel/ramp width (m)	8	
Length of access ramp (km)	2.3	Assume a 15° slope
<b>Repository</b>		
Approx. repository footprint (km <sup>2</sup> )	~ 4	Freeze et al. (2013); Jove-Colon et al. (2014)
Repository Depth (m)	600	

### 2.3 WASTE INVENTORY

The waste inventory assumed for the crystalline rock reference case is the same as that for the salt disposal system (Freeze et al., 2013) or the shale disposal system (Jove-Colon et al., 2014). Repository capacity is assumed to be 70,000 metric tons heavy metal (MTHM). For simplicity, the entire inventory is assumed to consist of pressurized water reactor (PWR) used nuclear fuel (UNF) assemblies. Each PWR UNF assembly contains 0.435 MTHM (91,000 MTHM/209,000 assemblies), with an assumed bounding fuel burn-up of 60 GWd/MTHM. The isotopic composition of 60 GWd/MTHM PWR inventory assumes an initial enrichment of 4.73% and 30-year out-of-reactor (OoR) decay storage, as reported in Carter et al. (2012, Table C-1). This reference case inventory can be augmented with boiling water reactor (BWR) and high-level waste (HLW) inventories as the performance assessment (PA) model matures.

**Table 2-6.** UNF Radionuclide Inventory for the Reference Case (Freeze et al., 2013)

Isotope	Waste inventory mass <sup>1</sup> (g/MTHM)	Molecular weight <sup>2</sup> (g/mol)	Mass fraction <sup>2</sup> (g / g UNF)	Mole fraction (mol / g UNF)
<sup>238</sup> U	9.10 x 10 <sup>5</sup>	238.05	6.32 x 10 <sup>-1</sup>	2.66 x 10 <sup>-3</sup>
<sup>237</sup> Np	1.24 x 10 <sup>3</sup>	237.05	8.61 x 10 <sup>-4</sup>	3.63 x 10 <sup>-6</sup>
<sup>241</sup> Am	1.25 x 10 <sup>3</sup>	241.06	8.68 x 10 <sup>-4</sup>	3.60 x 10 <sup>-6</sup>
<sup>242</sup> Pu	8.17 x 10 <sup>2</sup>	242.06	5.68 x 10 <sup>-4</sup>	2.34 x 10 <sup>-6</sup>
<sup>129</sup> I	3.13 x 10 <sup>2</sup>	129.00	2.17 x 10 <sup>-4</sup>	1.69 x 10 <sup>-6</sup>
<sup>234</sup> U	3.06 x 10 <sup>2</sup>	234.04	2.13 x 10 <sup>-4</sup>	9.08 x 10 <sup>-7</sup>
<sup>230</sup> Th	2.28 x 10 <sup>-2</sup>	230.03	1.58 x 10 <sup>-8</sup>	6.89 x 10 <sup>-11</sup>
<sup>233</sup> U	1.40 x 10 <sup>-2</sup>	233.04	9.73 x 10 <sup>-9</sup>	4.17 x 10 <sup>-11</sup>
<sup>229</sup> Th	6.37 x 10 <sup>-6</sup>	229.03	4.43 x 10 <sup>-12</sup>	1.93 x 10 <sup>-14</sup>
<sup>226</sup> Ra	3.18 x 10 <sup>-6</sup>	226.03	2.21 x 10 <sup>-12</sup>	9.77 x 10 <sup>-15</sup>

<sup>1</sup>From Carter et al. (2012, table C-1)

<sup>2</sup>From Sevougian et al. (2013, table 1)

The reference case PWR UNF inventory includes approximately 450 isotopes with a total mass of  $1.44 \times 10^6$  g/MTHM and a decay heat of 1.438 kW/MT (Carter et al. 2012, table C-1). The total mass of the PWR inventory includes actinides (dominated by <sup>238</sup>U), oxygen from the UO<sub>2</sub>, zirconium from cladding, and other fission and activation products. The mass inventory of these selected radionuclides in a reference case PWR UNF assembly (60 GWd/MTHM burn-up, 30-year OoR, 4.73% initial enrichment) is shown in Table 2-6. Smaller subset of radionuclides that are considered in the salt reference case (Freeze et al. 2013) are also assumed for the crystalline rock reference case, including neptunium series alpha-decay chain, uranium series alpha-decay chain, and <sup>129</sup>I, a non-sorbing radionuclide with a long half-life:

•

- Neptunium series alpha-decay chain (<sup>241</sup>Am → <sup>237</sup>Np → <sup>233</sup>Pa → <sup>233</sup>U → <sup>229</sup>Th)
- Uranium series alpha-decay chain (<sup>242</sup>Pu → <sup>238</sup>U → <sup>234</sup>U → <sup>230</sup>Th → <sup>226</sup>Ra → <sup>222</sup>Rn)
- <sup>129</sup>I - a non-sorbing radionuclide with a long half-life

Details of their half-life and decay constants are given in Freeze et al. (2013).

## 2.4 ENGINEERED BARRIER SYSTEM

The engineered barrier system (EBS) will include the following components: waste form, waste package, buffer materials, backfill materials, and seals (Jove-Colon et al., 2014).

### 2.4.1 Waste Forms

Waste forms considered in this reference case include PWR UNF waste and defense high-level waste (DHLW). Each irradiated PWR assembly is assumed to contain 0.435 MTHM and  $1.44 \times 10^6$  g/MTHM of isotopes, with mass fractions of the selected radionuclides as listed in Table 1. This corresponds to a total mass of  $6.27 \times 10^5$  g of isotopes per PWR assembly. The PWR waste forms are assumed to be predominantly  $UO_2$  with zircaloy cladding.  $UO_2$  has a solid density of  $10.97 \text{ g/cm}^3$  (Lide 1999, p. 4-94). Therefore, the solid volume of a PWR assembly can be approximated by  $(6.27 \times 10^5 \text{ g/assembly}) / (10.97 \times 10^6 \text{ g/m}^3) = 0.057 \text{ m}^3$ . Typical dimensions for unirradiated PWR assemblies are lengths of 111.8 to 178.3 in (2.84 – 4.53 m) and widths of 7.62 – 8.54 in (0.19 – 0.22 m) (Carter et al., 2012, table A-1). Based on these dimensions, the total volume of a PWR assembly can range from about 0.10 – 0.22  $\text{m}^3$ . The uranium loading (0.435 MTHM per assembly) is consistent with loadings, burn-ups, and enrichments of PWR assemblies listed in Carter et al. (2012, table A-3).

The release of radionuclides from UNF includes a fast/instant release fraction (IRF) and a slow release fraction. The IRF is predominantly released from radionuclides and fission gases located in the fuel and cladding gap, rod plenum regions (fission gases like Kr and Xe), and grain boundaries. The slow release fraction is released the dissolution of  $UO_2$  matrix. Sassani et al. (2012) describe the current state of knowledge of IRF processes in irradiated used fuels, structural considerations (e.g., accessible and inaccessible grain boundaries; Figure 2-6), and IRF models, and distributions for the IRF of radionuclides. The IRF distributions are based largely on empirical correlations depending on the state of the fuel and cladding, burnup rates, and irradiation history. For PA sampling, Sassani et al. (2012) advance the IRF implementation in two sets of distributions: (a) triangular distributions representing minimum, maximum, and mean (apex) values for LWR used fuel with burnup at or below 50 GWd/MT, and (b) a process model has yet to be developed with functional parametrics. Table 3.2 1 of Sassani et al. (2012) provides model and values of IRF (% of radioelement inventory) for spent fuel pellets of various burnups, for a variety of environment conditions, and from various regions of the fuel pellet samples.

For commercial UNF, the waste form is the UNF matrix, which is predominantly uranium dioxide ( $UO_2$ ). For the DHLW, the waste form is borosilicate glass. For both waste form types, the waste form degradation in the source-term model is represented with an annual fractional degradation rate (i.e., fraction of remaining waste mass degraded per year), with a distribution that captures potential range of degradation rates that could be expected in a generic crystalline repository environment. For the

commercial UNF waste form, uncertainty in the degradation rate is modeled with a log-triangular distribution with the mode of  $10^{-7} \text{ yr}^{-1}$  and lower and upper bounds of  $10^{-8} \text{ yr}^{-1}$  and  $10^{-6} \text{ yr}^{-1}$  respectively. The rate range is from the SKB spent nuclear fuel degradation model for its repository situated in a chemically reducing environment (SKB, 2006). For the borosilicate glass waste form, degradation is much less sensitive to the redox condition of water contacting the waste form. A fractional degradation rate model was developed using the literature data for degradation of similar glasses exposed in geologic environments. The rate model is expressed as log-uniform distribution with the minimum and maximum values of  $3.4 \times 10^{-6} \text{ yr}^{-1}$  and  $3.4 \times 10^{-3} \text{ yr}^{-1}$  respectively (Clayton et al., 2011).

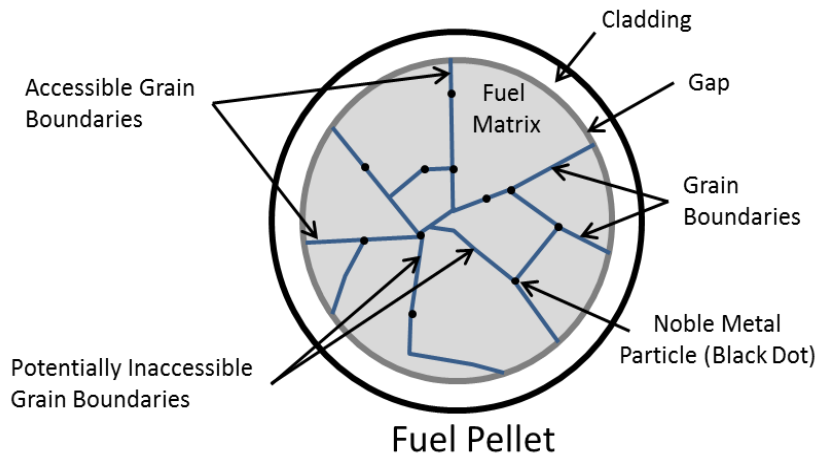


**Figure 2-6.** Schematic of a fuel pellet cross section showing the relative locations of radionuclide inventories for the gap, grain boundaries, fuel matrix, and noble metal particles. Also shown are the general locations of accessible grain boundaries and inaccessible grain boundaries (after Sassani et al. 2012).

## 2.4.2 Waste Packages

The reference case considers the design for two types of waste packages: the dual-purpose canister (DPC) that contains a used fuel waste inventory of 32-PWR UNF assemblies (Pressurized Water Reactor) and 12-PWR UNF assemblies. Waste package is composed of the stainless steel canister/container plus enclosing disposal overpack. Various types of disposal overpacks have been proposed in U.S. and international repository programs. Materials for disposal overpack can range from stainless steel, copper, and carbon steel depending on the barrier operational design (e.g., corrosion allowance) within the EBS concept. No decision on the disposal overpack material has been advanced so far but likely candidates are carbon- and stainless-steel. It is expected that implementation of the crystalline reference case with the generic disposal system analysis will consider waste package failure and thus provide the basis to make decisions on the disposal overpack material.

### *12-PWR Waste Package*

Similar to the reference case for disposal in salt (Freeze et al. 2013), the reference case for disposal in crystalline considers a waste package consisting of a canister containing a 12 PWR UNF assemblies with a disposal overpack. The 12-PWR waste package has a length of 5.0 m and a diameter of 1.29 m (Hardin et al., 2012, table 1.4-1). These outer dimensions include a 5.0 cm thick disposal overpack. Waste package dimensions are summarized in Table 2-7. This overpack thickness is considered sufficient to withstand general corrosion and ensure a retrievability period (if considered) of 50 years (Sevougian et al. 2013). More details of 12-PWR waste package are given in Freeze et al. (2013).

### *32-PWR Dual Purpose Canister (DPC) Waste package*

Hardin et al. (2013) discussed the characteristics of DPC while presenting the concept of direct disposal of DPC. The design capacity of a DPC can accommodate 32-PWR assemblies or 68-BWR assemblies (Figure 2-7). The average burnup for existing spent nuclear fuel (SNF) in dry storage is nominally 40 GWd/MT. We therefore assume a burnup of 40 GWd/MT for 32-PWR DPCs. Also, many of the cases developed by Greenberg et al. (2013) for scoping thermal calculations for DPCs use a 40 GWd/MT burnup. The nominal dimensions of DPCs have a length of 5 m and a diameter of 1.74 m based on the HI-STAR 100 Multi-Purpose Canister (MPC-32) (Greene et al. 2013). The exterior dimensions of the MPC-32 should include an additional 5.0 cm thick overpack for a total outer diameter of about 1.79 m. It should be noted that the HI-STAR 100 design includes a storage overpack with a wall thickness of 34.5 cm (Greene et al. 2013). Figure 5 shows a cross-section view of the MPC-32 for the HI-STAR 100 system. According to Hardin et al. (2013), DPCs having a 5 cm steel overpack would add about 30 MT in addition to approximately 50 MT of a fully loaded DPC.

**Table 2-7.** Canister dimensions for the waste package types

Canister type	Dimensions, m	Remarks
12-PWR	1.29 m (diameter) 5.0 m (length)	Source: (Hardin et al., 2012, Table 1.4-1)
32-PWR	1.79 m (diameter) 5.0 m (length)	Source: Greene et al. 2013

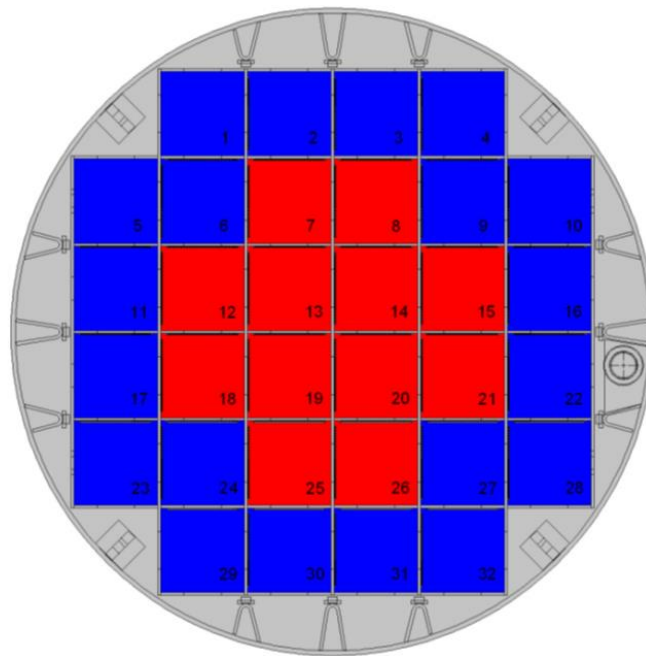


**Figure 2-7.** Cross-section view of dual-purpose canister MPC-32 for the HI-STAR 100 system (after Greene et al. 2013). Red and blue represent younger (higher dose) and older (lower dose) fuel assemblies, respectively.

Waste package failure rate is an important parameter that needs to be specified for a performance assessment calculation. Waste package failure can result from initial manufacturing defects or can be induced by various corrosion processes. Waste packages in the KBS-3 concept (Figure 2-8) are described in detail in SKB reports (e.g. SKB, 2011). The waste packages consist of a 5-cm copper shell with nodular cast iron inserts for structural integrity. Each canister contains approximately 7,400 kg of copper and 13,600 kg of cast iron (SKB, 2011). It is evaluated that the copper shell will be able to prevent waste failure for the first 60,000 years. For the reference case described here, a

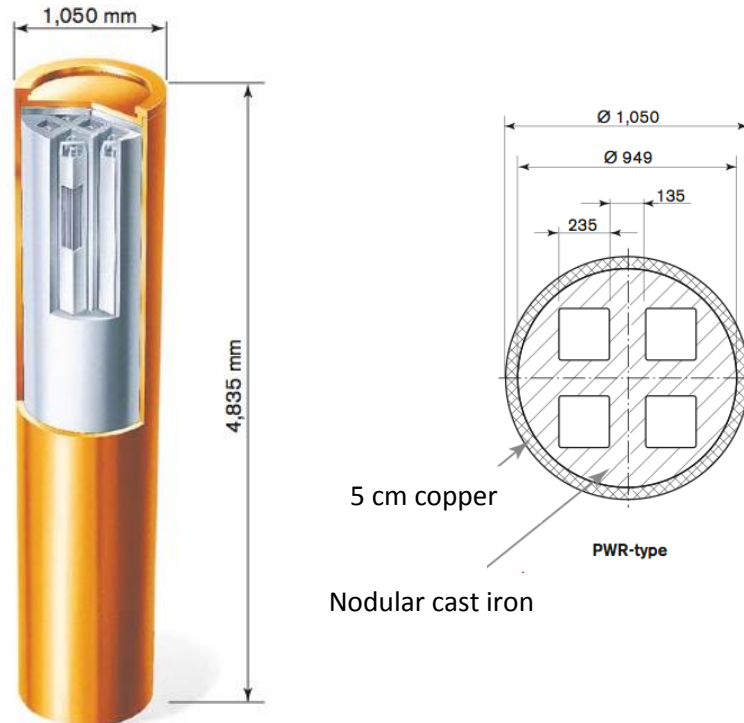


**Figure 2-8.** Waste package in the KBS-3 emplacement concept, assuming 4 PWR assemblies. Modified from SKB (2011).

waste package failure model yet needs to be developed.

### 2.4.3 Bentonite Buffer/Backfill

As described earlier, two different waste-package designs may be considered: (1) a DPC that contains a larger waste inventory of 32-PWR fuel assemblies, and (2) a 12-PWR canister. An engineered clay buffer backfill can be emplaced in a multi-layered configuration to optimize thermal, flow, and sorption properties of the buffer/backfill media. Figure 2-9 shows a double layer backfill configuration having two clay buffer materials for the 12-PWR canister. The choice of a double layer permits the use of two different clay buffer materials that can be tailored to optimize the barrier physical and chemical properties, while maintaining a low level of complexity in the overall EBS

design. While the double layer backfill configuration can certainly be applied to the disposal of DPCs, a single layer backfill configuration (as shown in Figure 2-10) could also be another option. It may be operationally challenging to install a two-layer backfill to accommodate the relatively large dimensions and substantial weight of a DPC. On the other hand, the high thermal load of a DPC would impose the partial sacrifice of the inner buffer layer closest to the waste package surface. The extent of such a “sacrificial layer” can be engineered with a tailored inner clay backfill layer as part of a double-layer system.

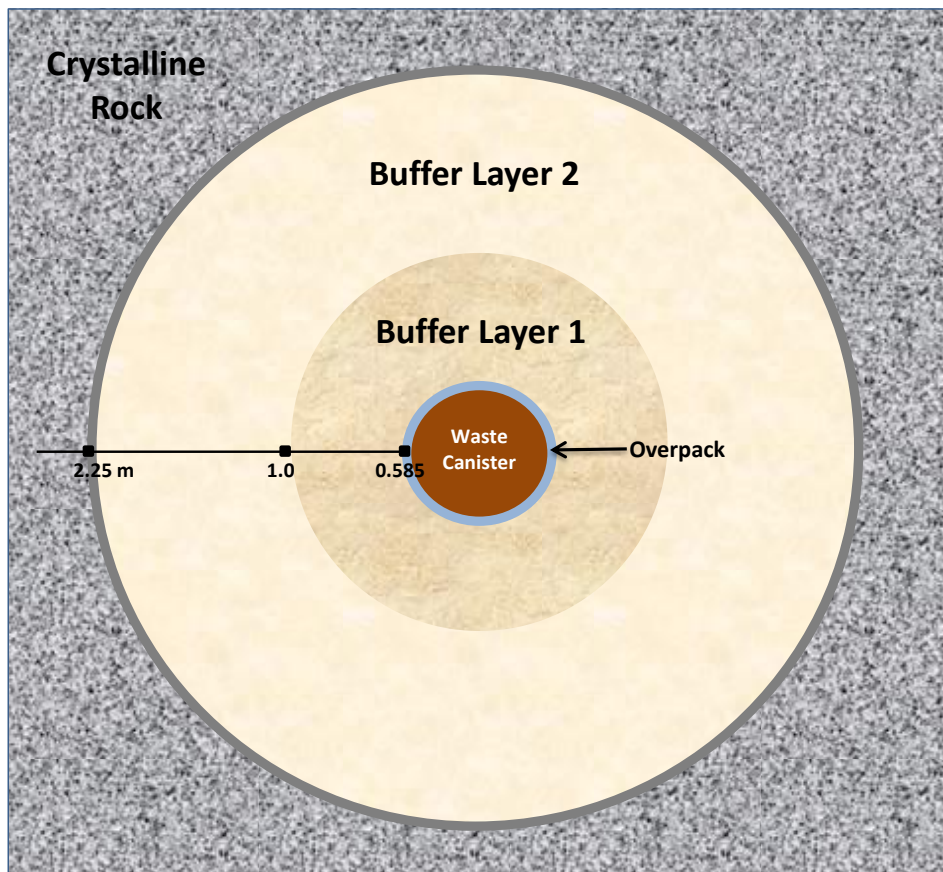


**Figure 2-9.** Schematic view of 2-D diagram of a double layer two-clay buffer layer EBS. Point values are radial distances in meters from the center of the waste canister (modified from Jove-Colon et al. 2013).

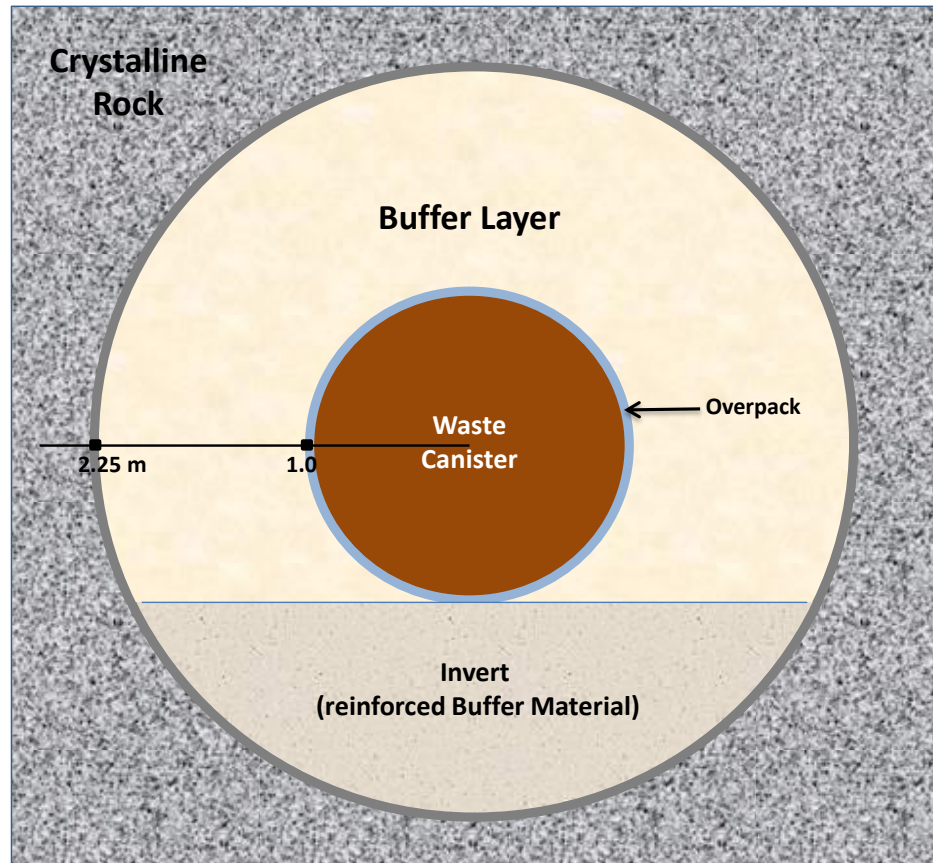


**Figure 2-10.** Geometry of a cross section of a drift for the disposal of DPC

The basic material in the backfill is typically bentonite which is an impure clay consisting mostly of smectite (montmorillonite), along with small amounts of other minerals such as quartz and feldspar. In some disposal concepts (ENRESA, 2000; SKB, 2006), the backfill contains bentonite exclusively, but mixtures of bentonite with graphite or silica phases (e.g., quartz) have also been considered in some disposal concepts to enhance thermal conductivity (e.g., JNC, 2000). Here we focus on the properties of two widely studied bentonites: FEBEX (ENRESA 2000) and MX-80 (SKB, 2006) bentonites. The properties of bentonite mixtures with other materials are not discussed here.

Table 2-8 lists typical thermal, hydrological and mechanical parameters for the two bentonites that have been studied as the backfill material for nuclear waste disposal. Thermal, hydrological and mechanical properties for bentonite vary a great deal with degree of compaction (dry density). Those properties listed in Table 2-8 are for the dry density range that is widely used in tests of different scales and are considered candidates for use in a future repository. For example, a dry density of around  $1650 \text{ kg/m}^3$  for FEBEX bentonite bricks has been used in the Mockup and In Situ test (ENRESA, 2000) and it is also the design used in the Spanish reference concept for high level nuclear

waste disposal (ENRESA, 2000). Properties for FEBEX and MX-80 bentonite in Table 2-8 are largely from ENRESA (2000) and SKB (2006).

Saturated permeability for FEBEX bentonite is typically around  $2-3 \times 10^{-21} \text{ m}^2$ , but a summary from various sources (ENRESA, 2000; Börgesson and Hernelind, 2005; Zheng et al., 2011) leads to a larger range of permeabilities. The relative permeability curve for FEBEX bentonite is typically given as:

$$K_{rl} = S^n \quad (2-1)$$

where  $K_{rl}$  is the relative permeability,  $S$  is the water saturation, and  $n$  is a constant. The exponent  $n$  ranges from 3 to 4.5 (ENRESA, 2000), but most models (Zheng et al. 2011; Sánchez et al. 2012) have used 3. The relative permeability curve for MX-80 bentonite is the same as in equation (1), with  $n$  ranging from 2 to 4 (Hökmark, 2004). Typically the van Genuchten (van Genuchten, 1980) function is used for water retention curve, which expresses the capillary pressure,  $s$ , as a function of water saturation,  $S$ :

$$S_w = S_r + (S_m - S_r) \left[ 1 + \left( \frac{s}{P_0} \right)^{\frac{1}{1-\lambda}} \right]^{-\lambda} \quad (2-2)$$

where  $S_r$  and  $S_m$  are the residual and maximum degree of water saturation,  $P_0$  is the material property that represents capillary strength, and  $\lambda$  is  $m$  in van Genuchten's notation, which represents the effects of the pore-size distribution. ENRESA (2000) lists a quite large range of  $\lambda$  and  $P_0$ , but in some modeling works (Zheng et al., 2011; Sánchez et al., 2012),  $\lambda$  is 0.18 and  $P_0$  is  $2 \times 10^7$  Pa; Villar et al. (2008) used the same value of  $\lambda$  but a slightly different value for  $P_0$  ( $2.8 \times 10^7$  Pa). The parameters  $\lambda$  and  $P_0$  for MX-80 bentonite are from Hökmark (2004). The specific heat capacity for MX-80 bentonite is from Man and Martino (2009).

**Table 2-8.** Thermal, hydrological and mechanical parameters for two bentonites

Parameter	FEBEX bentonite	MX-80 bentonite
Grain density [ $\text{kg}/\text{m}^3$ ]	2700	2700
Dry density [ $\text{kg}/\text{m}^3$ ]	1650-1700	1650-1700
Porosity $\phi$	0.41	0.41
Thermal conductivity [W/m °C] dry/wet	0.57/1.28	0.3/1.3
Saturated permeability [ $\text{m}^2$ ]	$1.75 \times 10^{-21} - 8 \times 10^{-21}$	$2.0 \times 10^{-21}$
Relative permeability, $k_{rl}$	$K_{rl} = S^3$	$K_{rl} = S^3$
van Genuchten $P_0$ (Pa)	$2 \times 10^7$ to $1 \times 10^8$	$0.9 \times 10^7$ to $2 \times 10^7$
van Genuchten $m$ (or $\lambda$ )	0.18-0.475	0.4-0.45
Compressibility, $\beta$ [1/Pa]	$3.2 \times 10^{-9}$	$3.2 \times 10^{-9}$

Thermal expansion coeff., [ $1/^\circ\text{C}$ ]	$1.0 \times 10^{-5}$	$1.0 \times 10^{-5}$
Dry specific heat, [ $\text{J/kg } ^\circ\text{C}$ ]	767-939	800
Tortuosity for vapor phase	$\phi^{1/3} S_g^{10/3}$	$\phi^{1/3} S_g^{10/3}$
Swelling pressure (MPa)	5-10	7.5-8

The chemical properties of the buffer layer are critical for the performance of a repository. First, these properties significantly affect the chemical environment in which canisters or overpack react with incoming formation water, particularly at elevated temperatures. Second, the buffer layer serves as the first barrier for retarding radionuclide migration, the effectiveness of that retardation is highly sensitive to the chemical conditions in the buffer.

Cation exchange capacity (CEC) is usually needed for reactive transport modeling of a repository system: it generally represents the sorption capacity of bentonite. FEBEX bentonite has a CEC of  $\sim 102$  meq/100 g (ENRESA, 2000; Fernandez et al., 2001) and MX-80 bentonite has a CEC of  $\sim 78.7$  meq/100 g (Bradbury and Baeyens, 2002). Table 2-9 shows the cation occupancies of the exchangeable sites.

**Table 2-9.** The CEC and exchangeable cations for FEBEX bentonite (Fernández et al. 2001) and MX-80 bentonite (Bradbury and Baeyens 2002)

Cations (meq/100 g)	MX-80 Bentonite	FEBEX Bentonite
$\text{Ca}^{+2}$	6.6	34.6
$\text{Mg}^{+2}$	4.0	34.0
$\text{Na}^+$	66.8	31.1
$\text{K}^+$	1.3	1.94
CEC (meq/100 g)	78.7	102

The radionuclide sorption properties of the clay material are represented in the form of  $K_d$  (distribution coefficients) or retardation factor,  $R_d$ .  $K_d$  is defined as the ratio of the sorbed radionuclide mass per unit mass of solid divided by the radionuclide solution mass concentration.  $R_d$  is defined as:

$$R_d = 1 + \frac{\rho_d}{\theta} K_d \quad (2-3)$$

where  $\rho_d$  is the dry bulk density of the soil and  $\theta$  is the volumetric water content.

The  $K_d$  approach and its variants have been widely adopted in transport calculations and have been calibrated to capture dependencies, such as aqueous phase and bulk rock chemistry.  $K_d$  values for various radionuclides have been determined for various types of materials. Current UFD work (experimental and modeling) is under way to assess diffusion data for U and other radionuclides in clay material. Reactive diffusion through clay is also part of this effort to mechanistically represent the effect of compacted porous clay on diffusive fluxes, particularly for charged species. Sorption data (expressed as a retardation factor,  $R_d$ ) for MX-80 bentonite were tabulated in Bradbury and Baeyens (2003b), with a subset of those tables shown in Table 2-10. A critical review of  $K_d$  for several bentonites and argillites are given in Miller and Wang (2012).

**Table 2-10.** In situ retardation factor  $R_d$  value ( $m^3/kg$ ) for the MX-80 bentonite at pH = 7.2 (Bradbury and Baeyens 2003b)

<b>Species</b>	<b>Retardation factor</b>	<b>Species</b>	<b>Retardation factor</b>
Cs(I)	0.12	Ra(II)	0.0021
Ce(III)	4.7	Ac(III)	26.8
PM(III)	4.7	Th(IV)	63
Sm(III)	4.7	Pa(V)	5
Eu(III)	4.7	U(IV)	49.1
Ho(III)	4.7	Np(IV)	63
Hf(IV)	81	Pu(III)	26.8
Pb(II)	7.9	Am(III)	26.8
Po(IV)	0.068	Cm(III)	26.8

Diffusion coefficients are important parameters that control the migration of radionuclides. Although the diffusion coefficient for major cations such as Na and trace elements such Sr and Cs have been widely studied—for example, García-Gutiérrez et al. (2001) for FEBEX bentonite and Ochs et al. (2001) for MX-80 bentonite—the diffusion coefficients for radionuclides are not widely reported. Table 11 lists the effective diffusion coefficients of several radionuclides for MX-80 bentonite (Brandberg and Skagius 1991).

**Table 2-11.** Effective diffusion coefficient for some elements for MX-80 (Brandberg and Skagius 1991)

Species	Effective diffusion coefficient (m <sup>2</sup> /s)
C-14	10 <sup>-10</sup>
I-129	2×10 <sup>-12</sup>
Sr-90	2×10 <sup>-8</sup>
Cs-137	2×10 <sup>-9</sup>
Na-22	2×10 <sup>-9</sup>
Pu-238	10 <sup>-10</sup>
Am-234	10 <sup>-10</sup>

#### 2.4.4 Seals

Seals comprise the isolation system emplaced in deep repository structures — such as shaft/tunnel/disposal gallery accesses and drift linings and/or support assemblies — to limit radionuclide mobility and fluid flow beyond the confines of the near-field environment. The shaft seal system is designed to limit access of formation water into the repository and disposal galleries. Conversely, it is also designed to restrict the outflow of contaminated fluids from the repository. Extensive work conducted at the WIPP repository provides the basis for the evaluation of the expected performance depending on the seal configuration and materials to be considered.

The design guidance items for a shaft seal system are given by Hansen et al. (2010):

- Limit waste constituents reaching regulatory boundaries
- Restrict formation water flow through the sealing system
- Use materials possessing mechanical and chemical compatibility
- Protect against structural failure of system components
- Limit subsidence and prevent accidental entry
- Utilize available construction methods and materials.

Seal materials include cement and clay that are consistent with shaft sealing material specifications and the repository makeup. In general, small amounts of groundwater (if any) are expected to percolate into the repository even with distal or proximal aquifers. Although cement and bentonite clay are regarded as stable seal materials, potential processes such as thermally-induced phase transformations and interactions with intrinsic or extrinsic fluids may cause degradation. However, significant degradation of this type is not expected to occur in a clay/shale repository, given the expected level of isolation.

Another aspect of seals is its close relationship to the disturbed rock zone (DRZ) as described by Bianchi et al. (2013). Permeability ranges for seals can be obtained from existing literature sources for cement and clay materials.

#### **2.4.5 Radionuclide transport in EBS**

Numerous modeling studies have been conducted by international research groups and by the UFDC on flow and radionuclide transport in the EBS. Some processes have long been identified as of great importance for the performance of a repository, such as diffusion and sorption. But the importance of some processes is not clear and requires more modeling and experimental studies. Here are the processes that are thought to be important and, therefore, have to be considered in the reference case:

- Heat transport by advection and conduction. An accurate prediction of the temperature profile in EBS is clearly important. The thermal limit in many countries (Hicks et al., 2009) is based on the temperature of the EBS.
- Fluid (water and vapor) flow by advection and diffusion. The hydrologic condition is also obviously important, because they affect heat transport, mechanical changes, and chemical reactions in the EBS.
- Mechanical changes in the EBS, which are also important because they affect the long-term stability of the EBS and drift.
- Chemical reactions including mineral precipitation/dissolution, sorption, and cation exchange are very important because they either directly control the migration of radionuclides or affect radionuclide transport indirectly through changes in the chemical conditions within the EBS. Cation exchange reactions also affect the volumes of the clay phase and thus the swelling properties.
- Interactions between the EBS and the canister materials, which have a significant impact on the redox environment and thus radionuclide solubility.

While the coupling between TH (e.g., heat transport by the advection of water), TC (e.g., change of mineral solubility with temperature), TM (e.g., thermal expansion and pressurization), and HC (e.g., solute transport by advection) are known to be important, recent modeling work sheds light on the importance of HMech (such as swelling due to moisture change) and MC (e.g. change in swelling pressure due to pore-water chemistry changes) couplings. Coupled THM models have been developed in Rutqvist et al. (2009, 2011, 2014a, 2014b). The results from the model developed in Rutqvist et al. (2014b) show that it takes about 2780 years to fully saturate the EBS bentonite if the interaction between micro- and macro-structures is considered. This is much longer than the saturation time for the EBS predicted with single-structure models. Coupled THMC models have also been developed (Liu et al. 2013; Zheng et al. 2014a) to evaluate the impact of chemical processes on mechanical behavior, specifically the effect of illitization, pore-water chemistry changes, and cation exchange on the swelling of EBS bentonite. Liu et al. (2013) showed that chemical changes result in a decrease in swelling pressure of 0.2–0.3 MPa (about 20–30% of the swelling capacity) for Kunigel-VI bentonite (JNC, 2000). In one extreme case, Kunigel-VI bentonite could loss up to 70%

of its swelling capacity, which suggests that MC coupling is important for Kunigel-VI bentonite. Zheng et al. (2014a) conducted modeling studies which consider FEBEX bentonite (ENRESA, 2000) as the EBS buffer/backfill material. Model results showed only a moderate decrease in swelling stress of about 0.08 MPa, accounting for just 2% of the swelling capacity of FEBEX bentonite. The possible reasons for FEBEX bentonite experiencing less swelling pressure loss than Kunigel-VI bentonite are as follows: (a) less illitization is predicted for FEBEX bentonite, and (b) FEBEX bentonite has much higher swelling capacity (5–8 MPa) than Kunigel-VI bentonite (around 1MPa). The tentative conclusion from current THMC models is that MC coupling does not necessarily need to be included in a performance assessment model. However, before making the determination that MC coupling could be neglected, coupled THMC modeling is warranted when site-specific data are available.

Mineral dissolution and precipitation are important processes controlling radionuclide transport in the EBS. It is generally assumed in a performance assessment calculation that secondary mineral phases precipitated from a solution remain in equilibrium with the solution, in other words, the dissolved concentration of a radioelement is determined by a solubility-controlling mineral phase. The solubility of relevant radioelements is given in Table 5-12.

**Table 5-12.** Solubility of relevant radioelements in granite repository environments

Element	Solubility	Units
Actinium (Ac)	6.00E-06	mol/L
Americium (Am)	6.00E-06	mol/L
Carbon (C)	No limit	mol/L
Curium (Cm)	6.00E-06	mol/L
Cesium (Cs)	No limit	mol/L
Iodine (I)	No limit	mol/L
Niobium (Nb)	4.00E-05	mol/L
Neptunium (Np)	1.00E-09	mol/L
Protactinium (Pa)	1.00E-09	mol/L
Lead (Pb)	No limit	mol/L
Paladium (Pd)	3.00E-06	mol/L
Plutonium (Pu)	2.00E-07	mol/L

Radium (Ra)	1.00E-06	mol/L
Antimony (Sb)	1.00E-07	mol/L
Selenium (Se)	4.00E-08	mol/L
Tin (Sn)	3.00E-08	mol/L
Strontium (Sr)	No limit	mol/L
Technetium (Tc)	3.00E-08	mol/L
Thorium (Th)	4.00E-07	mol/L
Uranium (U)	4.00E-10	mol/L
Zirconium (Zr)	2.00E-08	mol/L

Data sources: Mariner et al. (2011), table 2-5 (pH 7.5, T = 25 deg C).  
C, Cs, I, Sr, and Pb assumed infinitely soluble.

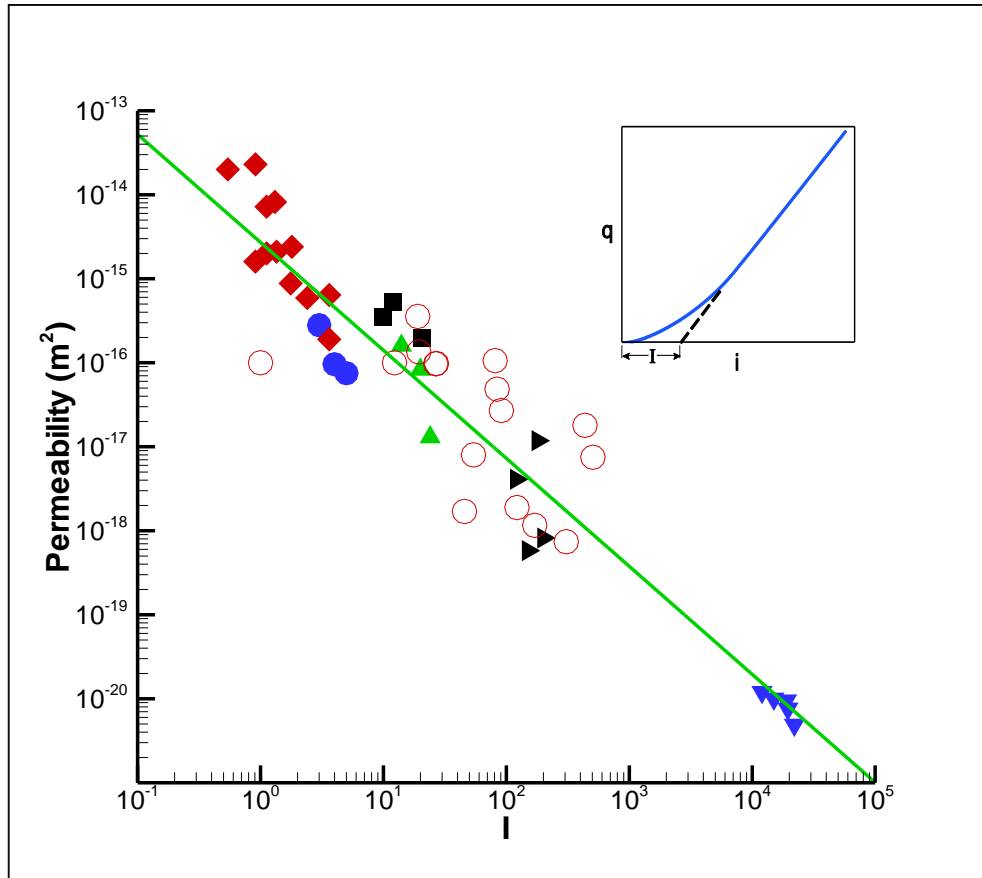


**Figure 2-11.** Non-Darcian flow in low permeability media (e.g. compacted clay) (Liu, 2014). In a low permeability medium, there exists a pressure gradient threshold below which no advective flow would be possible.  $I$  – pressure gradient threshold; and  $q$  – flow flux.

In a low-permeability medium such as compacted clay, water flow becomes non-Darcian and characterized by nonlinear relationship between water flux and hydraulic gradient (Liu, 2014). Thus, there exists a pressure gradient threshold below which no advective flow would be possible (Figure 2-11). Applying this concept to the buffer material around a waste package in the EBS, we postulate that advective flow is negligible and diffusion is thus dominant in radionuclide transport from a degraded waste form to the disturbed rock zone around the EBS. Radionuclide transport in the EBS is illustrated in Figure 2-12.

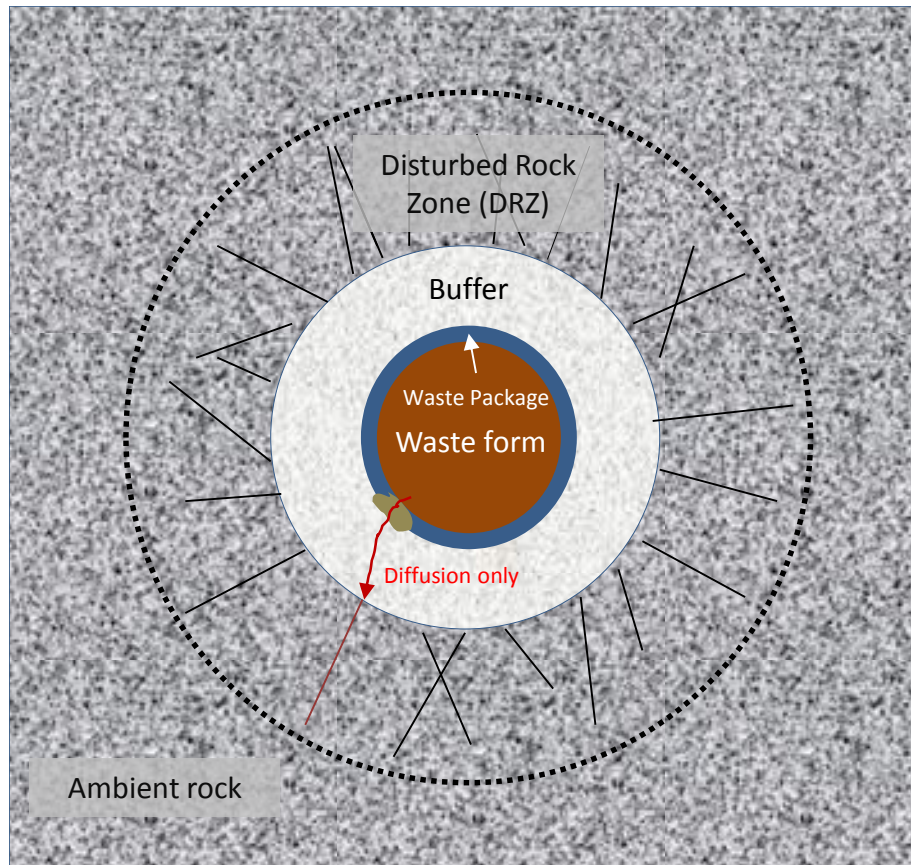


**Figure 2-12.** Illustration of radionuclide transport in the EBS. Because of the low permeability of buffer material, diffusion is predominant in radionuclide transport from a degraded waste form to the disturbed rock zone (DRZ).

## 2.5 NATURAL SYSTEM

Important processes to be considered in the natural system barrier include groundwater flow in fractures and deformation zones, advective transport and longitudinal dispersion of radionuclides within fractures, mixing at fracture intersections, and radionuclide retention by diffusion into rock matrix with sorption on matrix mineral grains.

### 2.5.1 Geologic Setting

Crystalline rocks are found in several distinct geologic and tectonic settings within the contiguous US:

- Northern Appalachians: Large areas of crystalline rocks are exposed across much of upstate New York, New Hampshire, and Vermont. The Adirondacks crystalline

- rocks are part of a shield area.
- Central and Southern Appalachians: Tectonically exposed Precambrian rocks forming considerable topography in the southeastern states of Virginia through Georgia. They are generally deformed and metamorphosed.
  - Central Midwest: Tectonically exposed crystalline basement rocks that form the Ouachita Mountains magmatic province of southern Oklahoma and the Llano uplift of central Texas.
  - Northern Midwest: Large areas of Wisconsin and Minnesota that contain Precambrian crystalline rocks that are part of the southern Canadian Shield.
  - Rocky Mountains: Mountain ranges running from the Canadian border to central New Mexico containing extensive Proterozoic crystalline-rock terrains.
  - Basin and Range: Region containing Proterozoic and Phanerozoic crystalline-rock terrains that are highly faulted and covered by Tertiary volcanic rocks.
  - Pacific Coast and the Sierra Nevada: A large region of the western US with outcrops of crystalline rock from the Mexican border through California and the length of the Sierra Nevada. Blocks also occur along the coast south of San Francisco and across the California-Oregon border. The Cordilleran batholiths are marginal to Precambrian basement.

Surface exposures for granitic rock in the contiguous United States based on data from Garrity and Soller (2009), a digital database of the geology of North America, are shown in Figure 2-6 (see also Perry et al. 2014) The surface exposures are color coded by surface slope. In addition, extent of previous glaciation is marked. Glaciation is a potential disruptive event for granitic repositories.

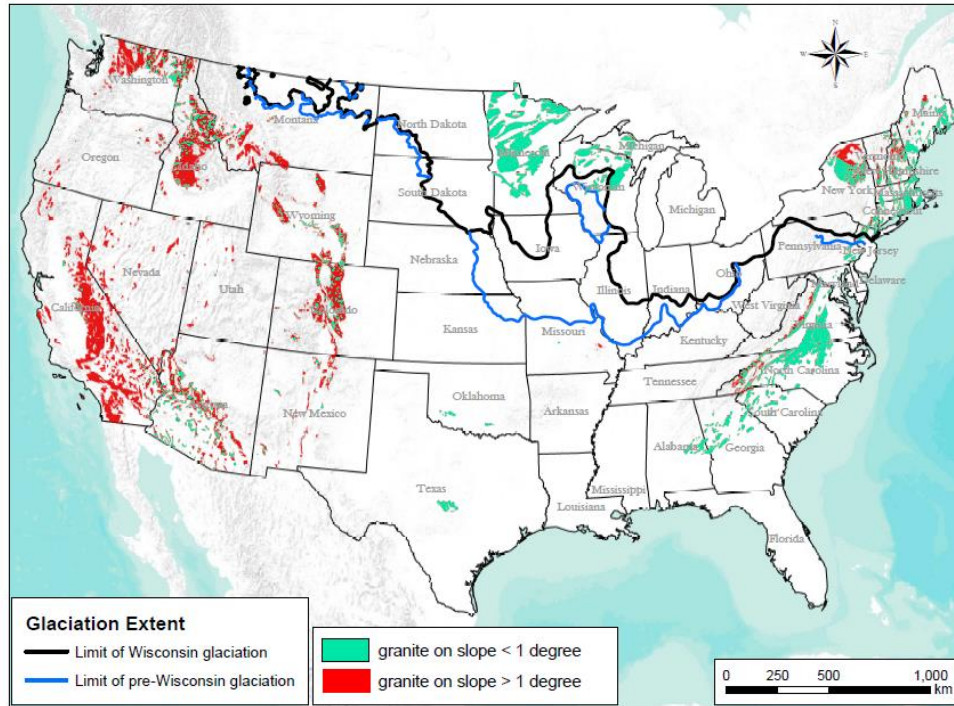


**Figure 2-13.** Distribution of crystalline rock surface exposures in the conterminous USA

The groundwater flow pattern is a key characteristic to specify when developing a reference case. In general, the groundwater table and flow patterns are controlled by geology, recharge, and surface topography. In regions where the groundwater recharge is relatively large, bedrock permeability is relatively small, and surficial deposits overlying the bedrock are relatively thin, the groundwater table is largely controlled by surface topography. That situation is the case for regions of Sweden and Finland that have been evaluated as potential sites for crystalline repositories. Gleeson et al. (2013) have delineated regions in the US where the groundwater table is likely to be controlled by topography (Figure 2-14). Note that there is significant overlap between the location of crystalline rock (Figure 2-13) and the topography-controlled regions.

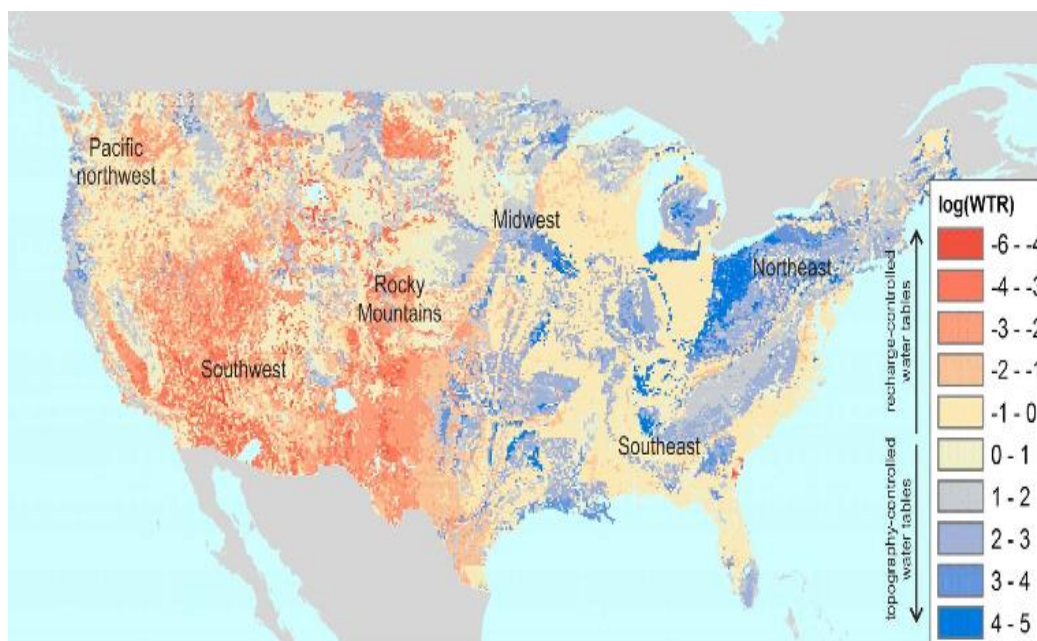


**Figure 2-14.** Regions where the groundwater system is likely to be controlled by topography. Figure modified from Gleeson et al. (2011). The water table ratio (WTR) is a dimensionless parameter that quantifies the relative importance of topography and recharge in controlling the water table. In areas with positive values of  $\log(\text{WTR})$ , groundwater flow is topography controlled and regional contributions to flow are likely to be insignificant.

Based on the overlap between the areas with topography-controlled groundwater flow systems in Figure 2-14 and the location of surface exposures for crystalline rock (Figure 2-13), the natural system for the granite reference case is chosen to have a topography-controlled flow system, which is regarded as local flow within by Tóth's classical schema (Tóth, 1963) for topography-driven flow.

### 2.5.2 Configuration of Generic Geologic Repository in Granite

The geometry for the generic natural system is shown in Figure 2-15. The site has a constant infiltration of 100 mm/y along the top and side of a hill and discharge to a topographically hypothetical repository location. Flow to the depression is enhanced by the presence of an intensely fractured deformation zone with enhanced porosity and permeability. Such zones are common in crystalline rock and represent an important feature to be considered. In addition, it is recommended to include surficial deposits of 1-2 m thickness at the discharge location. Although not necessarily significant in terms of groundwater travel times, radionuclides may sorb on such sediments increasing the radionuclide transport times. One possible release pathway of the disposal system is a nearby major fracture zone, which, in the reference case, is assumed to be located ~500 m

away from the edge of waste drifts (Figure 2-15). The thickness of the fracture zone is assumed to be 1 meter. Its hydrologic properties yet need to be determined.

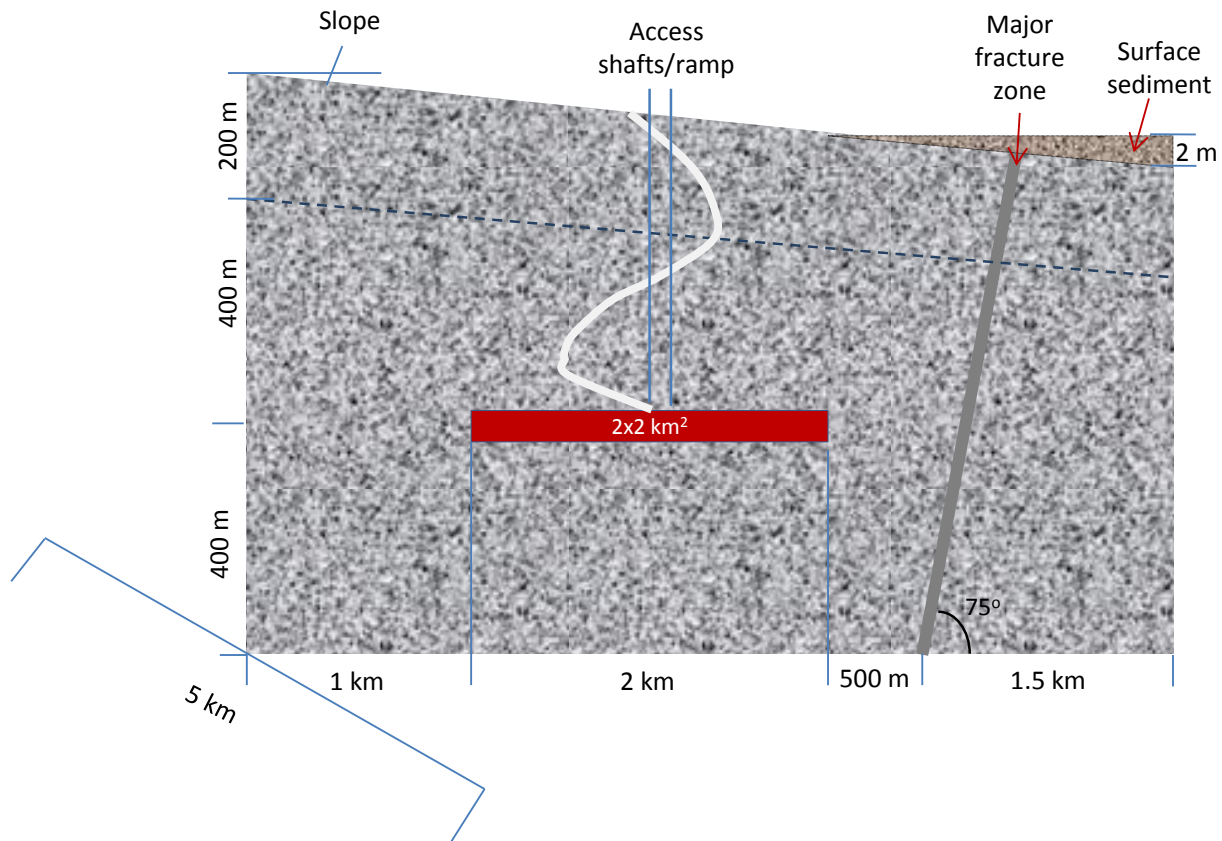


**Figure 2-15.** Configuration for generic natural system in granite (not to scale). The total model domain is  $\sim 5 \times 5 \times 1 \text{ km}^3$ .

### 2.5.3 Hydrologic Properties of Host Rock

Bulk permeability for fractured crystalline rock are typically in the  $10^{-18} \text{ m}^2$  to  $10^{-11} \text{ m}^2$  range (Bruce, 1980) but can be  $10^{-12} \text{ m}^2$  or higher at spatial scales relevant for model grid cells (Clauser, 1992). For modeling the well-characterized Forsmark site, bulk permeability values in the range  $3 \times 10^{-16} \text{ m}^2$  to  $10^{-14} \text{ m}^2$  were recommended (SKB, 2010a) for rock types other than those on the primary transport pathways, which were modeled by discrete fracture network approach. SKB (2010a) also recommended a value of  $10^{-5}$  for fracture kinematic porosity and flow wetted specific surface area of  $\sim 0.5 \text{ m}^2/\text{m}^3$ . Bulk flow properties recommended for generic modeling using a continuum porous medium approach are shown in Table 2-13. Parameters in a preliminary discrete fracture network model for DFN modeling of a generic site are shown in Table 2-14. It is important to note that these parameters are highly site-specific; thus, sensitivity studies about these generic values are recommended.

**Table 2-13.** Bulk properties for use in generic continuum porous medium flow and transport models

Parameter Description	Value	mean	Stdv	Units	Distribution Type	Index
Bulk Density	2700			kg/m <sup>3</sup>		1
Porosity	0.0018			[]		2
permeability	10 <sup>-20</sup> to 10 <sup>-19</sup>			m <sup>2</sup>		3
Longitude dispersivity	50			m		4
Equivalent flow rate	4.2x10 <sup>-6</sup> to 1.2x10 <sup>-4</sup>			m <sup>3</sup> /yr		5
Colloid concentrations	10			mg/l		6
Colloid concentrations (with dilute glacial melt water)	10			g/l		7
Hydraulic conductivity (for depth 200 to 400 m)	3x10 <sup>-9</sup> to 1x10 <sup>-7</sup>			m/s		8
Hydraulic conductivity (for depth > 400 m)	10 <sup>-13</sup> to 10 <sup>-10</sup>			m/s		9
Fracture zone mean fracture aperture	5x10 <sup>-4</sup>			m		10
Fracture aperture	10 <sup>-5</sup> to 3x10 <sup>-3</sup>			m		11
Fracture spacing	0.25 to 15			m		12
Fracture length	1.5 to 76			m		13
Heat conductivity	2.77 to 3.34			W m <sup>-1</sup> K <sup>-1</sup>		14
Heat capacity	2.17 to 2.24			MJ m <sup>-3</sup> K <sup>-1</sup>		15
	<b>Best estimate</b>	<b>Log<sub>10</sub>D<sub>e</sub> (m<sup>2</sup>/s)</b>	<b>Log<sub>10</sub>D<sub>e</sub> (m<sup>2</sup>/s)</b>			
Effective diffusivity (cations, non-charged solutes)	2.1x10 <sup>-14</sup>	-13.7	0.25	m <sup>2</sup> /s	Log-normal	16
Effective diffusivity (anions)	6.6x10 <sup>-15</sup>	-14.2	0.25	m <sup>2</sup> /s	Log-normal	17

1. SKB technical report TR-10-52, table 3-2
2. SKB technical report TR-10-52, table 3-2
3. Sandia report SAND2011-6203, p75-76 (Mariner et al., 2011)
4. SKB technical report TR-10-52, table 6-85
5. SKB technical report TR-10-50, table 3-5
6. SKB technical report TR-10-50
7. SKB technical report TR-10-50
8. SKB technical report TR-10-52, table 6-78
9. Sandia report SAND2011-6203, table 1-3 (Mariner et al., 2011)
10. Posiva 2010. Models and Data Report 2010. POSIVA 2010-01. Posiva Oy, Olkiluoto, Finland.
11. Kalinina et al. Paper "Analysis of the Effect of Heterogeneity on Heat Extraction in an EGS Represented with the Continuum Fracture Model", data from granite sites in US, Czech Republic, France, Spain, Portugal, Sweden, Egypt and Japan.
12. Kalinina et al. Paper "Analysis of the Effect of Heterogeneity on Heat Extraction in an EGS Represented with the Continuum Fracture Model", data from granite sites in US, Czech Republic, France, Spain, Portugal, Sweden, Egypt and Japan.
13. Kalinina et al. Paper "Analysis of the Effect of Heterogeneity on Heat Extraction in an EGS Represented with the Continuum Fracture Model", data from granite sites in US, Czech Republic, France, Spain, Portugal, Sweden, Egypt and Japan.
14. based on values at Forsmark and Laxemar (SKB 2006, table 9-4)
15. based on values at Forsmark and Laxemar (SKB 2006, table 9-4)
16. SKB technical report TR-10-52, Table 6-91
17. SKB technical report TR-10-52, Table 6-91

**Table 2-14.** Parameters for generic modeling using discrete fracture network approaches

Set	Orientation Distribution: Fisher			Size Distribution: Truncated Power Law			Fracture Density
	Mean Trend	Mean Plunge	Concentration $\kappa$	Exponent $\alpha$	Upper cutoff $R_u$ , m	Lower cutoff $R_l$ , m	Number of fractures in 1 km <sup>3</sup>
1. (NS)	90.0°	0.0°	22	2.5	500	15	2100
2. (NE)	135.0°	0.0°	22	2.7	500	15	2000
3. (HZ)	360.0°	90.0°	10	2.4	500	15	2300

#### 2.5.4 Disturbed Rock Zone

Excavation can cause the damage to the host rock around an excavated tunnel. In a crystalline rock, a typical result for the openings excavated by drill and blast is a damaged zone up to tens of centimeters thick, and the damage progressively diminishes with the distance from the opening (Backblom, 2008; NWMO, 2011). At Äspö, the DRZ as indicated micro-cracks has extension of 25 – 25 cm into the tunnel wall, and there is no significant axial hydraulic connectivity due to the few blast-induced fractures (Ericsson et al., 2009). As illustrated in Figure 2-12, the DRZ directly controls the communication between a waste package and the far field for water and radionuclide transport. For this reference case, we assume the extent of DRZ to be 1 meter into the tunnel. To minimize advective flows in the EDZs and waste drifts, we recommend arranging emplacement drifts perpendicular to the main groundwater flow direction (Figure 2-16).

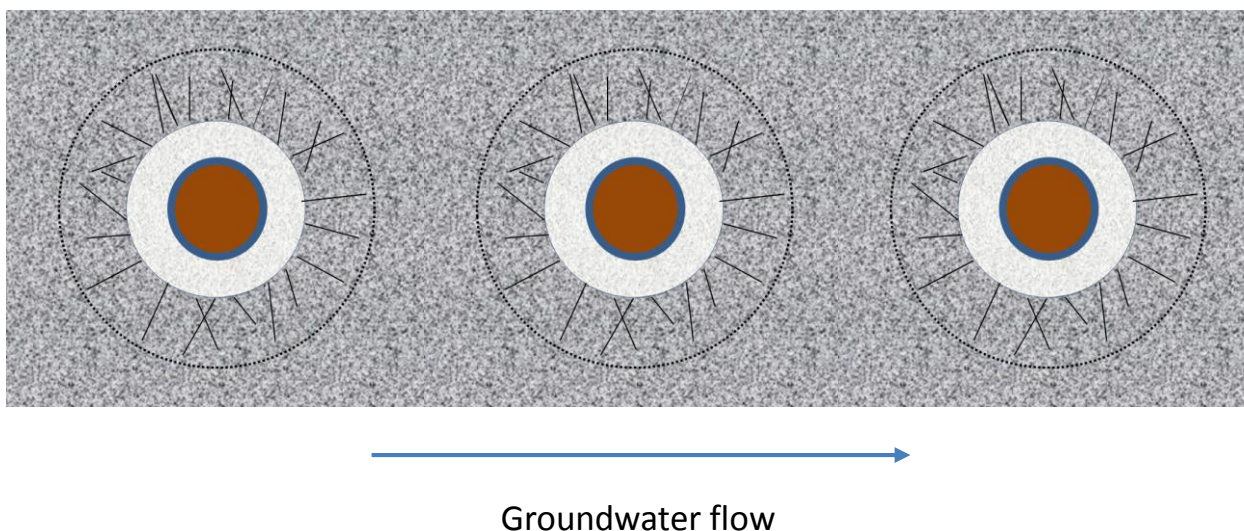


**Figure 2-16.** Minimizing advective flows in the EDZs and waste drifts by arranging emplacement drifts perpendicular to the main groundwater flow direction

### 2.5.5 Groundwater Chemistry and Radionuclide Transport

Groundwater chemistry directly affects chemical speciation and retention of radionuclides in both the near field and the far field. In crystalline rocks, at the depth of a typical deep geologic repository, groundwater is generally reducing with Eh values ranging from from -100 to -200 mV (Figure 2-17), due to the presence of  $\text{Fe}^{2+}$  or  $\text{S}^{2-}$ -containing minerals in the rock. Such conditions reduce the solubility of many redox-sensitive radionuclides (notably actinides) and enhance radionuclide sorption to geomaterials. Also, the salinity of groundwater as indicated by  $\text{Cl}^-$  concentration in granite sites generally increases with depth (Figure 2-18). High salinity can potentially destabilize colloidal particle suspensions in groundwater, therefore reducing the potential of colloid-facilitated radionuclide transport. The chemical compositions of groundwater from various sites are provided in Table 2-14.

Radionuclide sorption in the far field can occur on fracture walls, on fracture minerals, and in the matrix of granite. For the reference case, we assume that radionuclide sorption in the far field can be approximately described by a linear  $K_d$ -approach. The distribution coefficients ( $K_d$ ) for various radionuclides are given in Table 2-15. Note that  $K_d$  values are site specific, conditional to the mineralogy, groundwater chemistry and many other factors at a specific site. The values tabulated in Table 2-15 are first order approximations.

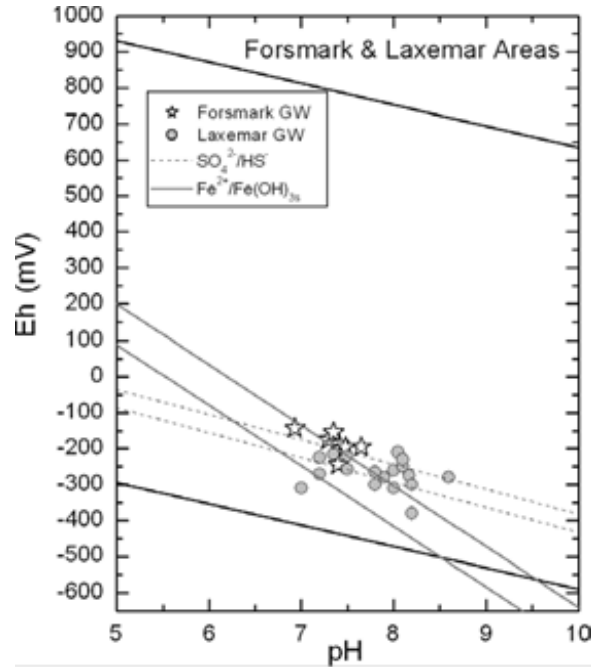


**Figure 2-17.** Eh and pH ranges at Swedish sites (Eh generally decreases with depth) (Laaksoharju et al., 2008).

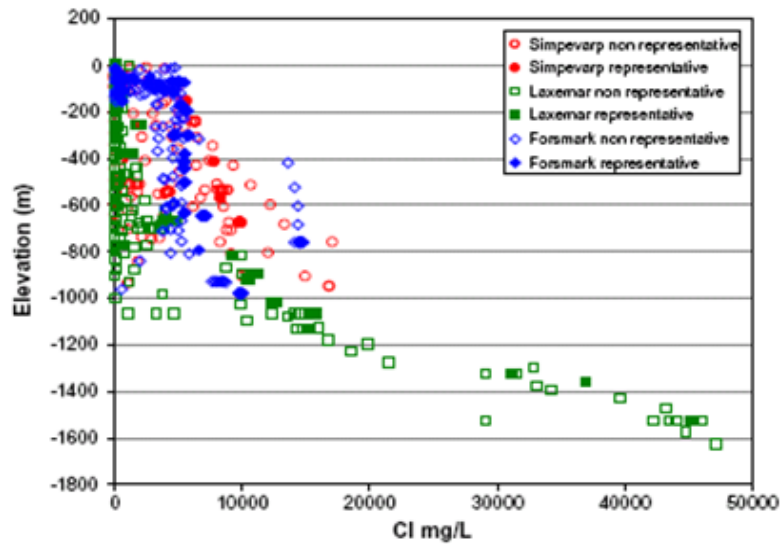


**Figure 2-18.** Chloride distribution with depth for Swedish granite sites (Laaksoharju et al., 2008): Laxemar (green), Simpevarp (red), Forsmark (blue). Open symbols represent samples considered unsuitable. Elevation indicated above sea level. Note: Chloride charge is balanced almost entirely by  $\text{Na}^+$  and  $\text{Ca}^{2+}$  (the sum of the concentrations of these two ions should be approximately 4/7ths that of  $\text{Cl}^-$  in mg/L).

**Table 2-14.** Groundwater Composition from various granite sites

Parameter	Olkiluoto, Finland	Olkiluoto, Finland	Olkiluoto, Finland	Laxemar, Sweden	Forsmark, Sweden	Pinawa, Canada	East Bull Lake, Canada
Borehole	OL-KR20	OL-KR10	OL-KR12	KLX03	KFM02A	WN-4	EBL-2
Depth (m)	360	487	708	380	512	513	538
TDS (g L <sup>-1</sup> )	10.5	22.1	49.5	2.8	9.3	7.5	2.3
Ionic strength (eq L <sup>-1</sup> )	0.22	0.48	1.18	0.05	0.19	0.16	0.05
pH	7.4	8	8.2	7.9	7.2	8.1	7.4
Na (mol L <sup>-1</sup> )	0.11	0.21	0.36	0.03	0.09	0.07	0.03
Ca (mol L <sup>-1</sup> )	0.03	0.09	0.25	0.01	0.02	0.03	0.01
K (mol L <sup>-1</sup> )	2.8E-04	3.6E-04	4.9E-04	1.4E-04	9.0E-04	5.3E-04	5.4E-05
Mg (mol L <sup>-1</sup> )	2.6E-03	1.6E-03	1.5E-03	4.4E-04	9.3E-03	1.1E-03	7.0E-05
Sr (mol L <sup>-1</sup> )	1.6E-04	3.7E-04	1.1E-03	nr	nr	nr	3.3E-05
Mn (mol L <sup>-1</sup> )	5.8E-06	7.3E-06	9.3E-06	nr	nr	nr	nr
Cl (mol L <sup>-1</sup> )	0.18	0.38	0.86	0.04	0.15	0.11	0.04
SO <sub>4</sub> (mol L <sup>-1</sup> )	2.1E-04	1.0E-05	5.0E-05	1.3E-03	5.2E-03	6.6E-03	1.4E-04
CO <sub>3</sub> (mol L <sup>-1</sup> )	5.5E-04	1.1E-04	4.0E-05	3.1E-03	2.2E-03	3.5E-03	5.0E-04
SiO <sub>2</sub> (mol L <sup>-1</sup> )	3.6E-04	2.8E-04	2.1E-04	nr	nr	nr	5.4E-05
Fe (mol L <sup>-1</sup> )	2.5E-06	2.0E-06	3.8E-07	8.0E-06	3.3E-05	nr	nr
S(-II) (mol L <sup>-1</sup> )	5.6E-06	<3.1 E-7	1.3E-06	3.0E-07	0.0E+00	nr	nr
Reference	Posiva (2010), Table 6-6	Posiva (2010), Table 6-6	Posiva (2010), Table 6-6	SKB (2006d), p. 382	SKB (2006d), p. 382	Gascoyne et al. (1987), Table 3	Gascoyne et al. (1987), Table 3

Note: nr =not reported

Data sources: Mariner et al. (2011), table 2-1 Sample groundwater composition in granite at depths from 360 to 708 m.

In a fractured granite rock, radionuclide transport can be modeled with a dual porosity approach. The diffusion of radionuclides into a matrix is an important process for radionuclide retention. It has been shown that solutes would spend an average of ten times as much time within the stagnant domain of diffusion porosity than within the flow porosity (Mariner et al., 2011). The matrix diffusion coefficients for the reference case are provided in Table 2-16. The diffusion porosity is given in Table 2-13.

**Table 2-15.** Distribution coefficients of radionuclides in granite

Species	Data (range) (unit: cc/g)	Geometric mean (cc/g)	Geometric STDV (dimensionless)	Mean of log10(data) data unit (m <sup>3</sup> /kg)	STDV of log10(data)
Am	220 - 190000	9096.03	4.306	0.959	0.634
Pu	0.2 - 401000	1736.9	13.957	0.24	1.145
Np	0.65 - 2720	31.61	5.667	-1.5	0.753
U	0 - 280000	16.04	9.215	-1.795	0.965
Tc	0.1 - 200000	15.5	56.54	-1.81	1.752
Sn	173 - 2940	688.4	2.754	-0.162	0.44
Cs	1 - 131000	135.76	7.991	-0.867	0.903
I	0.5 - 1.9	0.89	1.43	-3.052	0.155
Se	0 - 18	2.63	3.114	-2.579	0.493
Th	501 - 10000	1245.51	2.322	0.095	0.366
Pa	2.4 - 7.3	4.14	1.558	-2.383	0.193
Ra	30.1 - 3800	504.84	4.302	-0.297	0.634
Pb	1600 - 4400	2653.3	1.658	0.424	0.22
Sr	1 - 880	20.87	3.785	-1.68	0.578
Sb	450 - 519	483.27	1.074	-0.316	0.031
Zr	2.6 - 3160000	839.02	12.746	-0.076	1.105
Nb	7 - 142000	465.596	4.996	-0.332	0.699
Ac	83 - 40000	6687.15	8.17	0.825	0.912
Pd	142 - 82800	2256.63	5.301	0.353	0.724

Note: Data with de-ionized and other water chemistry that are obviously not relevant are not included except for Ac and Pd. For these two species no other data are available. Data sources: Japan JAEA database: <http://migrationdb.jaea.go.jp/english.html>

**Table 2-16.** Diffusion coefficients for matrix diffusion

Species	De : effective diffusivity (range)	Dp : pore diffusivity (range)	Mean (Dp)	Standard Deviation (Dp)
	(unit: m <sup>2</sup> /s)	(unit: m <sup>2</sup> /s)		
Am				
Pu	1.28e <sup>-13</sup> – 2.76e <sup>-13</sup>	2.61e <sup>-11</sup> – 5.63e <sup>-11</sup>	4.10E-11	1.07E-11
Np	2.10e <sup>-13</sup> – 5.41e <sup>-13</sup>	2.80e <sup>-11</sup> – 1.10e <sup>-10</sup>	6.99E-11	2.75E-11
U	2.20e <sup>-14</sup> – 4.40e <sup>-14</sup>	3.14e <sup>-12</sup> – 6.29e <sup>-12</sup>	5.14E-12	1.42E-12
Tc	4.20e <sup>-14</sup> – 4.20e <sup>-14</sup>	4.20e <sup>-12</sup> – 4.20e <sup>-12</sup>	4.20E-12	0
Sn				
Cs	5.04e <sup>-13</sup> – 1.80e <sup>-11</sup>	1.03e <sup>-10</sup> – 3.75e <sup>-10</sup>	2.11E-10	1.05E-10
I	3.90e <sup>-13</sup> – 2.60e <sup>-12</sup>	7.96e <sup>-11</sup> – 3.38e <sup>-10</sup>	1.57E-10	6.02E-10
Se	1.90e <sup>-12</sup> – 5.30e <sup>-12</sup>	8.26e <sup>-11</sup> – 9.46e <sup>-11</sup>	8.93E-11	5.00E-12
Th				
Pa				
Ra				
Pb				
Sr	2.00e <sup>-13</sup> – 1.60e <sup>-12</sup>	2.86e <sup>-11</sup> – 4.00e <sup>-10</sup>	6.65E-11	9.66E-11
Sb				
Zr				
Nb				
Ac				
Pd				

Note: Dp (pore diffusivity) ( $D_p = D_e/\text{porosity}$ ) is generally used in dual-porosity model as matrix diffusion coefficient. Data with de-ionized water are not included. Blank line means no data available. Data sources: Japan JAEA database: <http://migrationdb.jaea.go.jp/english.html>

## 2.6 BIOSPHERE

Development of a generic biosphere model is very challenging. In general the biosphere is highly site specific, and a generic biosphere model is therefore inherently highly uncertain. However, such a biosphere model can drive the performance measure of a generic repository, if the dose to a receptor is the repository performance measure. We here adopt a method from Lee et al. (2013).

A simple generic biosphere model based on the drinking water consumption such as the International Atomic Energy Agency's (IAEA) BIOMASS Example Reference Biosphere 1 (ERB 1) dose model (IAEA, 2003) is available. The ERB 1 dose model is deliberately designed to be very simple, being focused on a simple biosphere system and single exposure pathway. It is characterized by a drinking water well, bored through the

overburden into an aquifer that has been contaminated by radionuclide releases from the repository. Previous experience from more comprehensive biosphere modeling studies has shown that a drinking water well may sometimes represent a significant or even, depending on other aspects of the assessment context, a dominant pathway for release and exposure (IAEA, 2003).

For the reference case analysis, in order to avoid the issues associated with highly uncertain groundwater well discharge rates that are required as input to the BIOMASS ERB 1B dose model (IAEA, 2003), the BIOMASS ERB 1A dose model (IAEA, 2003) is used instead to convert the dissolved radionuclide concentrations in groundwater at a hypothetical drinking well location to an estimate of annual dose to a receptor based on drinking well water consumption. The ERB 1A dose model requires as input the radionuclide concentrations in the aquifer, from which an individual takes drinking water. The radionuclide concentrations in the aquifer are typically calculated by a geosphere model. The biosphere model assumes an individual water consumption rate of 1.2 m<sup>3</sup>/yr (IAEA, 2003), and uses the performance assessment model-calculated radionuclide concentrations in the far field at the site boundary. The ERB 1A parameters used to represent the biosphere are provided in Table 2-17.

**Table 2-17. IAEA ERB 1A Parameters Implemented in the Biosphere Model**

Well-water consumption rate: 1.2 m <sup>3</sup> /yr			
ERB 1 Dose Coefficient			
Isotope	Sv/Bq	Isotope	Sv/Bq
<sup>227</sup> Ac	0.00E+00	<sup>242</sup> Pu	2.40E-07
<sup>241</sup> Am	2.00E-07	<sup>226</sup> Ra	2.17E-06
<sup>243</sup> Am	2.01E-07	<sup>228</sup> Ra	0.00E+00
<sup>14</sup> C	5.80E-10	<sup>126</sup> Sb	0.00E+00
<sup>36</sup> Cl	9.30E-10	<sup>79</sup> Se	2.90E-09
<sup>245</sup> Cm	2.15E-07	<sup>126</sup> Sn	4.70E-09
<sup>135</sup> Cs	2.00E-09	<sup>90</sup> Sr	3.07E-08
<sup>137</sup> Cs	1.30E-08	<sup>99</sup> Tc	6.40E-10
<sup>129</sup> I	1.10E-07	<sup>229</sup> Th	6.13E-07
<sup>93</sup> Nb	0.00E+00	<sup>230</sup> Th	2.10E-07
<sup>237</sup> Np	1.11E-07	<sup>232</sup> Th	1.06E-06
<sup>231</sup> Pa	1.92E-06	<sup>232</sup> U	0.00E+00
<sup>210</sup> Pb	0.00E+00	<sup>233</sup> U	5.10E-08
<sup>107</sup> Pd	3.70E-11	<sup>234</sup> U	4.90E-08
<sup>238</sup> Pu	2.30E-07	<sup>235</sup> U	4.73E-08
<sup>239</sup> Pu	2.50E-07	<sup>236</sup> U	4.70E-08
<sup>240</sup> Pu	2.50E-07	<sup>238</sup> U	4.84E-08
<sup>241</sup> Pu	0.00E+00	<sup>93</sup> Zr	1.22E-09

Source: IAEA (2003), Table C.5.

## 2.6 REFERENCE SCENARIOS

As opposed to other media, disposal in crystalline rock relies more heavily on the EBS to contain radionuclides (Table 2-2). A principal function of the geosphere is to provide benign conditions for the EBS. A critical step in evaluating generic disposal systems is the specification of potential failure modes for the EBS. The detailed specification of failure modes is highly dependent on the local site conditions and repository design. For example, the KBS-3 concept depends on a nearly oxygen free copper canister that has low-to-negligible corrosion rates in reducing conditions. For that emplacement concept, disruptive events or manufacturing error are mechanisms that could lead to radionuclide release into the geosphere. For the emplacement-in-tunnel concept, however, the stainless steel package and carbon steel overpack are expected to degrade. Thus, we define three scenarios, depending on the emplacement concept and whether the repository is sited in locations that will be susceptible to disruptive events triggered by future glaciation (see Figure 2-13). In all three scenarios, transport in the geosphere is governed by similar processes, with the only difference being the potential for transient flow and chemistry in the glacial scenario. The repository evolution for the first two scenarios is illustrated in Figure 2-19.

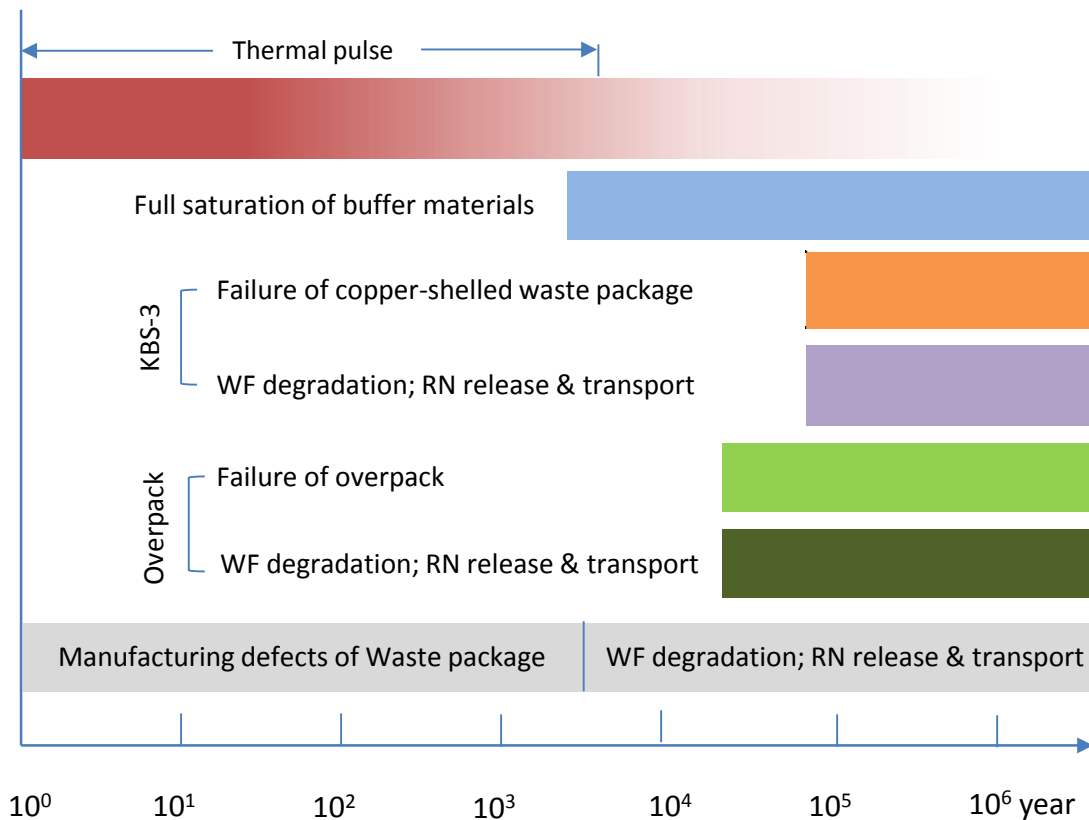


**Figure 2-19.** Schematic illustration of the evolution of a crystalline repository

### **Overpack Disposal Concept (Tunnel Emplacement)**

Generalized or localized corrosion of the stainless steel package and carbon steel overpack are potentially important processes to consider for the emplacement-in-tunnel concept. In evaluating the rate and timing of such corrosion, the effect of the waste form and concrete lining on the chemical conditions and corrosion potential and rate should be considered. In the nominal scenario, buffer function remains intact. In addition, the resulting corrosion products may provide additional retention capacity through sorption.

### **Copper-Shelled Waste packages (KBS-3 Concept)**

The KBS-3 concept depends on corrosion resistant copper canisters to contain waste for very long periods. An informative scenario to evaluate in this case is the situation where one or more waste packages have an initial defect. SKB's stylized treatment of that scenario presumes transport through a small-diameter penetration (pinhole) after the surrounding buffer materials become fully saturated. The penetration will then rapidly expand and lead to loss of the waste package containment function. The buffer remains intact and provides a diffusion/sorption barrier for radionuclides.

### **Buffer Erosion Driven by Glaciation Events (Both Concepts)**

The buffer erosion disruptive event is relevant for crystalline repositories sited in regions that will be subject to future glaciation events (see Figure 4-1). In this scenario, the passage of an ice sheet over the repository creates transient high infiltration, which may cause large flows of low ionic-strength water at repository depths. The low ionic-strength water then attacks the buffer eventually leading to erosion and localized loss of buffer barrier function.

## **2.7 MODELING APPROACHES**

Assessments of EBS degradation and transport processes when evaluating repositories in crystalline rock require similar approaches to that of argillite/shale, with the most significant difference being that groundwater flow rates at repository depths are expected to be highly heterogeneous in crystalline rock, which should be taken into account. To account for this spatial heterogeneity in flow and resulting effects on radionuclide transport, specialized modeling approaches are required.

Fractures are ubiquitous in crystalline rock and provide the primary migration pathways for radionuclides. Experience has shown that flow and transport in fractured rock are rarely represented adequately by uniform or mildly nonuniform isotropic continuum representations (Neuman, 2005) and a range of alternatives to the classical continuum representation have been developed. These alternative approaches may be grouped into three general classes: discrete fracture network representations, complex continua representations, and hybrid representations. Discrete fracture network (DFN) models depict the rock mass as an interconnected network of explicitly represented fractures. The approach is in the reductionist tradition, implicitly assuming that detailed statistical descriptions of small observable features will, once combined in numerical simulations, lead to understanding of the system as a whole. Networks of fractures are first stochastically generated using a stochastic model derived from site data. A computational

mesh is placed on each fracture plane usually ensuring that the mesh on each of a pair of intersecting fractures matches along the intersection. Groundwater flow equations are then solved using this computational mesh. The final step is then to simulate radionuclide transport using the computed flow field, usually by particle tracking. Most large-scale applications do not explicitly mesh the matrix volumes between adjacent fractures. Instead the effects of diffusion into the unrepresented matrix volume are represented (modeled) in the transport step (see e.g. Painter et al., 2008). DFN simulations were introduced first in theoretical studies; feasibility of detailed site-specific applications has also been clearly demonstrated (e.g. Cvetkovic et al., 2004, SKB, 2011).

Complex continua representations generalize a simple effective continuum representation to account for various flow and transport phenomena. Dual continuum models (Barenblatt et al., 1960) represent fractured porous rock as two overlapping and interacting continua. In its most general form (e.g. Duguid and Lee, 1977), known as the dual permeability model, flow and transport takes place in both the fracture and matrix continua while accounting for fluid and solute migration between the two continua in response to pressure and concentration differences. Commonly, flow in the matrix system is neglected relative to flow in the fracture system. In this case, the matrix acts as a non-conductive reservoir for fluid and/or solute storage and the fracture system provides the fluid migration pathways. In this variant, usually referred to as the dual porosity model, the fluid flow and the solute flux are proportional to the pressure and concentration differences between the two continua at a given location and time. The dual continuum class of models has also been generalized (Pruess and Narasimhan, 1985; Zyvoloski et al., 2008) to better represent gradients internal to the matrix blocks. In this approach, multiple continua are used to represent matrix processes. Flow between spatially adjacent matrix cells may be included or not represented, depending on the variant.

Regardless of how the matrix/fracture interactions are represented, multiple continuum models originally conceptualized the fracture flow system as having a representative elementary volume (REV) that establishes a spatial scale above which the flow properties become approximately independent of scale. For natural fracture patterns, which often have a broad distribution of fracture lengths, the existence of a classical REV scale may be questionable. Neuman proposed a stochastic continuum approach that does not require an REV (Neuman 1987, 2005). In his approach, an effective permeability tensor and other required flow/transport properties are assigned to each grid block in a conventional continuum conceptualization. However, the properties vary from grid cell to grid cell according to a stochastic model. Moreover, the stochastic model is dependent on the size of the grid block. Thus, a different stochastic model is required if the spatial discretization is changed. Parameterization of a stochastic continuum model, which generally requires inverse modeling of multiple pressure interference and solute tracer tests, has been demonstrated at the Apache Leap field site (e.g. Neuman 2005). The stochastic continuum model may be combined with any of the dual or multiple continua ideas to represent fracture/matrix interactions.

Hybrid methods adopt a reductionist view similar to DFN models but also use continuum representations for practical computational reasons (e.g. to reduce the overall size of the

computational mesh). Hybrid methods fall into two subclasses: nested and upscaled. In nested models, explicit DFN models are used along transport pathways or in other regions where high spatial resolution is required and continuum representations are used in regions that are of less interest. This approach allows for a DFN representation of transport in and near expected transport pathways while still modeling a sufficiently large region to honor natural hydraulic boundary conditions. In upscaled models, explicit DFN representations are constructed and stochastically generated. However, the flow problem is not solved on the full DFN. Instead, the DFN is used to establish, grid block by grid block, equivalent permeability tensors for use in a continuum model. Jackson et al. (2000), Svensson (2001) and Botros et al. (2008) provide examples of upscaling algorithms for the permeability tensors. Experience with upscaled models for flow has generally been good, but the approach is questionable for transport. Extensions that attempt to recover the transport effects of subgrid velocity variability through stochastic simulation have emerged (Painter and Cvetkovic, 2005) but have not been fully explored. Experience suggests that it should be possible to model a sufficiently well-characterized site in a variety of ways and that combinations of methods may allow for the most efficient use of available information. Extensive studies by the Swedish Nuclear Fuel and Waste Management Company in support a safety case for a proposed spent fuel repository (SKB, 2011) has clearly demonstrated practical utility of hybrid approaches to flow and transport modeling. Given this experience, DFN and DFN/continuum hybrids are expected to play an important role in future assessments of fractured hard rock sites.

For situations where the groundwater flow is adequately approximated as steady, a multistep procedure has been established (e.g. SKB, 2010b).

1. Model groundwater flow using a “fracture-aware” approach. This might involve only a DFN representation of the fractured rock, but in most applications a hybrid approach will likely be needed to allow the modeling domain to be large enough to intersect natural boundaries for regional groundwater flow. A hybrid approach may use permeability tensors upscaled from DFN models in an equivalent continuum porous medium (ECPM) representation or an explicit DFN representation embedded in an ECPM. In either case, experience has shown (e.g. Selroos and Painter, 2012) that the effect of repository tunnels and intensely fractured zones can be important and should be represented.
2. Calculation of transport pathways by streamline tracing. Hypothetical tracers that follow the groundwater flow without dispersion, diffusion, or sorption processes can be used to establish transport pathways from repository locations to potential discharge locations in the biosphere. If a DFN model is used to represent the flow, then the pathways may be established directly in the DFN-derived flow field assuming mixing at fracture intersections (Makedonska et al., 2014). If an ECPM is used to represent flow, then downscaling approaches (Painter and Cvetkovic, 2005) may be used to recover the velocity variability along the pathways, which is lost in the upscaled flow field.
3. EBS failure. Reactive transport modeling can be used to establish chemical conditions in the EBS, the rate of EBS degradation, and the times at which EBS

- containment function is lost. This part of the calculation is conceptually similar to that of the generic argillite/shale repository and is not discussed further here.
4. EBS transport after failure. A partially failed EBS may still provide significant radionuclide retention function through sorption, diffusion, and mineral precipitation. Three-dimensional radionuclide transport calculations should include those processes, which are similar to the argillite/shale repository situation. One potential complication is that it is computationally difficult to explicitly resolve transport around a small-diameter penetration (manufacturing defect scenario) and that specialized subgrid modeling approaches (Cliffe and Kelly, 2006) are available to avoid the very fine grid resolution that would be required.
  5. Radionuclide transport on the pathways. Radionuclide transport on the geosphere transport pathways established in Step 2 using the radionuclide releases from Step 5 is the final step. The relevant processes are advection, longitudinal dispersion, matrix diffusion, and sorption. Radionuclide transport may be simulated in a variety of ways, including conventional finite-difference, inverse Laplace methods, or time-domain particle tracking (Painter et al., 2008). The latter method is specifically designed for this application and is computationally advantageous.
  6. Biosphere. As discussed earlier, the biosphere representation depends on applicable regulations and site-specific scenarios regarding potential pathways from the geosphere to receptors of radionuclides. For the reference cases in UFDC, the biosphere conceptualization is based on the International Atomic Energy Agency (IAEA) BIOMASS Example Reference Biosphere 1B dose model (IAEA, 2003), which assumes that the receptor is an individual adult who obtains drinking water from a well drilled into the aquifer above the discharge locations from the repository host rock. Dissolved radionuclide concentrations in the aquifer are converted to estimates of annual dose to the receptor (dose from each radionuclide and total dose) based on the well pumping rate, the water consumption rate of the receptor, and radionuclide-specific dose conversion factors.

## 2.8 SUMMARY

Establishment of a generic reference case specifying the emplacement concept, waste inventory, waste form, waste package, backfill/buffer properties, EBS failure scenarios, host rock properties, and biosphere is an important step in developing a baseline for model development. A generic salt repository reference case was developed in Freeze et al. (2013) and a generic argillite/shale repository reference case was presented by Jove-Colon et al. (2014). The current section addresses the same for a generic crystalline repository, focusing on those elements of the reference case.

Three emplacement concepts were specified: waste packages containing 4 PWR assemblies emplaced in boreholes in the floors of tunnels (KBS-3 concept), a 12-assembly waste package emplaced in tunnels, and a 32-assembly dual purpose canister emplaced in tunnels. Alternative concepts such as a borehole array drilled between upper

and lower mined cavities were not considered here, but exploration of such alternative concepts would be a potential direction for future research.

Three failure scenarios were suggested for future use: a nominal scenario involving corrosion of the waste package in the tunnel emplacement concepts, a manufacturing defect scenario applicable to the KBS-3 concept, and a disruptive glaciation scenario applicable to both emplacement concepts.

A flow configuration for a generic natural barrier in a crystalline rock was developed, assuming that groundwater flow is controlled by topography. In the situation of topography-controlled flow, the regional contribution to flow is less important than local flow. The key parameters of a generic granite repository have been provided.

The computational approaches to analyzing EBS failure and transport processes in a crystalline rock repository are similar to those of argillite/shale, with the most significant difference being that the EBS in a crystalline rock repository will likely experience highly heterogeneous flow rates, which should be represented in the model. The computational approaches required to analyze radionuclide transport in the natural system are very different because of the highly channelized nature of fracture flow. Computational workflows tailored to crystalline rock based on discrete transport pathways extracted from discrete fracture network models are recommended.

## **2.9 REFERENCES**

- Backblom, G. 2008. Excavation Damage and Disturbance in Crystalline Rock – Results from Experiments and Analyses. SKB Technical Report TR 08-08, SKB Stockholm.
- Barenblatt, G.I., Zheltov Y.P., Kochina I.N., 1960. Basic concepts in the theory of seepage of homogeneous liquids in fissured rocks. *Journal of Applied Mathematics of Mechanics (English Translation)* 24, 1286–1303.
- Bianchi, M., Liu, H.-H., and Birkholzer, J. T., 2013. Diffusion Modeling in a Clay Repository: FY13 Report. . FCRD-UFD-2013-000228 Report, Lawrence Berkeley National Laboratory, Berkeley, USA.
- Börgesson, L. and Hernelind, J., 2005. Hydraulic bentonite/rock interactions in FEBEX experiment. In: *Advances in Understanding Engineered Clay Barriers* (E.E. Alonso and A. Ledesma, eds), pp. 391-412. Taylor & Francis Group, London, ISBN 04 1536 544 9.
- Botros F. E., Hassan A. E., Reeves D. M., and Pohll G., 2008. On mapping fracture networks onto continuum, *Water Resources Research* 44, W08435, doi:10.1029/2007WR006092.
- Bradbury, M.H. and Baeyens, B., 2002. Porewater chemistry in compacted re-saturated MX-80 bentonite: physico-chemical characterisation and geochemical modelling. PSI Bericht 02–10, Villigen PSI and NTB 01–08, Nagra, Wettingen, Switzerland.
- Bradbury M. and Baeyens, B., 2003b. Near Field Sorption Data Bases for Compacted MX-80 Bentonite for Performance Assessment of a High- Level Radioactive

- Waste Repository in Opalinus Clay Host Rock. PSI Bericht Nr. 03-07 August 2003 ISSN 1019-0643.
- Brandberg, F. and Skagius, K., 1991. Porosity, sorption and diffusivity data compiled for the SKB 91 study. SKB technical report 91-16.
- Bruce, W.F., 1980. Permeability of crystalline and argillaceous rocks. *Int. J. Rock Mech. Min. Sci. and Geomech. Abstr.* 17, 241–1251.
- Caporuscio F.A., Cheshire, M. C., McCarney, M., 2012. Bentonite Clay Evolution at Elevated Pressures and Temperatures: An experimental study for generic nuclear repositories, 2012 AGU fall meeting.
- Carter, J. T., Luptak, A. J., Gastelum, J., Stockman, C., and Miller, A., 2012. Fuel Cycle Potential Waste Inventory for Disposition. FCRD-USED-2010-000031, Rev. 5. U.S. Department of Energy, Office of Used Nuclear Fuel Disposition, Washington, DC.
- Cheshire, M. C., Caporuscio, F. A., Jové-Colon, C. and McCarney, M. K., 2013. Alteration of clinoptilolite into high-silica analcime within a bentonite barrier system under used nuclear fuel repository conditions. *International High-Level Radioactive Waste Management (2013 IHLRWM)*. Albuquerque, NM.
- Cheshire, M., Caporuscio, F., Rearick, M., Jové Colón, C., and McCarney, M. K., 2014. Bentonite evolution at elevated pressures and temperatures: an experimental study for generic nuclear repository designs. *American Mineralogist*: in press.
- Clauser, C., 1992. Permeability of crystalline rocks. *EOS Trans. Am. Geophys. Union* 73: 233-38.
- Clayton, D., Freeze, G., Hadgu, T., Hardin, E., Lee, J., Prouty, J., Rogers, R., Nutt, W.M., Birkholzer, J., Liu, H.H., Zheng, L., and Chu, S., 2011. Generic Disposal System Modeling – Fiscal Year 2011 Progress Report. FCRD-USED-2011-000184, SAND2011-5828P. U.S. Department of Energy, Office of Nuclear Energy, Used Fuel Disposition Campaign, Washington, DC.
- Cliffe, K. A., Kelly M., 2006. COMP23 v1.2.2 Users manual. SKB R-04-64, Svensk Kärnbränslehantering AB.
- Cvetkovic V., Painter S., Outters N., and Selroos J.-O., 2004. Stochastic simulation of radionuclide migration in discretely fractured rock near Aspo hard rock laboratory, *Water Resources Research* 40, W02404, doi:10.1029/2003WR002655.
- DOE, 2011. Used Fuel Disposition Campaign Disposal Research and Development Roadmap, FCRD-UFD-2011-000065REV0.
- Duguid J.O. and Lee P. C. Y., 1977. Flow in fractured porous rock, *Water Resources Research* 13, 558–566.
- ENRESA, 2000. Full-scale engineered barriers experiment for a deep geological repository in crystalline host rock FEBEX Project, European Commission: 403.
- Ericsson L.O., P. Brinkhoff, G. Gustafson and S.Kvartsberg. 2009. Hydraulic Features of the Excavation Disturbed Zone - Laboratory Investigations of Samples Taken from the Q and S- Tunnels at Äspö HRL. SKB Report R-09-45, Svensk Kärnbränslehantering AB, Stockholm.
- Fernández, A., Cuevas, J., Rivas, P., 2001. Pore-water chemistry of the FEBEX bentonite. *Mat. Res. Soc. Symp. Proc.* 663, 573–588.

- Freeze, G., W.P. Gardner, P. Vaughn, S.D. Sevougian, P. Mariner, V. Mousseau, G. Hammond. 2013. Enhancements to Generic Disposal System Modeling Capabilities. FCRD-UFD-2014-000062; SAND2013-10532P
- García-Gutiérrez, M., Missana, T., Mingarro, M., Samper, J., Dai, Z., and Molinero, J., 2001. Solute transport properties of compacted Ca-bentonite used in FEBEX project. *Journal of Contaminant Hydrology* 47(2–4): 127-137.
- Garrity, C. P. and Soller, D. R., 2009. Database of the Geologic Map of North America; adapted from the map by J.C. Reed, Jr. and others (2005). U.S. Geological Survey Data Series 424.
- Gleeson, T., Marklund, L, Smith, L. and Manning, A. H., 2011. Classifying the water table at regional to continental scales, *Geophys. Res. Lett.*, 38, L05401, doi:10.1029/2010GL046427.
- Greenberg, H. R., Wen, J., Buscheck, T. A., 2013. Scoping Thermal Analysis of Alternative Dual-Purpose Canister Disposal Concepts. LLNL-TR-639869.
- Greene, S.R., Medford, J.S. , and Macy, S.A., 2013. Storage and Transport Cask Data For Used Commercial Nuclear Fuel (2013 U.S. Edition), Report ATI-TR-130472013, EnergX, LLC: Oak Ridge, TN. 314 pp.
- Hansen, F.D., Hardin, E.L., Rechar, R. P., Freeze, G. A., Sassani, D.C., Brady, P.V., Stone, C. M., Martinez, M. J., Holland, J. F., Dewers, T., Gaither, K.N., Sobolik, S. R., and Cygan, R. T., 2010. Shale Disposal of U.S. High-Level Radioactive Waste. SAND2010-2843. Albuquerque, NM: Sandia National Laboratories.
- Hansen, F. D., E. L. Hardin, and A. Orrell 2011. Geologic Disposal Options in the USA. *International High-Level Radioactive Waste Conference 2011*, Albuquerque, NM, American Nuclear Society. 13:934-940.
- Hardin, E., J. Blink, H. Greenberg, M. Sutton, F. Massimiliano, J. Carter, M. Dupont, R. Howard, (2011). Generic Repository Design Concepts and Thermal Analysis (FY11). Sandia report SAND2011-6202.
- Hardin, E., T. Hadgu, D. Clayton, R. Howard, H. Greenberg, J. Blink, M. Sharma, M. Sutton, J. Carter, M. Dupont, and P. Rodwell, 2012. Repository Reference Disposal Concepts and Thermal Load Management Analysis. FCRD-UFD-2012-000219 Rev. 2. U.S. Department of Energy, Office of Used Nuclear Fuel Disposition, Washington, DC.
- Hardin, E., Clayton, D., Howard, R., Scaglione, J.M., Pierce, E., Banerjee, K., Voegelé, M.D., Greenberg, H., Wen, J., Buscheck, T.A., Carter, J.T., Severynse, T., Nutt, W.M., 2013. Preliminary Report on Dual-Purpose Canister Disposal Alternatives (FY13), August, 2013, FCRD-UFD-2013-000171 Rev. 0
- Hicks, T.W., White, M.J. and Hooker, P.J., 2009. Role of Bentonite in Determination of Thermal Limits on Geological Disposal Facility Design, Report 0883-1, Version 2, Falson Sciences Ltd., Rutland, UK, Sept. 2009.
- Hökmark, H., 2004. Hydration of the bentonite buffer in a KBS-3 repository. *Applied Clay Science* 26(1–4): 219-233.
- IAEA (International Atomic Energy Agency) 2003. Reference Biospheres for Solid Radioactive Waste Disposal. IAEA-BIOMASS-6. International Atomic Energy Agency, Vienna, Austria.

- Jackson, C., Hoch, A., Todman, S., 2000. Self-consistency of a heterogeneous continuum porous medium representation of a fractured medium, *Water Resour. Res.* 36 (1), 189-202.
- JNC, 2000. H12: Project to Establish the Scientific and Technical Basis for HLW Disposal in Japan. Second Progress Report on Research and Development for the Geological Disposal of HLW in Japan. Supporting Report 2: Repository Design and Engineering Technology. JNC TN1410 2000-003.
- Jove Colon, C., Greathouse, J. A., Teich-McGoldrick, S., et al., 2013. EBS Model Development and Evaluation Report, FCRD-UFD-2013-000312.
- Jove-Colon, C. F., Weck, P. F., Sassani, D. H., Zheng, L., Rutqvist, J., Steefel, C. I., Kim, K., Nakagawa, S., Houseworth, J., Birkholzer, J., Caproruscio, F. A., Cheshire, M., Rearick, M., S., McCarney, M. K., Zavarin, M., Benedicto, A., Kersting, A. B., Sutton, M., Jerden, J., Frey, K. E., Copple, J. M., and Ebert, W., 2014. Evaluation of Used Fuel Disposition in Clay-Bearing Rock, FCRD-UFD-2014-000056.
- Jove-Colon, C.F., J.A. Greathouse, S. Teich-McGoldrick, R.T. Cygan, T. Hadgu, J.E. Bean, M.J. Martinez, P.L. Hopkins, J.G. Argüello, F.D. Hansen, F.A. Caporuscio, and M. Cheshire, et al., 2012. Evaluation of Generic EBS Design Concepts and Process Models: Implications to EBS Design Optimization (FCRD-USED-2012-000140), U.S. Department of Energy, Washington DC., 250 pp.
- Kalinina et al., 2012. Analysis of the Effect of Heterogeneity on Heat Extraction in an EGS Represented with the Continuum Fracture Model. Proceedings of 37<sup>th</sup> Stanford Geothermal Reservoir Engineering Workshop, January 30 – February 1, 2012, Stanford, California.
- Laaksoharju, M., Smellie, J., Tullborg, E.-L., Gimeno, M.J., Molinero J., Gurban I., and Hallbeck L., 2008. Hydrogeochemical evaluation and modelling performed within the Swedish site investigation programme. *Applied Geochemistry*, Vol. 23, p1761-1795.
- Lee, J. H., Wang, Y., Simpson, M., 2013. Initial Performance Assessment to Evaluate Technical Feasibility of Direct Disposal of Electrorefiner Salt Waste in Salt Repository, FCRD-UFD-2013-000275.
- Lide, D.R., ed., 1999. *CRC Handbook of Chemistry and Physics*, CRC Press, Boca Raton, FL.
- Liu, H.H., 2014. Non-Darcian flow in low-permeability media: key issues related to geological disposal of high-level nuclear waste in shale formations, *Hydrology Journal* (in press).
- Liu, H.H., J. Houseworth, J. Rutqvist, L. Zheng, D.e Asahina, L. Li, V. Vilarrasa, F. Chen, S. Nakagawa, S. Finsterle, C. Doughty, T. Kneafsey and J. Birkholzer., 2013. Report on THMC modeling of the near field evolution of a generic clay repository: Model validation and demonstration, Lawrence Berkeley National Laboratory, August, 2013, FCRD-UFD-2013-0000244.
- Makedonska, M., Painter, S.L., Hsieh, T.-L., Bui, Q.M. and Gable, C.W., 2014. Particle tracking on discrete fracture network models with finite-volume meshes, in prep.
- Man A. and Martino J.B., 2009. Thermal , hydraulic and mechanical properties of sealing materials. NWMO TR-2009-20. December 2009, Atomic Energy and Canada Limited.

- Mariner, P. E., J. Lee, E. L. Hardin, F. D. Hansen, G. A. Freeze, A. S. Lord, B. Goldstein, and R. H. Price, 2011. *Granite Disposal of U.S. High-Level Radioactive Waste*. SAND2011-6203, Sandia National Laboratories, Albuquerque, NM.
- Neuman, S. P., 1987. Stochastic continuum representation of fractured rock permeability as an alternative to the REV and discrete fracture concepts. In Farmer I.W., Daemen J. J. K., Desai C.S., Glass C.E. Neuman S. P. (eds) *Rock Mechanics, Proceedings of the 28<sup>th</sup> US Symposium*, Tucson, Arizona. AA Balkema, Rotterdam.
- Neuman, S. P., 2005. Trends, prospects and challenges in quantifying flow and transport through fractured rocks, *Hydrogeology Journal* 13, 124–147.
- NWMO, 2011, *Excavation Damaged Zones Assessment*, DGR-TR-2-11-21.
- Ochs, M., Lothenbach, B., Wanner, H., Sato, H., and Yui, M., 2001. An integrated sorption–diffusion model for the calculation of consistent distribution and diffusion coefficients in compacted bentonite. *Journal of Contaminant Hydrology* 47(2–4): 283-296.
- Painter S. and Cvetkovic V., 2005. Upscaling discrete fracture network simulations: An alternative to continuum transport models, *Water Resources Research* 41, W02002, doi:10.1029/2004WR003682.
- Painter S., Cvetkovic V., Mancillas J., and Pensado O., 2008. Time domain particle tracking methods for simulating transport with retention and first-order transformation, *Water Resources Research* 44, W01406, doi:10.1029/2007WR005944.
- Perry, F. V., Kelley, R. E., Birdsell, S. M., Dobson, P. F., Houseworth, J. E., 2014. *Regional Geology: A GIS Database for Alternative Host Rocks and Potential Siting Guidelines*, LA-UR-14-20368. Los Alamos National Laboratory, Los Alamos, NM.
- Posiva, 2010. *Models and Data Report 2010*. POSIVA 2010-01. Posiva Oy, Olkiluoto, Finland.
- Pruess K. and Narasimhan, T.N., 1985. A practical method to modeling fluid and heat flow in fractured porous media. *Society Petroleum Engineers Journal* 25(1), 14–26.
- Pusch, R., Bluemling, P. and Johnson, L. (2003). Performance of strongly compressed MX-80 pellets under repository-like conditions, *Applied Clay Science* 23: 239–244.
- Pusch, R., Kasbohm, J. and Thao, H. T. M. (2010). Chemical stability of montmorillonite buffer clay under repository-like conditions—A synthesis of relevant experimental data. *Applied Clay Science* 47(1–2): 113-119.
- Rutqvist, J., Barr, D., Birkholzer, J., Fujisaki, K., Kolditz, O., Liu, Q.-S., Fujita, T., Wang, W., and Zhang, C.-Y., 2009. A comparative simulation study of coupled THM processes and their effect on fractured rock permeability around nuclear waste repositories. *Environmental Geology* 57(6): 1347-1360.
- Rutqvist, J., Ijiri, Y., and Yamamoto, H., 2011. Implementation of the Barcelona Basic Model into TOUGH–FLAC for simulations of the geomechanical behavior of unsaturated soils. *Computers & Geosciences* 37(6): 751-762.
- Rutqvist, J., Zheng, L., Chen, F., Liu, H.-H., and Birkholzer, J., 2014a. Modeling of Coupled Thermo-Hydro-Mechanical Processes with Links to Geochemistry

- Associated with Bentonite-Backfilled Repository Tunnels in Clay Formations. *Rock Mechanics and Rock Engineering* 47(1): 167-186.
- Rutqvist, J., Zheng, L., Chen, F., Liu, H.-H., and Birkholzer, J., 2014b. Investigation of coupled THMC process and reactive transport: FY14 progress. FCRD-UFD-2014-000497.
- Sánchez, M., Gens, A., and Olivella, S., 2012. THM analysis of a large-scale heating test incorporating material fabric changes. *International Journal for Numerical and Analytical Methods in Geomechanics* 36(4): 391-421.
- Sassani, D.C., C.F. Jové Colón, P. Weck, J.L. Jerden, K.E. Frey, T. Cruse, W.L. Ebert, E.C. Buck, R.S. Wittman, F.N. Skomurski, K.J. Cantrell, B.K. McNamara, and C.Z. Soderquist, 2012. Integration of EBS Models with Generic Disposal System Models (FCRD-UFD-2012-000277), U.S. Department of Energy: Washington D.C.
- Selroos, J.O. and Painter, S.L. 2012. Effect of transport-pathway simplifications on projected releases of radionuclides from a nuclear waste repository (Sweden). *Hydrogeology Journal* 20(8), 1467–1481.
- Sevougian, S.D., Freeze, G.A., Vaughn, P., Mariner, P., and Gardner, W.P., 2013. Update to the Salt R&D Reference Case. FCRD-UFD-2013-000368, SAND2013-8255P. Sandia National Laboratories, Albuquerque, NM.
- SKB, 2006. Buffer and backfill process report for the safety assessment SR-Can, SKB Technical Report TR-06-18.
- SKB, 2010a. Data report for the safety assessment SR-Site. Technical Report TR-10-52. Swedish Nuclear Fuel and Waste Management Co.
- SKB, 2010b. Radionuclide transport report for the safety assessment SR-Site. Technical Report TR-10-50. Swedish Nuclear Fuel and Waste Management Co.
- SKB. 2011. Long-term safety for the final repository for spent nuclear fuel at Forsmark: Main report of the SR-Site project. SKB-TR-11-01 (3 volumes).
- Svensson U., 2001. A continuum representation of fracture networks: Part I. Method and basic test cases, *Journal of Hydrology* 250, 170–186.
- Tóth, J., 1963. A theoretical analysis of groundwater flow in small drainage basins, *J. Geophys. Res.*, 68, 4795-4812.
- van Genuchten, M. T., 1980. A closed-form equation for predicting the hydraulic conductivity of unsaturated soils. *Soil science society of America journal* 44(5): 892-898.
- Villar, M. V., Sánchez, M., and Gens, A., 2008. Behaviour of a bentonite barrier in the laboratory: Experimental results up to 80 years and numerical simulation. *Physics and Chemistry of the Earth, Parts A/B/C* 33, Supplement 1(0): S476-S485.
- Wang, Y., Miller, A., Matteo, E., Reimus, P., Ding, M., Dittrich, T., Zheng, L., Houseworth, J., Zhao, P., Kersting, A., Dai, Z., Zavarin, M., 2013, Experimental and Modeling Investigation of Radionuclide Interaction and Transport in Representative Geologic Media, FCRD-UFD-2013-000314.
- Wersin P., Johnson, L.H. and McKinley, I.G., 2007. Performance of the bentonite barrier at temperature beyond 100°C: A critical review, *Physics and Chemistry of the Earth* 32: 780-788.

- Zheng, L., Samper, J., and Montenegro, L., 2011. A coupled THC model of the FEBEX in situ test with bentonite swelling and chemical and thermal osmosis. *Journal of Contaminant Hydrology* 126(1–2): 45-60.
- Zheng, L., Houseworth, J., Steefel, C., Rutqvist, J., Birkholzer, J. 2014a, Investigation of Coupled Processes and Impact of High Temperature Limits in Argillite Rock. FCRD-UFD-2014-000493, U.S. Department of Energy, Washington DC.
- Zyvoloski G. A, Robinson B. A, Viswanathan H. S., 2008. Generalized dual porosity: A numerical method for representing spatially variable sub-grid scale processes, *Advances in Water Resources* 31 (3) 535–544, DOI: 10.1016/j.advwatres.2007.11.006.



### **3. INVESTIGATION OF COUPLED THMC PROCESS AND REACTIVE TRANSPORT**

#### **3.1 INTRODUCTION**

The multi-barrier system in a nuclear waste repository typically consists of the natural barrier system (NBS), which includes the repository host rock and its surrounding subsurface environment, and the engineered barrier system (EBS). The EBS represents the man-made, engineered materials placed within a repository, including the waste form, waste canisters, buffer materials, backfill, and seals (OECD 2003).

Geological repositories in crystalline rock rely on clay buffers to provide hydrological and mechanical isolation of the waste and waste canisters from the host rock environment (Pusch et al. 2012, Lenhard et al. 2011). Smectite-rich clays (such as bentonite) have been identified as likely candidates for backfill/buffer inside access drifts and waste emplacement locations in crystalline-rock repositories (Pusch et al. 2012). In addition to their low permeability, strong sorption characteristics, and chemical buffering, smectite-rich clays are swelling clays that will fill up spaces left after initial emplacement, limiting water movement between the waste canister and the rock. Therefore, the clay buffer plays a significant role in the containment and long-term retardation of radionuclide release in crystalline rock.

During the lifespan of a geologic repository, the performance of the EBS, including the clay buffer, is affected by complex thermal, hydrogeological, mechanical, chemical, and biological processes, such as heat release due to radionuclide decay, multiphase flow (including gas release due to canister corrosion), swelling of buffer materials, radionuclide diffusive transport, waste dissolution, and chemical reactions. An in-depth understanding of these coupled processes is critical for the performance assessment (PA) of an EBS and the entire repository. Within the crystalline rock work package of the UFD Campaign, Lawrence Berkeley National Laboratory (LBNL)'s research is currently focused on two relevant areas related to clay buffer materials (bentonite), namely (1) thermal-hydrological-mechanical-chemical (THMC) processes, and (2) diffusive transport. The long-term goal of this work is to develop and verify models that can simulate these processes. The models can then be used to help provide a full understanding of how coupled processes impact interactions between the EBS components and the near-field host rock and radionuclide release and transport in the EBS.

LBNL's focus areas address key Features, Events and Processes (FEPs), which have been ranked in importance from medium to high, as listed in Tables 7 and 8 of the *Used Fuel Disposition Campaign Disposal Research and Development Roadmap* (FCR&D-USED-2011-000065 REV0) (Nutt 2011). Specifically, they address FEP 2.2.01, Excavation Disturbed Zone (EDZ) for shale by investigating the effects of coupled processes on interactions between shale (clay) disposal formations and the EBS; FEP 2.1.04.01, Buffer/Backfill; FEPs 2.1.07.02, 03, 04, 09, Mechanical Processes; FEPs 2.1.08.03, 07, 08, Hydrologic Processes; and FEP 2.1.11.04, Thermal Processes, by studying coupled

processes in the EBS; and FEPs 2.1.09.52, 53, 54, Chemical Processes—Transport, by investigating reactive-diffusive radionuclide transport in bentonite.

This report documents the progress that LBNL has made in its two R&D focus areas in FY14. Section 3.2 presents the modeling results of THMC processes within bentonite and the interaction between the EBS and a clay disposal formation in the near field. Section 3.3 documents the development of reactive-diffusive transport modeling approaches for radionuclide migration in bentonite. A summary and discussion of future work activities are given in Section 3.4.

## 3.2 MODELING COUPLED THMC PROCESSES IN THE EBS

The long-term chemical and mechanical stability of protective bentonite buffers and tunnel backfill is a key issue in the long-term performance of backfilled, multiple barrier nuclear waste repositories. For example, a certain swelling pressure should be maintained to keep the buffer homogenous, to prevent canister sinking, to prevent the adverse effect of external rock shear movements, to limit colloid transport, and to prevent the buffer from being a preferred pathway of radionuclide transport. The long-term stability of the buffer is governed by coupled THMC processes. These coupled THMC processes can be simulated by numerical modeling, e.g., by a coupling of LBNL's TOUGHREACT reactive transport simulator to a geomechanical code such as FLAC3D. However, this requires appropriate constitutive models describing couplings between the different processes.

In this section, we describe our ongoing work toward developing and applying coupled THMC models for the analysis of EBS coupled processes. We have previously implemented the Barcelona Basic Model (BBM) into the TOUGH-FLAC simulator for modeling coupled THM processes in bentonite, and have also developed a simplified approach that linked this model to chemical processes by coupling to the reactive transport simulator TOUGHREACT. This development and the results were summarized in a peer-reviewed journal article entitled "Modeling of Coupled Thermo-Hydro-Mechanical Processes with Links to Geochemistry Associated with Bentonite-Backfilled Repository Tunnels in Clay Formations," which has recently been published in *Rock Mechanics and Rock Engineering* (Rutqvist et al. 2014). The mechanical-chemical coupling approach in that study was focused on the evolution of primary and secondary swelling, in which the secondary swelling was caused by changes in ionic concentration. The model was used to simulate the effects of salt concentration on the swelling stress.

In the FY2013 milestone report "Investigation of Reactive Transport and Coupled THMC Processes in the EBS" (Davis et al., 2013), we presented progress toward the implementation and testing of a dual-structure model for expansive clay into TOUGH-FLAC. In a dual-structure model, the material consists of two structural levels: a microstructure in which the interactions occur at the particle level, and a macrostructure that accounts for the overall fabric arrangement of the material comprising aggregates and macropores (Figure 3.2.1) (Gens et al. 2006, Sánchez et al. 2005, Gens and Alonso 1992). A dual-structure model has important features for modeling the mechanical behavior of a bentonite buffer, such as irreversible strain during suction cycles. However,

most importantly, a dual-structure model provides the necessary link between chemistry and mechanics, enabling us to develop a fully coupled THMC model for the analysis of long-term EBS behavior. This approach enables mechanistic modeling of processes important for long-term buffer stability, including the effects of pore-water salinity on swelling (loss of swelling), conversion of smectite to nonexpansive mineral forms (loss of swelling), and swelling pressure versus exchangeable cations. In the FY2013 milestone report (Davis et al. 2013), we presented and applied one approach suggested by Gens (2010) for linking chemistry to the bentonite mechanics through the dual-structure model. In Gens' (2010) approach, some of the parameters related to micro-structural swelling depend on the concentration of each exchangeable cation.

In FY2014, we have made further significant progress in the development, testing, and application of the dual-structure model, as presented in this section of the milestone report. This includes additional testing and a demonstration of the capability of the implemented dual-structure model by modeling and reproducing observed behavior in a laboratory test of expansive clay. As observed in the experiments, the simulations yield nonreversible strain accumulation upon suction cycles and a decreasing swelling capacity with increasing confining stress. Finally, we present model simulations of a generic high-level nuclear waste repository with waste emplacement in horizontal tunnels backfilled with expansive clay and hosted in a clay rock formation. To our knowledge, this is the first time a dual-structure model has been applied to model coupled THM processes of a repository over a 100,000-year time period. We compared the THM results of the dual-structure model with those of the standard single-structure BBM, showing the importance of considering the dual-structure behavior of the expansive bentonite buffer material. We also upgrade the chemical and mechanical (CM) coupling scheme. Now the microstructural swelling depends not only the concentration of exchangeable cations, as implemented in FY2013 report (Davis et al. 2013), but also the mass fraction of smectite and the ion concentration of pore water. This coupling scheme needs to be validated with experimental data, and its effect on the long-term THMC behavior of EBS bentonite will be evaluated through THMC models that adopt dual-structure model and the upgraded CM coupling scheme in the future.

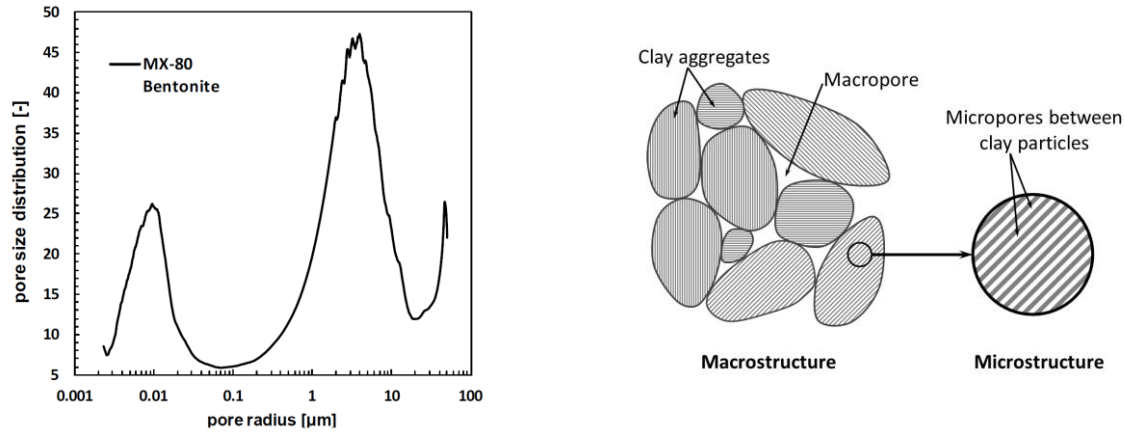


**Figure 3.2.1.** (a) Pore size distribution and (b) schematic representation of the two structural levels considered in the dual-structure model. Clay particles are represented by the gray lines.

### 3.2.1 Dual-Structure Model Implementation in TOUGH-FLAC

In this section, we present the development and implementation of a dual-structure model for expansive soils into TOUGH-FLAC. We first present an overview of the basic equations in the dual-structure model. We then summarize the implementation of this model into TOUGH-FLAC.

#### The Dual-Structure Approach

The dual-structure model considers the existence of a macrostructure, a microstructure, and the interactions between them. The macrostructure can be modeled with a constitutive model for unsaturated soils, such as the BBM. The BBM is able to describe many typical features of the mechanical behavior of unsaturated soils, including wetting-induced swelling or collapse strains (depending on the magnitude of the applied stress), as well as the increase in shear strength and apparent pre-consolidation stress with suction (Gens et al. 2006). The extension of BBM to a dual-structure model enables simulating the behavior of expansive soils, such as the dependency of swelling strains and swelling pressures on the initial stress state and on the stress path, strain accumulation upon suction cycles and secondary swelling. It is believed that such behavioral features are mainly related to the existence of coupled chemical-hydrogeological-mechanical phenomena between distinct levels of structure within the material (Alonso et al. 1999).

Conceptually, in a dual-structure model, as described by Alonso et al. (1999) and Sánchez et al. (2005), the total volume,  $V$ , of the material consists of the solid phase,  $V_s$ , the microstructural voids  $V_{vm}$ , and the macrostructure voids  $V_{vM}$

$$V = V_s + V_{vm} + V_{vM} = V_m + V_{vM} \quad , \quad (3.2.1)$$

where  $V_m$  is the volume of the microstructure.

Additionally, the total void ratio,  $e$ , and porosity,  $\phi$ , are the sum of their microstructural and macrostructural components according to

$$e = \frac{V_v}{V_s} = \frac{V_{vM}}{V_s} + \frac{V_{vm}}{V_s} = e_M + e_m, \quad (3.2.2)$$

$$\phi = \frac{V_v}{V} = \frac{V_{vM}}{V} + \frac{V_{vm}}{V} = \phi_M + \phi_m, \quad (3.2.3)$$

where  $V_v$  is the total volume of voids and the subscripts  $m$  and  $M$  refer to the microstructure and the macrostructure, respectively.

The microstructure can swell to invade the macroporosity, depending on the mechanical confinement and load level. This is relevant when considering permeability changes during the expansive soil swelling, because fluid flow takes place through the macroporosity, which is not proportional to the total strain and deformation of the expansive soil.

### Macrostructural Level

The macrostructural behavior is modeled based on the BBM, in which the yield surface is defined in the  $p-q-s$  space, where  $p$  is net mean stress (i.e., total stress minus gas-phase pressure),  $q$  is deviatoric stress (or shear stress), and  $s$  is suction (i.e., gas pressure minus liquid pressure). The size of the elastic domain increases as suction increases. This is shown in Figure 3.2.2 in the isotropic stress ( $s-p$  space) plane. The rate of increase of the elastic domain, represented by the loading-collapse (LC) curve, is one of the fundamental characteristics of the BBM (Gens et al. 2006).

The suction-dependent loading-collapse (LC) yield surface bounds the elastic region according to

$$f_{LC} = \frac{q^2}{g_y(\theta)^2} - \frac{M^2}{g_y(\theta=0)^2} (p + p_s)(p_0 - p) = 0 \quad (3.2.4)$$

where  $\theta$  is the Lode angle, the function  $g_y(\theta)$  describes the shape of the yield surface in the deviatoric plane,  $M$  is the constant slope of the critical state line,  $p_s = k_s s$  represents

the increase in cohesion with suction,  $k_s$  is an empirical material constant and the function

$$p_0 = p^c \left( \frac{p_0^*}{p^c} \right)^{[\lambda_{ps,0} - \kappa_{ps,0}] / [\lambda_{ps} - \kappa_{ps,0}]} \quad (3.2.5)$$

is the net mean yield stress (or apparent pre-consolidation stress) at the current suction, where  $p_0^*$  is the net mean yield stress (or pre-consolidation stress) at full saturation,  $p^c$  is a reference stress,  $\lambda_{ps,0}$  is a compressibility parameter in virgin soil states at zero suction,  $\lambda_{ps} = \lambda_{ps,0} [(1-r)\exp(-\xi s) + r]$  is a compressibility parameter in virgin soil states at suction  $s$ , and  $r$  is a constant related to the maximum stiffness of the soil (for an infinite suction),  $\xi$  is a parameter that controls the rate of increase of soil stiffness with suction, and  $\kappa_{ps,0}$  is the elastic stiffness parameter for changes in net mean stress at zero suction.

The flow rule is given by

$$g_{LC} = \frac{\alpha_a q^2}{g_y(\theta)^2} - \frac{M^2}{g_y(\theta=0)^2} (p + p_s)(p_0 - p) \quad (2.6)$$

where  $\alpha_a$  is a parameter that gives rise to a non-associative model, i.e.,  $g_{LC} \neq f_{LC}$ .

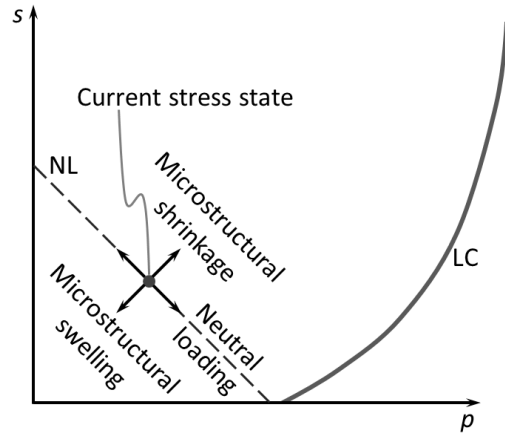


**Figure 3.2.2.** Schematic representation of the dual-structure model in the isotropic plane, including the neutral line (NL) and the loading-collapse (LC) yield surface. The NL moves with the current stress state, so that the current stress state is always contained within the NL. The stress state can change following one three stress paths: (i) microstructural shrinkage, if it moves to the right of the NL, (ii) microstructural swelling, if it moves to the left of the NL and (iii) neutral loading, if it moves along the NL, in which case the microstructure does not deform.

## Microstructural Level

The following assumptions are adopted related to microstructural behavior and its interaction with the macrostructure:

- The microstructure is mainly saturated and the effective stress concept holds.
- The microstructural behavior is elastic and volumetric.
- Mechanical, hydraulic, and chemical equilibrium exists between microstructure and macrostructure.
- Coupling between microstructure and macrostructure results in a possible buildup of macrostructural elastoplastic strains when elastic microstructural strains occur.

With these assumptions, the volumetric microstructural strain,  $d\varepsilon_{vm}^e$ , depends exclusively on variations in mean effective stress,  $d\hat{p} = d(\bar{p} - p_l) = d(\bar{p} - p_g + p_g - p_l) = d(p + s)$ , where  $\bar{p}$  is mean stress,  $p_l$  is liquid phase pressure and  $p_g$  is gas phase pressure. Therefore, a straight line  $p + s = \text{constant}$  can be drawn in the  $p-s$  space around the current state of stress and suction along which no microstructural strain takes place (Figure 3.2.2). This line, called the neutral line (NL), moves with the current stress state (C) and separates at each instant the zone of microstructural swelling from the zone of microstructural shrinkage in the  $p-s$  plane (Figure 3.2.2).

## Interaction Between Structural Levels

Microstructural swelling/shrinkage affects the structural arrangement of the macrostructure, inducing irreversible strains in the macroporosity. These irreversible macrostructural deformations induced by microstructural effects are considered proportional to the microstructural strain through interaction functions as

$$d\varepsilon_{v\beta}^p = f d\varepsilon_{vm}^e \quad (3.2.7)$$

where  $\varepsilon_{v\beta}^p$  is the macrostructural plastic strain arising from the interaction between both structures. Two interaction functions are defined:  $f = f_c$  for microstructural compression or shrinkage paths and  $f = f_s$  for microstructural swelling paths. These functions can adopt several forms (Sánchez et al., 2005), but they always depend on the ratio  $p/p_0$

$$f_c = f_{c0} + f_{c1} (p/p_0)^{n_c} \text{ and } f_s = f_{s0} + f_{s1} (1 - p/p_0)^{n_s}, \quad (3.2.8a)$$

or

$$f_c = f_{c0} + f_{c1} \tanh[f_{c2} (p/p_0 - f_{c3})] \text{ and } f_s = f_{s0} - f_{s1} \tanh[f_{s2} (p/p_0 - f_{s3})], \quad (3.2.8b)$$

where  $f_{ij}$  and  $n_i$  ( $i = \{c, s\}$  and  $j = \{0, 1, 2, 3\}$ ) are constants.

The ratio  $p/p_0$  is a measure of the distance from the current stress state to the yield locus for the macrostructure LC, and its inverse has the same meaning as the overconsolidation ratio for an isotropically consolidated soil. A low  $p/p_0$  implies a dense packing of the material. Under such dense packing (dense macrostructure), the microstructural swelling strongly affects the global arrangement of clay aggregates, which becomes more open. This results in a softening of the macrostructure, which implies that the macrostructural yield surface LC shrinks. Under this condition, expansion accumulates upon suction cycles. On the other hand, a high  $p/p_0$  implies a looser macrostructure. Under such loose packing conditions, the microstructural swelling produces an invasion of the macropores, which tends to close the macrostructure, and compression accumulates upon suction cycles. In such a case, the elastic domain increases and LC expands (Alonso et al. 1999; Sánchez et al. 2005).

### Elastic Strain

Equivalently to the BBM model, the macrostructural volumetric elastic strain increment for the dual-structure model is associated with changes in net mean stress  $dp$  and suction  $ds$  (Alonso et al. 1999)

$$d\varepsilon_{vM}^e = \frac{1}{K_M} dp + \frac{1}{K_s} ds, \quad (3.2.9)$$

where  $K_M$  is the macrostructural bulk modulus and  $K_s$  is the macrostructural modulus associated with suction strain.  $K_M$  and  $K_s$  are defined as

$$K_M = \frac{(1 + e_M)p}{\kappa_{Ps}(s)}, \quad (3.2.10)$$

$$K_s = \frac{(1 + e_M)(s + p_{atm})}{\kappa_{sp}(p, s)} \quad (3.2.11)$$

where  $\kappa_{Ps} = \kappa_{Ps0}(1 + s\alpha_{ps})$ ,  $\kappa_{sp} = \kappa_{sp0}(1 + \alpha_{sp} \ln(p/p_{ref}))\exp(\alpha_{ss}s)$ ,  $\kappa_{Ps0}$ ,  $\kappa_{sp0}$  are compressibility parameters for changes in net mean stress and suction, respectively,  $p_{ref}$  is a reference stress state for relating elastic compressibility to suction, and  $\alpha_{ps}$ ,  $\alpha_{sp}$  and  $\alpha_{ss}$  are empirical parameters.

The microstructural volumetric strain depends on the change in the microstructural effective stress

$$d\varepsilon_{vm}^e = \frac{1}{K_m} d\hat{p}, \quad (3.2.12)$$

where  $K_m$  is the microstructural bulk modulus for changes in mean effective stress  $d\hat{p}$ . Alonso et al. (1999) define two alternative expressions for the microstructural modulus

$$K_m = \frac{(1 + e_m)\hat{p}}{\kappa_m}, \quad (3.2.13a)$$

$$K_m = \frac{e^{\alpha_m \hat{p}}}{\beta_m}, \quad (3.2.13b)$$

where  $\kappa_m$ ,  $\alpha_m$  and  $\beta_m$  are compressibility parameters.

Thermal strains are purely volumetric

$$d\varepsilon_v^T = (\alpha_0 + 2\alpha_2 \Delta T)dT, \quad (3.2.14)$$

where  $\alpha_0$  and  $\alpha_2$  are material parameters corresponding to a temperature-dependent volumetric thermal expansion coefficient,  $T$  is temperature, and  $\Delta T = T - T_0$ , where  $T_0$  is a reference temperature. Finally,  $dT$  is the change in temperature from the initial temperature, which could be different from  $T_0$ .

The deviatoric elastic strain increment is defined as

$$d\varepsilon_q^e = \frac{1}{3G} dq, \quad (3.2.15)$$

where  $G$  is the shear modulus and may be obtained using a constant Poisson ratio  $\nu$  in

$$G = \frac{3(1-2\nu)}{2(1+\nu)} K_M. \quad (3.2.16)$$

Thus, the equations for elastic mechanical strain indicate the dependency of bulk modulus on suction (and hence fluid saturation), which in a dry clay can be significantly stiffer than in a water-saturated clay.

In total, the BBM is characterized by 18 parameters, with the dual-structure model incorporating between 8 and 11 additional parameters, depending on the microstructural bulk modulus and the interaction functions that are used.

### Plastic Strain

Macrostructural plastic strain occurs by two possible mechanisms: either when the stress lies on the LC yield surface, or as a result of microstructural shrinkage/swelling. While

the plastic strain by microstructural shrinkage/swelling is described by Eq. (3.2.7), the LC plastic strains are obtained from the plastic flow rule:

$$d\epsilon_{vLC}^p = d\Lambda \frac{\partial g_{LC}}{\partial p}, \quad (3.2.17)$$

$$d\epsilon_{qLC}^p = d\Lambda \frac{\partial g_{LC}}{\partial q}, \quad (3.2.18)$$

where  $d\Lambda$  is the plastic multiplier obtained from the consistency condition  $df_{LC} = 0$  (recall Equation (3.2.4)). The calculation of the plastic multiplier  $d\Lambda$  is detailed in Rutqvist et al. (2011).

The total plastic volumetric strain is the sum of both plastic mechanisms:

$$d\epsilon_v^p = d\epsilon_{vLC}^p + d\epsilon_{v\beta}^p. \quad (3.2.19)$$

The hardening variable of the macrostructure — the pre-consolidation pressure  $p_0^*$  — depends on the total plastic volumetric strain  $\epsilon_v^p$  as

$$\frac{dp_0^*}{p_0^*} = \frac{(1 + e_M)d\epsilon_v^p}{\lambda_{Ps0} - \kappa_{Ps0}}. \quad (3.2.20)$$

## Implementation into TOUGH-FLAC

We implemented the dual-structure model in TOUGH-FLAC, by extending our previous implementation of the BBM (Rutqvist et al. 2011) to include the microstructural level and its interactions with the macrostructure. This involves consideration of the sequential coupling of the TOUGH2 and FLAC<sup>3D</sup> simulators (Rutqvist et al. 2011), and constitutive stress-strain behavior in FLAC<sup>3D</sup>. TOUGH2 is a multiphase nonisothermal finite volume code; FLAC<sup>3D</sup> is a geomechanics finite difference code. Our implementation of the dual-structure model in FLAC<sup>3D</sup> was done using the user-defined constitutive model (UDM) option in FLAC<sup>3D</sup>, including C++ coding and dynamic link libraries. Specifically, the following calculation items were added:

1. Microstructural strain and effective stress
2. Macrostructural strain
3. Global elastic tensor depending on microscopic and macroscopic structural compliances
4. Micro/macrostructural interaction functions
5. Plastic macrostructural strain from structural interactions
6. Plastic corrections in the FLAC<sup>3D</sup> elastoplastic algorithm
7. Plastic hardening/softening factors.

Finally, at the end of each FLAC<sup>3D</sup> step, the hardening parameter, i.e., the pre-consolidation pressure  $p_0^*$ , the bulk modulus of both microstructure and macrostructure and the tangential bulk modulus, are updated based on the total plastic volumetric strain and stress state, and these are stored for use in the next step.

### 3.2.2 Testing of Implementation and Validation

In the FY2013 milestone report (Davis et al. 2013) we presented some initial testing of the implementation by modeling drying and wetting cycles as typically observed in laboratory data. Here we present new modeling of a laboratory experiment of Pousada (1982) to test and demonstrate the capability of the implemented dual-structure model. In the laboratory experiment of Pousada (1982), an expansive clay undergoes several suction (wetting-drying) cycles for two net mean stresses (Figures 3.2.3 and 3.2.4). Expansive clays show irreversible behavior when they undergo successive wetting-drying cycles. This phenomenon cannot be reproduced with the standard single-structure BBM model, but the incorporation of the interactions between the microstructure and the macrostructure of an expansive soil allows accumulating plastic strain upon suction cycles. Table 2.1 shows the parameters of the dual-structure model resulting from the calibration of the laboratory experiments of Pousada (1982).

**Table 3.2.1.** Parameters used to reproduce the suction cycles test of Pousada (1982)

---

<i>Parameters defining the Barcelona Basic Model for macrostructural behavior</i>						
$\kappa_{ps0}=0.005$	$\kappa_{sp0}=0.01$	$\lambda_{ps0}=0.024$	$p^c$ (MPa)=0.01	$r=0.85$	$\xi$ (MPa <sup>-1</sup> )=0.2	$p_0^*$ (MPa)=0.75
<i>Parameters defining the law for microstructural behavior</i>						
$\alpha_m$ (MPa <sup>-1</sup> )=1.2			$\beta_m$ (MPa <sup>-1</sup> )=0.02			
<i>Interaction functions between the microstructure and the macrostructure</i>						
$f_c = 1.975 + 0.185 \tanh[5(p/p_0 - 0.275)]$			$f_s = 1.825 - 0.4 \tanh[-0.4(p/p_0 - 0.3)]$			
$e_{micro}=0.45$		$e_{macro}=0.55$				

---

Figure 3.2.3 shows the calibration of a suction-cycles test, which comprises five suction cycles (suction ranges from 1.7 to 0.2 MPa in each suction cycle) at a very low net mean stress (0.01 MPa). The model can reproduce the plastic strain accumulation upon cycles and the tendency to reduce the amount of plastic strain accumulated between two successive suction cycles as cycles accumulate. The calibration of the experiment reproduces with a fair accuracy the end points of the wetting-drying cycles, as well as the strain evolution of the first suction cycle, which is curved. Nevertheless, the strain evolution of the subsequent cycles becomes quite linear in the laboratory experiment, but the numerical results maintain the curved evolution. To improve this change in the strain evolution pattern as suction cycles evolve, a more complex bulk modulus for both the microstructure and macrostructure may need to be implemented.

While the microstructure behaves elastically (Figure 3.2.3b), the macrostructure undergoes plastic strain that causes irreversible changes in macroporosity, which is related to the macrostructural void ratio through  $\phi_M = e_M / (1 + e)$  (Figure 3.2.3c). Macroporosity is enhanced at low net mean stress (low values of the  $p/p_0$  ratio) as a result of the interaction between the two levels of structures. Low values of the  $p/p_0$  ratio imply a dense macrostructure, so the swelling of the microstructure will open up the macrostructure, inducing expansion upon suction cycles. Thus, the plastic strain of the macrostructure induced by the elastic volumetric strain of the microstructure is higher during wetting than during drying (Figure 3.2.3d).

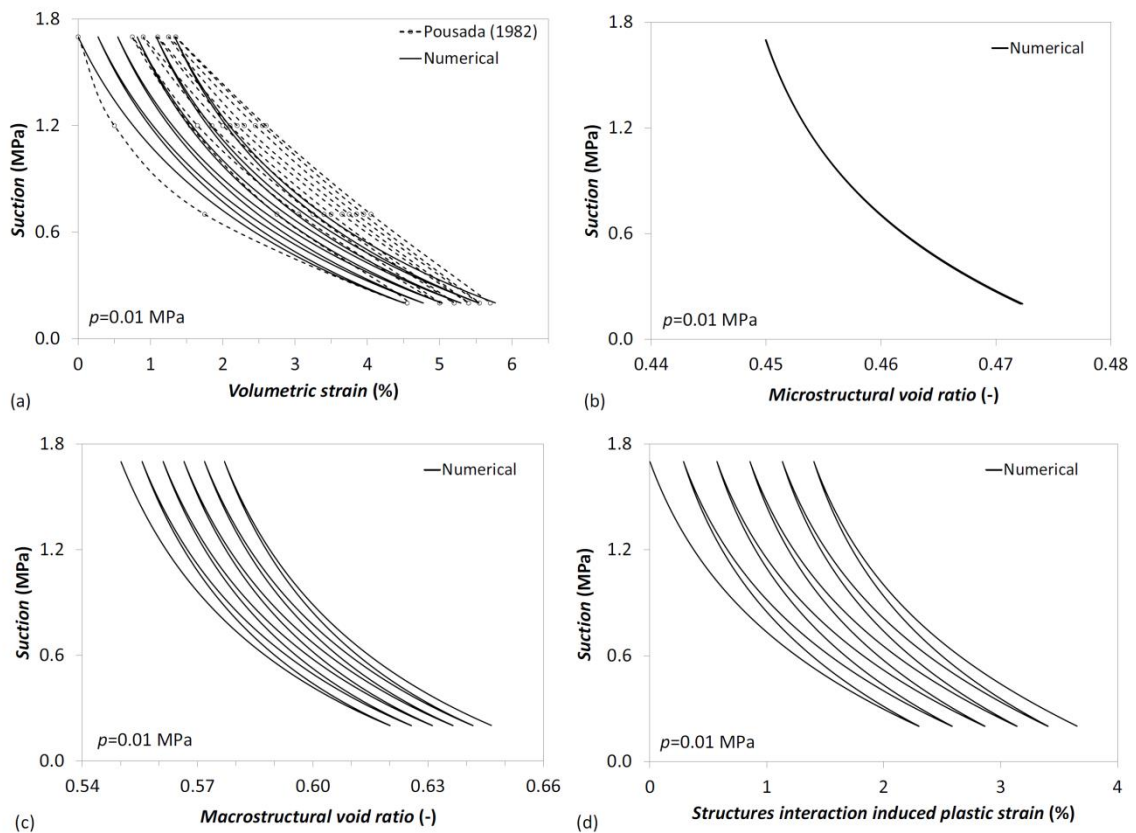


**Figure 3.2.3.** Evolution of (a) volumetric strain, (b) microstructural void ratio, (c) macrostructural void ratio and (d) plastic strain of the macrostructure due to micro/macrostructure interaction upon suction (wetting-drying) cycles for a net mean stress of 0.01 MPa. The experimental volumetric deformation of Pousada (1982) is also displayed in (a).

Figure 3.2.4 displays the results of the same experiment, but performed at a higher net mean stress of 0.1 MPa. Similarly to the experiment with a lower confining pressure, the numerical calibration reproduces fairly well the end points of the wetting-drying cycles

and the curved strain evolution of the first cycle. But for subsequent suction cycles, the experimental strain evolution becomes quasi-linear, while the numerical simulation keeps the curved evolution. Comparing Figures 3.2.3 and 3.2.4 reveals that the swelling capacity of the material is reduced as the confining stress increases. The rest of the characteristics remain the same: the microstructure is elastic, plastic strain accumulation is reduced with the number of cycles, and expansion accumulates upon cycles. The latter occurs because the  $p/p_0$  ratio is still relatively low and therefore, the macrostructure is dense. For a net mean stress that would yield a high  $p/p_0$  ratio, the macrostructure would be loose and the microstructure would invade macropores upon suction cycles. In this case, given the net mean stress and suction values, the microstructure deformation is almost independent of the confining stress (recall Figures 3.2.3b and 3.2.4b), because its stiffness is proportional to the effective stress [Equation (3.2.13)], which evolves very similarly in the two experiments. Apart from this, the higher net mean stress of 0.1 MPa (Figure 3.2.4) implies a higher  $p/p_0$  ratio, and therefore the suction cycles are closer to the equilibrium point between the wetting and the drying interaction functions. This causes a smaller plastic strain accumulation upon suction cycles due to the interaction between the two structural levels (compare Figures 3.2.3d and 3.2.4d).

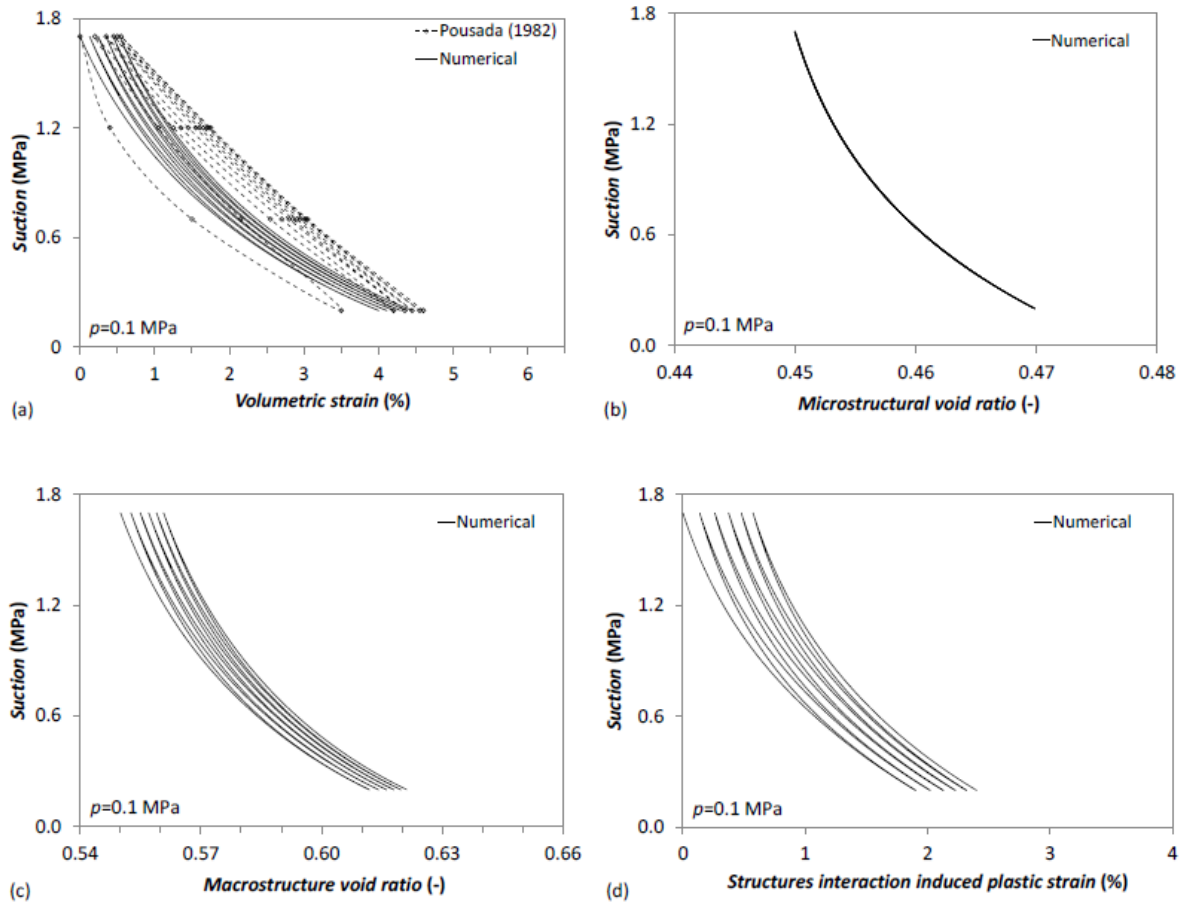


**Figure 3.2.4.** Evolution of (a) volumetric strain, (b) microstructural void ratio, (c) macrostructural void ratio and (d) plastic strain of the macrostructure due to suction (wetting-drying) cycles for a net mean stress of 0.1 MPa. The experimental volumetric deformation of Pousada (1982) is also displayed in (a).

The calibration of the dual-structure model with only these two available experiments becomes quite complicated, due to the large number of degrees of freedom that this model has. Though the simulated deformation paths differ somewhat from the experimental results, the global behavior of this expansive clay is satisfactorily captured. In general, more experiments would be required to back-calculate most of the parameters of the dual-structure model.

### 3.2.3 Application to a Generic Repository

We applied the dual-structure model and compared the THM results with those of the standard single-structure BBM in a generic repository similar to that considered in the Swiss nuclear waste disposal program. We assume that the host rock is Opalinus Clay. The tunnels containing the high-level waste are placed at 500 m depth and are spaced 50 m. Since the emplacement tunnels may typically be up to 1 km long, we model a 2D cross section of the repository and make use of the symmetry to model only one tunnel. We further assume that the tunnel is backfilled with FEBEX bentonite (Gens et al. 2009; Sánchez et al. 2012). The geometry of the model and the heat load of the waste are displayed in Figure 3.2.5.

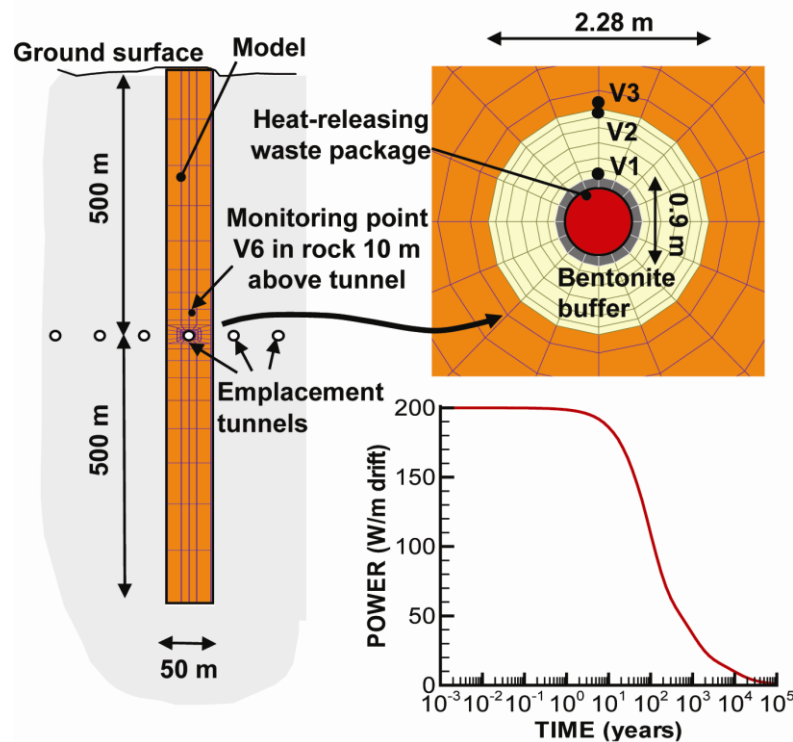


**Figure 3.2.5.** Model domain, numerical grid, monitoring points and heat power function for an assumed bentonite back-filled horizontal emplacement drift at 500 m depth in clay host rock.

Table 3.2.2 compiles the material parameters of the claystone host rock. The properties of the Opalinus Clay are taken from Gens et al. (2007) and Corkum and Martin (2007). The relative permeability curves follow the van Genuchten-Mualem model. The properties of the FEBEX bentonite for the standard single-structure BBM model were derived by Alonso et al. (2005) and Gens et al. (2009) (Table 2.3) and were also used in Rutqvist et al. (2014). The properties for the macrostructure of the dual-structure model are similar to those used in the single-structure BBM model, but some parameters have been adapted to obtain a global behavior of both the microstructure and the macrostructure comparable to that of the BBM model (see Table 3.2.4). The properties of the microstructure of the dual-structure model for the FEBEX bentonite are based on those proposed by Sánchez et al. (2012), but with some modifications (Table 3.2.4).

**Table 3.2.2.** Properties of the clay host rock (Gens et al., 2007; Corkum and Martin, 2007)

Property	Value
Porosity, $\phi$ (-)	0.15
Young's modulus, $E$ (GPa)	5
Poisson ratio, $\nu$ (-)	0.3
Grain density, $\rho_s$ (kg/m <sup>3</sup> )	2400
Grain Specific heat, $C_s$ (J/kg/°C)	900
Thermal conductivity, $\lambda_T$ (W/m/K)	2.2
Thermal expansion coefficient, $\alpha_0$ (°C <sup>-1</sup> )	1.0x10 <sup>-5</sup>
Intrinsic permeability, $k$ (m <sup>2</sup> )	5.0x10 <sup>-20</sup>
van Genuchten water retention parameter $m$ (-)	0.41
van Genuchten entry pressure, $P_0$ (MPa)	48
Residual liquid saturation, $S_{lr}$ (-)	0.1
Residual gas saturation, $S_{gr}$ (-)	0.01

**Table 3.2.3.** Material parameter values for the bentonite buffer used in the BBM model (Gens et al., 2009).

Property	Value
Initial dry density, $\rho_d$ (kg/m <sup>3</sup> )	1600
Compressibility parameter for stress-induced elastic strain, $\kappa_{ps0}$ (-)	0.05
Compressibility parameter for suction-induced elastic strain, $\kappa_{sp0}$ (-)	0.25
Poisson ratio, $\nu$ (-)	0.4
Parameter for stress-induced elastic strain, $\alpha_{ps}$ (MPa <sup>-1</sup> )	-0.003
Parameter for suction-induced elastic strain, $\alpha_{sp}$ (-)	-0.161
Parameter for suction-induced elastic strain, $\alpha_{ss}$ (-)	0
Reference stress state for relating elastic compressibility to suction, $p_{ref}$ (MPa)	0.01
Thermal expansion coefficient, $\alpha_0$ (°C <sup>-1</sup> )	1.5x10 <sup>-5</sup>
Compressibility parameter in virgin state soils at zero suction, $\lambda_{ps0}$ (-)	0.15
Parameter defining soil stiffness associated with loading collapse yield, $r$ (-)	0.925
Parameter for the increase of soil stiffness with suction, $\xi$ (MPa <sup>-1</sup> )	0.1
Parameter that describes the increase of cohesion with suction, $k_s$ (-)	0.1
A reference stress state for compressibility relation in virgin states, $p^c$ (MPa)	0.5
Slope of the critical state line, $M$ (-)	1.0
Non-associativity parameter in the plasticity flow rule, $\alpha_a$ (-)	0.53
Specific volume at reference stress state $p^c$ in virgin state, $v^c$ (-)	1.937
Net mean yield stress for saturated conditions at reference temperature, $p_0^*$ (MPa)	12.0
Initial porosity, $\phi_0$ (-)	0.398
Saturated reference permeability at reference porosity $\phi_0$ , $k_0$ (m <sup>2</sup> )	4.5x10 <sup>-27</sup>
Reference porosity for the permeability model, $\phi_0$ (-)	0.14
Model parameter for permeability, $b$ (-)	50
Relative permeability to liquid, $k_{rl}$ (-)	$k_{rl} = S_l^3$
Relative permeability to gas, $k_{rg}$ (-)	$k_{rg} = 1$
Klinkenberg parameter, $b_k$ (MPa)	2.5x10 <sup>5</sup>
van Genuchten water retention parameter $m$ (-)	0.32
van Genuchten entry pressure, $P_0$ (MPa)	30
Residual liquid saturation, $S_{lr}$ (-)	0.1
Residual gas saturation, $S_{gr}$ (-)	0
Grain Specific heat, $C_s$ (J/kg°C)	800
Thermal conductivity, $\lambda_T$ (W/m/K)	$0.5 + S_l(1.3 - 0.5)$

**Table 3.2.4.** Material parameter values of the bentonite buffer used in the dual-structure model (only the parameters of the macrostructure that differ from those used for the BBM model (Table 2.3) are included here) (Sánchez et al., 2012).

Property	Value
Compressibility parameter for stress-induced elastic strain, $\kappa_{ps0}$ (-)	0.079
Compressibility parameter for suction-induced elastic strain, $\kappa_{sp0}$ (-)	0.08
Reference stress state for relating elastic compressibility to suction, $p_{ref}$ (MPa)	0.03
Specific volume at reference stress state $p^c$ in virgin state, $v^c$ (-)	1.4935
Initial void ratio of the macrostructure, $e_M$ (-)	0.35
Initial void ratio of the microstructure, $e_m$ (-)	0.3
Parameter controlling the microstructural soil stiffness, $\alpha_m$ (MPa <sup>-1</sup> )	0.006
Parameter controlling the microstructural soil stiffness, $\beta_m$ (MPa <sup>-1</sup> )	0.0027
Interaction function for microstructural swelling paths	$f_s = 0.8 - 1.1 \tanh[20(p/p_0 - 0.25)]$
Interaction function for microstructural compression paths	$f_c = 1.0 + 0.9 \tanh[20(p/p_0 - 0.25)]$
Saturated reference permeability at reference porosity $\phi_0$ , $k_0$ (m <sup>2</sup> )	$3.0 \times 10^{-23}$
Reference porosity of the macrostructure for the permeability model, $\phi_{M0}$ (-)	0.14

We assume that the intrinsic permeability varies according to an exponential law that was proposed and calibrated against laboratory measurements by Sánchez et al. (2012) for the dual-structure model. This law depends on the porosity of the macrostructure as

$$\mathbf{k} = k_0 \exp[b(\phi_M - \phi_{M0})] \mathbf{I}, \quad (3.2.21)$$

where  $\mathbf{k}$  is the intrinsic permeability tensor,  $k_0$  is the intrinsic permeability at the reference porosity of the macrostructure  $\phi_{M0}$ ,  $b$  is a model parameter and  $\mathbf{I}$  is the identity matrix. For the single-structure BBM model, we adopt the same law, but change macroporosity to total porosity and adjust the value of  $k_0$ , so that the initial permeability is the same in the two cases ( $2.0 \times 10^{-21}$  m<sup>2</sup>). Furthermore, to account for the higher intrinsic permeability of clays to gas than to water (Olivella and Gens, 2000), we make use of the relationship given by Klinkenberg (1941)

$$\mathbf{k}_{gas} = \mathbf{k} \left( 1 + \frac{b_k}{p_g} \right), \quad (3.2.22)$$

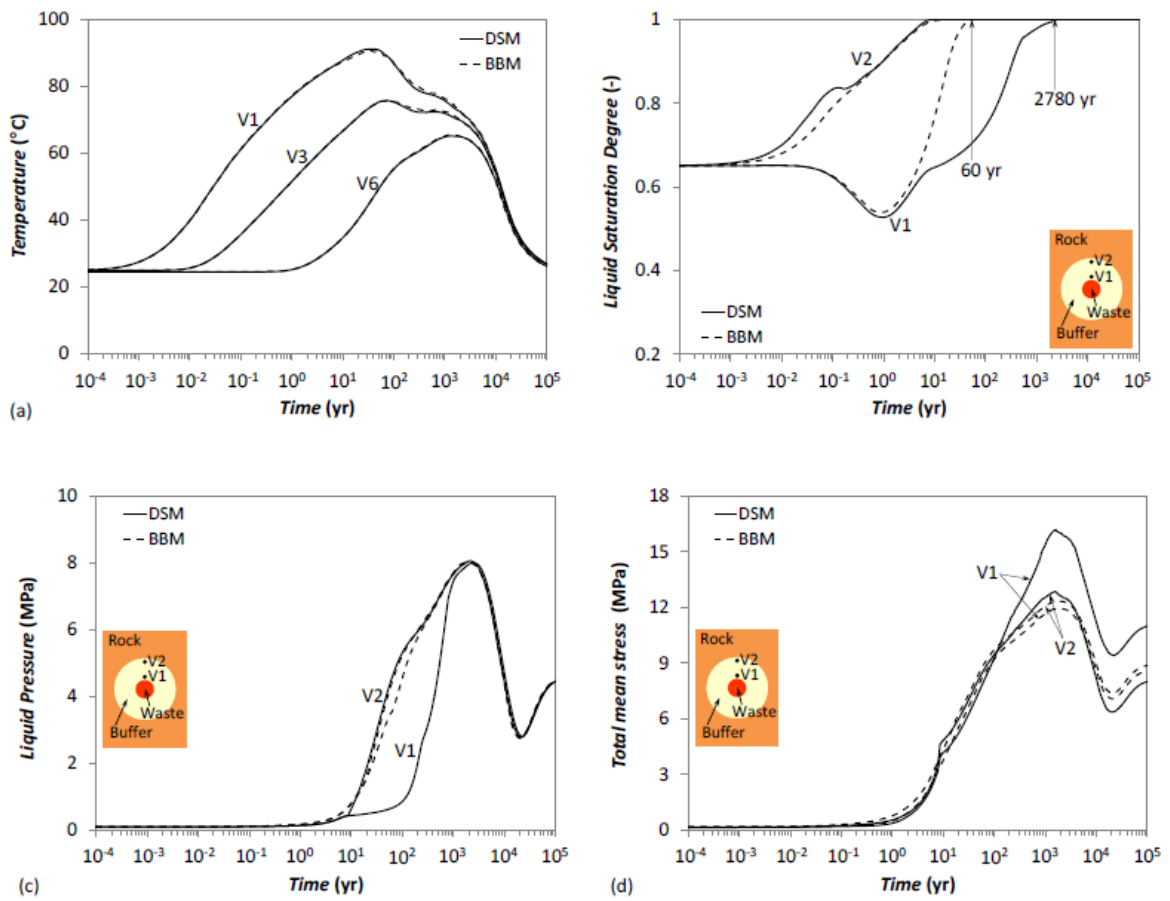
where  $b_k$  is the Klinkenberg parameter.

To calculate consistent initial conditions of the repository once the emplacement tunnel has been excavated and the backfill and the waste placed inside the tunnel, we calculate a sequence of stages. First, we calculate the pre-excavation equilibrium conditions. Mechanically, we assume that the stress field is isotropic and the vertical total stress increases linearly with depth and proportionally to a bulk density of  $24 \text{ kN/m}^3$ . Since the tunnel is located at 500 m depth, the pre-excavation mean stress is 11.8 MPa. The mechanical boundary conditions are no displacement perpendicular to the lateral and bottom boundaries and a constant pressure equal to atmospheric pressure at the upper boundary. Hydraulically, the groundwater table is located at the ground surface. Fluid pressure is imposed at the bottom of the model, at 1000 m depth, and is set to 9 MPa. The ground surface temperature and the temperature at the bottom of the model are fixed to  $10^\circ\text{C}$  and  $40^\circ\text{C}$ , respectively. Thus, the geothermal gradient is equal to  $30^\circ\text{C/km}$ . Next, we simulate the drift excavation by removing the elements in the tunnel and fixing the temperature at  $25^\circ\text{C}$  and the fluid pressure at 0.1 MPa until steady state is reached. Finally, the nuclear waste canister and the bentonite buffer are placed in the tunnel instantaneously, and the waste starts to release heat. The bentonite has an initial liquid degree of saturation of 0.65 and an initial gas pressure of 0.1 MPa.

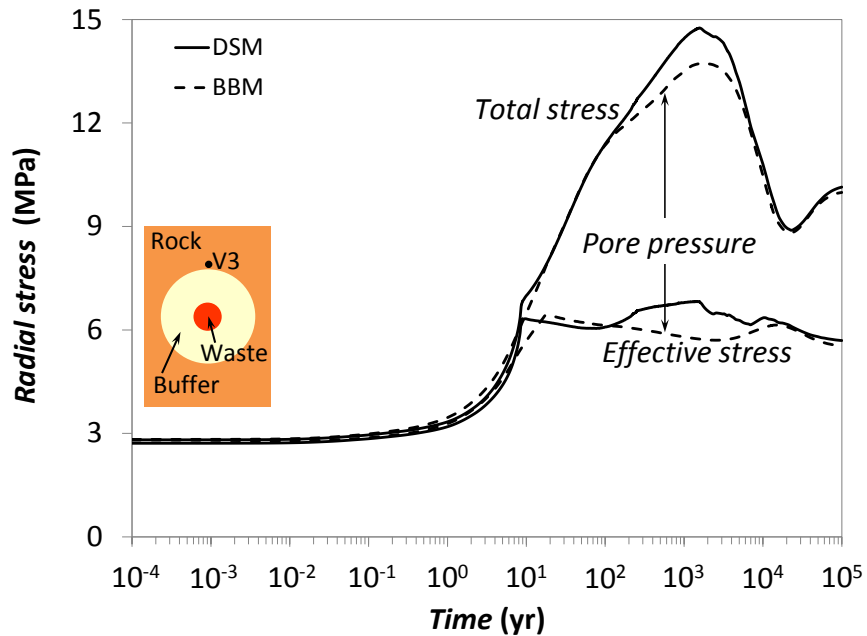
Figure 3.2.6 shows the evolution of temperature, liquid saturation degree, liquid pressure, and total mean stress at some points within the buffer and in the Opalinus Clay, obtained with both the BBM and the dual-structure model. Temperature evolution is similar for both mechanical constitutive models, though the temperature peak is slightly higher close to the canister for the dual-structure model, because the buffer becomes drier than for the standard single-structure BBM (Figure 3.2.6a). However, the hydration of the buffer is significantly affected by the mechanical constitutive model (Figure 3.2.6b). While the buffer close to the canister becomes fully saturated after 60 years for the BBM, it takes up to 2780 years when using the dual-structure model. Though the exact time at which the buffer will become fully saturated is very uncertain (because we do not know with precision all the parameters of the dual-structure model), the difference of two orders of magnitude between the saturation time predicted by the BBM and the dual-structure model shows the importance of using a constitutive model, which accounts for two structural levels to reproduce the thermo-hydro-mechanical behavior of expansive clays. This difference in the saturation time of the buffer occurs because in the dual-structure model, the porosity through which fluid flow occurs is limited to the porosity of the macrostructure and not the total porosity, as in the BBM. The deviation in the saturation evolution in the inner part of the buffer between the two models starts at early times (2–3 years), which is in agreement with the observations of the 10-year-long mock-up test for the FEBEX *in situ* test performed at the laboratory at CIEMAT, Madrid (Spain) (Sánchez et al. 2012). Furthermore, the delay in the saturation of the bentonite buffer causes a delay in its pressurization close to the canister (Figure 3.2.6c). Despite this significant delay in saturation at the inner parts of the buffer, the overall buffer swelling stress evolution is not severely retarded (Figure 3.2.6d). Indeed, the buffer is still functioning to provide sufficient swelling and support load to the tunnel wall and the EDZ (Figure 3.2.7).

Figure 3.2.8 displays the variables that control the dual-structure constitutive model, i.e., suction, mean net stress and effective stress. While suction and mean net stress are used to calculate the behavior of the macrostructure according to the BBM, the mean effective stress determines the elastic volumetric strain of the microstructure in the dual-structure model. Suction close to the tunnel wall decreases from the beginning of the simulation, because the host rock, which is fully saturated, supplies groundwater that gradually saturates the bentonite buffer (Figure 3.2.8a). However, suction initially increases close to the canister because the heat of the high-level nuclear waste dries the bentonite. Subsequently, the saturation of the entire bentonite buffer starts to take place, and suction decreases. The net mean stress (Figure 3.2.8b) is similar for both models close to the tunnel wall, because of the relatively quick saturation of this part of the buffer, which leads to a comparable high stiffness of the expansive clay (Figure 3.2.8d). However, close to the canister, the net mean stress becomes much higher for the dual-structure model than for the BBM, because the higher suction (recall Figure 3.2.8a) leads to a stiffer bentonite (Figure 3.2.8d). The effective mean stress evolution (Figure 3.2.8c) is similar to the suction evolution because the net mean stress is relatively low.

Figure 3.2.9 illustrates porosity evolution for simulation results of both constitutive models. The total porosity changes, though larger in the dual-structure model, are relatively similar for both models, especially in the region of the buffer close to the tunnel wall. However, a higher porosity reduction occurs close to the waste overpack, where a stronger drying takes place when accounting for the dual-structure model. Interestingly, the reduction in macroporosity is larger than the reduction in total porosity close to the waste overpack. This larger macroporosity reduction in the dual-structure model leads to a greater permeability reduction close to the waste overpack that impedes hydration of the buffer (Figure 3.2.10).



**Figure 3.2.6.** Evolution of (a) temperature (see Figure 3.2.5 for the location of the observation points), (b) liquid saturation degree, (c) liquid pressure and (d) total mean stress for the dual-structure model (DSM) and the standard single-structure Barcelona Basic Model (BBM).



**Figure 3.2.7.** Evolution of the total and effective radial stress at point V3 located at the tunnel wall for the dual-structure model (DSM) and the standard single-structure Barcelona Basic Model (BBM).

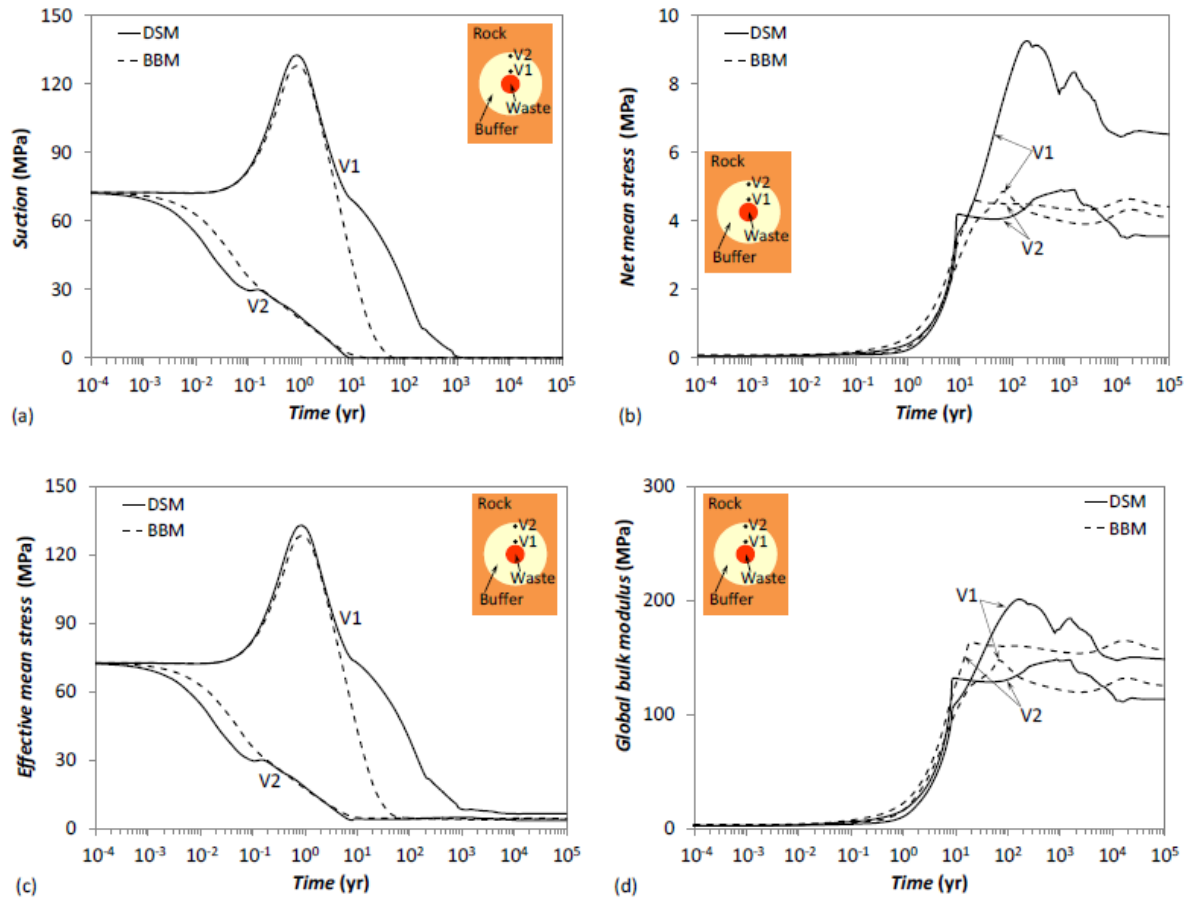


**Figure 3.2.8.** Evolution of (a) suction, (b) net mean stress, (c) effective mean stress and (d) global bulk modulus for the dual-structure model (DSM) and the standard single-structure Barcelona Basic Model (BBM).

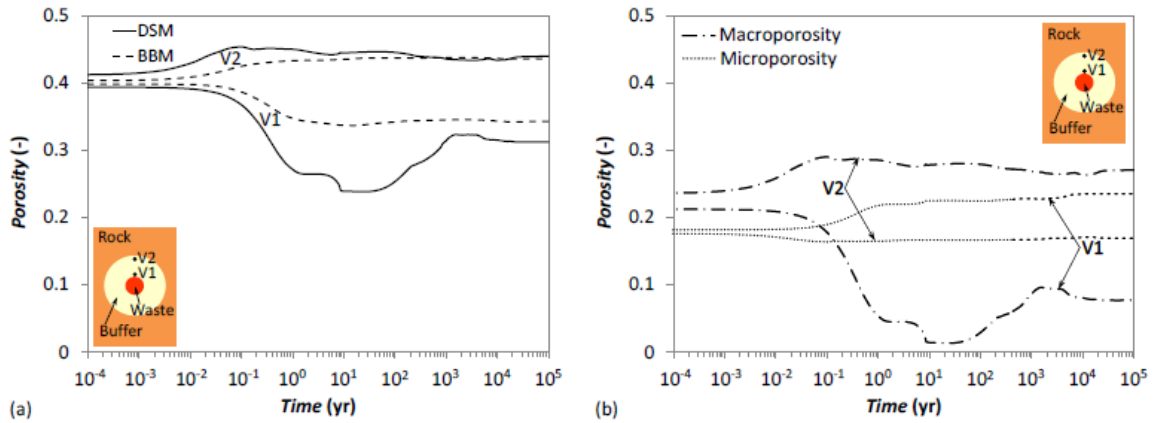


**Figure 3.2.9.** (a) Total porosity evolution for the dual-structure model (DSM) and the standard single-structure Barcelona Basic Model (BBM). (b) Macroporosity and microporosity evolution of the dual-structure model.

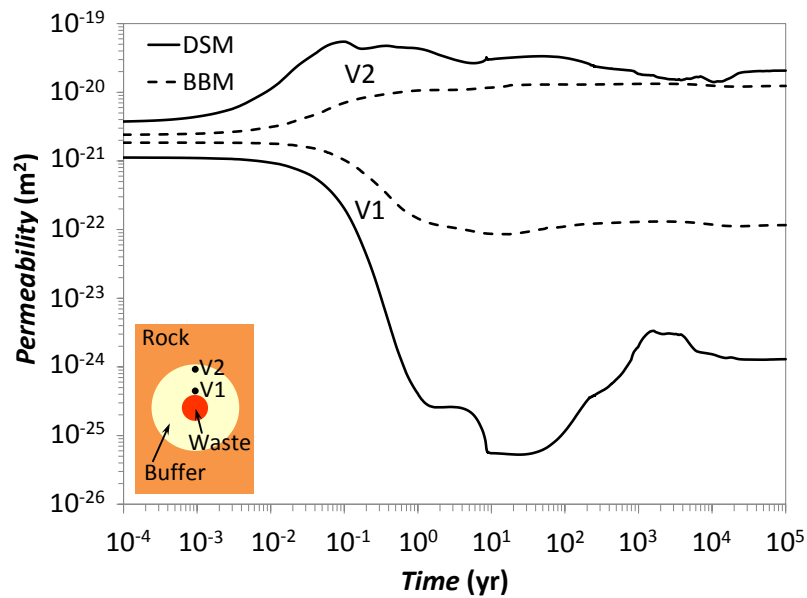


**Figure 3.2.10.** Permeability evolution for the dual-structure model (DSM) and the standard single-structure Barcelona Basic Model (BBM). Permeability is a function of the macroporosity in the dual-structure model.

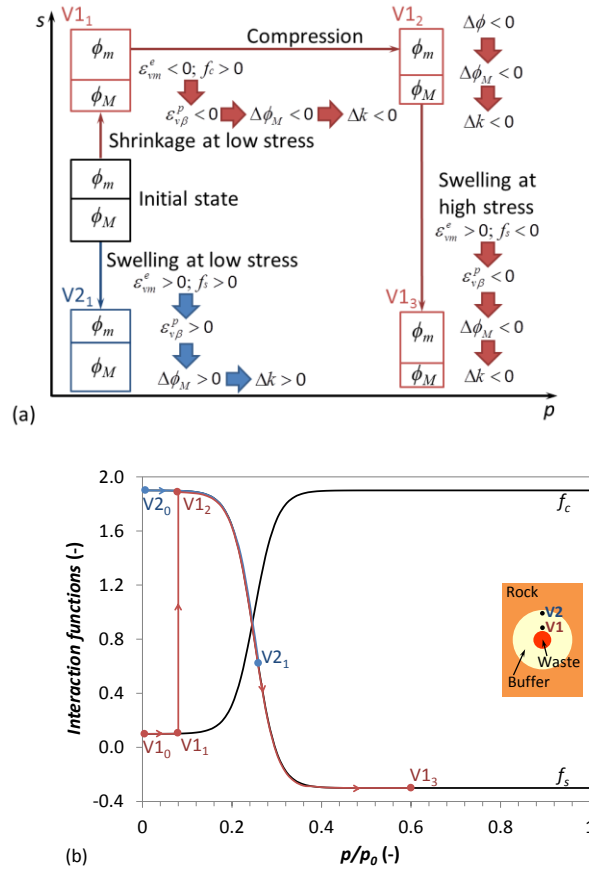


**Figure 3.2.11.** (a) Schematic evolution of the microporosity, macroporosity, plastic strain of the macrostructure due to micro/macrostructure interaction and permeability and (b) evolution of the interaction functions for a point close to the canister (V1) and a point close to the tunnel wall (V2).

Figure 3.2.11 schematically illustrates the evolution of the microporosity and the macroporosity at a point close to the canister and at another point close to the tunnel wall. The expansive clay close to the tunnel wall becomes saturated at a low mean stress. Thus, both the microstructure and the macrostructure swell (strain is positive) and since the interaction function of swelling at low stress is positive (Figure 3.2.11b), the plastic strain of the macrostructure due to interaction between the two structural levels is positive, i.e., the macrostructure expands (Figure 3.2.11a). Therefore, the permeability of the clay increases and full saturation occurs relatively quickly. On the other hand, close to the canister, the buffer dries during the first year of simulation, leading to shrinkage at low stress (strain is negative). In this case, since the interaction function of shrinkage at low stress is positive, the plastic strain of the macrostructure due to interaction between the two structural levels is negative, which implies shrinkage of the macrostructure and therefore, a permeability reduction. Later, the permeability is reduced even further because the mean stress of the buffer increases, which causes a compression of the pores. Finally, the region around the canister is saturated at high stress. Under these conditions,

the microstructure swells (strain is positive), but the interaction function of swelling at high stress is negative (Figure 3.2.11b). As a result, the plastic strain of the macrostructure due to interaction between the two structural levels is negative, i.e., the macrostructure shrinks. This shrinkage of the macrostructure is caused by an invasion of the microstructure, which closes the macropores when the expansive clay swells at high stress, contributing to reduce the permeability. This greater permeability reduction around the waste overpack when using the dual-structure model causes a significant delay in the time at which the buffer becomes fully saturated. These results are in agreement with those of Sánchez et al. (2012), who modeled a large-scale heating test—a mock-up test that lasted for 10 years for the FEBEX *in situ* test—performed in the laboratory. Their modeling results reproduce the experimentally observed delay of the saturation of the buffer in the short-term when using the dual-structure model instead of the BBM. In our study, we show how such a delay might affect the long-term THM evolution of a repository.

### 3.2.4 Coupled CM coupling through dual-structure model

To date we have considered and applied several CM coupling approaches, including an empirical model wherein we consider swelling stress caused by changes in ionic concentration and smectite volume fraction, and another approach in which the microstructural strain in the dual-structure model depends on the concentration of each exchangeable cation. The first model has been applied to simulate the effects of illitization on swelling pressure at high temperatures. This work and simulation results are presented in the upcoming FY2014 milestone report “Investigation of Coupled Processes and Impact of High Temperature Limits in Argillite Rock.” The second approach wherein microstructural strain is dependent on each exchangeable cation concentration was already demonstrated in a TOUGHREACT-FLAC modeling example presented in the FY2013 milestone report. In this report, the effect of ionic strength (or total ion concentration) on bentonite swelling and abundance of smectite has been implemented into the dual-structure model. The mathematical formulations for CM coupling are summarized below.

When CM coupling is considered, the dependence of microstructural volumetric strain on the change in the microstructural effective stress,

$$d\varepsilon_{vm}^e = \frac{f_s}{K_m} d\hat{p}, \quad (3.2.23)$$

where  $\hat{p} = p + s_m$ ,  $p$  is the effective mean stress; and  $s_m$  is the microstructural suction.  $f_s$  is the mass fraction of smectite in bentonite.  $K_m$  is given in Equations (3.2.13a and 3.2.13b).  $s_m$  has two components, matric suction,  $s$ , and osmotic suction,  $s_o$ , i.e.  $s_m = s + s_o$ . The effect of ionic strength of the pore water on microstructural strain is carried out via the osmotic suction, which is computed as:

$$s_o = -10^{-6} \frac{RT}{V_w} \ln(a_w), \quad (3.2.24)$$

where  $V_w$  is the molar volume of water (in  $\text{m}^3/\text{mol}$ ), and  $a_w$  is the activity of water.  $a_w$  is calculated in TOUGHREACT (Xu et al. 2011) as follows,

$$\ln(a_w) = -\Phi m^* \frac{1}{55.51}, \quad (3.2.25)$$

where  $\Phi$  is osmotic coefficient of the solution and  $m^*$  is the sum of the molalities of all species in solution.

The effect of exchangeable cations is linked to mechanics through the dependence of  $\beta_m$  (see Equation 2.24) on exchangeable cation concentration as shown in the following equation (Gens 2010):

$$\beta_m = \sum_i \beta_m^i x_i, \quad (3.2.26)$$

where  $x_i$  is the equivalent fraction of the exchangeable cation,  $i$ , ranging from 0 to 1, and  $\beta_m^i$  is the parameter that control the microstructure stiffness and defined for each of the exchangeable cations.

As shown in Equation (2.24), the larger the  $\beta_m$ , the more soil swells, and the soil is softer. Gens (2010) and Guimarães et al. (2013) proposed that  $\beta_m^i$  is proportional to the ionic hydrated radius and inversely proportional to its valence, and typically  $\beta_m^{Li} > \beta_m^{Na} > \beta_m^K$  and  $\beta_m^{monovalent} > \beta_m^{bivalent}$ . If this is true, one could infer that Na-smectite which contains exclusively Na in the interlayer space should swell more than Ca-smectite, provided that other conditions are the same. However, experimental results seem to be controversial.

Likos and Wayllace (2010) reported that “Water uptake, volume change, and swelling pressure were all more significant for Colorado ( $\text{Ca}^{2+}/\text{Mg}^{2+}$ ) bentonite than for Wyoming ( $\text{Na}^+$ ) bentonite.” Their results seem to support that Ca-Mg smectite exhibits more swelling than Na smectite. However, when two different types of bentonite are compared, material compositional differences between the bentonites can impact the results. Note that exchangeable cations in Colorado bentonite are dominated by Ca and Mg with 59% Ca and 38% Mg, whereas exchangeable cations in Wyoming bentonite are composed of 59% Na, 36% Ca and 5% Mg—Wyoming bentonite still contains a considerable amount of exchangeable Ca. Several facts have to be considered when the study by Likos and Wayllace (2010) is used as an example that Ca-Mg smectite exhibits more swelling than Na smectite. First, Colorado bentonite contains more smectite (90%) than Wyoming bentonite (70–90%). Second, in the free-swelling test, the Colorado bentonite is not

compacted to the same density as Wyoming bentonite. As shown in Figure 3.2.12 (the same as Figure 4 in Likos and Wayllace 2010), Colorado bentonite has an initial porosity ratio of 0.83, whereas Wyoming bentonite has an initial porosity ratio of 0.88. Because the higher degree of compaction (higher density) leads to the larger strain, the difference in initial density contributes the higher swelling of Colorado bentonite. Third, the comparison between Ca-exchanged Wyoming bentonite and untreated Wyoming bentonite reflects the effect of exchangeable cations on the swelling. Both samples have the same density, but one is 59% Na (untreated) and another is supposed to have 100% Ca. However, as shown in Figure 3.2.12(c), Ca-exchanged Wyoming bentonite actually swells less than untreated Wyoming bentonite.

Ironically, it is very well known that Na-smectite swells more than Ca-smectite. Mitchell and Soga (2005) state that “sodium and lithium montmorillonite may undergo almost unrestricted interlayer swelling provided water is available, the confining pressure is small, and the electrolyte concentration is low. On the other hand, divalent and trivalent forms of montmorillonite do not expand beyond a basal spacing of about 17 Å and form multi-particle clusters or aggregates, regardless of other environmental factors.”

To support the negative correlation of  $\beta_m$  with the valence of exchange cations, Guimarães et al. (2013) cited the work by Sridharan et al. (1986), who conducted a series of one-dimensional consolidation tests with homoionized bentonite. The initial moisture contents of samples are approximately 50% of the liquid limit. Since the Na-smectite has much higher liquid limit than Ca-smectite, the initial water content for different homoionized bentonite are very different, e.g., 257% for Na-bentonite and 89% for Ca-bentonite. As a result, the initial void ratios are different. To obtain a compressibility curve starting from the same point, the total compression at the end of each load increment ( $\delta$ ) is divided by the height of the soil solid ( $H_s$  as a percentage). Figure 3.2.13 (the same as Figure 4 in Sridharan et al. 1986) clearly shows that monovalence ions lead to more swelling than bivalence ions.

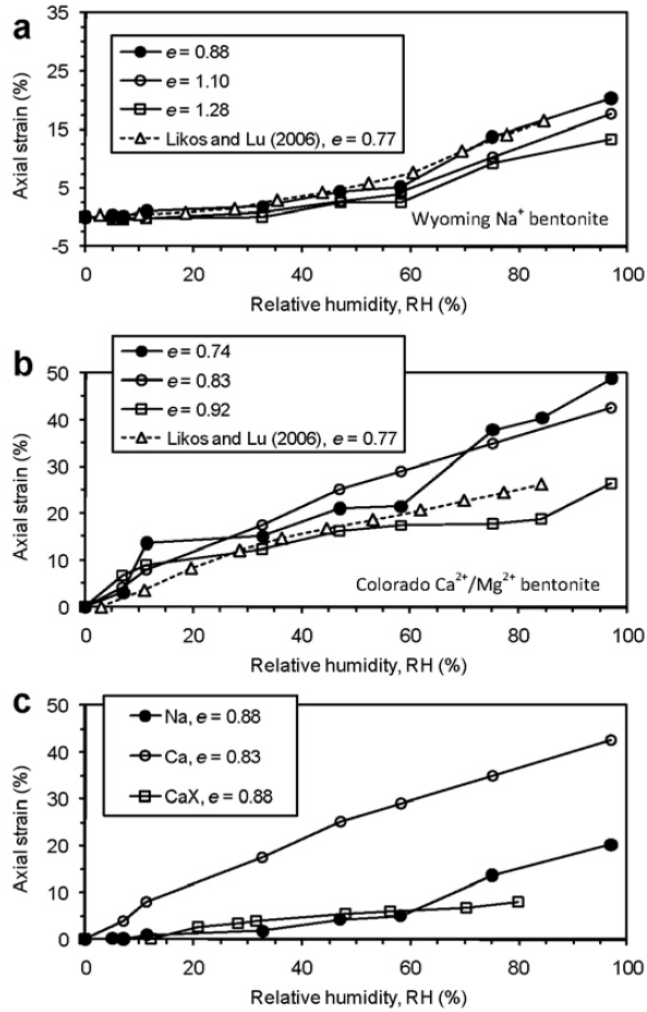


**Figure 2.12.** Axial-strain response measured along hydration paths under free swelling conditions: (a) Wyoming bentonite, (b) Colorado bentonite, (c) Wyoming, Colorado, and Ca<sup>2+</sup>-exchanged Wyoming bentonite (denoted CaX) (the same as figure 4 in Likos and Wayllace 2010).

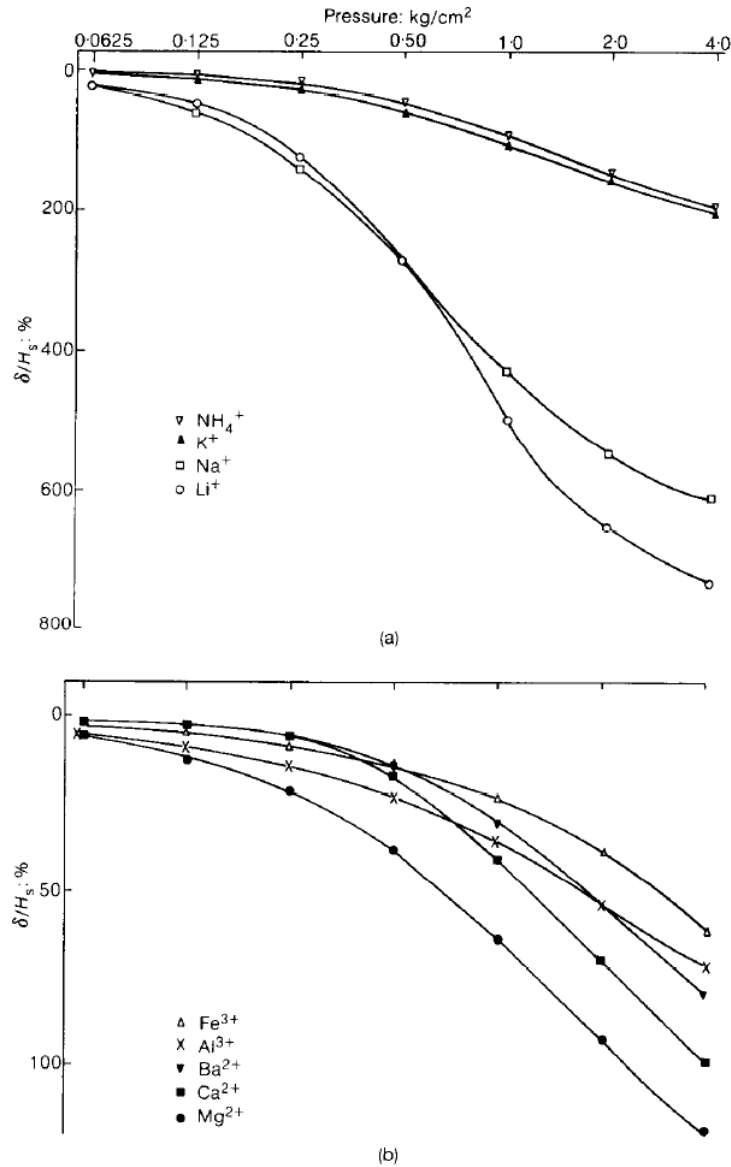


**Figure 3.2.13.** Percentage compression-pressure plots: (a) for monovalent bentonites; (b) for divalent and trivalent bentonites (Sridharan et al. 1986).

Similar experiments were also conducted in Di Maio (1996; 1998). In a series of conventional oedometer tests with Ponza bentonite (mainly composed of Na-smectite) having initial water content close to the liquid limit, specimens were exposed to saturated solutions ( $\text{NaCl}$ ,  $\text{KCl}$ , and  $\text{CaCl}_2$ ) with different concentrations. Then the void ratio versus effective stress and the volumetric strain change with time were measured. The following observations are fairly clear from the compression of saturated bentonite samples: (1) bentonite with higher valence cations has a low liquid limit and plastic limit, which is very well known by the soil mechanics community. Likos and Wayllace (2010) even use this as a confirmation of whether the bentonite is Ca-Mg bentonite or Na-

bentonite. It is also known that the more plastic the mineral, the more potential swelling and shrinkage (see p. 103 in Mitchell and Soga, 2005). So qualitatively, it seems that bentonite with higher valence cations has a lower swelling potential than bentonite with monovalence (but  $K^+$  might be an outlier).

After examining the published data, we propose the following equation to estimate  $\beta_m^i$  :

$$\beta_m^i = \kappa r^i / v^i, \quad (3.2.27)$$

where  $\kappa$  is a constant that has to be calibrated and  $r^i$  is hydrated radii of the cation and  $v^i$  is the valence of the cation. Equations (3.2.22) to (3.2.27) have been implemented in TOUGHREACT-FLAC and further testing will be conducted in the future.

The CM coupling through the dual-structure model represents the microscopic physical and chemical processes related to the swelling of bentonite. Therefore, it is likely to provide a more accurate prediction of the swelling behavior of bentonite under simultaneous heating, hydration, and chemical alteration as undergone by the EBS bentonite in a typical repository. However, validating such CM coupling by experimental data is quite difficult, because there are few measurements. Experiments that can be used to validate the CM coupling should at least have the following conditions: (1) the dual-structure BExM has been used to calibrate the stress/strain evolution, (2) hydrological conditions are measured, and (3) chemical conditions, including both the aqueous solution and solid phase, must be known. Based on our recent current literature survey, no published experiments have been conducted that capture all of these aspects.

### 3.2.5 Conclusions

We are developing and applying coupled THMC models for the analysis of EBS coupled processes in bentonite-backfilled repositories. We base this development on the extension of the Barcelona Basic Model (BBM) to a dual-structure model for expansive clay, such as bentonite. We have implemented the dual-structure model into TOUGH-FLAC and have tested the model against literature data from experiments and independent models. We have shown the capabilities of the dual-structure model by modeling and reproducing observed behavior for two laboratory tests performed by Pousada (1982) on expansive clay under increasing confining stress. The simulations yielded irreversible strain accumulation upon suction cycles and a decreasing swelling capacity as the confining stress increases, in agreement with Pousada's (1982) laboratory observations.

We have completed model simulations of a generic high-level nuclear waste repository with waste emplacement in horizontal tunnels backfilled with expansive clay and hosted in a clay-rock formation. To our knowledge, this the first time a dual-structure model has been applied to model coupled THM processes of a repository over a 100,000-year time period. We compared the THM results of the dual-structure model with those of the standard single-structure BBM, showing the importance of considering the dual-structure behavior of the expansive soil material when modeling the THM behavior of a nuclear waste repository involving a protective bentonite buffer. The main difference between the

two models is that the dual-structure model predicts that the time for full saturation of the expansive clay is on the order of thousands of years, while the BBM yields a time on the order of tens of years. The numerical simulation shows that this delay is caused by the fact that the fluid flow conducting macrostructure is invaded by the microstructure, with associated reduction in permeability for water flow. Such a delay has previously been observed in large-scale laboratory and *in situ* experiments; here we show this might affect the long-term performance of a repository. However, the modeling results also showed that despite a significant delay in saturation along the inner parts of the buffer, the overall buffer swelling stress evolution was not severely retarded. That is, the buffer is still functioning to provide sufficient swelling and support load to the tunnel wall and the EDZ.

We also upgraded the chemical and mechanical (CM) coupling scheme based on the dual-structure model for expansive clay. Now the microstructural swelling depends not only on the concentration of exchangeable cations, as implemented in FY2013 report (Davis et al., 2013), but also on the mass fraction of smectite and the ion concentration of pore water. This coupling scheme was implemented in coupled THMC code TOUGHREACT-FLAC3D, but it needs to be validated with experimental data, and its effect on the long-term THMC behavior of EBS bentonite will be evaluated through THMC models that adopt the dual-structure model and the upgraded CM coupling scheme in the future. Moreover, another CM coupling not considered to date is the effects of silica precipitation (cementation) on the mechanical behavior of the bentonite buffer. It is expected that cementation could make the buffer brittle, i.e., prone to fracturing when exposed the thermal stresses. This is another CM process that we will explore in the future.

### 3.3 ION ADSORPTION AND DIFFUSION IN SMECTITE CLAY BARRIERS

The long-term management of nuclear waste repositories requires reliable predictions of diffusion through waste-containment barriers, such as compacted bentonite. For clays, cation diffusion processes are influenced by: (1) the electrical charge of the diffusing solute, (2) the degree of compaction, and (3) the electrical double-layer structure at the clay/water interface. Most currently available diffusion models do not specifically include the expected changes in metal-diffusion rates due to these variations. A “decoupling” of parameters and processes is necessary to ensure an accurate prediction of apparent diffusion rates under the chemical gradients expected within engineered barrier systems.

In order to achieve this goal, laboratory-scale diffusion experiments were performed, and in collaboration with colleagues, the data were described by reactive diffusive transport of calcium and bromide through lightly compacted montmorillonite.

#### 3.3.1 Background

Smectite minerals are swelling clay minerals that have the form of flake-shaped particles, that are ubiquitous in soils and sedimentary environments, with a mica-like structure and

characteristic dimensions on the order of 1 nm in thickness and ~200 nm in diameter (Tournassat et al. 2003). Because of their high specific surface area and cation exchange capacity, these natural “nano”-particles can strongly influence the geochemistry, mass-transfer properties, and mechanics of porous media in which they are present. For example, smectites play key roles in the isolation of landfills and high-level radioactive waste repositories (Altmann et al. 2012).

A recurrent theme in studies of the properties of smectite-rich media is the existence of strong couplings between their chemistry, mechanics, microstructure, and transport properties. These couplings are thought to arise because the pore width in clayey media is similar to the thickness of the electrical double layer (EDL), the interfacial region in which surface charge is screened by counter-ion adsorption and co-ion exclusion. According to the well-known Gouy-Chapman theory, the co-ion exclusion distance, a measure of the thickness of the EDL, equals twice the Debye length  $\kappa^{-1}$ , or about 6 nm and 2 nm at  $T = 298$  K for a 1:1 electrolyte at ionic strengths ( $I$ ) = 0.01 and 0.1, respectively, whereas a large number of the pores have a size of ~1 to 10 nm in clay shales and engineered clay barriers (Holmboe et al., 2012). Because of this similarity between pore width and EDL thickness, much of the pore water in smectite-rich media has properties distinct from those of bulk liquid water.

Current theories of the couplings between chemistry, transport, and mechanics in clayey media consistently use a conceptual model of overlapping EDLs in a single slit-shaped pore between parallel, uniformly-charged clay surfaces (Figure 3.3.1). Within this conceptual framework, a widely accepted model of the pore-scale details has yet to emerge. The simplest models assume that all pores have the same width and that the EDL consists only of a diffuse ion swarm interacting with the surface through long-range, nonspecific interactions. The resulting models have a single adjustable parameter, the geometric factor  $G$ . These simple models can qualitatively predict the coupled properties of compacted smectite clay barriers, but their quantitative agreement with experimental data is quite poor.

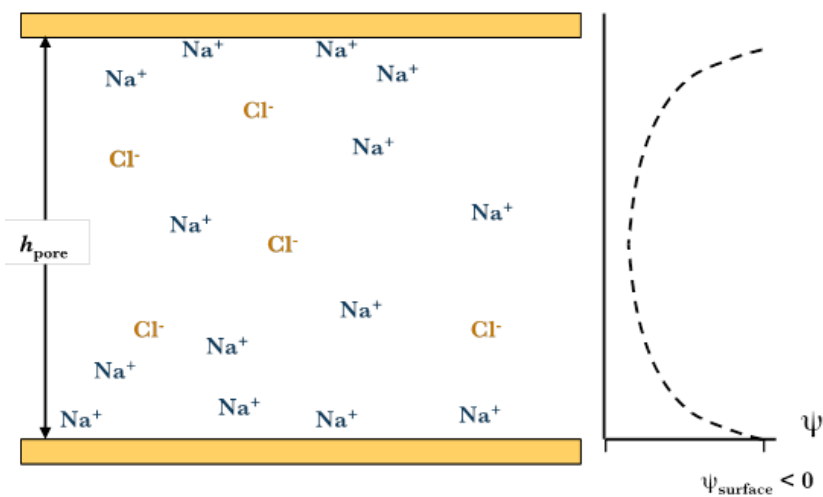


**Figure 3.3.1.** Pore-scale conceptual model used by models of coupled phenomena in compacted smectite clay barriers.

The persistence of very different models suggests that available macroscopic-scale data do not strongly constrain current theories of the properties of clay barriers. The present situation results from several challenges. The first challenge is that the microstructure of clay barriers is arduous to characterize with sufficient resolution to constrain existing models. X-ray diffraction techniques can detect the smallest pores present in smectite clay barriers (crystalline hydrates with a pore width of 0.3 to 0.9 nm) as well as some larger-scale features such as osmotic hydrates and interstratified stacking arrangements, but they provide limited information on larger-scale stacking arrangements, and they may be sensitive to sample preparation techniques. Electron microscopy techniques are not yet able to probe the microstructure of hydrated compacted clay on the length scale of the smallest pores, because of difficulties associated with beam damage and microstructural changes during sample drying. The second challenge is that the structure of the EDL in clayey media has never been directly observed: existing models are based on theoretical calculations, Monte Carlo simulations, and molecular dynamics (MD) simulations.

Despite these limitations, it is possible to test the plausibility of a series of pore models by carefully evaluating the physical meaning of their related fitting parameters on a single set of data. It must be noted that the many published models have not yet been benchmarked on a single and relevant set of data. In last year's EBS report, we presented new macroscopic-scale measurements of the adsorption and diffusion of trace levels of  $\text{Ca}^{2+}$ ,  $\text{Br}^-$ , and HTO in a loosely compacted water-saturated Na-montmorillonite, a smectite mineral that is the main constituent of the bentonite used for engineered clay-barrier applications. In this report these data are modeled using a multicomponent reactive transport (diffusion) approach with various conceptual models to describe the electrical double layer, anion-accessible porosity, and other properties of interlayer pore structure. In addition, MD simulations are presented of adsorption and diffusion in

individual clay interlayer nanopores, carried out under similar conditions (solid-liquid ratio, electrolyte composition) as the laboratory diffusion experiment. These results allow us to critically evaluate the ability of various EDL models to link molecular and macroscopic-scale adsorption and diffusion in compacted smectite.

Calcium was selected for the diffusion experiment in Na-montmorillonite, due to its relevance for U(VI) solution speciation and sorption behavior (Davis et al. 2013). Impurities of calcium minerals have to be expected, both in the bentonite buffer as well as the bordering cement-based layer in engineered barrier systems. Hence, a calcium concentration gradient and the diffusive transport of Ca within barrier systems are very likely. At this point, only a few diffusion studies have been performed for Ca in bentonite; data for Ca diffusion in Na-montmorillonite is even more scarce (Kozaki et al. 2001). However, these data will be very relevant for the interpretation of uranium(VI) diffusion behavior in Na-montmorillonite at varying Ca concentrations. Furthermore, using calcium bromide as a salt allowed us to study the diffusion behavior of a fairly nonreactive anion (bromine) in a sodium chloride background electrolyte solution.

### **3.3.2 Experimental and modeling methods**

#### ***Materials***

Acids, bases, and salt solutions used in experiments were of TraceSelect (Sigma Aldrich) or a comparable grade in order to minimize calcium background concentrations. Aqueous solutions were prepared with Nanopure water (Barnstead ultrapure water system).

A commercially available, well-characterized and standardized source clay (Na-montmorillonite, SWy-2, Clay Minerals Society) was selected in order to allow for a subsequent comparison with other data from the literature. The material is known to contain considerable amounts of impurities, such as quartz (8%), feldspars (16%), and calcite. The clay was pretreated to remove major mineral impurities, and to minimize a potential calcium release due to calcite dissolution during experiments.

#### ***Calcium bromide through-diffusion experiment***

The calcium bromide through-diffusion experiment largely followed procedures previously described in detail in the literature (Molera and Eriksen 2002). The experimental setup consisted of the diffusion cell containing the clay packing, the high-concentration and low-concentration reservoirs, the tubings and fittings connecting the reservoirs with the diffusion cell, and a peristaltic pump. All solutions used in the experiment were repeatedly adjusted to pH 7 using small volumes of acid/base solutions (TraceSelect grade NaOH and HCl) prior to their contact with the mineral phase.

At the beginning of the experiment, a weighed aliquot of dry, Na-montmorillonite was packed into the “ring-like” component of the diffusion cell (PEEK, D=1.0 cm, L=0.5 cm) to give the desired dry density ( $\sim 1.0 \text{ g/cm}^3$ ). The clay packing was contained between stainless-steel metal filters and carefully compacted with a custom-made PEEK rod. Then, high-concentration (200 mL) and low-concentration (20 mL) reservoirs were filled with background electrolyte solution (0.1 M NaCl, pH=7), and the clay was saturated

with electrolyte by circulating the solutions through the cell with a peristaltic pump (0.7 mL/min) for about 4.5 weeks.

After clay saturation, the solution in the high-concentration reservoir was exchanged for a background electrolyte containing 1 mM  $\text{CaBr}_2$ , and the solution in the low-concentration reservoir was replaced with a 20 mL aliquot of fresh,  $\text{CaBr}_2$ -free electrolyte. Over the following weeks, the circulation of solutions through the diffusion cell was continued at the same flow rate. However,  $\text{CaBr}_2$ -free background electrolyte solutions in the low-concentration reservoir were continuously exchanged by replacing reservoir vials. This provided a nearly constant concentration gradient between high- and low-concentration reservoirs. The vials were weighed to correct for volume losses due to evaporation, sampled for Ca and Br analysis by IC and FIA analysis, respectively, and pH values were measured. Small volumes (1.5 mL) of the high-concentration reservoir solution were repeatedly sampled for Ca and Br analysis, in order to monitor solute concentrations and determine the concentration gradient over the course of the experiment. This procedure was continued until the diffusive fluxes for both Ca and Br reached steady-state conditions, and a series of data points were then collected at steady state.

After reaching steady-state conditions for Ca and Br diffusion, the solution in the high-concentration reservoir was replaced with a  $\text{CaBr}_2$ -free background electrolyte solution containing approximately 1000 Bq/mL (27 nCi/mL) of tritiated water (HTO). As before, low-concentration reservoir solutions were continuously replaced, and tritium activities analyzed by liquid scintillation counting until the diffusive flux of HTO had reached steady-state conditions.

#### ***Determination of anion-accessible porosity***

Preliminary modeling results showed a difference between the diffusion-accessible porosity of packed Na-montmorillonite for tritiated water (HTO) and the anion (bromide). A separate experiment was conducted in order to experimentally determine the anion-accessible porosity. For this experiment, the same setup and procedures were used except that the diffusion cell was connected to two large (200 mL), high-concentration (0.1 M NaCl, 0.002 M NaBr) reservoirs at the beginning of the experiment. The background electrolyte (0.1 M NaCl, pH=7) and the bromide concentration (0.002 M Br as NaBr) were the same as in the through-diffusion experiment described above.

After equilibrating the clay with the reservoir solutions, the wet clay packing was extruded and dried at 150°C to determine its water content by weight difference and compute the exact dry density. After grinding the clay, bromide was extracted based on the procedure of Glaus et al. (2010). Weighed aliquots of Na-montmorillonite were mixed with 10 mL of Nanopure water. After mixing for 3 days, the suspensions were centrifuged, and the resulting supernatant solutions filtered with 0.2  $\mu\text{m}$  filters (first 1 mL discarded). The solutions were analyzed for bromide concentrations by ICP.

#### ***Multi-component transport modeling***

The diffusion data were modeled using PHREEQC v3.0 in a 1D geometry using the multi-component diffusion (MCD) capabilities of the code and in collaboration with C.

Tournassat (BRGM, France). Diffusion coefficients of individual chemical species were taken from the PHREEQC.dat database. No temperature correction was done. Filter diffusion properties were explicitly taken into account as well as the dead-volume at the end of the experimental device. Filter transport parameters were derived from a previous study (Molera et al. 2003), because the same material was used in this study:  $\theta_f = 0.25$ ,  $G = 2.33$ , height = 0.082 cm. Molera and co-workers found identical  $G_f$  values for  $\text{Na}^+$ ,  $\text{Cs}^+$  and  $\text{Sr}^{2+}$  diffusion, and we considered that diffusion parameters of the filters were identical for all chemical species. Details of the system geometry are given in Figure 3.3.2. Constant concentrations of tracers were assigned to the upper reservoir. The renewal of the lower reservoir at each sampling time has a non-negligible effect on the diffusion gradient and thus on the recorded fluxes (Glaus et al. 2013). This effect was fully taken into account during the simulation: tracers accumulated as a function of time in the numerical cell representative of the lower reservoir; this numerical cell was reset to a zero concentration for tracers at each sampling time, and the simulation was restarted. The solution in the dead-volume was not reset to a zero concentration, thereby mimicking the “storage” effect of the solution in the tubing of the peristaltic pump. Using this calculation method, the calculated concentrations in the lower reservoir could be compared directly to the measured concentrations at each sampling time without any data pre-treatment.

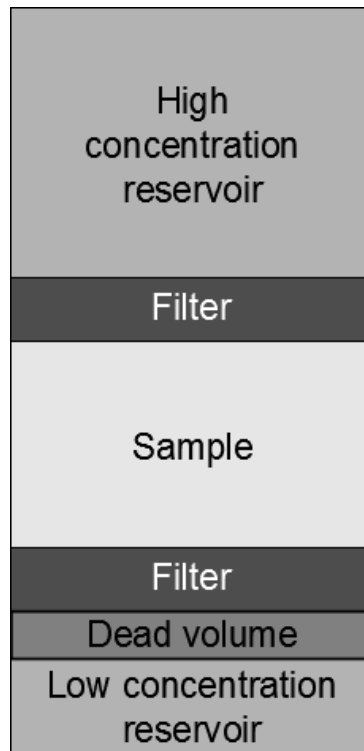


**Figure 3.3.2.** Sketch of the modeled diffusion cell system.

### *Molecular dynamics simulations*

MD simulations of Na-Ca-Cl-Br aqueous solutions confined in a 31.5 Å wide nanopore between parallel smectite basal surfaces were carried out as in the previous research of Holmboe and Bourg (2014), in collaboration with M. Holmboe (Uppsala University, Sweden). The methodology is known to accurately predict the diffusion coefficients and activation energies of diffusion of water and sodium in smectite interlayer nanopores for pore widths ranging from 0.3 to 30 Å and temperatures ranging from 278 to 353 K (Holmboe and Bourg 2014). In brief, simulations were carried out with the program LAMMPS. Inter-atomic interactions were described with the SPC/E water model of liquid water and the CLAYFF model of mineral-water interactions. Water molecules were kept rigid using the SHAKE algorithm. Production runs were carried out in the *NVT* ensemble (constant composition, volume, and temperature) using two different initial configurations for a total duration of 105 ns (with a 1 fs time step) and were preceded by 1 ns of equilibration in the *NPT* ensemble (at  $P = 1$  bar) and 5 ns of equilibration in the *NVT* ensemble. Electrostatic and dispersion interactions beyond 12 Å were computed with the particle-particle particle-mesh (PPPM) solver. Two-dimensional diffusion coefficients ( $D_{\text{pore}}$ ) in the  $xy$  plane of the interlayer nanopores were calculated with the well-known Einstein relation:

$$D_{\text{pore}} = \frac{1}{2n} \lim_{\tau \rightarrow \infty} \frac{d\langle l^2 \rangle}{d\tau} \quad (3.3.1)$$

where  $n = 2$  for diffusion in the  $xy$  plane, and  $\langle l^2 \rangle$  is the mean-square displacement of the species of interest as a function of time  $\tau$ . The infinite-time limit in the Einstein relation was evaluated using the slope  $\langle l^2 \rangle$  versus  $\tau$  for  $\tau = 150$  to 250 ps, as calculations using shorter probe time scales may not accurately reflect the infinite-time diffusive limit (Bourg and Sposito 2011).

In order to calculate  $D$  as a function of distance from the surface, the pore was divided into 0.2 Å thick slices parallel to the clay surfaces. To circumvent the effect of the finite residence time within each slice, normally being only a fraction of  $\tau$ , the mean square displacement within each slice was analyzed with Equation.(3.3.1) using a mended single particle trajectory. This mended single particle trajectory was constructed from all segments of trajectory data belonging to each slice by (1) appending all particles trajectories into a single particle trajectory and (2) iteratively removing the last record of any preceding trajectory segment, and then translating the succeeding segment of trajectory data so that its first trajectory record replaced the removed record in the preceding trajectory segment.

The simulated system contained 180 clay unit cells of average unit cell formula  $\text{Si}_8(\text{Al}_{3.33}\text{Mg}_{0.67})\text{O}_{20}(\text{OH})_4$ , 9000 water molecules, 116  $\text{Na}^+$  ions, 4  $\text{Ca}^{2+}$  ions, 3  $\text{Cl}^-$  ions, and 1  $\text{Br}^-$  ion (total of 34324 atoms) in a  $93.305 \times 90.030 \times 40.913$  Å simulation cell. The system was designed to approximate the conditions of a macroscopic diffusion experiment. The average unit cell formula used in our simulations was close to that of the

clay used in the experiment. The solid-liquid ratio,  $M = 0.81 \text{ kg dm}^{-3}$ , calculated using a smectite particle thickness of  $9.4 \text{ \AA}$  (Bourg and Sposito, 2011) was close to that used in the experiments. The average composition of the nanopore water ( $0.712 \text{ M Na}^+$ ,  $0.247 \text{ M Ca}^{2+}$ ,  $0.019 \text{ M Cl}^-$ ,  $0.006 \text{ M Br}^-$ ) was selected to be roughly similar to that of the nanopore water in the diffusion experiment.

### 3.3.3 Results

#### *Measurements of adsorption and diffusion at the macroscopic scale*

Figure 3.3.3 illustrates the characteristics of the data collected. The low-concentration reservoir solution was changed very frequently during the experiment to assure that the concentration gradients between the high- and low-concentration reservoirs were nearly constant throughout the experiment. However, it was not possible to change the low-concentration reservoir solution on an even schedule, and thus, the concentrations of diffused solutes varied significantly from sample to sample, with higher concentrations observed when the elapsed time between solution changes was greater (Fig. 3.3.3).

One can observe from these data that the relative Br concentration (sampled concentration divided by the high concentration reservoir) was increasing faster than that for tritium, suggesting that the anion diffused faster because of charge repulsion or a lower accessible porosity than that available for tritium. Relative Ca concentrations increased much more slowly, taking weeks before significant breakthrough into the low-concentration reservoir solution (Fig. 3.3.3), illustrating that Ca breakthrough was likely retarded by sorption or ion exchange processes.

#### *Anion accessible porosity*

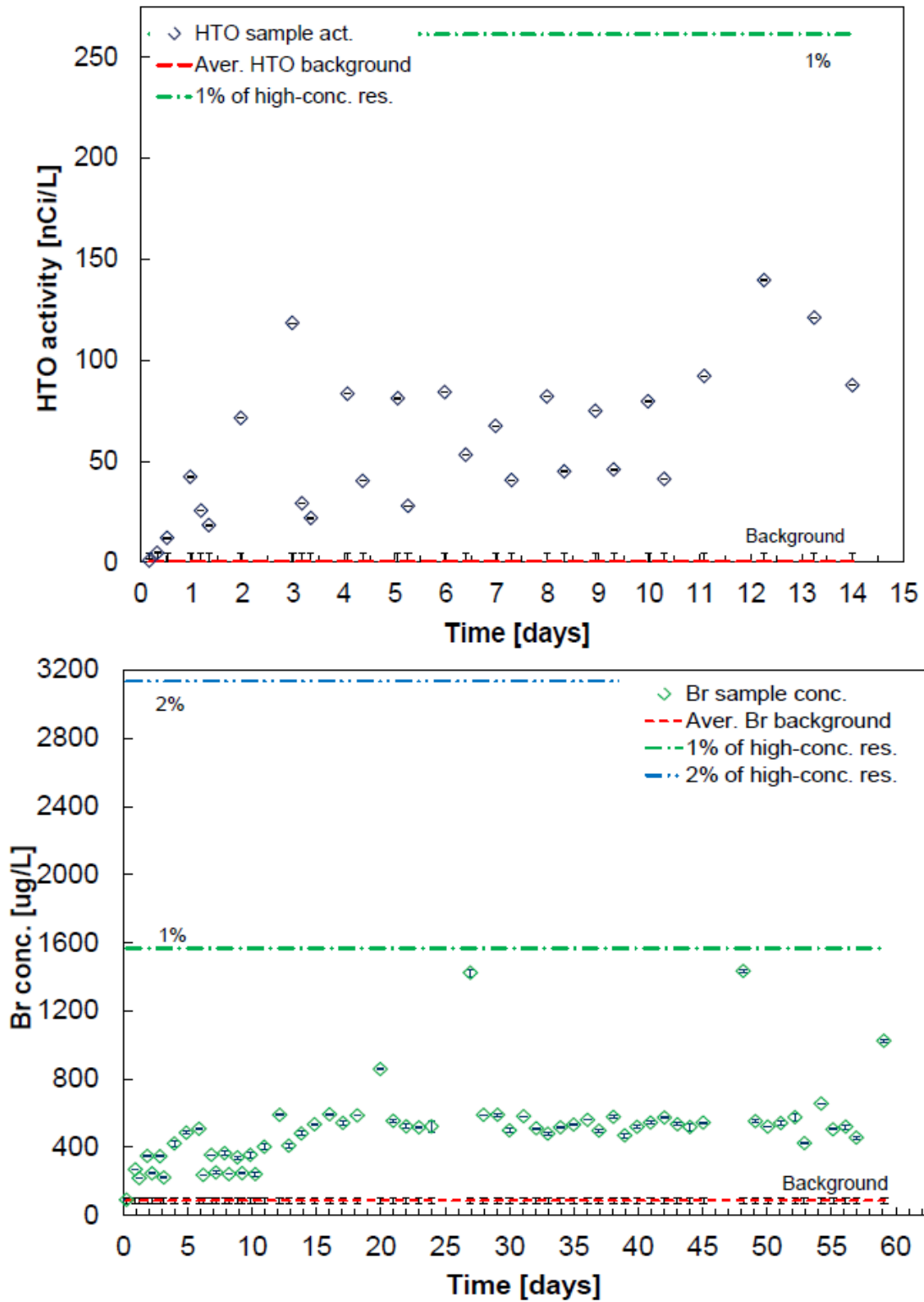
The static experiments yielded a total porosity of  $\theta = 0.74$  based on the water-content value and a bromide concentration of  $6.3 \times 10^{-5} \text{ mol kg}_{\text{water}}^{-1}$  when normalized to the total porosity. The external bromide concentration was  $8.5 \times 10^{-4} \text{ mol kg}_{\text{water}}^{-1}$ . A bromide accessible porosity  $\theta_{\text{Br}} = 0.55$  can be inferred from these measurements, corresponding to 74% of the total porosity.

#### *Reactive transport modeling of adsorption and diffusion in the clay*

Porosity and mean pore size determination: The clay was compacted at a dry density value of  $\rho_{\text{dry}} = 0.79 \text{ kg dm}^{-3}$ , based on the mass of clay packed and the volume of the cell. The crystal density of clay layers (or grain or specific density,  $\rho_g$ ) is about  $2.84 \text{ kg dm}^{-3}$ . Neglecting the impurities (mostly fine grained quartz), the total porosity, of the material is given by:

$$\theta = 1 - \frac{\rho_{\text{dry}}}{\rho_g} \quad (3.3.2)$$

which yields a value of 0.72. This value is in excellent agreement with the value determined by water loss upon drying at 150°C ( $\theta = 0.74$ ) after the experiment. Accordingly, the total porosity of the material was set to 0.72 for modeling purposes.



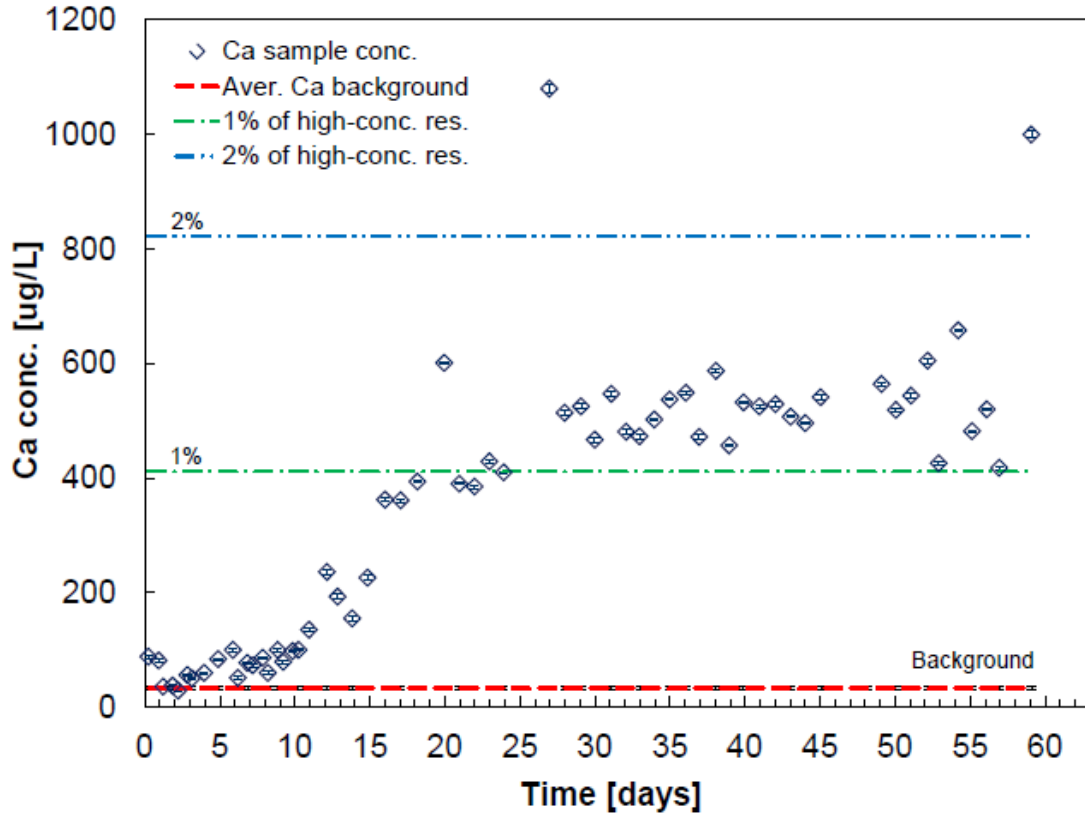


**Figure 3.3.3.** Concentrations of tritiated water (top), bromide (middle) and calcium (bottom) in samples from the low-concentration reservoir. Concentrations varied significantly due to the time lapse between changes of the low concentration reservoir solution. Dashed green curve shows the concentration that is 1% of the high concentration reservoir.

The total specific area of montmorillonite layers is  $SSA=770 \text{ m}^2 \text{ g}^{-1}$ . The cation exchange capacity of Swy-2 montmorillonite is circa  $0.85\text{-}0.9 \text{ mol kg}^{-1}$  and it follows that the surface charge is circa.  $\sigma_0 = -0.11 \text{ Coulomb-m}^{-2}$ .

By considering that the layers have a perfect parallel and homogeneous spatial arrangement, an average pore thickness,  $d_{pore}^{hom}$ , can be estimated from:

$$d_{pore}^{hom} = \frac{\theta}{SSA/2 \times \rho_{dry} \times 10^6} \quad (3.3.3)$$

which yields the value  $23.7 \text{ \AA}$ .

**Modeling Step 1:** The modeling strategy used here is similar to the one developed in Appelo et al. (2010). In the first step, a HTO, Br, and Ca diffusion experiment were modeled, with independent model parameters in order to derive species dependent

accessible porosity/rock capacity values with related pore-diffusion coefficients. In a second step, different models were built according to various conceptual models available in the literature in order to be able to simulate the whole set of data within a single conceptual approach.

For tritiated water (HTO), the rock capacity factor equals the total porosity (no specific retention is considered). Figure 3.3.4 shows that it is possible to fit HTO diffusion data by considering the total porosity value determined from sample bulk dry density (0.72) and adjusting only the geometrical factor,  $G$ , for the clay material ( $1/G = 0.047$ ). However, it should be noted that an equally good fit could be obtained with lower or higher porosity values and corresponding lower and higher values for  $G$  (not shown). This observation demonstrates the lack of accuracy in determining HTO transport parameters at high porosities from diffusion curves only. The good agreement between the experimental measurement of water porosity content (0.74) and the calculation from sample bulk dry density (0.72) constrains this problem. In the following, we will consider a total porosity value of  $\theta = 0.72$  and a  $1/G$  value of 0.047. With these parameters,  $D_p(\text{water}) = 1.0 \times 10^{-10} \text{ m}^2 \text{ s}^{-1}$  and  $D_e(\text{water}) = 7.3 \times 10^{-11} \text{ m}^2 \text{ s}^{-1}$ . (see Appelo et al. 2010 for the relationships that determine these parameters).

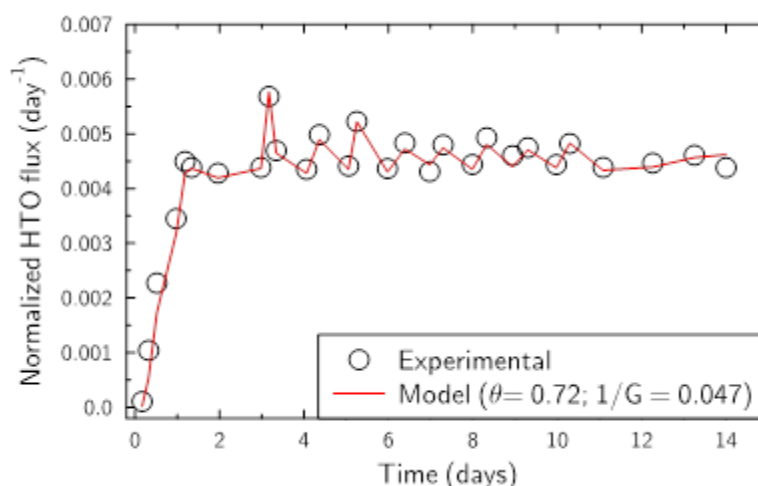


**Figure 3.3.4.** Comparison of experimental and modeled tritium flux into the low-concentration reservoir solution at a set porosity value of 0.72 and a fit value of  $1/G$ .

For Br, the rock capacity factor equals the  $Br^-$ -accessible porosity (no retention). Given the very low compaction of the material, the geometrical factor for anions should not be much different from that for the water tracer. Consequently, in a first modeling attempt, we used  $G_{Br} = G_{water} = 1/0.047$ . Figure 3.3.5 shows that experimental results are well reproduced if the porosity value is reduced to 0.46 as compared to 0.72 for water, i.e., the  $Br^-$ -accessible porosity is 64% of the total porosity. This result is in good agreement with the experimentally measured Br- accessible porosity (described above) of 74% of the total porosity. Figure 3.3.5 shows that a porosity of 0.53 instead of 0.46 only decreases the  $1/G_{Br}$  value to 0.041, and the available diffusion data are not sufficiently accurate to

decide which is the better set of parameters. Only a comparison with independently obtained data will make it possible to refine the model. The  $1/G_{Br}$  value (0.041) is lower than the  $1/G_{HTO}$  (0.047), in agreement with the usually observed higher tortuosity in clay material for anions than for neutral species (Glaus et al. 2010).

Because  $Ca^{2+}$ -accessible porosity is expected to be essentially the same as that of water, we expect also that the  $Ca^{2+}$  geometrical factor should not be much different from that of water. However, for  $Ca^{2+}$ , the rock capacity factor is different from the accessible porosity due to  $Ca^{2+}$  adsorption to the clay surfaces. If we consider that  $Ca^{2+}$  can diffuse with a pore diffusion coefficient,  $D_p(Ca)$ , whether it is adsorbed or not, the diffusion equation simplifies to:

$$\Phi \frac{\partial c}{\partial t} = \frac{\partial}{\partial x} \left( \frac{\Phi D_p(Ca)}{G} \frac{\partial c}{\partial x} \right) \quad (3.4)$$

where  $\Phi$  is a nonphysical, effective porosity (usually  $\Phi > 1$  for adsorbing species). It is possible to reproduce steady-state Ca diffusion data with  $1/G = 0.047$  and with a nonphysical effective porosity  $\Phi$  equal to 11 (Figure 3.3.6), but this model overestimates the Ca flux in the early, transient period, thereby showing that retardation mechanisms must take place. Only the effective diffusion coefficient at steady state can be estimated:  $D_e(Ca) = 4.1 \times 10^{-10} \text{ m}^2 \text{ s}^{-1}$ .

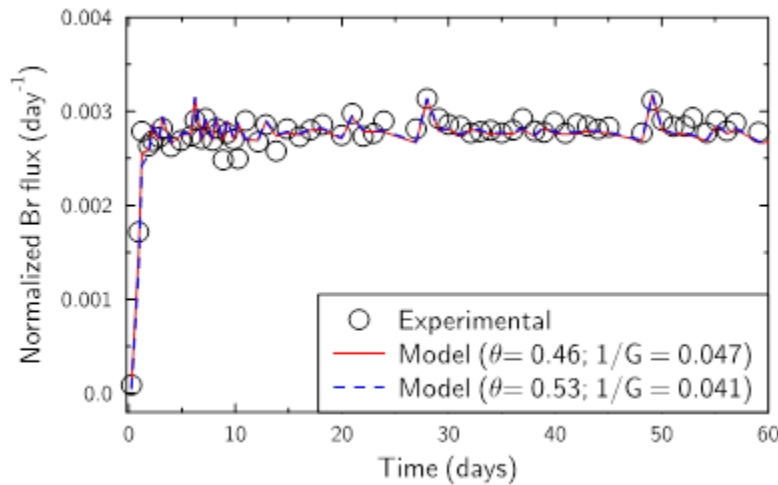


**Figure 3.3.5.** Comparison of experimental and modeled bromide ion flux into the low-concentration reservoir solution at set values of  $1/G$  and fit porosity values.

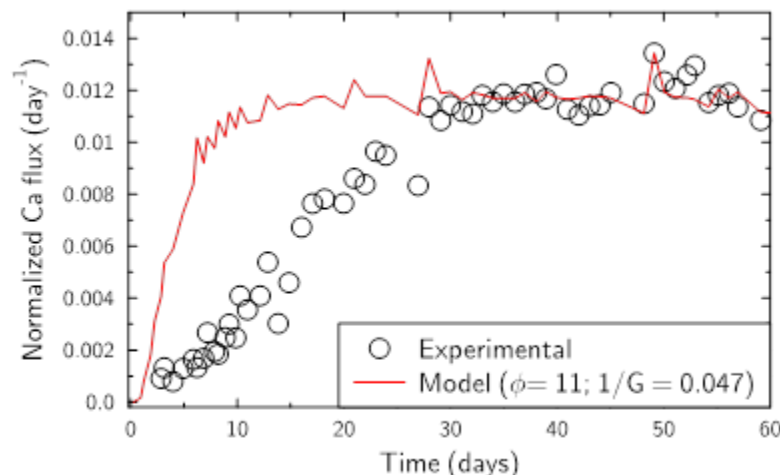


**Figure 3.3.6.** Comparison of experimental and modeled calcium ion flux into the low-concentration reservoir solution at set values of  $1/G$  and fit rock capacity values.

**Modeling step 2:**

*Classical pore model:* We first consider a model in which Ca and Br diffuse in the same accessible porosity, and where Ca adsorbs on the clay through a cation exchange mechanism that is responsible for its higher observed rock capacity factor. The porosity was set to 0.53 in agreement with Br accessible porosity, and two different geometric factors were considered for Br and Ca. Ca could undergo cation exchange with Na, all exchanged species being considered as immobile. For Br,  $1/G_{Br}=0.041$  and this simulation is strictly equivalent to the one shown in Figure 3.3.6. It is also possible to fit the Ca experimental data by adjusting the  $1/G_{Ca}$  value to a value of 0.47 together with a Na-Ca exchange selectivity coefficient of  $\log K_{Na-Ca} = 0.5$  (using the Gaines and Thomas convention that is implemented in PHREEQC) (Figure 3.3.7), i.e., a value in close agreement with the values usually reported for this exchange reaction (Bourg and Sposito, 2011). As  $1/G_{Ca}$  is an order of magnitude higher than  $1/G_{Br}$  and  $1/G_{HTO}$ , it means that Ca diffusion is enhanced by a factor of ten as compared to HTO or Br diffusion, while having access to a similar porosity.

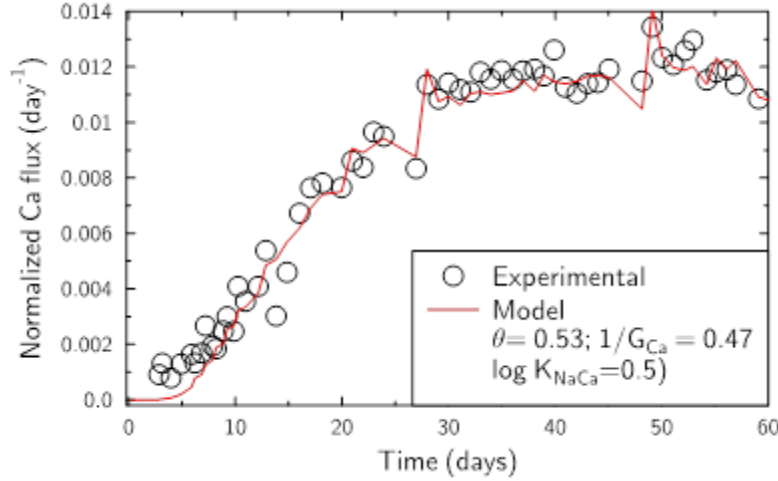


**Figure 3.3.7.** Comparison of experimental and modeled calcium ion flux into the low-concentration reservoir solution at a set value of  $1/G$ , ion exchange, and fit porosity value.

Single porosity with diffuse layer model: In this model, the clay-layer surface charge is compensated by the condensation of cations and the exclusion of anions in a diffuse layer. Diffusion of water and ions is attributed to the additive contributions of the “free” water, where electro-neutrality prevails, and of the diffuse layer water, where cation concentration is higher than anion concentration (Appelo et al. 2010). The diffuse layer average composition is not obtained by solving the Poisson-Boltzmann equation, but by using a so-called “Donnan” equilibrium model, i.e., a mean potential model, assuming a mean water density of  $1 \text{ kg dm}^{-3}$  in the diffuse layer. The distribution of water among the “free” water and the diffuse layer water can be calculated according to the method from Appelo et al. (2010) as explained below.

If we consider that a fraction,  $f$ , of the porosity is “free” water and a fraction  $1-f$  to be located in the diffuse layer, it follows that:

$$\theta_{Br} \times C_{Br,free} = f\theta_{HTO} \times C_{Br,free} + (1-f)\theta_{HTO}C_{Br,EDL} \quad (3.3.5)$$

where  $C_{Br,free}$  and  $C_{Br,EDL}$  are the bromide concentration in the free water and in the diffuse layer respectively. The mean concentration in the diffuse layer is related to the concentration in the free water through:

$$C_{Br,EDL} = C_{Br,free} \exp\left(\frac{F\psi_D}{RT}\right) \quad (3.3.6)$$

And it follows:

$$\frac{F\psi_D}{RT} = \ln\left(\frac{\frac{\theta_{Br}}{\theta_{HTO}} - f}{1 - f}\right) \quad (3.3.7)$$

Next, we define  $\sigma_D$  as the surface charge that is compensated in the diffuse layer and that is thus related to the charge balance in the diffuse layer:

$$(1 - f)\theta_{HTO} \sum_i z_i C_{i,EDL} = -1000 \times SSA \times \frac{\sigma_D}{F} \times \rho_{dry} \quad (3.3.8)$$

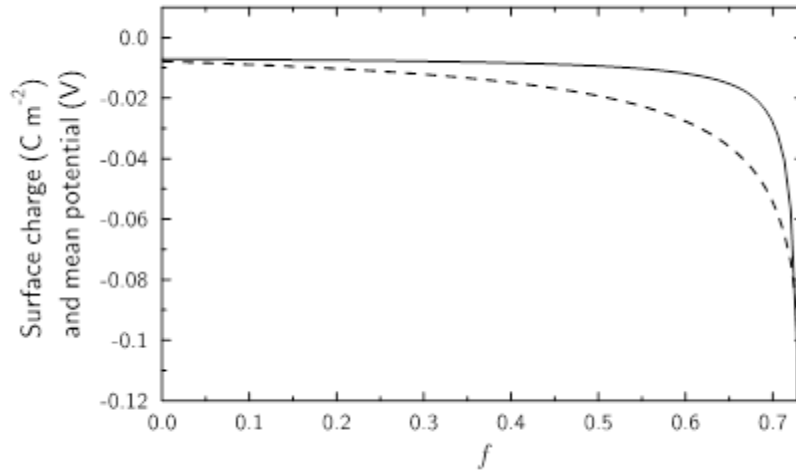
For the conditions of Br diffusion (and for the case where no Ca has diffused yet, *i.e.* only Na compensates the surface charge):

$$\begin{aligned} (1 - f)\theta_{HTO} \left( C_{Na,Bulk} \exp\left(\frac{-F\psi_D}{RT}\right) - C_{Na,Bulk} \exp\left(\frac{F\psi_D}{RT}\right) \right) \\ = -1000 \times SSA \times \frac{\sigma_D}{F} \times \rho_{dry} \end{aligned} \quad (3.3.9)$$

Rearranging,

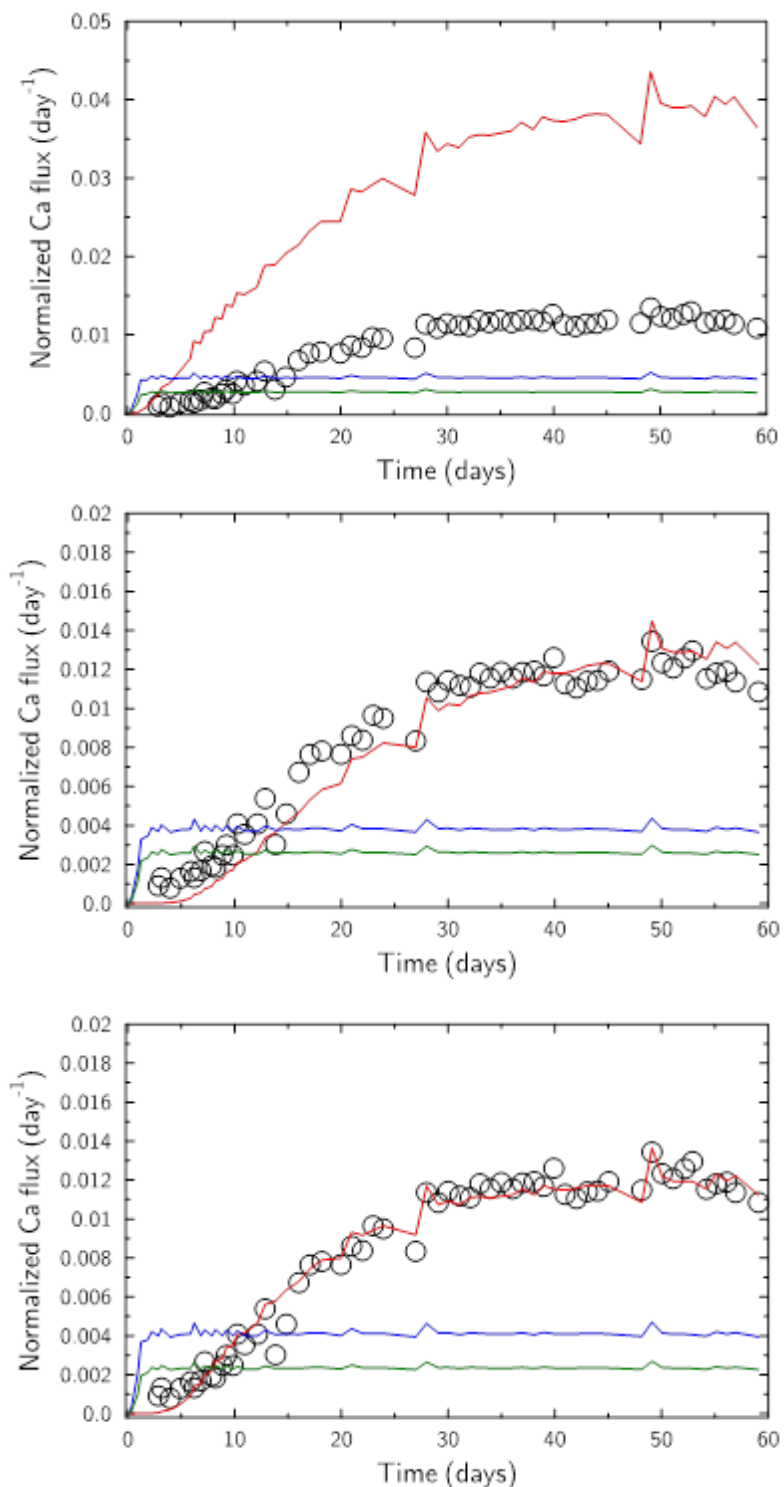
$$\sigma_D = \frac{-2F\theta_{HTO}C_{Na,Bulk}(1 - f) \sinh\left(-\ln\left(\frac{\frac{\theta_{Br}}{\theta_{HTO}} - f}{1 - f}\right)\right)}{1000 \times SSA \times \rho_{dry}} \quad (3.3.10)$$

Figure 3.3.8 shows that for our experimental conditions, if the total surface charge is compensated in the diffuse layer, it follows that the  $f$  value is about the same as the  $\frac{\theta_{Br}}{\theta_{HTO}}$  value ( $\sim 0.74$ ), meaning that Br is almost entirely confined in the free water volume. On the other hand, if all the porosity volume is considered to be occupied by the diffuse layer (*i.e.*,  $f = 0$ ), then the effective surface charge must be less than 10% of the total surface charge, meaning that more than 90% of the charge must be screened by surface-complexing cations.



**Figure 3.8.** Relationship between the diffuse layer mean potential, surface charge compensated in the diffuse layer, and ratio of free water in the porosity, via Equations. (3.3.7)-(3.3.10).

Next, we consider for a first simulation run that: (i) the diffuse layer has the same diffusion properties as bulk water, and (ii) no surface charge compensation occurs other than the compensation in the diffuse layer. The geometrical factor of Ca is set equal to that of HTO. Figure 3.3.9 shows that the calculated Ca flux is too high in comparison to the experimental data. Moreover, the Ca retardation is not sufficient.



**Figure 3.3.9.** Single porosity model with diffuse layer and surface complexation. Top: no surface complexation, diffusion properties of the diffuse layer are the same as the diffusion properties of the bulk water. Middle: surface complexation according to model 1 ( $\log K_{Na} = -0.7$ ). Bottom: surface complexation model according to model 2 ( $\log K_{Na} = 0.8$ ).

These two deficiencies in the model can be solved: (i) by considering that the diffusivity in the diffuse layer is less than in bulk water, and/or (ii) by considering Ca (and Na) surface complexation. Na and Ca surface complexation were taken into account by considering the following reactions in the framework of a double layer surface complexation model (Parkhurst and Appelo, 1999):



As explained in Appelo et al. (2010),  $\log K_{\text{Ca}}$  is constrained by the relative affinities of Ca and Na for the surface with  $\log K_{\text{Ca}} - 2 \log K_{\text{Na}} \sim 0.5-1$ . Varying the  $\log K_{\text{Na}}$  value enables one to vary the extent of surface charge compensation by surface complexes. A large range of  $K_{\text{Na}}$  values can be found in the literature, depending on the model used and the representation of the interface between the clay surface and the solution. With a  $\log K_{\text{Na}} = -0.7$  (Appelo et al. 2010, EDL model 1), 74% of the surface charge is compensated by the diffuse layer, thus corresponding to a “free” pore water volume of 70% of the total porosity (Figure 3.3.9, middle). With a  $\log K_{\text{Na}} = 0.8$ , 30% of the surface charge is compensated by the diffuse layer, thus corresponding to a “free” pore-water volume of 60% of the total porosity (Figure 3.3.9, bottom). Hence, for our system, the choice of  $\log K_{\text{Na}}$  within a reasonable range of values has little influence on the volume repartition between the diffuse layer and the “free” water.

Ca diffusion data can be reproduced using either EDL models 1 ( $\log K_{\text{Na}} = -0.7$ ) or 2 ( $\log K_{\text{Na}} = 0.8$ ) by adjusting the  $\log K_{\text{Ca}}$  value together with the diffusivity in the diffuse layer, thereby showing the cross-correlation of the three parameters and reminding us that available macroscopic-scale data do not strongly constrain current theories of the clay properties (Figure 3.3.9).

### **Molecular Dynamics Simulations of Smectite Nanopores**

As mentioned in the Methods section above, the simulated system contained 180 clay unit cells of average unit cell formula  $\text{Si}_8(\text{Al}_{3.33}\text{Mg}_{0.67})\text{O}_{20}(\text{OH})_4$ , 9000 water molecules, 116  $\text{Na}^+$  ions, 4  $\text{Ca}^{2+}$  ions, 3  $\text{Cl}^-$  ions, and 1  $\text{Br}^-$  ion (total of 34,324 atoms) in a  $93.305 \times 90.030 \times 40.913 \text{ \AA}$  simulation cell. Molecular dynamics simulations of the average density of ions and water as a function of distance from the clay surface are shown in Figure 3.3.10. Simulation results are broadly consistent with our previous study of Na-Ca-Cl solutions of higher salinity (0.3 to 1.8  $\text{mol}_c \text{ dm}^{-3}$ ) in 6 nm wide clay interlayer nanopores (Bourg and Sposito, 2011), despite significant methodological differences (our previous simulations used higher concentrations and a larger pore size, as noted above, as well as a different MD simulation code, different inter-atomic potential parameters for  $\text{Na}^+$  and  $\text{Cl}^-$ , and a rigid clay framework). The simulation predicts the existence of three ordered water layers at  $z = 6.1, 9.5, \text{ and } 12.4 \text{ \AA}$ . If the peak locations are expressed relative to the plane of surface O atoms (with a rescaled coordinate  $z^* = z - 3.22 \text{ \AA}$ ), the water density peaks are located at  $z^* = 2.9, 6.3, \text{ and } 9.2 \text{ \AA}$ . The spacing between the water

density peaks is close to the diameter of a water molecule, showing that the water layering arises from the steric packing of water molecules on the clay surface. Ion density profiles show that  $\text{Na}^+$  and  $\text{Ca}^{2+}$  are attracted to, and  $\text{Cl}^-$  and  $\text{Br}^-$  are repulsed from, the vicinity of the clay surface, as expected from the negative structural charge of the clay lamellae. For all four ionic species, the density profiles show two peaks near the clay surface: a first peak at  $z = 7.65 \pm 0.1 \text{ \AA}$  (for all four ions) and a second peak at  $z = 9.95 \pm 0.1 \text{ \AA}$  (for cations) or  $10.35 \pm 0.1 \text{ \AA}$  (for anions). In the context of the well known triple-layer model (TLM), the two peaks of the cation density profiles indicate adsorption as outer-sphere surface complexes (OSSC) and in the diffuse ion swarm (DIS). The OSSC density peaks accounts for 35% of  $\text{Na}^+$  ions and 65% of  $\text{Ca}^{2+}$  ions in our system. The existence of two peaks in the anion density profiles are inconsistent with mean-field theories of ion adsorption on charged surfaces, such as the TLM, which suggests that these features arise from ion-ion or ion-water correlations that are not taken into account by these theories. The coincidence of the cation and anion density peaks suggest that the position of the peaks is strongly influenced by water density layering at the clay-water interface, even though the position of the peaks is not perfectly registered with the water-density features (the first ion density peak is located close to the minimum between the first and second water layers, whereas the second ion density peak almost coincides with the second water layer).

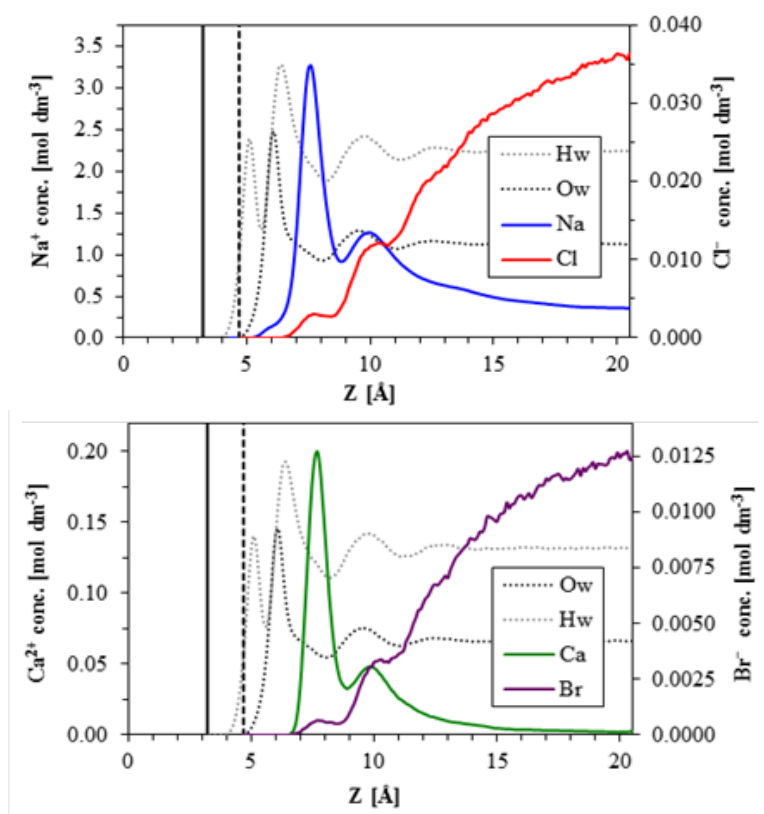


**Figure 3.3.10.** MD simulation of the average density profiles of water and ions as a function of distance in the direction normal to the clay surface, from the mid-plane of the clay sheet ( $z = 0 \text{ \AA}$ ) to the mid-plane of a nanopore ( $z = 20.45 \text{ \AA}$ ). Vertical lines show the location of the plane of surface O atoms (solid line,  $z = 3.23 \text{ \AA}$ ) and the location of the Gibbs dividing surface (dashed line,  $z = 4.7 \text{ \AA}$ ). The solid curves show the density profiles of  $\text{Na}^+$  and  $\text{Cl}^-$

(upper figure) and  $\text{Ca}^{2+}$  and  $\text{Br}^-$  (lower figure) using a different vertical scale for each ion. The dotted black and gray lines show the density profiles of water O and H atoms with an arbitrary vertical scale.

Values of the average ion concentration in the mid-plane of the nanopore, reported in Table 3.3.1, show that water in the mid-plane contains significantly more moles of cationic charge ( $q_+ = 0.3659 \text{ mol}_c \text{ dm}^{-3}$ ) than moles of anionic charge ( $q_- = 0.0484 \text{ mol}_c \text{ dm}^{-3}$ ). This indicates that the EDLs formed on the two clay surfaces overlap in the center of the nanopore, a phenomenon that is known to strongly influence the swelling properties and semi-permeable membrane properties of compacted clays. To a first approximation, we can apply a Donnan equilibrium model to estimate the composition of a hypothetical bulk-liquid-like component that would be in equilibrium with the water in the mid-plane of our interlayer nanopore, by applying a charge-balance relation to ion concentrations,  $C_{i,\text{bulk}}$ , in the hypothetical bulk solution:

$$\sum_i z_i C_{i,\text{bulk}} = 0 \quad (3.3.13)$$

where  $z_i$  is the valence of the ion  $i$  of interest, and a Boltzmann relation between concentrations at the interlayer mid-plane ( $C_{i,\text{mid-plane}}$ ) and in the bulk solution:

$$C_{i,\text{mid-plane}} = C_{i,\text{bulk}} e^{\frac{-z_i F \psi_{\text{mid-plane}}}{RT}} \quad (3.3.14)$$

where  $\psi_{\text{mid-plane}}$  is the electrostatic potential at the interlayer mid-plane (relative to a value of zero in the hypothetical bulk solution),  $F$  is Faraday's constant,  $R$  is the ideal gas constant, and  $T$  is absolute temperature. Application of Equations (3.3.13)-(3.3.14) to the values of  $C_{i,\text{mid-plane}}$  in Table 3.3.1 yields  $\psi_{\text{mid-plane}} = -25.9 \text{ mV}$  and the values of  $C_{i,\text{bulk}}$  shown in the last row in Table 3.3.1.

Alternatively, the full Poisson-Boltzmann (PB) equation can be solved numerically and the "free" water chemical composition can be adjusted to match the MD concentration profiles. A distance of closest approach corresponding to the position of first adsorption peak maximum was chosen: the effective pore size was thus reduced to  $25.8 \text{ \AA}$ . The surface charge was set to  $-0.114 \text{ C m}^{-2}$ . Na, Ca, Cl, and Br concentrations in "free" water were varied to match the MD concentration profiles. Actually, only Na and Ca concentrations were fitted due to (i) the electroneutrality condition in free water and (ii) the relationship  $C_{\text{Cl}} = 3 \times C_{\text{Br}}$ . From the concentration profiles, it is possible to calculate a mean concentration in the pore. The excellent agreement for anion profiles between MD calculations and PB prediction justifies the use of the PB equation to estimate the anion accessible porosity in pores of similar size and for similar ionic strength and solution composition (Figure 3.3.11).

The values of  $C_{i,\text{pore}}$  and  $C_{i,\text{free}}$  in Table 3.1 allow us to quantify several ion adsorption (or negative adsorption) coefficients at the nanopore scale. The amount of adsorbed solute per mass of clay  $q_i$  can be calculated according to the relation:

$$q_i = \frac{C_{i,\text{pore}} - C_{i,\text{free}}}{M} \quad (3.3.15)$$

MD simulation predictions of the diffusion coefficients of water and ions in bulk liquid water ( $D_{\text{bulk}}$ ) and in the clay interlayer nanopore ( $D_{\text{pore}}$ ), shown in Table 3.3.2, indicate that all species diffuse more slowly in the nanopores than in bulk liquid water. The influence of confinement, quantified by the nanopore confinement effect  $q_{\text{nano}} = D_{\text{pore}}/D_{\text{bulk}}$ , is identical for all species except  $\text{Ca}^{2+}$  (Table 3.3.2). This effect is thought to arise from the fact that calcium is strongly concentrated near the clay surface, where water and solutes tend to diffuse more slowly. Predictions of the self-diffusion coefficient of water O atoms as a function of distance from the surface (Figure 3.3.12) indicate that in the region between the first and second water layers (where a large fraction of the cations is adsorbed as OSSC), water diffuses roughly 80% as fast as bulk liquid water.

**Table 3.3.1.** Molecular dynamics simulation predictions of the average ion concentration in the entire pore ( $C_{i,\text{pore}}$ ), in the mid-plane of the pore ( $C_{i,\text{mid-plane}}$ ), and in a hypothetical bulk solution in Donnan equilibrium with the mid-plane of the pore ( $C_{i,\text{bulk}}$ ).

	Br	Cl	Ca	Na
	MD			
$C_{\text{pore}}$ (mol dm <sup>-3</sup> )	6.17x10 <sup>-3</sup>	1.85x10 <sup>-2</sup>	2.47x10 <sup>-2</sup>	7.16x10 <sup>-1</sup>
$C_{\text{mid-plane}}$ (mol dm <sup>-3</sup> )	1.25x10 <sup>-2</sup>	3.59x10 <sup>-2</sup>	2.40x10 <sup>-3</sup>	3.61x10 <sup>-1</sup>
	Donnan			
$C_{\text{bulk}}$ (mol dm <sup>-3</sup> )	3.42x10 <sup>-2</sup>	9.83x10 <sup>-2</sup>	3.2x10 <sup>-4</sup>	1.32x10 <sup>-1</sup>
	Poisson-Boltzmann			
$C_{\text{bulk}}$ (mol dm <sup>-3</sup> )	3.42x10 <sup>-2</sup>	1.03x10 <sup>-1</sup>	3.5x10 <sup>-4</sup>	1.36x10 <sup>-1</sup>
$C_{\text{pore}}$ (mol dm <sup>-3</sup> )*	5.7x10 <sup>-3</sup>	1.7x10 <sup>-2</sup>	1.9x10 <sup>-2</sup>	6.52x10 <sup>-1</sup>
$q$ (mol kg <sup>-1</sup> )	-3.46x10 <sup>-2</sup>	-9.83x10 <sup>-2</sup>	3.0x10 <sup>-2</sup>	7.19x10 <sup>-1</sup>
$\phi_a/\phi$ (-)	0.180	0.188	n.a.	n.a.
$K_d$ (dm <sup>3</sup> kg <sup>-1</sup> )	n.a.	n.a.	93.8	5.45

\* normalized to the total pore size (x25.8/35.54)

**Table 3.2.** MD simulations of the average diffusion coefficients of ions and water in the clay nanopores ( $D_{\text{pore}}$ ) and in bulk liquid water ( $D_{\text{bulk}}$ ). Values of  $D_{\text{bulk}}$  are corrected for the artifact that causes a simulation cell size dependence of  $D$  in MD simulations of bulk fluids; for  $D_{\text{pore}}$  no correction is needed, as shown in our previous study (Holmboe and Bourg, 2014). The last row shows the nanopore confinement effect  $q_{\text{nano}} = D_{\text{pore}}/D_{\text{bulk}}$ .

	Br	Cl	Ca	Na	H <sub>2</sub> O
$D_{\text{pore}}$ (10 <sup>-9</sup> m <sup>2</sup> s <sup>-1</sup> )	1.32±0.15	1.22±0.07	0.47±0.04	0.80±0.01	2.05±0.01
$D_{\text{bulk}}$ (10 <sup>-9</sup> m <sup>2</sup> s <sup>-1</sup> )	1.58±0.02	1.68±0.08	0.85±0.04	1.08±0.09	2.68±0.03
$q_{\text{nano}}$ (-)	0.83±0.09	0.73±0.05	0.55±0.05	0.74±0.06	0.77±0.01

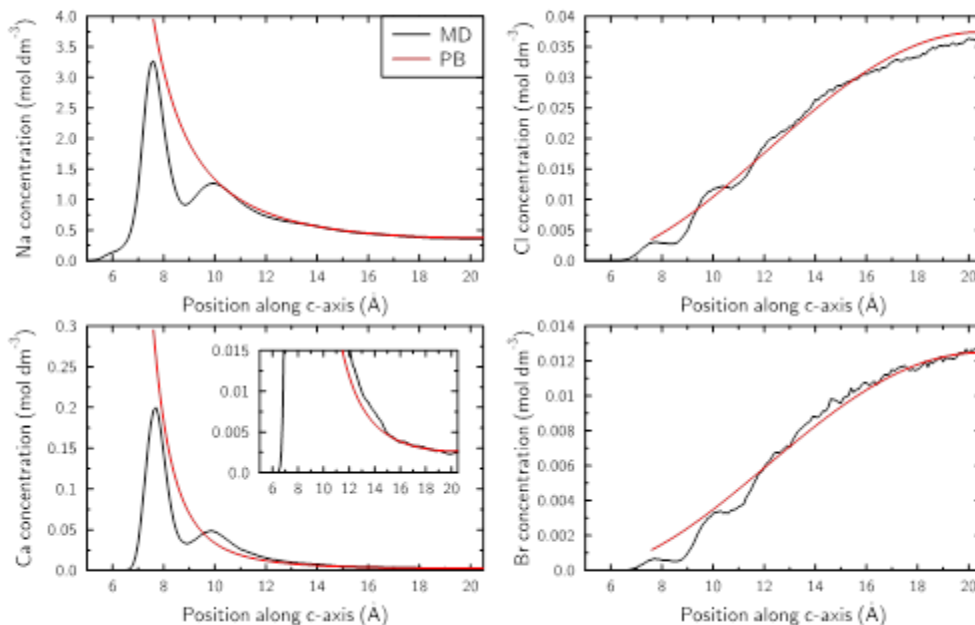


**Figure 3.3.11.** Comparison of cation and anion profiles between MD results and Poisson-Boltzmann equation resolution.

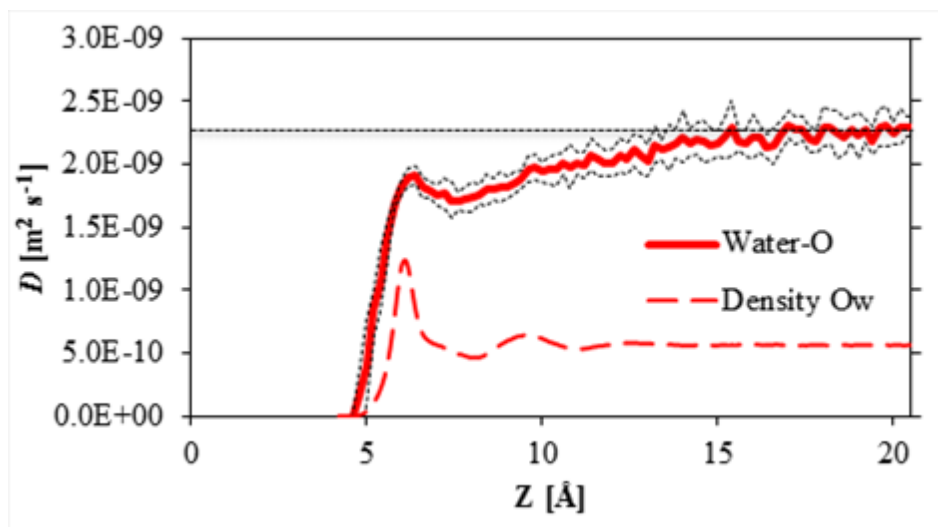


**Figure 3.3.12.** Molecular dynamics simulation of the average diffusion coefficient of water O atoms in the  $xy$ -plane as a function of distance from the clay surface (solid line, with confidence intervals shown as dashed lines). The density profile of water O atoms is shown by the thick dashed line. The self-diffusion coefficient of bulk liquid water is shown by the horizontal dashed line.

### 3.3.4 Discussion

#### Is free water present in compacted montmorillonite?

The present experiment deals with a loosely compacted montmorillonite. However, the mean pore size ( $\sim 23.7 \text{ \AA}$ ) is on the order of eight water layers. In similar conditions, the resolution of the Poisson-Boltzmann equation and the MD results agreed, and the solution in the center of the pore was found to be charge unbalanced, with more cationic charges than anionic charges. Note that these calculations were representative of slightly larger pore and ionic strength than those of the diffusion experiment, meaning that the charge unbalance was even underestimated as compared to the value that could be calculated with actual experimental conditions. From those considerations, it should then be concluded that no free water was present in the porosity of the clay sample, and that a single porosity model with the diffuse layer occupying all the space might be appropriate, as for example the model proposed by Birgersson and Karnland (2009). However, this kind of model leads to an overestimation of the actually measured anion exclusion as exemplified by Figure 3.3.8. MD results support this conclusion by showing too much anion exclusion, as compared to the measurement in conditions that are otherwise less favorable to anion exclusion than the experimental one. Finally, the excellent agreement of MD results with the resolution of the Poisson-Boltzmann equation justifies the use of the PB model to estimate anion exclusion accurately (Figure 3.3.11). However, such a calculation yields too much anion exclusion. Consequently, homogeneous pore models where only a diffuse layer is present cannot be successful at describing correctly the mass balance between surface charge, anions, and cations in the porosity, and it is necessary to consider that free water is present in the porosity.

#### Is an average pore model with free water and diffuse layer/surface complexation physically relevant?

The model result depicted in Figure 3.3.7 is representative of a single pore model with surface complexation, where all the surface charge is compensated by adsorbed cations, leaving no charge to be compensated in a diffuse layer. Br and Ca diffusion data are fitted adequately using this model, but it is not possible to fit HTO data (not shown) satisfactorily, because the considered porosity corresponds to the anion accessible porosity and not the total porosity. This problem could be circumvented by considering the adsorption of the water molecule corresponding to the hydration shells of adsorbed Na and Ca (not shown). The Ca diffusivity in the bulk water must be increased by a factor of ten, as compared to the diffusivity of Br, in order to fit the data. It is difficult to justify the physical meaning of such an increase of the Ca diffusion coefficient, unless it is considered that this increase compensates the assumed zero mobility of surface complexed Ca. Indeed, the MD results indicate that outer-sphere surface complexes of Na and Ca have a non-negligible mobility parallel to the surface. This single pore model can thus be successful at describing the system as a whole, if the adsorption of water molecules is considered and if the mobility of adsorbed ions/molecules is taken into account. However, it remains in poor agreement with the MD results that predict the presence of a diffuse layer in accordance with the Poisson-Boltzmann model prediction.

If the presence of a diffuse layer is considered in a single porosity model, then it must agree quantitatively with the relationship that governs the distribution of water between free and diffuse layer water. Figure 3.3.9 shows clearly that this model implies the necessary assumptions of: (1) the presence of non- (or negligibly) mobile surface complexes to explain the Ca retardation, and (2) a lower diffusivity of Ca in the diffuse layer than in the bulk water. These two features are supported by the MD results. The diffusion data alone do not enable one to quantify with precision the surface complexation model parameters (especially  $\log K_{Na}$ ). In addition, the necessary decrease in Ca mobility in the diffuse layer is not in quantitative agreement with the decrease in the Ca diffusion coefficient that is calculated with the MD trajectories. Finally, it is possible to estimate a mean diffuse layer thickness with:

$$d_D = \frac{\theta_{EDL}}{SSA \times \rho_{dry} \times 10^6} \quad (3.3.16)$$

The resulting value is  $d_D = 3.6 \text{ \AA}$ . This value is clearly nonphysical: it represents only one water molecule diameter. As a conclusion, this last single pore model fails at giving a physically consistent picture of the processes at work.

Obviously, the single porosity model is an oversimplification of a complex system, and the corresponding derived parameters consistent with that model result from the integration of several processes, thus explaining why so many different models are available to describe very similar data in the literature. The model differences depend strongly on the authors' choices for the processes that are coupled together.

The above detailed evaluation of single pore models with regards to molecular information (on the one hand) and experimental diffusion and static data (on the other) is good evidence that the distribution of pore size (at least interlayer, mesopores, and macropores) is indeed an important feature that must be taken into account to understand water, anion, and cation diffusivity in clay materials (Tournassat and Appelo, 2011). In this work, multi-porosity models were not proposed because parameterization of such models would have been underconstrained by the available data. Detailed characterization of clay-material pore structure down to the resolution of the interlayer size would greatly help to constrain such models.

### 3.3.5 Conclusion

This section examines the consistency of macroscopic measurements, electrical double layer (EDL)-based models, and molecular-scale simulations of clay media. Macroscopic-scale measurements of the adsorption and diffusion of trace levels of calcium ( $\text{Ca}^{2+}$ ), bromide ( $\text{Br}^-$ ), and tritiated water (HTO) in a loosely compacted, water-saturated Namontmorillonite are presented. In order to aid in the interpretation of the macroscopic-scale data, as well as to challenge the fundamental assumptions inferred by different pore/transport models commonly used in the diffusion literature, molecular dynamics (MD) simulations of adsorption and diffusion in individual clay interlayer nanopores are presented at similar solid-liquid ratio and electrolyte composition as in the laboratory

diffusion experiments.

The results from the macroscopic-scale adsorption and diffusion experiments and MD simulations of the montmorillonite diffusion experiment allow a critical test of various transport/pore models, by carefully evaluating the physical meaning of their related fitting parameters on a single set of data. Hence, by evaluating the results using a multi-component reactive transport (diffusion) approach with the different transport/pore models, we highlight the difficulty in constraining current theories of the properties of clay barriers using transport modeling alone.

The following conclusions can be reached with regard to “average pore” models:

- Some models cannot reproduce the data: a simple Donnan model applied to the whole porosity simply does not comply with the actual measured anion accessible porosity;
- The “classical pore model” without diffuse layer consideration enables modeling of the Br and Ca diffusion data, but for Ca we need to consider a very high diffusivity as compared to water. This is not in agreement with the MD calculation and does not make sense from a physical point of view;
- Pore models with the consideration of the diffuse layer can reproduce the data well in a single run, and diffusion or surface complexation parameters appear to have physically meaningful values. But the calculated diffuse layer thickness with these models is nonsensical, and the diffusivity in the diffuse layer is far too low compared to that estimated from MD simulations.
- The detailed evaluation of single pore models presented in this report, with regard to molecular information on the one hand and experimental diffusion and static data on the other hand, demonstrates the need to consider a *distribution* of pore size as the important feature that must be taken into account to understand water, anion, and cation diffusivity in clay materials.

### 3.4 SUMMARY

#### Modeling Coupled THMC Processes in the EBS

We are developing and applying coupled THMC models for the analysis of EBS coupled processes in bentonite-backfilled repositories. We based this development on the extension of the Barcelona Basic Model (BBM) to a dual-structure model for expansive clay, such as bentonite. The dual-structure model has been found to give results that are in better agreement with observations, in particular the rate of buffer resaturation, by representing identifiable physical mechanisms not treated by the original BBM model. Therefore, this model improvement reduces the modeling uncertainty for THM processes in a bentonite buffer. Specific accomplishments are as follows:

- We completed implementation of the dual-structure model into TOUGH-FLAC, tested the model against literature data from experiments and independent models, and have successfully modeled and reproduced observed behavior for laboratory tests on expansive clay under increasing confining stress.

- We completed simulations for a generic high-level nuclear waste repository showing the importance of considering the dual-structure behavior on the resaturation and swelling of the buffer, including a delayed resaturation as has also been experimentally observed.
- We applied the previously developed and implemented CM coupling model and TOUGHREACT-FLAC3D to simulate the effect of illitization on swelling pressure at high temperature for a generic repository.
- We upgraded the CM coupling scheme based on the dual-structure model for expansive clay and implement the new scheme into the TOUGHREACT-FLAC3D simulator.

Recommended work for FY15 includes:

- Continue to validate and improve the dual-structure model by testing it on new experimental data available through international collaborative DECOVALEX and Mont Terri projects, as well as any new data available in the literature.
- Based on modeling of long-term evolution and the outcome of model validations against experimental data, develop an experimental protocol for validation and for determining key parameters that will minimize uncertainties in the long-term model predictions.
- Testing and validation TOUGHREACT-FLAC3D with the newly developed and implemented CM model against experimental data.
- Evaluate the long-term THMC behavior of EBS bentonite through a mechanistic THMC analysis using TOUGHREACT-FLAC and the dual-structure model with new the CM coupling scheme.
- Develop CM coupling relationships to describe effects of cementation (silica precipitation) on mechanical properties of bentonite (transition from plastic to brittle).

### **Ion Adsorption and Diffusion in Smectite Clay Barriers**

Section 3.3 examines the consistency of macroscopic measurements, electrical double layer (EDL)-based models, and molecular-scale simulations of clay media for adsorption and diffusion of trace levels of calcium ( $\text{Ca}^{2+}$ ), bromide ( $\text{Br}^-$ ), and tritiated water (HTO) in a loosely compacted, water-saturated Na-montmorillonite. Molecular dynamics (MD) simulations are also conducted and used to aid the interpretation of adsorption and diffusion processes in individual clay interlayer nanopores. The MD simulations allow a critical test of various transport/pore models by carefully evaluating the physical meaning of their related fitting parameters on a single set of data. These results highlight the difficulty in constraining current theories of the properties of clay barriers using transport modeling alone. Specific accomplishments and conclusions are as follows:

- Some models cannot reproduce the data: a simple Donnan model applied to the whole porosity simply does not comply with the actual measured anion accessible porosity;
- The “classical pore model” without diffuse layer consideration enables modeling of the Br and Ca diffusion data, but for Ca we need to consider a very high

diffusivity as compared to water. This is not in agreement with the MD calculation and does not make sense from a physical point of view;

- Pore models with the consideration of the diffuse layer can reproduce the data well in a single run, and diffusion or surface complexation parameters appear to have physically meaningful values. But, the calculated diffuse layer thickness with these models is nonsensical and the diffusivity in the diffuse layer is far too low as compared to that estimated from MD simulations;
- The detailed evaluation of single pore models presented in this report, with regard to molecular information on the one hand and experimental diffusion and static data on the other hand, demonstrates the need to consider a *distribution* of pore size as the important feature that must be taken into account to understand water, anion, and cation diffusivity in clay materials.

Recommended work for FY15 includes:

- Conduct detailed characterization of clay-material pore structure down to the resolution of the interlayer size to provide sufficient data to constrain and use more complex multi-porosity models.

### 3.5 REFERENCES

- Alonso, E.E., Alcoverro, J., Coste, F., Malinsky, L., Merrien-Soukatchoff, V., Kadiri, I., Nowak, T., Shao, H., Nguyen, T.S., Selvadurai, A.P.S., Armand, G., Sobolik, S.R., Itamura, M., Stone, C.M., Webb, S.W., Rejeb, A., Tijani, M., Maouche, Z., Kobayashi, A., Kurikami, H., Ito, A., Sugita, Y., Chijimatsu, M., Borgesson, L., Hernelind, J., Rutqvist, J., Tsang, C., Jussila, P. The FEBEX benchmark test: case definition and comparison of modeling approaches. *Int. J. Rock Mech. Min. Sci.*, 42, 611–638 (2005).
- Alonso, E.E., Vaunat, J., Gens, A. Modelling the mechanical behaviour of expansive clays. *Engineering Geology*, 54, 173–183 (1999).
- Altmann, S., Tournassat, C., Goutelard, F., Parneix, J.C., Gimmi, T., Maes, N., 2012. Diffusion-driven transport in clayrock formations. *Applied Geochemistry* 27, 463–478.
- Appelo, C.A.J., Van Loon, L.R., Wersin, P., 2010. Multicomponent diffusion of a suite of tracers (HTO, Cl, Br, I, Na, Sr, Cs) in a single sample of Opalinus Clay. *Geochimica et Cosmochimica Acta* 74, 1201–1219.
- Birgersson, M., Karnland, O., 2009. Ion equilibrium between montmorillonite interlayer space and an external solution: Consequences for diffusional transport. *Geochimica et Cosmochimica Acta* 73, 1908–1923.
- Bourg, I.C., Sposito, G., 2011. Ion exchange phenomena, in: *Handbook Soil Science*, second edition.
- Corkum, A.G., Martin, C.D., 2007. The mechanical behaviour of weak mudstone (Opalinus Clay) at low stresses. *Int. J. Rock Mech. Min. Sci.*, 44, 196–209.
- Davis J., Rutqvist J., Steefel C., Tinnacher R., Vilarrasa V., Zheng L., Bourg I., Liu H.-H., and Birkholzer J. Investigation of Reactive Transport and Coupled THMC

- Processes in the EBS: FY13 Report. Prepared for U.S. Department of Energy, Used Fuel Disposition, FCRD-UFD-2013-000216, Lawrence Berkeley National Laboratory (2013).
- Di Maio, C. Exposure of bentonite to salt solution: osmotic and mechanical effects. *Géotechnique* 46(4): 695-707 (1996).
- Di Maio, C., Discussion on exposure of bentonite to salt solution: osmotic and mechanical effects. *Geotechnique* XVVIII (3), 433–436 (1998).
- Gens, A, Alonso, E. A framework for the behaviour of unsaturated expansive clays. *Can. Geotech. J.* 29, 1013–1032 (1992).
- Gens, A. Soil - environmental interactions in geotechnical engineering. *Geotechnique*, 60, 3–74 (2010).
- Gens, A., Sánchez, M., Guimarães, L. do N., Alonso, E.E., Lloret, A., Olivella, S., Villar, M.V., Huertas, F. A full-scale in situ heating test for high-level nuclear waste disposal: observations, analysis and interpretation. *Geotechnique*, 59(4), 377–399 (2009).
- Gens, A., Sánchez, M., Sheng, D. On constitutive modelling of unsaturated soils. *Acta Geotechnica*, 1, 137–147 (2006).
- Gens, A., Vaunat, J., Garitte, B., Wileveau, Y. In situ behaviour of a stiff layered clay subject to thermal loading, observations and interpretation. *Geotechnique*, 57(2), 207–228 (2007).
- Glaus, M.A., Frick, S., Rosse, R., Van Loon, L.R., 2010. Comparative study of tracer diffusion of HTO, Na-22(+) and Cl-36(-) in compacted kaolinite, illite and montmorillonite. *Geochimica et Cosmochimica Acta* 74, 1999–2010.
- Glaus, M.A., Loon, L.R. van, Laer, L. van, Aertsens, M., Bruggeman, C., Govaerts, J., Maes, N., 2013. Benchmark experiments for the investigation of the diffusive behaviour of  $^{85}\text{Sr}^{2+}$  in compacted Na-illite, In: *Migration, Loughborough*.
- Guimarães, L. D. N., Gens, A. Sánchez, M. Olivella S. A chemo-mechanical constitutive model accounting for cation exchange in expansive clays. *Géotechnique* 63, 221-234 (2013).
- Holmboe, M. and Bourg, I.C., 2014, Molecular dynamics simulations of water and sodium diffusion in smectite interlayer nanopores as a function of pore size and temperature, *J. Phys. Chem. C*, 118, 1001-1013.
- Holmboe, M., Wold, S., Jonsson, M., 2012. Porosity investigation of compacted bentonite using XRD profile modeling. *Journal of Contam. Hydrol.* 128, 19–32.
- Klinkenberg, L.J. The Permeability of Porous Media to Liquids and Gases, in *API Drilling and Production Practice*, 200–213 (1941).
- Kozaki T., Inada K., Sato S., Ohashi H., 2001, Diffusion mechanism of chloride ions in sodium montmorillonite. *J. Contam. Hydrol.*, 47, 159-170.
- Lenhard, R., Fedors, R., Manepally, C., Pabalan, R., Ofoegbu, G., Chiang, K., Bradbury, J., Markley, C. Buffer and backfill workshop report, U.S. Nuclear Regulatory Commission, Contract NRC–02–07–006, 2011.
- Likos, W. J. and Wayllace, A. Porosity evolution of free and confined bentonites during interlayer hydration. *Clays and Clay Minerals* 58(3): 399-414 (2010).
- Mitchell J., Soga, K. *Fundamentals of Soil Behavior*, Third edition, John Wiley & Sons, INC. ISBN-13: 978-0471463023, (2005).

- Molera, M. and Eriksen, T., 2002, Diffusion of  $^{22}\text{Na}^+$ ,  $^{85}\text{Sr}^{2+}$ ,  $^{134}\text{Cs}^+$  and  $^{57}\text{Co}^{2+}$  in bentonite clay compacted to different densities: experiments and modeling, *Radiochim. Acta* 90, 753–760.
- Molera, M., Eriksen, T., Jansson, M., 2003, Anion diffusion pathways in bentonite clay compacted to different dry densities, *Applied Clay Science* 23, 69–76.
- Nutt, M., Used Fuel Disposition Campaign Disposal Research and Development Roadmap (FCR&D-USED-2011-000065 REV0), U.S. DOE Used Fuel Disposition Campaign, 2011.
- OECD, Engineering barrier systems and the safety of deep geological repositories (State-of-the-art Report), ISBN 92-64-18498-8, 2003.
- Olivella, S., Gens, A. Vapour transport in low permeability unsaturated soils with capillary effects. *Transport In Porous Media*, 40, 219–241 (2000).
- Parkhurst, D.L. and Appelo, C.A.J., 1999. User's guide to PHREEQC (version 2) - a computer program for speciation, reaction-path, 1D-transport, and inverse geochemical calculations. US Geol. Surv. Water Resour. Inv. Rep. 99-4259, 312p.
- Pousada, P.E. Deformabilidad de arcillas expansivas bajo succión controlada. Ph. D. Thesis, Technical University of Madrid, Spain (1982).
- Pusch, R., Knutsson, S., Mohammed, M.H. Isolation of hazardous waste in crystalline rock, *Journal of Earth Sciences and Geotechnical Engineering*, vol.2, no. 3, 57-75, 2012.
- Rutqvist J., Barr D., Birkholzer J.T., Chijimatsu M., Kolditz O., Liu Q.-S., Oda Y, Wang W.-Q. and Zhang C.-Y. Results from an international simulation study on coupled thermal, hydrological, and mechanical (THM) processes near geological nuclear waste repositories. *Nuclear Technology*, 163, 101–109 (2008).
- Rutqvist, J., Ijiri, Y. Yamamoto, H. Implementation of the Barcelona Basic Model into TOUGH-FLAC for simulations of the geomechanical behavior of unsaturated soils. *Computers & Geosciences*, 37, 751–762 (2011).
- Rutqvist, J., Zheng, L., Chen, F., Liu, H.-H., Birkholzer, J. Modeling of coupled thermo-hydro-mechanical processes with links to geochemistry associated with bentonite-backfilled repository tunnels in clay formations. *Rock Mech. Rock Eng.*, 47, 167–186 (2014).
- Sánchez, M., Gens, A., Guimarães, L. do N., Olivella, S. A double structure generalized plasticity model for expansive materials. *Int. J. Numer. Anal. Meth. Geomech.*, 29, 751–787 (2005).
- Sánchez, M., Gens, A., Olivella, S. THM analysis of a large-scale heating test incorporating material fabric changes. *Int. J. Numer. Anal. Meth. Geomech.*, 36, 391–421 (2012).
- Sridharan, A., Rao, S. M. and Murthy, N. S. Compressibility behaviour of homoionized bentonites. *Géotechnique* 36, 551-564 (1986).
- Tournassat, C., Appelo, C.A.J., 2011, Modelling approaches for anion-exclusion in compacted Na-bentonite. *Geochimica et Cosmochimica Acta* 75, 3698–3710.
- Tournassat, C., Neaman, A., Villiéras, F., Bosbach, D., Charlet, L., 2003, Nanomorphology of montmorillonite particles: Estimation of the clay edge sorption site density by low-pressure gas adsorption and AFM observations. *American Mineralogist* 88, 1989–1995.

Xu, T., N. Spycher, E. Sonnenthal, G. Zhang, L. Zheng and K. Pruess. TOUGHREACT Version 2.0: A simulator for subsurface reactive transport under non-isothermal multiphase flow conditions. *Computers & Geosciences* 37(6): 763-774 (2011).



## **4. DEMONSTRATION OF DISCRETE FRACTURE NETWORK MODELING CAPABILITY**

### **4.1 INTRODUCTION**

Relatively impermeable hard rocks such as fractured granite and fractured welded tuffs have been considered previously as potential repository host media. Fractures are ubiquitous in such media and provide the primary migration pathways for radionuclides. Experience has shown that flow and transport in fractured rock are rarely described adequately by uniform or mildly nonuniform isotropic continuum representations (Neuman 2005) and a range of alternatives to the classical continuum representation have been developed. These alternative approaches may be grouped into three general classes: discrete fracture network representations, complex continua representations, and hybrid representations.

Discrete fracture network (DFN) models depict the rock mass as an interconnected network of explicitly represented fractures. The approach is in the reductionist tradition, implicitly assuming that detailed statistical descriptions of small observable features will, once combined in numerical simulations, lead to understanding of the system as a whole. Networks of fractures are first stochastically generated using a stochastic model derived from site data. A computational mesh is placed on each fracture plane usually ensuring that the mesh on each of a pair of intersecting fractures matches along the intersection. Groundwater flow equations are then solved using this computational mesh. The final step is then to simulate radionuclide transport using the computed flow field, usually by particle tracking. Most large-scale applications do not explicitly mesh the matrix volumes between adjacent fractures. Instead the effects of diffusion into the unrepresented matrix volume are represented (modeled) in the transport step (see e.g. Painter et al. 2008). DFN simulations were introduced first in theoretical studies; feasibility of detailed site-specific applications has also been clearly demonstrated (e.g. Cvetkovic et al. 2004, Svensk Kärnbränslehantering 2011, Painter et al., 2012; Hyman et al., 2014).

Complex continua representations generalize a simple effective continuum representation to account for various flow and transport phenomena. Dual continuum models (Barenblatt et al. 1960; Warren and Root 1963) represent fractured porous rock as two overlapping and interacting continua. In its most general form (e.g. Duguid and Lee, 1977), known as the dual permeability model, flow and transport takes place in both the fracture and matrix continua while accounting for fluid and solute migration between the two continua in response to pressure and concentration differences. Commonly, flow in the matrix system is neglected relative to flow in the fracture system. In this case, the matrix acts as a non-conductive reservoir for fluid and/or solute storage and the fracture system provides the fluid migration pathways. In this variant, usually referred to as the dual porosity model, fluid and solute flux are proportional to the pressure and concentration differences between the two continua at a given location and time. The dual continuum class of models has also been generalized (Pruess and Narasimhan 1985; Zyvoloski et al. 2008) to better represent gradients internal to the matrix blocks. In this approach, multiple continua are used to represent matrix processes. Flow between

spatially adjacent matrix cells may be included or not represented, depending on the variant.

Regardless of how the matrix/fracture interactions are represented, multiple continuum models originally conceptualized the fracture flow system as having a representative elementary volume (REV) that establishes a spatial scale above which the flow properties become approximately independent of scale. For natural fracture patterns, which often have a broad distribution of fracture lengths, the existence of a classical REV scale may be questionable. Neuman proposed a stochastic continuum approach that does not require an REV (Neuman 1987, 2005). In his approach, an effective permeability tensor and other required flow/transport properties are assigned to each grid block in a conventional continuum conceptualization. However, the properties vary from grid cell to grid cell according to a stochastic model. Moreover, the stochastic model is dependent on the size of the grid block. Thus, a different stochastic model is required if the spatial discretization is changed. Parameterization of a stochastic continuum model, which generally requires inverse modeling of multiple pressure interference and solute tracer tests, has been demonstrated at the Apache Leap field site (e.g. Neuman 2005). The stochastic continuum model may be combined with any of the dual or multiple continua ideas to represent fracture/matrix interactions.

Hybrid methods adopt a reductionist view similar to DFN models but also use continuum representations for practical computational reasons (e.g. to reduce the overall size of the computational mesh). Hybrid methods fall into two subclasses: nested and upscaled. In nested models, explicit DFN models are used along transport pathways or in other regions where high spatial resolution is required and continuum representations are used in regions that are of less interest. This approach allows for a DFN representation of transport in and near expected transport pathways while still modeling a sufficiently large region to honor natural hydraulic boundary conditions. In upscaled models, explicit DFN representations are constructed and stochastically generated. However, the flow problem is not solved on the full DFN. Instead, the DFN is used to establish, grid block by grid block, equivalent permeability tensors for use in a continuum model. Jackson et al. (2000), Svensson (2001) and Botros et al. (2008) provide examples of upscaling algorithms for the permeability tensors. Experience with upscaled models for flow has generally been good, but the approach is questionable for transport. Extensions that attempt to recover the transport effects of subgrid velocity variability through stochastic simulation have emerged (Painter and Cvetkovic 2005) but have not been fully explored.

Experience suggests that it should be possible to model a sufficiently well-characterized site in a variety of ways and that combinations of methods may allow for the most efficient use of available information. Extensive studies by the Swedish Nuclear Fuel and Waste Management Company in support a safety case for a proposed spent fuel repository (Svensk Kärnbränslehantering 2011) has clearly demonstrated practical utility of hybrid approaches to flow and transport modeling. Given this experience it is likely that DFN and DFN/continuum hybrids will play an important role in future assessments of fractured hard rock sites. However, modern and non-proprietary modeling tools for

supporting such assessments and for addressing key unresolved scientific issues are lacking.

This section addresses Topic P1 of the R&D Plan for UFDC Natural Systems Evaluation and Tool Development – Development of Discrete Fracture Models. The longer-term objective is to develop discrete fracture network (DFN) flow and transport modeling capability, which was identified as a capability gap. The DFN software development process related to requirements definition, algorithm design, validation, and prototyping were summarized previously (Painter et al., 2014). This chapter provides a demonstration example using data from the site of the proposed Forsmark repository in Sweden.

**Table 4-1.** DFN parameters used in simulations of the Forsmark site

Set	Orientation Distribution: Fisher			Size Distribution: Power Law			Fracture Density  Number of fractures in 1 km <sup>3</sup>
	Mean Trend	Mean Plunge	Concentration  $\kappa$	$\alpha$	$R_x$ , m	$R_o$ , m	
1. (NS)	90.0°	0.0°	21.7	2.5	500	15	2093
						20	1019
						25	583
2. (NE)	135.0°	0.0°	21.5	2.7	500	15	2000
						20	920
						25	503
3. (HZ)	360.0°	90.0°	8.2	2.38	500	15	2285
						20	3887
						25	7711

## 4.2 APPLICATION TO THE FORSMARK SITE

The Swedish Nuclear Fuel and Waste Management Company (SKB) recently submitted an application for a license to construct a final repository for spent nuclear fuel. SKB is

owned by the utilities producing electricity by nuclear power in Sweden and is responsible for the handling of all spent nuclear fuel and other radioactive wastes generated as a result of nuclear power production in Sweden. If the application is approved and the repository constructed within the estimated time frame, it will be among the first, if not the very first, deep geological repository for spent nuclear fuel. The repository is to be constructed at approximately 500 m depth in crystalline bedrock according to the KBS-3 principle (Svensk Kärnbränslehantering, 2011), which implies a system of independently functioning barriers. The Forsmark area is located in northern Uppland within the municipality of Östhammar, about 120 km north of Stockholm. The Forsmark area consists of crystalline bedrock that has been affected by both ductile and brittle deformation. The ductile deformation has resulted in large-scale, ductile high-strain belts and more discrete high-strain zones. Tectonic lenses, in which the bedrock is less affected by ductile deformation, are enclosed between the ductile high strain belts. The proposed repository location is in the north-westernmost part of one of these tectonic lenses. The brittle deformation has given rise to reactivation of the ductile zones in the colder, brittle regime and the formation of new brittle fracture zones of variable size.

As a demonstration test of the new DFN capability, the DFN inferred (Svensk Kärnbränslehantering, 2011) for Forsmark was simulated. The purpose of the numerical experiments is to demonstrate that the new capability can be deployed in applications. Three fracture sets are represented. The stochastic parameters for the three fracture sets are given in Table 4-1. A three-dimensional domain of size 1000 m × 1000 m × 1000 m was used. The three sets of fractures are of circular shape and oriented according to Fisher distribution:

$$f(\theta) = \frac{\kappa \cdot \sin\theta \cdot e^{\kappa \cos\theta}}{e^{\kappa} - e^{-\kappa}}, \quad (4.1)$$

where  $\theta$  is the deviation of the fracture pole orientation from the mean orientation and the parameter  $\kappa > 0$  is the concentration parameter. The concentration parameter quantifies the degree of clustering; values approaching zero represent a uniform distribution on the sphere and large values imply small average deviations from the mean direction.

The fractures sizes at Forsmark obey a truncated power-law distribution with lower and upper cut-off radii of  $R_0$  and  $R_x$ , respectively. The power-law distribution is sampled by first generating a random number  $u$  from a uniform distribution between 0.0 and 1.0. The radius is then calculated as

$$R = R_0 \cdot \left[ 1 - u + u \cdot \left( \frac{R_0}{R_x} \right)^\alpha \right]^{-1/\alpha}. \quad (4.2)$$

Fracture transmissivity,  $\sigma$ , was estimated using a power-law relationship a correlated transmissivity model (Svensk Kärnbränslehantering, 2011)

$$\log(\sigma) = \log(a \cdot R^\beta), \quad (4.3)$$

with parameters  $a=1.6 \times 10^{-9}$ ,  $\beta=0.8$ . The fracture aperture,  $b$ , and fracture permeability,  $k$ , were partially correlated to fracture size and calculated using the cubic law (Adler et al. 2012)

$$\sigma = \frac{b^3}{12}, \quad k = \frac{b^2}{12}. \quad (4.5)$$

Pressure boundary conditions are applied to horizontal faces of the domain, assuming fluid flow from bottom to top along the  $z$  direction. The steady state pressure solutions and permeability fields are shown in Fig. 4-1 for one realizations of the network.

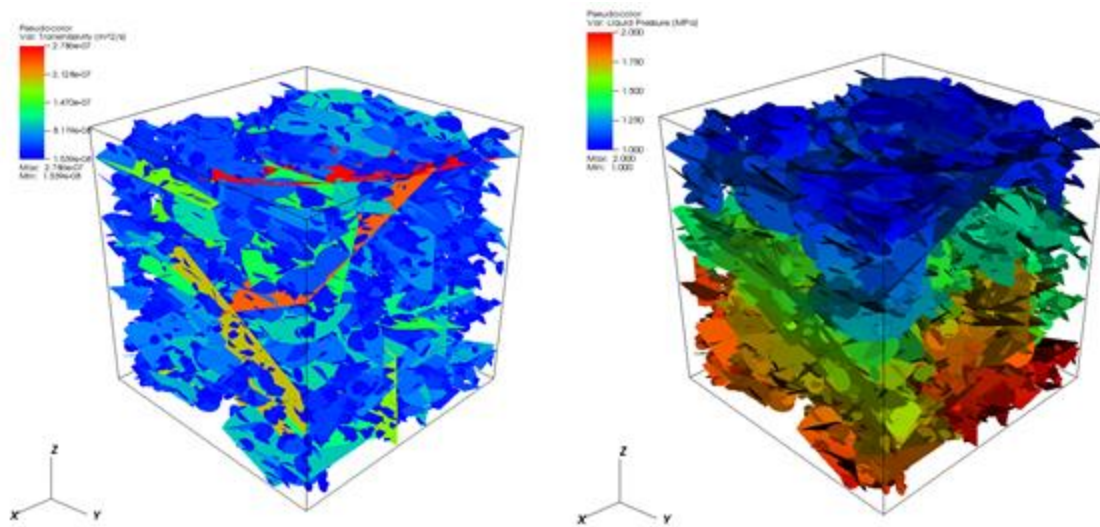


**Figure 4-1.** DFN (left) and resulting pressure distribution (right) using fracture network parameters similar to the Forsmark site. The simulated volume is  $1 \text{ km} \times 1 \text{ km} \times 1 \text{ km}$  and the fracture lower radius cutoff is 15 m.

In the first numerical experiment on particle tracking on the DFN all particles were placed initially on a small region ( $20\text{m} \times 20\text{m}$ ) in the center of inflow boundary. This experiment allows us to observe how fast particle trajectories diverge from their initial common location (Fig. 4-2) due to high topological variety of the DFN and probabilistic method used on fracture intersection. Final positions of particles are captured at the out-flow boundary and plotted in Fig. 4-2 (right image). A wide dispersion in space is observed, but so is channeling, with higher particle density on large fractures edge.

Travel time cumulative distributions are shown in Fig. 4-3, assuming uniform and flux-weighted injection of particles on the upstream side. With flux injection, the travel time distribution is well approximated by a power-law distribution. It should be noted that power-law distributions are fundamentally inconsistent with the advection dispersion equation. With uniform (residence) injection, the distribution is not well approximated by a power-law distribution, and shows instead two regions with different characteristic power-law exponents and a finite cutoff. Larger domains will be necessary to ensure ergodic conditions and eliminate the large realization-to-realization variability. Two realizations on a larger spatial domain are shown in Fig. 4-4. These examples are on a domain of size  $1000 \text{ m} \times 1000 \text{ m} \times 1000 \text{ m}$  and used the 15 m lower cutoff in fracture radius.

The relative importance of interfracture and intrafracture variability on solute transport is a long-standing scientific issue. Previous studies (e.g. Cvetkovic et al. 1999) of the transport effects of flow channeling in variable-aperture fractures typically considered a single fracture isolated from the rest of the network. Although these studies yield some clear insights into the process, the unrealistic boundary conditions for flow limit the usefulness of the results for field-scale applications. Flow in an individual fracture is controlled not only by the aperture variability, but also by the boundary conditions that are determined by connections with other fractures in the network. Fluid may enter and leave a fracture only where the fracture intersects other fractures. Those connections may represent a relatively small fraction of the fracture surface. This limited connection to other fractures introduces a certain degree of flow channeling independent of that caused by aperture variability. The relative importance of the two channeling mechanisms – heterogeneity-induced or geometry-induced – cannot be investigated without considering heterogeneous fractures embedded in a three-dimensional network. Previous attempts to address that issue (Painter, 2006) were limited by lack of reliable numerical tools. The new DFN simulation capability described here has been extended to incorporate both fracture-to-fracture and within-fracture variability (see Figs. 2-5 and 2-6), thus allowing the importance of single-fracture aperture variability to be reliably assessed at the field scale. Travel time statistics on that network are shown in Fig. 2-7 for different values of correlation length of aperture variability on individual fractures. The results are nearly independent of the correlation length, which suggests that the intrafracture variability is relatively unimportant at the field scale.

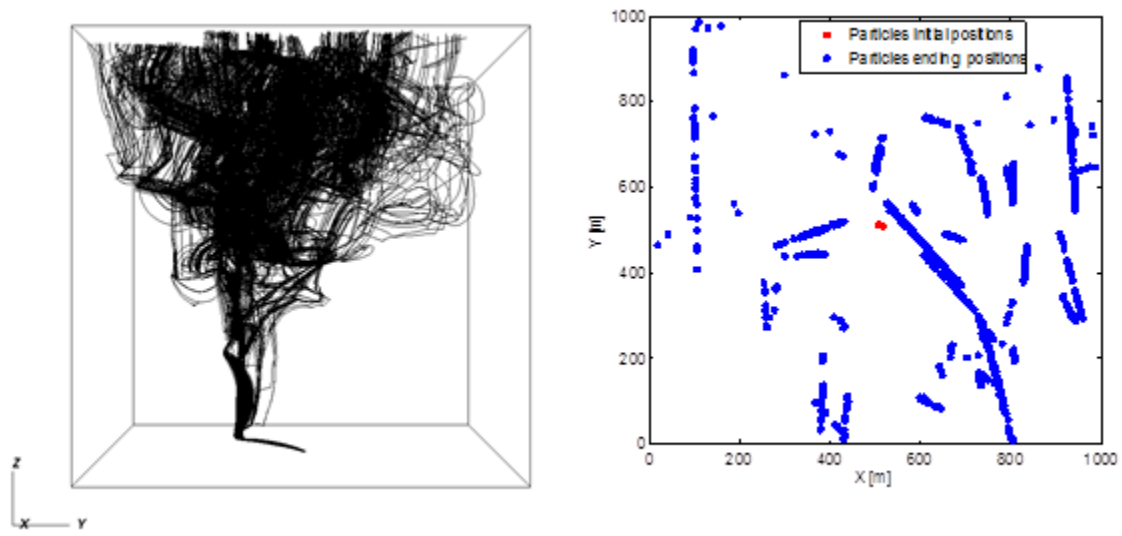


**Figure 4-2.** Particle trajectories (left) and horizontal projection of initial and exit locations (right).

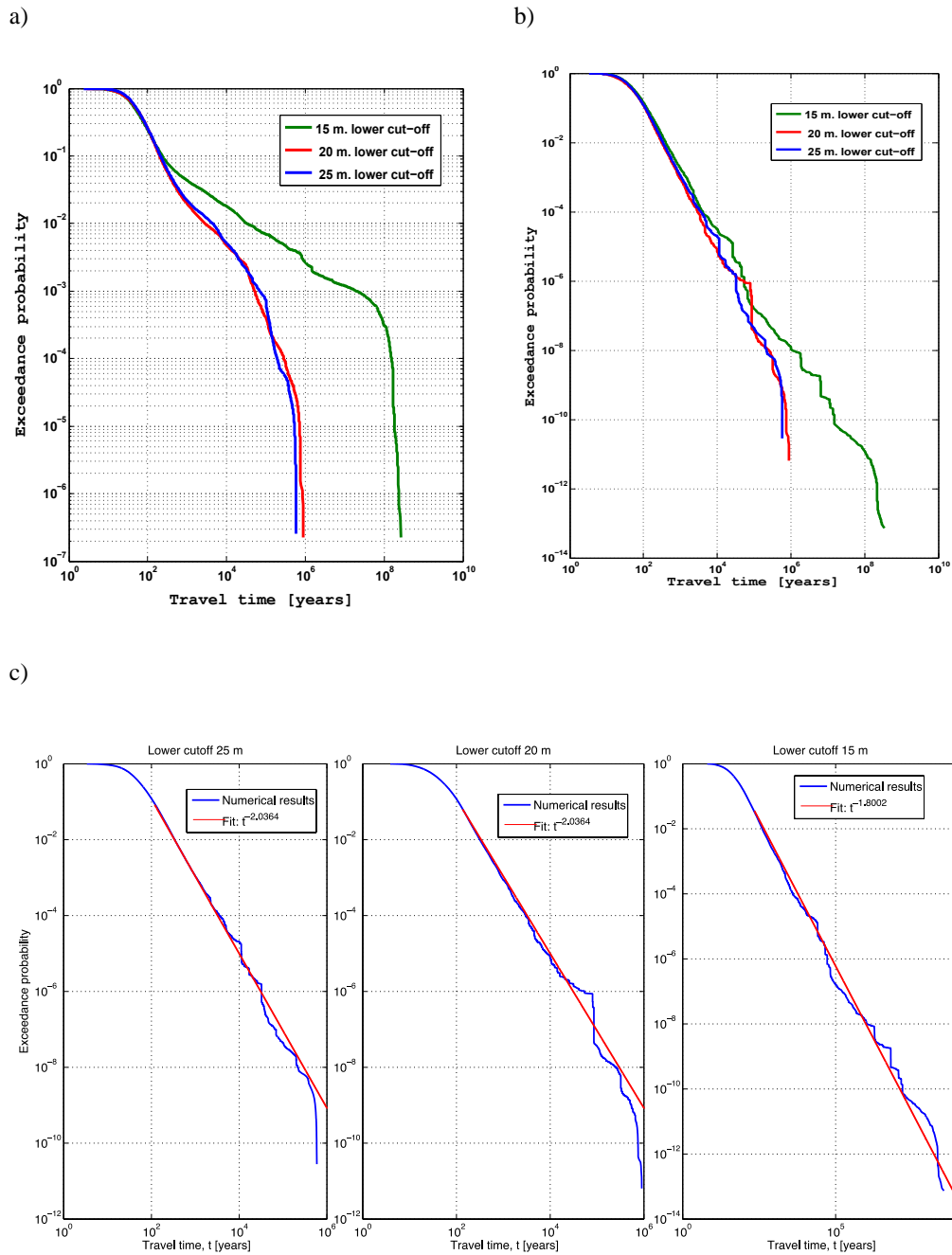


**Figure 4-3.** Cumulative distribution of particle travels time: a) uniformly weighted at starting positions; b) flux-weighted at starting positions; c) power law fit applied to the flux weighted results.

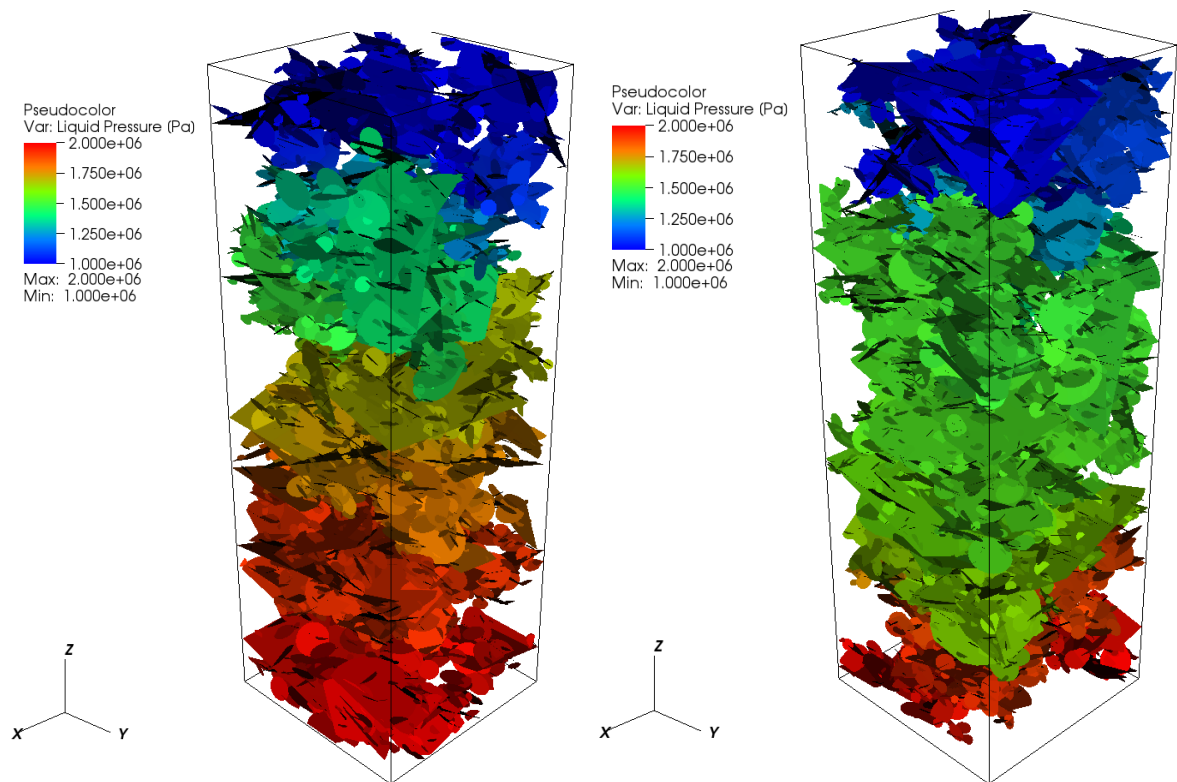


**Figure 4-4.** Two realizations of the pressure solution on a DFN simulated in a  $1 \text{ km} \times 1 \text{ km} \times 3 \text{ km}$  volume.

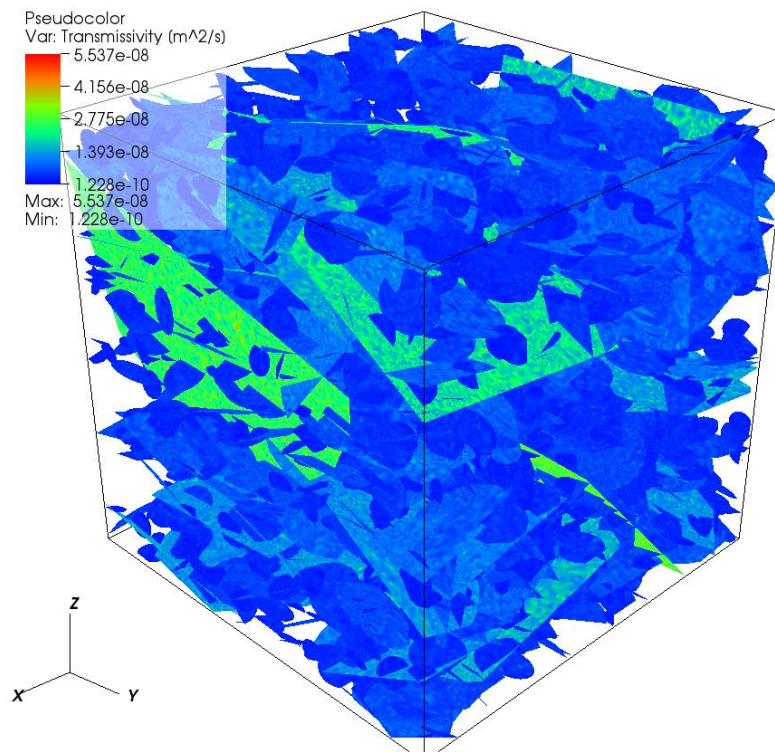


**Figure 4-5.** Realization with internal variability in fracture aperture and transmissivity

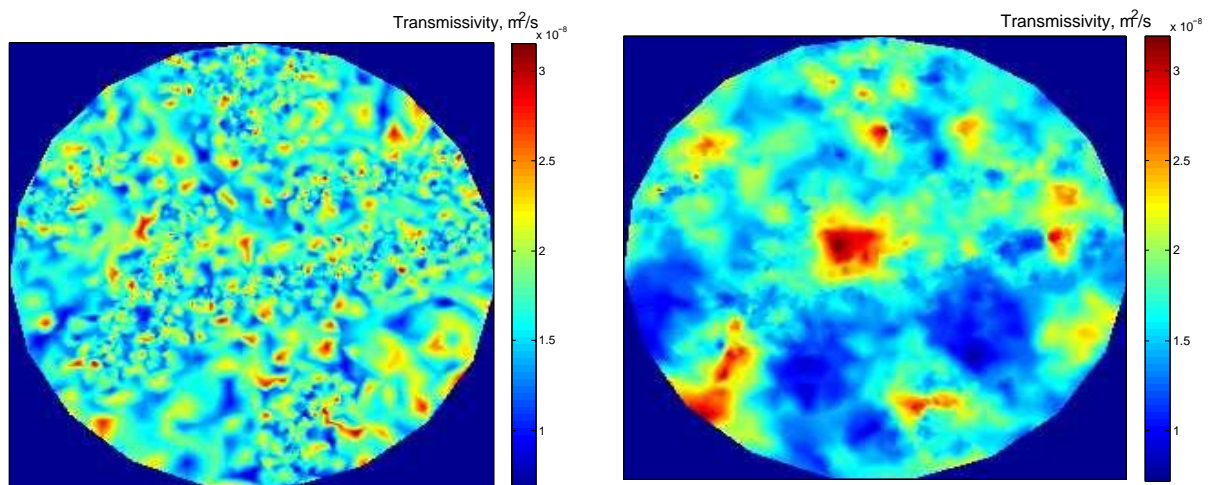


**Figure 4-6.** Transmissivity field on single fracture with correlation length of 10 m (left) and 50 m (right)

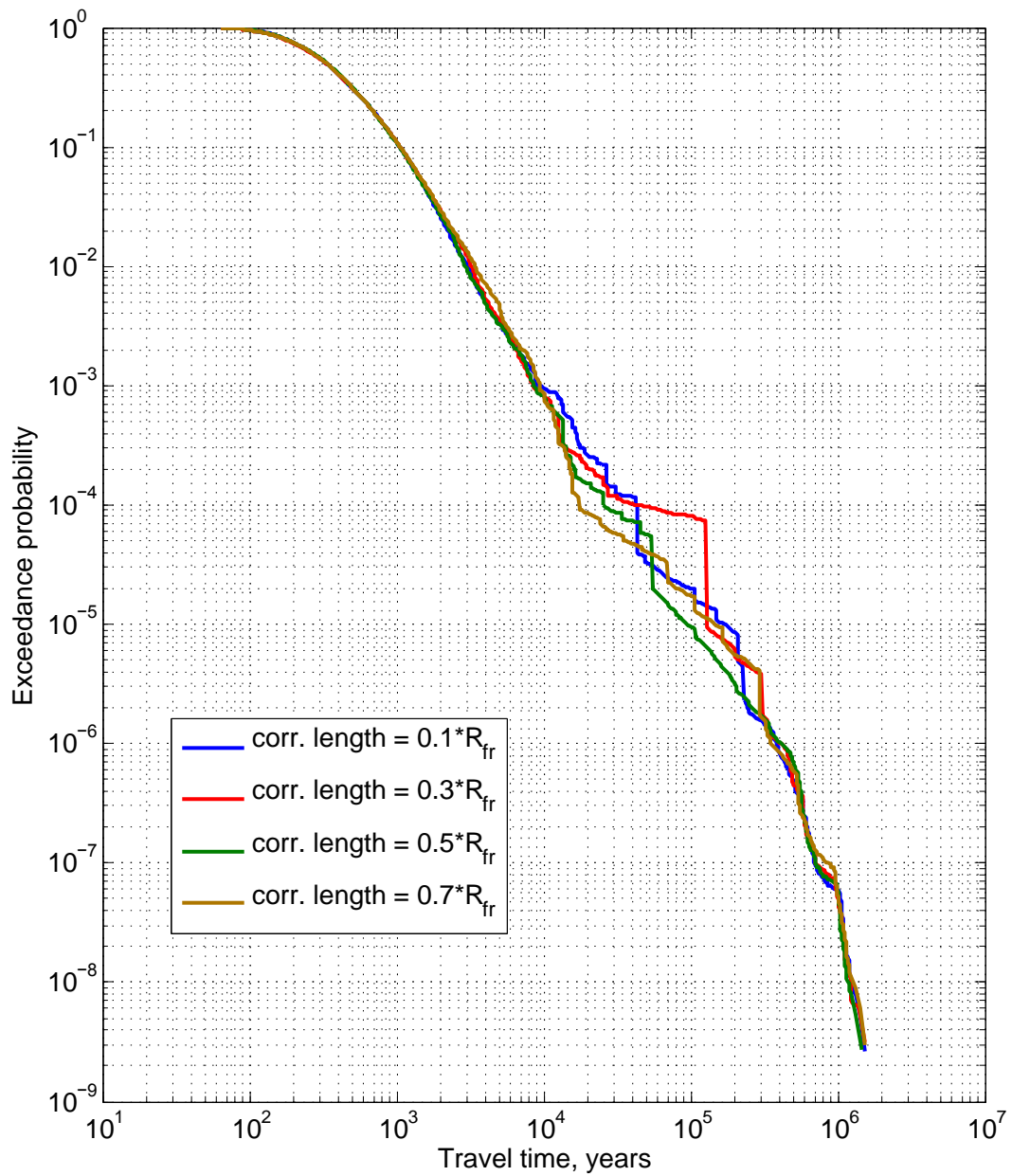


**Figure 4-7.** Distribution of travel times through a 1 km<sup>3</sup> DFN assuming intrafracture variability in aperture and transmissivity with different correlation lengths. Flux-weighted injection is assumed.

### 4.3 MODELING OF BRIE EXPERIMENT

The Swedish Nuclear Fuel and Waste Management Company (SKB) is currently conducting a multiyear flow experiment in the fractured crystalline rock at the Äspö Hard Rock Laboratory (Äspö HRL). The Bentonite Rock Interaction Experiment (BRIE, [www.chalmers.se/en/projects/Pages/brie.aspx](http://www.chalmers.se/en/projects/Pages/brie.aspx), Bockgård et al., 2010) is focused on the interaction between rock and bentonite in a borehole similar to those planned for emplacement of waste in the KBS concept for disposal in crystalline rock. The main objectives of the BRIE are better understanding of the movement of water across the bentonite-rock interface, better prediction of wetting of the bentonite, and better characterization methods for emplacement boreholes. The site selected for BRIE is located at 420 m depth in the TASO-tunnel of Äspö HRL.

Details of the BRIE can be found elsewhere (Bockgård et al., 2010). The main part of the experiment comprises two bentonite-filled boreholes that are monitored as water flows from the surrounding fracture network into the bentonite. The experiment involved several phases: characterization of the site, drawdown of the water table near the two emplacement boreholes, emplacement of the bentonite, wetting of the bentonite, and post-experiment recover and analyses of the bentonite. Tunnel and borehole geometry in the vicinity of the BRIE is shown in Figure 4-8. The two arrows indicate the positions of the boreholes in which bentonite was placed. Five pilot boreholes shown in Figure 4-8 were first drilled in the bottom of the tunnel. These boreholes and the nearby tunnels made it possible to infer the position of three major fractures, which are shown in Figure 4-9. The pilot boreholes were then pumped to draw down the water table. Two emplacement boreholes were then drilled to a diameter of 30 cm and the bentonite emplaced. The bentonite contained relative humidity sensors to allow the saturation of the bentonite to be monitored.

This section summarizes the status of the UFDC's efforts to model the BRIE experiment using the new DFN modeling capability. The main objectives of the work are to trial and refine the DFN modeling capability using the BRIE site as a relatively well characterized demonstration site. This work is part of SKB's Task Force on Groundwater Flow and Transport Modeling (Bockgård et al., 2010), which involves modeling teams from several countries.

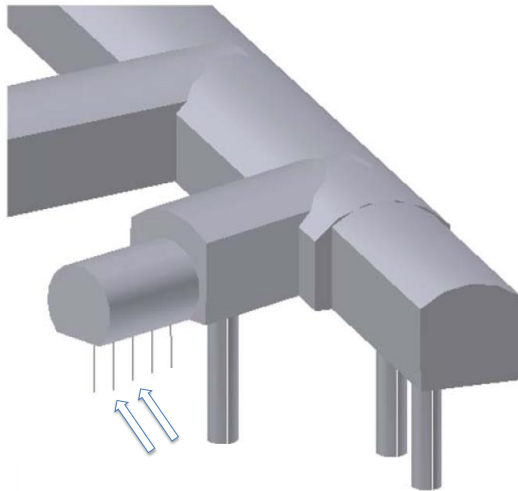


**Figure 4-8.** Tunnel geometry in the vicinity of the BRIE. The two arrows indicate the positions of the bentonite boreholes. Modified from Bockgård et al. (2010).

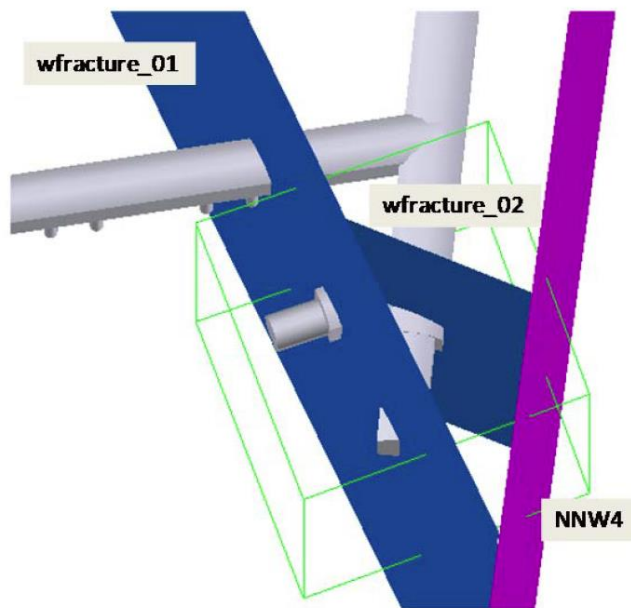


**Figure 4-9.** Location of known fractures near the BRIE. The green box shows the location of the modeling domain. Modified from Bockgård et al (2010).

### 4.3.1 Model Development Required to Support the BRIE Modeling Effort

The scope of the modeling task is to model wetting of the bentonite in the emplacement boreholes. This requires that flow in the fracture network near the boreholes also be modeled. The DFN grids are locally two-dimensional whereas the emplaced bentonite requires a conventional three-dimensional space-filling grid. As preliminary step in the BRIE modeling, the UFDC's DFN modeling capability needed to be extended to allow for hybrid DFN/volume grids.

The procedure used to create hybrid DFN/volume meshes is illustrated in Figure 4-10. In this example, the interior of a cylinder is to be meshed and merged with a DFN grid in the nearby rock volume. A DFN is first generated using the procedures described previously (Painter et al. 2012, Hyman et al. 2014). The generated DFN ignores the volume to be meshed. However, before the DFN is meshed, interfaces between fractures and the cylinder to be meshed are identified. A two-dimensional mesh is then created on each fracture in a way that conforms to the fracture intersections and to the fracture-volume interfaces (Figure 4-10a). The fracture grids are then merged, as described previously and in Hyman et al. (2014). In the second step, nodes on the fractures within the volume to be meshed are removed (Figure 4-10b). A tetrahedral mesh that conforms to the fracture intersection is then created within the cylinder. In the final step, the tetrahedral mesh and the DFN mesh are merged and duplicate nodes removed (Figure 4-10c). The LaGriT software (Los Alamos Grid Toolbox, 2013) was used to execute the meshing calculations.

### 4.3.2 Scoping Calculations

A set of scoping calculations were first performed to test the capability to solve for flow in hybrid tetrahedral/DFN grids. Those scoping calculations used a single fracture intersecting the bentonite volume. The FEHM software was used (Zyvolosky, 2007). FEHM has an option for defining the same node multiple times. It then imposes a constraint that the unknowns be the same for a multiply defined node. That capability simplifies the construction of the mesh because it avoids having to merge control volumes at the interface between the three-dimensional and two-dimensional meshes, which would create issues with property assignments at the merged control volumes.

The van Genuchten model (van Genuchten, 1980) was used for both the bentonite and the rock fracture. In the van Genuchten model, liquid saturation  $s_l$  is related to capillary pressure as

$$s_l = \left[ 1 + \left( \frac{P_g - P_l}{P_0} \right)^{\frac{1}{1-\lambda}} \right]^{-\lambda} \quad (4.6)$$

where  $P_g$  is gas pressure,  $P_l$  is liquid pressure, and  $P_0$  and  $\lambda$  are empirical parameters. The reference case parameters used for the fracture and bentonite are provided in Table 1. The initial saturation of the bentonite was specified as 36%. The fracture was initially saturated with water. The boundary conditions on the fracture edges were specified at 2 MPa. Richards model was used for the reference case.

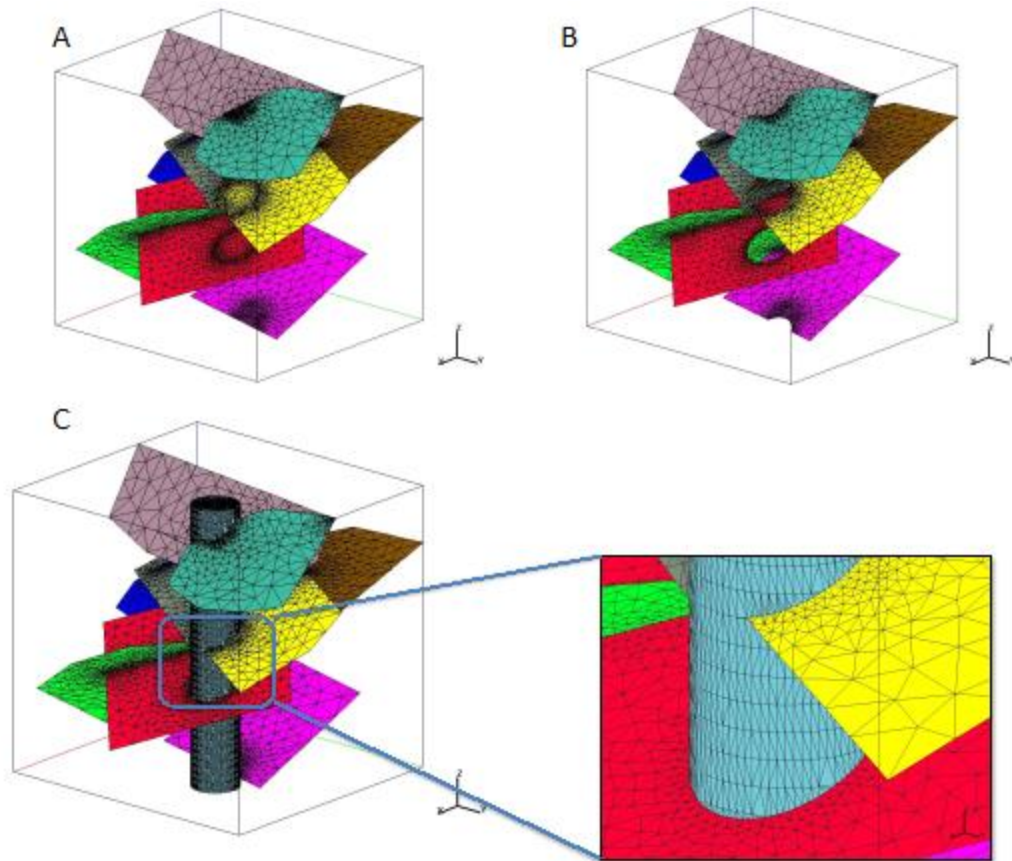


**Figure 4-10.** Example showing the creation of a hybrid tetrahedral/DFN mesh. Such hybrid meshes were required to model the rewetting of bentonite in the BRIE.

**Table 4-2.** Parameter Values Used in the Scoping Calculations (Bockgård et al., 2010)

Parameter	Bentonite	Fracture
van Genuchten pressure parameter $P_0$ [MPa]	9.23	1.74
van Genuchten shape parameter $\lambda$ [-]	0.3	0.6
Hydraulic conductivity [m/s]	$6.4 \times 10^{-14}$	Not applicable
Porosity [-]	0.44	Not applicable

Transmissivity [m <sup>2</sup> /s]	Not applicable	$5 \times 10^{-10}$
Transport Aperture [m]	Not applicable	$10^{-4}$

Results for the reference case at 10 days, 6 months and 1 year are shown in Figure 4-11. The top row of images shows the liquid saturation in three-dimensional view. The bottom row shows the saturation at a horizontal cut at the fracture plane. After about 1 year, enough water has been imbibed into the bentonite to raise the saturation in the bentonite at the location of the fracture to approximately 65%. Water is also starting to migrate upward in the bentonite.

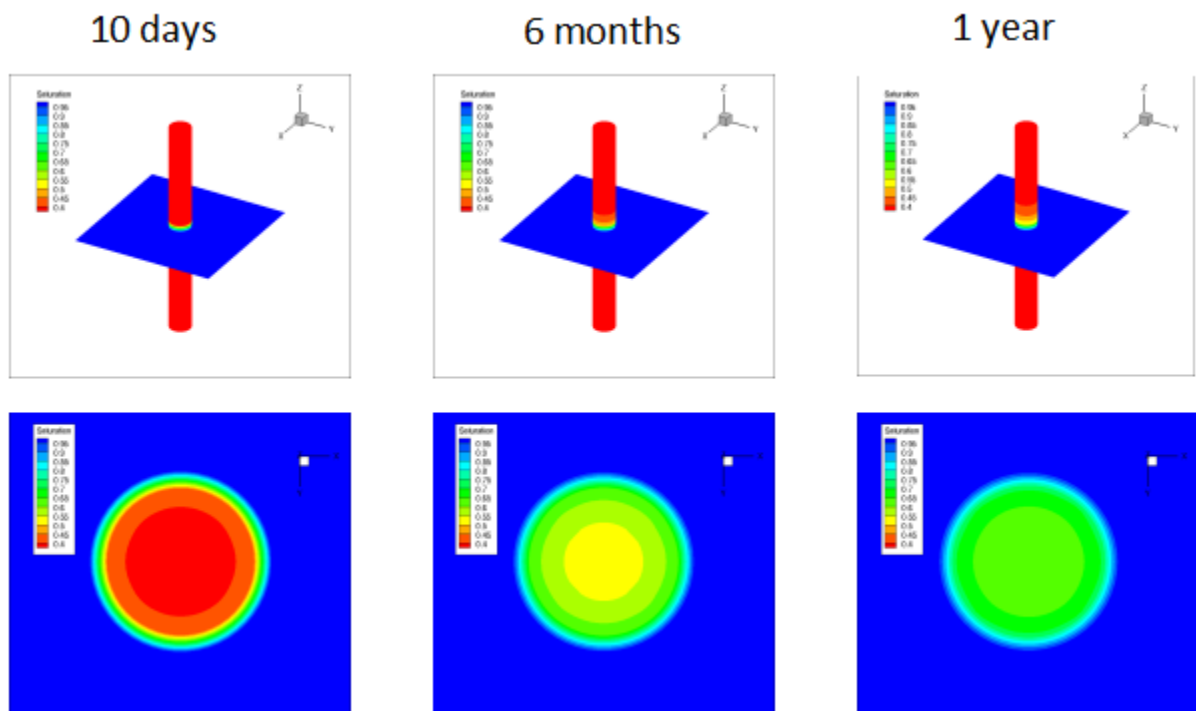


**Figure 4-11.** Liquid saturation for a scoping calculation using a single fracture and a bentonite cylinder representing one of the BRIE boreholes. The images in the bottom row are at the plane of the fracture.

A comparison between the Richards equation representation, which treats gas as a passive phase and ignores the conservation equation for air, and a more complete representation that solves the two-component system is shown in Figure 4-12. There is no

significant difference between the two representations at 1 year, which suggests that the Richards equation representation is adequate for representing the rewetting process. This comparison would need to be revisited for longer simulation times, however.

Liquid saturation at 1 year for the reference case is compared to two variant cases in Figure 4-13. The images on the left show liquid saturation for a variant case in which bentonite permeability is higher by an order of magnitude. The images on the right are for the case with an annular gap at the outer edge of the bentonite cylinder. The effect of the annular gap is represented by increasing vertical permeability in the outermost ring of cells. In both variant cases, the bentonite wetting progresses faster than in the reference case. A variant case with higher fracture permeability was also run. That result was not significantly from the reference case and is not shown.

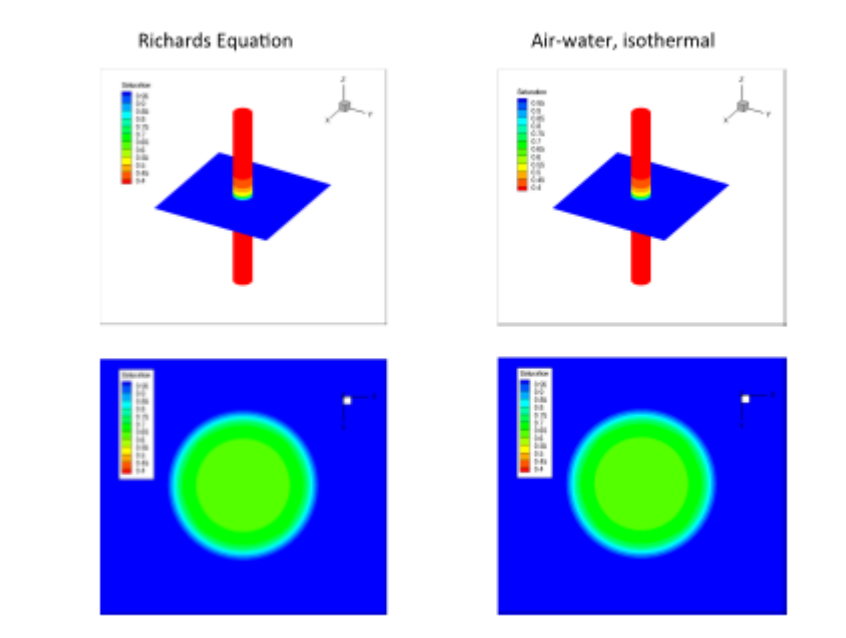


**Figure 4-12.** Comparison between the Richards equation representation and a more complete two-component representation. Shown is liquid saturation at 1 year.

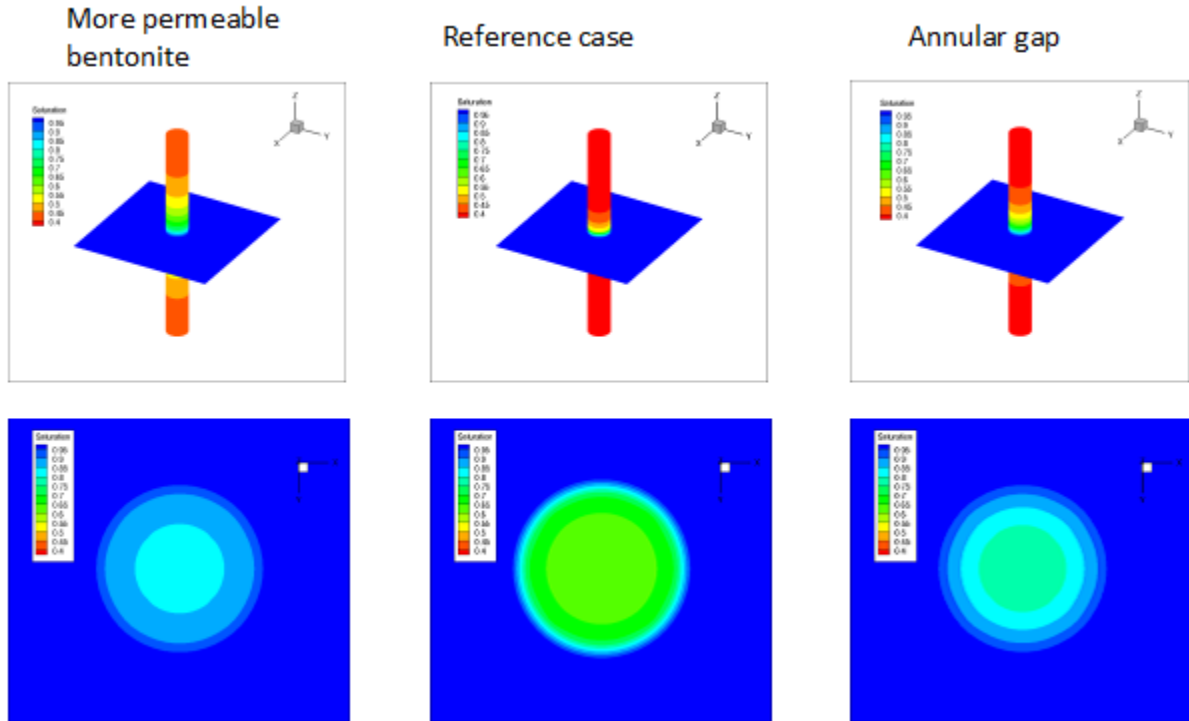


**Figure 4-13.** Comparison between the reference case scoping run and two variant cases. Shown is liquid saturation at 1 year.

### 4.3.3 Model Setup

A primary goal of this work is to gain experience in applying advanced DFN models in practical applications that involve complicated geometries and boundary conditions. Task 8d of SKB's Task Force on Groundwater Flow and Transport Modeling is a valuable application for that purpose. In Task 8d, the flows in the fractured granite surrounding the two BRIE boreholes as well as flow in the boreholes themselves are being modeled. This section describes preliminary model setup for Task 8d.

Model geometry is shown in Figure 4-9. The domain of interest is a 40 m × 40 m × 40 m cube. The model domain contains multiple tunnels, the two BRIE boreholes, and three deterministic fractures. For this work, the task description (Bockgård et al., 2010) specified a DFN model for stochastically simulating unobserved fractures (Table 4-3). This model used the isotropic Fisher distribution (Fisher, 1953) for fracture orientation

$$f(\theta) = \frac{\kappa \sin \theta e^{\kappa \cos \theta}}{e^{\kappa} - e^{-\kappa}} \quad (4.7)$$

where  $t$  is the deviation of the fracture pole orientation from the mean orientation and the parameter  $k > 0$  is the concentration parameter. The concentration parameter quantifies the degree of clustering; values approaching zero represent a uniform distribution on the sphere and large values imply small average deviations from the mean direction.

**Table 4-3.** DFN Parameters for the Fractured Rock Mass Near the BRIE Boreholes (Bockgård et al., 2010)

Set	Orientation Distribution: Fisher			Size Distribution: Power Law		Fracture Density
	Mean Trend	Mean Plunge	Concentration Parameter	Lower Cutoff $r_0$	Exponent $k_r$	Area per Volume $P_{32}$
1	280°	20°	10	0.25 m	2.6	1.1 m <sup>-1</sup>
2	20°	10°	15	0.25 m	2.6	2 m <sup>-1</sup>
3	120°	50°	10	0.25 m	2.6	0.75 m <sup>-1</sup>

A workflow was developed for modeling the BRIE experiment. The major steps are:

1. A realization of the DFN model is created using stochastic simulation. The stochastically generated fractures are combined with the three deterministic fractures.
2. Two meshes are created. In the first, the DFN model is meshed without the boreholes. In the second, the DFN is meshed in combination with a tetrahedral mesh for the interior of the boreholes using the methods described in Section 4.3. These two meshes do not include tunnels.
3. The tunnel is represented in both meshes by specifying all nodes that fall inside the tunnel as boundary nodes with pressure specified as atmospheric.
4. Boundary conditions are mapped to the faces of the cube in both meshes. Pressure results from a larger simulation were provided for that purpose.
5. A steady-state flow simulation is performed without the boreholes to establish pre-experiment conditions in the fracture network.
6. The result of Step 5 is used as initial condition for a transient flow simulation with the BRIE boreholes represented. The liquid saturation index in the bentonite is initially 36%. Of interest is the rewetting of the bentonite.

The result of Step 2, a meshed realization of the DFN with the three deterministic fractures and the two BRIE boreholes is shown in Figure 4-14. For this preliminary simulation the lower cutoff was increased to 1.0 m to reduce the size of the network, with appropriate adjustments to the fracture density. The network contains approximately 3500 stochastically generated fractures. The result of Step 3, a computational mesh with tunnel nodes identified is shown in Figure 4-15. The tunnel nodes are blue and green. Non-tunnel nodes are shown in red.

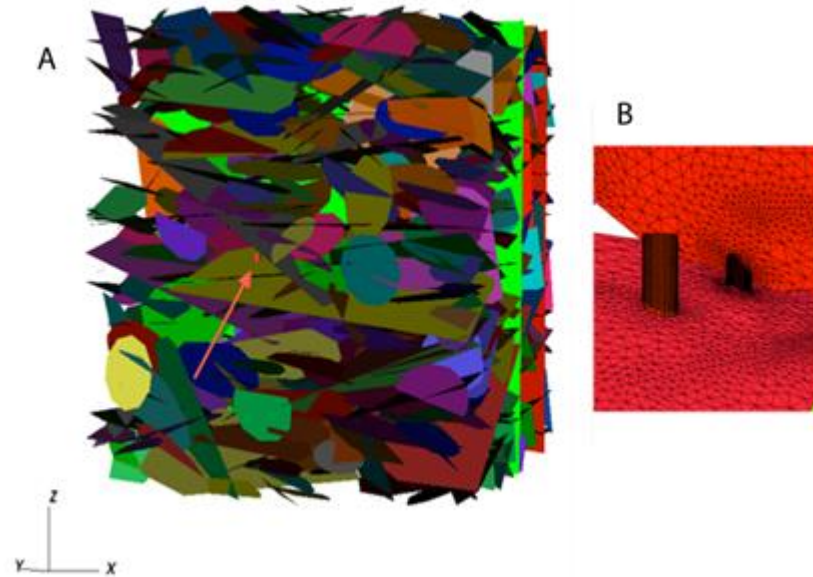


**Figure 4-14.** Computational mesh for the three-dimensional model of the BRIE experiment. The DFN and boreholes are shown in A. The arrow indicates the position of one of the boreholes. A detail from the computational mesh showing the merged DFN and tetrahedral mesh is shown in B.

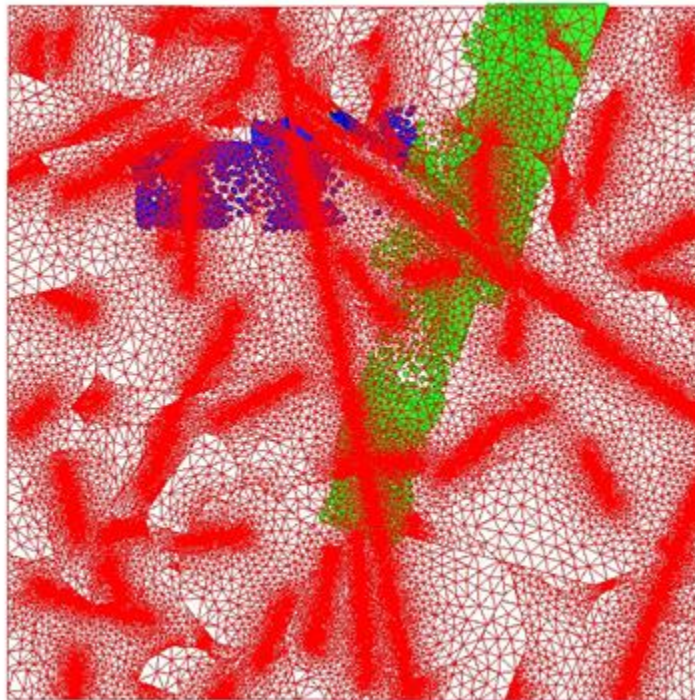


**Figure 4-15.** Computational mesh with tunnel nodes tagged (blue and green).

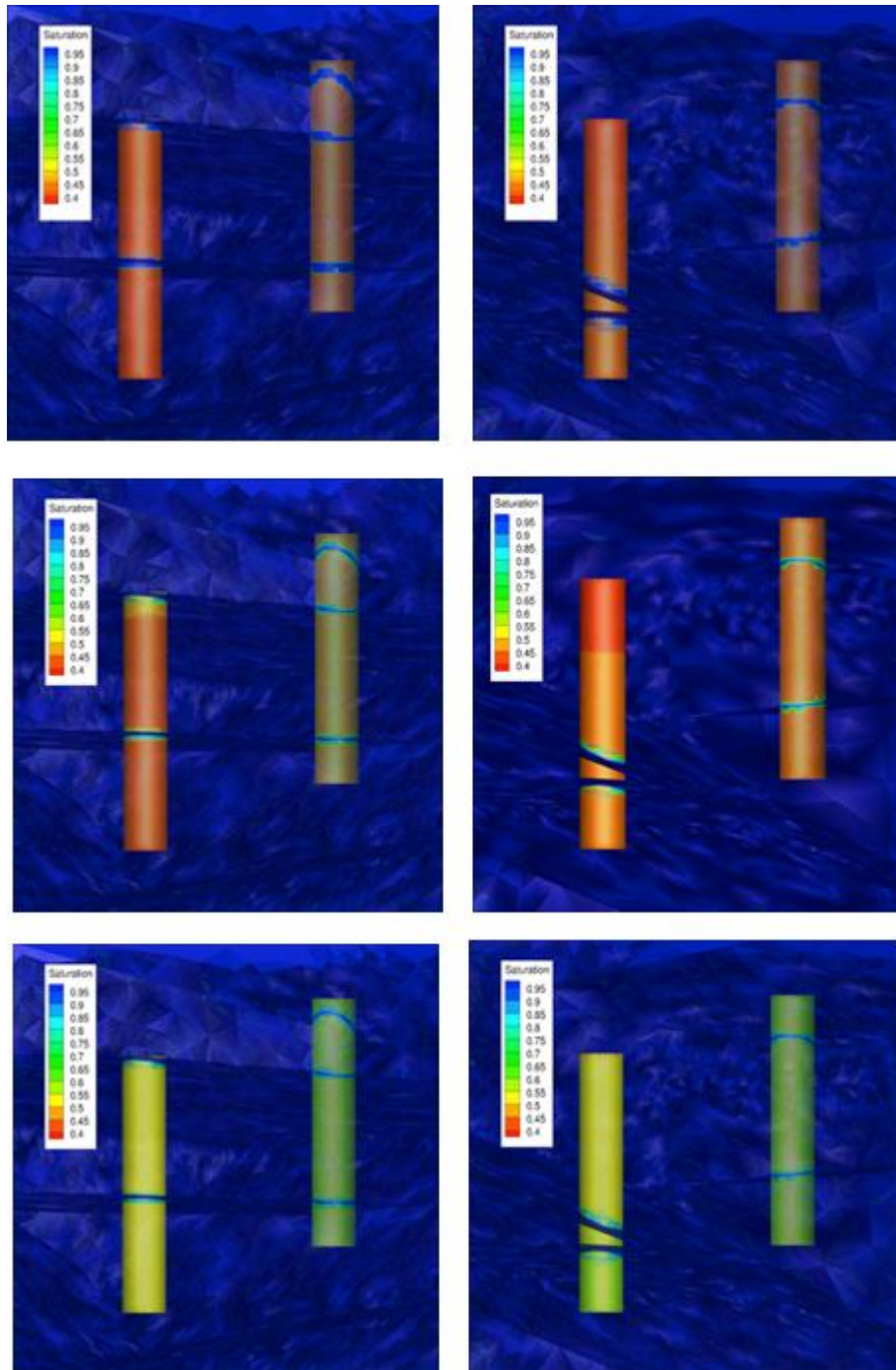


**Figure 4-16.** Details from two simulations of rewetting of the BRIE experiment boreholes. Results from one realization of the DFN are shown in each of the two columns. The top row is at 3 months, the middle row is at 6 months, and the bottom row is after one year of rewetting.

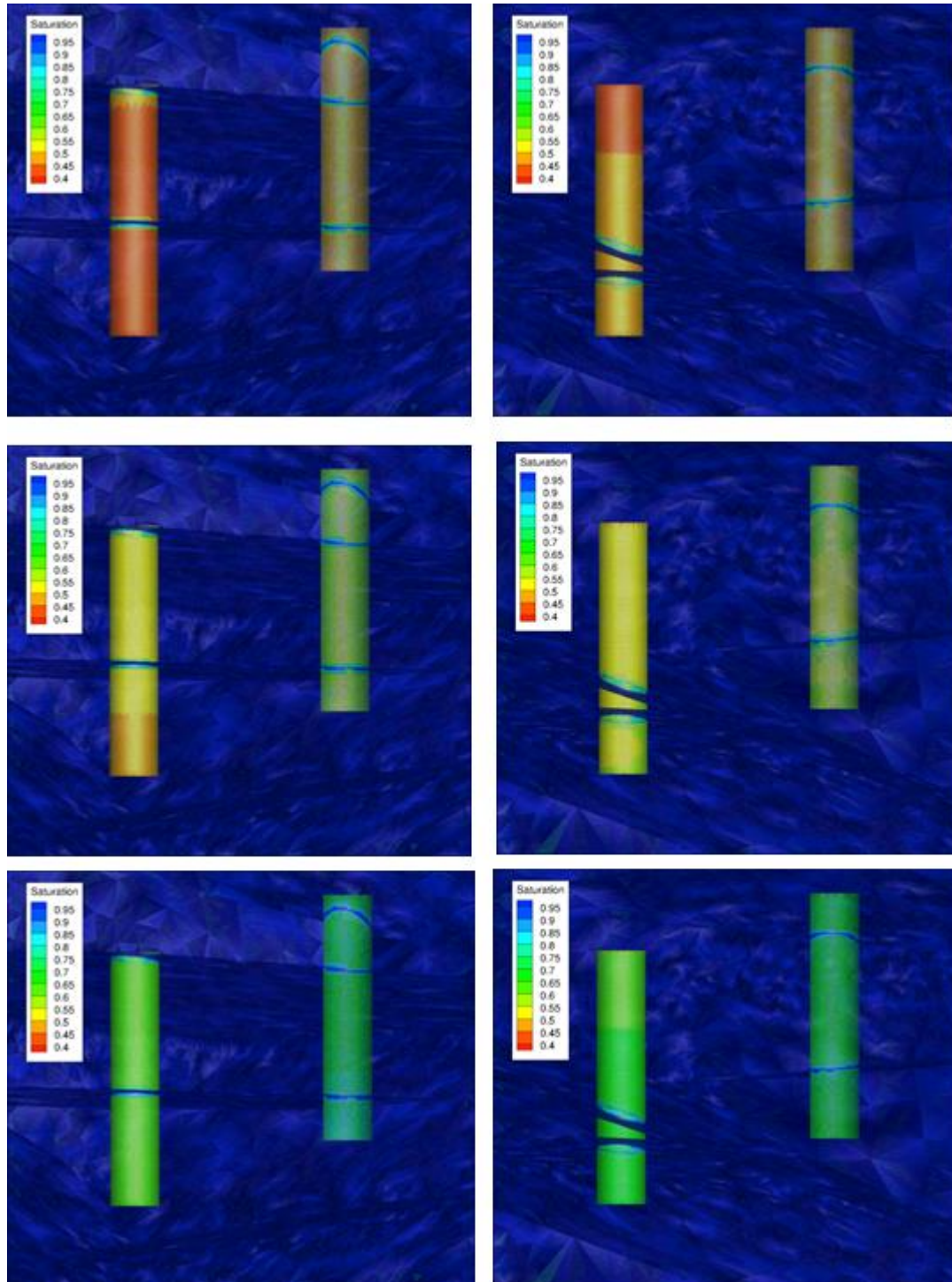


**Figure 4-17.** Details from two simulations of rewetting of the BRIE experiment boreholes, assuming higher values of permeability in the boreholes. Results from one realization of the DFN are shown in each of the two columns. The top row is at 3 months, the middle row is at 6 months, and the bottom row is after one year of rewetting.

#### 4.3.4 Initial Results

Initial results for rewetting of the BRIE experiment boreholes for two realizations of the DFN are shown in Figure 4-16 at 3 months, 6 months, and 12 months. Little difference is noted between the two realizations. Both realizations show a steep gradient in liquid saturation in the bentonite near where it intersects with fractures. Away from that intersection, the bentonite is rewetting relatively uniformly. This dependence of saturation on distance from the fracture intersection is attributed to the shape of the capillary pressure versus saturation curve, which provides for strong suction at lower saturation values. Corresponding results assuming larger values of the permeability of bentonite are shown in Figure 4-17.

#### 4.4 SUMMARY

DFN generation, parallel flow solutions, and particle tracking were demonstrated at application-relevant scales using fracture parameters from a well-characterized site. We also developed and demonstrated the capability to simulate intrafracture variability within a full-scale DFN network. The ability to produce high-quality computational DFN meshes suitable for state-of-the-art parallel subsurface flow codes is a unique capability that will allow large DFNs to be considered in applications. The ability to reliably track particles on DFN control volume grids is also a unique capability.

There are two overarching motivations for this work on DFN modeling tools. First, the tools under development will be necessary should the UFDC be asked to evaluate a potential future site in fractured rock. Second, there are several unresolved generic scientific issues associated with flow and transport in fractured rock that these tools will be able to address. Of the component pieces of the work, the generation of a high-quality DFN computational mesh is largely complete for the situation where the space between fractures is not meshed. Further work is required to develop meshing capability for the spaces between fractures, which may be needed to address some of the unresolved issues associated with transport in fractured rock. In addition, testing of the DFN capability has revealed that the current computational bottleneck is in the DFN generation step. Although progress has recently been made in improving that computational bottleneck, additional optimization of the algorithm and software would be advantageous to enable larger and more detailed DFNs to be considered.

Refinement and extension of the UFDC's DFN modeling capability was undertaken to enable representation of the tetrahedral mesh within the DFN mesh. The two realizations of the DFN with boreholes in place for the BRIE project is an important demonstration of an advanced modeling capability combining volume and DFN meshes, and incorporating complex geometries. These simulations used the FEHM code to merge the volume and DFN meshes. FEHM has unique capability to use define redundant computational nodes, which greatly facilitated the merging of the meshes. Modification of the PFLOTRAN code to introduce similar capability would be useful to allow for parallel simulations. Comparison of simulated and measured saturation values in the BRIE borehole is underway.

## 4.5 REFERENCES

- Adler, P.M., Thovert. J.-F., Mourzenko, V.V., Fractured Porous Media, Oxford University Press, 2012.
- Arbogast T., Cowsar L. C., Wheeler M. F., Yotov I., 2000. Mixed finite element methods on non-matching multiblock grids, *SIAM Journal Numerical Analysis* 37(4), 1295-1315.
- Barenblatt, G.I., Zheltov Y.P., Kochina I.N., 1960. Basic concepts in the theory of seepage of homogeneous liquids in fissured rocks. *Journal of Applied Mathematics of Mechanics (English Translation)* 24, 1286–1303.
- Bockgård, N., Vidstrand, P., Åkesson, M., Fransson, Å. and Stigsson, M. (2010) Task 8: Modelling the Interaction between Engineered and Natural Barriers – an Assessment of a Fractured Bedrock Description in the Wetting Process of Bentonite at Deposition Tunnel Scale. SKB report 2010-04-14. SKB, Stockholm. Revised 10/10/2012.
- Botros F. E., Hassan A. E., Reeves D. M., and Pohll G., 2008. On mapping fracture networks onto continuum, *Water Resources Research* 44, W08435, doi:10.1029/2007WR006092.
- Cordes C. and Kinzelbach W., 1992. Continuous groundwater velocity field and path lines in linear, bilinear, and trilinear finite elements, *Water Resources Research* 28(11), 2903-2911.
- Cvetkovic V, Selroos J-O, Cheng H (1999) Transport of reactive tracers in rock fractures. *J Fluid Mech* 378:335–356
- Cvetkovic V., Painter S., Outters N., and Selroos J.-O., 2004. Stochastic simulation of radionuclide migration in discretely fractured rock near Aspo hard rock laboratory, *Water Resources Research* 40, W02404, doi:10.1029/2003WR002655.
- Duguid J.O. and Lee P. C. Y., 1977. Flow in fractured porous rock, *Water Resources Research* 13, 558–566.
- Ewing R., Lazarov R., Lin T., and Lin Y., 2000. The mortar finite volume element methods and domain decomposition. *East-West Journal of Numerical Mathematics* 8, 93–110.
- Fisher, R.A., 1953. Dispersion on a Sphere. *Proc. Roy. Soc. London Ser. A.*, 217: 295-305
- Jackson, C., Hoch, A., Todman, S., 2000. Self-consistency of a heterogeneous continuum porous medium representation of a fractured medium, *Water Resour. Res.* 36 (1), 189-202.
- Hyman, J., Gable, C.W., Painter, S.L., and Makedonska, N. 2014. Conforming Delaunay Triangulation of Stochastically Generated Three Dimensional Discrete Fracture Networks: A Feature Rejection Algorithm for Meshing Strategy. *SIAM Journal on Scientific Computing* 36(4), A1871-A1894.
- Los Alamos Grid Toolbox, LaGriT, 2011. Los Alamos National Laboratory, <<http://lagrit.lanl.gov>>.
- Lichtner, P.C., Hammond, G.E., Bisht, G., Karra, S., Mills, R.T., and Kumar, J., 2013. PFLOTRAN User's Manual: A Massively Parallel Reactive Flow Code.

- Mosé R., Siegel P., Ackerer P., and Chavent G., 1994. Application of the mixed hybrid finite element approximation in a groundwater flow model: Luxury or necessity?, *Water Resources Research* 30(11), 3001–3012, doi:10.1029/94WR01786.
- Neuman, S. P., 1987. Stochastic continuum representation of fractured rock permeability as an alternative to the REV and discrete fracture concepts. In Farmer I.W., Daemen J. J. K., Desai C.S., Glass C.E. Neuman S. P. (eds) *Rock Mechanics, Proceedings of the 28<sup>th</sup> US Symposium*, Tucson, Arizona. AA Balkema, Rotterdam.
- Neuman, S. P., 2005. Trends, prospects and challenges in quantifying flow and transport through fractured rocks, *Hydrogeology Journal* 13, 124–147.
- Painter S. and Cvetkovic V., 2005. Upscaling discrete fracture network simulations: An alternative to continuum transport models, *Water Resources Research* 41, W02002, doi:10.1029/2004WR003682.
- Painter S. 2006. Effect of single-fracture aperture variability on field- scale transport. SKB R-06-25, Svensk Kärnbränslehantering AB,, Stockholm.
- Painter S., Cvetkovic V., Mancillas J., and Pensado O., 2008. Time domain particle tracking methods for simulating transport with retention and first-order transformation, *Water Resources Research* 44, W01406, doi:10.1029/2007WR005944.
- Painter S., Gable C., and Kelkar S., 2011. Pathline tracing on fully unstructured control volume grids. *Computational Geosciences* 16(4) 1125–1134.
- Painter, S., Gable, C., Makedonska, N., Hyman, J., Hsieh, T.-L. Bui, Q., Liu, H.H., Birkholzer, J., 2012. Fluid Flow Model Development for Representative Geologic Media. Los Alamos National Laboratory. LAUR-12-26878. FCRD-UFD-2013-000058.
- Pichot G., Erhel, J., de Dreuzy, J. R., 2010. A mixed hybrid Mortar method for solving flow in discrete fracture networks. *Applicable Analysis: An International Journal* 89 (10), 1629–1643.
- Pruess K. and Narasimhan, T.N., 1985. A practical method to modeling fluid and heat flow in fractured porous media. *Society Petroleum Engineers Journal* 25(1), 14–26.
- Pruess K., Oldenburg C., and Moridis G., 1999. TOUGH2 Users Guide, Version 2.0, LBNL-43134, Lawrence Berkeley National Laboratory, Berkeley CA.
- Svensk Kärnbränslehantering AB, 2011. Long-term safety for the final repository for spent nuclear fuel at Forsmark, SKB TR-11-01, Svensk Kärnbränslehantering AB
- Svensson U., 2001. A continuum representation of fracture networks: Part I. Method and basic test cases, *Journal of Hydrology* 250, 170–186.
- van Genuchten, M., 1980. A closed-form equation for predicting the hydraulic conductivity of unsaturated soil, *Soil. Sci. Soc. Am. J.*, 44(5), 892-898.
- Wang, Y.F., 2011. Research and Development Plan for Natural System Evaluation and Tool Development. U.S. Department of Energy.
- Warren J.E. and Root P.J., 1963. The behavior of naturally fractured reservoirs. *Society of Petroleum Engineers Journal* 3, 245–255.

- Zyvoloski G. A., 2007. FEHM: A control volume finite element code for simulating subsurface multi-phase multi-fluid heat and mass transfer. Los Alamos Unclassified Report LA-UR-07-3359.
- Zyvoloski G. A, Robinson B. A, Viswanathan H. S., 2008. Generalized dual porosity: A numerical method for representing spatially variable sub-grid scale processes, *Advances in Water Resources* 31 (3) 535–544, DOI: 10.1016/j.advwatres.2007.11.006

## **5. DESCRIBING URANIUM TRANSPORT IN A FRACTURED CRYSTALLINE ROCK USING MINI-COLUMN EXPERIMENTS**

### **5.1 INTRODUCTION**

In FY 2014, Los Alamos National Laboratory (LANL) focused on refining an experimental methodology for describing and parameterizing radionuclide transport in a more robust and less conservative manner than a simple  $K_d$ -type equilibrium partitioning model but at the same time without resorting to a full geochemical description of the rock-water-nuclide system. The motivation for improving on the former is that  $K_d$ -type models are often overly conservative and do not take full credit for all the retardation processes that may be occurring in a given system – this can lead to overly conservative and expensive repository system designs. The motivation related to detailed geochemical descriptions is that every system is ultimately unique and must be investigated for site-specific behaviors, including processes such as slow desorption kinetics and bond-aging phenomena that are often not accounted for in geochemical models. We do not propose abandoning detailed geochemical descriptions of radionuclide transport, but we believe that a focused set of initial experiments, such as those described here, can provide reasonable semi-empirical descriptions of radionuclide transport processes that can be used in performance assessment calculations to evaluate the need for more detailed descriptions (using a risk-informed basis) while also serving to identify key processes that may require more detailed investigation in subsequent experiments. We believe that this is a cost-effective approach of taking credit for radionuclide retardation processes in performance assessments, particularly for moderately adsorbing radionuclides for which risk estimates can be quite sensitive to assumptions and uncertainties associated with adsorption and desorption processes.

We expanded on our previous work of method development to incorporate longer desorption periods and tighter control of pH conditions in an effort to gain better understanding of uranium transport and improve efforts in upscaling to the longer time scales needed for repository design and reliable risk assessments. Our focus has been on a method and results that can be readily incorporated into systems models used for nuclear waste repository risk assessments. If spent nuclear fuel is to be disposed of without any reprocessing, uranium is likely to be an important radionuclide in risk or dose calculations for most geologic repository systems because of its large inventory in used fuel and its relatively weak adsorption in many geochemical environments. Our current effort has focused on uranium transport in a saturated, fractured crystalline rock system, using the Grimsel Test Site (GTS) in Switzerland as a source of geologic materials, although we have purposely lowered the pH of the site-specific groundwater to be more consistent with other crystalline rock systems and to provide greater amounts of U adsorption (the ambient pH at the GTS is ~9, and U sorption is negligible at this pH). We also conducted our experiments under oxidizing conditions to avoid redox processes that would further complicate U transport behavior and not necessarily apply to other radionuclides, although we recognize that many deep crystalline rock environments are inherently reducing and such redox processes may ultimately need to be considered for a

redox-sensitive element like uranium. The Grimsel granodiorite system was chosen for this study for several reasons: (1) it is representative of a generic crystalline rock repository, (2) it avoids any perceived ties to potential future U.S. repository locations, (3) materials from this site are readily available, (4) field transport experiments involving uranium and other radionuclides are being conducted at the site, and (5) the UFD is involved in a formal collaboration with the CFM project at the GTS.

Although this study is focused on a crystalline rock system, the intent is to develop methods that can be widely applied to any geologic system being considered for nuclear waste disposal, including engineered barrier systems. It has been mentioned in past reports that we have contemplated transitioning our studies to  $^{237}\text{Np}$  from uranium, but we have continued our efforts with uranium to provide a full analysis of the granodiorite and uranium system. As is discussed in another chapter of this report, we have expanded this methodology to also investigate americium desorption from bentonite colloids in the GTS granodiorite system.

This chapter focuses on experimental and modeling results for long-term mini-column experiments involving transport of uranium-bearing solutions through a fracture fill material (FFM) from the GTS. The FFM is more representative of the sorption processes that can be expected at the GTS than the parent granodiorite, as the main flowpaths in the formation occur within the weathered fractures. We found significant uranium sorption occurred in columns packed with FFM at pH values of  $\sim 7$  and  $\sim 8$ , and switching the injection solution to uranium-free water resulted in long desorption tails that are relevant to upscaling.

## 5.2 MATERIALS AND METHODS

We conducted a series of uranium breakthrough experiments with small columns packed with Grimsel fracture fill material (FFM) at pH 6.9 and 7.9. The injection solution was then switched to uranium-free groundwater of various pH values to investigate the long-term desorption behavior.

### 5.2.1 Groundwater

The groundwater used in all experiments was a synthetic Grimsel groundwater (SGGW) that matched the water chemistry of the water found in the shear zone at the GTS. The recipe is given in Table 5-1. The SGGW was made by adding reagent-grade chemicals to high-purity water ( $> 18 \text{ M}\Omega \text{ cm}$  resistivity). The water was allowed to equilibrate with the atmosphere in Los Alamos, NM (2,231 m above sea level) before use in the experiments.

**Table 5-1. Synthetic Grimsel Groundwater Recipe**

Compound	g L <sup>-1</sup>
Na <sub>2</sub> SO <sub>4</sub>	0.1440
KCl	0.0048
MgCO <sub>3</sub>	0.0427
NaHCO <sub>3</sub>	0.2733
CaCl <sub>2</sub>	0.0130
H <sub>4</sub> SiO <sub>4</sub>	0.0341
pH	8.8-9.1

This water chemistry was slightly adjusted to account for additional Mg and carbonate that would be contributed from an engineered barrier consisting of FEBEX bentonite [ENRESA, 1998, and personal communication with I. Blechschmidt, NAGRA]. The SGGW had a pH range of 8.8-9.1, which agrees well with the measured pH of GTS groundwater. Since previous results at pH 8.9 showed negligible uranium adsorption (Kersting et al., 2012, Ch. 5) and because we are interested in potential applications different from the GTS system, the pH of our experimental solutions were lowered to allow for measurement of uranium sorption in a pH range that may be present in other crystalline rock systems. N-morpholino-ethanesulfonic acid (MES) was used to buffer the SGGW to lower values. MES was selected as the buffer because it offers effective buffering in the pH 6-8 range while having a low tendency to complex with metal ions (Good et al., 1966), including uranyl ion (U(VI)<sup>2+</sup>). Buffering with inorganic acid/base pairs such as a carbonate or phosphate could affect the aqueous speciation and transport behavior of uranium by forming uranyl complexes (carbonate) and possibly uranyl precipitates (phosphate). MES has also been used as a buffer by other groups for uranium and actinide studies (Giammar and Hering, 2001).

The breakthrough experiments conducted for this study required the lowering of the SGGW pH from 8.9 to pH 6.9 and 7.9 to observe sufficient uranium sorption to satisfy our objectives. Our work from FY 2013 showed that SGGW/MES solutions at pH 6.9 and 7.9 remained stable for at least 6 months. Uranium adsorption partition coefficients (K<sub>d</sub> values) onto many different minerals have been reported to vary over several orders of magnitude between pH 7 and 9 (Waite et al., 1994; Echevarria et al, 2001; Davis and Curtis, 2003; Joseph et al., 2013), with essentially zero K<sub>d</sub> at pH of 9 or higher. For a given pCO<sub>2</sub>, uranium exhibits much stronger adsorption at the low end of this pH range because of the greater abundance of positively-charged uranyl species (U(VI)<sup>2+</sup> and U(OH)<sup>+</sup>) and the lesser abundance of nonsorbing neutral and negatively-charged uranyl carbonate or uranyl-Ca/Mg-carbonate complexes at neutral pH. Table 5-2 shows relative abundances of uranium-bearing species in SGGW as predicted by PHREEQC (Parkhurst and Appelo, 2013) using the llnl.dat database (Johnson, 2010) with the addition of uranyl-calcium-carbonate and uranyl-magnesium-carbonate complexation constants from Dong and Brooks (2006).

**Table 5-2.** PHREEQC calculations of fractional abundance and speciation of uranium with SGGW water chemistry as a function of pH

Constituent	pH 6.9	pH 7.9	pH 8.8
$\text{UO}_2\text{Ca}(\text{CO}_3)_3^{2-}$	0.478	0.562	0.563
$\text{UO}_2\text{Mg}(\text{CO}_3)_3^{2-}$	0.181	0.217	0.230
$\text{UO}_2(\text{CO}_3)_2^{2-}$	0.141	0.0171	0.00261
$\text{UO}_2\text{Ca}_2(\text{CO}_3)_3^0$	0.0868	0.0998	0.0900
$\text{UO}_2(\text{CO}_3)_3^{4-}$	0.0785	0.0943	0.105
$\text{UO}_2(\text{CO}_3)^0$	0.0180	0.00022	---
$\text{UO}_2\text{Mg}_2(\text{CO}_3)_3^0$	0.00790	0.00935	0.00943
$\text{UO}_2(\text{OH})^+$	8.5e-5	1.1e-6	2.4e-8
$\text{UO}_2^{2+}$	2.5e-6	1.9e-9	8.8e-12
<b>SUM</b>	<b>0.9910</b>	<b>0.9993</b>	<b>0.9999</b>

### 5.2.2 Porous Medium

Weathered fracture fill material (also known as fault gouge) was collected during coring operations of the MI shear zone at the Grimsel Test Site (GTS) in Switzerland. The shear zone is not currently exposed in the CFM tunnel (where the field experiments were conducted), so the material was collected in an adjacent tunnel. The samples were collected by hand from a zone identified as a shear zone, where a fracture in the granite rock had been exposed to hydrothermal solutions and was highly altered over time. Samples were shipped by our collaborators at the GTS to Los Alamos National Laboratory in pieces ranging from micron size up to larger pieces that were 10-15 cm long. Due to the small quantity of material available, all pieces less than 1 cm in size were combined and crushed using a percussion mortar, sieved into 75-150, 150-355, and 355-500  $\mu\text{m}$  size fractions, and thoroughly rinsed in high-purity water to removal all fines. The samples were rinsed with synthetic SGGW until the electrical conductivity of solution in contact with the material for 24 hours was within 5% of the electrical conductivity of the SZW. Samples were then oven dried for 12 hours at 60 °C and stored in glass jars. Optical microscope (Wild Heerbrugg, M420) microphotographs for the 150-355  $\mu\text{m}$  size fraction of granodiorite parent material and the fracture fill material show that the FFM appears to have a larger fraction of dark grains (Figure 5-1).



**Figure 5-1.** Microphotographs of crushed and sieved Grimsel granodiorite (left) and fracture fill material (right) for the 150-355  $\mu\text{m}$  size fraction

The mineralogy for the FFM was determined from quantitative x-ray diffraction (QXRD) at the GGRL lab at LANL and Table 5-3 lists the major mineral fractions for the unaltered granodiorite, a scraping from the shear zone surface, and a bulk sample of the crushed FFM that we used for all experiments in this section. Table 5-4 shows the bulk chemical analysis by x-ray fluorescence. The main differences in unaltered granodiorite and FFM were a significant enrichment in Mg, minor enrichment in K and Fe, and minor depletions of Si, Na, and Ca. Surface area was determined by the BET method with krypton gas (Micromeritics Analytical Services) and was measured as  $0.23 \text{ m}^2 \text{ g}^{-1}$  for the 150-355  $\mu\text{m}$  size fraction used in the column experiments.

**Table 5-3.** Quantitative x-ray diffraction interpretation (wt%) of Grimsel granodiorite, the shear zone surface, and bulk FFM materials.

Mineral	Granodiorite	Shear Zone Surface	FFM
Quartz	32	18	13
Microcline	10	8	5
Albite	42	44	34
Biotite	5	11	31
Chlorite	1	--	
Muscovite	10	19	16
Epidote	<1	--	--
Smectite	--	--	1
Calcite	--	<1	<1

**Table 5-4.** Bulk chemical analysis of granodiorite and FFM materials by X-ray fluorescence analysis (wt%)

<b>Constituent</b>	<b>Granodiorite bulk</b>	<b>FFM bulk</b>	<b>Detection Limits</b>
fuse ratio	7:1	7:1	7:1
Na <sub>2</sub> O	4.01	3.15	0.0451
MgO	0.725	4.28	0.0300
Al <sub>2</sub> O <sub>3</sub>	14.0	14.3	0.0313
SiO <sub>2</sub>	70.9	63.4	0.1507
P <sub>2</sub> O <sub>5</sub>	0.115	0.124	0.0049
K <sub>2</sub> O	4.22	4.90	0.0112
CaO	1.90	1.03	0.0084
TiO <sub>2</sub>	0.436	0.491	0.0092
MnO	0.081	0.086	0.0252
Fe <sub>2</sub> O <sub>3</sub>	3.10	3.83	0.0041
V	29	41	13
Cr	bdl	bdl	10
Co	bdl	bdl	15
Ni	bdl	bdl	5
Cu	bdl	bdl	5
Zn	31	53	5
Ge	bdl	bdl	24
As	bdl	bdl	15
Rb	110	192	4
Sr	135	71	5
Zr	217	236	6
Ba	403	372	19
W	bdl	bdl	43
U	bdl	bdl	4
LOI	0.35	4.28	
total	99.931	99.970	

bdl = below detection limit

LOI = loss on ignition

### 5.2.3 Uranium and Tritiated Water

The uranium used in all experiments was a combination of  $^{233}\text{U}$  (Eckert and Ziegler) and natural uranium from a 1000 mg/L ICP-MS standard (SpexCertiPrep). For all solutions, approximately 98% of the uranium was natural uranium and about 2% of the uranium was  $^{233}\text{U}$  added to ensure accurate quantification of concentrations by liquid scintillation counting (LSC). Several thousand samples were analyzed over the course of the experiments, so the rapid and inexpensive LSC analysis method was very important. It was assumed that the  $^{233}\text{U}$  radiotracer and the  $^{238}\text{U}$  comprising the vast majority of the uranium in the ICP-MS standard would behave identically with respect to adsorption and speciation in all experiments. The uranium solution used in all breakthrough experiments had a total concentration of  $6.5\mu\text{M}$ , which is near the solubility limit for uranium at neutral pH in the SGGW. This concentration was verified experimentally to be under the solubility limit at all test pHs, and it was also predicted to be under the limit in PHREEQC calculations (with the exception of a slight supersaturation with respect to soddyite,  $(\text{UO}_2)_2\text{SiO}_4 \cdot 2\text{H}_2\text{O}$ , at pH 6.9). A relatively high uranium concentration was desirable to maximize sorption site occupancy in the small-scale column experiments. Tritium in the form of tritiated water was co-injected with uranium in all column experiments as an ideal conservative tracer to provide mean groundwater residence times and dispersivities in the columns.

### 5.2.4 Analytical Measurements

Uranium and tritium concentrations were measured by liquid scintillation counting, or LSC (Perkin Elmer Tri-Carb 2550 or Perkin-Elmer Quantulus), with energy ranges of 0-20 keV for tritium and 100-260 keV for uranium. An aliquot of a groundwater sample was weighed and diluted to 6 mL with deionized water to ensure uniform sample volume. The diluted sample was then poured into a 20 mL polypropylene scintillation vial and 14 mL of liquid scintillation cocktail (Packard, Ultima Gold AB) was added, followed by vigorous shaking of the samples for at least 15 seconds. Samples were subjected to two 15 minute counts and the results were averaged. The transformed index of an external  $^{133}\text{Ba}$  standard (tSIE) was used to correct for variable quenching of the samples, especially with respect to tritium. pH measurements were made using a pH meter (Orion Model 290) and a glass pH electrode (Fisher AccuPrest). The electrode was calibrated with commercially available pH 4.01, 7.00 and 9.01 buffers (Ricca Chemical Company).

### 5.2.5 Column Transport Experiments

Column transport experiments were conducted in duplicate at pHs of 6.9 and 7.9 by injecting pH-adjusted SGGW spiked with uranium and tritium through “mini” columns filled with FFM. The mini columns were constructed from 6 cm lengths of 0.95 cm diameter Teflon<sup>®</sup> tubing. The ends of the tubes were tapped to accept Teflon<sup>®</sup> compression fittings. The inside openings were covered with a small disk of 75  $\mu\text{m}$  PEEK screen (Spectrum Labs) to retain the column material while minimizing resistance to flow and straining of fines or colloids. Teflon<sup>®</sup> tubing and 3-way polycarbonate stopcocks were used to connect the columns to 50 mL Teflon<sup>®</sup> syringes (Torviq, TS-50)

adapted for use with syringe pumps (KD Scientific, Model 100). The Teflon<sup>®</sup> syringes were used to eliminate interactions between uranium and the syringes, which were observed in our FY 2013 column experiments in which polypropylene syringes were used. 3-way stopcocks allowed for refilling syringes and switching suspensions or solutions while minimizing flow and pressure disturbances. Flow was directed upward to help maintain saturation and to minimize the potential for air bubbles collecting in the column. An additional length of Teflon<sup>®</sup> tubing was connected to the top (outlet side) of the column and directed column effluent to a fraction collector (Gilson, FC-220) filled with 13 × 100 mm polystyrene test tubes. The fraction collector was enclosed in an acrylic plastic chamber with evaporation pans to minimize evaporation before sample analysis. Figure 5-2 shows photos of the column setup with Teflon<sup>®</sup> syringes mounted in syringe pumps injecting solution through columns taped to the side of the fraction collector, and effluent from the top of the columns passing through the side of the fraction collector chamber to deposit in racks of test tubes.

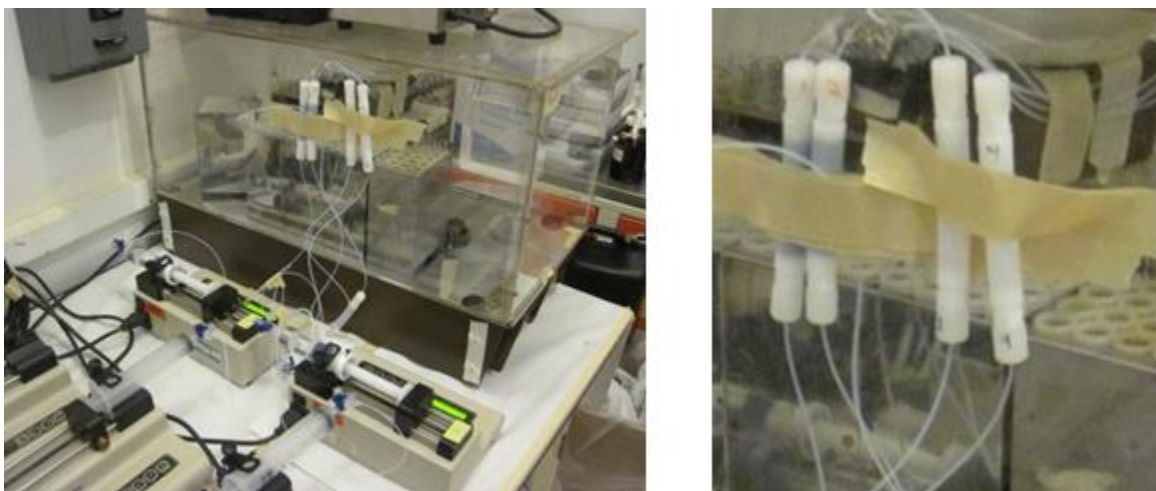


**Figure 5-2.** Image of column set-up with 5 columns running in parallel with syringe pumps, tubing, and fraction collector (left) and a close-up of the FFM and control columns (right)

Columns were packed with 5.0 g of dry FFM and the syringe pump flow rate was set to 0.3 mL h<sup>-1</sup>. Breakthrough experiments were also conducted in control columns in which all components were identical to the FFM columns except that the columns contained no FFM. These experiments were conducted to screen for interactions between uranium and the materials used in the flow systems. The columns were initially flushed with uranium- and tritium-free SGGW for 7 days, and the pH was monitored to ensure the effluent pH stabilized within 0.1 pH unit before the start of the uranium and tritium injections.

To begin each column breakthrough experiment, the influent solution was switched to SGGW containing uranium and tritium. Syringes were refilled several times during the experiment and were eventually changed to SGGW without uranium and tritium to observe the desorption behavior of the uranium from the FFM. Samples were collected

at varying intervals, and the sample mass was weighed with a digital balance (Mettler, PL1200) and subtracted from the empty test tube weight to calculate the actual flow rates ( $\sim 0.28 \text{ mL h}^{-1}$ ). Uranium and tritium activity were measured in every sample. pH was measured and recorded for at least one of the duplicate columns. Our previous experience with columns packed with GTS granodiorite (Wang et al., 2013b, Ch. 5) indicated that subtle changes in pH could result in significant and difficult-to-interpret rapid changes in uranium concentrations due to the extreme sensitivity of uranium adsorption to pH, so we took great care to ensure that the pH remained as steady as possible in the FY 2014 experiments. However, late in each column experiment, the pH was purposely changed to induce uranium desorption and provide additional insights into the desorption process. The experimental conditions in all columns are summarized in Table 5-5.

**Table 5-3.** Summary of FFM column experimental conditions. (2 Teflon<sup>®</sup> columns with 150-355  $\mu\text{m}$  at pH 6.9 and 7.9). Flow rate in all columns  $\sim 0.28 \text{ mL h}^{-1}$ .

Injection Solution (pH 6.9)	Approximate Start Time, hr	Approximate Start Volume, ml
6.5 $\mu\text{M}$ U, pH 6.9	0	0
U-free SGGW, pH 6.9	834	228
U-free SGGW, pH 9.0	3412	736
0.1 M HCl, pH 1.2	5202	1226

**Injection Solution (pH 7.9)**

### 5.2.6 Batch Adsorption/Desorption Experiments

No new batch adsorption or desorption experiments were conducted in FY 2014, but the results of batch experiments conducted in FY 2013 were compared to the FY 2014 column experiment results to gain additional insights into the results of the latter experiments. The batch experiments were conducted at pHs of 6.9 and 7.9 with the same 150-355  $\mu\text{m}$  size fraction of FFM material that was used in the columns. The experiments were conducted in Teflon centrifuge tubes with 10 ml of uranium-spiked SGGW placed in contact with 0.2, 0.5, or 1.0 g of FFM. Control experiments were conducted at each pH in the same centrifuge tubes without the geologic materials present to evaluate adsorption to container walls and correct for this if necessary. All experiments were conducted in duplicate. The tubes were not shaken automatically, but they were manually inverted several times at least once a day. 0.75-ml samples were collected after 10, 100, 1000, 5900, 17200, and 18600 minutes. After 18600 minutes, all SGGW except for  $\sim 0.5 \text{ ml}$  was removed from each centrifuge tube, and then 9.5 ml of pH-adjusted uranium-free SGGW was added to each tube to bring the solution volume

back to 10 ml. 0.75-ml samples were then removed after 10, 100, 1000, 8300, and 17100 minutes to observe the desorption behavior of the uranium from the FFM material. The results of the batch experiments that are of relevance to the column experiments are discussed in Section 5.2.4 of this report, with the reader being referred to our FY 2013 UFD milestone report (Wang et al., 2013b, Ch. 5) for additional details of the experiments.

### 5.2.7 Interpretive Modeling

The batch and column experiments were interpreted using a multisite/multirate reaction modeling approach where each different type of site could be assigned different adsorption and desorption rate constants as well as different surface site densities. Two separate Fortran programs were used for modeling the two different types of experiments, although the equations used to model the adsorption and desorption reactions in each program were identical. The governing equations in the batch experiment model were:

$$\frac{\partial s_i}{\partial t} = k_{fi}c \left(1 - \frac{s_i}{s_{mi}}\right) - k_{ri}s_i \quad (5-1)$$

$$\frac{\partial c}{\partial t} = \frac{M}{V} \left[ -\sum_i k_{fi}c \left(1 - \frac{s_i}{s_{mi}}\right) + \sum_i k_{ri}s_i \right] \quad (5-2)$$

where,  $c$  = concentration in aqueous phase, mol/ml

$s_i$  = concentration on surface sorption site  $i$ , mol/g

$t$  = time, hr

$k_{fi}$  = adsorption rate constant for sorption site  $i$ , ml/g-hr

$k_{ri}$  = desorption rate constant for site  $i$ , hr<sup>-1</sup>

$s_{mi}$  = surface site density (maximum adsorption capacity) for sorption site  $i$ , mol/g

$M$  = mass of solids, g

$V$  = volume of solution, ml.

The governing equations for the column transport model were equation (5-1) plus the following equation for the mobile aqueous phase:

$$\frac{\partial c}{\partial t} - v \frac{\partial c}{\partial x} + D \frac{\partial^2 c}{\partial x^2} + \frac{\rho_B}{\phi} \left[ -\sum_i k_{fi}c \left(1 - \frac{s_i}{s_{mi}}\right) + \sum_i k_{ri}s_i \right] \quad (5-3)$$

where,  $v$  = flow velocity, cm/hr

$D$  = dispersion coefficient, cm<sup>2</sup>/hr

$\rho_B$  = bulk density of solids, g/cm<sup>3</sup>

$\phi$  = porosity

In addition to solving equations (5-1) and (5-2), the batch model allowed the volume of solution in the reactor to be changed at specified times to simulate sampling, and it also allowed for a specified volume of uranium-free water to be added to the reactor to simulate the start of the desorption phase of the experiments. Equations (5-1) and (5-2) were solved using a 4<sup>th</sup>-order Runge-Kutta algorithm.

The column model solved equations (5-1) and (5-3) simultaneously using an implicit finite difference algorithm. The model allowed for arbitrary injection functions to be specified at the column entrance ( $x = 0$ ), and it also allowed for flow rate changes and changes to the reaction parameters  $k_{fi}$ ,  $k_{ri}$ , and  $s_{mi}$  to be specified multiple times during an experiment simulation. Changes to the reaction parameters could be specified when the pH of the injection solution was changed. The changes to reaction parameters were propagated through the columns in the same manner as a conservative tracer.

The approach to interpreting the column experiments was to try to match the uranium breakthrough curve(s) with as few reaction parameters and adsorption site types as possible. It was recognized that allowing more sites with adjustable reaction rates could always provide a better match to the data sets, so the goal was to use only as many sites as necessary to achieve reasonable matches. The first step in the interpretation procedure was to fit the tritiated water breakthrough curves to obtain estimates of the mean water residence time and Peclet number (length divided by longitudinal dispersivity) in the columns. These parameters were then assumed to apply to the uranium, and the uranium breakthrough curves during the portion of the experiments conducted at the initial pH were matched by adjusting only the reaction parameters (adsorption and desorption rate constants, number of sites, and site surface densities). Then the number of sorption sites and the surface densities of these sites that were found to be necessary to fit the initial pH data were carried forward into the remainder of the experiments, so only the adsorption and desorption rate constants for each site were allowed to vary to fit the remainder of the uranium breakthrough curves. The resulting parameters were then compared to the parameters obtained from fitting the batch adsorption/desorption experimental data to gain additional insights into the adsorption and desorption processes.

An automated parameter estimation algorithm, such as PEST (Doherty, 2009, 2010), was not employed to obtain the matches to the data. Such tools are certainly desirable for future endeavors, but the complexity and subtleties of the data-matching exercise coupled with the limited time between data collection and reporting made it impractical to employ these tools at this stage. Often it was considered important to match subtle data features containing only a few observations even if it meant a poorer match to features containing many data points that would have dominated a least-squares or other minimization exercise.

### 5.3 RESULTS

In presenting and discussing the results of the column experiments, we place more emphasis on the results of the pH 6.9 experiments than the pH 7.9 experiments because the pH 6.9 experiments involved introducing a desorption pH of 9, the ambient pH at the Grimsel Test Site, prior to introducing a solution of pH of ~1 to induce rapid desorption and close the experiment mass balance. The pH 7.9 column experiments involved only a pH 1 desorption step to close the mass balance (this decision was made because ~97% of the uranium mass was calculated to be recovered during the pH 7.9 portion of the experiment). Also, the pH 6.9 batch experiments yielded much more consistent results

across the different solid-to-solution ratios than the pH 7.9 experiments, which we attribute to the significantly greater uranium sorption at pH 6.9. Stronger adsorption, particularly at the relatively low solid-to-solution ratios that were employed in the batch experiments, should reduce experimental errors and yield more consistent results.

### 5.3.1 Column Experimental Results

Results of the duplicate control column breakthrough experiments (without FFM) at pH 6.9 and pH 7.9 are shown in Figure 4-3. It is apparent that, despite the switch to the Teflon<sup>®</sup> syringes and the minimization of reactive components in the flow systems, there was still slight retention of the uranium at pH 6.9, although the retention was much less than in the FY 2013 experiments with polypropylene syringes (Kersting et al., 2012, Ch. 5). Retention to flow system components at pH 7.9 appeared to be negligible, although the uranium concentration reached only 90-95% of its injection concentration in the effluent of both control columns. The retention at both pHs was considered to be low enough relative to the retention observed in the FFM column experiments that it did not have to be accounted for in the interpretation of the FFM experiments.

Importantly, the desorption tails at both pH 6.9 and pH 7.9 matched the tritium curves quite well.

The results of the duplicate FFM column transport experiments at pH 6.9 and 7.9 are shown in Figures 5-4 and 5-5, respectively. These figures show the breakthrough curves plotted on a logarithmic scale at the right to highlight the desorption behavior in the experiments. The reproducibility of the duplicate experiments was remarkably good, with the uranium breakthrough curves essentially falling on top of each other in each pair of experiments (c.f. Figure 5-6).

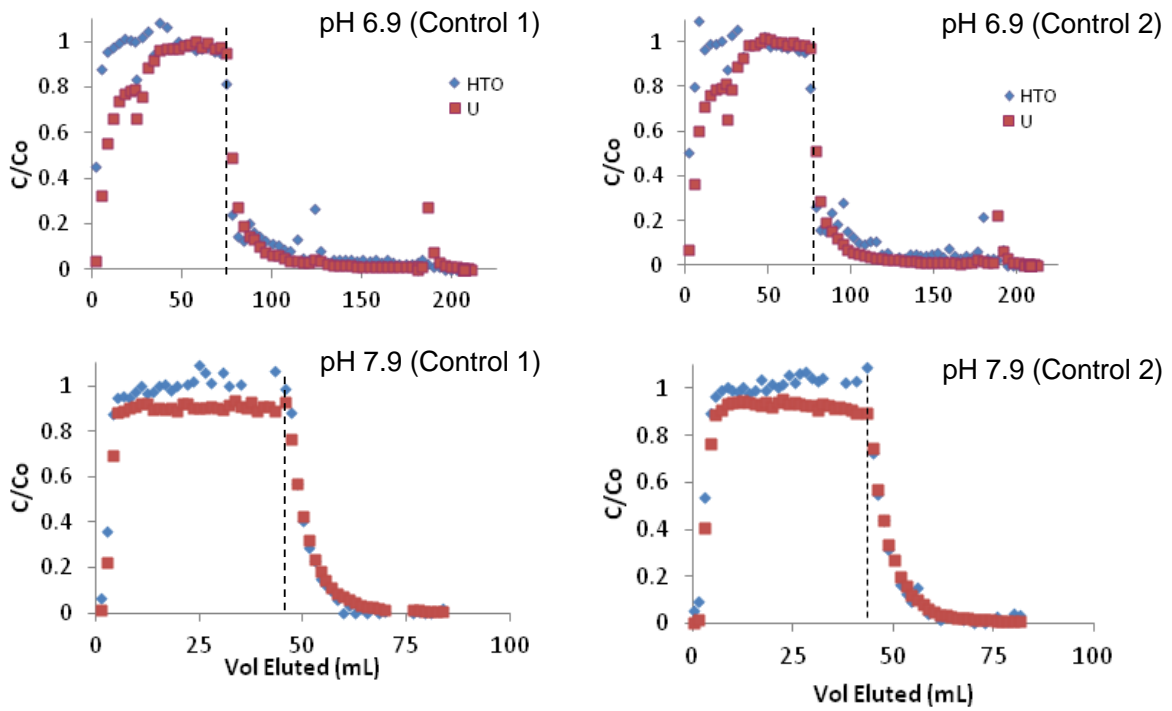


**Figure 5-3.** Control breakthrough experiments without FFM for duplicate columns with uranium solutions of pH 6.9 (top) and pH 7.9 (bottom). Dashed lines denote when injection solution was switched to uranium- and tritium-free solution.

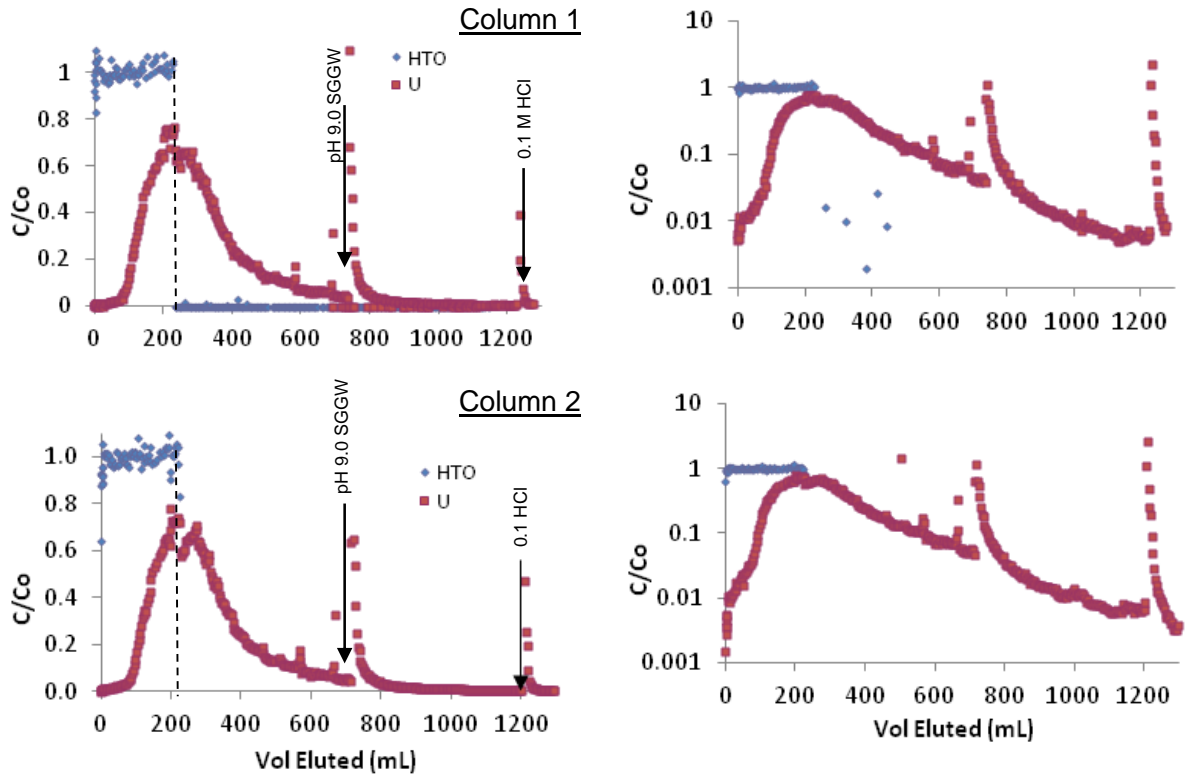


**Figure 5-4.** Breakthrough curves for duplicate FFM breakthrough experiments with pH 6.9 uranium solutions plotted on a linear concentration scale (left) and logarithmic scale (right) to highlight the desorption behavior. Dashed lines denote when injection solution was switched to uranium- and tritium-free solution.

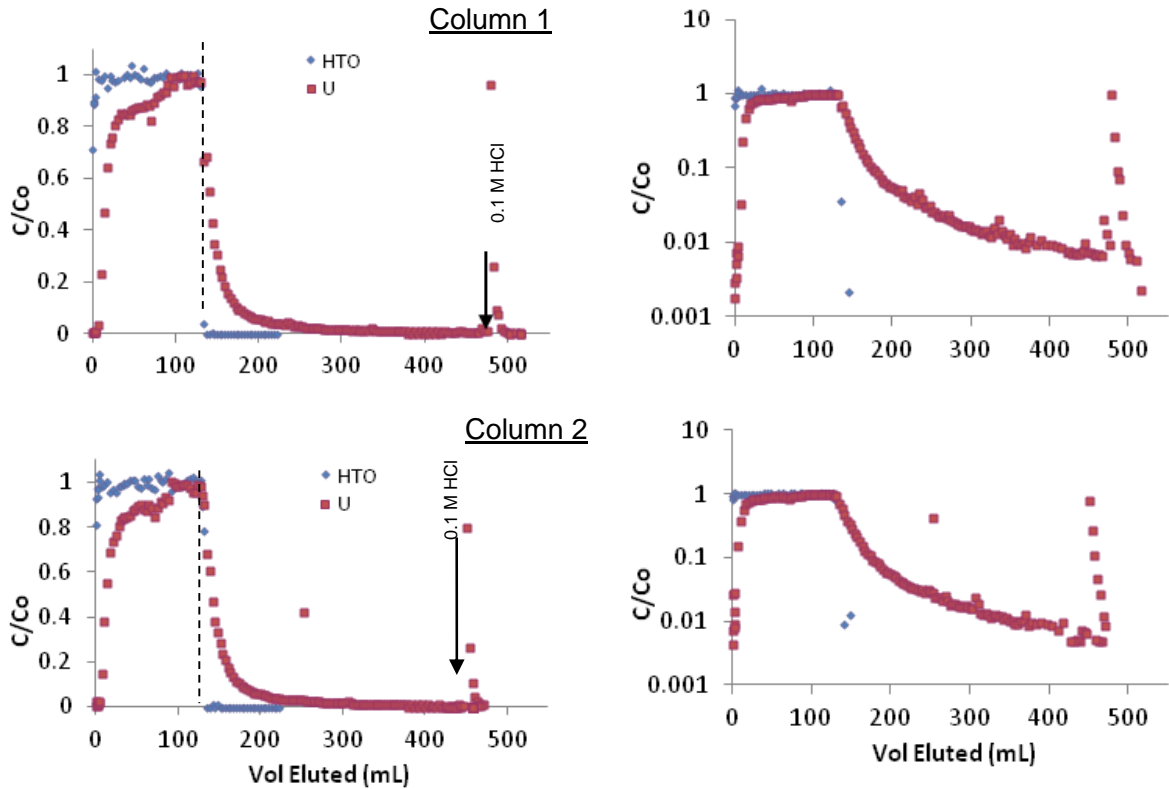


**Figure 5-5.** Breakthrough curves for duplicate FFM breakthrough experiments with pH 7.9 uranium solutions plotted on a linear concentration scale (left) and logarithmic scale (right) to highlight the desorption behavior. Dashed lines denote when injection solution was switched to uranium- and tritium-free solution.

### 5.3.2 Column Experiment Interpretations

#### *pH 6.9 Experiments*

The best model fit to the pH 6.9 uranium breakthrough curves is shown in Figure 5-6. The two breakthrough curves from the duplicate columns are both shown in this figure to illustrate how well they agreed with each other (only a single model fit was considered necessary to match both breakthrough curves). The only significant differences between the two observed breakthrough curves were the slight shifts in the volumes at which the pH changes occurred, which is a result of the slight differences in the flow rates through the two columns (the changes occurred at the same times, not the same volumes). We were not concerned with inexact matches to the volumes at which the pH changes occurred because they did not affect the reaction parameter estimates. The fits to the tritium data (not shown) indicated a mean column pore volume of about 1.4 ml and a Peclet number of about 100.

The reaction parameters corresponding to the model fits of Figure 4-6 are listed in Table 4-5. Note that a minor decrease in the uranium desorption rate constant for the first sorption site was assumed when the uranium-bearing water was switched to uranium- (and tritium-) free water; this assumption was necessary to fit the sudden drop in uranium concentrations that occur at the time of the switch (believed to be due to a subtle drop in the alkalinity of the solution, as the pH was constant throughout the pH 6.9 portion of the experiments, at least within the precision of our measurements).

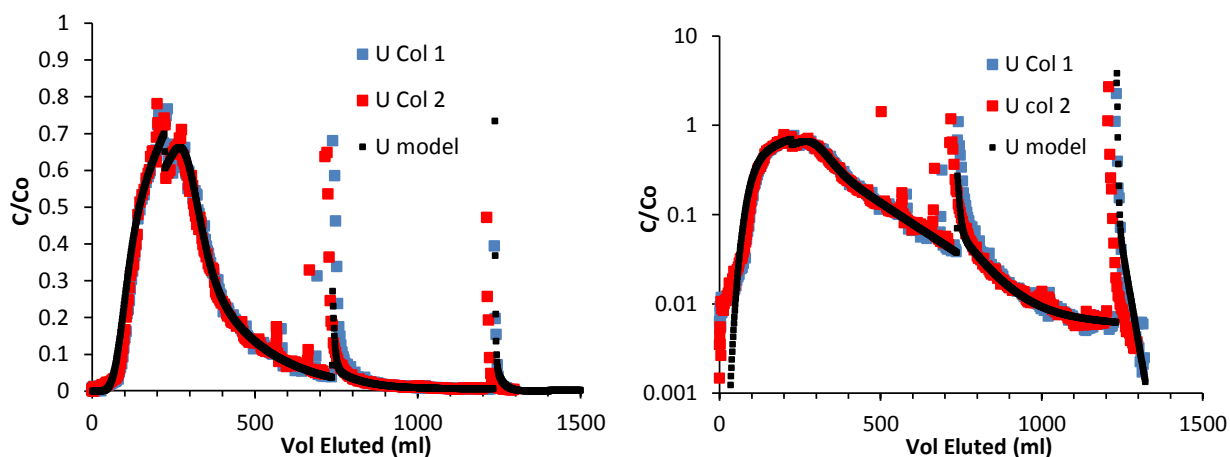


**Figure 5-6.** Best fit of three-site model to the duplicate uranium breakthrough curves in FFM column experiments at pH 6.9, plotted on a linear concentration scale (left) and logarithmic scale (right). Best-fitting reactive transport parameter estimates are listed in Table 4-5.

It is of interest to discuss the sensitivity of the model fits to the parameter estimates of Table 5-5, as well as the uniqueness of the fits. The early breakthrough of the uranium is dictated primarily by the adsorption and desorption rate constants of the first adsorption site, which is the site with the highest surface density and the fastest rate constants. The ratio of the adsorption to desorption rate constant of this site dictates the timing of the uranium arrival, and the value of the adsorption rate constant dictates the slope of the arrival, with a faster rate constant resulting in a steeper slope. The second and third sites have slower rate constants than the first site. Without a second site, the modeled uranium concentration would rapidly rise to  $C/C_0 = 1$  and it would also rapidly decrease from  $C/C_0 = 1$  after uranium-free water is introduced to the column (Fig. 5-7). A second, slower site helps keep the uranium concentration from reaching  $C/C_0 = 1$  while still allowing a relatively rapid rise in concentration, and it also helps fit the tail of the uranium breakthrough curve.

**Table 5-4.** Reactive transport parameter estimates providing the best three-site model fit to the uranium breakthrough curves at pH 6.9 (Figure 5-6).

Starting Vol., ml (Approx.)	Adsorption Site	$k_f$ , ml/g-hr	$k_r$ , hr <sup>-1</sup>	$S_m$ , $\mu\text{mol/g}$
0 (pH 6.9)	1	2.1	0.07 (0.06)*	1.3+**
	2	0.07	0.0022	0.39
	3	0.007	0.00003	0.104
	4	0.001	0.00003	0.026
736 (pH 9 flush)	1	0.1	0.06	1.3+
	2	0.02	0.0035	0.39
	3	0.0018	0.00011	0.104
	4	0.0002	0.00011	0.026
1226 (pH 1 flush)	1	0.01	0.1	1.3+
	2	0.003	0.2	0.39
	3	0.0001	0.2	0.104
	4	0.0001	0.013	0.026

\* Value in parentheses was used after uranium-free water was introduced at ~228 ml.

\*\* Model is insensitive to surface density of first site as long as it is greater than 1.3  $\mu\text{mol/g}$ .

Figure 5-7 shows best fits to the uranium breakthrough curves assuming only a single sorption site and also assuming two sites (note that only the portion of the breakthrough curves before the pH increase to 9 are shown for clarity). Two separate curves are shown for the two-site model; one in which the second site is assumed to have a relatively large surface site density, and one in which the surface site density is assumed to be quite limited. The rate constants and surface site density of the second site can be varied systematically to achieve similar fits because these parameters are correlated (negatively), resulting in nonuniqueness of the best-fitting parameter estimates. When the density of the second site is decreased, the adsorption rate constant can be increased to achieve similar amounts of adsorption to the second site. However, a limit is reached where the fit significantly degrades after the site density drops below a critical value (or

the adsorption rate constant rises above a certain value). The two-site model curve of Figure 5-7 with a more limited number of second sites is a poorer fit to the uranium breakthrough curve because the second site density is lower than the critical value yielding reasonably good fits. In fact, the best fits can always be obtained with a very large number of sites because the adsorption rate constants can always be adjusted to provide good matches to the data.

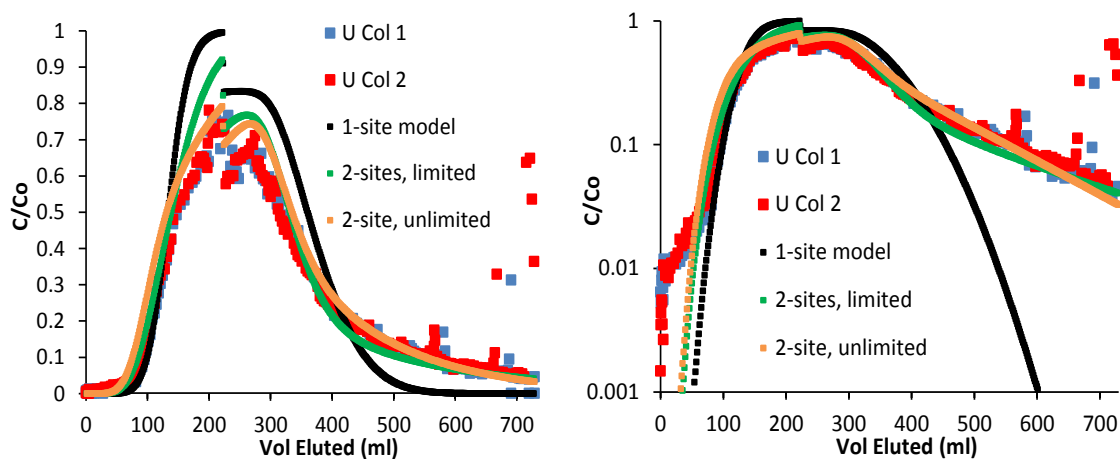


**Figure 5-7.** One-site and two-site model fits to the duplicate uranium breakthrough curves in FFM column experiments at pH 6.9. The one-site model has an adsorption rate constant of 3.0 ml/g-hr and a desorption rate constant of  $0.066 \text{ hr}^{-1}$ . The two-site limited model has adsorption rate constants of 2.1 and 0.12 ml/g-hr for the first and second sites, respectively, and desorption rate constants of 0.07 and  $0.0016 \text{ hr}^{-1}$  for the two sites, with a second site density of  $0.11 \text{ } \mu\text{mol/g}$ . The two-site unlimited model has adsorption rate constants of 2.1 and 0.07 ml/g-hr and desorption rate constants of 0.07 and  $0.0025 \text{ hr}^{-1}$ , respectively (with a second site density of  $0.39 \text{ } \mu\text{mol/g}$ , which we found to be not limiting).

While the two-site model curves of Figure 5-7 are clearly an improvement over the single-site curve, they still fail to fully explain the observed data. As Figure 5-6 shows, the addition of a third site helps achieve an excellent match to the data. In effect, the third site serves as an irreversible sink for the uranium over the time scale of pH 6.9 portion of the experiment, which allows the model curve to be adjusted downward to correct for the over-prediction of concentrations near the peak of the breakthrough curve that results when only two sites are assumed. The third site does not necessarily have to be specified as irreversible – it merely must have a small enough desorption rate constant to effectively retain most of the adsorbed uranium for the remainder of the pH 6.9 portion of the experiment after the uranium-free water is introduced. Note that although Table 5-5 lists four sites, the third and fourth sites are effectively the same site during the pH 6.9 portion of the experiment (and the pH 9 portion as well) because they have the same

desorption rate constant - their adsorption rate constants can be added to obtain an overall adsorption rate constant for a combined site. A fourth site is specified only to achieve a match to the pH ~1 portion of the experiment. It should also be noted that the same negative correlation between the adsorption rate constant and surface site density mentioned above for the second site also applies to the third site – the third site density can be decreased with a corresponding increase in adsorption rate constant to achieve a similar fit, resulting in a certain amount of nonuniqueness in the model fits. However, as with the second site, there is a lower limit of surface site density below which the fits degrade significantly.

The model curve of Figure 5-6 during the pH 6.9 portion of the column experiments is quite insensitive to the desorption rate constant of the third site provided the rate constant is less than a critical upper limit above which a significant amount of the uranium adsorbed to the third site begins to desorb over the time scale of the experiment. Figure 5-8 shows three extrapolations of the pH 6.9 model curve (assuming no increase to pH 9) with three different values of the third site desorption rate constant. The largest value ( $0.00013 \text{ hr}^{-1}$ ) results in the model curve deviating from the log-linear trend in the tail of the breakthrough curve almost immediately after the end of the pH 6.9 data. The intermediate value ( $0.00003 \text{ hr}^{-1}$ ) shows a deviation sometime after the end of the pH 6.9 data, and the smallest value ( $0.000003 \text{ hr}^{-1}$ ) shows a deviation occurring at about the detection limit of uranium by our LSC method. While each curve obviously explains the *observed* data equally well, each has significantly different implications for long-term and large-scale transport. As will be shown in Section 5.4, the smaller the desorption rate constant of the third site, the greater will be the predicted retardation of uranium over large scales.

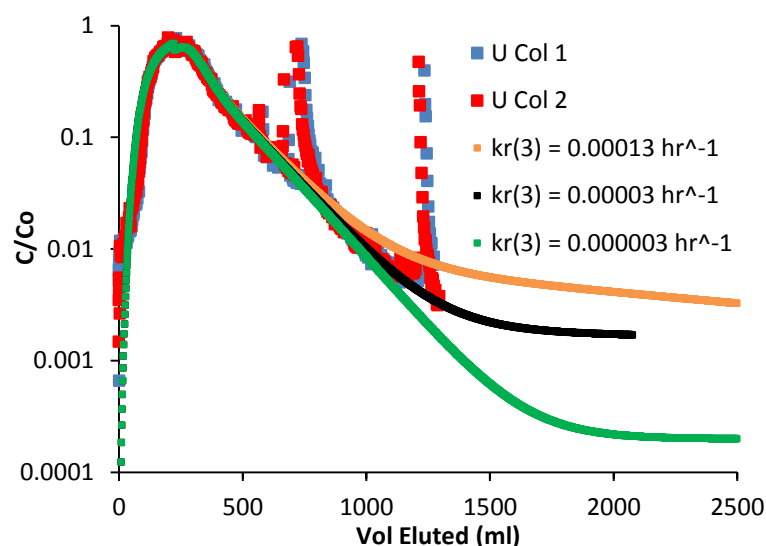


**Figure 5-8.** Extrapolations of the model-simulated pH 6.9 uranium breakthrough curves assuming no pH changes and three different desorption rate constants for the third site,  $k_r(3)$ . All other parameters are the same as in Table 5-5. Note that fourth site of Table 5-5 is combined with third site.

A valid question is: Why was the pH increased to 9 before a deviation was observed in the tail of uranium breakthrough curve? If one were really trying to interrogate the slowest desorption rates at a pH of 6.9, the logical procedure would be to extend the breakthrough curves until a deviation was observed or until the concentrations drop below detection limits, whichever comes first. If the log-linear tails are simply extrapolated to infinite time, it is predicted that only about 84% of the uranium would be recovered, with the implication being that over 15% of the uranium must have a zero desorption rate. Even if a log-log extrapolation is done, which involves some upward curvature of the trend on a log-linear scale, the predicted recovery is only ~91%, and thus 9% of the uranium is predicted to have a zero desorption rate. In both of these cases, the large-scale retardation of uranium would be very great because some of the uranium would be predicted to be irreversibly adsorbed. In reality, it is quite uncertain to make such extrapolations, and it is clearly non-conservative to assume any irreversible adsorption sites without direct evidence – evidence which, almost by definition, is impossible to obtain without running infinitely long experiments and having extremely low detection limits.

Rather than extend the experiments at pH 6.9, we decided to increase the pH to 9, which is the ambient Grimsel pH, to see how much desorption would be induced by this pH increase. We had previously shown (Kersting et al., 2012, Ch. 5) in both batch and column experiments that there was no observable *adsorption* to Grimsel granodiorite at pH 9, so it was fully expected that raising the pH to 9 would induce considerable desorption. While Figures 5-5 and 5-6 show that this clearly occurred, it is interesting

that the desorption was not complete (about 8% of the injected uranium was rapidly desorbed, i.e., the large concentration spike, whereas ~20% of the injected uranium was retained in the columns when the pH was initially switched to 9). It is even more interesting that the tail occurring after the large spike appears to resume the log-linear trend observed prior to the pH increase. Although we cannot know for sure, this observation suggests that the trend at pH 6.9 would have likely continued at least until the end of the pH 9 injection, especially when one considers that desorption rates should have been significantly higher at pH 9 than pH 6.9. Thus, we feel quite comfortable in using the intermediate value of the third-site desorption rate constant of Figure 5-7 ( $0.00003 \text{ hr}^{-1}$ ) as an upper limit for the desorption rate constant of this site *at pH 6.9*. Thus, this intermediate value is listed in Table 5-5. Further implications of the parameter estimates of Table 5-5, as well as a discussion of how the column results compare to the batch experiment results is provided in Section 5.4.

The fact that there is clearly some slow desorption occurring at pH 9 indicates that while observable adsorption did not occur at this pH in either column or batch experiments (Kersting et al., 2012, Ch. 5), uranium that was adsorbed at lower pHs does not necessarily desorb rapidly when subjected to pH 9 solutions. We considered the possibility that there may be a slow-diffusion component to the release of uranium from the FFM, but this possibility seems remote given (1) the rapid desorption of a portion of the uranium mass, which was obviously not diffusion-limited, and (2) the steep slope of the uranium decrease on a log-log plot after the initial rapid desorption, which was much steeper (slope of less than -2.5) than would be predicted from a diffusion-dominated process [slope of -1.5, Tsang (1995)].

The pH ~1 flush of the columns resulted in nearly complete recovery of the uranium from the columns: 95% recovery for Column 1 and 97% for Column 2. While not a perfect mass balance closure, we consider this extremely good mass balance for experiments of this duration. This result indicates that systematic errors in the uranium concentration measurements were relatively small over the course of the experiments. Perhaps more importantly, the significant spike in concentrations after introducing the pH 1 solution confirms that there was indeed a significant amount of uranium remaining on the FFM after the pH 9 solution had been flushing the columns for considerable time. About 6% of the injected uranium was desorbed during the pH 1 flush in both columns, confirming that the pH 9 flush left behind a significant fraction of the uranium that was adsorbed to the FFM at the start of the flush (6% of the 20% that was adsorbed at the start of the flush). The lack of complete mass balance closure suggests that it is possible that even the pH 1 flush did not remove all the adsorbed uranium, although we must also accept the possibility that there was a systematic mass balance error of 3-5% in the experiments.

### *pH 7.9 Experiments*

The best model fit to the pH 7.9 uranium breakthrough curves is shown in Figure 5-9. As in the case of the pH 6.9 column experiments, the two breakthrough curves from the duplicate columns are in very good agreement and only a single model fit was considered necessary to match both breakthrough curves. The reaction parameters corresponding to the model fits of Figure 5-9 are listed in Table 5-6.

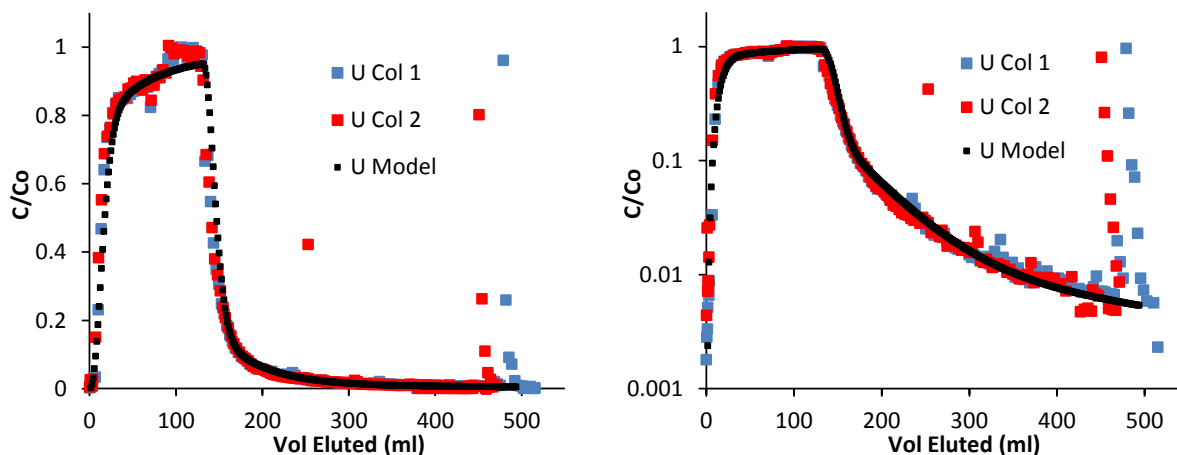


**Figure 5-9.** Best fit of three-site model to the duplicate uranium breakthrough curves in FFM column experiments at pH 7.9, plotted on a linear concentration scale (left) and logarithmic scale (right). Best-fitting reactive transport parameter estimates are listed in Table 5-6. Note that the change to pH 1 at around 490 ml was not modeled (pH was assumed constant at 7.9).

As with the pH 6.9 column experiments, three adsorption sites were found to be necessary to obtain a good match to the uranium breakthrough curves at pH 7.9. However, it was clear that the uranium adsorbed much less strongly to the FFM at pH 7.9 than at pH 6.9, and the tails of the breakthrough curves had upward curvature consistent with much more rapid desorption than at pH 6.9. Over 97% of the uranium was calculated to be recovered before the pH 1 flush was started, and a log-log extrapolation of the tail of the pH 7.9 breakthrough curve indicated that about 99% would have been recovered had the log-log trend continued to infinite time. The mass balance after the pH 1 flush came to slightly greater than 100% (101% and 100.7% in columns 1 and 2, respectively), which suggests that the uranium recoveries at the end of the pH 7.9 portion of the experiment may have been as much as 1% lower than calculated; i.e., there was slightly greater uranium retention than calculated. This excellent mass balance closure is well within the precision of our measurements, especially considering background alpha activities in the SGGW, and it suggests that the our systematic errors are less than the 3-5% mass shortfall calculated in the pH 6.9 experiments.

In hindsight, it may have been informative to introduce a pH 9 flush before the pH 1 flush, although the ~97% recovery at the end of the pH 7.9 portion of the experiment prompted us to simply induce the remaining ~3% of the adsorbed uranium to rapidly desorb to close the mass balance. The long-term and large-scale implications of the reaction parameters deduced from the pH 7.9 column interpretations are discussed in Section 5.4

**Table 5-5.** Reactive transport parameter estimates providing the best three-site model fit to the uranium breakthrough curves at pH 7.9 (Figure 5-9).

Adsorption Site	$k_f$ , ml/g-hr	$k_r$ , hr <sup>-1</sup>	$S_m$ , $\mu\text{mol/g}$
1	0.5	0.12	1.3+*
2	0.014	0.0058	0.39
3	0.0035	0.0007	0.104

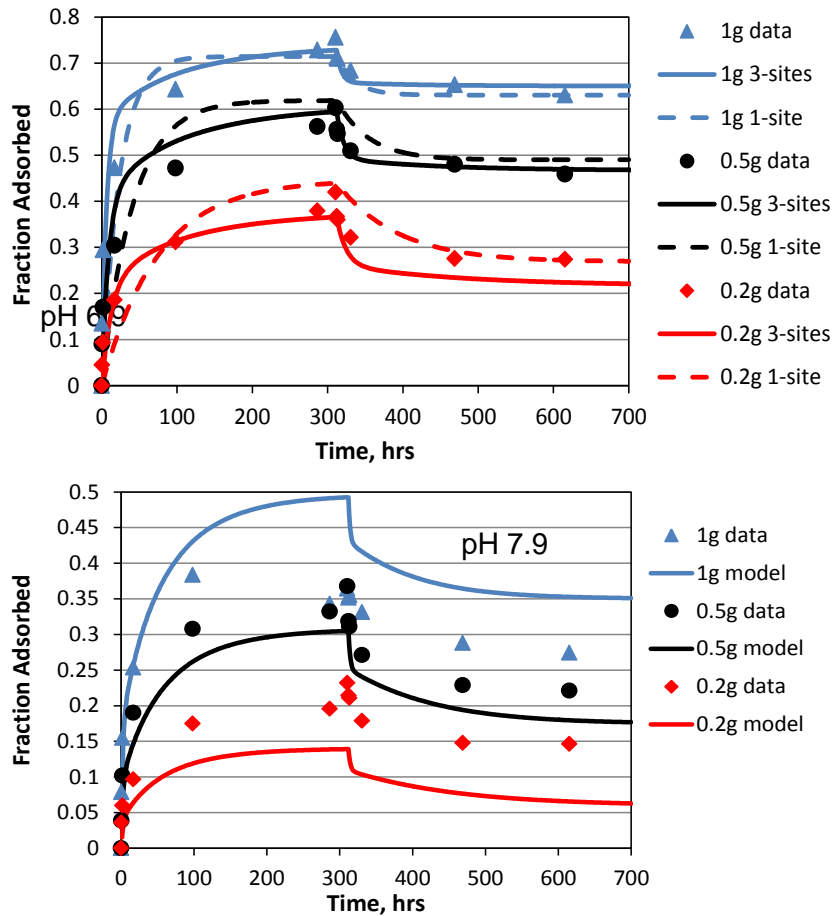
\* Model is insensitive to surface density of first site as long as it is greater than 1.3  $\mu\text{mol/g}$ .

## 5.4 DISCUSSION

### 5.4.1 Comparison with Batch Experiment Results

It is of interest to qualitatively compare the results of the column experiments with the batch adsorption/desorption experiments that were conducted in FY 2013. Figure 5-10 reproduces the results of fitting the batch experiments with both a one-site and a three-site adsorption model (3-site model only for pH 7.9), and Table 5-7 lists the best-fitting parameters (from our FY 2013 milestone report, Wang et al., 2013b, Ch. 5). These fits were constrained by assuming that the same reaction parameters must apply to all the

solid-to-solution ratios, which is why the model over-predicts the observed sorption at the highest ratio for pH 7.9 and under-predicts the observed sorption at the lowest ratio for this pH. Considering only the pH 6.9 results, it is apparent that while a three-site model is superior to a one-site model, consistent with the column experiments, the batch adsorption reaction rate constants are somewhat slower than the column rate constants and the batch desorption rate constants are somewhat faster.



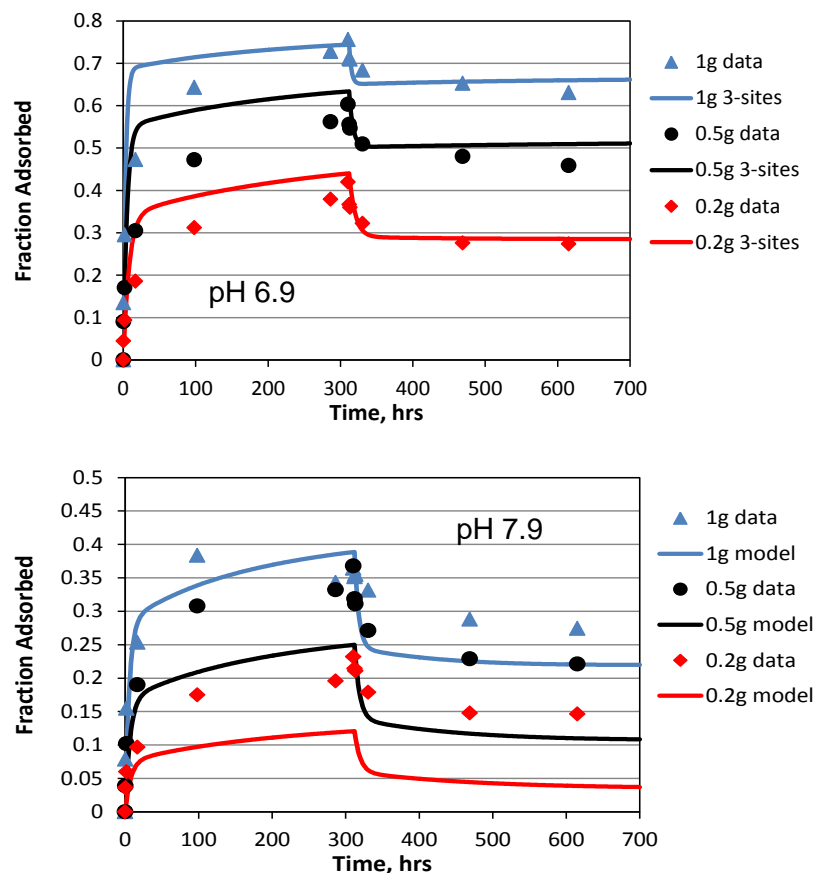
**Figure 5-10.** FY 2013 FFM batch adsorption and desorption data at pH 6.9 (top) and pH 7.9 (bottom), with 3-site and 1-site model fits to the pH 6.9 data and a 3-site model fit to the pH 7.9 data. Legend indicates grams of FFM material per 10 ml of initial solution. Data points are averages of two observations.

Figure 5-11 shows the model predictions for the batch experiments using the reaction parameters for the three-site model that provided the best matches to the column experiments. In this case, the column parameters at pH 6.9 provide reasonably good matches to the batch results (although the adsorption rates are over-predicted), but the column parameters at pH 7.9 significantly underpredict the batch results at the two smaller batch solid-to-solution ratios. It is not surprising that the best match at pH 7.9 is

at the highest batch solid-to-solution ratio because the solid-to-solution ratio in the columns was much larger than in any of the batch experiments (approximately 5 g to 2.5 ml). The poor model matches to the pH 7.9 batch data in both Figures 5-10 and 5-11 suggest that there may have been some problems or inconsistencies with these data. One would intuitively expect that the fractions adsorbed in the batch experiments at pH 7.9 would decrease significantly as the solid-to-solution ratios are decreased because of the relatively weak adsorption at this pH, but clearly the decrease is not nearly as great as the model can fit or predict. We suspect that there may have been some experimental artifacts that either suppressed uranium adsorption at the highest solid-to-solution ratio at pH 7.9 or, more likely, increased it at the lower solid-to-solution ratios. The most likely such artifact would be a lower alkalinity in the reactors with lower solid-to-solution ratios, which would increase the adsorption in these reactors. We did not measure the alkalinity in the reactors (or in the column effluents) because this measurement requires much more sample than we had to spare. Interestingly, if one ignores the failure to predict the fractions adsorbed at the two lower solid-to-solution ratios at pH 7.9, the rate and amount *desorbed* in these experiments is actually quite well predicted (much better than at the highest ratio – c.f. Figure 5-10)

**Table 5-6.** Reaction model parameters yielding matches to FFM batch adsorption-desorption data shown in Figure 5-10.

<b>pH 6.9</b>	<b><math>k_f</math>, ml/g-hr</b>	<b><math>k_r</math>, hr<sup>-1</sup></b>	<b><math>S_m</math>, <math>\mu</math>mol/g</b>
1-site model	0.3	0.005	1.3+
3-site model, site 1	0.8	0.06	1.3+
3-site model, site 2	0.1	0.003	0.104
3-site model, site 3	0.07	0.001	0.026
<b>pH 7.9</b>			
3-site model, site 1	0.8	0.4	1.3+
3-site model, site 2	0.05	0.005	0.039
3-site model, site 3	0.05	0.001	0.013



**Figure 5-11.** FY 2013 FFM batch adsorption and desorption data at pH 6.9 (top) and pH 7.9 (bottom), showing 3-site model predictions using the best-fitting reaction parameters from the column experiments.

The batch experiments were conducted at relatively low solid-to-solution ratios with the hope of possibly observing some effects of reaching surface site saturations, particularly at the lowest solid-to-solution ratio of 0.2 g to 10 ml. These effects would be manifested by a decrease in the apparent partition coefficient at smaller solid-to-solution ratios, and if observed, they might provide some constraints on the total uranium adsorption site capacity (i.e., site density) on the FFM surfaces at the experimental pHs, as well as perhaps some constraints on the site densities of the second and third sites (via model fitting). However, these effects were not observed at either pH, and in fact, the apparent partition coefficients increased rather than decreased as solid-to-solution ratios decreased at pH 7.9. Table 5-8 lists the apparent adsorption and desorption partition coefficients in the batch experiments as determined from the final concentrations observed during both the adsorption and desorption phases of the batch experiments. We are left to conclude that the batch experiments did not yield meaningful constraints on the surface densities of the adsorption sites in the column experiments, and they also seemed to under-predict the adsorption rates observed in the pH 6.9 column experiments (although the agreement with the observed column rate constants was better at pH 7.9). The under-prediction of adsorption rates might be a result of greater mass transfer limitations in the batch

experiments than in the column experiments, although this seems counterintuitive if good mixing was achieved in the batch tests. The estimation process for the rate constants inherently accounts for differences in solid-to-solution ratios in different experiments.

Despite the inability to obtain good constraints on adsorption site densities from the batch experiments and also good agreement between the batch and column reaction rate parameters, the batch adsorption partition coefficients predict the arrival times of the uranium in the column experiments reasonably well at both pHs. Given that the porosity in the columns was about 50%, resulting in a bulk density of about  $1.325 \text{ g/cm}^3$ , the predicted retardation factors in the columns are  $1 + 1.325(K_d)/0.5$ , or  $1 + 2.65(K_d)$ . Table 5-9 lists the column retardation factors calculated using the adsorption partition coefficients of Table 5-8 along with the observed column retardation factors based on when the uranium concentration reached half its peak concentration. These results suggest that the batch experiments were useful for predicting when the early arrival of uranium occurred in the column experiments. The greater desorption partition coefficients of Table 5-8 relative to the adsorption coefficients are also consistent with the extended tailing observed in the column experiments, which suggest lower desorption rates than adsorption rates.

Overall, we conclude that the FY 2013 batch experiments were of limited value in gaining additional insights into the observed uranium column transport behavior, although they did predict the early breakthrough times in the column experiments reasonably well. Suggested improvements for batch experiments include (1) continually adding more uranium after some adsorption has occurred until uranium adsorption per unit mass of added uranium clearly decreases, (2) replacing the desorption solution with uranium-free water multiple times to induce more desorption and better interrogate slow desorption rate constants, and (3) generally using higher mass to solution ratios to more closely mimic column or field conditions. The first and second suggestions would help place better constraints on surface site densities of the different sorption sites, which we do not believe were very well constrained by the column experiments. The second suggestion could also be carried out until detection limits are reached in the solution phase, which, in principle, minimizes the desorption rate constants that can be interrogated. The third suggestion is mainly to avoid artifacts and data scatter that can occur when small sample sizes are used with materials of high mineralogical heterogeneity, which may have been a factor in the batch experiments with the small solid-to-solution ratios.

**Table 5-7.** Experimentally-observed partition coefficients ( $K_d$  values) in batch experiments based on final concentrations measured during adsorption and desorption phases of experiments.

<b>pH 6.9</b>	<b>Adsorption <math>K_d</math> (ml/g)</b>	<b>Desorption <math>K_d</math> (ml/g)</b>
1g : 10 ml	24.0	46.2
0.5 g : 10 ml	26.7	46.0
0.2 g : 10 ml	24.0	60.3
<b>pH 7.9</b>	<b>Adsorption <math>K_d</math> (ml/g)</b>	<b>Desorption <math>K_d</math> (ml/g)</b>
1g : 10 ml	5.3	14.4
0.5 g : 10 ml	8.6	20.9
0.2 g : 10 ml	11.3	60.1

**Table 5-8.** Comparison of retardation coefficients predicted from batch adsorption partition coefficients (Table 4-8) with retardation coefficients observed in column experiments (leading edge of breakthrough curves).

<b>pH 6.9</b>	<b>Batch Ret. Coef.</b>	<b>Column Ret. Coef.</b>
1g : 10 ml	64.6	
0.5 g : 10 ml	71.1	80
0.2 g : 10 ml	64.6	
<b>pH 7.9</b>	<b>Batch Ret. Coef.</b>	<b>Column Ret. Coef.</b>
1g : 10 ml	15.1	
0.5 g : 10 ml	23.8	10.3
0.2 g : 10 ml	30.9	

## 5.4.2 Implications for Large-Scale Transport

To evaluate the implications of the column experiment results over longer time and distance scales, the three-site model was used with the best-fitting reaction parameters of Tables 4-5 and 4-6 to simulate large-scale reactive transport at pHs of 6.9 and 7.9, respectively. Simulations were also conducted using a single fast site with a partition coefficient equal to either the adsorption or desorption  $K_d$  value that was experimentally observed at the highest solid-to-solution ratio in the batch experiments (Table 5-8).

The results of the pH 6.9 simulations are shown in Figure 5-12. In these simulations, the mean water residence time is 1 year and the upper plot shows the results for a steady input of 6.5  $\mu\text{M}$  uranium while the lower plot shows the results for a 50-year pulse of 6.5  $\mu\text{M}$  uranium. A Peclet number of 120 was used in all simulations (i.e., minimal dispersion). With a mean residence time of one year and a large Peclet number, the effective uranium retardation factor is the number of years taken to reach  $C/C_0 = 0.5$  in the continuous-input plots. The three curves of Figure 5-12 labeled as using the column parameters had identical values of all reaction parameters (i.e., Table 5-5) except for the desorption rate constant of the third site, for which values of 0.0013, 0.00003, and 0.000003  $\text{hr}^{-1}$  were used (figure legend); i.e., the same three values used to generate the model curves of Figure 5-8.

Two features of the plots of Figure 5-12 are noteworthy. First, it is apparent that curves generated using the column parameters have significantly greater uranium retardation factors than either of the curves generated using the batch  $K_d$  values. Also, while the response to a continuous uranium input is relatively insensitive to the desorption rate constant of the third site, the response to a 50-year-pulse input shows considerable sensitivity to this parameter. We attribute the latter behavior to a greater influence of the low-abundance third site when the average uranium concentration is lower, as it is when the input function is of limited duration. The continuous injection of uranium tends to saturate the less-abundant third site and thus lessens the influence of the desorption rate constant of this site on the uranium breakthrough.

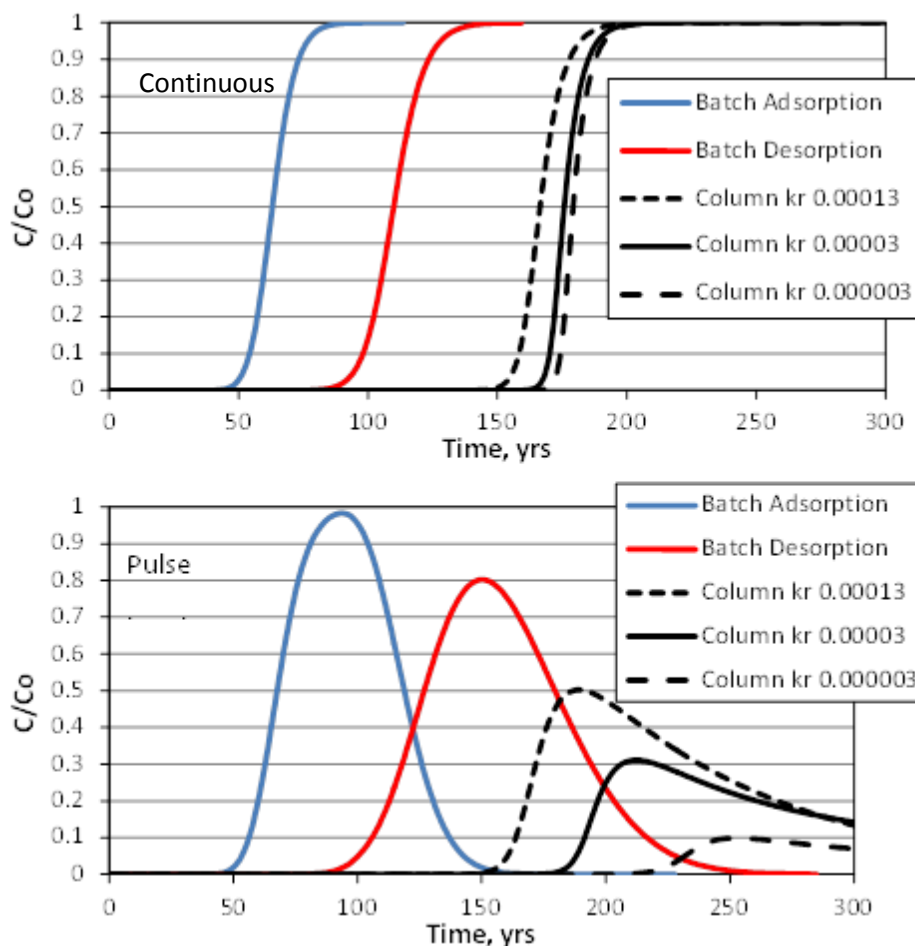


**Figure 5-12.** Uranium transport predictions over large scales at pH 6.9 using one-site model with partition coefficients from batch experiments (blue and red) and three-site model with reaction rate constants from column experiments (black). Mean water residence time is one year and uranium input concentration is  $6.5 \mu\text{M}$ . Top plot shows response to continuous uranium input and bottom plot show response to a 50-year pulse input.  $k_r$  values in legend are desorption rate constant of third sorption site.

Figure 5-13 shows the results of the large-scale model simulations at pH 7.9. The same assumptions were used in these simulations as in the simulations at pH 6.9 except that the finite pulses in the lower plot were only 10 years instead of 50 years. Also, only one curve is shown using the column parameters because the desorption rate constant of the third site was better constrained in the column experiments at pH 7.9 than at pH 6.9 (the uranium recovery at pH 7.9 was nearly complete).

In Figure 5-13, it is apparent that the column parameters predict a uranium retardation factor that is greater than the one-site simulation using the batch adsorption  $K_d$  value but less than the simulation using the batch desorption  $K_d$  value. Furthermore, this behavior

is observed for both a continuous input and a pulse input. The reason for the different behavior at pH 7.9 compared to pH 6.9 is attributed to the similarity of the ratios of the adsorption to desorption rate constants for all three sites at pH 7.9 and also to the smaller range of the desorption rate constants as well as the greater value of the slowest desorption rate constant at this pH. In effect, all three sites have similar individual partition coefficients at pH 7.9, with the only difference being their relative adsorption and desorption rates. These characteristics all contribute to well-behaved transport that is consistent with a single partition coefficient at large scales (i.e., when the time scale is large compared to the time scales of all the reactions). In contrast, at pH 6.9 the third site has a significantly greater ratio of adsorption to desorption rate constant and hence a greater effective partition coefficient than the other two sites. This disparity, coupled with the limited number of slower sites and the very small desorption rate constant of the third site gives rise to greater retardation relative to that predicted from the batch experiments and also to a large sensitivity of the pulse input breakthrough curves to the third-site desorption rate constant.

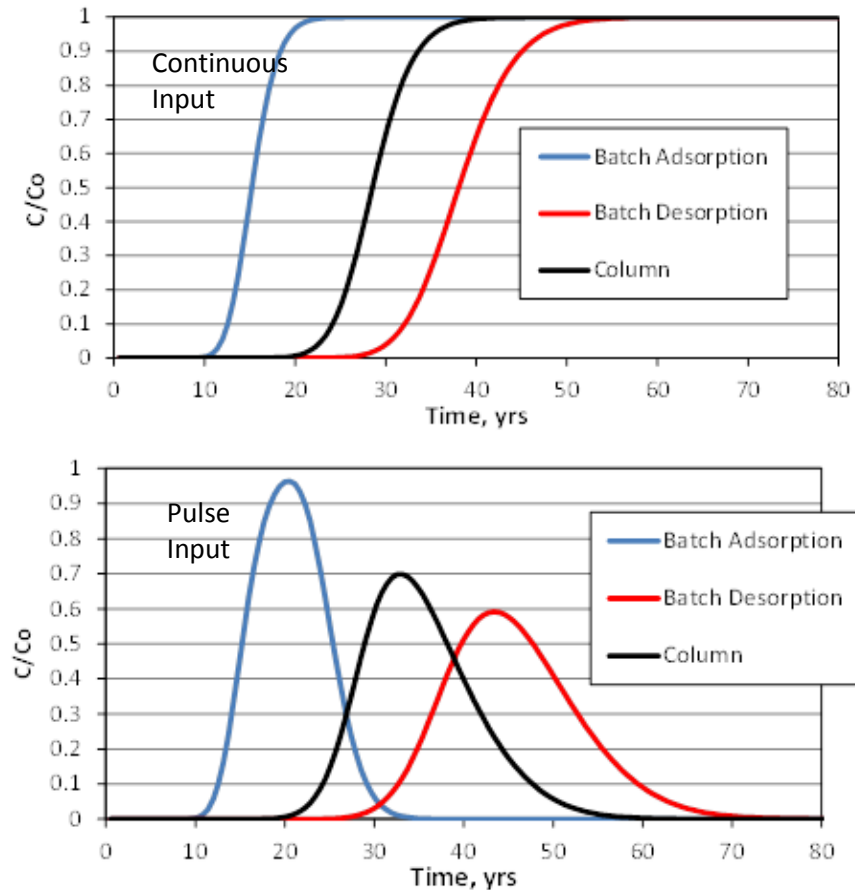


**Figure 5-13.** Uranium transport predictions over large scales at pH 7.9 using one-site model with partition coefficients from batch experiments (blue and red) and three-site model with reaction rate constants from column experiments (black). Mean water residence time is one year and uranium input concentration is 6.5  $\mu\text{M}$ . Top plot shows response to continuous uranium input and bottom plot show response to a 50-year pulse input.

At pH 6.9, the desorption rate constant of the third site is probably the most important reaction parameter affecting the large-scale transport behavior of uranium. Unfortunately, it is also the most uncertain and the most difficult parameter to estimate of any of the reaction parameters. The adsorption site densities are also somewhat uncertain, but the impact of their uncertainty is lessened by the negative correlation between the adsorption rate constant and the site density for any given site when these parameters are estimated. This negative correlation tends to be self-compensating because sites that have smaller densities tend to have larger adsorption rate constants to match the same experimentally-observed rates and amounts of adsorption. Nonetheless, obtaining better constraints on site densities would reduce uncertainties in larger-scale transport predictions. It is worth noting that the column experiments imposed some loose lower limit constraints on surface densities of the slower sites because the fits degraded as surface densities were decreased below certain values (a point was reached where increasing the adsorption rate constants of these sites could no longer compensate for the decreased surface densities).

An important implication of the above discussion is that even a very small number of sites that are effectively irreversible (zero desorption rate constant) could have a dramatic influence on large-scale transport predictions provided that plume concentrations and durations remain low enough that irreversible sites do not become saturated. Although it is technically not possible to measure desorption rates of zero (we can only place upper limits on very low rates), the lack of complete recovery predicted by conservative log-log extrapolations of the tails of the uranium breakthrough curves in the pH 6.9 column experiments suggests that there may be some desorption rates that are low enough at this pH to have a very significant impact on the large-scale transport of uranium. Interrogating these slow desorption rates, while difficult, clearly has a big payback in terms of improving (and removing conservatism from) large-scale transport predictions.

## 5.5 CONCLUSIONS

We believe that we have made significant progress in effectively demonstrating a method of interrogating and taking defensible credit for slow desorption rates to improve reactive transport predictions over long time and distance scales. We chose uranium in Grimsel Test Site granodiorite as a study case, but the method could be applied to any moderately sorbing radionuclide in any hydrogeologic system. Although we did not demonstrate a large difference between uranium transport predictions using column transport data and batch adsorption data, the former of which was intended to interrogate slow desorption sites and the latter of which did not interrogate these slow sites, we think that our approach is valid and that it could be readily improved to reduce conservatism in large-scale predictions. The most important improvement would be to carry out the flushing phase of the column experiments (at the same solution conditions as the injection/loading phase) until curvature is observed in the log-linear tailing of the breakthrough curves or until detection limits are reached. This would allow the lowest possible estimates of the *upper limits* of slow desorption rate constants. Another improvement would be the introduction of flow interruptions during the log-linear tailing portions of the breakthrough curves to get better constraints on very low desorption rates (we tried this

approach in FY 2013 experiments, but it was inconclusive, mainly because solution conditions were not maintained strictly constant). We also believe that our inducement of desorption (by introducing a higher pH in the case of uranium) has validity in obtaining conservative estimates of slow desorption rate constants. Additional improvements could also be made in the batch experiments (discussed at the end of Section 5.4.1) to better constrain both slow desorption rates and surface site densities and thus better complement the column experiments.

From a practical standpoint, the three-site kinetic model that yielded good fits to the uranium column transport data at both investigated pHs is easy to implement in performance assessment models with little additional computational burden over a simple linear partition coefficient ( $K_d$ ) model. This approach is consistent with multirate models, although we believe that three or four sites is probably sufficient to explain most experimental data sets, and it is not necessary (and less defensible) to employ continuous distributions of rate constants or to constrain all the reactions to have the same effective partition coefficient, as has sometimes been done with multirate models (Liu et al., 2008). The three-site kinetic model is also consistent with more sophisticated geochemical modeling approaches where, for instance, uranium transport has been shown to be effectively simulated using three types of surface complexation sites (weak, strong and very strong) in a classic geochemical modeling framework (e.g., Davis and Curtis, 2003). We also showed that when the ratio of the adsorption to desorption rate constants of all sites are similar in magnitude and the time scale of the slowest desorption reaction is fast relative to the time scale of transport, a simple linear partition coefficient ( $K_d$ ) approach can be effectively used to describe reactive transport over long time and distance scales.

## 5.6 REFERENCES

- Davis, J. A. and Curtis, G. P., 2003. Application of Surface Complexation Modeling to Describe Uranium(VI) Adsorption and Retardation at the Uranium Mill Tailings Site at Naturita, Colorado, *NUREG/CR-6820*, United States Geological Survey (for Nuclear Regulatory Commission), Menlo Park, CA.
- Doherty, J.E., 2009. *Manual for PEST: Model Independent Parameter Estimation*, in: J.E. Doherty (Ed.). Watermark Numerical Computing, Brisbane, Australia, p. 336.
- Doherty, J.E., 2010. *Addendum to the PEST Manual*, in: J.E. Doherty (Ed.). Watermark Numerical Computing, Brisbane, Australia, p. 131.
- Dong, W. and Brooks, S., 2006. Determination of the formation constants of ternary complexes of uranyl and carbonate with alkaline earth metals ( $Mg^{2+}$ ,  $Ca^{2+}$ ,  $Sr^{2+}$ , and  $Ba^{2+}$ ) using anion exchange method. *Env. Sci. Tech.*, **40**(15), pp. 4689–4695.
- Echevarria, G., Sheppard, M. I., and Morel, J. L., 2001. Effect of pH on the sorption of uranium in soils. *J. Env. Radioactivity*, **53**(2), pp. 257-264.
- ENRESA, 1998. FEBEX, Full-scale Engineered Barriers Experiment in crystalline host rock – Pre-operational stage summary report, Technical Publication 01/98, Madrid, Spain.
- Giammar, D. E. and Hering, J. G., 2001. Time scale for sorption-desorption and surface precipitation of uranyl on Goethite. *Env. Sci. Tech.*, **35**(16), pp. 3332–3337.

- Good, N. E., Winget, G. D., Winter, W., Connolly, T. N., Izawa, S., Singh, R. M. M. 1966. Hydrogen ion buffers for biological research. *Biochemistry*, **5**(2), pp. 467-477.
- Johnson, J., 2010. llnl.dat 4023 2010-02-09. Data from 'thermo.com.V8.R6.230' prepared by Jim Johnson at Lawrence Livermore National Laboratory, in Geochemist's Workbench format. Converted to PHREEQC format by Greg Anderson with help from David Parkhurst.
- Joseph, C., Stockmann, M., Schmeide, K., Sachs, S., Brendlet, V., and Bernhard, G., 2013. Sorption of U(VI) onto Opalinus clay: Effects of pH and humic acid. *Applied Geochemistry*, **36**, pp. 104-117.
- Kersting et al. 2012. Radionuclide Interaction and Transport in Representative Geologic Media, Used Fuel Disposition Campaign Milestone Report FCRD-UFD-2012-000154; Chapter 5, Laboratory Testing Complementing Grimsel Field Work: Conservative Tracer Screening and Preliminary Radionuclide Transport Experiments.
- Liu, C., Zachara, J. M., Qafoku, N. P., and Wang, Z., 2008. Scale-dependent desorption of uranium from contaminated subsurface sediments. *Water Resour. Res.*, **44**(8), DOI: 10.1029/2007WR006478
- Parkhurst, D. L. and Appelo, C. A. J., 2013. PHREEQC (Version 3.0.4) - A computer program for speciation, batch speciation, one-dimensional transport, and inverse geochemical calculations, U.S. Geological Survey Techniques and Methods, Book 6, Chapter A43, 497 p., <http://pubs.usgs.gov/tm/06/a43/>.
- Tsang, Y. W. 1995. Study of alternative tracer tests in characterizing transport in fractured rocks, *Geophys. Res. Letters*, **22**(11), 1421-1424.
- Waite, T. D., Davis, J. A., Payne, T. E., Waychunas, G. A., and Xu, N., 1994. Uranium(VI) adsorption to ferrihydrite – Application of a surface complexation model. *Geochim Cosmochim. Acta*, **58**(4), pp. 5465-5478.
- Wang, Y., et al. 2013a. Natural System Evaluation and Tool Development – International Collaborations: FY13 Progress Report, Used Fuel Disposition Campaign Milestone Report FCRD-UFD-2013-000628; Chapter 2, Interpretations of Colloid-Facilitated Transport Experiments at the Grimsel Test Site from 2008 through 2012.
- Wang, Y., et al. 2013b. Experimental and Modeling Investigation of Radionuclide Interaction and Transport in Representative Geologic Media, Used Fuel Disposition Campaign Milestone Report FCRD-UFD-2013-000314; Chapter 5, An Experimental Methodology for Improving Radionuclide Transport Process Models using Uranium and Grimsel Granodiorite as a Case Study.

## 6. LABORATORY INVESTIGATION OF COLLOID-FACILITATED TRANSPORT OF AMERICIUM BY BENTONITE COLLOIDS IN A GRANODIORITE SYSTEM

### 6.1 INTRODUCTION

The objective of this study was to quantify the colloid-facilitated transport potential of americium (Am) through a weathered fractured granodiorite system. Am was adsorbed to bentonite clay colloids before injection through columns packed with geologic media to provide estimates of desorption rate constants (from colloids) that are important for performance assessment calculations. While our studies focused on a specific crystalline rock system, the method(s) we developed can, in principle, be applied to any geologic setting in which colloid-facilitated transport in groundwater is a potential mechanism for radionuclide release to the accessible environment. The methods are intended to especially provide insights into upscaling of colloid-facilitated radionuclide transport predictions in time and space.

A specific area of interest is to evaluate and quantify the potential transport of Am in deep fractured crystalline rock formations (especially when initially adsorbed to mobile mineral colloids). We selected a fractured/weathered granodiorite at the Grimsel Test Site (GTS) in Switzerland as a model crystalline rock repository system because the system has been thoroughly studied (Huber et al., 2011), and field experiments involving actinides have already been conducted at this site (Geckeis et al., 2004; Chapter 4 of this report). Working on this system provides a unique opportunity to compare lab experimental results with field-scale observations.

Field experiments and observations have shown that Am transport can be enhanced by the presence of colloids. Penrose et al. (1990) found Am released as part of a treated waste stream into a canyon at Los Alamos National Laboratory was detected over 3 km from the source and was sorbed very strongly to colloids in the 25-430 nm size range. Geckeis et al. (2004) conducted two *in situ* experiments at the GTS by injecting radionuclides adsorbed to bentonite colloids in a fractured shear zone and found that most of the Am(III) migrated without retardation in association with colloids. Significant transport of both Am and Pu were attributed to slow desorption kinetics from mobile colloids; up to 60% of the Am was removed from collected samples by centrifugation. Vilks and Baik (2001) investigated Am transport through a natural fracture in a granite block and found that dissolved Am was completely adsorbed to fracture surfaces, but injecting dissolved Am and colloids together resulted in a small amount of transport.

Laboratory experiments with Am, granite, and bentonite colloids have also been conducted and show the need for more quantitative analysis to determine the role of desorption rates in Am transport. Murali and Mathur (2002) investigated Am adsorption to bentonite and granite as a function of contact time, pH, liquid-solid ratio, radionuclide concentration, and the presence of competing cations and found that Freundlich and Langmuir isotherms seem to accurately predict Am/bentonite sorption. Iijima et al. (2008) attributed differences in Am  $R_d$  values (effective retardation factors for colloid-facilitated transport) reported in the literature to be due to differences in solution

composition and reactive site capacity as a function of particle size and surface area. Iijima et al. (2010) investigated the effect of addition order on sorption rate coefficients and reversibility in batch experiments with Am, GTS granite, and bentonite colloids and found Am adsorption to bentonite to be largely reversible. Huber et al. (2011) also investigated Am adsorption and desorption in the ternary system containing GTS groundwater, GTS fracture fill material (FFM) and bentonite colloids, and they measured slow desorption rates of Am from the bentonite colloids in the presence of FFM.

For our experiments, weathered FFM from the GTS and bentonite used as a repository backfill in experiments at the GTS were characterized with various analytical methods (e.g., BET, SEM/EDS, QXRD), and batch and breakthrough column experiments were conducted and analyzed to elucidate the dominant parameters and provide insight into potential Am transport in a crystalline rock repository. Am solutions were prepared in synthetic groundwaters that matched the natural water chemistry found in the GTS. FFM samples were crushed, rinsed, and equilibrated with synthetic groundwater and sorted to yield a 150-355  $\mu\text{m}$  size fraction. In colloid-facilitated transport experiments, bentonite was crushed, sodium-saturated, equilibrated with synthetic Grimsel groundwater, and allowed to settle by gravity to yield a stable suspension. These bentonite suspensions were then equilibrated with Am before use. Sorbing Am onto bentonite colloids prior to injection into the columns resulted in >50% of the americium being transported through the columns. Subsequent reinjection of unanalyzed effluent showed that the Am was not irreversibly adsorbed to binding sites on the bentonite colloids.

## 6.2 MATERIALS AND METHODS

We conducted a series of three breakthrough experiments with small columns packed with the same GTS fracture fill material (see Section 5.2). The unanalyzed effluent from the first set of columns (run in duplicate) was injected through a second column, and the unanalyzed effluent from the second column was injected through a third column. This repeat injection procedure was conducted to determine if colloids that transported through one column were more likely to transport through a second or third column, and likewise to determine if Am that transported through one column while adsorbed to colloids was more likely to remain associated with the colloids and transport more efficiently through a second or third column. If either of these outcomes were observed, it would suggest a distribution of colloid filtration rate constants and/or a distribution of Am desorption rate constants from colloids, which would have important implications for the scale dependence of colloid-facilitated transport of Am. In effect, the repeat-injection experiments were designed to interrogate slow colloid filtration rates and slow desorption rates better than single-pass experiments. Slow rates have a much greater influence on large-scale performance assessment calculations of colloid-facilitated transport than faster rates (see Section 6, Discussion section of this report). Faster rates can mask the presence of slow rates in single-pass column experiments.

### 6.2.1 Groundwater

The groundwater used in all experiments was synthetic shear zone water (SZW) that matched the water chemistry of the water found in the shear zone at the Grimsel Test Site. The SZW was prepared by adding analytical grade reagents to filtered, high-purity water ( $> 18 \text{ M}\Omega \text{ cm}$  resistivity) according to the concentrations of constituents listed in Table 6-1.

The ionic strength (0.66 mM) was calculated from the added reagents and pH 8.0 was measured for the solution equilibrated with the atmosphere in Los Alamos, NM (2,231 m above sea level). The carbonate concentration listed in Table 6-1 is as it was prepared, not after equilibration with the atmosphere.

**Table 6-1.** Synthetic shear zone water constituents

Constituent	mg/L
Na	14.97
K	0.20
Mg	0.02
Ca	5.60
Cl	5.67
SO <sub>4</sub>	5.85
F	6.00
Si	9.96
CO <sub>3</sub> +HCO <sub>3</sub>	20.06
Ionic Strength	0.66 mM
pH	8.0

### 6.2.2 Porous Medium

Weathered fracture fill material (also known as fault gouge) was collected during coring operations of the MI shear zone at the Grimsel Test Site (GTS) in Switzerland (see Section 5.2). The shear zone is not currently exposed in the CFM tunnel (where the field experiments were conducted), so the material was collected in an adjacent tunnel. The shear zone occurs where a fracture in the granite rock had been exposed to hydrothermal

solutions and was highly altered over time. Samples were shipped to Los Alamos National Laboratory in pieces ranging from micron size up to 10-15 cm long. Due to the small quantity of material available, all pieces less than 1 cm in size were combined and crushed using a percussion mortar, sieved into 75-150, 150-355, and 355-500  $\mu\text{m}$  size fractions, and thoroughly rinsed in high-purity water to removal all fines. The samples were then rinsed with synthetic Grimsel shear zone water (SZW) until the electrical conductivity of solution in contact with the material for 24 hours was within 5% of the electrical conductivity of the SZW. Samples were then oven dried for 12 hours at 60 °C and stored in glass jars. Optical microscope (Wild Heerbrugg, M420) photographs of the 150-355  $\mu\text{m}$  size fraction of the FFM and the unaltered granodiorite matrix show that the FFM appears to have a larger fraction of dark grains (Figure 5-1). The mineralogy of the granodiorite and FFM were determined by quantitative X-ray diffraction (QXRD) at Los Alamos. Table 5-3 lists the major fractions for the unaltered granodiorite, a scraping from the shear zone surface, and a bulk sample of the crushed FFM that we used for all experiments discussed in this section. Table 5-4 shows the bulk chemical analysis of the granodiorite and bulk FFM by X-ray florescence. The main differences between the unaltered granodiorite and FFM were a significant enrichment in Mg, minor enrichment in K and Fe, and minor depletions of Si, Na, and Ca. Surface area of the FFM was determined by the BET method with krypton gas (Micromeritics Analytical Services) and was measured as 0.23  $\text{m}^2 \text{g}^{-1}$  for the 150-355  $\mu\text{m}$  size fraction used in all column experiments.

### 6.2.3 Bentonite Colloids

Bentonite colloids were processed from a brick of compressed FEBEX bentonite shipped to us by our project partners at the Grimsel Test Site in Switzerland. Samples of the brick were crushed in a ceramic mortar and pestle and sieved to retain the size fraction less than 75  $\mu\text{m}$ .

The bentonite colloids were sodium saturated to enable comparison of our results with other published results (Huber et al., 2011). 20 g of material was added to 800 mL of 1 M NaCl and was placed on a shaker table for 7 days. The supernatant was decanted and the removed liquid was replaced with new 1 M NaCl and placed on the shaker for 7 additional days. This process was repeated 3 times and the solution



**Figure 6-1.** Preparation of colloid suspension from FEBEX bentonite brick

conductivity was measured (VWR Series 500, Model 2052 meter and VWR 525 conductivity dip cell/electrode, Model 23198-020) to ensure stability. The resulting suspension was settled and the supernatant was decanted and replaced with SZW. This process was repeated 6 times until the conductivity of the supernatant was reduced below 2.5 mS and the colloids did not readily settle. The suspension was then placed in a sonic bath for 30 minutes, centrifuged for 12 h, and the supernatant removed and replaced with SZW. This process was repeated 10 times until the resulting conductivity of the bentonite suspension was within 1% of the SZW (Figure 6-1).

The suspension was then diluted to 25 g L<sup>-1</sup> with SZW and was settled in 1 L graduated cylinders for 2 weeks to obtain a stable experimental suspension. The top 700 mL was decanted and Stokes' Law was applied to calculate a theoretical maximum particle size of less than 1 μm. The final stock suspension was then passed through a 1 μm filter to remove any larger particles. A single particle counter was used to measure the particle size distribution of the stock suspension. Very few particles larger than 220 μm were present (Figure 6-2).

The concentration of the stock suspension was calculated to be (1540 mg L<sup>-1</sup>) by drying 25 mL of suspension on a watch glass (in triplicate) and determining the weight difference after drying. The stock suspension was diluted to 100 mg L<sup>-1</sup> and was stored in a sealed glass bottle. Surface area was measured by the BET method with nitrogen gas to be 56.1 m<sup>2</sup>·g<sup>-1</sup>.

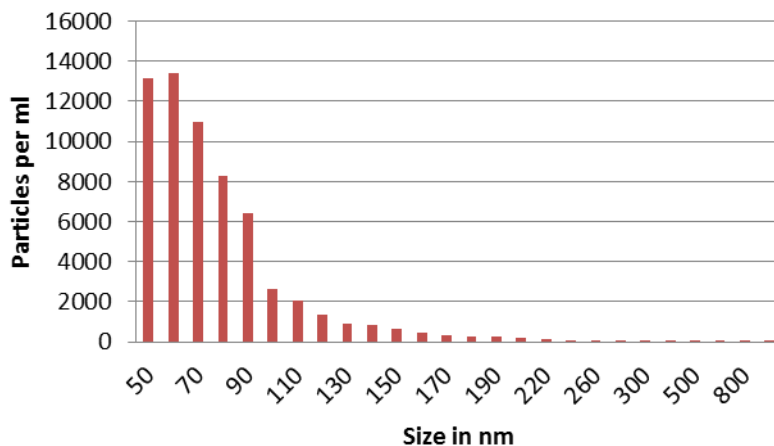


**Figure 6-2.** Particle size distribution of FEBEX bentonite colloid suspension as measured by a single particle counter. Note that the concentration scale on the y-axis does not account for sample dilution.

#### 6.2.4 Americium and Tritiated Water

The Am used in all experiments was a  $^{241}\text{Am}$  solution stabilized with HCl (Eckert and Ziegler). The Am was processed by the supplier within 3 weeks of ordering and was determined to be >99.8% americium with very little ingrowth of Np. SZW with 100 mg L<sup>-1</sup> concentration of bentonite colloids was spiked with ~1000 dpm  $^{241}\text{Am}$ , which is calculated to be  $5.5 \times 10^{-10}$  M. The suspensions were allowed to equilibrate for 1 week. PHREEQC calculations for similar water chemistry confirmed that the suspension is below the solubility product of all Am species present. All suspensions were stored in Teflon® bottles until use in experiments. It should be noted that we attempted to make a  $5.5 \times 10^{-10}$  M solution of dissolved Am without colloids and over 75% of the  $^{241}\text{Am}$  was lost to the bottle surfaces, resulting in less than 25% of the original Am remaining in solution. When bentonite colloids were added at the same time as the addition of Am, all of the Am remained in the suspension, with > 97% being sorbed to the colloids and < 3% remaining in the dissolved phase or being sorbed to the bottle surfaces. These suspensions were measured once a week over the course of the experiments and remained stable without any measureable loss of Am for 3 months. Tritium in the form of tritiated water was added to the Am and bentonite suspensions and was used as a conservative tracer to provide groundwater residence times and dispersivities in the column experiments.

#### 6.2.5 Analytical Measurements

Am and tritium concentrations were measured by liquid scintillation counting, or LSC (Perkin Elmer Tri-Carb 2550) with energy ranges of 0-20 keV for tritium and 100-250 keV for Am. A 1 mL aliquot of sample was combined with 5 mL of deionized water and 14 mL of liquid scintillation cocktail (Packard, Ultima Gold AB) in a polypropylene scintillation vial to yield 20 mL total. The vial was vigorously shaken for at least 15 seconds to ensure mixing between the cocktail and the sample, and samples were counted for two 15 minute increments and the results were averaged. The transformed index of an external  $^{133}\text{Ba}$  standard (tSIE) was used to correct for variable quenching of the samples, especially with respect to tritium.

Total Am concentrations were measured with uncentrifuged column effluent and dissolved Am was measured by centrifuging the sample at 15,000 RPM for 12 hours and then analyzing 1 mL of the supernatant for Am concentration. Colloid-associated Am was then calculated as the difference between the total and dissolved americium concentration for each sample.

pH of the solutions, suspensions, and breakthrough experiment samples were measured using a pH meter (Orion, Model 290) and a glass pH electrode (Fisher, AccupHast) calibrated with 4.01, 7.00, and 9.01 pH buffer solutions (Ricca Chemical Corp.).

Colloid concentrations of the bentonite suspensions were measured using both UV-Visible light scattering and turbidimetry for the first set of columns. After interference was observed in the colloid suspensions with low concentrations, turbidimetry was used exclusively for the remaining column breakthrough experiments. A turbidimeter (Hach, 2100N) was calibrated with standards (0.1, 1, 5, 10, 20, 40, 60, 80, 100 mg L<sup>-1</sup>) and the

same 12 mm borosilicate glass test tube was used for every measurement to reduce error from test tube variability. Colloid concentration was calculated using a correlation function derived to relate colloid concentration with the measured NTU (nephelometric turbidity units) of the sample.

### 6.2.6 Column Transport Experiments

Am column transport experiments were conducted by eluting Am and bentonite suspensions through columns packed with FFM in the 150-355  $\mu\text{m}$  size range. Small columns were constructed from 6 cm lengths of 0.95 cm diameter Teflon<sup>®</sup> tubing. The ends of the tubes were tapped to accept Teflon<sup>®</sup> compression fittings. The inside openings were covered with a small disk of 75  $\mu\text{m}$  PEEK screen to retain the column material while providing minimum resistance to flow and causing negligible straining of colloids. Teflon<sup>®</sup> tubing (1/16<sup>th</sup>-inch ID) and 3-way polycarbonate stopcocks were used to connect the columns to 50 mL Teflon<sup>®</sup> syringes (Torviq, TS-50) adapted for use with syringe pumps (KD Scientific, Model 100). 3-way stopcocks allowed for refilling syringes and switching suspensions or solutions while minimizing flow and pressure disturbances that may affect colloid retention. Flow was directed upward to help maintain saturation and to minimize the potential for air bubbles collecting in the column. An additional length of 1/16<sup>th</sup>-inch ID Teflon<sup>®</sup> tubing was connected to the top (outlet side) of the column and directed column effluent to a fraction collector (Gilson, FC-220) filled with 13  $\times$  100 mm polystyrene test tubes. The fraction collector was enclosed in an acrylic plastic chamber with evaporation pans filled with deionized water to minimize evaporation before sample analysis. Figure 6-3 shows a picture of the column experiment setup.

Columns were packed with 5.0 g of dry FFM (or no fill for control columns) and the flow rate was set to 0.3 mL h<sup>-1</sup>. The columns were initially flushed with Am-, tritium-, and colloid-free SZW for 7 days and the pH was monitored to ensure effluent pH stabilized within 0.1 pH units of the influent solution (pH 8.0  $\pm$  0.1) before the start of the radionuclide/colloid injection.

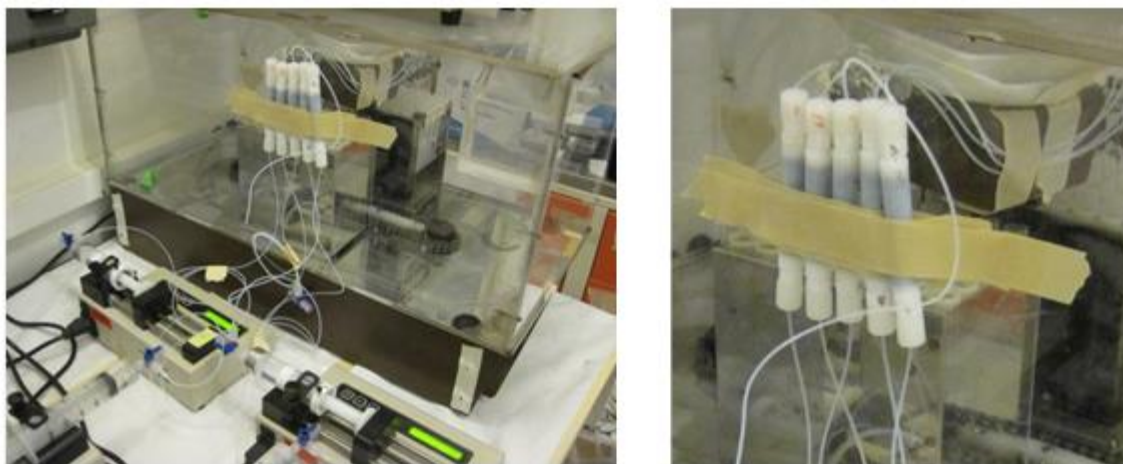


**Figure 6-3.** Photos of column setup with 5 columns running in parallel with syringe pumps, tubing, and fraction collector

To begin each breakthrough experiment, the background solution was switched to a suspension containing tritium and Am presorbed to the bentonite colloids. Syringes were refilled several times during the experiment and were eventually changed to SZW free of tritium, Am, or bentonite colloids to observe the flushing of the colloids and Am from the columns. Samples were collected at 12 hr intervals and the sample mass was weighed with a digital balance (Mettler, PL1200) and subtracted from the empty test tube weight to calculate the actual flow rates. pH measurements were measured and recorded for one of the duplicate columns. Total and dissolved Am activity, tritium activity, and colloid concentration were measured for every sample early in the breakthrough and were then reduced to every other sample to ensure adequate effluent was available for reinjection.

The unanalyzed effluent from the duplicate FFM columns was stored in a Teflon<sup>®</sup> bottle. This combined effluent was then injected into another FFM-filled column that had not been previously exposed to colloids or Am. This process was repeated again, with the unanalyzed effluent from the second FFM injection being stored and then injected into an additional unexposed FFM-filled column. A control column was run in parallel with each successive FFM injection. A flowchart of the procedure is shown in Figure 6-4.

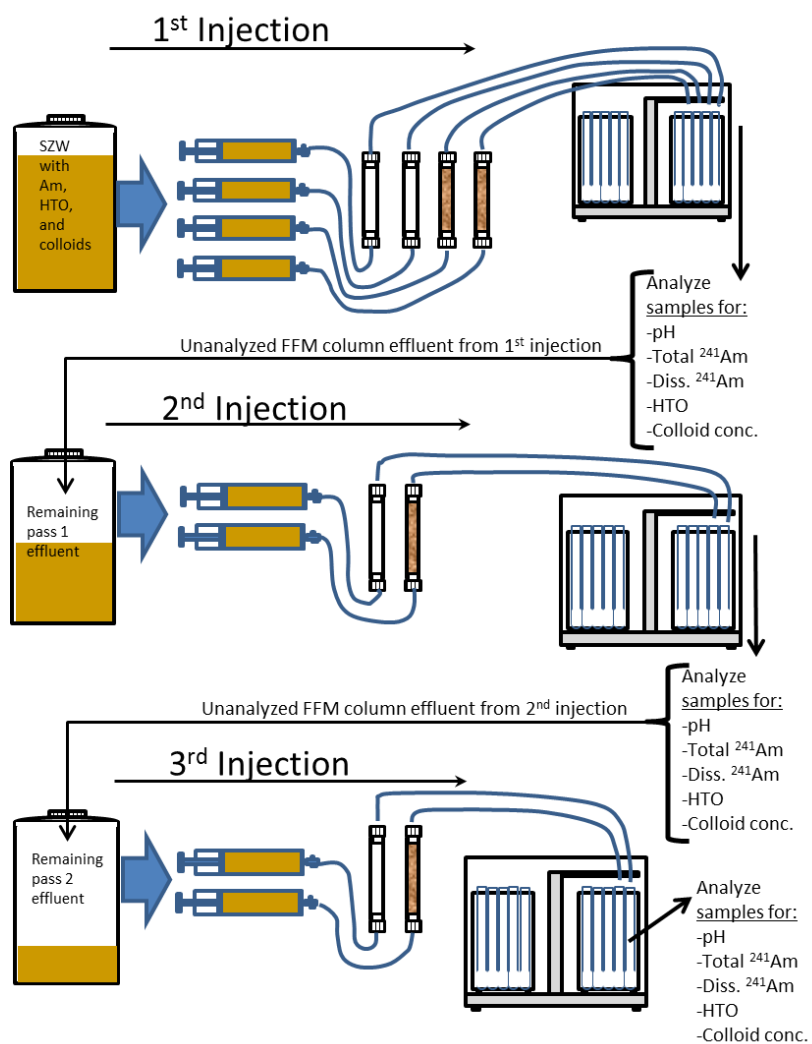


**Figure 6-4.** Flowchart of Am-colloid column experiments. A SZW/bentonite suspension with <sup>241</sup>Am and HTO added was injected through two columns filled with FFM and two control columns. Aliquots of effluent were analyzed for pH, total and dissolved <sup>241</sup>Am, HTO, and colloid concentrations and the remaining effluent was combined in a Teflon<sup>®</sup> bottle and injected through a second column filled with FFM and a second control column. Aliquots of the second injection effluent were measured for the above parameters and the remainder was combined and injected through a third column filled with FFM and a third control column. Aliquots of the third injection were measured for the above parameters.

### 6.2.7 Interpretive Modeling

The breakthrough results ( $C/C_0$  versus time) were modeled using the RELAP semi-analytical model (Reimus et al., 2003), which can simulate 1-D advective-dispersive transport with either filtration (colloids) or adsorption (solutes). Filtration or adsorption are described using a first-order reaction that can be either fast or slow and either reversible or irreversible. The model was first used to fit the normalized tritium breakthrough curves (without reactions) to determine the mean water residence time and longitudinal dispersion coefficient (or Peclet number, which is the column length divided by dispersivity) in each column. These parameters were then assumed to apply to the colloids so that a colloid filtration rate constant could be estimated by fitting the colloid breakthrough curves. Finally, the Am breakthrough curves were fitted in the same manner as the colloids, and the Am desorption rate constant from the colloids was taken to be the difference between the first order rate constant needed to fit the Am data and the colloid filtration rate constant. This last step was based on the assumption that the observed reduction in Am concentration was the result of both Am desorption from the colloids and the filtration of colloids to which Am was adsorbed. Thus, the colloid filtration rate constant must be subtracted from the overall rate constant describing Am removal to estimate the desorption rate constant of Am from the colloids. This procedure assumes that any Am that desorbs from the colloids rapidly adsorbs to immobile FFM surfaces and is effectively removed from the system because of the huge abundance of the FFM surfaces relative to the colloid surfaces

## 6.3 RESULTS

### *Control Experiments*

Initial stock solutions of  $5.5 \times 10^{-10}$  M Am (~1000 DPM) were prepared by adding a small spike of concentrated dissolved  $^{241}\text{Am}$  (25  $\mu\text{L}$ ) to 800 mL of SZW in a 1 L Teflon<sup>®</sup> bottle. An 800 mL stock suspension of 100 mg  $\text{L}^{-1}$  bentonite colloids, SZW, and  $^{241}\text{Am}$  was also prepared. 1 mL samples were collected and measured for Am activity at specified intervals, with the results shown in Figure 6-5.

Almost 75% of the Am in the dissolved stock solutions was lost to the Teflon<sup>®</sup> bottle surface within the first 3 hours, and the solution stabilized to a consistent concentration after 23 h (note that one of the two stock solutions in Figure 6-5 appears to take longer than 3 hrs to reach 75% adsorption, but no samples were taken from this bottle until over 100 hrs after the first very rapid sample). Shaking the bottles had no measureable effect on the Am concentrations, leading us to conclude that precipitation of Am was an unlikely cause of this loss of Am. When bentonite colloids were present, all of the Am remained in the suspension.

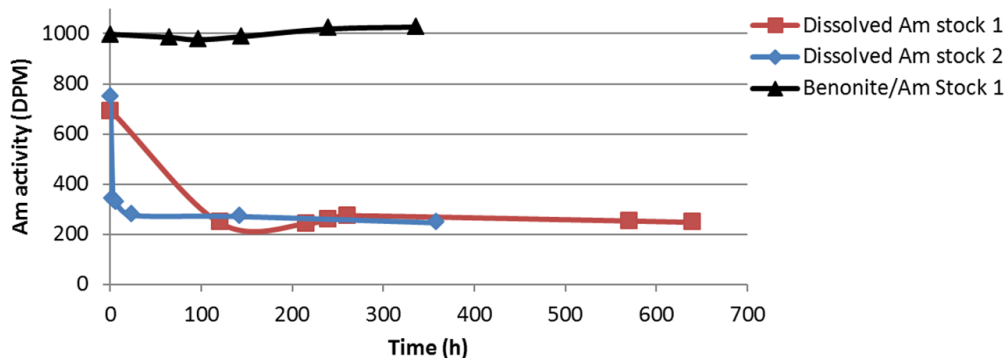


**Figure 6-5.** Concentration of Am in stock solutions/suspensions stored in Teflon bottles. Initial concentrations of all stocks were ~1000 DPM <sup>241</sup>Am.

Control experiments with various experimental materials were conducted with a  $1.4 \times 10^{10}$  M dissolved americium solution (245 DPM). This was the same solution that had equilibrated with the Teflon® bottles shown in Figure 6-5. 15 mL of solution were added to 50 mL Teflon® Oak Ridge centrifuge tubes, 50 mL Teflon® syringes, and 50 mL polycarbonate test tubes. 8 mL of solution were added to 8 mL polystyrene test tubes and 15 mL polypropylene centrifuge tubes. 1 mL samples were removed at specified time intervals and measured for dissolved americium activity by LSC. All experiments were conducted in duplicate, with the averaged results shown in Figure 6-6.

All materials resulted in a significant loss of Am from solution. Polystyrene and polycarbonate materials resulted in the least amount of Am loss while polypropylene and Teflon® resulted in the most loss. These results led us to focus on the transport of the Am/bentonite suspensions through FFM and not conduct dissolved Am batch and column experiments (because of the large amounts of adsorption to experimental material surfaces that would have to be corrected for).

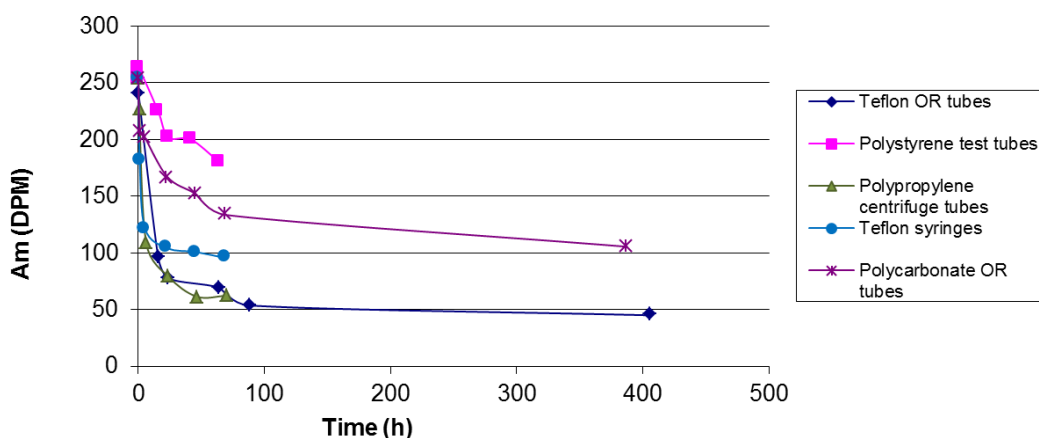


**Figure 6-6.** Material compatibility with dissolved Am solution. Materials tested were Teflon® Oak Ridge centrifuge tubes, polystyrene test tubes, polypropylene centrifuge tubes, Teflon® syringes, and polycarbonate Oak Ridge centrifuge tubes.

In addition to the batch control experiments, column breakthrough control experiments (using all experimental materials except the FFM) with Am/bentonite suspension were also conducted. As described in Section 6.2.6, a series of breakthrough experiments were conducted by injecting the effluent from the first column into a second column, and then injecting the effluent from the second column into a third column. Control breakthroughs were conducted in the same manner, and the FFM breakthrough experiments were normalized for the loss of Am in the control experiments. The results of the control breakthrough experiments are shown in Figure 6-7. Duplicate columns were used for the first control experiment and are shown in the top and middle graphs. The syringes were refilled after 40, 59, and 74 mL of cumulative volume and the same syringe was used without rinsing. The noticeable increases in Am concentration for each time the syringe was filled suggests that americium that is initially sorbed to the bentonite is being sorbed to the Teflon<sup>®</sup> in the system. Less Am is lost with each refill (Figure 6-8), indicating that the capacity for Teflon<sup>®</sup> to sorb Am is being approached. The loss of americium in the dissolved Am batch experiments and in the syringes during the column experiments indicates that Teflon<sup>®</sup> does have some affinity for Am at pH 8.0.

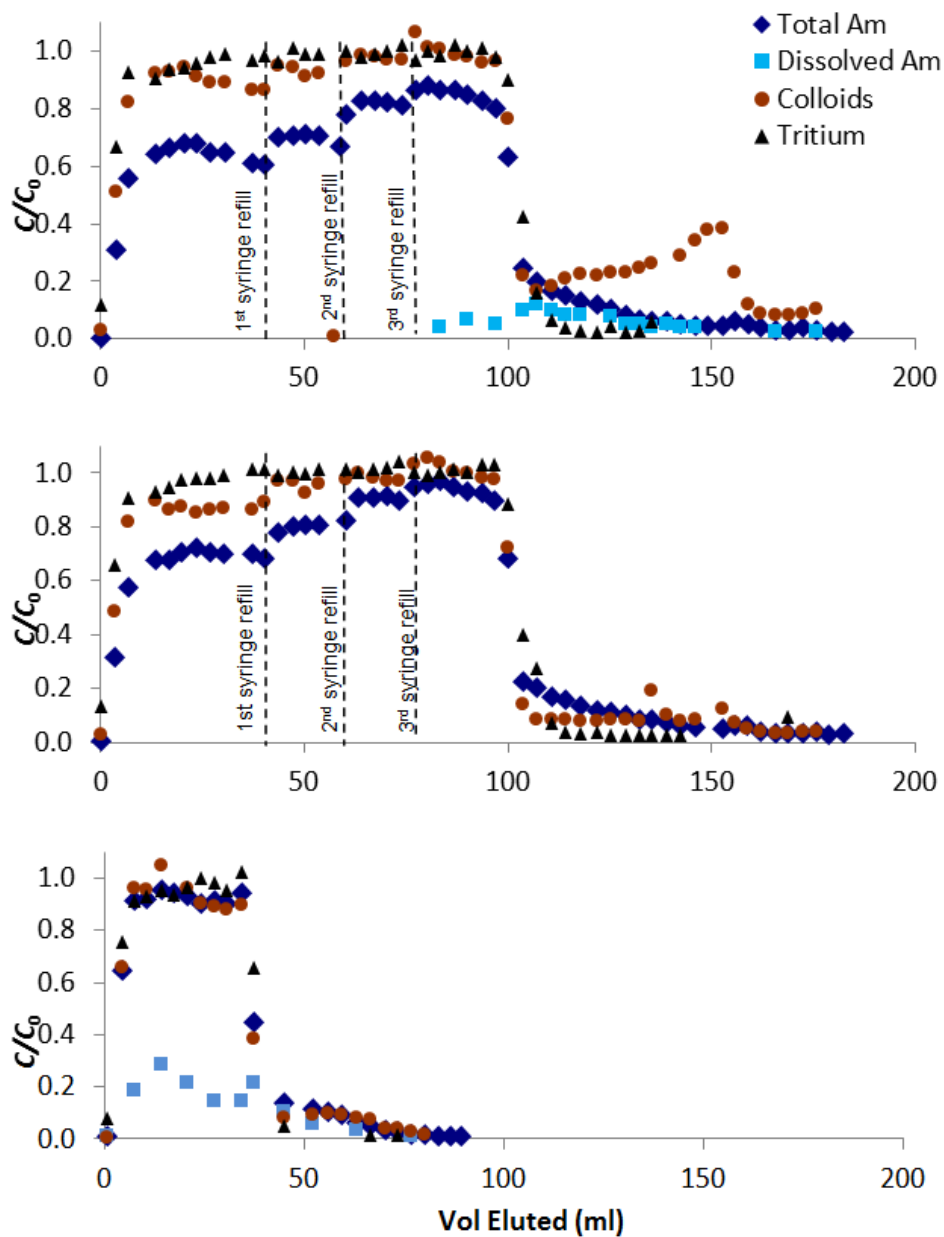


**Figure 6-7.** Results of control breakthrough experiments (system components only with no FFM). The top and middle graphs are duplicate controls for the first pass (stock solution) and the bottom graph is for the second pass (effluent from first FFM column injected through an empty column). The injection concentration ( $C_0$ ) used for the bottom graph was the effluent concentration coming out of the first FFM column.

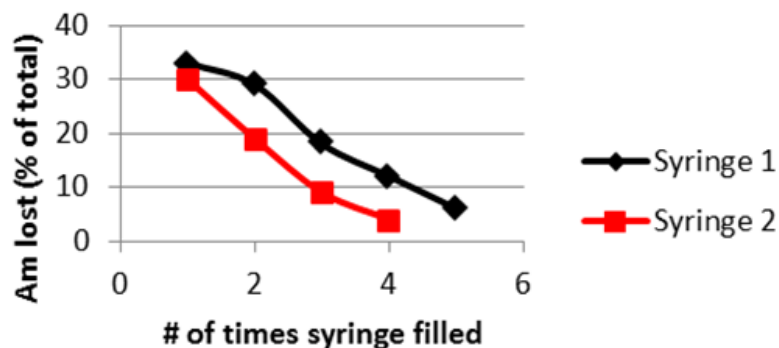


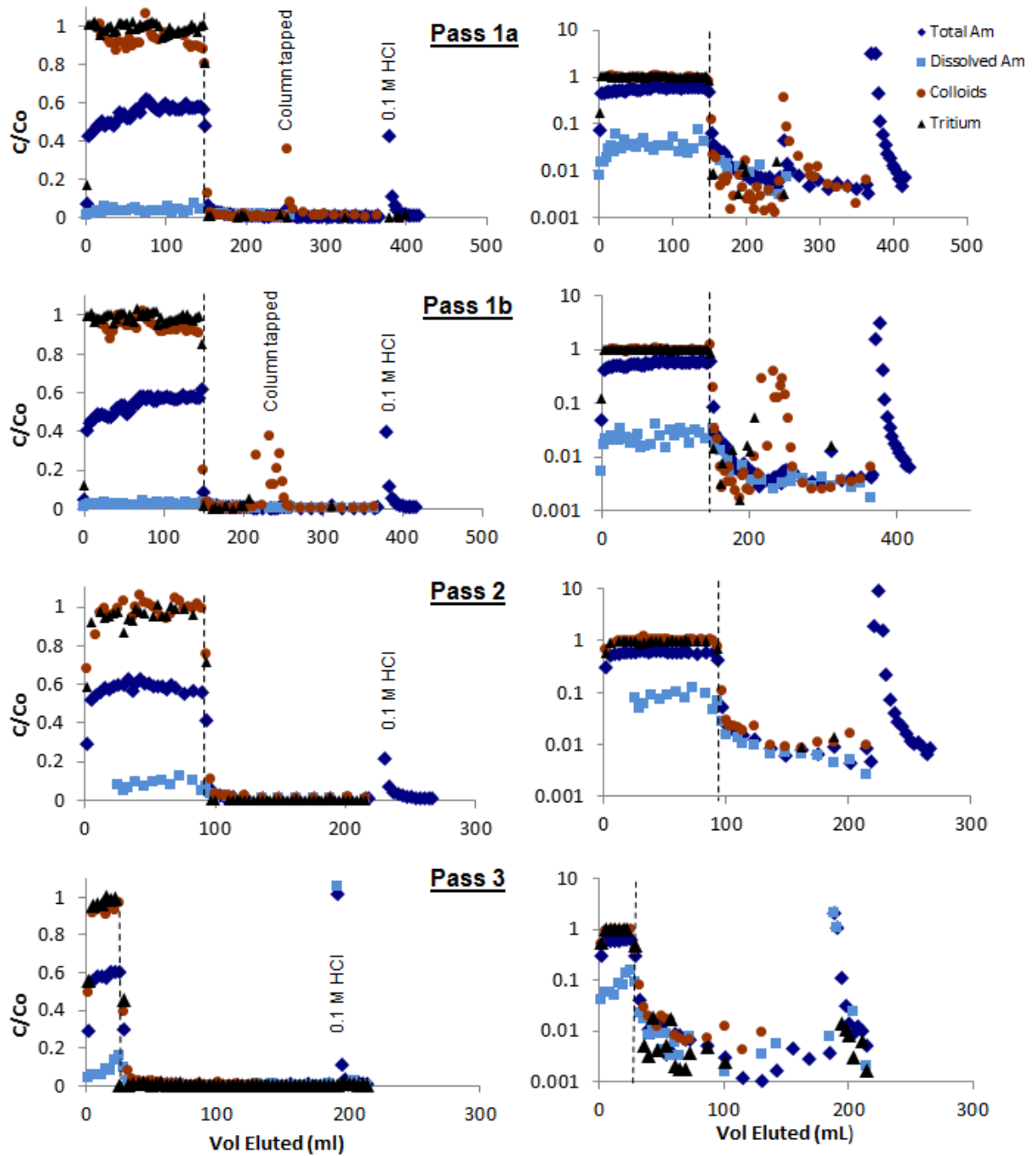
**Figure 6-8.** Am loss from Am/bentonite suspension in control experiments as a function of number of times syringes were refilled.

### *Column Breakthrough Experiments*

Figure 5-10 shows the results of the FFM column experiments with the injection of Am pre-equilibrated with bentonite colloids. Column results were highly reproducible for first injection columns that were conducted in duplicate. Colloid breakthrough occurred within the first pore volume and closely matched the conservative tracer, except the tritium tracer reached  $C/C_0$  of 1.0 while the colloid breakthrough reached a plateau greater than  $C/C_0$  of 0.95 but below 1.0. Am was also measured in the column effluent within the first pore volume, although attenuation from sorption to the FFM resulted in plateau of  $C/C_0$  values of about 0.58-0.60. Most of the Am that was transported through the column remained adsorbed to the bentonite colloids, with 2-3% of the measured Am being in the dissolved phase and remaining in the sample after centrifugation. After the injection suspension was switched to tritium-, Am-, and bentonite-free solution, very little bentonite or Am was measured in the effluent. Am in the effluent was measured to be less than 2% of the influent concentration. For the first injection, both columns were tapped on the side 4-5 times with the handle of a screwdriver to examine for trapped air bubbles at around 250 mL of cumulative effluent. It can be seen in Figure 5-10 that a significant pulse of colloids exited the column for the next few pore volumes due to this physical disturbance, but there was not a corresponding pulse of Am. After more than 200 mL of effluent was collected for the tail portion of the breakthrough, the injection solution was switched to 0.1 M HCl with a pH of ~1. An additional pulse of Am in the effluent was observed, however most of the americium that was sorbed on the FFM remained adsorbed after the acid injection.

For the second and third injections, the  $C_0$  values used in the calculations were the effluent Am and colloid concentrations from the previous column. There was no measureable difference in the effluent colloid concentration between the first, second, and third injections (they were always very close to  $C/C_0 = 1$ ). The normalized Am concentration for the second and third injections was about 0.57 and 0.58, respectively, which were very similar to the breakthrough concentrations from the first injection. The amount of dissolved Am in the effluent increased from the first to the third injections.

Less than 5% of the total Am was in the dissolved phase for the first injection, and this



increased to 5-10% for the second injection and 10-15% for the third injection.

**Figure 6-9.** Results of breakthrough experiments with  $C/C_0$  on linear scale (left) and log scale (right). The top two rows are duplicate experiments for the first pass of stock solution through FFM (Pass 1a and Pass 1b). The third row is for the second injection, which passed the effluent from the first columns through a new FFM column. The bottom row is for the third pass, which was the injection of effluent from the second pass through a new FFM column. The vertical dashed line denotes when the suspension injection was stopped and injection of americium- and colloid-free SZW was started.

The breakthrough results modeled with the RELAP model (Reimus et al., 2003) are shown in Figure 6-10. Only the breakthrough portion of the data was fitted with the model. Important fitted parameters from the model are listed in Table 6-2.

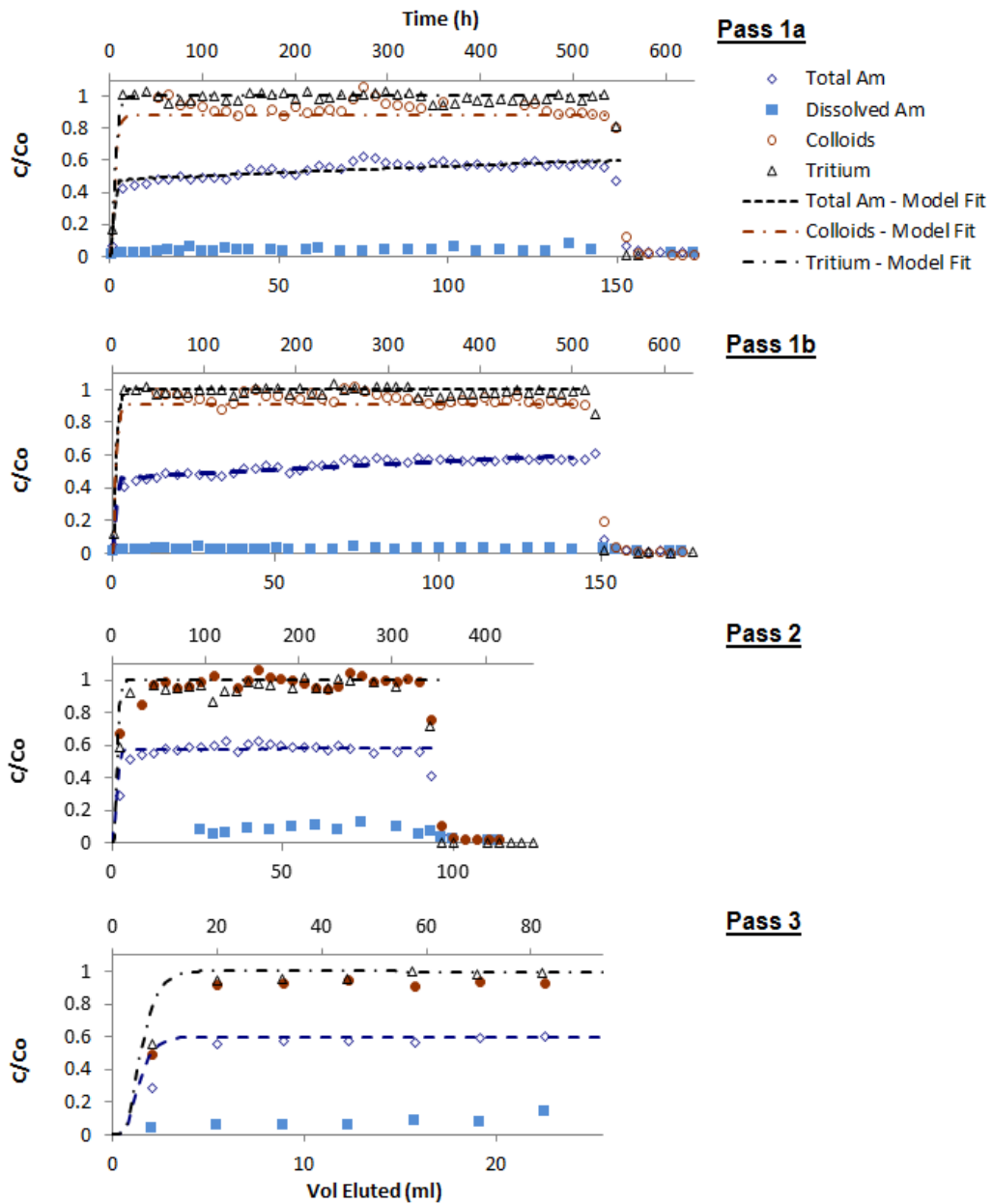


**Figure 6-10.** Model fits for americium breakthrough experiments with bentonite colloids. Results are shown for the first injection (Pass 1a and Pass 1b), second injection (Pass 2), and third injection (Pass 3).

**Table 6-2.** Parameters deduced from RELAP model fits to FFM column breakthrough curves.

	Pass 1a	Pass 1b	Pass 2	Pass 3
Colloid filtration rate constant $k_f$ ( $\text{hr}^{-1}$ )	0.01	0.02	-	-

<b>Am desorption rate constant <math>k_f</math> (hr<sup>-1</sup>)</b>	0.094*	0.097*	0.098	0.091
<b>Mean residence time (hr)</b>	6.5	6.5	6	6
<b>Peclet number</b>	5	5	10	10

\*These rate constants were estimated by matching the final Am  $C/C_0$  values in the first pass (first column) just before the colloid and Am-free water was injected, as this was the only time period during these passes in which the control columns reached  $C/C_0 \sim 1$  for the Am.

We did not attempt to model the breakthroughs of the dissolved Am in the column experiments; this has been reserved for future work. It is possible that these breakthroughs represent Am that was adsorbed to colloids that were too small to be removed by centrifugation, not true dissolved Am. If this were the case, then the desorption rate constants of the Am from the colloids would decrease slightly with each column injection because the recovery of this ‘dissolved’ fraction increased with each injection.

The good agreement of the model-deduced Am desorption rate constants for each of the column passes (Table 6-2) suggests that Am adsorption and desorption behavior on the bentonite colloids is well described by a single type of adsorption site on the colloids. If the desorption rate constant had decreased significantly with each pass, then it would be logical to conclude that Am adsorbed to different types of sorption sites on the colloids that had different effective desorption rate constants. Alternatively, a bond-aging process might be implicated in which Am that is adsorbed to colloids for longer times tends to become more strongly associated with the colloids and thus desorbs more slowly over time. Interestingly, the single-site adsorption/desorption behavior deduced from modeling the column experiments is in agreement with the conclusion that a single-site model provided the best description of colloid-facilitated Am transport behavior in a Grimsel Test Site field experiment (see Section 7 of this report).

Huber et al. (2011) conducted batch desorption experiments in a ternary system with Am, bentonite colloids, and FFM. Modeled desorption rates for initial Am concentrations of  $1.4 \times 10^{-9}$  M and  $8.0 \times 10^{-9}$  M adsorbed to the colloids) were  $0.009 \text{ hr}^{-1}$  and  $0.0037 \text{ hr}^{-1}$ , respectively. The higher rate, which corresponds to the initial concentration that is closest to our initial concentration of  $5.5 \times 10^{-10}$  M Am, is about an order of magnitude lower than the rates we estimated in our column experiments (Table 6-2). However, in the experiments of Huber et al. (2011), the solid mass to solution volume ratio was 1g FFM to 4 ml, whereas in our columns we calculate that this ratio was approximately 1 g FFM to 0.3 ml; i.e., about one order of magnitude higher in our experiments. Furthermore, the reported BET surface area of the FFM material used by Huber et al. (2011) was in very good agreement with our FFM surface area measurements. Thus, if the rate constants are normalized to either the FFM mass to solution volume ratio or the FFM surface area to solution volume ratio, the rate constants in the two sets of experiments are in excellent agreement; i.e., around 0.002 to 0.003 ml/g-hr in both sets of experiments.

## 6.4 DISCUSSION

During FY 2014 we have continued to make advances toward our objective of developing experimental methodologies to improve process models of radionuclide transport in nuclear waste repository environments. In this chapter we demonstrated a repeat-injection column method for evaluating and parameterizing colloid-facilitated radionuclide transport, using bentonite colloids, Am, and Grimsel Test Site granodiorite FFM as a model system. The method is designed to better interrogate the slower rates (either colloid filtration rates or radionuclide desorption rates from colloids) that will have the biggest impact in performance assessment calculations over long time and distance scales. The specific insights into Am colloid-facilitated transport in the Grimsel FFM system obtained during this study include:

- For strongly adsorbing radionuclides like Am, it is extremely important to test experimental components and materials for unwanted interactions using careful control experiments. Even with the use of almost entirely Teflon<sup>®</sup> components, control experiments indicated a significant loss of Am to system surfaces other than the FFM, which is important to account for when interpreting results.
- Bentonite colloid breakthroughs in all three repeat column injections were relatively reproducible with nearly complete recoveries, suggesting that there is not a significant fraction of colloids that are highly prone to filtration (which would have been expressed as a significantly lower colloid recovery in the first column). There was also very little release of the colloids once filtered in the FFM, although some release was induced (and a small amount of filtration confirmed) by physically disrupting the columns during the flushing phase of the first pass. The apparent weak interactions between bentonite colloids and FFM surfaces is not surprising, as both the colloids and FFM have a negative surface charge at a pH of 8, and thus electrostatic attachment is not favored after collisions between the colloids and FFM surfaces.
- Am colloid-facilitated transport in the FFM system appears to be governed by the desorption of Am from a single type of binding site on the bentonite colloids. In a series of three sequential column injections, the normalized effluent concentration ( $C/C_0$ ) leveled off at between 0.58 and 0.60 even though the concentration of Am being injected into the column was reduced by 46% and 65%, between the first and second and second and third injections, respectively. These results indicate that the desorption rate constant for Am from the colloids did not change with time, with overall Am concentration, or with the ratio of colloid to Am concentrations.

Although we did not observe different colloid filtration rates or different Am desorption rates in the sequential column injections of this study, we believe that this experimental method has the potential to effectively interrogate slow kinetic processes associated with

colloid-facilitated radionuclide transport. An increase in colloid recoveries in successive column injections would suggest a fraction of colloids that is relatively susceptible to filtration, and the colloids that remain mobile in later injections will have smaller apparent filtration rate constants that are more relevant for use in large-scale performance assessment calculations. Similarly, an increase in colloid-facilitated radionuclide recoveries in successive column injections would suggest multiple types of adsorption sites on colloids with different desorption rates or perhaps bond-aging processes that cause the radionuclide to be more strongly associated with colloids over time. In either case, a smaller desorption rate constant will be observed with each successive column injection, resulting in the interrogation of the stronger radionuclide-colloid interactions that are most relevant to colloid-facilitated transport over long time and distance scales.

## 6.5 REFERENCES

- Geckeis, H., Schäfer, T., Hauser, W., Rabung, Th., Missana, T., Degueldre, C., Möri, A., Eikenberg, J., Fierz, Th., and Alexander, W., 2004. Results of the colloid and radionuclide retention experiment (CCR) at the Grimsel Test Site (GTS), Switzerland – impact of reaction kinetics and speciation on radionuclide migration. *Radiochim. Acta.* **92**, 765-774.
- Huber, F., Kunze, P., Geckeis, H., and Schäfer, T., 2011. Sorption reversibility kinetics in the ternary system radiocnuclide-bentonite colloids/nanoparticles-granite fracture filling material. *Appl. Geochem.* **26**, 2226-2237.
- Iijima, K., Tomura, T., Tobita, M., and Suzuki, Y. 2010. Distribution of Cs and Am in the solution- bentonite colloids-granite ternary system: effect of addition order and sorption reversibility. *Radiochim. Acta* **98**, 729-736.
- Iijima, K., Shoji, Y., and Tomura, T. 2008. Sorption behavior of americium onto bentonite colloid. *Radiochim. Acta* **96**, 721-730.
- Murali, M., and Mathur, J., 2002. Sorption characteristics of Am(III), Sr(II) and Cs(I) on bentonite and granite. *J. Radioanal. Nucl. Ch.* **254**(1) 129-136.
- Penrose, R., Polzer, W., Essington, E., Nelson, D., and Orlandini, K., 1990. Mobility of plutonium and americium through a shallow aquifer in a semiarid region. *Environ. Sci. Technol.* **24**, 228-234.
- Reimus, P. W., Pohll, G., Mihevc, T., Chapman, J., Papelis, L., Lyles, B., Kosinski, S., Niswonger, R., and Sanders, P., 2003. Testing and parameterizing a conceptual model for radionuclide transport in a fractured granite using multiple tracers in a forced-gradient test, *Water Resour. Res.*, **39**(12), 1350, doi:10.1029/2002WR001597.
- Vilks P., and Baik, M. 2001. Laboratory migration experiments with radionuclides and natural colloids in a granite fracture. *J. Contam. Hydrol.* **47**, 197-210.

## **7. EVALUATION OF ALTERNATIVE DESCRIPTIONS OF DESORPTION OF TRI- AND TETRAVALENT SOLUTES FROM BENTONITE COLLOIDS IN TRACER TESTS AT THE GRIMSEL TEST SITE**

### **7.1 INTRODUCTION**

Between 2008 and 2012, four colloid-facilitated transport experiments were conducted in a saturated shear zone in a granodiorite at the Grimsel Test Site (GTS) in Switzerland by the Colloids Formation and Migration (CFM) project. The shear zone, called the MI shear zone, is a planar feature (large conductive fracture) with channelized flow. The CFM project is hosted and led by NAGRA (Swiss Nuclear Waste Cooperative), and it includes participants from Germany, Finland, United Kingdom, Spain, Japan, South Korea, and the United States. The CFM testbed is schematically illustrated in Fig. 7-1. All of the transport experiments discussed in this section were conducted with injections of tracer solutions into borehole/interval CFM 06.002i2 while extracting water from the Pinkel surface packer located at the tunnel wall approximately 6.2 m from the injection interval. The tests included three colloid-homologue tracer tests: 08-01, 10-01 and 10-03, where the first number indicates the year, and the second number indicates the sequential test for that year. These tests were conducted at different Pinkel extraction flow rates and therefore had significantly different transport residence times in the MI shear zone. The homologues included Th(IV), Hf(IV), Eu(III), and Tb(III), which were selected to represent tri- and tetra-valent actinides. The fourth test (12-02) was conducted in 2012 with a colloid-radionuclide injection in the same test configuration, and it included the actinides Pu(IV) and Am(III). This configuration was chosen for all tests because a radionuclide-doped bentonite plug will be inserted into borehole/ interval CFM 06.002i2 in late 2013 or early 2014 and allowed to remain in place for at least two years while collecting flow from the Pinkel surface packer. Thus, the four colloid-facilitated transport tests have provided information on how colloids and radionuclides released as a result of swelling and erosion of the bentonite plug will transport through the shear zone.

Model interpretations of the four colloid-facilitated transport tests were provided in the FY 2013 milestone on UFD international activities (Wang, et al., 2013. Ch. 2). The current chapter focuses on refining the interpretations of the tri- and tetravalent homologue and actinide breakthrough curves in these tests, with emphasis on evaluating alternative descriptions of the desorption process of the solutes from the bentonite colloids and determining which description best explains the test observations. The best description of the desorption process should provide the most accurate upscaled predictions of colloid-facilitated transport. This exercise has relevance to providing better upscaled predictions of colloid-facilitated radionuclide transport in any hydrogeologic setting for the UFD program.

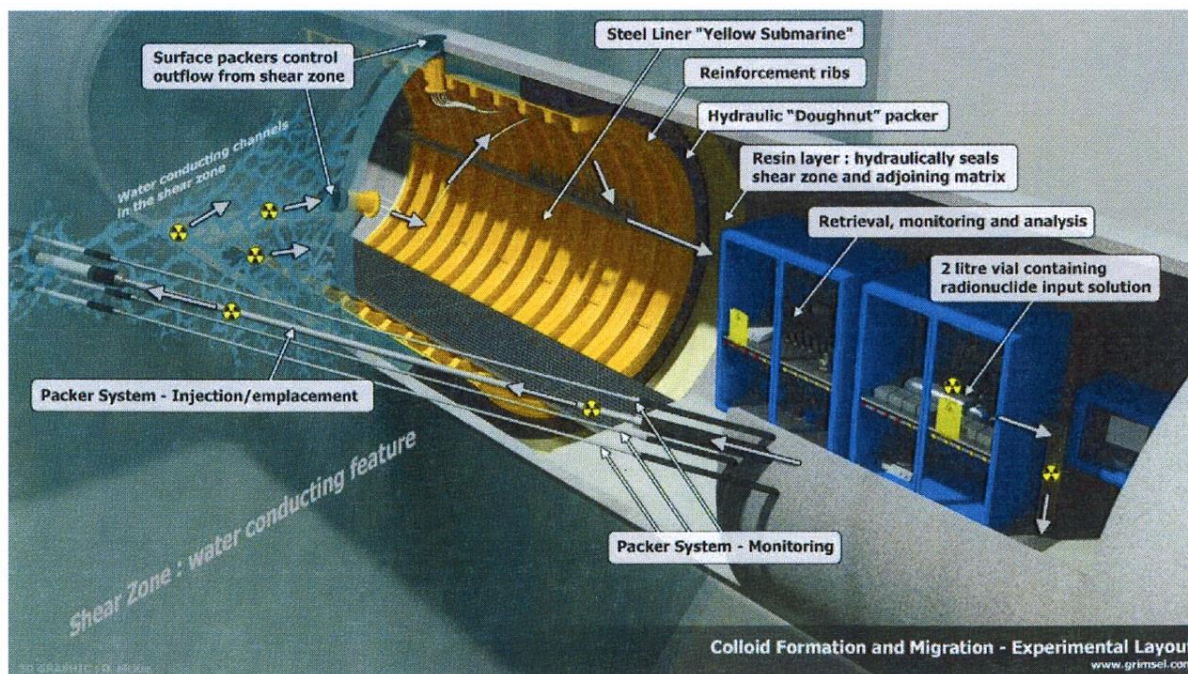


**Figure 7-1.** Schematic illustration of the CFM field test bed

## 7.2 SUMMARY OF CFM COLLOID-FACILITATED TRANSPORT TESTS

Wang et al. (2013), Chapter 2 (FY 2013 UFD progress report on CFM activities) provide a thorough summary of the four colloid-facilitated transport tests conducted at the GTS from 2008 to 2012, so only an abbreviated overview is provided here. The reader is referred to the earlier report for more details.

The experimental parameters and test conditions associated with each of the CFM colloid-facilitated transport experiments are summarized in Table 7-1. Additional information about each experiment can be obtained from the Quick-Look reports issued for the tests (Schäfer et al., 2008; Rosli et al., 2010; Schäfer et al., 2010; Achtziger and Kontar, 2011; Schäfer, 2012; Kontar and Gräfe, 2012). The colloid and solute breakthrough curves in the experiments are presented with the model results in Section 7.4.

For some perspective on the differences between the tests, Figure 7-2 shows the extraction-side normalized conservative tracer breakthrough curves in each test multiplied by their respective dilution factors (extraction flow rate divided by injection flow rate) along with the normalized injection concentration histories for each test. Note that the curves for test 10-03 are corrected an apparent decay of the uranine in the injection loop (Appendix 2-A of Wang et al., 2013). The curves are plotted as a function of volume extracted (instead of time) to facilitate their comparison at the vastly different extraction flow rates. It is apparent from Figure 6-2 that the extraction concentrations very closely follow the injection concentration histories after the extraction

concentrations have peaked, which is a clear indication that the tails of the observed extraction breakthrough curves are dictated by the slow decline in concentrations in the injection loops during the tests. Note that the injection function for test 08-01 was estimated assuming a well-mixed injection interval even though the injection interval in this test was not actively circulated (there were no direct measurements of injection interval concentrations in this test because a conservative dye tracer was not used).

The tracer breakthrough curves corresponding to transport exclusively through the shear zone in each test must be deduced by deconvolving the injection functions from the extraction functions, which is accomplished by matching the extraction functions using an advection-dispersion model while assuming that the injection functions are the observed injection concentration histories. Figure 7-3 shows the shear-zone-only normalized tracer breakthrough curves as a function of volume eluted for each test obtained from this deconvolution process (see Section 7.3 for modeling approach). The breakthrough curves of this figure were calculated assuming that a 1.5-hr tracer pulse was injected directly into the shear zone (to match the 1.5-hr injection during the 08-01 test), with the normalized concentrations being divided by the extraction flow rate of each test to make the areas under the curves the same. The shear-zone mean residence times, Peclet numbers (transport distance divided by longitudinal dispersivity) deduced for each test and used to generate the curves of Figure 7-3 are listed in Table 7-2.

**Table 7-1.** Summary of experimental parameters and test conditions in the CFM colloid-facilitated transport tests

Parameter	Test 08-01	Test 10-01	Test 10-03	Test 12-02
Extraction Flow Rate, mL/min	160-165	48	10	25
Injection Flow Rate, mL/min	10	0.56	0.28	0.33
Injection Interval Volume, mL	4574	2000	3000	3250
Injection Loop Circulation Flow, mL/min	0	45-50	39.5	20
Inj. To Ext. Head Difference, m	0.37-0.675	0.073-0.06	1.16-1.19	0.35
Conservative Tracer Mass Injected, mg	---	5 (Uranine)	9 (Uranine)	3.7 (AGA)
Colloid Mass Injected, mg	15±4.2 (LIBD)	47.2 (LIBD)	~210 (Al)	~220 (Al)
Th(IV) mass injected, µg	19.8±1.3 (97%)	14.9±1.6 (100%)	49.8±0.9 (99%)	---
Hf(IV) mass injected, µg	23.4±1.4 (98%)	12.8±0.6 (99%)	51.6±0.1 (100%)	---
Tb(III) mass injected, µg	14.3±1.2 (89%)	10.2±0.5 (97%)	45.4±1.1 (99%)	---
Eu(III) mass injected, µg	---	12.0±0.4 (95%)	45.5±0.7 (99%)	---
<sup>242</sup> Pu(IV) mass injected, µg	---	---	---	1.6±0.1 (99+%)
<sup>243</sup> Am(III) mass injected, µg	---	---	---	0.035±0.004 (99+%)

AGA – amino-G acid

LIBD – Laser-induced breakdown detection (analytical method for colloids)

Al – Aluminum concentrations measured by ICP-MS used to estimate colloid concentrations

It is apparent from Figure 7-3 that although that the tests were conducted using the same injection and extraction locations, there was considerable variability in tracer transport through the shear zone in the different tests. Even when the injection and extraction flow rates were the same, as in the 08-01 and 08-02 tests, the breakthrough curves were significantly different; the breakthrough curve the 08-01 test in Figure 7-3 exhibits essentially no dispersion in the shear zone (perfect plug flow), whereas the 08-02 test has a significantly later arrival and much more dispersion than 08-01. However, the lack of dispersion deduced in test 08-01 may be an artifact of assuming that the injection interval was well mixed despite the fact that there was no active circulation of the injection loop in this test. The shear zone breakthrough curves for tests 10-01 and 12-02 were the most similar of any pair of tests, even though test 12-02 was conducted after 3 small monitoring boreholes were drilled in the immediate vicinity of CFM06.002i2. Interestingly, these two tests also had similar initial injection flow rates (0.488 vs. 0.556 ml/min) despite the fact that test 10-01 was a passive injection (allowing the tracers to be flushed out of the injection interval by natural flow in the shear zone) and test 12-02 was actively injected by pumping into the injection interval. Test 10-03 also involved a passive injection, whereas Test 08-01 was an active injection.

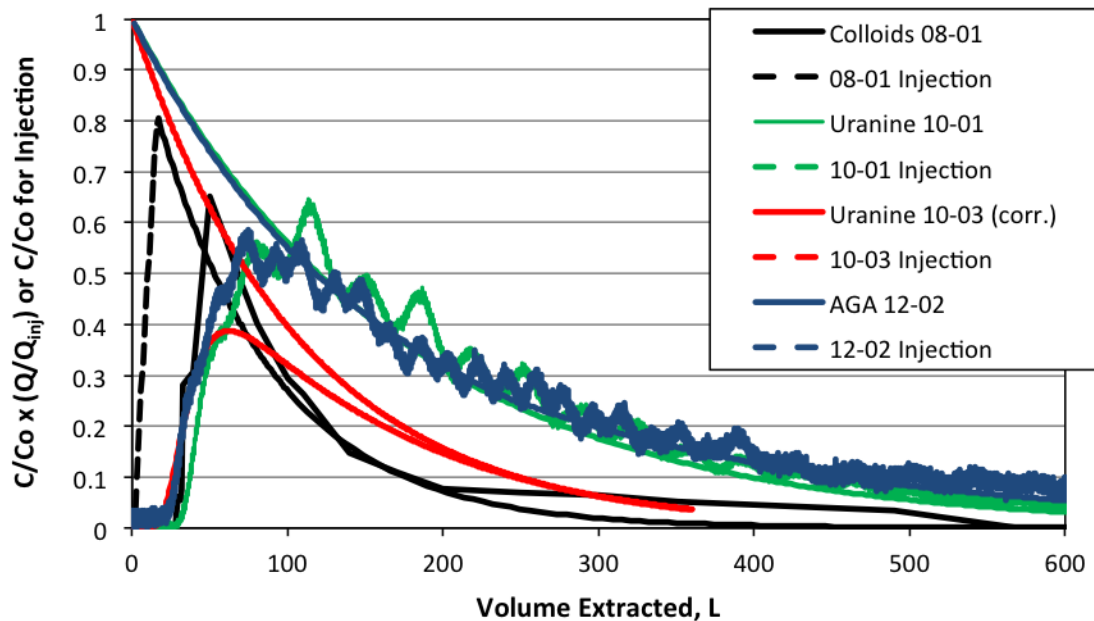


**Figure 7-2.** Normalized extraction and injection concentration histories in each test plotted as a function of volume extracted. Uranine in test 10-03 is corrected for injection loop decay.

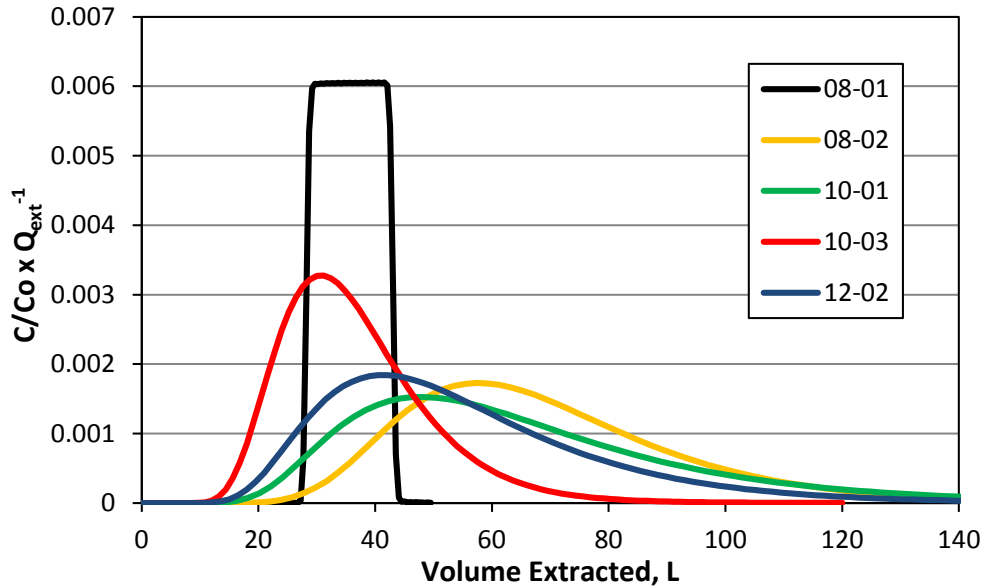


**Figure 7-3.** Deduced shear-zone-only breakthrough curves in each test

**Table 7-2.** Mean residence times and Peclet numbers in shear zone for curves of Figure 7-3

Parameter	Test 08-01	Test 08-02	Test 10-01	Test 10-03	Test 12-02
Mean Residence Time, hr	3.6	6.25 13.5	22	60	34 6.5
Peclet number	10000		9	17	

### 7.3 INTERPRETIVE MODELING APPROACH

Wang et al. (2013), Chapter 2 (FY 2013 UFD progress report on CFM activities) provide a thorough description of the interpretive modeling approach for the CFM colloid-

facilitated transport tests, and much of this is reiterated here for completeness, with emphasis on refinements to the model and the approach.

### 7.3.1 Description of Model and Interpretive Procedure

The first step in interpretation procedure for each test was to estimate the injection flow rate into the shear zone by plotting the log of the conservative tracer concentration in the injection loop vs. time and fitting a straight line to the data. The slope of this line is equal to  $-Q/V$ , where  $Q$  is the flow rate (mL/min) out of the interval and  $V$  is the known injection interval volume (mL). In cases where the slope changed during a test, different line segments were fitted to different portions of the data. Examples are provided in Appendix 2-A of Wang et al. (2013), which documents the corrections for uranine decay in the injection loop in test 10-03. For test 08-01, a conservative tracer was not used, so an injection flow rate of 10 mL/min was assumed because the flow rate was controlled by a pump and measured in this test. The injection function for each test was taken to be  $C = C_0 \exp(-Qt/V)$ , where  $C_0$  = initial concentration in injection loop, and  $t$  = time.

The RELAP (REactive transport LAPlace transform) model (Reimus et al., 2003) was then used to fit the conservative tracer extraction breakthrough curves by adjusting the mean residence time and Peclet number in the shear zone (Peclet number is transport distance divided by longitudinal dispersivity) as well as the fractional tracer mass participation in each test. The exponentially-decaying injection functions were directly input into RELAP to conduct these analyses. RELAP is a semi-analytical model that uses a Fourier transform inversion method to solve the Laplace-domain transport equations in either a single- or a dual-porosity system. The model can account for diffusion between fractures and matrix, as well as linear, first-order reactions in both fractures and matrix. The very rapid execution of the model makes it ideal for the numerous simulations needed for transport parameter estimation. The fractional mass participation in each test was allowed to be an adjustable parameter because some of the tests did not have complete tracer recovery, indicating that some of the tracer mass drifted out of the hydraulic capture zone induced by extraction at the Pinkel surface packer at the tunnel wall. A matrix porosity of 0.02 that extended 1 cm into the matrix from the fracture wall(s) was assumed in the shear zone for all test interpretations (the matrix was assumed to have a porosity of zero at distances greater than 1 cm from the fracture walls), and a solute matrix diffusion coefficient of  $1 \times 10^{-6}$  cm<sup>2</sup>/sec was also assumed in all interpretations. Also, a fracture aperture of 2 mm was assumed in all test interpretations. The mean residence time, Peclet number and fractional mass participation estimated for the conservative tracers using these matrix diffusion parameters were not significantly different from estimates obtained assuming no matrix diffusion.

In addition to providing estimates of shear-zone transport parameters for the conservative tracers, RELAP was also used to estimate colloid transport parameters (filtration and resuspension rate constants). These estimates were obtained by assuming that the mean residence time, Peclet number and fractional mass participation estimated for the

conservative tracers also applied to the colloids, and then the filtration rate parameters were adjusted to fit the colloid data.

The resulting best-fitting parameters from RELAP were used as initial parameter estimates in a 2-D numerical model that could account for processes that RELAP does not explicitly account for. The most important of these processes were the variable injection flow rates observed in test 12-02 and the simultaneous transport of colloids and reactive solutes in all the tests (RELAP does not account for interacting species). In effect, RELAP was used to obtain initial estimates for the more robust numerical model. This procedure was found to be highly effective for refinement of parameter estimates; only relatively minor adjustments to the RELAP-estimated parameters were necessary, and these adjustments could be made rather quickly by hand. The mean residence times and Peclet numbers of the shear zone listed in Table 7-2 were obtained using this refinement procedure.

The 2-D numerical model simultaneously solves the following equations:

Colloid Transport in Fractures:

$$\text{Mobile: } \frac{\partial C_{col}}{\partial t} + v_f \frac{\partial C_{col}}{\partial x} - D_c \frac{\partial^2 C_{col}}{\partial x^2} + k_{fc} C_{col} - k_{rc} S_{col} + k_{fci} C_{col} - P_{col} = 0 \quad (7-1)$$

$$\text{Immobile: } \frac{\partial S_{col}}{\partial t} - k_{fc} C_{col} + k_{rc} S_{col} - k_{fci} C_{col} = 0 \quad (6-2)$$

Solute Transport in Fractures:

$$\begin{aligned} & \frac{\partial C}{\partial t} + v_f \frac{\partial C}{\partial x} - D_f \frac{\partial^2 C}{\partial x^2} + k_{1f} C C_{col} \left(1 - \frac{C_1}{C_{col} S_1^0}\right) + k_{2f} C C_{col} \left(1 - \frac{C_2}{C_{col} S_2^0}\right) + \\ & \left(\frac{\rho_f}{\eta}\right) k_{fa} C \left(1 - \frac{S_a}{S_a^0}\right) + \left(\frac{\rho_f}{\eta}\right) k_{fb} C \left(1 - \frac{S_b}{S_b^0}\right) + k_{1f} C S_{col} \left(1 - \frac{C_{filt,1}}{S_{col} S_1^0}\right) + k_{2f} C S_{col} \left(1 - \frac{C_{filt,2}}{S_{col} S_2^0}\right) - \\ & k_{1b} C_1 - k_{2r} C_2 - k_{1b} C_{filt,1} - k_{2r} C_{filt,2} - \left(\frac{\rho_f}{\eta}\right) k_{ra} S_a - \left(\frac{\rho_f}{\eta}\right) k_{rb} S_b - \frac{\phi D_m}{b} \frac{\partial C_m}{\partial y} \Big|_{y=b} = 0 \end{aligned} \quad (7-3)$$

Solute Transport on mobile colloids (in fractures) while adsorbed to colloid sites 1 and 2:

$$\begin{aligned} & \frac{\partial C_1}{\partial t} + v_f \frac{\partial C_1}{\partial x} - D_c \frac{\partial^2 C_1}{\partial x^2} - k_{1f} C C_{col} \left(1 - \frac{C_1}{C_{col} S_1^0}\right) - k_{rc} C_{filt,1} + \\ & k_{1r} C_1 + k_{fc} C_1 - P_{col} S_a = 0 \end{aligned} \quad (7-4)$$

$$\begin{aligned} & \frac{\partial C_2}{\partial t} + v_f \frac{\partial C_2}{\partial x} - D_c \frac{\partial^2 C_2}{\partial x^2} - k_{2f} C C_{col} \left(1 - \frac{C_2}{C_{col} S_2^0}\right) - k_{rc} C_{filt,2} + \\ & k_{2r} C_2 + k_{fc} C_2 - P_{col} S_b = 0 \end{aligned} \quad (7-5)$$

Solute Transport in Matrix:

$$\frac{\partial C_m}{\partial t} - D_m \frac{\partial^2 C_m}{\partial y^2} + \left( \frac{\rho_b}{\phi} \right) k_{fam} C_m \left( 1 - \frac{S_{am}}{S_{am}^0} \right) + \left( \frac{\rho_b}{\phi} \right) k_{fbm} C_m \left( 1 - \frac{S_{bm}}{S_{bm}^0} \right) - \left( \frac{\rho_b}{\phi} \right) k_{ram} S_{am} - \left( \frac{\rho_b}{\phi} \right) k_{rbm} S_{bm} = 0 \quad (7-6)$$

Immobile Solute in Fractures (sorption sites a and b):

$$\frac{\partial S_a}{\partial t} - k_{fa} C \left( 1 - \frac{S_a}{S_a^0} \right) + k_{ra} S_a = 0 \quad (7-7)$$

$$\frac{\partial S_b}{\partial t} - k_{fb} C \left( 1 - \frac{S_b}{S_b^0} \right) + k_{rb} S_b = 0 \quad (7-8)$$

Immobile Solute in Matrix (sorption sites a<sub>m</sub> and b<sub>m</sub>):

$$\frac{\partial S_{am}}{\partial t} - k_{fam} C \left( 1 - \frac{S_{am}}{S_{am}^0} \right) + k_{ram} S_{am} = 0 \quad (7-9)$$

$$\frac{\partial S_{bm}}{\partial t} - k_{fbm} C \left( 1 - \frac{S_{bm}}{S_{bm}^0} \right) + k_{rbm} S_{bm} = 0 \quad (7-10)$$

Immobile Solute adsorbed onto Immobile Colloids in Fractures (colloid sites 1 and 2):

$$\frac{\partial C_{filt,1}}{\partial t} - k_{1f} C S_{col} \left( 1 - \frac{C_{filt,1}}{S_{col} S_1^0} \right) - (k_{fc} + k_{fci}) C_1 + k_{rc} C_{filt,1} + k_{1r} C_{filt,1} = 0 \quad (7-11)$$

$$\frac{\partial C_{filt,2}}{\partial t} - k_{2f} C S_{col} \left( 1 - \frac{C_{filt,2}}{S_{col} S_2^0} \right) - (k_{fc} + k_{fci}) C_2 + k_{rc} C_{filt,2} + k_{2r} C_{filt,2} = 0 \quad (7-12)$$

where,  $C_{col}$  = concentration of colloids in solute phase, g/cm<sup>3</sup>

$S_{col}$  = colloid concentration on fracture surfaces, g/cm<sup>3</sup>

$C$  = solution concentration of solute in fractures, g/cm<sup>3</sup>

$C_m$  = solution concentration of solute in matrix, g/cm<sup>3</sup>

$S_a$  = sorbed concentration of solute on fracture surface site  $a$ , g/g

$S_b$  = sorbed concentration of solute on fracture surface site  $b$ , g/g

$C_1$  = concentration of solute sorbed to site 1 on mobile colloids, g/cm<sup>3</sup>

$C_2$  = concentration of solute sorbed to site 2 on mobile colloids, g/cm<sup>3</sup>

$C_{filt,1}$  = concentration of solute sorbed to site 1 on immobile colloids, g/cm<sup>3</sup>

$C_{filt,2}$  = concentration of solute sorbed to site 2 on immobile colloids, g/cm<sup>3</sup>  
 $S_{am}$  = sorbed concentration of solute on matrix surface site  $a_m$ , g/g  
 $S_{bm}$  = sorbed concentration of solute on fracture surface site  $b_m$ , g/g  
 $P_{col}$  = colloid production rate in fractures, g/cm<sup>3</sup>-hr  
 $v_f$  = fluid velocity in fractures, cm/hr  
 $D_f$  = solute dispersion coefficient in fractures, cm<sup>2</sup>/hr  
 $D_c$  = colloid dispersion coefficient in fractures, cm<sup>2</sup>/hr  
 $D_m$  = solute molecular diffusion coefficient in matrix, cm<sup>2</sup>/hr  
 $\rho_f$  = effective bulk density within fractures, g/cm<sup>3</sup>  
 $\rho_B$  = bulk density in matrix, g/cm<sup>3</sup>.  
 $\eta$  = porosity within fractures  
 $\phi$  = matrix porosity  
 $b$  = fracture half aperture, cm  
 $k_{fc}$  = colloid filtration rate constant (1/s) =  $\lambda v_f$ , where  $\lambda$  = filtration coefficient (1/cm)  
 $k_{rc}$  = reverse colloid filtration (detachment) rate constant, 1/hr  
 $k_{fci}$  = irreversible colloid filtration rate constant, 1/hr  
 $k_{fa}$  = rate constant for sorption of solute onto fracture surface site  $a$ , ml/g-hr  
 $k_{ra}$  = rate constant for desorption of solute from fracture surface site  $a$ , 1/hr  
 $k_{fb}$  = rate constant for sorption of solute onto fracture surface site  $b$ , ml/g-hr  
 $k_{rb}$  = rate constant for desorption of solute from fracture surface site  $b$ , 1/hr  
 $k_{fam}$  = rate constant for sorption of solute onto matrix surface site  $a_m$ , ml/g-hr  
 $k_{ram}$  = rate constant for desorption of solute from matrix surface site  $a_m$ , 1/hr  
 $k_{fbm}$  = rate constant for sorption of solute onto matrix surface site  $b_m$ , ml/g-hr  
 $k_{rbm}$  = rate constant for desorption of solute from matrix surface site  $b_m$ , 1/hr  
 $k_{1f}$  = rate constant for sorption of solute onto colloid surface site 1, ml/g-hr  
 $k_{1r}$  = rate constant for desorption of solute from colloid surface site 1, 1/hr

$k_{2f}$  = rate constant for sorption of solute onto colloid surface site 2, ml/g-hr

$k_{2r}$  = rate constant for desorption of solute from colloid surface site 2, 1/hr

$S_1^0$  = maximum solute capacity on colloid sorption site 1, g/g colloid

$S_2^0$  = maximum solute capacity on colloid sorption site 2, g/g colloid

$S_a^0$  = maximum solute capacity on fracture sorption site  $a$ , g/g solid

$S_b^0$  = maximum solute capacity on fracture sorption site  $b$ , g/g solid

$S_{am}^0$  = maximum solute capacity on matrix sorption site  $a_m$ , g/g solid

$S_{bm}^0$  = maximum solute capacity on matrix sorption site  $b_m$ , g/g solid

Figure 7-4 shows the system geometry and boundary conditions assumed in the numerical model. The parallel-plate fracture domain is one node wide, implying that concentration gradients across the fracture aperture are rapidly leveled by diffusion and/or advective mixing. Solute diffusion between fractures and matrix is assumed to be perpendicular to the fracture flow direction. The matrix nodes can be specified to have variable spacing with different porosities and different solute diffusion coefficients as a function of distance away from the fracture wall. Thus, fracture coatings or gradients in porosity or diffusion coefficients can be simulated. The above equations and the geometry of Figure 7-4 also apply to RELAP, although simplifications are necessary to use the RELAP semi-analytical solution method (Reimus et al., 2003).

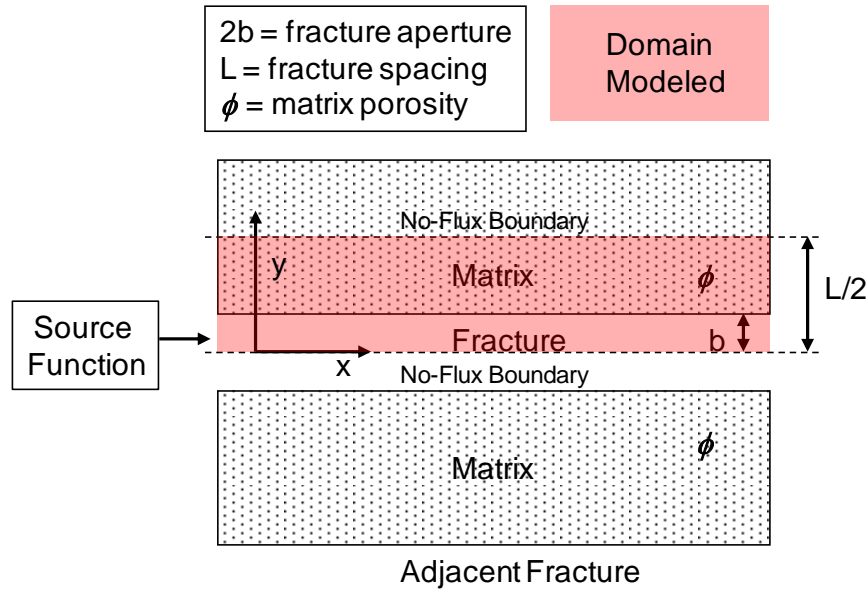


**Figure 7-4.** System geometry and boundary conditions assumed in the numerical model (also applies to the RELAP model).

### 7.3.2 Refinements to Evaluate Solute Desorption Processes from Colloids

It was found in FY 2013 that once appropriate mean residence times, Peclet numbers and fractional mass participations were determined for the conservative tracer breakthrough curves in each test, and filtration parameters were determined for the colloids, the model fits to the colloid-facilitated solute breakthrough curves were sensitive mainly to the desorption rate constants of the solutes from the colloids. The best fits to the tri- and tetravalent solute data were obtained when (1) the rate constants for solute adsorption to the shear zone surfaces were large enough that the solutes rapidly adsorbed to these surfaces after they desorbed from the colloids and (2) the rate constants for solute desorption from the shear zone surfaces were small enough that the solutes effectively did not desorb from these surfaces for the remainder of the tests. Under these conditions, the shear zone surfaces act as a fast and irreversible sink once desorption from colloids occurs. The strong dependence on the solute desorption rates from the colloids is also due in part to the nearly complete adsorption of the tri- and tetravalent solutes to the bentonite colloids in the injection cocktails.

Because the tri- and tetravalent solute desorption process from colloids is so important, the model presented in Section 7.3.1 was modified somewhat to provide some alternative descriptions of the solute associations with the colloids and hence of the desorption process. The following modifications were implemented:

- 1) The solute mass initially adsorbed to the colloids could be distributed between the two adsorption sites on the colloids in any specified ratio, which effectively adds one adjustable parameter to the model; i.e., the fraction on the first site (with one

minus the fraction on the first site being assigned to the second site). This feature of the model was actually in place in FY 2013, but it was not used then because only one site was assumed on the colloids in FY 2013.

- 2) An “bond-aging” reaction can be simulated on the colloid surfaces. This reaction involves a simple first-order conversion of sorbed solute from site 1 to site 2 on colloid surfaces. The reaction occurs whether solutes are adsorbed to colloids in the injection loop prior to entering the shear zone or are in the shear zone (and either on mobile or immobile colloids). The aging reaction is effectively captured through the addition of two ordinary differential equations that are solved simultaneously with equations (7-1)-(7-12):

3)

$$\frac{\partial C_1}{\partial t} = -\frac{\partial C_2}{\partial t} = -k_{age} C_1 \quad (7-13)$$

$$\frac{\partial C_{filt,1}}{\partial t} = -\frac{\partial C_{filt,2}}{\partial t} = -k_{age} C_{filt,1} \quad (7-14)$$

where  $k_{age}$  is the aging rate constant ( $\text{hr}^{-1}$ ) (another adjustable parameter).

The aging reaction is considered to be irreversible.

- 4) An alternative aging process, suggested by CFM project participants, can be specified in which there is only a single adsorption site on colloids, but the desorption rate constant for this site decays with time according to:
- 5)

$$k_{1r}(t) = k_{1r,0} e^{-t/A} \quad (7-15)$$

where  $k_{1r,0}$  is the initial rate constant ( $\text{hr}^{-1}$ ), and  $A$  (hr) is a time constant for the decay process. This introduces two additional adjustable parameters to the model.

The two alternative bond-aging representations cannot be implemented together. It can be shown that the second representation (equation 7-15) can be quite well mimicked by the first representation if the desorption rate constant of the second site is set equal to zero in the first representation. However, the second representation cannot mimic the first when the desorption rate constant of the second site is nonzero or when a fraction of the sorbed solute is initially assigned to the second site. Equation (7-15) also has the disadvantage of being less mechanistic than equations (7-13) and (7-14) in that it implies a continuum of different types of sites with a continuum of desorption rate constants.

Table 7-3 summarizes the different descriptions of the solute desorption process from colloids that were considered when attempting to fit the tri- and tetravalent solute breakthrough curves in the colloid-facilitated transport tests. The 2-site hybrid model involves a combination of (7-1) and (7-2) above, where aging from site 1 to site 2 is allowed, but there is also the ability to specify the fraction of solute associated with each site initially. Only the one-site model with no aging or decay was considered in the FY 2013 interpretive modeling efforts.

**Table 7-3.** Different descriptions of the solute desorption process from colloids used for interpreting the tri- and tetravalent solute breakthrough curves

Model Name	Adjustable Parameters	Comments
1-site	$k_{1r}$	
1-site exp decay	$k_{1r,0}, A$	See eq. 15
Aging to 2 <sup>nd</sup> site	$k_{1r}, k_{2r}, k_{age}$	Only 2 adjustable parameters if $k_{2r} = 0$
2-site, no aging	$f(1), k_{1r}, k_{2r}$	Only 2 adjustable parameters if $k_{2r} = 0$
2-site hybrid	$f(1), k_{1r}, k_{2r}, k_{age}$	Only 3 adjustable parameters if $k_{2r} = 0$

Note:  $f(1)$  = fraction of adsorbed solute mass initially adsorbed to first site ( $f(2) = 1 - f(1)$ ).

### 7.3.3 Process for Selecting the Best Description of Desorption from Colloids

Each of the variants listed in Table 6-3 was evaluated for its ability to fit the tri- or tetravalent solute breakthrough curves in each of the CFM colloid-facilitated transport tests. The procedure for determining which variant best described the desorption process was as follows:

- (1) Each model variant was fitted to a given data set by minimizing the sum of squares differences between the model and data (i.e., the residual sum of squares). The best fits were obtained by manual adjustment of the parameters, as an automated parameter estimation algorithm was not successfully interfaced with the model during the time available to complete this report. However, it was not apparent that an automated algorithm would have helped significantly in any cases except where there were four adjustable parameters (only the 2-site hybrid model) because the parameter space was quite thoroughly interrogated for all cases of up to three adjustable parameters. The response surface for the 4-parameter hybrid model was quite complex, so there was less confidence in manually finding a global minimum with this model.
- (2) For variants with the same number of adjustable parameters, the one with the lowest residual sum of squares value was taken to be the best-fitting model.
- (3) For variants with different number of adjustable parameters, a  $F$  (Fisher-Snedecor) statistic was calculated as follows:

$$F(1:2) = \frac{(SS_1 - SS_2)/(df_1 - df_2)}{SS_2/df_2} \quad (7-16)$$

where  $F(1:2) = F$  statistic for evaluating improvement in fit offered by model 2 over model 1, where model 2 has more adjustable parameters than model 1.

$SS_x$  = sum of squares of residual differences between model x and data

$df_x$  = degrees of freedom for model x (number of data points minus number of adjustable parameters used to fit data)

- (4) The  $F$  statistic of equation (7-16) was compared to an  $F$  value taken from a standard  $F$ -distribution table (e.g., Draper and Smith, 1981) to determine whether model 2 offers a *statistically significant* improvement over model 1 in explaining the data. The tabulated  $F$  values depend on (1) the difference in the degrees of freedom between the two models, (2) the number of the degrees of freedom of the model with more parameters, and (3) the confidence level of the  $F$  test. As an example, if a model with 2 parameters is compared to a model with 3 parameters for a data set that contains 25 data points, and one wants to be confident at the 95% level that the 3-parameter model is better than the 2-parameter model, then the appropriate  $F$ -distribution value is  $F(1,22,0.05)$ , where  $0.05 = 1 - 0.95$ .
- (5) If the  $F$  statistic calculated from equation (7-16) was greater than the appropriate tabulated  $F$ -distribution value for a 95% level of confidence, then the model with more parameters was accepted as being a *statistically significant improvement* over the model with less parameters at this confidence level.

We note that the fitting procedure did not involve any transformations or weighting of the colloid or homologue breakthrough curve data sets. Somewhat different results would have likely been obtained had the data been transformed or weighted in some way. A logarithmic transformation is often used to avoid biasing fits toward the data points with the largest numerical values (i.e., the peak concentrations), but we chose not to use a log transformation because (1) the highest concentrations also tend to have the least amount of uncertainty from analytical error, so it is somewhat justified to allow the fits to be biased slightly toward the high-concentration points, and (2) concentrations of zero were considered significant, especially in the tails of the breakthrough curves, and zeroes cannot be log-transformed unless they are set to a minimum value like a detection or quantification limit. For Run 08-01, we also excluded the early data points (all points before the peaks) from the fitting procedure because of the very rapid rise in the colloid and solute concentrations in this test. These rapid rises caused very large sum-of-squares differences between the models and data for a few of the early points, and it was quite apparent that the best fits were being heavily biased by these points at the expense of much poorer fits to the peaks and tails of the breakthrough curves. It was considered more important for explaining solute desorption behavior to obtain better fits to the peaks and tails than to fit the sharp early rise of the breakthrough curves.

## 7.4 INTERPRETIVE MODELING RESULTS

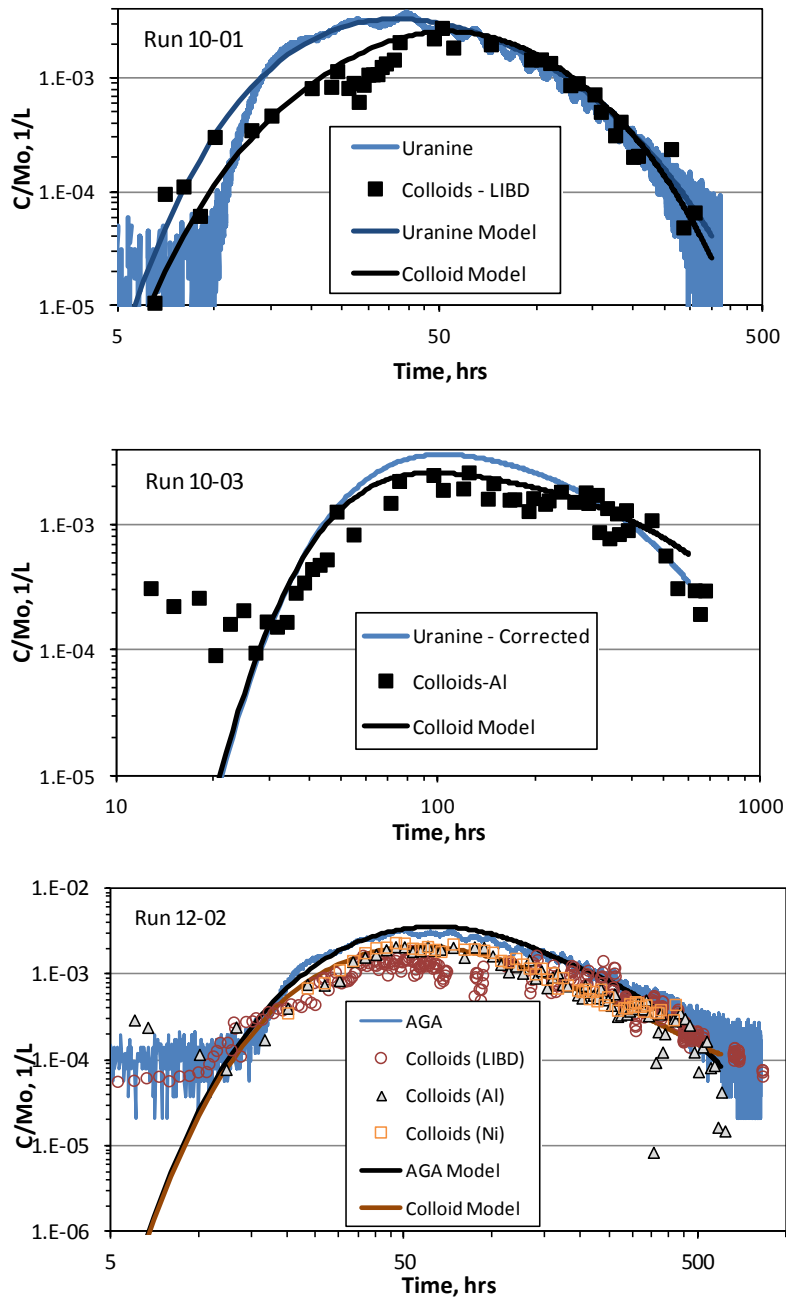
Table 7-2 (Section 7.2) lists the best-fitting mean residence times and Peclet numbers obtained by fitting the conservative tracer breakthrough curves with the RELAP model (and refined with the numerical model). The fractional mass participations deduced for each test were 1.0 for test 08-01, 0.9 for test 10-01, 0.6 for test 10-03 (estimated after correcting for the uranine decay in the injection loop), and 0.99 for test 12-02. The parameter estimates for tests 08-01 and 12-02 in Table 7-2 are slightly different than the estimates reported in FY 2013 (Wang et al., 2013, Ch. 2) because of some minor differences in the way the breakthrough curves were fitted for these tests.

Table 7-4 lists the colloid transport parameters providing the best fits to the colloid breakthrough curves in each test, and the best-fitting model curves for both the conservative dye tracer and the colloids in Runs 10-01, 10-03 and 12-02 are shown in Figure 7-5 (Run 08-01 is not shown because there was no conservative tracer, but a colloid model curve for 08-01 is shown in Figure 6-6). In Run 08-01, a single irreversible filtration rate constant provided a good fit to the colloid data, whereas in Runs 10-03 and 12-02, a reversible reaction describing colloid filtration and detachment provided a better match to the colloid data. In Run 10-01, the best fit was obtained by assuming both an irreversible and a reversible colloid filtration reaction were occurring simultaneously. The reversible processes are invoked either to (1) account for a delay in the initial arrival of colloids relative to the conservative tracer (Run 10-01) or (2) provide an improved fit to the tail of the colloid breakthrough curve by allowing for some colloid detachment (10-03 and 12-02).

**Table 7-4.** Colloid transport parameter estimates in the CFM tracer tests.

<b>Test</b>	$k_{fci} \text{ hr}^{-1}$	$k_{fc} \text{ hr}^{-1}$	$k_{rc} \text{ hr}^{-1}$
08-01	0 (0.015)*	0	0
10-01	0.0065	0.2	0.286
10-03	0	0.01	0.0042
12-02	0	0.016	0.0005

\*Number in parentheses is best estimate of  $k_{fci}$  in Run 08-01 if the raw colloid data are fitted (i.e., not forcing the colloid concentrations to exceed the homologue concentrations). If it is assumed that the colloid concentrations must exceed the homologue concentrations (which is logical), then the best estimate of  $k_{fci}$  is zero.



**Figure 7-5.** Simulated and experimental breakthrough curves for the conservative dye tracers and colloids in CFM Runs 10-01, 10-03 and 12-02. Best-estimate parameters are listed in Tables 6-2 (conservative tracers) and 6-4 (colloids). Three colloid breakthrough curves are shown for Run 12-02 because three analytical methods were used to quantify the colloid concentrations.

The reasons for the differences in the deduced filtration processes in the different tests are unknown. They may reflect the different flow pathways accessed in the different tests, which are evident from Figure 7-3, or perhaps they are influenced by the different flow rates and residence times in the different tests. It should be pointed out that there is more uncertainty in the colloid transport parameters estimated for Run 10-03 than for the other tests because they were obtained by comparing the colloid breakthrough curve to a *corrected* uranine breakthrough curve (shown in Figure 7-5), which had greater inherent uncertainty than the conservative dye tracer breakthrough curves in the other tests. Nonetheless, the forward filtration rate constants in all tests are in relatively good agreement (ignoring the rapid forward rate constant for the reversible reaction deduced for Run 10-01), varying between  $0.0065 \text{ hr}^{-1}$  and  $0.015 \text{ hr}^{-1}$ , which is a range of less than a factor of 2.5. However, to model the colloid-facilitated transport of the homologues in Run 08-01, it was necessary to assume no filtration at all of the colloids because the normalized breakthrough curves of both Th and Hf were higher than that of the colloids in that test, which was considered impossible. The estimate of  $0.015 \text{ hr}^{-1}$  mentioned above and listed in parentheses in Table 7-4 for Run 08-01 was obtained by matching the colloid recovery, which, based on the raw colloid data, was less than 100%.

Table 7-5 lists the best-fitting desorption rate parameters associated with several of the model variants of Table 6-3 for the four CFM tracer tests. In some cases, models with more parameters offered no improvement over models with less parameters; i.e., the fits converged to a rate or decay constant of zero, or to no initial adsorption to a second site, which effectively reduced them to a simpler model. Models offering no improvement over simpler models are not listed in Table 7-5. Run 08-01 provides a good example of this situation, where the one-site model was not improved on by any of the more complex models for any of the homologues. In fact, if the modeled colloid breakthrough curve was not artificially adjusted to be slightly higher than the Th and Hf breakthrough curves in this test, the best fits to these curves would have had no desorption at all. Figs. 7-6 through 7-9 show the best-fitting model curves for each of the tri- and tetravalent solutes in each test, respectively. The dashed lines in these figures are the best-fitting single-site model curves in cases where a single-site model did not provide the best fit to the breakthrough curves.

The sums of squares of the residual differences between the models and the breakthrough curves associated with each of the models and corresponding parameter sets listed in Table 7-5 are listed in Table 7-6. Listed next to each residual sum of squares value is the *F* statistic calculated using equation (7-16) and the appropriate tabulated *F* value to which the *F* statistic is compared to make a determination of whether the model with more parameters offers a statistically better fit than the model with less parameters (i.e., provides a better description of the solute desorption process). A discussion of the implications of these model results is provided in Section 7.5

**Table 7-5.** Best-fitting solute desorption parameters for selected model variants.

Run/Solute	Model	$k_{r1}$	$k_{r2}$	$f(1)$	$k_{age}$	$k_{r1,0}$	$A, hr$
08-01/Th	1-site	0.0136					
08-01/Hf	1-site	0.081					
08-01/Tb	1-site	0.192					
	Aging to 2 <sup>nd</sup> site	0.17	0.9		0.016		
10-01/Th	1-site	0.0253					
	Aging to 2 <sup>nd</sup> site	0.0176	0.12		0.0058		
	2-site, hybrid	0.015	0.12	0.979	0.0073		
10-01/Hf	1-site	0.0368					
	2-site, no aging	0.0403	0	0.949			
10-01/Tb	1-site	0.074					
	Aging to 2 <sup>nd</sup> site	0.06	0.2		0.0096		
	2-site, hybrid	0.0585	0.2	0.972	0.00955		
10-01/Eu	1-site	0.086					
	1-site exp decay					0.0935	350
	Aging to 2 <sup>nd</sup> site	0.092	0		0.00078		
	2-site, no aging	0.139	0.107	0.893			
10-03/Th	1-site	0.003					
	1-site exp decay					0.026	53
	Aging to 2 <sup>nd</sup> site	0.029	0		0.016		
	2-site, no aging	0.3	0	0.24			
	2-site, hybrid	0.03	0	0.731	0.0101		
10-03/Hf	1-site	0.0021					
	1-site exp decay					0.0185	54
	Aging to 2 <sup>nd</sup> site	0.0215	0		0.0155		
	2-site, no aging	0.3	0	0.192			

	2-site, hybrid	0.03	0	0.743	0.0139		
10-03/Tb	1-site	0.0415				0.052	480
	1-site exp decay						
	Aging to 2 <sup>nd</sup> site	0.051	0		0.00045		
	2-site, no aging	0.4	0	0.88			
10-03/Eu	1-site	0.026				0.0405	260
	1-site exp decay						
	Aging to 2 <sup>nd</sup> site	0.0382	0		0.00124		
	2-site, no aging	0.18	0	0.76			
	2-site, hybrid	0.0545	0	0.874	0.00068		
12-02/Am	1-site	0.0163					
12-02/Pu	1-site	0.0077					
	Aging to 2 <sup>nd</sup> site	0.0045	0.052		0.002		
	2-site, hybrid	0.0016	0.052	0.898	0.0024		

Note: Red text indicates model best explaining the data set (see Table 6-6).

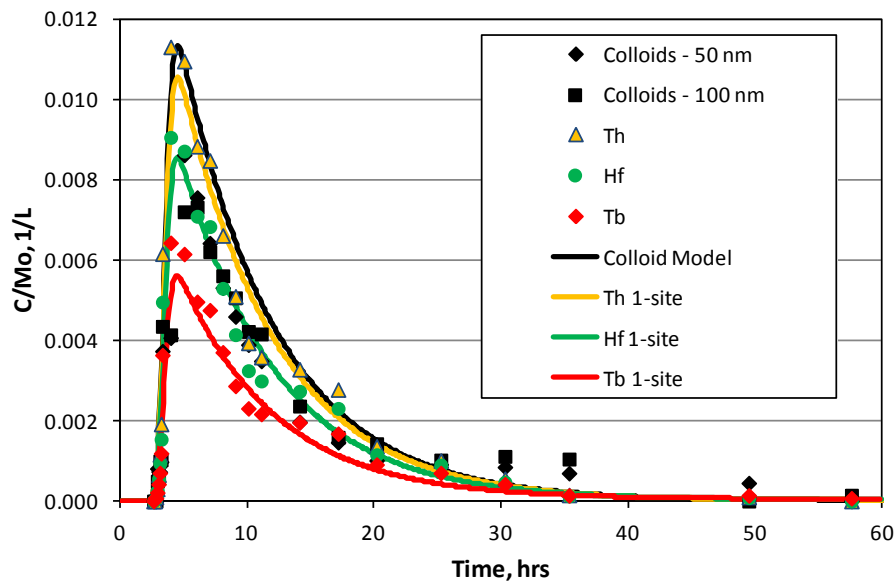


**Figure 7-6.** Simulated and experimental breakthrough curves for the colloids and homologues in CFM Run 08-01. Best estimate parameters are listed in Table 7-5.

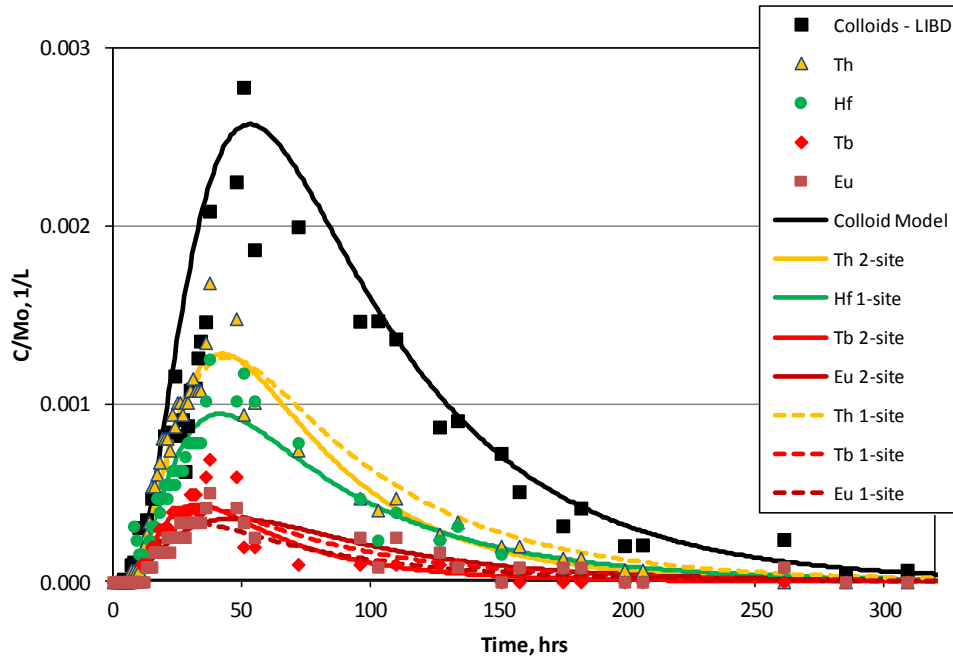


**Figure 7-7.** Simulated and experimental breakthrough curves for the colloids and homologues in CFM Run 10-01. Best estimate parameters are listed in Table 7-5.

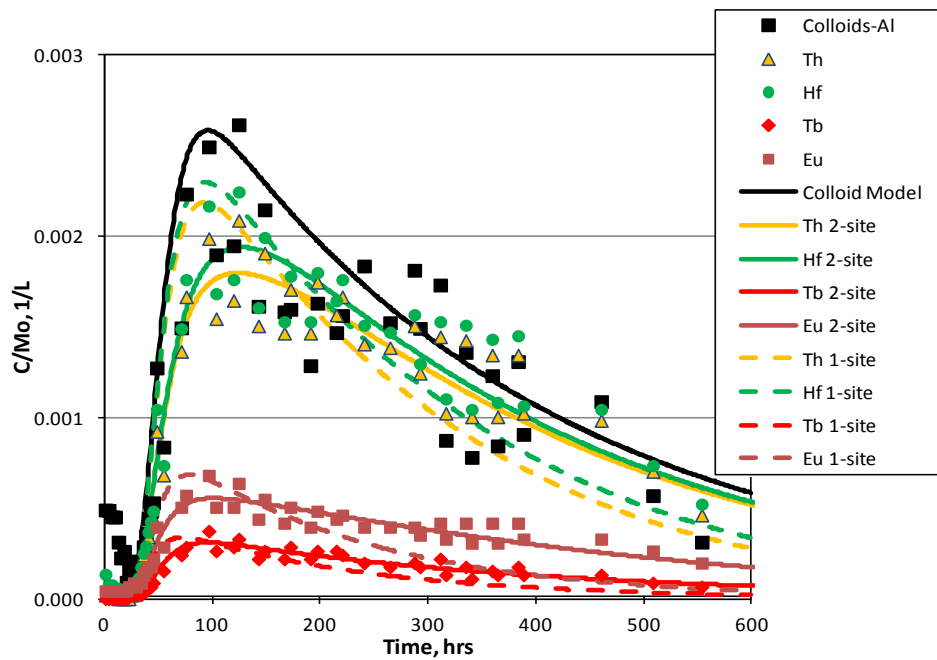


**Figure 7-8.** Simulated and experimental breakthrough curves for the colloids and homologues in CFM Run 10-03. Best estimate parameters are listed in Table 7-5.

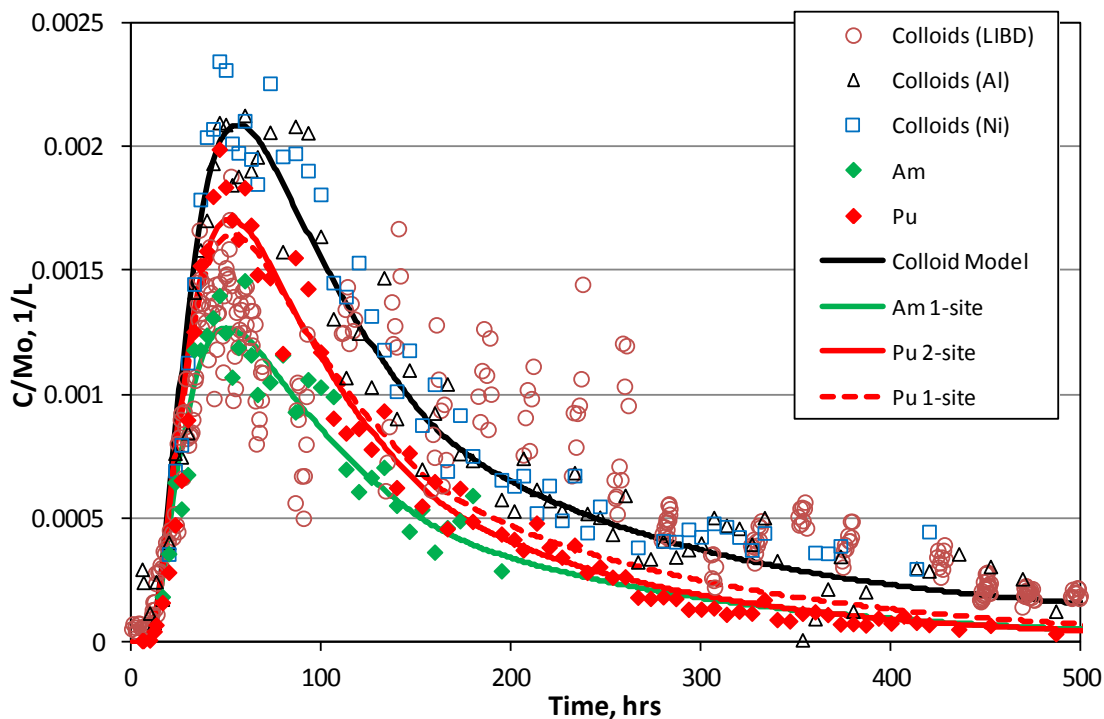


**Figure 7-9.** Simulated and experimental breakthrough curves for the colloids and actinides in CFM Run 12-02. Best estimate parameters are listed in Table 7-5.

**Table 7-6.** Sum of squares residuals,  $F$  statistics and tabulated  $F$  values (95% confidence level) for the model variants of Table 6-5 and for determinations of which variant best explains the solute desorption process.

Run/Solute	Model	$SS_{res}$	$F_{model-data}$	$F_{sig, 0.05}$
08-01/Th	1-site	$9.57 \times 10^{-6}$	-	-
08-01/Hf	1-site	$5.51 \times 10^{-6}$	-	-
08-01/Tb	1-site	$2.74 \times 10^{-6}$	-	-
	Aging to 2 <sup>nd</sup> site	$2.25 \times 10^{-6}$	3.05	4.06
10-01/Th	1-site	$9.46 \times 10^{-7}$	-	-
	Aging to 2 <sup>nd</sup> site	$6.89 \times 10^{-7}$	20.5 (vs. 1-site)	3.17
	2-site, hybrid	$6.78 \times 10^{-7}$	0.88 (vs. Aging)	4.02
10-01/Hf	1-site	$5.46 \times 10^{-7}$	-	-
	2-site, no aging	$5.35 \times 10^{-7}$	1.15 (vs. 1-site)	4.01

10-01/Tb	1-site	$2.87 \times 10^{-7}$	-	-
	Aging to 2 <sup>nd</sup> site	$2.41 \times 10^{-7}$	10.5 (vs. 1-site)	
	2-site, hybrid	$2.40 \times 10^{-7}$	0.23 (vs. Aging)	4.02
10-01/Eu	1-site	$1.86 \times 10^{-7}$	-	-
	1-site exp decay	$1.52 \times 10^{-7}$	11.4 (vs. 1-site)	4.01
	Aging to 2 <sup>nd</sup> site	$1.54 \times 10^{-7}$	10.6 (vs. 1-site)	4.01
	2-site, no aging	$1.15 \times 10^{-7}$	34.6 (vs. Decay)	4.01
10-03/Th	1-site	$3.91 \times 10^{-6}$	-	-
	2-site, no aging	$2.05 \times 10^{-6}$	46.3 (vs. 1-site)	4.03
	Aging to 2 <sup>nd</sup> site	$1.26 \times 10^{-6}$	107 (vs. 1-site)	4.03
	1-site exp decay	$1.25 \times 10^{-6}$	109 (vs. 1-site)	4.03
	2-site, hybrid	$1.13 \times 10^{-6}$	5.31 (vs. Decay)	4.03
10-03/Hf	1-site	$3.74 \times 10^{-6}$	-	-
	2-site, no aging	$2.24 \times 10^{-6}$	34.2 (vs. 1-site)	4.03
	1-site exp decay	$1.44 \times 10^{-6}$	28.3 (vs no-age)	4.03
	Aging to 2 <sup>nd</sup> site	$1.44 \times 10^{-6}$	28.3 (vs no-age)	4.03
	2-site, hybrid	$1.40 \times 10^{-6}$	1.43	4.03
10-03/Tb	1-site	$2.07 \times 10^{-7}$	-	-
	1-site exp decay	$6.78 \times 10^{-8}$	105 (vs. 1-site)	4.03
	Aging to 2 <sup>nd</sup> site	$7.18 \times 10^{-8}$	96 (vs. 1-site)	4.03
	2-site, no aging	$3.75 \times 10^{-8}$	40.4 (vs. Decay)	4.03
10-03/Eu	1-site	$7.73 \times 10^{-7}$	-	-
	2-site, no aging	$2.08 \times 10^{-7}$	139 (vs. 1-site)	4.03
	1-site exp decay	$1.80 \times 10^{-7}$	168 (vs. 1-site)	4.03
	Aging to 2 <sup>nd</sup> site	$1.62 \times 10^{-7}$	192 (vs. 1-site)	4.03
	2-site, hybrid	$1.49 \times 10^{-7}$	4.36 (vs. Aging)	4.03
12-02/Am	1-site	$4.90 \times 10^{-7}$	-	-
	1-site	$1.07 \times 10^{-6}$	-	-

12-02/Pu	Aging to 2 <sup>nd</sup> site	8.31 x 10 <sup>-7</sup>	10.4 (vs. 1-site)	3.98
	2-site, hybrid	8.21 x 10 <sup>-7</sup>	1.0 (vs. Aging)	3.98

Note: Red text indicates best-fitting model (see Table 7-5).

## 7.5 EVALUATION OF ALTERNATIVE DESCRIPTIONS OF SOLUTE DESORPTION PROCESS FROM COLLOIDS

The evaluation of alternative descriptions of solute desorption from colloids met with mixed results. For the most part, a two-site model offered a significant improvement over a one-site model, although a one-site model with a single desorption rate constant was considered superior for all of the colloid-facilitated solute data sets in Test 08-01, for Hf in Test 10-01 and Am in Test 12-02. By far the most significant improvement offered by a two-site model was for the solute data sets of Test 10-03, which exhibited relatively low peak concentrations followed by long, high tail concentrations, with the ratio of the normalized homologue concentrations to normalized colloid concentrations decreasing throughout the test and approaching one in the tails of the breakthrough curves for Th and Hf. These patterns can only be explained by a decrease in the average desorption rate of the solutes from the colloids over time during the test, and the only way that such a decrease can be accounted for is with at least one second, slower desorption site. This second site must either have sufficient initial solute mass adsorbed to account for the long solute tail, or there must be an aging reaction converting some of the solute mass from the faster site to the slower site during the test. In the case of the Th and Hf in Test 10-03, invoking an aging process offers a significant improvement over no aging process. The single-site model with an exponentially decaying first order rate constant fit the Test 10-03 homologue data reasonably well, but, as discussed in the next paragraph, this model can be interpreted as representing two sites rather than the literal interpretation of a single site with a time-dependent rate constant.

Table 7-6 shows that for each of the solute data sets in Run 10-03 and for the Eu data set in Test 10-01, the single-site exponential decay model yielded almost identical sum-of-squares differences as the two-site model with all of the solute initially adsorbed to the first site and a first-order aging reaction that converted the adsorbed solute from the first site to the second site that had a desorption rate constant of zero (i.e., irreversible). Both of these model variants have two adjustable parameters: the initial desorption rate constant and a time constant for decay of this rate constant in the case of the single-site model with a decaying rate constant, and the rate constant for the first adsorption site and an aging rate constant in the case of the two-site model (with the second site having a desorption rate constant of zero). The fact that these two variants yield nearly identical sum-of-squares differences and nearly identical fits in all cases in which the second site was assumed to be irreversible suggests that the two model variants are essentially equivalent from the standpoint of explaining the solute data. We consider the two-site aging model variant to be a more plausible description of the desorption process than the single-site variant with an exponentially-decaying rate constant because the latter does not have a sound mechanistic basis (i.e., it implies a continuum of different sites with

different desorption rate constants rather than an aging reaction converting solute from one site to another, although the net effect of the decaying rate constant is to effectively mimic the aging process with an irreversible second site).

The improvement of the model fits to the solute breakthrough curves offered by including a second adsorption site on colloids (over a single site model) was much less significant for tracer tests other than Test 10-03, and as mentioned above, there was actually no improvement for the three solute data sets in Test 08-01, Hf in Test 10-01 and Am in Test 12-02. While it was concluded that a two-site model was statistically justified over a single-site model in explaining 8 of the 13 colloid-facilitated solute transport data sets, the best-fitting parameters in these cases suggest that there was no consistency in the description of the two-site desorption process. In three cases (i.e., Th and Tb in Test 10-01 and Pu in Test 12-02), the best fits were obtained assuming an aging process and a second site that had a *faster* desorption rate constant than the first site. The inference in these cases is that the solute desorbed from the colloids more rapidly near the end of the respective tests than at the beginning, which is in contrast to the results obtained for all the solutes in Run 10-03 and Eu in Test 10-01.

These inconsistencies from one test to another, particularly with the same solutes in Tests 08-01, 10-01 and 10-03, suggest that either the colloid-facilitated transport processes are truly varying from one test to another or that there is enough random and/or systematic errors in the breakthrough curve data that the similarity in transport behavior of the colloid-associated homologues between tests is masked by these errors. The first explanation seems more plausible, although the second cannot be entirely ruled out. The variability in colloid-facilitated transport processes from one test to the next could have a number of possible causes. Subtle differences in the preparation procedure for the colloids and the tracer cocktails could potentially result in differences in the association of the solutes with the colloids, leading to stronger or weaker associations or perhaps to differences in aging processes in different tests. Even with complete consistency in cocktail preparations, differences in time elapsed between tracer cocktail preparation and tracer injection in different tests could also influence solute-colloid associations during the tests if aging processes are significant. The different tests also had different apparent shear zone flow pathways (Figure 7-3), so it is quite possible that even if the tracer cocktails were completely identical in all respects, the colloids and solutes may have come in contact with different shear zone surfaces during the different tests, thus resulting in differences in solute desorption parameters. The different flow rates in otherwise similar flow pathways could have influenced solute desorption parameters by subtly influencing colloid collision frequencies with shear zone surfaces or collision efficiencies with respect to inducing solute desorption from colloids. Finally, it is possible that the greater ratio of colloid to solute concentrations in Test 10-03 relative to Tests 08-01 and 10-01 might have resulted in some differences in the colloid-facilitated transport of the solutes in this test. It should be noted that all of these explanations could potentially also explain differences in colloid filtration parameters between the different tests.

It is worth noting that the apparent time-varying changes in desorption rate constants for some of the solutes in some of the tests may have also been caused by differences in transport characteristics of the early and late shear-zone flow pathways in the tests. Although the residence times in the shear-zone pathways were always quite short compared to the test durations, which suggests that most of the observed tailing can be attributed to the slowly-decaying injection functions rather than dispersion in shear-zone pathways (see Figure 7-2), it is still possible there were some differences in the shear zone pathways early and late in the tests that may have resulted in apparent changes to desorption rate constants. This could explain why in some cases (Th and Tb in Test 10-01, and Pu in Test 12-02) there was an apparent increase in the desorption rate constant with time when one would normally expect an aging process to result in a decrease in the desorption rate with time.

The possibility that random or systematic errors in the breakthrough curve data could have masked a similarity in the colloid-associated transport behavior of the solutes between the tests seems less likely than the above potential explanations for the observed differences. In the absence of direct information on these types of errors in the colloid, homologue and actinide analytical data, we use a qualitative and empirical measure of how much “noise” is in each data set. This measure is the ratio of the sum of squares of differences between the data and best-fitting models to the sum of squares of the model predictions (normalized concentrations) at each observation, which is listed for each data set in Table 7-7. This ratio effectively provides a measure of the ability of the models to explain the data sets (similar to the ratio of the sum-of-squares regression to total sum of squares, which provides a quantitative measure in the case of a *linear* regression model). It is apparent that the greatest data scatter relative to the model fits for the solute breakthrough curves occur in Test 10-01. All other tests had smaller ratios that were comparable to each other, which suggests that greater confidence can be placed in the fits for these tests than for Test 10-01. This result can be qualitatively deduced by looking at the plots of the model curves and data curves in Figures 6-6 to 6-9. Besides the considerable data scatter in Test 10-01, the relatively high early peaks in solute concentrations followed by steep drops to relatively low tail concentrations made it difficult to fit the 10-01 breakthrough curves, resulting in large ratios in Table 6-7. These features also result in the conclusion that two of the four solute breakthrough curves in Run 10-01 are best explained by an aging process with a second adsorption site on the colloids that has a faster desorption rate constant than the first site (this drives the tails lower more quickly).

**Table 7-7.** Ratios of sum of squares of residuals (between model and data) to sum of squares of model predictions for all the best-fitting model simulations.

Run/Solute	Model	Ratio
08-01/Th	1-site	0.02
08-01/Hf	1-site	0.018

08-01/Tb	1-site	0.02
10-01/Th	Aging to 2 <sup>nd</sup> site	0.027
10-01/Hf	1-site	0.037
10-01/Tb	Aging to 2 <sup>nd</sup> site	0.067
10-01/Eu	2-site, no aging	0.054
10-03/Th	2-site, hybrid	0.018
10-03/Hf	1-site exp decay	0.021
	Aging to 2 <sup>nd</sup> site	0.021
10-03/Tb	2-site, no aging	0.025
10-03/Eu	2-site, hybrid	0.025
12-02/Am	1-site	0.018
12-02/Pu	Aging to 2 <sup>nd</sup> site	0.017

It should be noted that some of the scatter in the data sets might be attributable to earth tides that caused periodic fluctuations in the conservative dye tracer breakthrough curves in the longer tests (Figs. 7-7 and 7-9). Because the frequency of concentration data was much lower for the offline analyses of colloids and solutes than for the inline fluorescence analyses of the dye tracers, the impact of the earth tides on the colloid and solute concentrations is somewhat uncertain. We speculate that the impact may have been greater for Test 10-01 than for the other tests, although other unknown factors may have played a role in the larger data scatter of this test.

## 7.6 DISCUSSION

### 7.6.1 Implications for Nuclear Waste Repository Performance Assessments over Long Time and Distance Scales

To assess the implications of the CFM tracer test results for colloid-facilitated radionuclide transport over longer time and distance scales, it is of interest to examine the scaling behavior of the desorption parameters for the tri- and tetravalent solutes from the colloids in the CFM Tests 08-01, 10-01, 10-03 and 12-02. Figure 7-10 shows desorption rate constants from the colloids for the trivalent solutes as a function of residence time in the shear zone for the four tracer tests, and Figure 7-11 shows an analogous plot for the tetravalent solutes. In both cases, the plots reflect the desorption rate constants obtained

when only a single adsorption site was assumed on the colloids. The desorption rate constants for a second site and any aging process on the colloid surfaces are not reflected in these plots so as to keep the evaluation consistent across all tests. We note that a similar plot of the scale dependence of colloid filtration rate constants is not presented here because the filtration rate constants did not exhibit any clear trend with time scale (Table 7-4). Also, there was also an inconsistency between tests of whether the colloid filtration process was reversible or irreversible or both.

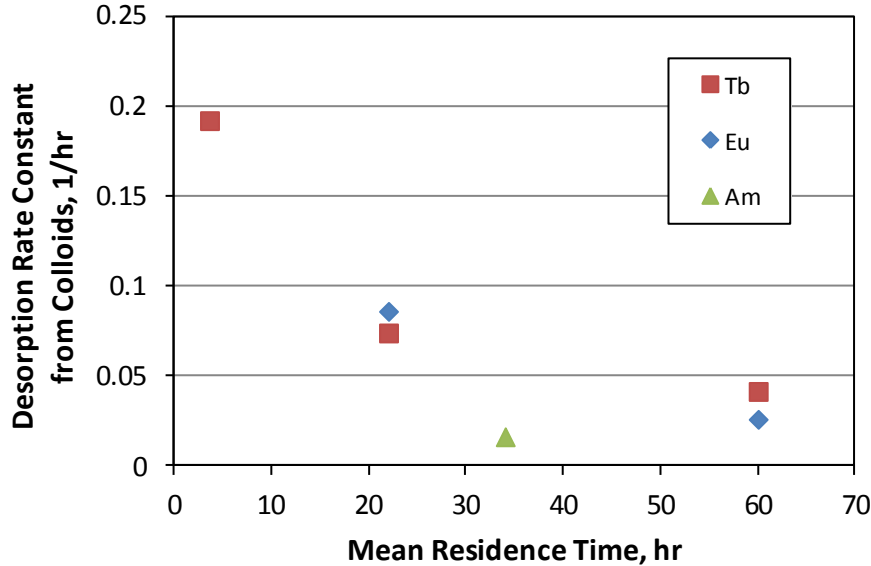


**Figure 7-10.** Desorption rate constants from colloids vs. time for trivalent homologues and Am(III) in the four CFM tracer tests

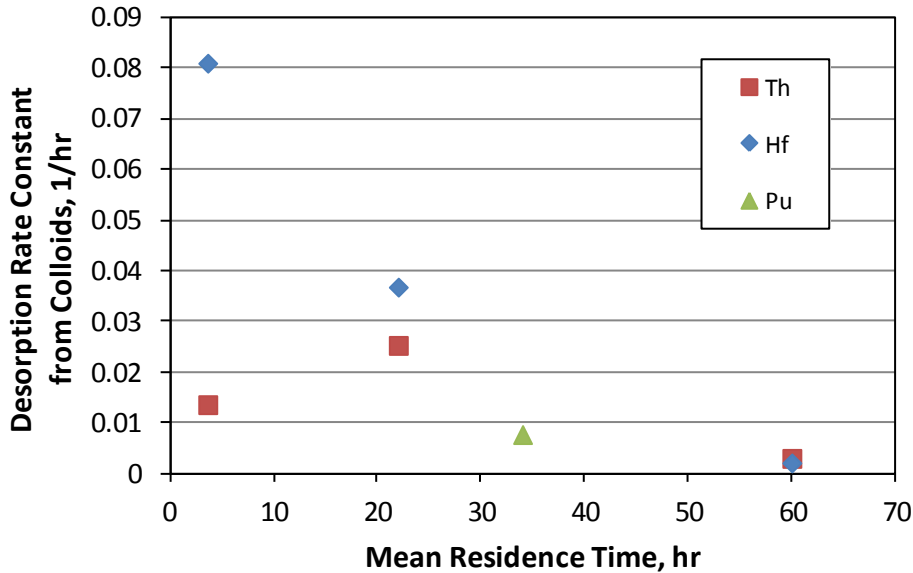


**Figure 7-11.** Desorption rate constants from colloids vs. time for tetravalent homologues and Pu(IV) in the four CFM tracer tests.

In both Figures 7-10 and 7-11, there is a tendency for the desorption rate constants to decrease with residence time. Linear regression fits to the log-log transformed data of Figures 7-10 and 7-11 are shown in Figure 7-12. It is apparent that the tetravalent solutes desorb more slowly than the trivalent solutes in any given test, although both species have nearly the same slope, implying a similar time-scale dependence. Extrapolation of the desorption rate constant regressions to longer times yields predictions that 99% of the trivalent solutes will desorb from the colloids after a residence time of about 500 hours and 99% of the tetravalent solutes will desorb after a residence time of about 1 year. Of course, the uncertainties associated with these extrapolations are quite large, especially for the actinides Am and Pu, which although combined with the tri- and tetravalent homologues for the regressions of Figure 7-12, were each only used in one test (12-02). The possibility of more than one adsorption site on colloids and an aging process that converts one type of site to another, as indicated by the best model fits to several of the data sets, casts additional uncertainty on extrapolations of desorption rate constants to longer times. Nonetheless, the tracer test data suggest that the time scales for desorption of the tri- and tetravalent solutes from the colloids should be relatively short compared to time scales for performance assessment, implying negligible colloid-facilitated transport of Am and Pu over time scales of multiple years, even if colloid filtration is minimal.

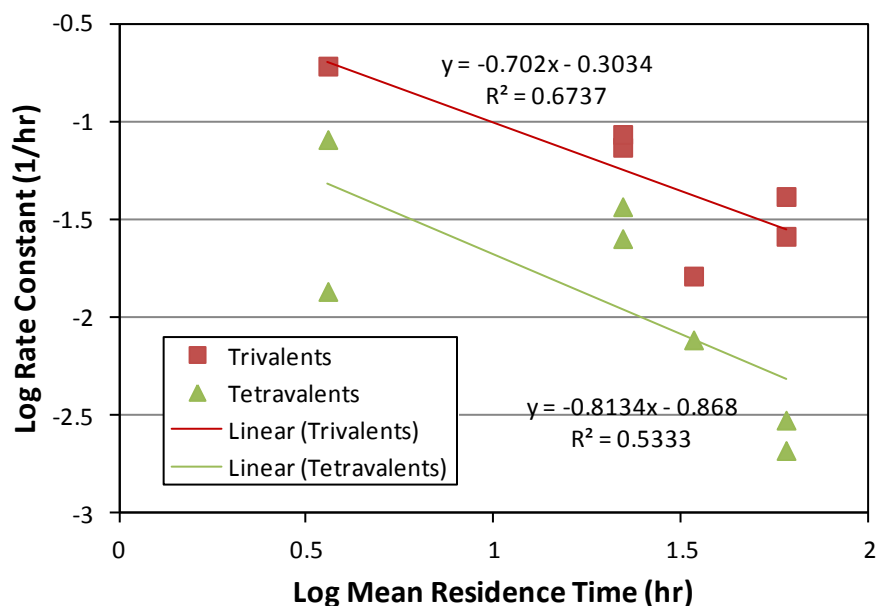


**Figure 7-12.** Trends of log desorption rate constants from colloids vs. log time (trivalent and tetravalent solutes) in the CFM tracer tests

The apparent time-scale dependence of the desorption rate constants in Figures 7-10 through 7-12 are worthy of further discussion. Mechanistically, time-dependent rate constants for specific reactions are not supported by theory or literature data (this point

was previously made in Section 7.5 in connection with the single-site, exponentially-decaying rate constant desorption model). However, a simple example can illustrate how a small number of reactions or, more accurately, a small number of different types of sorption sites with different corresponding desorption rates, could result in the observed time-dependent behavior. Figure 7-13 shows the desorption rate constants for the tetravalent solutes as a function of residence time in the CFM tracer tests (data of Figure 7-11) along with a line generated from a simple calculation of the *apparent* rate constant in a system in which there are 3 types of sorption sites on the colloids, with desorption rate constants of  $0.1 \text{ hr}^{-1}$ ,  $0.0005 \text{ hr}^{-1}$ , and  $0.00001 \text{ hr}^{-1}$ , respectively. One-third of the mass of the tetravalent solute was assumed to occupy each of the sites at time zero. Even though each of the sorption sites has a time-invariant desorption rate constant, the overall system exhibits time-dependent desorption rate behavior similar to that observed in the CFM tracer tests.

The key point in Figure 7-13 is that the extrapolation of the CFM tracer test data to longer time scales will critically depend on the presence or absence of desorption rate constants that are significantly smaller than the rate constants that can be effectively interrogated in the CFM tests. More specifically, it will depend on the presence or absence of some fraction of sorption sites on colloids that have extremely low desorption rate constants. Even a very small fraction of such sites could result in significant observable colloid-facilitated transport of an actinide over long time and distance scales – of course it would also be necessary for a significant fraction of colloids to remain unfiltered over such time scales. The dashed lines in Figure 7-13 are intended to qualitatively illustrate the range of potential extrapolations that could occur over longer time and distance scales depending on the presence or absence of very small rate constants. If there are no rate constants much smaller than those deduced from the CFM tests, then the extrapolations would flatten out, and colloid-facilitated transport would not be predicted to be a problem over longer time scales. However, if there are significantly smaller rate constants that were not interrogated by the CFM tracer tests, then colloid-facilitated transport might still be a problem over longer time scales.

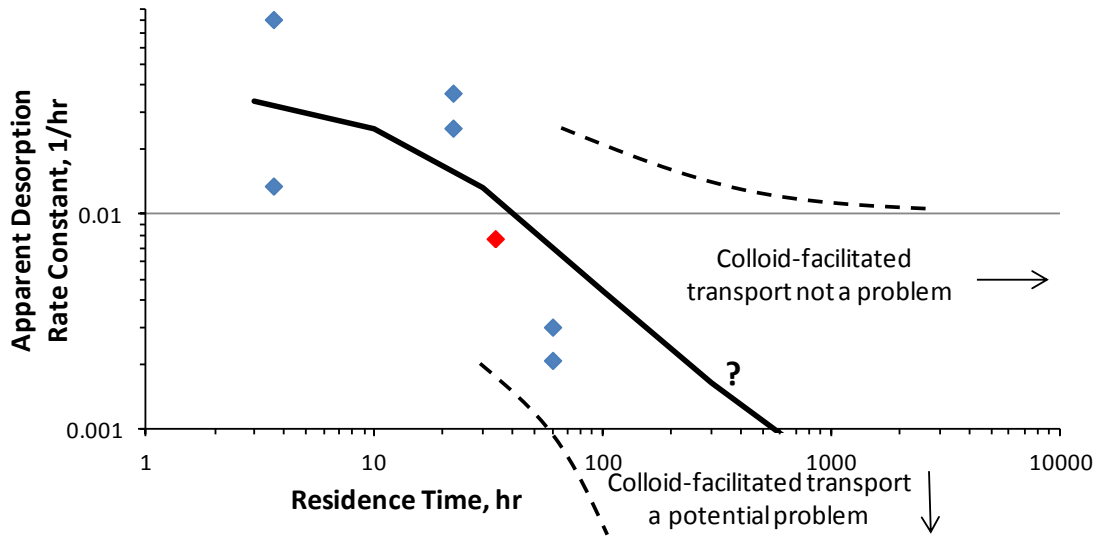


**Figure 7-13.** Apparent desorption rate constants from colloids for the tetravalent species as a function of residence time in the CFM tracer tests. Red data point is Pu in Run 12-02.

If we consider the ability to observe solute desorption from colloids in the CFM tracer tests to be equivalent to the ability to observe a 5% difference between the recoveries of the colloids and the colloid-adsorbed solutes (the breakthrough curve data suggest at least a 5% uncertainty), then the *minimum* colloid filtration rate constant or solute desorption rate constant that can be interrogated in the CFM tests is approximately  $0.0002 \text{ hr}^{-1}$ . This value is calculated from  $\ln(0.95)/(-100 \text{ hr})$ , where 0.95 corresponds to a 95% recovery (difference of 5%), and 100 hrs is approximately the maximum residence time of the CFM tests. This expression comes from a simple manipulation of the equation for the exponential decay of an initial concentration,  $C_0$ , associated with a first-order reaction with rate constant  $k$ :

$$\frac{C}{C_0} = e^{-kt} \quad (7-17)$$

All of the extrapolated mass recoveries vs. time discussed above were based on equation (7-17). Even if the experimental and measurement errors were small enough to observe a 1% difference in recoveries, the minimum observable rate constant would only be  $4.4 \times 10^{-5} \text{ hr}^{-1}$ , and this rate constant would predict that less than 0.01% colloid-associated radionuclides would still remain adsorbed to colloids after about 25 years. Using a minimum measurable rate constant of  $0.0002 \text{ hr}^{-1}$ , corresponding to a 5% observable difference in recoveries, the prediction would be only about 5 years to reach 0.01% of the solutes remaining adsorbed to colloids. Clearly, with a maximum practical shear zone residence time of around 100 hrs (beyond which recoveries are not guaranteed because of the high ambient flows in the shear zone), the CFM testbed has a limited ability to interrogate the very small rate constants that could mean the difference between

significant colloid-facilitated transport or no colloid-facilitated transport over performance assessment time scales. The problem is further compounded by the presence of any sorption sites on colloids from which solutes tend to desorb rapidly because this will result in observed behavior that completely masks the effects of very slow desorption rates. In effect, if there is any significant observable solute desorption from colloids over the relatively short time scales of the CFM tracer tests, it will be extremely difficult to see the effects of very slow desorption rates that will matter for performance assessments over long time scales.

### **7.6.2 Suggestions for Future CFM Colloid-Facilitated Transport Tests**

The above discussion is not intended to imply that the CFM test bed is useless for obtaining colloid-facilitated transport information relevant to long time and distance scales. Rather, it is intended to point out the limitations of directly extrapolating the CFM test data to longer time and distance scales. The discussion also helps provide insights into how future tests might be conducted to better interrogate both colloid filtration rate constants and solute desorption rate constants that might matter in long-term performance assessments. Although a clear scale dependence of colloid filtration rate constants was not apparent from the CFM tests, such a scale dependence is still very important for performance assessment predictions because if there is no fraction of colloids that has very slow filtration rate constants, colloid-facilitated transport will not be a problem no matter how strongly adsorbed radionuclides are to colloids. The transport time scales achievable in the CFM test bed have practical limitations, so suggestions for improvements must necessarily focus on pre-conditioning of the colloids used in the injection cocktails and/or on pre-conditioning of the injection cocktails themselves. Two suggestions are put forward here for consideration, although many variations of these, as well as alternative suggestions, are certainly possible:

- Subject the colloids generated by dispersing bentonite in synthetic GTS water to experiments that tend to eliminate or reduce the number of colloids that are more susceptible to filtration prior to injecting them in a CFM field test. For instance, the dispersed colloids could be run through a large laboratory column containing GTS shear zone material, and only the colloids exiting the column could be used in the field injection cocktail. Based on the column residence time and observed column recovery of the colloids, it will be possible to estimate the maximum effective filtration rate constant of the recovered colloids (although this rate constant won't necessarily strictly apply to the shear zone itself).
- Adsorb the target homologues or radionuclides onto the colloids isolated above, and then perform large-scale desorption experiments using shear zone materials in the presence of the colloids to remove homologues or radionuclides that are adsorbed to weaker colloid sorption sites. The maximum effective desorption rate constants associated with homologues or radionuclides that remain adsorbed to the colloids after a certain amount of desorption time could then be estimated, and

the remaining colloids and associated homologues could be used as part of an injection cocktail in a GTS field tracer test.

One obvious variation of these suggestions would be to perform a large column transport experiment *after* adsorbing solutes to the dispersed bentonite colloids and effectively isolating both filtration-resistant colloids and the more strongly adsorbed solutes in one step. Using an injection cocktail pre-conditioned in these ways in a CFM field test would, in principle, increase the probability of interrogating the small colloid filtration rate constants and small desorption rate constants that will matter over performance assessment time scales.

## 7.7 REFERENCES

- Achtziger, P., and Kontar, K. 2011. *GTS Phase VI Homologue Tracer Test Run 10-03*, Quick-Look Report A-1588-25/28, CFM Project, Switzerland.
- Draper, N. and Smith, H. 1981. *Applied regression analysis*, 2<sup>nd</sup> ed. John Wiley and Sons, New York, New York.
- Kontar, K. and Gräfe, K. 2012. *GTS Phase VI CFM Project Tracer Test Run 12-02*, Quick-Look Report, AN 12-302, CFM Project, Switzerland.
- Reimus, P. W., Pohll, G., Mihevc, T., Chapman, J., Papeis, L., Lyles, B., Kosinski, S., Niswonger, R., and Sanders, P., 2003. Testing and parameterizing a conceptual model for radionuclide transport in a fractured granite using multiple tracers in a forced-gradient test, *Water Resour. Res.*, **39**(12), 1350, doi:10.1029/2002WR001597.
- Rösli, U., Achtziger, P., and Kontar, K. 2010. *GTS CFM Homologue Tracer Test Run 10-01*, Quick-Look Report AN 10-271, CFM Project, Switzerland.
- Schäfer, T., Geyer F., Hauser, W., Seher H., Walther, C., Trick, T., Degueldre C., Missana T., Alonso, U., Suzuki, M., Baer, T., and Blechschmidt, I. 2008. *GTS CFM Homologue Tracer Test Run 08-01*, Quick-Look Report A1588-4, CFM Project, Switzerland.
- Schäfer, T., Geyer F., Hauser, W., Heck, S., and Walther, C. 2010. *GTS CFM Homologue Tracer Test Run 10-01, Part II*, Quick-Look Report AN 10-271, CFM Project, Switzerland.
- Schäfer, T., Geyer F., Hauser, W., Heck, S., and Walther, C. 2012. *GTS Phase VI Tracer Test Run 10-03, Part II*, Quick-Look Report, AN 12-182, CFM Project, Switzerland.
- Wang, Y., et al. 2013a. Natural System Evaluation and Tool Development – International Collaborations: FY13 Progress Report, Used Fuel Disposition Campaign Milestone Report FCRD-UFD-2013-000628; Chapter 2, Interpretations of Colloid-Facilitated Transport Experiments at the Grimsel Test Site from 2008 through 2012.

## **8. Pu SORPTION, DESORPTION AND INTRINSIC COLLOID STABILITY UNDER GRANITIC CHEMICAL CONDITIONS**

### **8.1 STABILITY OF PLUTONIUM INTRINSIC COLLOIDS IN THE PRESENCE OF CLAY AT ELEVATED TEMPERATURES: DISSOLUTION KINETICS**

#### **8.1.1 Introduction**

The large volumes of plutonium (Pu) designated for storage in high-level nuclear waste repositories are predicted to impact repository performance under certain scenarios (Kaszuba and Runde, 1999; Management, 2002). Plutonium can migrate in the subsurface associated with the colloidal fraction of groundwater (Kersting et al., 2012). Colloid facilitated Pu transport has been reported on the scale of kilometers at sites both in the US (Kersting et al., 1999; Santschi et al., 2002b) and Russia (Novikov et al., 2006). Despite the recognized importance of colloid-facilitated Pu transport, geochemical and biochemical mechanisms controlling Pu colloid formation and stability over the range of concentrations expected in the environment have not been identified. In particular, kinetic information under environmental conditions is lacking. The temperature in the vicinity of radiological waste packages is expected to be elevated for some time. Thus, understanding Pu behavior at elevated temperatures is necessary. The paucity of thermodynamic and kinetic data limits the efficacy of current transport model predictions (Altmaier et al., 2013; Rao et al., 2011).

Pu can be associated with the colloidal fraction of groundwater in two forms. Pu can either form an intrinsic colloid or sorb onto mineral, organic, or microbial colloids to form pseudo-colloids. At high concentrations where actinide ions in solution exceed the solubility product, Pu will precipitate and form Pu hydroxide intrinsic colloids (Neck et al., 2007d; Neck and Kim, 2001). Transport of intrinsic Pu colloids is controlled by its stability (both physical and chemical). At low concentrations, Pu will sorb onto inorganic or organic colloids, resulting in the formation of pseudo-colloids. Transport of Pu pseudo-colloids is determined by the Pu sorption/desorption kinetics. Both forms of Pu colloids may exist simultaneously under some subsurface conditions.

The identity of naturally occurring mineral colloids will be a function of the host rock mineralogy. Among the most ubiquitous mineral colloids are aluminosilicate clays that are commonly observed as mobile colloids due to their inherently small particle size and prevalence as alteration minerals from original host rock material (Kersting et al., 1999). Clays are known to sorb Pu (Begg et al., 2013b; Bertetti et al., 1998; Keeney-Kennicutt and Morse, 1985; Kozai et al., 1996; Kozai et al., 1993; Lujanienė et al., 2007; Powell et al., 2004; Powell et al., 2005; Powell et al., 2008; Sabodina et al., 2006b; Sanchez et al., 1985; Turner et al., 1998). In addition, the proposed use of bentonite within some engineered barrier systems scenarios for high-level nuclear waste repositories provides additional importance to understanding Pu interaction with smectite aluminosilicate clays (Sabodina et al., 2006b). Smectite clay may represent a key phase that will control transport of Pu pseudo-colloids in repository near and far fields.

Batch sorption has been the most common method used to measure the affinity of a contaminant for a mineral surface. Data obtained from a conventional sorption experiment are the concentrations of the contaminant in the liquid phase before and after sorption. Filtration and/or centrifugation are commonly used to separate solids from liquid after equilibrium is reached. The quantity sorbed is calculated based on the difference of the total and aqueous concentrations. However, if the contaminant is involved in multiple processes that all form solid phases (i.e., sorption, colloids formation and/or precipitation), these data cannot distinguish between them.

In order to distinguish between precipitated, colloidal, and sorbed states of Pu, we employed dialysis membranes to segregate Pu intrinsic colloids from pseudo colloids in the current study. Dialysis membranes are commonly used to separate suspended solutes or particles of different dimensions in a liquid mixture. Desirable size separation by dialysis can be achieved by selecting the membrane pore-size molecular weight cutoff (MWCO). A membrane pore size of 5 kilo Daltons (kDa) is able to separate soluble species from particles >1 nm. Dialysis membranes provide a unique opportunity to segregate Pu intrinsic colloids (2–5 nm) from its pseudo-colloids (>100-nm on mineral phases) while allowing aqueous species (<1 nm) to interact with both colloidal phases.

In the present study, we examined the stability of Pu intrinsic colloids relative to Pu-montmorillonite pseudo-colloids using a novel experimental design and modeling approaches. We employed dialysis membranes in an effort to segregate Pu intrinsic colloids (2–5 nm) from montmorillonite colloids (>100 nm) and allow aqueous Pu to establish equilibrium between both colloidal phases. Using the dialysis membrane approach, we monitored the dissolution of PuO<sub>2</sub> intrinsic colloids in the absence and presence of montmorillonite, and formation of Pu pseudo-colloids. The data provide new insights into stability of plutonium intrinsic colloids in the presence of clay at 25 and 80 °C.

### 8.1.2 Materials and Methods

#### Pu Stock and Intrinsic Pu colloid preparation

All reagents were of analytical grade or better and used as received. De-ionized water from a Barnstead Milli-Q Water (MQW) purification system (resistivity: 18.2 megaohm-cm) was used for all procedures and solution preparation. Pu stock solutions with two different Pu isotopic ratios were used. A relatively pure alpha-emitting <sup>238</sup>Pu stock solution was used in low- and intermediate Pu concentration experiments. The <sup>238</sup>Pu, <sup>239</sup>Pu, <sup>240</sup>Pu, and <sup>241</sup>Pu mass percent in the stock was 76.83%, 21.03%, 2.01%, and 0.142%, respectively. The major isotope contributing to alpha activity in this stock was <sup>238</sup>Pu (~99.9% by activity). The second Pu stock solution, used in the high Pu concentration experiments, was a <sup>242</sup>Pu solution spiked with ~1% of the <sup>238</sup>Pu stock. The <sup>238</sup>Pu, <sup>239</sup>Pu, <sup>240</sup>Pu, <sup>241</sup>Pu, and <sup>242</sup>Pu mass percent in this stock was 0.75%, 0.21%, 0.13%, 0.04%, and 98.87%, respectively. The major isotopes contributing to alpha activity in this stock were <sup>238</sup>Pu (96.75%) and <sup>242</sup>Pu (2.93%). Both Pu stock solutions were purified

using AG®1-x8 100-200 mesh anion exchange resin from Bio-Rad Laboratories, and filtered through an Amicon Ultra 0.5 mL centrifugal filter with membrane MWCO of 3 kDa from EMD Millipore. The oxidation state of Pu(IV) was confirmed using both UV-Vis and solvent extraction. The aqueous Pu(IV) starting solution was prepared by diluting the stock solution into a pH 8 buffer solution and gradually adding microliters of NaOH (1 N or 6 N) to adjust pH to ~pH 8. The intrinsic PuO<sub>2</sub> colloids were prepared by neutralizing Pu(IV) stocks using NaOH solution and adjusting solution pH to 9 to 10. After aging for more than a week, the Pu colloids were centrifuged at an RCF of 9168 for 1 hr, and the supernatant was removed. The Pu colloid particle size cut-off based on centrifugation was 14 nm. However, the average particle size of the aggregates (intrinsic Pu nano-colloids) was 30 nm and the sizes of crystallite within the aggregates ranged from 2.5 to 4.5 nm (Figure 8-1). The Pu colloids were re-suspended in Milli-Q water. The Pu colloid starting solutions were prepared by adding a spike of Pu colloids into the pH 8 buffer solution without further pH adjustment. Pu concentrations in samples were analyzed by a PerkinElmer Tri-Carb 2900TR Liquid Scintillation Analyzer. The fraction of soluble Pu in the Pu colloid stock solution, based on the 3 kDa MWCO filtrate, was 1 to 3%.

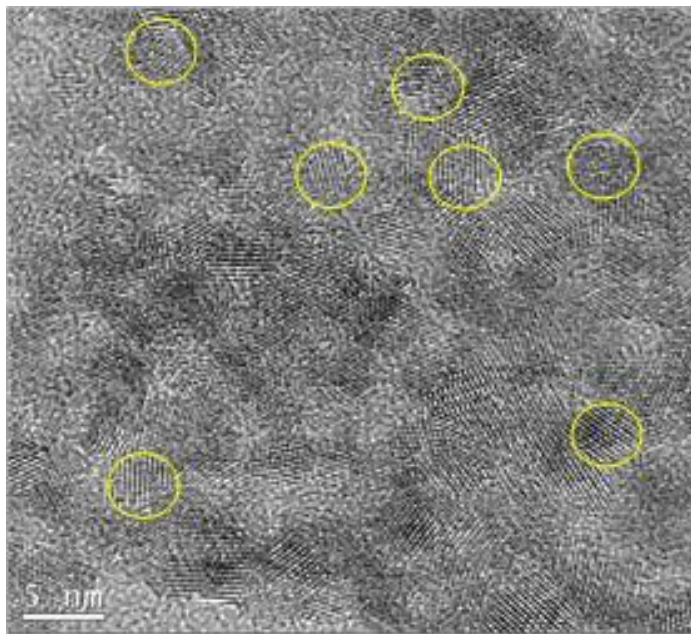


**Figure 8-1.** TEM image of mat of Pu intrinsic colloids. Several individual Pu colloids are highlighted by yellow circles. The measured average particle sizes was 3.5 nm with a range of 2.5-4.5 nm.

## Montmorillonite

SWy-1 montmorillonite (Clay Minerals Society) was pre-treated using 1 mM HCl (to dissolve any carbonate minerals) followed by addition of 0.1% H<sub>2</sub>O<sub>2</sub> (to oxidize organic contaminants and reduced metals (e.g., Fe<sup>2+</sup>). The pre-treated montmorillonite was centrifuged to remove excess liquid, and the wet paste was transferred to a 6 to 8 kDa MWCO dialysis tube suspended in 0.01 M NaCl solution to produce a homoionic Na-montmorillonite. The clay minerals were dialyzed for seven days, and the NaCl solution was changed at least once per day. The clay minerals were then suspended in Milli-Q water and centrifuged to obtain the fraction of particle sizes from 50 nm to 2 microns. The wet solids were dried at 40 °C until a constant weight was obtained. A stock montmorillonite suspension was made by mixing 4 g of dried montmorillonite in 400 mL of pH 8 buffer (5 mM NaCl/0.7 mM NaHCO<sub>3</sub>). Quadrasorb SI surface area and pore size analyzer from QuantaChrome Instruments was used for BET measurements. The surface area of montmorillonite measured by N<sub>2</sub>(g)-BET was 31.45 ± 0.17 m<sup>2</sup>/g, which is comparable to the reported value of 31.8 m<sup>2</sup>/g (Clay Minerals Repository).

## Dissolution Experiments

Intrinsic Pu(IV) colloid stability was evaluated using the experimental design shown in Figure 8-2. Briefly, intrinsic Pu colloids are placed inside the dialysis bag, while the clay colloids are placed outside the dialysis bag. Thus, the colloidal montmorillonite is isolated from the intrinsic Pu colloids while exchange of truly aqueous (non-colloidal) ions between both solid phases is permitted. Pu detected outside the dialysis membrane over time represents dissolved Pu species that diffuse across the dialysis membrane. In the presence of montmorillonite, the dissolved Pu can either remain in solution or sorb to montmorillonite. The dissolution rate of intrinsic Pu colloids is expected to be a function of its solubility, surface area, composition, solution ionic strength, pH and temperature. The sorption rate of Pu to montmorillonite is affected by the Pu speciation, solution Eh/pH, ionic strength, and temperature.

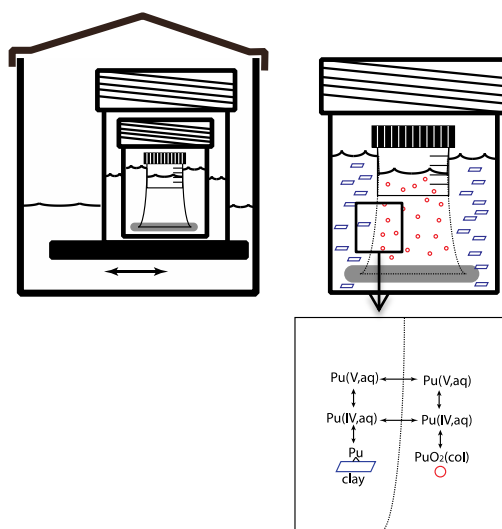


**Figure 8-2.** Experimental design using dialysis membrane to separate intrinsic Pu colloids (placed inside dialysis tubing), from mineral colloids (placed outside the tubing). For Pu-montmorillonite sorption to occur, Pu intrinsic colloids must dissolve and diffuse through the membrane.

A total of 16 experiments (excluding a control blank) were performed to test the experimental design and quantify dissolution of intrinsic Pu colloids in the presence of montmorillonite (Table 8-1). The dialysis membrane used was Spectra/Por® 7 standard RC pre-treated dialysis tubing with MWCO 1 kDa, from Spectrum Laboratories, Inc. The experiments were performed at two temperatures, 25°C (8 experiments) and 80°C (8 experiments) to evaluate the effect of temperature. At each temperature, Pu was initially added either in an aqueous form (to test simple diffusion and sorption of Pu) or as intrinsic colloids (to test intrinsic colloid dissolution, diffusion and sorption of Pu). The initial Pu concentrations bracketed the PuO<sub>2</sub>(am, hyd) solubility ( $\sim 5 \times 10^{-9}$  M) (Neck et al., 2007c). In addition, montmorillonite-free solutions (spiked blanks) with initial Pu concentrations below and near PuO<sub>2</sub>(am, hyd) solubility were used to compare with sorption experiments and evaluate Pu loss to container walls and dialysis membranes.

**Table 8-1.** Experimental conditions and data summary

Exp	Temperature °C	Inside dialysis bag				Outside dialysis bag		Kinetic constant					Equilibrium constant	
		Pu colloids	Pu <sup>4+</sup>	PuO <sub>2</sub> <sup>+</sup>	<sup>3</sup> H	Clay <sup>a</sup>	Final % Pu	k <sub>1</sub>	k <sub>2</sub>	k	k <sub>3</sub>	k <sub>3</sub>	k <sub>3</sub> =k <sub>1</sub> /SSA	K = k <sub>3</sub> /k <sub>3</sub>
		mol L <sup>-1</sup>				g L <sup>-1</sup>		day <sup>-1</sup>					mol m <sup>-2</sup> day <sup>-1</sup>	
1	25	1.13E-11				1	45	0.025					6.2E-07	160
2		9.09E-10				1	33	0.06				1.5E-06		
3		2.01E-07				1	10	0.4				9.9E-06		
4		9.13E-10				0	2		0.06	0.8	0.005			
5	80	1.14E-11				1	88	0.17				4.2E-06	25	
6		8.31E-10				1	70	0.3				7.4E-06		
7		2.01E-07				1	15	0.15				3.7E-06		
8		9.13E-10				0	35		0.3	20	0.8			
9	25		5.93E-12			1	55		30				28	
10			6.20E-10			1	37		30					
11			6.52E-12			0	3		30	0.14	0.005			
12	80		5.93E-12			1	100	0.15				3.7E-06	0.007	
13			6.20E-10			1	63	0.2				5.0E-06		
14			6.52E-12			0	28		0.3	0.002	0.03			
15	25			1.30E-10	4.90E-11	0	89/98 <sup>b</sup>		25/40 <sup>b</sup>					
16	80			1.30E-10	4.70E-11	0	42/87 <sup>b</sup>		30/40 <sup>b</sup>					

a. Swy-1 Montmorillonite

b. values represent as PuO<sub>2</sub><sup>+/3</sup>H

All batch experiments were conducted in 450-mL Teflon jars with air-tight closures. 225 mL of pH 8 buffer (5 mM NaCl / 0.7 mM NaHCO<sub>3</sub>) was mixed with 25 mL of montmorillonite stock suspension to yield a 250-mL montmorillonite suspension of 1 g/L. A sealed dialysis tubing containing 30 mL of either aqueous Pu(IV) or intrinsic Pu colloids was then placed in the 250 mL pH buffer solution with or without montmorillonite. The 450-mL Teflon jars were submerged in 1-L Teflon containers filled with Milli-Q water to minimize evaporative losses and provide secondary containment to the radioactive samples. Over the course of the experiment, the 25°C samples were placed on a top-loading orbital shaker, and the 80°C samples were submerged in an Innova 3100 water bath shaker from New Brunswick Scientific. All samples were shaken at an orbital speed of 100 rpm.

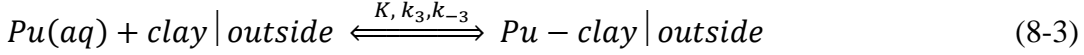
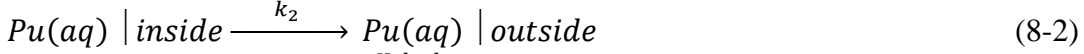
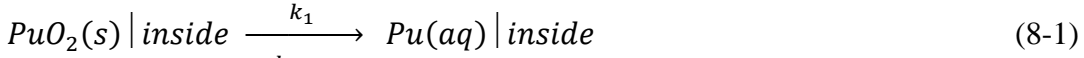
Each experiment was sampled as a function of time over a three-month period. At each sampling interval, aliquots of the montmorillonite suspension were collected, centrifuged and analyzed for total Pu, Pu in the supernatant, and solution pH. Alternatively, aqueous Pu was determined by measuring the filtrate Pu concentration after filtering the suspension through 3kDa pore size centrifugal filters. The montmorillonite concentration in the suspension was also measured based on light scattering at a wavelength range of 300–500 nm using a Cary 500 Scan UV-Vis-NIR spectrophotometer (Varian). The pH of the clay suspension was monitored and maintained at pH 8 ± 0.5 at all times.

### 8.1.3 Results and Discussion

#### Kinetics

The formation of Pu-montmorillonite pseudo-colloids due to the dissolution of intrinsic Pu colloids in the system involves a series of processes including Pu colloids dissolution, Pu(IV)/Pu(V) redox reactions, aqueous Pu species diffusion and sorption. To simplify the discussion, we focus on the essential processes, which follow a sequential order: PuO<sub>2</sub>

colloids dissolve to produce aqueous Pu species inside the dialysis membrane (Eq. 8-1); the aqueous Pu species diffuse across the membrane (Eq. 2) and Pu species sorb onto clay that is placed outside of the dialysis membrane (Eq. 8-3).



where  $k_1$  and  $k_2$  represent apparent kinetic constants of Eq. 8-1 and Eq. 8-2, respectively.  $K = k_3/k_{-3}$  is the sorption equilibrium constant and  $k_3$  and  $k_{-3}$  are the sorption and desorption rate constants.

To a first order approximation, we assume that the rates are proportional to the reactant concentrations in above equations. Therefore, a pseudo 1<sup>st</sup> order reaction model was used for all three reactions. As a result, kinetic rate constants can be compared directly to determine the rate limiting steps. However, it should be noted that  $k_1$  is a product of intrinsic Pu colloids' specific surface area and dissolution rate constant. Similarly,  $k_2$  reflects the characteristics of an ion's diffusion coefficient but is also a function of experimental parameters, including the configuration/dimensions of the dialysis systems, the number of membrane pores and their sizes, and shaker speed used in the experiments. By placing either aqueous or solid Pu species inside dialysis bag, and analyzing the total Pu concentration outside of dialysis bag, we are able to determine  $k_1$  and  $k_2$ . By analyzing concentrations of total and aqueous Pu in clay suspension outside of the bag, we can obtain equilibrium constant  $K$ .

### Apparent Diffusion in the System

To determine the rate of aqueous species diffusion from inside the dialysis bag, through the membrane, and to the outside of the dialysis bag, tritium and aqueous Pu(V) were placed inside the dialysis bag and small aliquots of the solution outside dialysis bag were taken as function time and monitored for both Pu and tritium (i.e. Eq. 8-2). The concentrations of  $^3H$  or  $PuO_2^+(aq)$  inside and outside of dialysis bag can be described by the following:

$$\frac{dC_{in}}{dt} = -k_2 C_{in} \quad (8-4)$$

$$C_{out} V_{out} = C^0 (V_{in} + V_{out}) - C_{in} V_{in} \quad (8-5)$$

$$C^0 = C_{in}^0 * V_{in} / (V_{in} + V_{out}) \quad (8-6)$$

$$C_{out} = C^0 [1 - \exp(-k_2 t)] \quad (8-7)$$

where  $C_{in}$  and  $C_{out}$  are  $^3H$  or  $PuO_2^+$  concentrations (in mol L<sup>-1</sup>) inside and outside of the dialysis bag at time  $t$  (days), respectively;  $C_{in}^0$  is the initial concentration inside a dialysis

bag at time zero.  $V_{in}$  and  $V_{out}$  (in L) are the solution volumes inside and outside of dialysis bag, respectively.

The data obtained from diffusion experiments are plotted in Fig. 8-3, which shows that tritium data obtained from both temperatures (Fig. 8-3a) and  $\text{PuO}_2^+$  data obtained from 25 °C (dash line in Fig. 8-3b) experiments fit well to a 1<sup>st</sup> order reaction model. The obtained rate constants were 40 and 23 day<sup>-1</sup> for tritium at both temperatures and  $\text{PuO}_2^+$  at 25 °C, respectively. The 1<sup>st</sup> order reaction model only fits the initial data points of  $\text{PuO}_2^+$  at 80 °C with a rate constant of 30 day<sup>-1</sup>. As time progresses, Pu concentrations at 80 °C decreased. The decrease may reflect slow sorption to container walls, sorption to the dialysis membrane, and/or oxidation/reduction of Pu(V). This data could be fit with a first order reaction followed by kinetically controlled sorption process (Eq. 8-2 and Eq. 8-3) (Fig. 8-3b). All fitted rate constants are listed in Table 8-1. The fitted rate constants indicate that diffusion of aqueous species across the dialysis membrane will occur on timescale of  $\ll 1$  day.

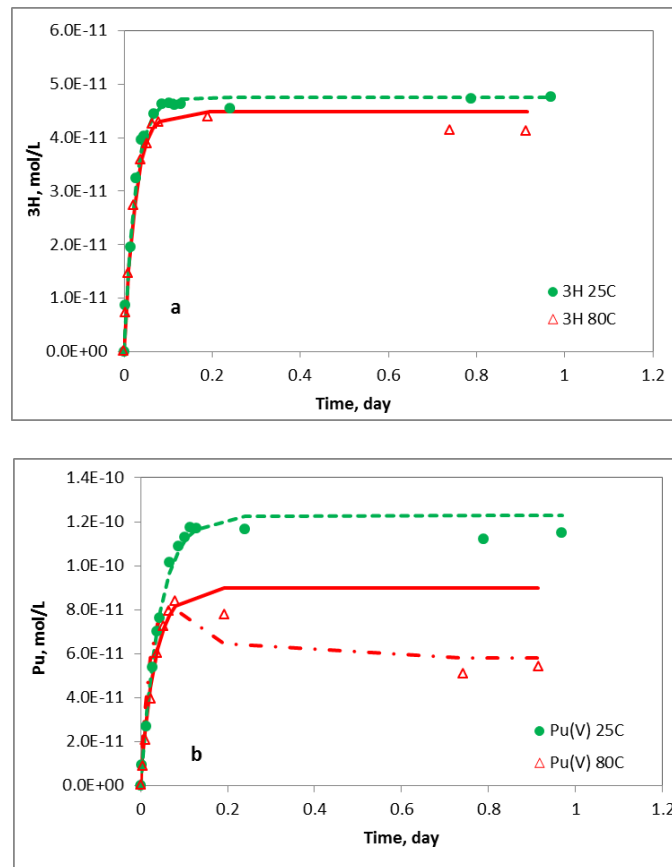


**Figure 3.** Diffusion of (a)  $^3\text{H}$  and (b)  $\text{Pu(V)}$  as function of time (Solid circles= $25^\circ\text{C}$  and open triangles= $80^\circ\text{C}$ ). Dash ( $25^\circ\text{C}$ ) and solid lines ( $80^\circ\text{C}$ ) are fitted curves using Equation 8-7. The dash-dotted line ( $\text{PuO}_2^+$  at  $80^\circ\text{C}$ ) is fitted by including a kinetic sorption process..

### Kinetics of Intrinsic Pu Colloid Dissolution

In these experiments (Exp. 1-3, 5-7 in Table 8-1), intrinsic Pu colloids were placed inside the dialysis bag, which was suspended in a clay suspension. Small aliquots of the clay suspension outside dialysis bag were taken as function of time and concentrations of total and aqueous Pu was monitored. If the total Pu concentration in the clay suspension is used to evaluate the system, then the system can be simplified to containing only two processes (dissolution and diffusion). Assuming 1<sup>st</sup> order rates for Pu colloid dissolution and diffusion, the kinetics can be described by two first order reactions in sequence (Lasaga, 1998a):

$$C_{out} = C^0 \left[ 1 + \frac{k_1 \exp(-k_2 t) - k_2 \exp(-k_1 t)}{k_2 - k_1} \right] \quad (8-8)$$

where  $C_{out}$  in  $\text{mol L}^{-1}$  represents the total Pu concentration in the clay suspension as a function of time ( $t$ ), and  $k_1$  and  $k_2$  are first order rate constants representing dissolution and diffusion. In the case where rate constants  $k_1$  and  $k_2$  differ by orders of magnitude, the rate-limiting process can be identified and the model can be further simplified to a first order rate model. Equations (8-7) and (8-8) provided equivalent quality of fits to the

data and suggests that the dissolution process is the rate-limiting step. The rate constants ranged from 0.025-0.40 day<sup>-1</sup> at 25 °C and 0.15-0.30 day<sup>-1</sup> at 80 °C, one to two orders of magnitude lower than the rate constants determined in the diffusion experiments. The experimental data are plotted in Fig. 8-4 and the rate constants are summarized in Table 8-1. Dissolution of minerals with low solubility is more likely to be controlled by reactions at sites on the surface rather than material transport, either in aqueous solution or through protective surface layers (Berner, 1981). As PuO<sub>2</sub> is a low solubility solid phase, our results are consistent with this interpretation.

Our results also show that the dissolution rates vary with the initial Pu colloids concentration and temperature. We will discuss temperature effects in a later section. In a heterogeneous system and at constant pressure and temperature, the overall dissolution rate of a metal oxide can be described as the sum of the rates of proton-promoted, hydroxide-promoted, ligand-promoted and reductant or oxidant-promoted, if any redox reaction involves in the dissolution. In other words, the dissolution rate is actually the sum of all the parallel dissolution rates of different metal centers (Stumm, 1997). We cannot distinguish between these processes here. However, the dissolution rate clearly increases with the intrinsic Pu colloid concentration, as would be expected for a surface-controlled dissolution process.

In the high colloid concentration samples, the overall rate may decrease significantly as the system reaches equilibrium (Lasaga, 1981; Lasaga and Luttge, 2004). The impact of solution saturation can explain the decrease in kinetic constant obtained in the highest Pu concentration experiment at 80 °C (Experiment 7, Table 8-1). The result also implies that the solubility of Pu colloids may be lower at elevated temperatures.

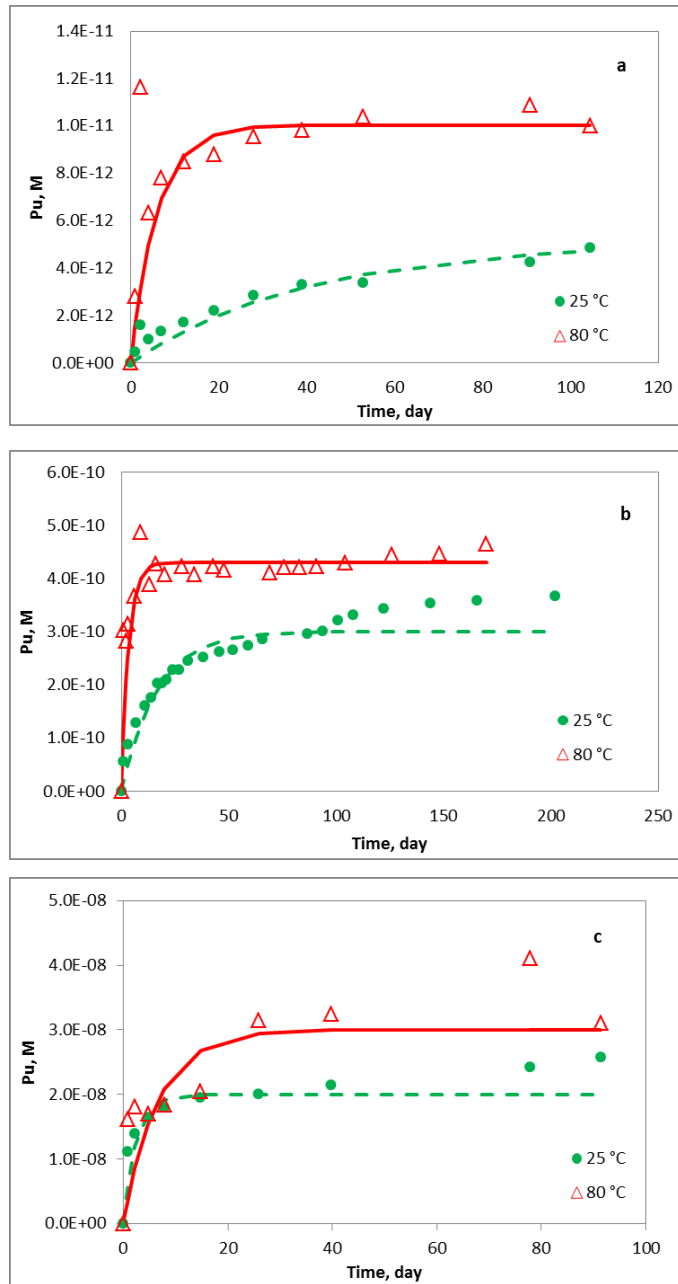


**Figure 8-4.** Dissolution and diffusion of Pu colloids in the presence of clay at 25 and 80 °C. Solid circles (25 °C) and open triangles (80 °C) are the experimental data points. Dash (25 °C) and solid lines (80 °C) are fitted curves using psuedo<sup>1<sup>st</sup></sup> order reaction model. Initial Pu colloids concentrations were 4a:  $1.1 \times 10^{-11} \text{ mol L}^{-1}$ ; 4b:  $9 \times 10^{-10} \text{ mol L}^{-1}$ ; 4c:  $2 \times 10^{-7} \text{ mol L}^{-1}$

### Sorption Kinetics in the Aqueous Pu(IV)-Montmorillonite System

Four experiments (Exp. 9, 10, 12, 13) were performed using aqueous Pu(IV) instead of intrinsic Pu colloids. The purpose of these experiments was to investigate Pu speciation effects on the kinetics. The experimental data are plotted along with fitting curves in Fig. 8-5 and the obtained rates constants are listed in Table 8-1. The fast rates ( $30 \text{ day}^{-1}$ ) observed at  $25 \text{ }^\circ\text{C}$  suggest that these experiments were diffusion controlled and that the rate of aqueous Pu(IV) sorption to montmorillonite was much faster (Begg et al., 2013b). However, the rate constants obtained from the  $80 \text{ }^\circ\text{C}$  experiments (Exp. 12 and 13) were much lower ( $0.15\text{-}0.2 \text{ day}^{-1}$ ) and similar to those obtained from intrinsic Pu colloid-montmorillonite experiments. In fact, these rate constants are 200X slower than the ones observed at  $25 \text{ }^\circ\text{C}$ . This observation suggested that aqueous Pu(IV) species formed intrinsic Pu colloids or  $\text{PuO}_2$  solids at  $80 \text{ }^\circ\text{C}$  at the start of the experiment. Once these intrinsic Pu colloids formed inside the dialysis bag, they slowly dissolved and diffused across the membrane. Thus, at  $80 \text{ }^\circ\text{C}$ , aqueous Pu(IV) initially formed intrinsic Pu colloids which then slowly dissolved, and aqueous Pu species diffused, and formed stable Pu-clay pseudo-colloids. Hydrolysis of Pu(IV) is endothermic and, as a result, high temperatures will favor the formation of intrinsic Pu colloids (Cleveland, 1979). In addition, the ionization constant of water,  $K_w$ , increases with temperature which can lead to a 30X increase in hydroxide concentration at pH 8 between 25 and  $80 \text{ }^\circ\text{C}$ . This will also enhance  $\text{Pu}^{4+}$  hydrolysis. Endothermic hydrolysis behavior of aqueous Pu and other actinide species has been reported in numerous studies (Altmaier et al., 2013; Rao et al., 2004; Rao et al., 2011; Runde et al., 2002).

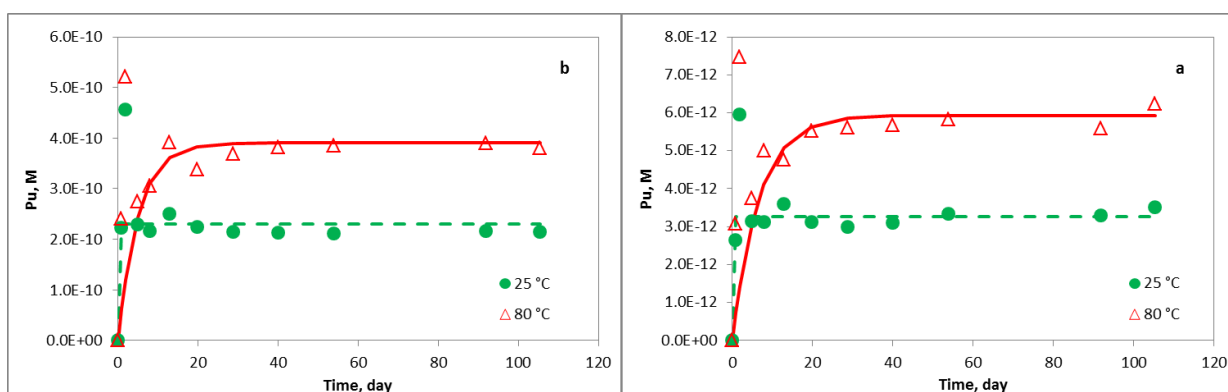
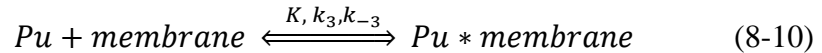
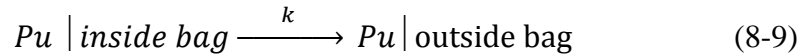


**Figure 8-5.** Kinetics of aqueous Pu(IV)-montmorillonite system at temperatures 25 and  $80 \text{ }^\circ\text{C}$ . Solid circles ( $25 \text{ }^\circ\text{C}$ ) and open triangles ( $80 \text{ }^\circ\text{C}$ ) are the experimental data points. Dash ( $25 \text{ }^\circ\text{C}$ ) and solid lines ( $80 \text{ }^\circ\text{C}$ ) are fitted curves using 1<sup>st</sup> order kinetic model. Initial Pu colloids concentrations 5a:  $6 \times 10^{-12} \text{ mol L}^{-1}$ , 5b:  $6.2 \times 10^{-10} \text{ mol L}^{-1}$ .

### Kinetics in the Absence of Montmorillonite

Four experiments (exp. 4, 8, 11, 14) using both intrinsic Pu colloids and aqueous Pu(IV) as were performed in the absence of a montmorillonite clay suspension. These experiments served as control experiments to evaluate the sorption of Pu to the container walls, dialysis membrane and other materials. The experimental data are plotted along with fitting curves in Fig. 8-6. At 25 °C, Pu concentrations in the solution outside of the dialysis bag were initially higher than at 80 °C, and then decreased over time, indicating there was significant sorption to the dialysis bag and/or container wall over time. To first order, the processes in this system can be described as a 1<sup>st</sup> order reaction followed by a sorption reaction:



The Pu concentration outside of the dialysis bag as a function of time is governed by Equation 8-11:

$$C_{out} = C^0 \left[ 1 - \exp(-kt) - \frac{k_3}{k_3 + k_{-3}} \left( 1 + \frac{k \exp(-(k_3 + k_{-3})t) - (k_3 + k_{-3}) \exp(-kt)}{k_3 + k_{-3} - k} \right) \right] \quad (8-11)$$

where  $k$  represents kinetic constant of either PuO<sub>2</sub> dissolution or aqueous Pu(aq) diffusion across the membrane;  $K = k_3/k_{-3}$  is sorption equilibrium constant, and  $k_3$  and  $k_{-3}$  are the sorption and desorption rate constants.

Table 8-1 lists the curve fitting results and shows that rate constants are consistent with the ones obtained from dissolution or diffusion experiments depending upon Pu initial speciation and experimental temperatures. In the intrinsic Pu colloid –buffer solution system (exp. 4 and 8), rate constants were 0.06 and 0.3 day<sup>-1</sup> for experiments performed at 25 and 80 °C, respectively. These values match  $k_1$  values obtained in the intrinsic Pu colloid – montmorillonite experiments (exp. 2 and 6), indicating that kinetics in the intrinsic Pu colloid - buffer solution system was governed by the PuO<sub>2</sub> dissolution. In the aqueous Pu(IV)-buffer solution system (exp. 11 and 14), the rates constants were 30 and 0.3 day<sup>-1</sup> in the 25 and 80 °C experiments, respectively. The 30 day<sup>-1</sup> rate constant matches aqueous Pu(IV) diffusion rate constants obtained from Exp. 9 and 10, indicating that the diffusion process was controlling the system. Thus, we can conclude that the presence of clay impacts neither diffusion rates of Pu species nor dissolution rates of intrinsic Pu colloids. At elevated temperature, the 0.3 day<sup>-1</sup> rate constant matches those obtained from intrinsic Pu colloid dissolutions experiments with or without clay (Exp. 6 and 8), suggesting that aqueous Pu(IV) underwent fast hydrolysis to form intrinsic Pu colloids, whose dissolution became a rate-limiting step governing the observed kinetics. Although the presence of clay doesn't affect the kinetics of these systems, it stabilizes Pu and increased total amount of Pu in the solution phase (see Table 1 for column of %Pu in solution phase outside of dialysis bag to compare exp. 2 with 4, exp. 6 with 8, exp. 9 with 11 and exp. 12 with 14).

Our results show that there is moderate sorption for Pu to the container walls and dialysis membrane and the sorption equilibrium constant,  $K$ , ranges from 0.067 at 80 °C to 160 at 25 °C. The sorption of Pu to these materials appears to be stronger at 25 °C than that at 80 °C. Pu speciation may have affected this apparent sorption behavior. Pu oxidation state analysis using solvent extraction indicated that a much higher fraction of aqueous Pu(IV) existed in the intrinsic Pu colloid suspension at 25 °C than that at 80 °C (see section “ $K_d$  of Pu-clay and the thermodynamics” for more details), thus stronger sorption is expected from Pu(IV) species at 25 °C.

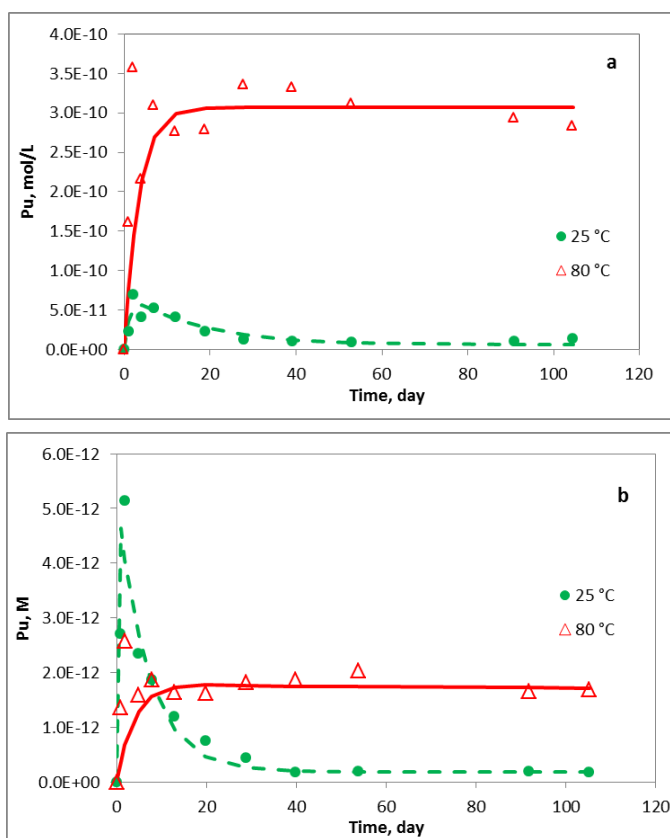


**Figure 8-6.** Kinetics of Pu colloids and aqueous  $\text{Pu}^{4+}$  in the absence of montmorillonite at temperatures 25 and 80 °C. Solid circles (25 °C) and open triangles (80 °C) are the experimental data points. Dash (25 °C) and solid lines (80 °C) are fitted curves using kinetics model pseudo<sup>1<sup>st</sup></sup> order intermediate with equilibrium. 6a: Pu colloids-buffer systems,  $C^0 = 9.13 \times 10^{-10}$  mol/L; 6b: aqueous Pu(IV)-buffer systems,  $C^0 = 6.52 \times 10^{-12}$  mol/L.

## Temperature Effects

High temperature can enhance Pu(IV) hydrolysis as the process is endothermic (Altmaier et al., 2013; Cleveland, 1979). In addition, a significant increase in water ionization due to decreasing in  $pK_w$  ( $\sim 12.50$ ) at 80 °C also drives reaction towards Pu(IV) hydrolysis. As a result, the solubility of intrinsic Pu colloids under our experimental conditions decreased at higher temperature. A Pu(IV) solubility decrease in J-13 and UE-25p #1 groundwaters in the vicinity of Yucca Mountain, NV at elevated temperatures has also been reported despite possible existence of higher oxidation states of Pu(V, VI) and/or multi solid phases controlling Pu solubility (Efurd et al., 1998; Nitsche et al., 1993; Nitsche et al., 1994; Runde et al., 2002).

In general, the overall process of dissolution of a solid in an aqueous solution contains two essential steps: various chemical reactions occurring at the solid surface and the transport of dissolved species to and from the surface. The kinetics of the dissolution can be controlled by surface chemical reactions, transport of soluble species to and from the surface or a combination of both processes (Berner, 1981). The values of the dissolution activation energy ( $E_a$ ) not only provide very important temperature dependence of the rate of dissolution, but also offer important clues to the dissolution mechanisms. According to Lasaga (Lasaga, 1998b), for mineral dissolutions in water phase, typical values of  $E_a < 21 \text{ kJ mol}^{-1}$  were for transport-controlled processes and  $E_a > 42 \text{ kJ mol}^{-1}$  for the processes controlled by chemical reactions on solid surfaces. Intermediate values may be found for mixed-control (transport and surface) of the dissolution reaction (Hocsman et al., 2006). The relationship between a rate constant and the activation energy is described by Arrhenius equation:

$$k_1 = A_{diss} \exp\left(-\frac{E_a}{RT}\right) \quad (8-12)$$

and  $E_a$  can be calculated using rate constants at two different temperatures:

$$\ln \left[ \frac{k_1(T_2)}{k_1(T_1)} \right] = -\frac{E_a}{R} \left( \frac{1}{T_2} - \frac{1}{T_1} \right) \quad (8-13)$$

where  $A_{diss}$  is the pre-exponential factor, which is a constant for a given reaction,  $k_1(T_1)$  and  $k_1(T_2)$  are dissolution rate constant  $k_1$  at absolute temperatures  $T_1$  and  $T_2$  in kelvin, respectively,  $E_a$  is the activation energy for the reaction, and  $R = 8.314 \text{ J mol}^{-1}$  is the gas constant.

We used  $k_1$  values obtained from low Pu colloids concentration experiments, in which the systems were far from solution equilibrium (exp. 1, 2, 5, 6), to calculate apparent  $E_a$ . The average of apparent activation energy ( $E_a$ ) for  $\text{PuO}_2$  colloids dissolution process was  $28 \text{ kJ mol}^{-1}$ . This intermediate value may indicate that the intrinsic Pu colloid dissolution process is controlled by a combination of both surface reaction and mass transport at the surface (Hocsman et al., 2006).

### Temperature Dependence of Pu Sorption

The  $K_d$  values for Pu-montmorillonite can be calculated using the measured Pu activity on montmorillonite and in the supernatant. The resulting  $K_d$  values from the various experiments are plotted in Figure 8-7. Many factors including Pu speciation, oxidation state, and temperature can impact  $K_d$  values. Figure 7 indicates that at the same temperature,  $K_d$ s obtained from intrinsic Pu colloid experiments tend to have lower values than those obtained from aqueous Pu(IV) experiments. Furthermore,  $K_d$ s in intrinsic Pu colloids experiments increased over time to approach values from aqueous Pu(IV) experiments. This phenomenon can be explained by the change of Pu oxidation states during sorption processes. Pu(V) is the predominant species formed as a result of dissolution of intrinsic Pu colloids and this oxidation state exhibits a weaker sorption to clay relative to Pu(IV) (Altmaier et al., 2013; Begg et al., 2014; Neck et al., 2007a; Neck et al., 2007b). Over time, Pu(V) tends to reduce to Pu(IV) on the montmorillonite surface which leads to an increasing  $K_d$  over time (Begg et al., 2013b). Figure 7 also indicates that the  $K_d$  increases with temperature which implies that the sorption process is endothermic and that higher temperatures lead to greater Pu sorption to montmorillonite.

The van't Hoff equation as expressed in Eq. 8-14 and Gibbs free energy as described in Eq.8-15 can be used to calculate the changes in enthalpy ( $\Delta H^\circ$ , J mol<sup>-1</sup>), entropy ( $\Delta S^\circ$ , J mol<sup>-1</sup> K<sup>-1</sup>) and Gibbs free energy ( $\Delta G^\circ$ , J mol<sup>-1</sup>) of Pu-clay sorption at standard atmospheric pressure:

$$\ln K_d = -\frac{\Delta H^\circ}{RT} + \frac{\Delta S^\circ}{R} \quad (8-14)$$

$$\Delta G^\circ = \Delta H^\circ - T\Delta S^\circ \quad (8-15)$$

where T is the absolute temperature in kelvin and R = 8.314 J mol<sup>-1</sup> K<sup>-1</sup> is the gas constant. The calculated thermodynamic parameters are summarized in Table 8-2. The positive value of  $\Delta H^\circ$  (38 kJ mol<sup>-1</sup>) confirms endothermic nature of the Pu-clay sorption, and negative values of  $\Delta G^\circ$  indicate that the sorption reaction is spontaneous. A more negative value of  $\Delta G^\circ$  obtained from elevated temperature confirms that the Pu pseudo-colloids are more stable at higher temperature. However, as described in the following paragraph, the thermodynamic parameters derived from these experiments are only approximate since redox conditions, pH, and Pu oxidation states were not strictly controlled.

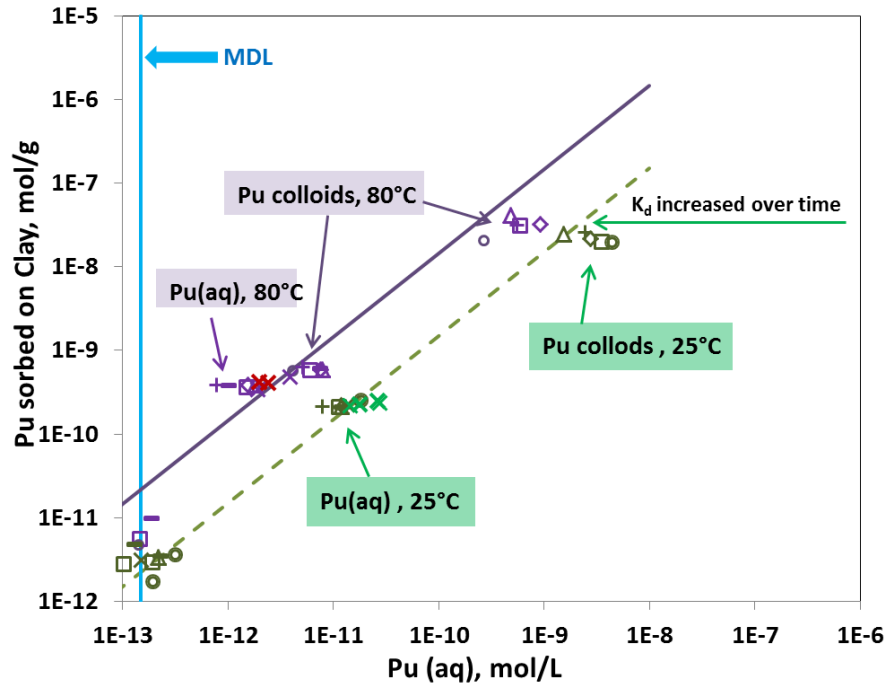


**Figure 8-7.** Pu sorption data from both colloidal and aqueous Pu(IV) experiments with montmorillonite at 25 and 80 °C. Dash (25 °C) and solid lines (80 °C) represent the average  $K_d$  values at each temperature.

At the termination of the experiments, Pu oxidation state distribution in the supernatants of both intrinsic Pu colloids and Pu-clay pseudo colloids were analyzed using solvent extraction (Figure 8-8). We show that in the Pu-clay suspension, higher oxidation states  $\text{PuO}_2^+$  and  $\text{PuO}_2^{2+}$  were the predominant species at 25 °C, while  $\text{Pu}^{4+}$  was more prevalent at 80 °C (Fig. 9a). This suggests that elevated temperatures led to more reducing solution conditions. This may, in part, explain the higher Pu  $K_{ds}$  at 80 °C. Although the Pu oxidation state distribution changed at different temperatures and colloidal solutions, and they made significant impact on the Pu sorption behavior, the processes controlling Pu speciation in solution or on mineral surface is not yet clear and requires further investigation.

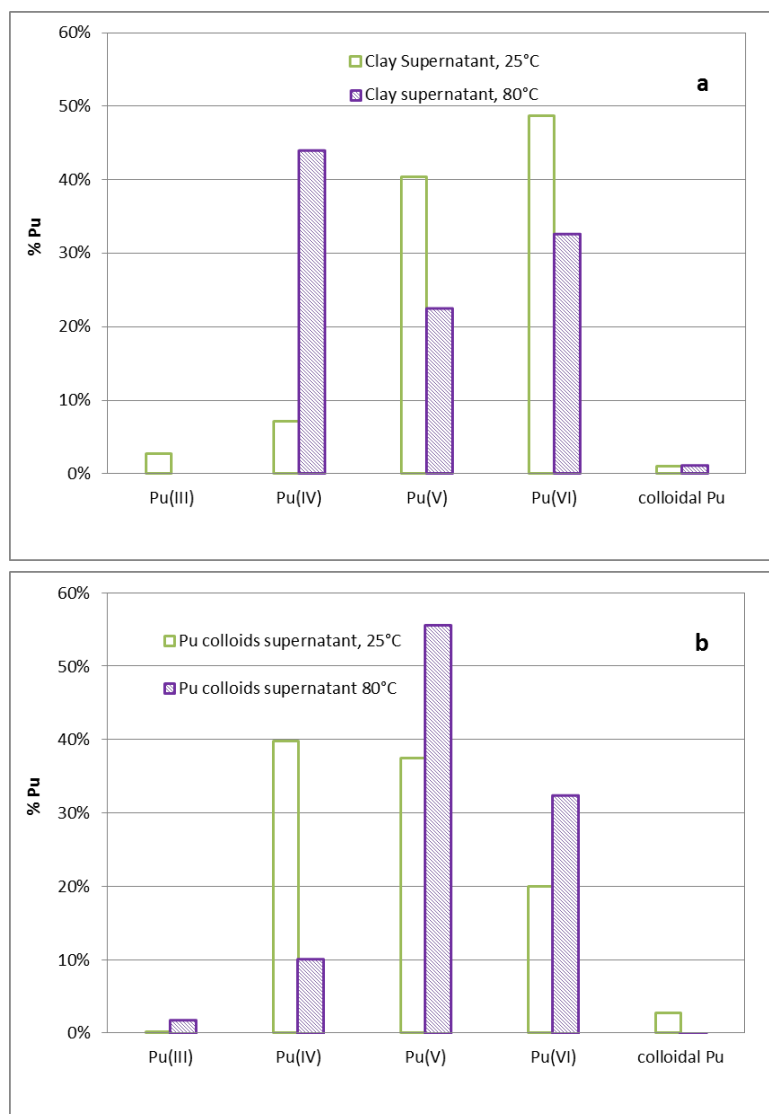


**Figure 8-8.** Pu oxidation states distributions at 25 °C (open bars) and 80 °C (filled bars). 9a. Clay supernatant outside of dialysis bag; 9b. Supernatant of Pu colloidal solution inside dialysis bag.

**Table 8-2.** Thermodynamic parameters for sorption of Pu onto montmorillonite at 25 and 80 °C.

Temperature	Average $K_d$ (mL/g)	T (Kelvin)	$\Delta H^\circ$ , kJ/mol	$\Delta S^\circ$ , kJ/mol K	$\Delta G^\circ$ , kJ/mol
25 °C	1.70E+04	298.15	38.0	0.21	-24.1
80 °C	1.85E+05	353.15	38.0	0.21	-35.6

#### 8.1.4 Conclusions

A study of the dissolution of intrinsic Pu colloids in the presence of montmorillonite at different temperatures was successfully accomplished using a novel experimental setup containing a dialysis device. This device enables us to separate two solid phases, but let them interact with each other via aqueous Pu ions. Kinetics of a series processes involved in intrinsic Pu colloid dissolution was modeled using 1<sup>st</sup> order reactions to compare the rate constant of different processes. We show that the kinetic constants for dissolution were one to two orders of magnitude lower than that of diffusion of aqueous Pu species in the system. Therefore the dissolution processes was the rate-limiting step. Although the presence of clay changes neither the colloids dissolution nor diffusion rates of Pu, it can stabilize dissolved Pu species and drive intrinsic Pu colloid dissolution and the formation of more stable Pu pseudo-colloids. Temperature enhances dissolution of intrinsic Pu colloids by overcoming a moderate activation energy (28 kJ mol<sup>-1</sup>). Our thermodynamic study shows that the sorption of Pu on montmorillonite is endothermic as a positive change in enthalpy for the sorption has been obtained. The affinity of Pu for the clay increases with increasing temperature, resulting in higher  $K_d$  at elevated temperature. The negative values of change of Gibbs free energy for Pu-clay sorption confirm that sorption of Pu onto clay occurs spontaneously and Pu pseudo-colloids are thermodynamically quite stable at both temperatures of 25 to 80 °C.

Although the fact that intrinsic Pu colloids tend to dissolve in the presence of montmorillonite may limit the migration of intrinsic Pu colloids, the subsequent formation of thermodynamically more stable Pu pseudo-colloids can play important role in Pu transport in the environment over significant temporal and spatial scales.

## 8.2 STABILITY OF PLUTONIUM INTRINSIC COLLOIDS IN THE PRESENCE OF CLAY AT ELEVATED TEMPERATURES: INFLUENCE OF MORPHOLOGY ON PuO<sub>2</sub> REACTIVITY

### 8.2.1 Introduction

PuO<sub>2</sub> dissolution is an important issue with respect to many fields including Pu transport behavior in the environment, storage and treatment of radioactive wastes from both laboratories and industries, and in reprocessing of spent nuclear fuels. From an environmental perspective, plutonium (Pu) is expected to be one of the dominant long-term dose contributors for high-level nuclear waste repositories because of its toxicity, long half-life (<sup>239</sup>Pu half-life = 24,100 yrs.) and large inventory. In an effort to design a long-term barrier system for the safe disposal of nuclear waste, it is important to understand how Pu may migrate in the natural system once it breaches the waste package. Determining the fate and transport of Pu depends both on the initial chemical form at the source and the geochemistry and hydrology of the source location and along the down-gradient transport paths. Colloid-facilitated transport of low levels of Pu in both groundwater and surface water has been documented at several DOE sites (Dai et al., 2005; Kersting et al., 1999; Santschi et al., 2002a). Pu sorbed to iron oxide colloids has also been detected over 4 km from its original source in Mayak, Russia (Novikov et al., 2006). These field studies indicate that the Pu associated with mobile colloids has moved on the scale of kilometers, yet the mechanisms are not well understood. Without a conceptual understanding of the dominant processes and a quantitative understanding of the relevant reaction chemistry, current transport models cannot effectively predict Pu concentrations and transport rates in the field.

Pu can be associated with the colloidal fraction of groundwater in two different forms. Pu can migrate as either an intrinsic Pu colloids or sorb on to naturally occurring inorganic, organic or microbial species as pseudo-colloids. When concentrations of Pu exceed its solubility, Pu can hydrolyze to form intrinsic Pu colloids (Cleveland, 1979). In the case of Pu(IV), the solubility-limiting concentration may be as low as  $\sim 10^{-10}$  M under ambient conditions (Neck et al., 2007b). The transport of intrinsic Pu colloids will be controlled by their stability (both physical and chemical). In contrast, if concentrations of Pu ions are below their solubility, Pu ions can sorb on to naturally occurring colloidal forms including organic, inorganic, or microbial species resulting in the formation of Pu pseudo-colloids. The transport of Pu pseudo-colloids is determined by Pu sorption/desorption rates on the colloidal materials under given conditions. Efforts to model the transport of Pu from a near-field to a far-field environment are currently limited due to the lack of understanding of how intrinsic Pu colloids will persist along a changing geochemical flow path away from a high-level nuclear waste repository where intrinsic Pu colloids are most likely to form (Kersting, 2013).

In addition to a broad range of geochemical processes and conditions (e.g. temperature, Eh / pH, isotopic composition) that can affect the overall stability of intrinsic Pu colloids once they are formed, the initial formation conditions also play a critical role in their

long-term stability. The morphology of a solid phase including crystal structure, the crystallite size and aggregation is among the important factors that greatly influences the reactivity of the solid. Previous investigations on intrinsic Pu colloids showed that the ultimate morphology is strongly dependent on the conditions of formation and age of solution (Walther and Denecke, 2013). In particular, the degree of crystallinity, which can be affected by aging, temperature and original formation conditions, will affect the stability of intrinsic Pu colloids (Farr et al., 2004; Haire et al., 1971; Rai and Ryan, 1982; Runde et al., 2002). Published thermodynamic data for Pu(IV) oxide and hydroxide show a range of  $pK_{s,0}$  for  $\text{PuO}_2(\text{hyd})$  and  $\text{PuO}_2(\text{cr})$  from 50.2 to 58.8 and 60.2 to 64.0, respectively (Lemire, 2001). These data illustrate how crystallinity can have a significant impact on the solubility and stability of  $\text{PuO}_2$ .

In the current study, we performed long-term dissolution experiments of three different forms of intrinsic Pu colloids in the presence of montmorillonite at two different temperatures. All three intrinsic Pu colloids used were formed under elevated temperature conditions. The results are compared to experiments performed with hydrous Pu dioxide prepared in a weak alkaline solution at room temperature and reported in Section 8.1 of this report. Scanning electron microscopy (SEM) and transmission electron microscopy (TEM) were used to characterize the morphology of intrinsic Pu colloids including crystal structure, orientations of single crystallites within  $\text{PuO}_2$  aggregates and particle sizes. The combination dissolution experiments and morphology characterization of intrinsic Pu colloids was used to identify the impact of  $\text{PuO}_2$  formation conditions, morphological characteristics, and crystallinity on the stability of  $\text{PuO}_2$  solid phases.

## 8.2.2 Material and Methods

All reagents were of analytical grade or better and used as received. De-ionized water from a Barnstead Milli-Q Water (MQW) purification system (resistivity: 18.2 megaohm-cm) was used for all procedures and solution preparation.

### Calcination of High-Fired $^{239}\text{Pu}$ Oxides

Reactor fuel grade Pu oxide was used to make the high-fired Pu oxides. The Pu isotopic ratios in mass percentage for  $^{238}\text{Pu}$ ,  $^{239}\text{Pu}$ ,  $^{240}\text{Pu}$ ,  $^{241}\text{Pu}$  and  $^{242}\text{Pu}$  were 0.046%, 88.0%, 11.6%, 0.25% and 0.065%, respectively. The starting material was dissolved in concentrated nitric acid containing a small admixture of HF. After filtering, Pu was converted to the +3 oxidation state using hydroxylamine ( $\text{NH}_2\text{OH}$ ) in dilute nitric acid. Pu(III) was then precipitated by the addition of oxalic acid to form Pu(III) oxalate. The precipitate was allowed to settle for 30-60 minutes, filtered, washed with DI water, alcohol, and then dried under vacuum at room temperature. The dried Pu(III) oxalate was then calcined at temperatures of either 300°C (high-fired  $\text{PuO}_2$  #1) or 800°C (high-fired  $\text{PuO}_2$  #2) to convert Pu(III) oxalate to  $\text{PuO}_2$ . To prepare samples for our dissolution experiments, the Pu dioxide powders were suspended in Milli-Q water, allowed to settle for 10 minutes. The supernatant, including  $\text{PuO}_2$  fines, was discarded. This Milli-Q water rinse was repeated three times. The Pu concentration of the two high-fired Pu dioxide suspensions was determined by  $^{241}\text{Pu}$  using beta liquid scintillation counting

(LSC). For logistical and safety reasons, the two high-fired Pu dioxides prepared in this manner were not colloidal sized. Grinding these samples to produce colloid-sized particles was not practical due to sample dispersal safety concerns. However, in this report, we refer to these samples as intrinsic Pu colloids.

### **Peptization of PuO<sub>2</sub> Colloidal Sols**

A <sup>242</sup>Pu stock solution consisting of alpha emitters <sup>238</sup>Pu, <sup>239</sup>Pu, <sup>240</sup>Pu, and <sup>242</sup>Pu with activity percentages of 15.8%, 0.062%, 5.0%, and 79.1%, respectively, was purified using an AG1x8 100-200 mesh anion exchange resin column. The intrinsic Pu colloids were prepared by heating  $1.6 \times 10^{-3}$  M Pu(IV, aq) in 0.1 M HNO<sub>3</sub> solution on a hotplate at 60-80 °C for 30 min. The dark brown Pu(IV) solution turned to a green color immediately upon heating. The formation of intrinsic Pu colloids was confirmed by UV/VIS. The fraction of soluble Pu in the intrinsic Pu colloid solution was determined to be < 0.2% using a 3kDa NMWL (Nominal Molecular Weight Limit) ultra-centrifugal filter. After aging for two years, a dilution of the intrinsic Pu colloids (Pu concentration of  $3 \times 10^{-5}$  M) was made in pH 8 buffer solution (5 mM NaCl/0.7 mM NaHCO<sub>3</sub>) and used in our experiments.

### **Precipitation of Intrinsic Pu Colloids in an Alkaline Solution**

A relatively pure alpha-emitting <sup>238</sup>Pu stock solution was used in low- and intermediate-Pu-concentration experiments. The isotopic ratios in mass percentage for <sup>238</sup>Pu, <sup>239</sup>Pu, <sup>240</sup>Pu, and <sup>241</sup>Pu were 76.83%, 21.03%, 2.01%, and 0.142%, respectively. The major isotope contributing to alpha activity in this stock was <sup>238</sup>Pu (~99.9% by activity). Pu stock solution was purified using AG@1-×8 100-200 mesh anion exchange resin from Bio-Rad Laboratories, and filtered through an Amicon Ultra 0.5 mL centrifugal filter with membrane MWCO of 3 kDa from EMD Millipore. The intrinsic Pu colloids were prepared by neutralizing Pu(IV) stocks using NaOH solution and adjusting solution pH to pH 9–10. After aging for more than a week, the intrinsic Pu colloids were centrifuged at an RCF of  $9168 \times g$  for 1 hr, and the supernatant was removed. The intrinsic Pu colloid particle size cut-off based on centrifugation was 14 nm. The intrinsic Pu colloids were re-suspended in Milli-Q water. The intrinsic Pu colloid starting solutions were prepared by adding a spike of intrinsic Pu colloids into the pH 8 buffer solution without further pH adjustment. Pu concentrations in samples were analyzed by a PerkinElmer Tri-Carb 2900TR Liquid Scintillation Analyzer. The concentration of soluble Pu in the intrinsic Pu colloid starting solutions, measured in 3kDa NMWL filtrate were 1~3% of the total concentrations.

### **Preparation of Montmorillonite**

SWy-1 Montmorillonite from the Clay Minerals Society was used in our experiments. Detailed summary on the preparation of the homo-ionic Na-montmorillonite can be found in (Begg et al., 2013b), and then the prepared clay minerals were suspended in Milli-Q water and centrifuged to obtain the fraction of particle sizes from 50 nm to 2 microns (see detailed description in Section 8.1 of this report).

## Determinations of Pu Concentrations

Two different Pu sources ( $^{242}\text{Pu}$  and reactor fuel grade  $^{239}\text{Pu}$ ) were used in this study. For the intrinsic Pu colloids made from  $^{242}\text{Pu}$  stock solution, alpha liquid scintillation counting (LSC) was used to determine Pu concentrations. The reactor fuel grade Pu dioxide contained  $^{241}\text{Am}$ , the daughter of  $^{241}\text{Pu}$ , as a predominant alpha emitter, which contributed > 90% of the total alpha activity in the samples. It was not possible to use alpha LSC to quantify Pu concentrations in our dissolution experiments. Therefore, beta LSC was used to measure activity of  $^{241}\text{Pu}$  in samples, and Pu isotopic ratios were used to determine the total Pu concentrations in the samples. For beta LSC quantification, a  $^{241}\text{Pu}$  quenching curve was generated from a NIST traceable standard and used to determine the LSC counting efficiency for each sample.

## Dialysis Experiments

In the context of this report, we have chosen to refer to all solid phase plutonium oxides used in these experiments as intrinsic Pu colloids. As will be shown in the SEM images, some forms of plutonium oxides were not colloidal sized. In some cases, plutonium oxide aggregates were not colloidal-sized but the individual crystallites that formed the aggregates were colloidal-sized. Detailed morphological characterization of the various samples are provided in the following sections. However, in the discussion, we broadly define all plutonium oxides used in these experiments as intrinsic Pu colloids.

A total of 7 dialysis experiments were performed to investigate the stability of intrinsic Pu colloids in the presence of montmorillonite and compared to the results from previous experiments (see part I of the report). Experiments were performed at 25 °C (4 experiments) and 80 °C (3 experiments) to evaluate the effect of temperature on colloid stability of these intrinsic Pu colloids. The experimental conditions and parameters are listed in Table 8-3. All batch experiments were conducted in 450-mL Teflon jars with airtight closures. A sealed dialysis bag containing 15 mL of an intrinsic Pu colloid suspension was placed in the 250 mL of pH 8 montmorillonite suspension with a solid to liquid ratio of 1g : 1L. The 450-mL Teflon jars were submerged in 1-L Teflon containers filled with Milli-Q water to minimize evaporative losses and provide secondary containment to the radioactive samples. Over the course of the experiment, the 25°C samples were placed on a top-loading orbital shaker, and the 80 °C samples were submerged in a heated water bath (Innova 3100) and shaken at an orbital speed of 100 rpm. Pu concentrations in the clay suspension outside of dialysis bag were monitored as functions of time over a six-month or longer period. At each sampling interval, aliquots of the montmorillonite suspension were collected and analyzed for total Pu. At the termination of the experiments, total Pu concentrations in the clay suspensions were measured. The pH of the clay suspension was monitored and maintained at  $\text{pH } 8 \pm 0.5$  at all times.

**Table 8-3.** Conditions of intrinsic Pu colloid stability experiments at 25 and 80 °C.

Expt	Expt. Temp.	Pu oxides used	PuO <sub>2</sub> formed temperature	Initial Pu conc. inside dialysis bag	Pu upper limit in clay susp.	Montmorillonite suspension	MWCO
	°C		°C	mol L <sup>-1</sup>	mol L <sup>-1</sup>	g L <sup>-1</sup>	kDa
1	25	high-fired PuO <sub>2</sub> -1	calcined at 300	3.6×10 <sup>-6</sup>	2.7×10 <sup>-7</sup>	1	1000
2	25	high-fired PuO <sub>2</sub> -1	calcined at 300	2.2×10 <sup>-7</sup>	2×10 <sup>-8</sup>	1	500 -1000
3	25	high-fired PuO <sub>2</sub> -2	calcined at 800	1.1×10 <sup>-6</sup>	6×10 <sup>-8</sup>	1	1000
4	25	peptized PuO <sub>2</sub> -3	peptized in dilute acid at 70	3.9×10 <sup>-5</sup>	3.6×10 <sup>-6</sup>	1	500 -1000
5	80	high-fired PuO <sub>2</sub> -1	calcined at 300	4.9×10 <sup>-8</sup>	2.8×10 <sup>-9</sup>	1	1000
6	80	high-fired PuO <sub>2</sub> -2	calcined at 800	3.9×10 <sup>-6</sup>	2.2×10 <sup>-7</sup>	1	1000
7	80	peptized PuO <sub>2</sub> -3	peptized in dilute acid at 70	1.4×10 <sup>-6</sup>	8×10 <sup>-8</sup>	1	1000

## Instrumentation

Intrinsic Pu colloids and high-fired Pu oxides were characterized using scanning electron microscopy (SEM) and transmission electron microscopy (TEM) for their morphology, crystal structure and chemical composition. SEM analysis was performed using a JEOL 7401-F field emission scanning electron microscope equipped with an Everhart-Thornley secondary-electron detector and a solid state backscattered electron detector for imaging. The SEM is also equipped with an Oxford X-Max (80 mm<sup>2</sup>) silicon drift detector and Oxford Aztec software to perform X-ray energy dispersive spectroscopy (EDS) measurements of chemical elements. TEM was performed using a Philips CM300-FEG transmission electron microscope with a field emission electron gun operating at 300 kV. The CM300-FEG microscope is equipped with an Oxford X-ray detector for EDS measurements. Solution UV/Vis spectra were taken from Cary 500 Scan UV-Vis-NIR spectrophotometer. Liquid scintillation counting was performed on a PerkinElmer Tri-Carb 2900TR liquid scintillation analyzer.

## 8.2.3 Results and Discussion

### Characterization

SEM and TEM images of three different types of intrinsic Pu colloids prior to dissolution experiments were obtained to compare their morphologies and particle sizes. Figure 8-9a and 9c show general morphology of the intrinsic Pu colloid samples in low magnified SEM images. An average particle size of 4 μm was observed by SEM for the two high-fired samples. However, high-fired PuO<sub>2</sub>-1 contained a significant number of smaller particles that were submicron in sizes. It is observed that the variation of particle sizes was closely related to calcination temperatures (Fig. 8-9b and d). PuO<sub>2</sub> formed by calcination at lower temperature showed significant spreading of particle size distribution. However, the mass distributions of the PuO<sub>2</sub> as function of particles sizes

were not very sensitive to the calcination temperatures (Machuron-Mandard and Madic, 1996). Our observations are consistent with the findings reported by Machuron-Mandard and Madic. Both samples contain highly porous and layered square platelets. The higher magnified SEM images (Fig. 8-9b and d) show that these square platelets are polycrystalline in nature and consist of individual crystallites with size distribution range from a few nanometers to >300 nm. Sample PuO<sub>2</sub>-1 calcined at 300 °C shows a wide spreading grain size distribution (Fig. 8-9b) ranging from a 4 to > 300 nm. The average particles size was estimated to be 5 nm for high-fired PuO<sub>2</sub>-1 due to predominance of particle sizes <10 nm. This estimation was based on size measurements for particles of >10 nm and area measurements for particles of <10 nm from SEM images. On the other hand, high-fired PuO<sub>2</sub>-2 calcined at 800 °C exhibits a much more uniform size distribution with majority of the crystallite sizes within a narrow range of 20-50 nm. The average particle size for high-fired PuO<sub>2</sub>-2 was measured to be 31 nm by SEM image analysis. Our TEM observations (not shown here) also confirmed this result.

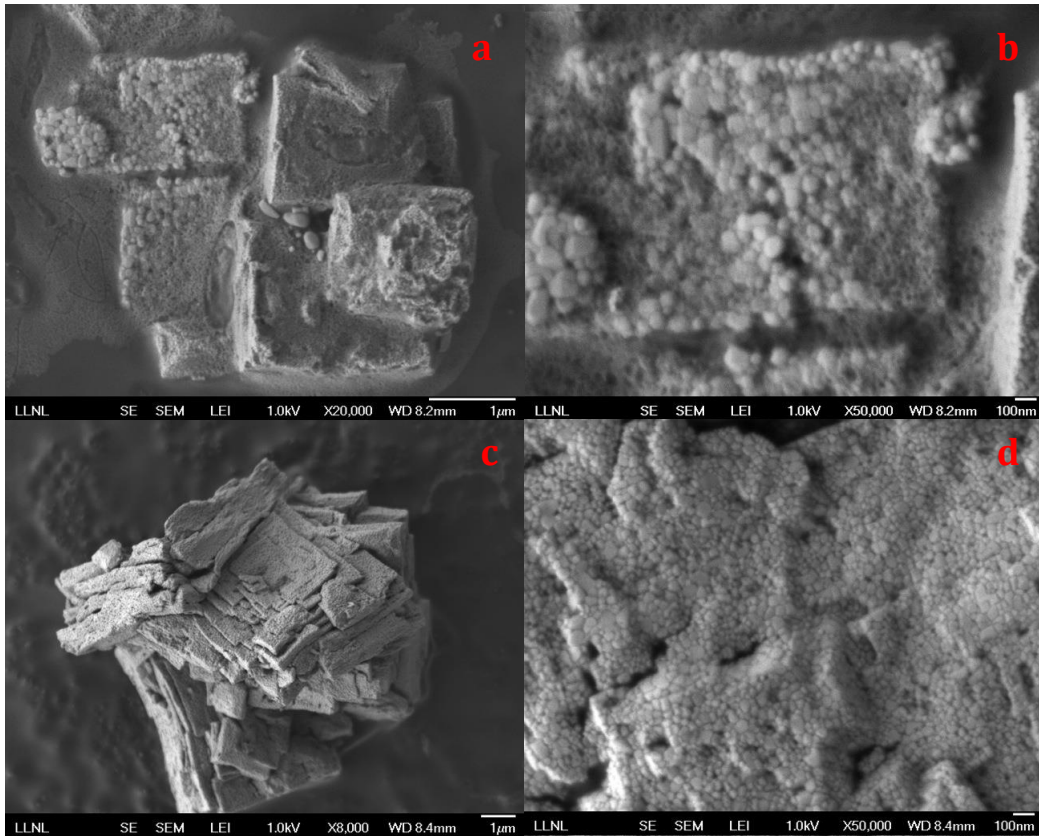


**Figure 8-9.** Secondary electron SEM observations of high-fired PuO<sub>2</sub> particles. a. PuO<sub>2</sub> calcined at 300 °C forming layered porous square platelets with uneven grain size distribution. b. High magnification image of PuO<sub>2</sub> calcined at 300 °C showing wide range of grain size distribution from few nanometers to > 100 nm. C. PuO<sub>2</sub> calcined at 800 °C forming layered porous square platelets with relative even grain size distribution. 1d High magnification image of PuO<sub>2</sub> calcined at 800 °C showing majority of grain sizes distribute between 20-50 nm.

Figure 8-10 shows transmission electron microscopy (TEM) observations of intrinsic Pu colloids prepared by either peptization of Pu hydroxide colloidal sol in 0.1 M HNO<sub>3</sub> solution or precipitation from weak alkaline solution of pH 9~10. The intrinsic Pu colloids peptized in dilute nitric acid solution are well defined spherical aggregates of PuO<sub>2</sub> single crystallites. The measured average size of the aggregates was 31 nm, while the measured average size of individual PuO<sub>2</sub> crystallites in each aggregate was 2.5 nm. The electron diffraction spectrum (EDS) of peptized intrinsic Pu colloids matched typical PuO<sub>2</sub> FCC crystal structure. Although the individual crystallites form rough outer surface of the aggregates, HRTEM image of one aggregate (Fig. 8-10b) reveals that individual crystallites fuse together and exhibit a preferential crystal structure orientation. This is the first time that we report the image of this quasi-single-crystal structure in intrinsic Pu colloids. This unique character may cause peptized PuO<sub>2</sub> aggregates to share some features of larger single crystals. On the other hand, intrinsic Pu colloids precipitated from alkaline solution flocculated in solution formed aggregates with poorly defined shapes (see Fig. 8-10c). These aggregates also consist of individual PuO<sub>2</sub> crystallites of sizes 2.5-4.5 nm (see Fig. 8-10d), however, the individual crystallites didn't show any preferred crystal structure alignment within the aggregates. Instead, they exhibit completely random orientations (Fig. 8-10d). Neither the freshly prepared nor the aged intrinsic Pu colloids prepared in a alkaline solution (up to 1 year) showed any change in their crystallite orientations. The various intrinsic Pu colloids used in these experiments have different particle sizes and ultimately different surface areas. Due to the health and safety concerns inherent in working with potentially dispersible Pu powders, the high-fired Pu oxides could not be ground to finer sizes. The surface area of these Pu oxides/colloids was estimated based on the sizes of crystallites as well as the sizes of the aggregates and the data are tabulated in Table 8-4. It is noticeable that specific crystallite surface area of samples PuO<sub>2</sub>-1, PuO<sub>2</sub>-3 and PuO<sub>2</sub>-4 were similar within a range of 104 to 227 m<sup>2</sup> g<sup>-1</sup> and the ones for PuO<sub>2</sub>-2 was one order of magnitude smaller. On the other hand, samples PuO<sub>2</sub>-1 and 2 have same specific particle surface area of ~0.1 m<sup>2</sup>/g<sup>-1</sup>, while samples PuO<sub>2</sub>-3 and 4 have similar specific particle surface area around ~20 m<sup>2</sup> g<sup>-1</sup>. Due to limited quantities of the materials, BET measurements were not performed for these tested samples. However, PuO<sub>2</sub> surface areas have been measured previously and the measured values are in the range of 1.2 to 12.3 m<sup>2</sup> g<sup>-1</sup> (Machuron-Mandard and Madic, 1996) at calcination temperatures from 1050 to 450 °C, and 5 to 41 m<sup>2</sup> g<sup>-1</sup> for PuO<sub>2</sub> treated at 1750 °C (Mewhinney et al., 1987), respectively. These measured specific areas are equivalent to particle size ranges of 43 ~ 430 and 13 ~ 100 nm, respectively, which more or less reflect the sizes of Pu oxides aggregates used in our study.

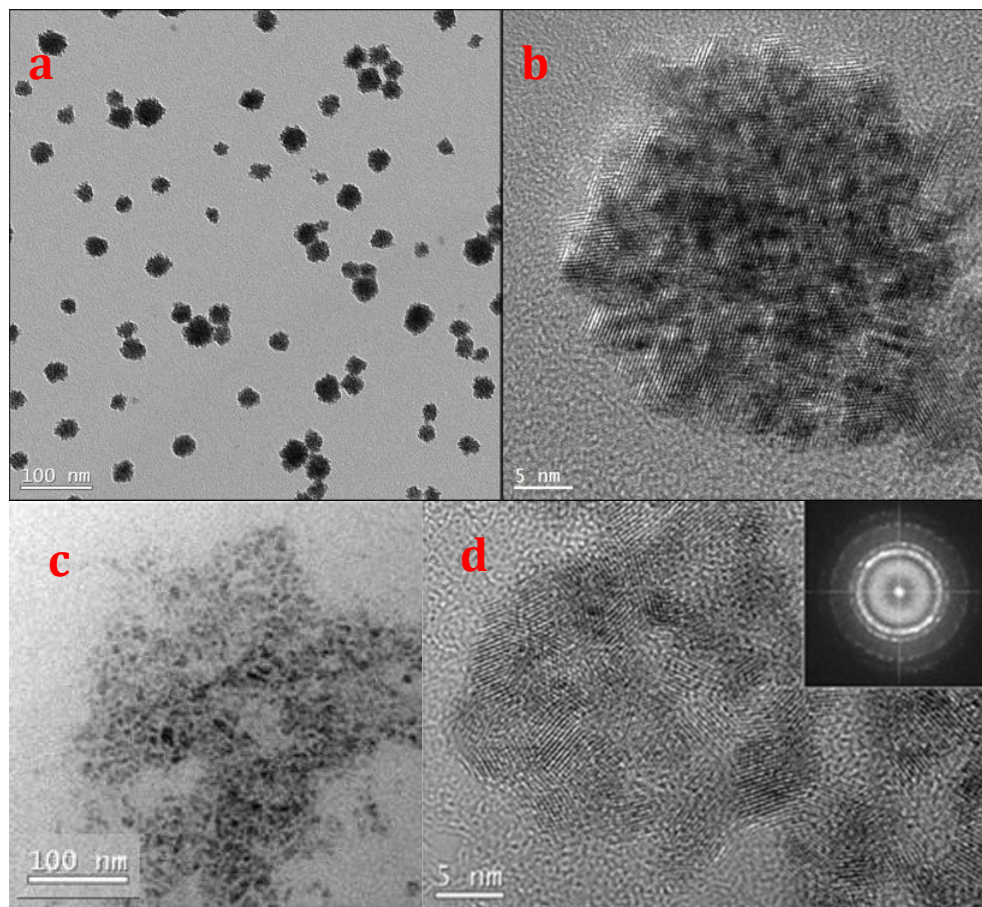


**Figure 8-10.** Bright-field TEM images of Pu-colloids. a. Dispersed spherical PuO<sub>2</sub> clusters formed by peptization in dilute nitric acid solution. b. HRTEM images of one peptized PuO<sub>2</sub> polycrystalline cluster with 2-3 nm sized individual crystallites. These individual crystallites exhibit a preferential crystal structure orientation. c. Flocculated PuO<sub>2</sub> with irregular shape formed by precipitation of Pu(IV) in weak alkaline solution. d. HRTEM images of one precipitated PuO<sub>2</sub> particle showing polycrystalline structure with 2-5 nm individual crystallites. Individual crystallites exhibit random crystal structure orientation. The inset electron diffraction pattern shows FCC crystal structure of PuO<sub>2</sub>.

**Table 8-4.** Particle sizes and surface area of intrinsic Pu colloids and montmorillonite used in this study.

Intrinsic Pu colloid/clay	Density	Crystallite			Aggregate		
		Avg Diameter	Diameter Range	Surface Area	Avg Diameter	Diameter Range	Surface Area
	g/cm <sup>3</sup>	nm	nm	m <sup>2</sup> /g	nm	nm	m <sup>2</sup> /g
High-fired PuO <sub>2</sub> #1 (PuO <sub>2</sub> -1)	11.5	5	3-335	104	4000	0.1-10	0.13
High-fired PuO <sub>2</sub> #2 (PuO <sub>2</sub> -2)	11.5	31	10-105	17	4000	2-10	0.13
Peptized <sup>242</sup> PuO <sub>2</sub> (PuO <sub>2</sub> -3)	11.5	2.3	2-3.1	227	31	16-50	17
Precipitated <sup>238</sup> PuO <sub>2</sub> (PuO <sub>2</sub> -4)	11.5	3.5	2.5-4.5	149	30	10-50	17
Montmorillonite <sup>a</sup>	2.83	71		30	300	50-2000	7

a. N<sub>2</sub>(g)-BET measurement was 31.45 ± 0.17 m<sup>2</sup>/g

## Dissolution of Intrinsic Pu Colloids

The kinetics studies of intrinsic Pu colloids precipitated from weak alkaline solution (both freshly prepared and aged up to 1 year) was studied in the presence of montmorillonite at 25 and 80 °C previously (Section 8.1 of this report: kinetics studies). Colloid stability at three different intrinsic Pu colloid concentrations ( $10^{-11}$ ,  $10^{-9}$  and  $10^{-7}$  M) was examined. These intrinsic  $^{238}\text{Pu}$  colloids were aged for 1 month to >1 year prior to use in the stability experiments. However, no difference in behavior was observed between the fresh and aged samples. The dissolution rate constants obtained from those experiments were ranged from  $6 \times 10^{-7}$  to  $1 \times 10^{-5}$  and  $4 \times 10^{-7}$  to  $7 \times 10^{-7}$  mol m<sup>-2</sup> day<sup>-1</sup> at 25 and 80 °C, respectively. We have found that the apparent dissolution rates in our experiments were a function of the formation conditions of the intrinsic Pu colloid, intrinsic Pu colloid surface area and colloids concentration, and solution temperature. Although 7 experiments using calcined PuO<sub>2</sub> and peptized Pu hydroxide colloids were performed in over prolonged periods from 6 month to 8 months (see Table 8-3), only two experiments (exp. 4 and 6) showed signs of intrinsic Pu colloid dissolution. Figure 8-11 plots the Pu concentration in the clay suspension as function of time for these two experiments. In contrast to our previous intrinsic Pu colloid dissolution (Pu hydroxides precipitated in alkaline solution) in which nearly complete dissolution was achieved in three months, Pu concentrations in these experiments were detectable in clay suspensions only after ~100 days, implying very slow dissolution kinetics. A first order reaction model was applied to the data obtained from exp. 4 and 6, and could only qualitatively fit the dissolution curves (see Figure 4), especially for exp. 6. The rate constants obtained from curve fitting were  $1.6 \times 10^{-7}$  and  $1.7 \times 10^{-8}$  mol m<sup>-2</sup> day<sup>-1</sup> for samples PuO<sub>2</sub>-3 at 25 °C (exp. 4) and PuO<sub>2</sub>-2 at 80 °C (exp. 6), respectively. These values were 1 to 2 orders of magnitude lower than those obtained from experiments using sample PuO<sub>2</sub>-4 (precipitated PuO<sub>2</sub> in alkaline solution). Given that the specific crystallite surface area of PuO<sub>2</sub>-3 is even slightly higher than that of PuO<sub>2</sub>-4, and both samples had very similar specific particle area, the observed difference in dissolution rate was more likely due to the difference in their morphologies, especially the degree of crystallinity. The higher the degree of crystallinity, the more stable the intrinsic Pu colloids, and thus, lower dissolution rate was observed. Sample PuO<sub>2</sub>-2 appeared to dissolve at 80 °C, although it had highest degree of crystallinity with smallest specific crystallite surface areas. Again the observed dissolution could not be explained by its surface area. Without additional experimental information and further investigations, we are unable to give a satisfactory explanation for this result.

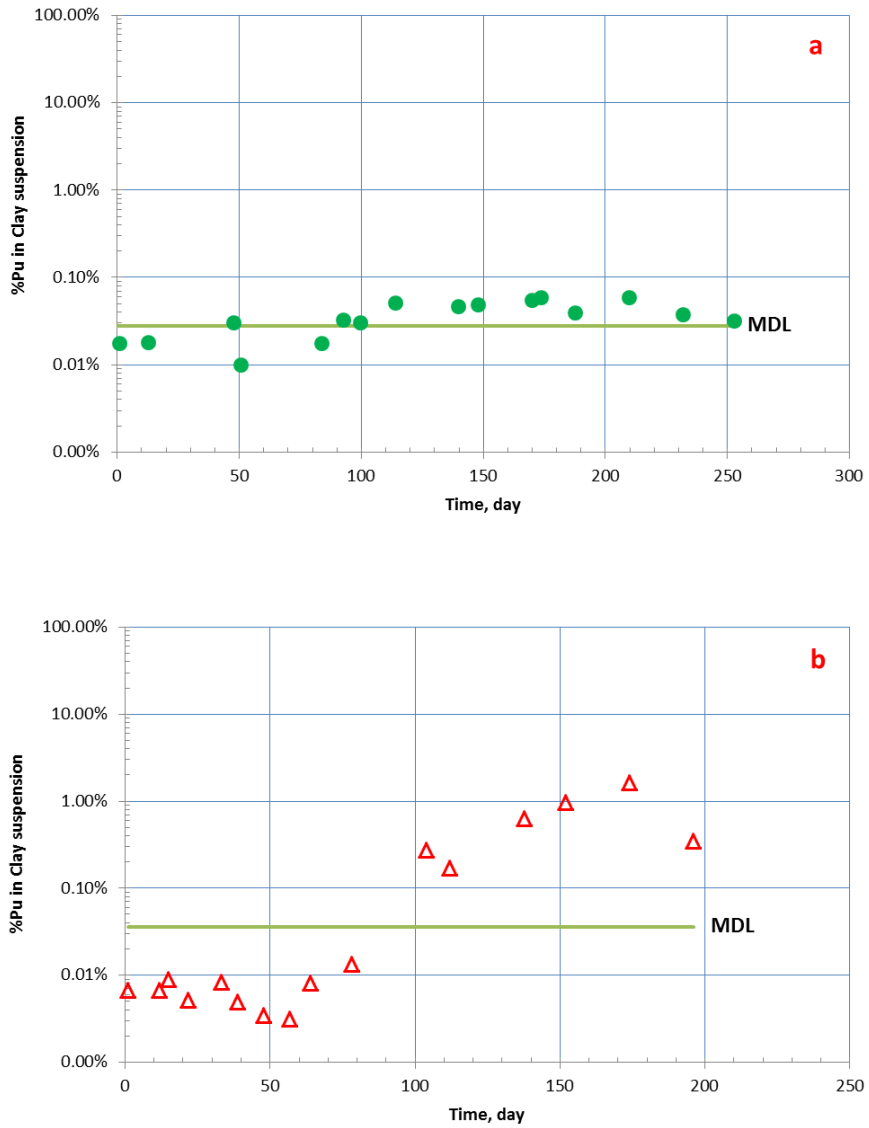


**Figure 8-11.** Dissolution kinetics of intrinsic Pu colloids. Solid circles and open triangles are experimental data at 25 and 80 °C, respectively. Solid lines are the method detection limits (MDL). a. Dissolution of peptized  $^{242}\text{PuO}_2$  at 25 °C. b. Dissolution of calcined  $^{239}\text{PuO}_2$  at 80 °C.

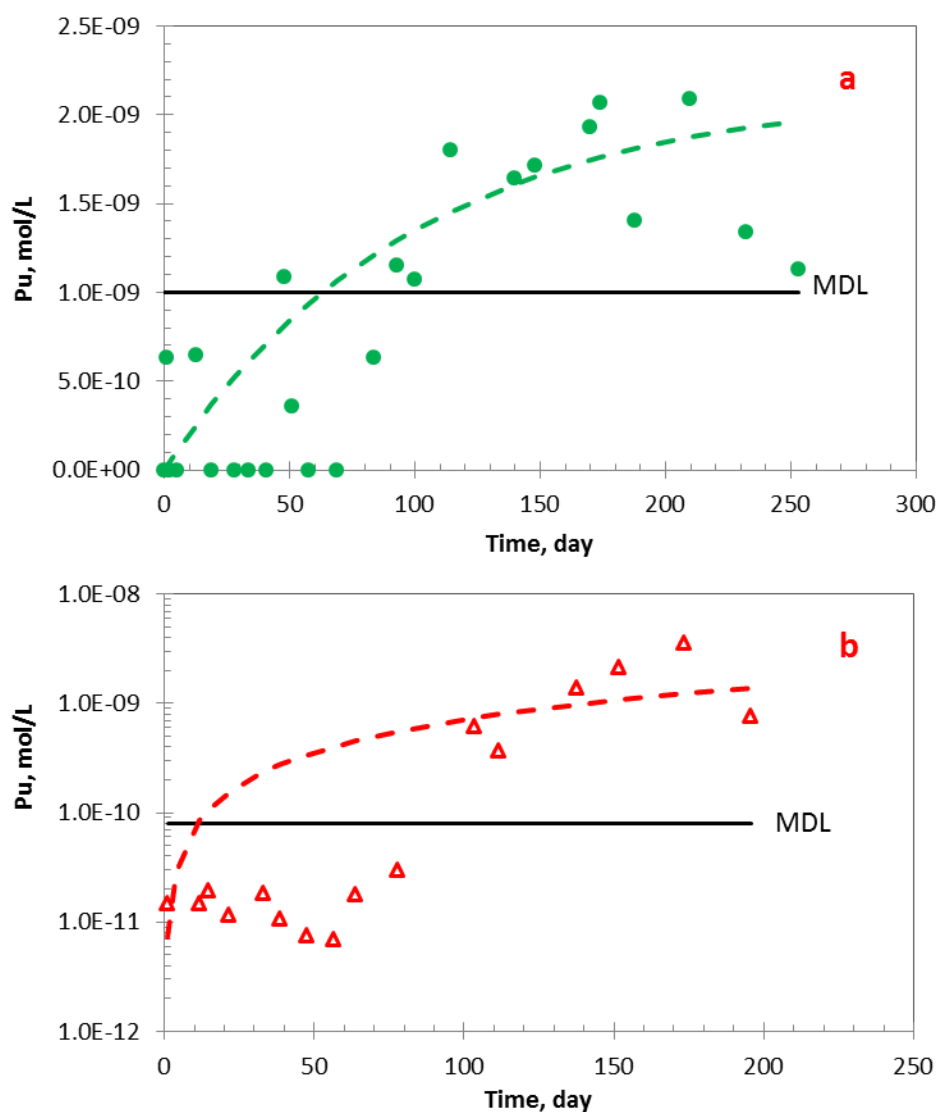


**Figure 8-12.** Dissolution kinetics were modeled using a first order reaction model. Solid circles and open triangles are experimental data at 25 and 80 °C, respectively. Solid lines are the method detection limits (MDL), and dashed lines are model fitting curves. a. Dissolution of peptized <sup>242</sup>PuO<sub>2</sub> at 25 °C. The obtained dissolution rate constant was  $1.6 \times 10^{-7}$  mol/m<sup>2</sup>/day. b. Dissolution of calcined <sup>239</sup>PuO<sub>2</sub>-2 at 80 °C. The obtained dissolution rate constant was  $1.7 \times 10^{-8}$  mol/m<sup>2</sup>/day.

Conservative predictions of Pu concentrations in the clay suspension were calculated using the dissolution rate constants obtained from sample PuO<sub>2</sub>-4 and the estimated crystallite surface areas of each of the intrinsic Pu colloids tested. The resulting Pu dissolution rates were compared to experimental results. These results are summarized in Table 8-5. For all cases, the predicted Pu concentrations are higher than either measured Pu concentrations in clay suspension or MDLs for the individual experiments. Moreover,

the TEM observations (not shown here) from sample PuO<sub>2</sub>-3 at the end of the dissolution 25 and 80 °C experiments did not show any significant signs of dissolution. All these results confirm that the dissolution rates of samples PuO<sub>2</sub>-1 to 3 were much slower than that of PuO<sub>2</sub>-4. Aside from crystallinity considerations, radiation effects from <sup>238</sup>Pu have also been reported to damage the crystallinity of <sup>238</sup>Pu oxides which led to an increased solubility of <sup>238</sup>PuO<sub>2</sub> (Park et al., 1973). The combined amorphous nature of the intrinsic Pu colloids and the high <sup>238</sup>Pu activity leads to the highest dissolution rates in sample PuO<sub>2</sub>-4. However, further experiments of the radiation effects are needed to quantitatively compare Pu oxides dissolution behavior and processes.

**Table 8-5.** Summary of dissolution experiment results, MDL and Pu conc. at the termination of experiments

Expt	Expt Temp.	PuO <sub>2</sub> used	Crystallite diameter	Calculated surface area	Pu upper limit in clay suspension	Apparent min k <sub>s</sub> from previous exp	Expt duration	MDL	Measured final Pu conc.	Predicted Pu conc.
	°C		nm	m <sup>2</sup> mol <sup>-1</sup>	mol L <sup>-1</sup>	mol m <sup>-2</sup> day <sup>-1</sup>	day	mol L <sup>-1</sup>	mol L <sup>-1</sup>	mol L <sup>-1</sup>
1	25	PuO <sub>2</sub> -1	5	2.8×10 <sup>4</sup>	2.7×10 <sup>-7</sup>	6.2×10 <sup>-7</sup>	196	6×10 <sup>-11</sup>	1.5×10 <sup>-8</sup> <sup>a</sup>	2×10 <sup>-8</sup>
2	25	PuO <sub>2</sub> -1	5	2.8×10 <sup>4</sup>	2×10 <sup>-8</sup>	6.2×10 <sup>-7</sup>	252	6×10 <sup>-11</sup>	< MDL	2×10 <sup>-9</sup>
3	25	PuO <sub>2</sub> -2	31	4.6×10 <sup>3</sup>	6×10 <sup>-8</sup>	6.2×10 <sup>-7</sup>	196	6×10 <sup>-11</sup>	1.5×10 <sup>-9</sup> <sup>b</sup>	3×10 <sup>-9</sup>
4	25	PuO <sub>2</sub> -3	2.3	6.2×10 <sup>4</sup>	3.6×10 <sup>-6</sup>	6.2×10 <sup>-7</sup>	253	3×10 <sup>-10</sup>	2.5×10 <sup>-9</sup> <sup>c</sup>	4×10 <sup>-7</sup>
5	80	PuO <sub>2</sub> -1	5	2.8×10 <sup>4</sup>	2.8×10 <sup>-9</sup>	3.7×10 <sup>-6</sup>	191	6×10 <sup>-11</sup>	< MDL	4×10 <sup>-10</sup>
6	80	PuO <sub>2</sub> -2	31	4.6×10 <sup>3</sup>	2.2×10 <sup>-7</sup>	3.7×10 <sup>-6</sup>	196	6×10 <sup>-11</sup>	4.5×10 <sup>-9</sup> <sup>c</sup>	3×10 <sup>-8</sup>
7	80	PuO <sub>2</sub> -3	2.3	6.2×10 <sup>4</sup>	8×10 <sup>-8</sup>	3.7×10 <sup>-6</sup>	182	3×10 <sup>-10</sup>	< MDL	1×10 <sup>-8</sup>

- Pu concentration was not detected for 140 days, and then it jumped to this value on 150 days and stayed on it to the termination of the experiment. It is concluded that the detected Pu was due to the decay of the integrity of dialysis membrane after a long-lasting experiment.
- Pu concentration was not detected for 170 days, and then it jumped to this value on last sampling day. It is concluded that the detected Pu was due to the decay of integrity of the dialysis membrane after a long-lasting experiment.
- Dissolution of PuO<sub>2</sub> may have been observed in these experiments.

### Temperature Effects on PuO<sub>2</sub> Morphology and Reactivity

Intrinsic Pu colloids were retrieved from inside dialysis bags after the dissolution experiments (exp. 4 and 7) for TEM imaging (Fig. 5). The HRTEM images of the samples revealed that the aggregates tend to fuse at their edges with a preferential alignment in the 25 °C experiment (Fig. 8-13a). The signs of particle fusion were not as developed at 80 °C (Fig. 8-13b). These observations indicate that PuO<sub>2</sub> aggregates exhibit stronger relationship with each other at 25 °C than that at 80 °C. It suggests that intrinsic

Pu colloids are more reactive at 25 °C. These observations may explain why we observed some intrinsic Pu colloids dissolution at 25 °C, but not at 80 °C for sample PuO<sub>2</sub>-3.

In the current study, we show that intrinsic Pu colloids formed at elevated temperatures resulted in greater crystallinity and larger single crystals (PuO<sub>2</sub>-1 and PuO<sub>2</sub>-2 in Fig. 8-9). In the liquid phase, temperature effects led to intrinsic Pu colloids forming well defined aggregate shapes and the incipient alignment of the crystallites within the aggregates (PuO<sub>2</sub>-3 compared to PuO<sub>2</sub>-4 in Fig. 8-10). These features likely reduced the surface energy and surface reactivity of the intrinsic Pu colloids. Thermal treatments have been shown to be one of the very important factors influencing PuO<sub>2</sub> surface chemistry including its reactivity and heterogeneous dissolution kinetics (Farr et al., 2004). Increasing temperatures can effectively decrease Pu oxides solubility in groundwaters (Nitsche et al., 1993; Runde et al., 2002). The temperature effect on intrinsic Pu colloids was attributed to the increased crystallinity of the solubility controlling solids (Runde et al., 2002) and crystal growth (Machuron-Mandard and Madic, 1996) during formation of PuO<sub>2</sub>. It is apparent from our experiments that intrinsic Pu colloids formed at elevated temperatures are more stable and less reactive than those formed at room temperature. The various formation temperatures influence morphological features including crystallinity, crystal growth, aggregation and particle shapes and sizes. These morphological difference will have a substantial effect of the stability and dissolution rates of intrinsic Pu colloids.

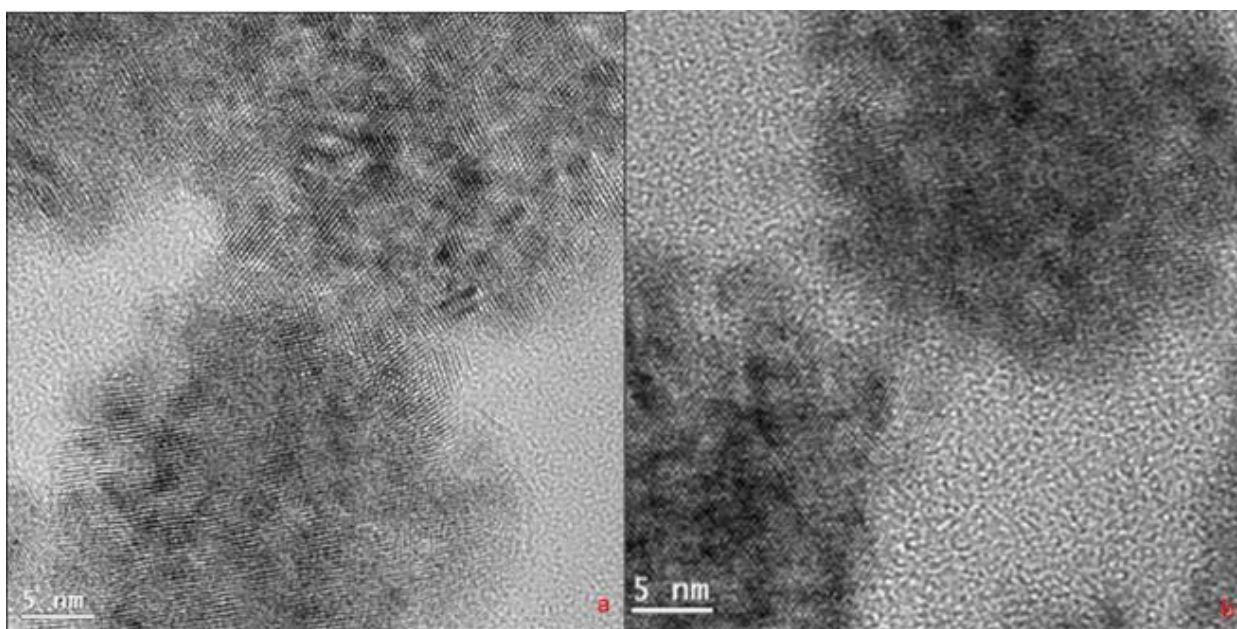


**Figure 8-13.** HRTEM images of sample PuO<sub>2</sub>-3 from inside dialysis bag after dissolution experiments. a: Sample from experiment at 25 °C. The aggregates tend to fuse at their edges with preferential alignment. b: Sample from experiment at 80 °C. The aggregates show minimum fusion at their edges.

## **8.2.4 Conclusions**

We have examined the reactivity of three different types of intrinsic Pu colloids in the presence of montmorillonite at 25 and 80°C under atmospheric conditions. Scanning electron microscopy (SEM) and transmission electron microscopy (TEM) have been used to characterize their morphology. Pu oxides calcined at 300 and 800 °C and intrinsic Pu colloids produced from acidic solution are quite stable under our experimental conditions. Only two out of seven experiments showed signs of intrinsic Pu colloid dissolution after 100 days. Predicted Pu concentrations calculated using dissolution rate constants obtained from intrinsic Pu colloids formed in alkaline solution are much higher than the measured Pu concentrations, suggesting that these three types of intrinsic Pu colloids are more stable, thus less reactive than the ones formed in alkaline solution. The differences in the reactivity among investigated intrinsic Pu colloids are attributed to their morphological features including crystallinity, crystal growth, aggregation and particle shapes and sizes, all of which are greatly influenced by temperatures during formation of these intrinsic Pu colloids. Intrinsic Pu colloids and/or Pu oxides formed at elevated temperatures are more stable and may play an important role in the migration of intrinsic Pu colloids away from nuclear waste repository setting. Our results suggest that repository scenarios that include higher heat loading may result in stabilization of Pu oxide phases, which can lead to greater migration of intrinsic Pu colloids. However, the repository temperature history, combined with the predicted timing of canister failure and re-saturation of the repository near field will all play a role in the evolution of any specific repository scenario and the potential for Pu mobilization.

## **8.3 FUTURE WORK**

### **8.3.1 Stability of Intrinsic Pu Colloids Across a Range of Repository Conditions**

The FY15 effort will build on FY14 experiments summarized in this report. We will extend our current intrinsic Pu colloid stability experimental program to a broader range of geochemical conditions that spans the generic disposal scenarios presently under investigation (salt, argillite, and granite). This work builds on a research program initiated in FY12, where a novel design was developed to study the stability of intrinsic Pu colloids in the presence of montmorillonite clay. In FY14, we completed our study of the stability of intrinsic Pu colloids as a function of temperature and aging in the presence of inorganic colloids at near neutral pH and low salinity groundwater. We determined that the formation conditions of PuO<sub>2</sub> have a dramatic effect on the stability of the colloidal and solid phases in these waters. However, we do not yet know how the wide ranging groundwater conditions in the various repository scenarios may affect the stability of these PuO<sub>2</sub> phases.

In FY15 we will investigate the stability of both low temperature and high fired intrinsic Pu oxides across a wide range of ionic strengths, solution conditions, and temperature that brackets a wider range of repository conditions. Particular focus will be placed on the stabilization of Pu clusters in solution at higher ionic strengths, as observed by Soderholm et al. (2008). Their work suggests that nano-clusters of Pu may be stabilized in high ionic strength solutions due to the specific interaction between PuO<sub>2</sub> clusters and

Cl counterions. However, the implications to Pu transport in repository environments has not been examined. Stabilization of Pu nano-clusters in higher ionic strength solution could substantially increase Pu mobility in certain repository environments.

### 8.3.2 Temperature Effects on Bentonite Alteration and Sorption of Actinides

Adsorption and desorption reactions between minerals and radionuclides, which are used to predict their transport in nuclear waste repository scenarios, are routinely performed at temperatures below 303 K.(Begg et al., 2013a; Geckeis et al., 2004; Huber et al., 2011; Sabodina et al., 2006a) However, repository scenarios are likely to involve temperatures at least as high as 360 K.(Cornell, 1993; Rutqvist et al., 2014) There have been a limited number of studies that have demonstrated the importance of temperature on the adsorption of radionuclides such as Cs and Pu.(Long et al., 2013; Lu et al., 2003) Further, previous work has identified that the aqueous complexation U, Np and Pu will change as a function of temperature.(Rao et al., 2010) However a systematic study of the effects of temperature on both adsorption and desorption processes of radionuclides and minerals relevant to nuclear waste repository scenarios is lacking. Furthermore, the effect of temperature on mineral alteration and their subsequent sorption behavior has been given very little attention. In FY15, we seek to constrain the effects of temperature on the adsorption/desorption of Pu(IV) and Pu(V) with montmorillonite and its alteration products. This effort will build on our existing experience with Pu and montmorillonite at both ambient and elevated temperatures.(Begg et al., 2013a; Zhao et al., 2012) We will take advantage of the availability of large-volume titanium Parr bomb reactors at LLNL to prepare hydrothermally altered montmorillonite and bentonite rock (6 months alteration at 200°C). The sorption/desorption of Pu(IV) and Pu(V) to both pristine and hydrothermally altered rock will be investigated as a function of pH (4-10) and temperature (25-80°C).

### 8.3.3 Modeling Colloid Facilitated Pu Transport at the Grimsel CFM Facility

Colloid-facilitated transport of actinides in natural systems and the production/stability of pseudo-colloids as a result of bentonite erosion must be quantified for repository performance assessment. Laboratory sorption/desorption models developed in FY13 and FY14 need to be tested in field-scale demonstrations. In FY15, we will test our sorption/desorption kinetic models using the field data available to the UFD program through the CFM international project at the Grimsel facility, Switzerland.

Due to its swelling properties, plasticity, ion exchange, sorption and sealing capability, bentonite is a good candidate for backfill material proposed to be used in nuclear waste repository scenarios.(Guyen, 1990) However, one of the concerns with the use of bentonite as a backfill material is that it can form colloidal particles which may enhance the migration of radionuclide species.(Geckeis et al., 2004; Kersting et al., 1999) As a result, radionuclide (including Pu) adsorption to mineral colloids has been the subject of considerable study. In contrast, desorption reactions have been far less well studied. This is problematic because application of thermodynamic equilibrium parameters in field

transport models which incorrectly represent desorption processes are likely to be flawed.(Artinger et al., 2002)

Recently, we have developed a numerical model to describe the adsorption and desorption behavior of Pu with montmorillonite (a primary constituent of bentonite) colloids.(Begg et al., In Prep) To further test the assumptions in our approach, we propose to apply this numerical model to data generated in recent Pu-colloid transport experiments performed at the Grimsel Test Site. Comparison of the model and observed behavior will allow us to verify the applicability of our in field-scale conditions or will otherwise highlight areas of weakness in our understanding of Pu adsorption/desorption mechanisms.

#### 8.4 REFERENCES

- Altmaier, M., Gaona, X., and Fanghaenel, T., 2013. Recent Advances in Aqueous Actinide Chemistry and Thermodynamics. *Chemical Reviews* **113**, 901-943.
- Artinger, R., Schuessler, W., Schaefer, T., and Kim, J. I., 2002. A kinetic study of Am(III)/humic colloid interactions. *Environ Sci Technol* **36**, 4358-4363.
- Begg, J. D., Zavarin, M., and Kersting, A. B., 2014. Plutonium Desorption from Mineral Surfaces at Environmental Concentrations of Hydrogen Peroxide. *Environ Sci Technol* **48**, 6201-6210.
- Begg, J. D., Zavarin, M., Zhao, P., Tumey, S. J., Powell, B., and Kersting, A. B., 2013a. Pu(V) and Pu(IV) sorption to montmorillonite. *Environ Sci Technol* **47**, 5146-5153.
- Begg, J. D., Zavarin, M., Zhao, P. H., Tumey, S. J., Powell, B., and Kersting, A. B., 2013b. Pu(V) and Pu(IV) Sorption to Montmorillonite. *Environ Sci Technol* **47**, 5146-5153.
- Begg, J. D. C., Zavarin, M., and Kersting, A., In Prep. Desorption of plutonium from montmorillonite: An experimental and modeling study.
- Berner, R. A., 1981. Kinetics of Weathering and Diagenesis. In: Lasaga, A. C. and Kirkpatrick, R. J. Eds.), *Kinetics of Geochemical Processes*. BookCrafters, Inc., Chelsea, Michigan
- Bertetti, F. P., Pabalan, R. T., and Almendarez, M. G., 1998. Studies on neptunium(V) sorption on quartz, clinoptilolite, montmorillonite, and  $\alpha$ -alumina. In: Jenne, E. A. (Ed.), *Adsorption of Metals by Geomedia*. Academic Press, San Diego.
- Cleveland, J. M., 1979. The Chemistry of Plutonium. American Nuclear Society, La Grange Park.
- Cornell, R. M., 1993. Adsorption of cesium on minerals: A review. *Journal of Radioanalytical and Nuclear Chemistry* **171**, 483-500.
- Dai, M. H., Buesseler, K., and Pike, S. M., 2005. Plutonium in groundwater at the 100K-Area of the US DOE Hanford site. *Journal of Contaminant Hydrology* **76**, 167-189.
- Efurd, D. W., Runde, W., Banar, J. C., Janecky, D. R., Kaszuba, J. P., Palmer, P. D., Roensch, F. R., and Tait, C. D., 1998. Neptunium and plutonium solubilities in a Yucca Mountain groundwater. *Environ Sci Technol* **32**, 3893-3900.

- Farr, J. D., Schulze, R. K., and Neu, M. P., 2004. Surface chemistry of Pu oxides. *Journal of Nuclear Materials* **328**, 124-136.
- Geckeis, H., Schafer, T., Hauser, W., Rabung, T., Missana, T., Degueldre, C., Mori, A., Eikenberg, J., Fierz, T., and Alexander, W. R., 2004. Results of the colloid and radionuclide retention experiment (CRR) at the Grimsel Test Site (GTS), Switzerland - impact of reaction kinetics and speciation on radionuclide migration. *Radiochim Acta* **92**, 765-774.
- Guven, N., 1990. Longevity of bentonite as buffer material in a nuclear-waste repository. *Engineering Geology* **28**, 233-247.
- Haire, R. G., Lloyd, M. H., Beasley, M. L., and Milligan, W. O., 1971. Aging of Hydrated Plutonium Dioxide *JOURNAL OF ELECTRON MICROSCOPY* **20**, 8-16.
- Hocsman, A., Di Nezo, S., Charlet, L., and Avena, M., 2006. On the mechanisms of dissolution of montroydite [HgO(s)]: Dependence of the dissolution rate on pH, temperature, and stirring rate. *J Colloid Interf Sci* **297**, 696-704.
- Huber, F., Kunze, P., Geckeis, H., and Schafer, T., 2011. Sorption reversibility kinetics in the ternary system radionuclide-bentonite colloids/nanoparticles-granite fracture filling material. *Applied Geochemistry* **26**, 2226-2237.
- Kaszuba, J. P. and Runde, W. H., 1999. The aqueous geochemistry of neptunium: Dynamic control of soluble concentrations with applications to nuclear waste disposal. *Environ Sci Technol* **33**, 4427-4433.
- Keeney-Kennicutt, W. L. and Morse, J. W., 1985. The redox chemistry of Pu(V)O<sub>2</sub>+ interaction with common mineral surfaces in dilute solutions and seawater. *Geochimica Et Cosmochimica Acta* **49**, 2577-2588.
- Kersting, A. B., 2013. Plutonium Transport in the Environment. *Inorg Chem* **52**, 3533-3546.
- Kersting, A. B., Efurud, D. W., Finnegan, D. L., Rokop, D. J., Smith, D. K., and Thompson, J. L., 1999. Migration of plutonium in ground water at the Nevada Test Site. *Nature* **397**, 56-59.
- Kersting, A. B., Zavarin, M., Zhao, P., and Dai, Z., 2012. Radionuclide interaction and transport in representative geologic media 2012. Sandia National Laboratory.
- Kozai, N., Ohnuko, T., Matsumoto, J., Banba, T., and Ito, Y., 1996. A study of the specific sorption of neptunium(V) on smectite in low pH solution. *Radiochim. Acta* **75**, 149-158.
- Kozai, N., Ohnuky, T., and Muraoka, S., 1993. Sorption characteristics of neptunium by sodium-smectite. *J. Nuclear Sci. Tech.* **30**, 1153-1159.
- Lasaga, A. C., 1981. Transition State Theory. In: Lasaga, A. C. and Kirkpatrick, R. J. Eds.), *Kinetics of Geochemical Processes*. BookCrafters, Inc., Chelsea, Michigan
- Lasaga, A. C., 1998a. *Kinetic Theory in the Earth Sciences*. Princeton University Press, Princeton, NJ.
- Lasaga, A. C., 1998b. *Kinetic Theory in the Earth Sciences*. Princeton University Press, Princeton, NJ.
- Lasaga, A. C. and Lutge, A., 2004. Mineralogical approaches to fundamental crystal dissolution kinetics. *Am Mineral* **89**, 527-540.
- Lemire, R. J., 2001. *Chemical Thermodynamics of Neptunium and Plutonium, Volume 4*. Elsevier Science (September 9, 2001)

- Rao, L., Guoxin, T., Yuanxian, X., Judah, I. F., PierLuigi, Z., and Plinio Di, B., 2010. Bridging the Gap in the Chemical Thermodynamic Database for Nuclear Waste Repository: Studies of the Effect of Temperature on Actinide Complexation, *Nuclear Energy and the Environment*. American Chemical Society.
- Long, H., Wu, P., and Zhu, N., 2013. Evaluation of Cs<sup>+</sup> removal from aqueous solution by adsorption on ethylamine-modified montmorillonite. *Chemical Engineering Journal* **225**, 237-244.
- Lu, N. P., Reimus, P. W., Parker, G. R., Conca, J. L., and Triay, I. R., 2003. Sorption kinetics and impact of temperature, ionic strength and colloid concentration on the adsorption of plutonium-239 by inorganic colloids. *Radiochim Acta* **91**, 713-720.
- Lujanienė, G., Motiejunas, S., and Sapolaite, J., 2007. Sorption of Cs, Pu and Am on clay minerals. *Journal of Radioanalytical and Nuclear Chemistry* **274**, 345-353.
- Machuron-Mandard, X. and Madic, C., 1996. Plutonium dioxide particle properties as a function of calcination temperature. *Journal of Alloys and Compounds* **235**, 216-224.
- Management, O. o. C. R. W., 2002. Yucca Mountain Science and Engineering Report: Technical Information Supporting Site Recommendation Consideration. U.S. Department of Energy.
- Mewhinney, J. A., Rothenberg, S. J., Eidson, A. F., Newton, G. J., and Scripsick, R. C., 1987. Specific Surface-Area Determinations of U and Pu Oxide Particles. *J Colloid Interf Sci* **116**, 555-562.
- Neck, V., Altmaier, M., and Fanghaenel, T., 2007a. Thermodynamic data for hydrous and anhydrous PuO<sub>2+x</sub>(S). *Journal of Alloys and Compounds* **444**, 464-469.
- Neck, V., Altmaier, M., and Fanghanel, T., 2007b. Solubility of plutonium hydroxides/hydrous oxides under reducing conditions and in the presence of oxygen. *Cr Chim* **10**, 959-977.
- Neck, V., Altmaier, M., Seibert, A., Yun, J. I., Marquardt, C. M., and Fanghanel, T., 2007c. Solubility and redox reactions of Pu(IV) hydrous oxide: Evidence for the formation of PuO<sub>2+x</sub>(s, hyd). *Radiochimica Acta* **95**, 193-207.
- Neck, V., Altmaier, M., Seibert, A., Yun, J. I., Marquardt, C. M., and Fanghanel, T., 2007d. Solubility and redox reactions of Pu(IV) hydrous oxide: Evidence for the formation of PuO(2+x)(s, hyd). *Radiochim Acta* **95**, 193-207.
- Neck, V. and Kim, J. I., 2001. Solubility and hydrolysis of tetravalent actinides. *Radiochim Acta* **89**, 1-16.
- Nitsche, H., Gatti, R. C., Standifer, E. M., Lee, S. C., Muller, A., Prussin, T., Deinhammer, R. S., Maurer, H., Becraft, K., Leung, S., and Carpenter, S. A., 1993. Measured solubilities and speciations of neptunium, plutonium, and americium in a typical groundwater (J-13) from the Yucca Mountain region. Los Alamos National Laboratory, Los Alamos, NM.
- Nitsche, H., Roberts, K., Prussin, T., Muller, A., Becraft, K., Keeney, D., Carpenter, S. A., and Gatti, R. C., 1994. Measured solubilities and speciations from oversaturation experiments of neptunium, plutonium, and americium in UE-25p #1 well from the Yucca Mountain region. Los Alamos National Laboratory, Los Alamos.
- Novikov, A. P., Kalmykov, S. N., Utsunomiya, S., Ewing, R. C., Horreard, F., Merkulov, A., Clark, S. B., Tkachev, V. V., and Myasoedov, B. F., 2006. Colloid transport

- of plutonium in the far-field of the Mayak Production Association, Russia. *Science* **314**, 638-641.
- Park, J. F., Catt, D. L., Craig, D. K., Olson, R. J., and Smith, V. H., 1973. Solubility Changes of  $^{238}\text{Pu}$  Oxide in Water Suspension and Effect on Biological Behavior after Inhalation by Beagle Dogs., U.S. Department of Commerce, National Technical Information Service.
- Powell, B. A., Fjeld, R. A., Kaplan, D. I., Coates, J. T., and Serkiz, S. M., 2004.  $\text{Pu(V)O}_2^+$  adsorption and reduction by synthetic magnetite ( $\text{Fe}_3\text{O}_4$ ). *Environ Sci Technol* **38**, 6016-6024.
- Powell, B. A., Fjeld, R. A., Kaplan, D. I., Coates, J. T., and Serkiz, S. M., 2005.  $\text{Pu(V)O}_2^+$  adsorption and reduction by synthetic hematite and goethite. *Environ Sci Technol* **39**, 2107-2114.
- Powell, B. A., Kersting, A. B., and Zavarin, M., 2008. Sorption and Desorption Rates of Neptunium and Plutonium on Goethite. In: Zavarin, M., Kersting, A. B., Lindvall, R. E., and Rose, T. P. Eds.), *Hydrologic Resources Management Program and Underground Test Area Project, FY 2006 Progress Report*. Lawrence Livermore National Laboratory, Livermore, CA.
- Rai, D. and Ryan, J. L., 1982. Crystallinity and Solubility of  $\text{Pu(IV)}$  Oxide and Hydrated Oxide in Aged Aqueous Suspensions. *Radiochim Acta* **30**, 213-216.
- Rao, L. F., Srinivasan, T. G., Garnov, A. Y., Zanonato, P. L., Di Bernardo, P., and Bismondo, A., 2004. Hydrolysis of neptunium(V) at variable temperatures (10-85 degrees C). *Geochimica Et Cosmochimica Acta* **68**, 4821-4830.
- Rao, L. F., Tian, G. X., Di Bernardo, P., and Zanonato, P., 2011. Hydrolysis of Plutonium(VI) at Variable Temperatures (283-343 K). *Chem-Eur J* **17**, 10985-10993.
- Runde, W., Conradson, S. D., Wes Efurud, D., Lu, N., VanPelt, C. E., and Tait, C. D., 2002. Solubility and sorption of redox-sensitive radionuclides (Np, Pu) in J-13 water from the Yucca Mountain site: comparison between experiment and theory. *Applied Geochemistry* **17**, 837-853.
- Rutqvist, J., Zheng, L. G., Chen, F., Liu, H. H., and Birkholzer, J., 2014. Modeling of Coupled Thermo-Hydro-Mechanical Processes with Links to Geochemistry Associated with Bentonite-Backfilled Repository Tunnels in Clay Formations. *Rock Mech. Rock Eng.* **47**, 167-186.
- Sabodina, M. N., Kalmykov, S. N., Sapozhnikov, Y. A., and Zakharova, E. V., 2006a. Neptunium, plutonium and  $^{137}\text{Cs}$  sorption by bentonite clays and their speciation in pore waters. *Journal of Radioanalytical and Nuclear Chemistry* **270**, 349-355.
- Sabodina, M. N., Kalmykov, S. N., Sapozhnikov, Y. A., and Zkharova, E. V., 2006b. Neptunium, plutonium and  $^{137}\text{Cs}$  sorption by bentonite clays and their speciation in pore waters. *J. Radioanal. Nucl. Chem.* **270**, 349-355.
- Sanchez, A. L., Murray, J. W., and Sibley, T. H., 1985. The adsorption of plutonium IV and V on goethite. *Geochimica Et Cosmochimica Acta* **49**, 2297-2307.
- Santschi, P. H., Roberts, K. A., and Guo, L. D., 2002a. Organic nature of colloidal actinides transported in surface water environments. *Environ Sci Technol* **36**, 3711-3719.

- Santschi, P. H., Roberts, K. A., and Guo, L. D., 2002b. Organic nature of colloidal actinides transported in surface water environments. *Environ Sci Technol* **36**, 3711-3719.
- Stumm, W., 1997. Reactivity at the mineral-water interface: dissolution and inhibition. *Colloids and Surfaces A: Physicochemical and Engineering Aspects* **120**, 143-166.
- Turner, D. R., Pabalan, R. T., and Bertetti, F. P., 1998. Neptunium(V) sorption on montmorillonite: An experimental and surface complexation modeling study. *Clays and Clay Minerals* **46**, 256-269.
- Walther, C. and Denecke, M. A., 2013. Actinide Colloids and Particles of Environmental Concern. *Chemical Reviews* **113**, 995-1015.
- Zhao, P., Kersting, A. B., Dai, Z., and Zavarin, M., 2012. Pu(IV) Intrinsic Colloid Stability in the Presence of Montmorillonite at 25 & 80 C.



## **9. MIXED POTENTIAL MODEL FOR USED FUEL DEGRADATION: APPLICATION TO CRYSTALLINE ARGILLITE ENVIRONMENTS**

### **9.1 INTRODUCTION**

The high-level objective for this work is to develop a used fuel degradation model that:

- Calculates the dissolution rate of used fuel based on the corrosion potential and redox reaction currents of electrochemical reactions (most importantly the anodic reaction releasing  $\text{UO}_2^{2+}$  into solution, which is the fuel dissolution rate) that are established at the fuel/solution interface.
- Produces surface area-scalable results that can be used to define a fractional fuel degradation rate for performance assessment models.
- Accounts for interfacial redox reaction kinetics, radiolytic oxidants ( $\text{H}_2\text{O}_2$ ), and the catalytic behavior of the noble metal particles (NMP) present within the fuel.
- Accounts for the evolution of fuel burnup and the related temperature and dose histories of the exposed fuel.

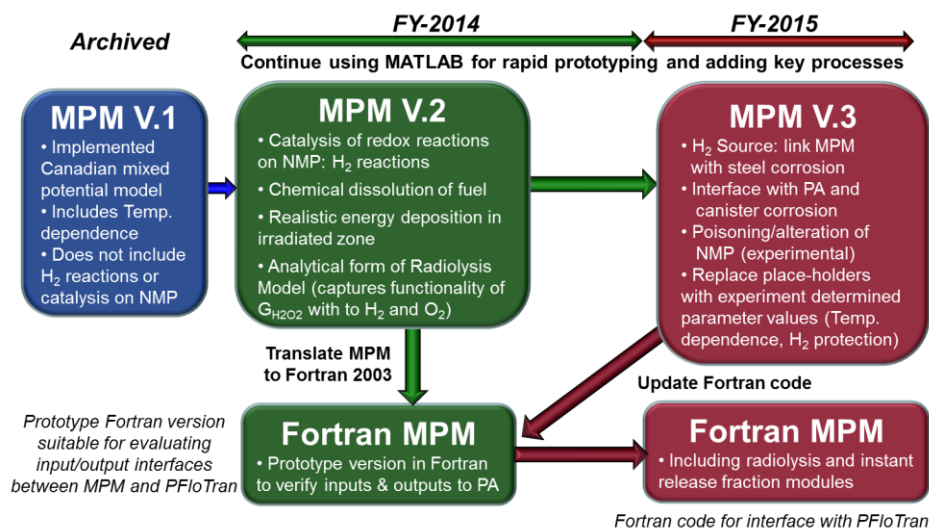
The objectives specifically addressed in FY2014 are shown in the context of previous and future work in Figure 9-1. Briefly, MPM V.1 represents the implementation of the model developed in Canada with modifications to facilitate including additional processes affecting fuel dissolution. Specifically, MPM V.2 includes separate  $\text{UO}_2$  and NMP phases to model catalytic effects, a more sophisticated radiolysis model, and a modified diffusion model that facilitates calculations over long times. Other planned modifications include adding a steel corrosion module to quantify hydrogen generation, modifying the catalytic efficiency of NMP to account for the effects of catalytic poisons in the groundwater (e.g., bromide) and corrosion, and evolving the reactive surface area of the corroding fuel. This report focuses on the progress made during FY 2014 in the following areas:

- Integrating the MPM with the Radiolysis Model (RM) developed at PNNL (e.g., Buck et al., 2013).
- Updating the MPM parameter database based on an ongoing literature review.
- Performing sensitivity runs with the updated MPM.
- Translating MPM (with RM subroutine) to Fortran 2003 to facilitate integration with performance assessment models.

A generalization of the envisioned relationships between the MPM and the generic performance assessment models for the argillite and crystalline rock disposal concepts is shown in Figure 2. Updates to the parameter database and the information exchange between the MPM and PA models summarized in Figure 9-2 are discussed in this section.

Part of the proposed scope of FY2015 will be to begin the process of actually integrating the MPM into the generic performance assessment models for argillite and crystalline repositories. Specifically the MPM will be used to calculate the dissolution rate or

fractional degradation rate of used fuel to provide source terms for radionuclides released from a breached waste package. Work to extend the MPM to include the chemical and redox effects of canister corrosion (primarily the hydrogen source term in the waste package) will be coordinated with container breaching models being developed in other UFD activities. The extensive parameter database used by the MPM V2 (presented below) makes it applicable to a wide range of geochemical settings; however, more experimental data are required to reduce uncertainties in key functionalities such as the pH and temperature dependencies of rate constants.



Figure

9-1. Schematic flow diagram highlighting progress made in the development of the MPM and future priorities based on sensitivity results from MPM V.2.

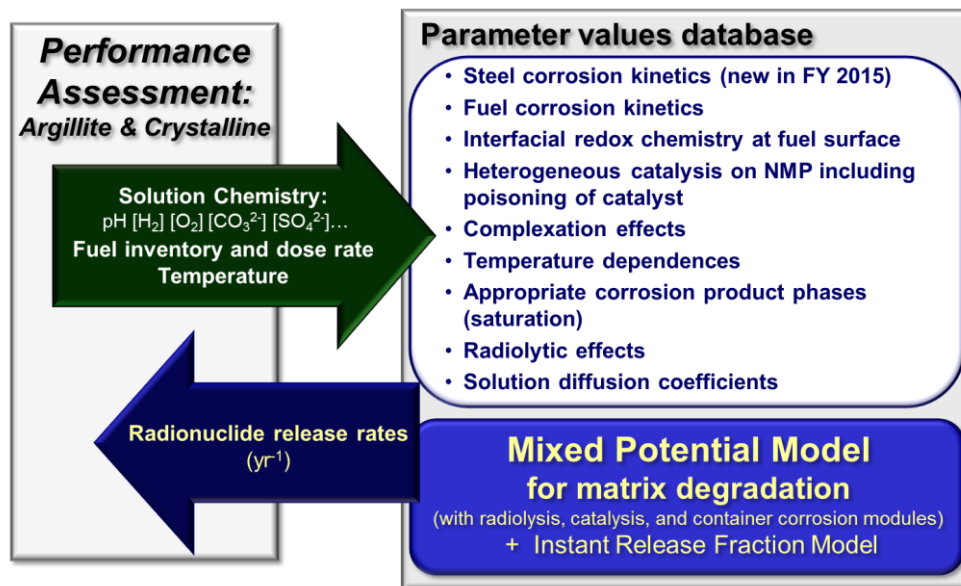


Figure 9-2. Schematic flow diagram showing relationships between the MPM and the generic performance assessment models

## 9.2 CHEMICAL ENVIRONMENTS OF CRYSTALLINE AND ARGILLITE REPOSITORIES

Clayrock/shale (here synonymous with argillite) bedrock formations are recognized as promising repository host rocks. For example, Callovo-Oxfordian formations at Bure France, the Boom Clay at Mol Belgium, the Boda formations at Mecsek Hungary, the Opalinus Clay at Mont Terri Switzerland, the Oxford Clay in the UK and the Queenston formation in Canada (list from Gaucher et al., 2009). Due to their low permeability, it is difficult to extract undisturbed water samples from clayrock formations; therefore, modeling techniques base on equilibrium with dominant mineral assemblages have been developed (e.g., Gaucher et al., 2009). Table 9-1 shows a typical modeled clayrock/shale pore water composition and a measured pore water composition from The Callovo-Oxfordian in France (Vinsot et al., 2008). These values can be used to place the MPM V2 model runs within the contexts of the geologic environments in question. Crystalline shield sites that have been identified as promising as repository settings include rock units in Canada, Finland and Sweden. Examples of crystalline rock groundwater chemistries are shown in Table 9-2.

**Table 9-1.** Measured and modeled pore water compositions from a clayrock or argillite formation. The model assumes that the water is in equilibrium with the mineral assemblage illite-calcite-dolomite-iron chlorite-quartz-pyrite-celestite. The measured composition is from the Callovo-Oxfordian formations in France.

	Model (Gaucher et al., 2009)	Measured (Vinsot et al., 2008)
pH	7.1	7.2
Eh <sub>SHE</sub> (mV)	-163	-199
	(moles/kg)	(moles/kg)
Inorganic C	2.19E-3	4.2E-3
Cl	3.01E-2	4.1E-2
S	3.39E-2	1.9E-2
Na	3.21E-2	5.6E-2
K	7.09E-3	9.0E-4
Ca	1.49E-2	7.6E-3
Mg	1.41E-2	5.9E-3
Sr	1.12E-3	2.5E-4
Si	9.41E-5	1.4E-4

Al	7.39E-9	----
Fe	2.14E-4	1.5E-5

**Table 9-2.** Modeled and measured pore water compositions from crystalline rock units (compiled by Guimera et al., 2006). The model is for a fracture hosted groundwater after 5,000 years of a deglaciation period at repository depth (for discussion see Guimerà et al., 2006).

Components	Forsmark groundwater	Grimsel groundwater	5,000 year old Forsmark water (modeled)
pH	7.0	9.6	9.8
Eh <sub>SHE</sub> (mV)	-143	-200	-240
	(moles/L)	(moles/L)	(moles/L)
HCO <sub>3</sub> <sup>-</sup>	1.77E-3	4.50E-4	9.28E-5
Cl	1.53E-1	1.60E-4	4.04E-4
S	6.80E-3	6.10E-5	----
Na	8.88E-2	6.90E-4	6.90E-4
K	8.75E-5	5.00E-6	3.18E-4
Ca	2.33E-2	1.40E-4	2.17E-4
Mg	9.30E-3	6.20E-7	6.20E-7
Si	1.85E-4	2.50E-4	5.60E-4
Br	2.98E-4	3.80E-7	3.80E-7
Fe	3.31E-5	3.00E-9	2.91E-7

As will be discussed below, the chemical properties of the groundwater examples shown in Tables 9-1 and 9-2 that will influence the MPM fuel dissolution rate calculations are the pH, Eh, dissolved carbonate and dissolved iron. Chloride and bromide are also important species because they are radiolytically active. It is expected that future versions of the MPM will account for radiolytically active halides after planned experiments to quantify their effects on the fuel dissolution rate. The MPM V2 sensitivity runs discussed below account for the full ranges of groundwater compositions expected from different argillaceous and crystalline repository environments.

### 9.3 MIXED POTENTIAL MODEL PROCESS OVERVIEW

As shown in Figure 9-1, the Argonne MPM was developed based on the Canadian-mixed potential model for  $\text{UO}_2$  fuel dissolution of King and Kolar, 2003 and was implemented using the numerical computing environment and programming language MATLAB (Jerden et al., 2013). The MPM is a 1-dimensional reaction-diffusion model that accounts for the following processes:

- Rate of oxidative dissolution of the fuel matrix U(VI) as determined by interfacial redox reaction kinetics (quantified as a function of the corrosion potential) occurring at the multiphase fuel surface (phases include  $\text{UO}_2$  and the noble metal fission product alloy phase (NMP), often referred to as the epsilon phase).
- Chemical (solubility-based) dissolution of the fuel matrix U(IV).
- Complexation of dissolved uranium by carbonate near the fuel surface and in the bulk solution.
- Production of hydrogen peroxide (which is the dominant fuel oxidant in anoxic repository environments) by alpha-radiolysis.
- Diffusion of reactants and products in the groundwater towards and away from the reacting fuel surface.
- Precipitation and dissolution of a U-bearing corrosion product layer on the fuel surface.
- Diffusion of reactants and products through the porous and tortuous corrosion product layer covering the reacting fuel surface.
- Arrhenius-type temperature dependence for all interfacial and bulk reactions.

In the MPM, the fuel degradation rate is calculated using mixed potential theory to account for all relevant redox reactions at the fuel surface, including those involving oxidants produced by solution radiolysis. Because the MPM is based on fundamental chemical and electrochemical principles, it is flexible enough to be applied to the full range of repository environments and conditions.

Of particular interest is the surface chemical properties of the NMP, which have been shown to catalyze redox reactions at the fuel/solution interface (e.g., Broczkowski et al., 2005, Shoesmith, 2008, Trummer, et al., 2009, Cui et al., 2010). These studies show that the degradation rate of the used fuel may be dramatically affected if dissolved hydrogen is present. Therefore, this process was incorporated into the MPM V2 using user-input hydrogen concentrations (Jerden et al., 2013).

In FY2014, the MPM V2 with the catalytic NMP domain was run for a number of conditions to determine the relative effects of key variables such as temperature, dose rate, and solution chemistry. As discussed below, the most important process in terms of fuel dissolution rate is the reaction of hydrogen at the NMP domains. The main source of hydrogen in the repository near field and waste package will be as a by-product of the anoxic corrosion of steel. This process and its relationships to the MPM calculated used fuel degradation rate are shown in Figure 9-3. Figure 9-3a illustrates the abundance of

steel surrounding the fuel in a generic waste package. Figure 9-3b shows the chemical and redox couples between the fuel dissolution (i.e., the reaction releasing  $\text{UO}_2^{2+}$  into the solution between corroding steel and the fuel). The reaction releasing  $\text{UO}_2^{2+}$  into solution is the key reaction modeled by the MPM and is defined as the fuel dissolution rate



The MPM is designed to quantify the effects of other reactions and processes on the kinetics of that reaction through chemical and electrochemical couples. The diagram in Figure 9-3c shows the catalyzed oxidation of hydrogen on the NMP surface and the transfer of electrons from NMP sites to the fuel matrix are coupled chemically through the dissolved hydrogen concentration. The electrical coupling between NMP and fuel grains establishes a galvanic link that effectively protects the fuel from oxidative dissolution by mitigating the reaction in Equation (9-1). The poisoning of NMP shown on the right side represents catalytic deactivation due to the formation of surface coatings and corrosion. The kinetics of the steel oxidation to release  $\text{H}_2$  and the effects of poisoning of NMP remain to be included in the MPM; this is planned for FY 2015.

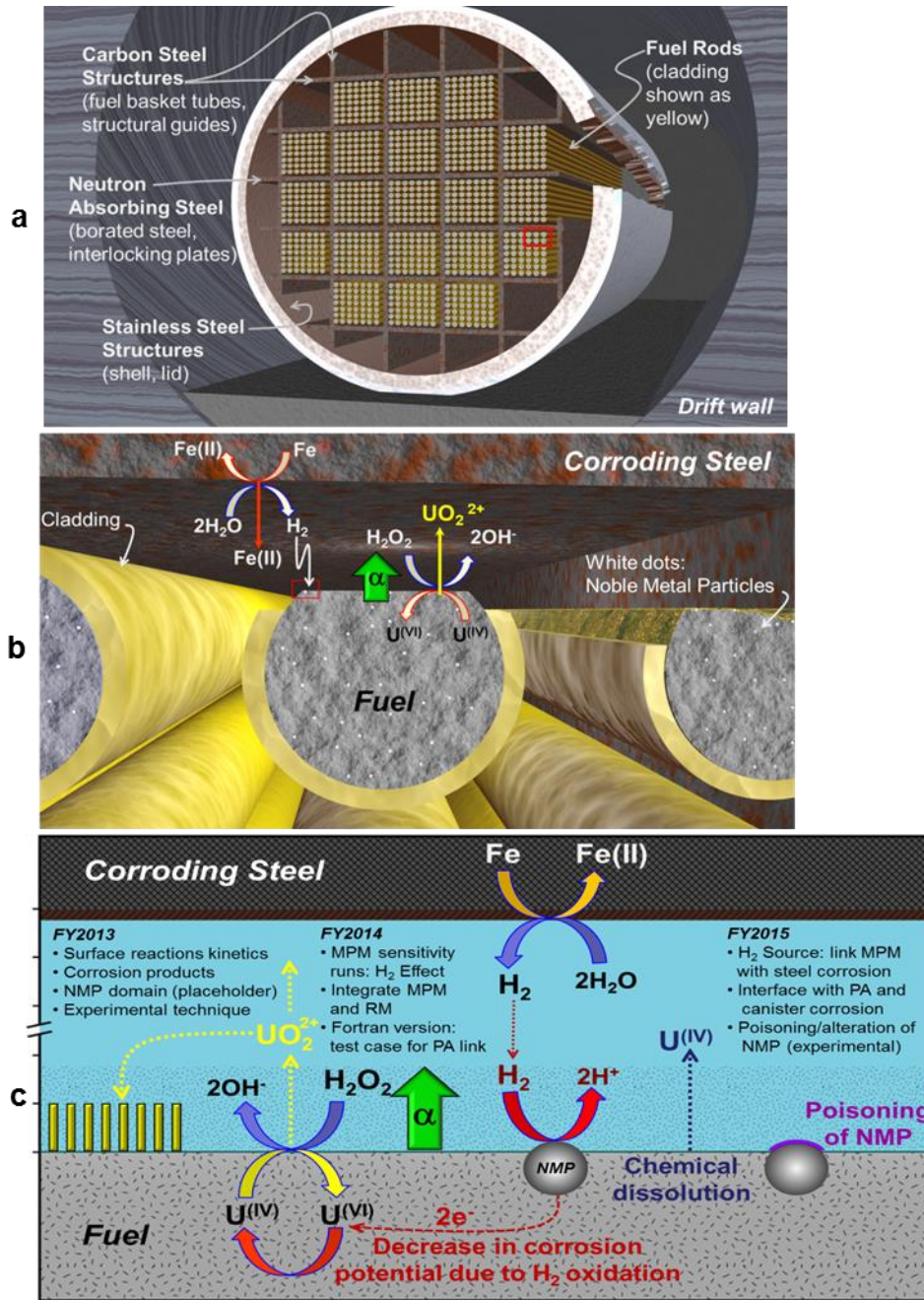


**Figure 9-3.** Conceptual diagrams of a used fuel waste package (a), exposed fuel (b), and a summary of the key interfacial processes that determine the overall degradation rate highlighting when each process was/will be incorporated into the MPM (c).

#### 9.4 UPDATED MPM PARAMETER DATABASE

Tables 9-3 – 9-7 show the MPM parameter database that has been updated based on recent literature and used in sensitivity runs discussed in below. Although there remain

quite a few estimated values that require experimental evaluation to quantify model uncertainties, the sensitivity runs yield important information about the relative (order of magnitude) effects that different variables have on the predicted fuel dissolution rate. The results can be used to prioritize which parameters are experimentally verified.

The extensiveness of the MPM parameter database makes it possible to use the model to calculate used fuel dissolution rates over a wide range of geochemical and electrochemical conditions. For example, the model accounts for the range of temperature, pH and carbonate concentrations anticipated in both argillite and crystalline rock repositories (e.g., Tables 9-1 and 9-2).

**Table 9-3.** Parameter and variable inputs used for in sensitivity runs with MPM V2.

<b>Variables set by user</b> (these will ultimately be inputs from other PA models)	<b>Range of values used in Sensitivity runs</b>	<b>Notes</b>
Temperature	25 °C to 200 °C	The evolution of the waste form temperature will be the output of other models accounting for burnup, fuel age, repository design, etc.
Dose rate	1 – 500 rad/s	Dose evolution will also be the output of other models accounting for fuel burnup and age.
Environmental concentration of dissolved oxygen	Zero to millimolar	This key variable will be determined by a number of interdependent kinetic processes within the waste package and near-field, but the dominant buffer may be the geologic environment: Argillite vs. Crystalline Rock.
Environmental concentration of dissolved carbonate	Zero to millimolar	This is a key variable determined by specifics of the geologic environment: Argillite vs. Crystalline Rock.
Environmental concentration of dissolved ferrous iron	Zero to millimolar	This key variable will be determined by a number of interdependent kinetic processes within the waste package and near-field, but the dominant source will be corroding steel components.

Environmental concentration of dissolved hydrogen	Zero to millimolar	This key variable (the most important for the present work) will also be determined by a number of interdependent kinetic processes within the waste package and near-field, but the dominant source will be anoxic corrosion of steel components.
pH	4 to 9.5	The effect of pH is incorporated into the MPM V2 by modifying the rate constants for fuel dissolution (Table 4) based on the experimental results of Torrero et al., 1997 which yield: $r \text{ (mol/m}^2\text{s)} = 3.5\text{E-}8[\text{H}^+]^{0.37}$ for pH 3.0 to 6.7 and $r \text{ (mol/m}^2\text{s)} = 3.5\text{E-}8$ for pH values greater than 6.7.  <i>Note:</i> groundwaters in Argillite and Crystalline environments are anticipated to have pH > 6.7 (e.g., Tables 1 and 2).

---

*Space and Time Parameters*

Length of diffusion grid in model	3 mm	Arbitrary, can be changed by user to represent system of interest.
Number of calculation nodes (points) in diffusion grid	200	Arbitrary, can be changed by user to optimize calculation efficiency.
Duration of simulation	100,000 years	Arbitrary, can be changed by user to represent duration of interest.

---

*Radiolysis Parameters*

Alpha-particle penetration depth	35 micrometers	The basis for this value was re-examined in FY 2014, but remains unchanged (confirmed). See section 2.1 for discussion.
Generation value for H <sub>2</sub> O <sub>2</sub>	Calculated by new Radiolysis Model subroutine	In MPM V2, this value varies depending on the dose rate and dissolved concentrations of O <sub>2</sub> and H <sub>2</sub> within the irradiation zone (see Section 2.2 below)

---

*Physical Interfacial Parameters*

Surface coverage of NMP	Zero to 1%	Based on qualitative examination of photomicrographs of spent fuels of different burnups e.g., Tsai, 2003.
Resistance between UO <sub>2</sub>	Constant 1.0E-3	Assumed that fuel and NMP are electrically

and NMP domains	V/Amp	well-coupled
Porosity of schoepite corrosion layer	50%	Reasonable assumption based on qualitative assessment of photomicrographs of schoepite layers e.g., Finch and Ewing, 1992.
Tortuosity factor of schoepite corrosion layer	0.1	Reasonable assumption based on analogy of schoepite layer with compacted clay (King and Kolar, 2003)

**Table 9-4.** Rate constants for all relevant reactions and their associated activation energies used in MPM V2. The far right column provides notes on recent updates based on our on-going literature survey.

Reaction	Rate Constant (mol/m <sup>2</sup> s)	Activation energy (J/mole)	Updates based on literature review
<i>Fuel Dissolution Reaction</i>			
$\text{UO}_2^{\text{fuel}} \rightarrow \text{UO}_2^{2+} + 2\text{e}^-$	5.00E-08	6.00E+04	Zeroth-order electrochemical rate constant for the irreversible oxidation of $\text{UO}_2$ from King and Kolar, 2003.
$\text{UO}_2^{\text{fuel}} + 2\text{CO}_3^{2-} \rightarrow \text{UO}_2(\text{CO}_3)_2^{2-} + 2\text{e}^-$	1.30E-08	6.00E+04	Electrochemical rate constant for the irreversible oxidation of $\text{UO}_2$ in carbonate solution from King and Kolar, 2003. (the reaction order with respect to carbonate is $m = 0.66$ ).
$\text{UO}_2^{\text{fuel}} \rightarrow \text{UO}_2(\text{aq})$	8.60E-12	6.00E+04	Based on solubility of $\text{UO}_2$ in reducing conditions. Calculated using GWB and YMP data0 R5 thermodynamic database.
<i>Reactions at Fuel Surface</i>			
$\text{H}_2\text{O}_2 \rightarrow \text{O}_2 + 2\text{H}^+ + 2\text{e}^-$	7.40E-08	6.00E+04	1 <sup>st</sup> -order electrochemical rate constant for irreversible oxidation of $\text{H}_2\text{O}_2$ on $\text{UO}_2$ estimated based on assumption that, at a potential of 0.08 VSCE, the oxidation and reduction rates of $\text{H}_2\text{O}_2$ on $\text{UO}_2$ are equal and that the Tafel slopes are identical: from King and Kolar, 2003.
$\text{H}_2\text{O}_2 + 2\text{e}^- \rightarrow 2\text{OH}^-$	1.20E-12	6.00E+04	1 <sup>st</sup> -order electrochemical rate constant for irreversible reduction of $\text{H}_2\text{O}_2$ on $\text{UO}_2$ : from King and Kolar, 2003.

$O_2 + 2H_2O + 4e^- \rightarrow 4OH^-$	1.40E-12	6.00E+04	1 <sup>st</sup> -order electrochemical rate constant for irreversible reduction of $O_2$ on $UO_2$ : from King and Kolar, 2003.
<i>Reaction at NMP surface</i>	<i>(m/s)</i>	<i>(J/mole)</i>	
$H_2O_2 \rightarrow O_2 + 2H^+ + 2e^-$	7.40E-07	6.00E+04	1 <sup>st</sup> -order electrochemical rate constant for irreversible oxidation of $H_2O_2$ on NMP catalyst, assumed to be one order of magnitude faster than on oxide - needs experimental evaluation.
$H_2O_2 + 2e^- \rightarrow 2OH^-$	1.20E-11	6.00E+04	1 <sup>st</sup> -order electrochemical rate constant for irreversible reduction of $H_2O_2$ on NMP catalyst: assumed to be one order of magnitude faster than on oxide - needs experimental evaluation.
$O_2 + 2H_2O + 4e^- \rightarrow 4OH^-$	1.40E-11	6.00E+04	1 <sup>st</sup> -order electrochemical rate constant for irreversible reduction of $O_2$ on NMP catalyst: assumed to be one order of magnitude faster than on oxide - needs experimental evaluation.
$H_2 \rightarrow 2H^+ + 2e^-$	5.00E-04	6.00E+04	1 <sup>st</sup> -order electrochemical rate constant for irreversible oxidation of $H_2$ on NMP catalyst: based on data for Pt-Ru catalyst (Uchida et al., 2009) - needs experimental evaluation.
<i>Corrosion Reactions</i>	<i>Layer</i>	<i>(/s)</i>	<i>(J/mole)</i>
$UO_2^{2+} + 2H_2O \rightarrow UO_3 \cdot 2H_2O + 2H^+$	1.00E-03	6.00E+04	Estimate based on residence time of $UO_2^{2+}$ in supersaturated solution - needs experimental/literature evaluation. Rate law from King and Kolar, 2003:  $1.0E-3 * \exp(6.0E4 * dT) / (2.4 * [UO_2^{2+}]_{saturation})^4$
$UO_2(CO_3)_2^{2-} + 2H_2O \rightarrow UO_3 \cdot H_2O + 2CO_3^{2-} + 2H^+$	1.00E-04	6.00E+04	Estimate based on residence time of $UO_2^{2+}$ in supersaturated solution containing carbonate - needs experimental/literature evaluation. Rate law from King and Kolar, 2003:  $1.0E-4 * \exp(6.0E4 * dT) / (2.4 * [UO_2(CO_3)_2^{2-}]_{saturation})^4$
$UO_3 \cdot H_2O + 2CO_3^{2-} + 2H^+ \rightarrow UO_2(CO_3)_2^{2-} + 2H_2O$	6.30E-12	6.00E+04	Based on data for dissolution of soddyite in carbonate solution: from King et al., 2001.
<i>Key Bulk Reactions</i>	<i>(/s)</i>	<i>(J/mole)</i>	

$\text{H}_2\text{O}_2 \rightarrow \text{H}_2\text{O} + 0.5\text{O}_2$	4.50E-07	6.00E+04	Personal communication with Rick Wittman of PNNL on 3/12/2014, the overall reaction rate constant comes from runs using the PNNL Radiolysis model which uses rate constants from Pastina and Laverne, 2001.
	(m/mol s)	(J/mole)	
$\text{O}_2 + 4\text{Fe}^{2+} + 8\text{OH}^- \rightarrow 4\text{H}_2\text{O} + 2\text{Fe}_2\text{O}_3$	5.90E-01	6.00E+04	Rate is highly pH dependent below 8.0. Derived from experimental data at pH = 8.7 by King and Kolar, 2003.
$\text{H}_2\text{O}_2 + 2\text{Fe}^{2+} + 4\text{OH}^- \rightarrow 3\text{H}_2\text{O} + \text{Fe}_2\text{O}_3$	6.90E-01	4.20E+04	From King and Kolar, 2003, notes that pH dependence unknown - needs experimental evaluation.
$\text{UO}_2^{2+} + 2\text{Fe}^{2+} + 6\text{OH}^- \rightarrow \text{UO}_2 + 3\text{H}_2\text{O} + \text{Fe}_2\text{O}_3$	1.00E-02	6.00E+04	Assumed value based on similar redox reactions, from King and Kolar, 2003.
$\text{UO}_2(\text{CO}_3)_2^{2-} + 2\text{Fe}^{2+} + 6\text{OH}^- \rightarrow \text{UO}_2 + 2\text{CO}_3^{2-} + 3\text{H}_2\text{O} + \text{Fe}_2\text{O}_3$	1.00E-03	6.00E+04	Assumed value based on similar redox reactions, from King and Kolar, 2003.

**Table 9-5.** Electrochemical parameters for all relevant reactions and their associated temperature dependence used in MPM V2. The far right column provides notes on recent updates based on our on-going literature survey.

Reactions	Charge Transfer Coefficient	Standard Potential (Volts <sub>SCE</sub> )	Temperature Dependence (Volts <sub>SCE</sub> /K)	Updates based on literature review
<i>Fuel Dissolution</i>				
$\text{UO}_2^{\text{fuel}} \rightarrow \text{UO}_2^{2+} + 2\text{e}^-$	9.60E-01	0.169	-2.48E-04	From King and Kolar, 2003
$\text{UO}_2^{\text{fuel}} + 2\text{CO}_3^{2-} \rightarrow \text{UO}_2(\text{CO}_3)_2^{2-} + 2\text{e}^-$	8.20E-01	-0.173	2.10E-03	From King and Kolar, 2003
<i>Reactions at Fuel Surface</i>				
$\text{H}_2\text{O}_2 \rightarrow \text{O}_2 + 2\text{H}^+ + 2\text{e}^-$	4.10E-01	-0.121	-9.93E-04	From King and Kolar, 2003
$\text{H}_2\text{O}_2 + 2\text{e}^- \rightarrow 2\text{OH}^-$	4.10E-01	-0.973	-6.98E-04	From King and Kolar, 2003

$O_2 + 2H_2O + 4e^- \rightarrow 4OH^-$	5.00E-01	-0.426	-1.23E-04	From King and Kolar, 2003
--	----------	--------	-----------	---------------------------

---

*Reaction at NMP surface*

$H_2O_2 \rightarrow O_2 + 2H^+ + 2e^-$	4.10E-01	-0.121	-9.93E-04	Assumed to be equal to values on $UO_2$ surface - needs experimental evaluation.
$H_2O_2 + 2e^- \rightarrow 2OH^-$	4.10E-01	-0.973	-6.98E-04	Assumed to be equal to values on $UO_2$ surface - needs experimental evaluation.
$O_2 + 2H_2O + 4e^- \rightarrow 4OH^-$	5.00E-01	-0.426	-1.23E-04	Assumed to be equal to values on $UO_2$ surface - needs experimental evaluation.
$H_2 \rightarrow 2H^+ + 2e^-$	1	-0.421	0	Standard potential from Lide, R.D. (Ed.), 1999. Handbook of Chemistry and Physics, 80th ed. Charge transfer coefficient and temperature dependence need experimental evaluation.

---

**Table 9-6.** Diffusion coefficients and associated temperature dependence used in MPM V2. The far right column provides notes on recent updates based on our on-going literature survey.

Species	Diffusion coefficient (cm <sup>2</sup> /s)	Activation energy (J/mole)	Updates based on literature review
UO <sub>2</sub> <sup>2+</sup>	7.66E-10	1.50E+04	Changed from 5.0E-10 (estimate King et al., 2001) based on Kerisit and Liu, 2010.
UO <sub>2</sub> (CO <sub>3</sub> ) <sub>2</sub> <sup>2-</sup>	6.67E-10	1.50E+04	Changed from 5.0E-10 (estimate King et al., 2001) based on Kerisit and Liu, 2010.
U(IV)O <sub>2</sub> (aq)	5.52E-10	1.50E+04	Assumed to be neutral species and set equal to neutral UO <sub>2</sub> CO <sub>3</sub> (aq) from Kerisit and Liu, 2010.
CO <sub>3</sub> <sup>2-</sup>	8.12E-10	1.50E+04	Changed from 5.0E-10 (estimate King et al., 2001) based on Kerisit and Liu, 2010.
O <sub>2</sub>	1.70E-09	1.50E+04	No change: from From King and Kolar, 2003.
H <sub>2</sub> O <sub>2</sub>	1.70E-09	1.50E+04	No change: from From King and Kolar, 2003.
Fe <sup>2+</sup>	7.19E-10	1.50E+04	Added from Lide, R.D. (Ed.), 1999. Handbook of Chemistry and Physics, 80th ed.
H <sub>2</sub>	5.00E-09	1.50E+04	Added from Macpherson and Unwin, 1997.

**Table 9-7.** Saturation concentrations and associated temperature dependence used in MPM V2. The far right column provides notes on recent updates based on our on-going literature survey.

Species	Saturation Concentration (mole/m <sup>3</sup> )	Activation energy (J/mole)	Updates based on literature review
UO <sub>2</sub> <sup>2+</sup>	3.00E-02	-6.00E+04	Changed from 3.2E-2 mole/m <sup>3</sup> based on GWB runs using YMP data0 R5 equilibrium constant database. The negative activation energy reflects the observations of Murphy and Codell (1999) that common uranyl minerals exhibit retrograde solubility.
UO <sub>2</sub> (CO <sub>3</sub> ) <sub>2</sub> <sup>2-</sup>	9.00E-02	-6.00E+04	Changed from 5.12(mol/cm <sup>3</sup> ) <sup>0.34</sup> mole/m <sup>3</sup> based on GWB runs using YMP data0 R5 equilibrium constant database. The negative activation energy reflects the observations of Murphy and Codell (1999) that common uranyl minerals exhibit retrograde solubility
Fe <sup>++</sup>	5.00E-02	6.00E+04	Changed from 3.2E-2 mole/m <sup>3</sup> based on GWB runs using YMP data0 R5 equilibrium constant database.

## 9.5 ALPHA PARTICLE PENETRATION DEPTH AND DOSE RATE PROFILE USED IN MPM V2.

In the MPM, the primary oxidant driving the oxidative dissolution of the fuel is H<sub>2</sub>O<sub>2</sub> formed by radiolysis and the width of the irradiated zone in which H<sub>2</sub>O<sub>2</sub> is produced is of fundamental importance. (This was shown conceptually as the length of the green arrow labeled  $\alpha$  in Figure 9-3c). Thus far, the Argonne MPM has used the value of 35 micrometers from the fuel surface as the width of the irradiated zone (also referred to as the alpha particle penetration depth), which is the value used in the Canadian mixed potential model of King and Kolar 2003. The basis for this value and its applicability was reexamined because the Canadian work assumed only CANDU fuel assemblies.

The width of the alpha penetration depth is determined by the energy of the alpha particles emitted from the fuel surface. The 2013 version of the well-established and validated code “The Stopping and Range of Ions in Matter” (SRIM, 2013) was used to determine the relationship between alpha particle energy and penetration depth in water (Figure 9-4). The results show that the alpha penetration depth can vary from between 35  $\mu$ m for and alpha energy of around 5 MeV up to 55  $\mu$ m for and alpha energy of 6.5 MeV. 5 – 6.5 MeV is the reasonable range of alpha energies emitted from used fuel.

Based on the used fuel energy spectra shown in Radulescu (2011), a reasonable argument can be made for using an energy value of 5 MeV for used fuel alpha particles. Furthermore, Radulescu (2011) show that the alpha energy spectra does not change dramatically with time; therefore it is also reasonable to use a constant alpha penetration depth of 35  $\mu\text{m}$  throughout the duration of MPM simulations.

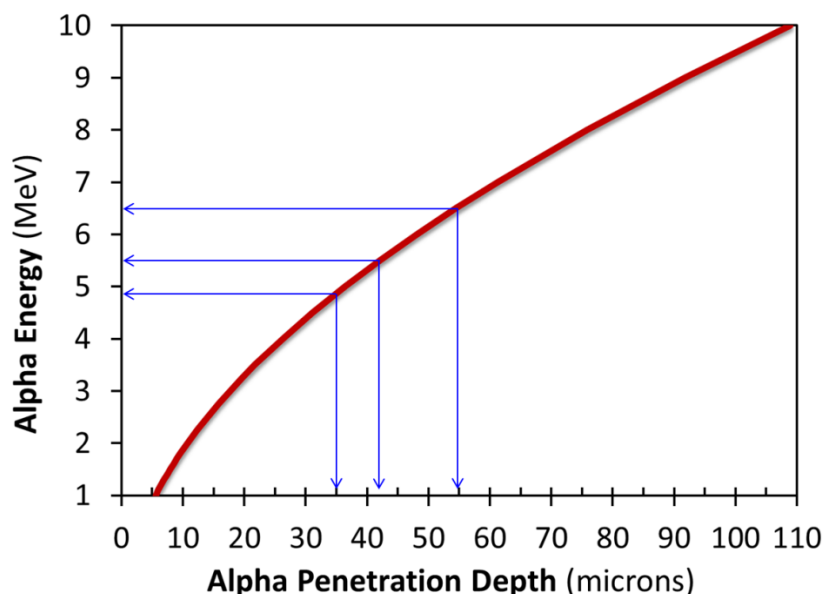


**Figure 9-4.** Alpha particle penetration depths vs. the alpha particle energy based on the stopping power of water, calculated using SRIM, 2013.

Another key physical quantity that determines the amount of radiolytic oxidants, and thus the local solution oxidative potential, is the dose rate within the alpha penetration zone. The earlier version of the MPM used a constant dose rate (step-function) across the entire 35  $\mu\text{m}$  alpha irradiation zone. This assumption was conservative (produced the maximum amount of radiolytic oxidants) but was also physically unrealistic. This step function has been replaced in MPM V2 with an exponentially decreasing alpha dose rate within the alpha penetration zone (Figure 9-5). The analytical function shown the curve in Figure 9-5 was fit to the dependence measured by Nielsen and Jonsson, 2006 (blue circles).

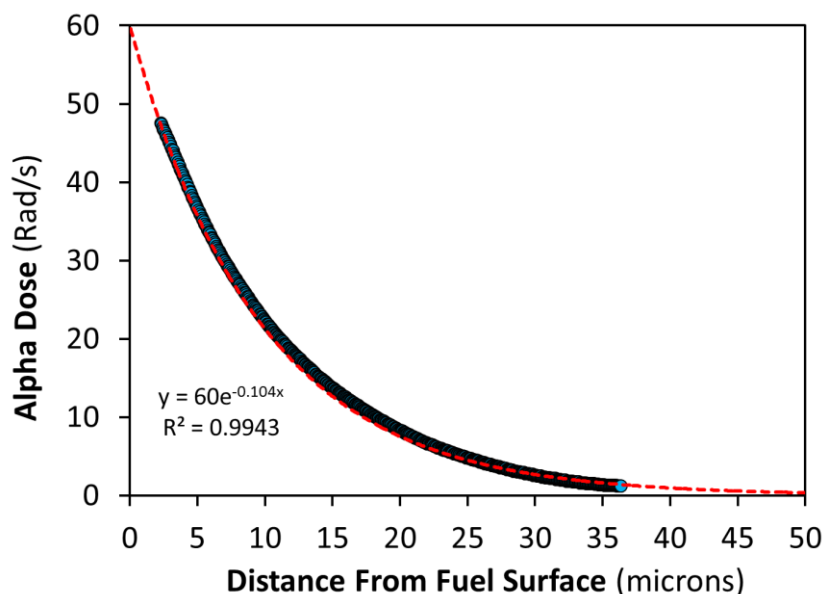


**Figure 9-5.** Alpha dose rate profile used in the MPM V2 (red line,  $Y=60e^{-0.104x}$ ), which is a fit to the data points of Nielsen and Jonsson, 2006.

## 9.6 INCORPORATION OF RADIOLYSIS MODEL ANALYTICAL FUNCTION INTO MPM V2

In January 2014, Rick Wittman and Edgar Buck of PNNL produced a straight forward analytical function that captures the functional dependence of the effective or conditional generation value of  $H_2O_2$  ( $G_{H_2O_2}$ ) on the local dissolved concentrations of  $H_2$  and  $O_2$ . A description of the PNNL Radiolysis Model and the quantitative definition of the conditional  $G_{H_2O_2}$  can be found in Buck et al, 2013 and a forthcoming FY2014 PNNL report.

The function provided by PNNL was converted from Fortran to MATLAB and incorporated as a subroutine into the MPM V2 (Appendix D). The radiolysis model function essentially replaces the constant  $G_{H_2O_2}$  value that had been used in MPM V1. The following relationship describes the basic equation for  $H_2O_2$  production as a function of space and time used in MPM V2:

$$\text{Molar yield of } H_2O_2(x,t) = [G_{H_2O_2}](H_2, O_2) * [\text{Dose Rate}](x,t) * g(x)$$

The amount of  $H_2O_2$  produced is determined as the product of  $G_{H_2O_2}$ , which is a function of local solution chemistry (radiolysis model subroutine), the dose rate, which varies in both time (as fuel decays) and space (see Figure 5), and a geometrical factor  $g(x)$ . The geometrical factor accounts for how the diffusion of aqueous species is modified by the tortuosity of the uranyl corrosion layer (schoepite). The subroutine written in MATLAB code is shown in Appendix D.

The topology of the radiolysis model function that determines  $G_{H_2O_2}$  in the MPM V2 is shown in Figure 6. The striking feature of this function is the precipitous decrease in the

value of  $G_{\text{H}_2\text{O}_2}$  from around 1.0 (the value used in the previous MPM version) down to less than 0.1 for conditions of low dissolved  $\text{O}_2$  and moderate to high concentrations of  $\text{H}_2$ . This feature is strongly dependent on the dose rate, as shown in the plots at the bottom Figure 6. The impact this  $G_{\text{H}_2\text{O}_2}$  “cliff” on the dissolution rate of used fuel calculated by the MPM V2 has been explored as part of the sensitivity runs discussed in Section 9.7 below.

Sensitivity runs show that even at a low starting  $[\text{O}_2] = 1.0\text{E-}9$  moles/L, the dissolved concentration of  $\text{O}_2$  rarely drops below  $1.0\text{E-}7$  moles/L. This is due to the production of  $\text{O}_2$  as  $\text{H}_2\text{O}_2$  decomposes at the fuel surface by the reaction  $\text{H}_2\text{O}_2 \rightarrow \text{O}_2 + 2\text{H}^+ + 2\text{e}^-$ .

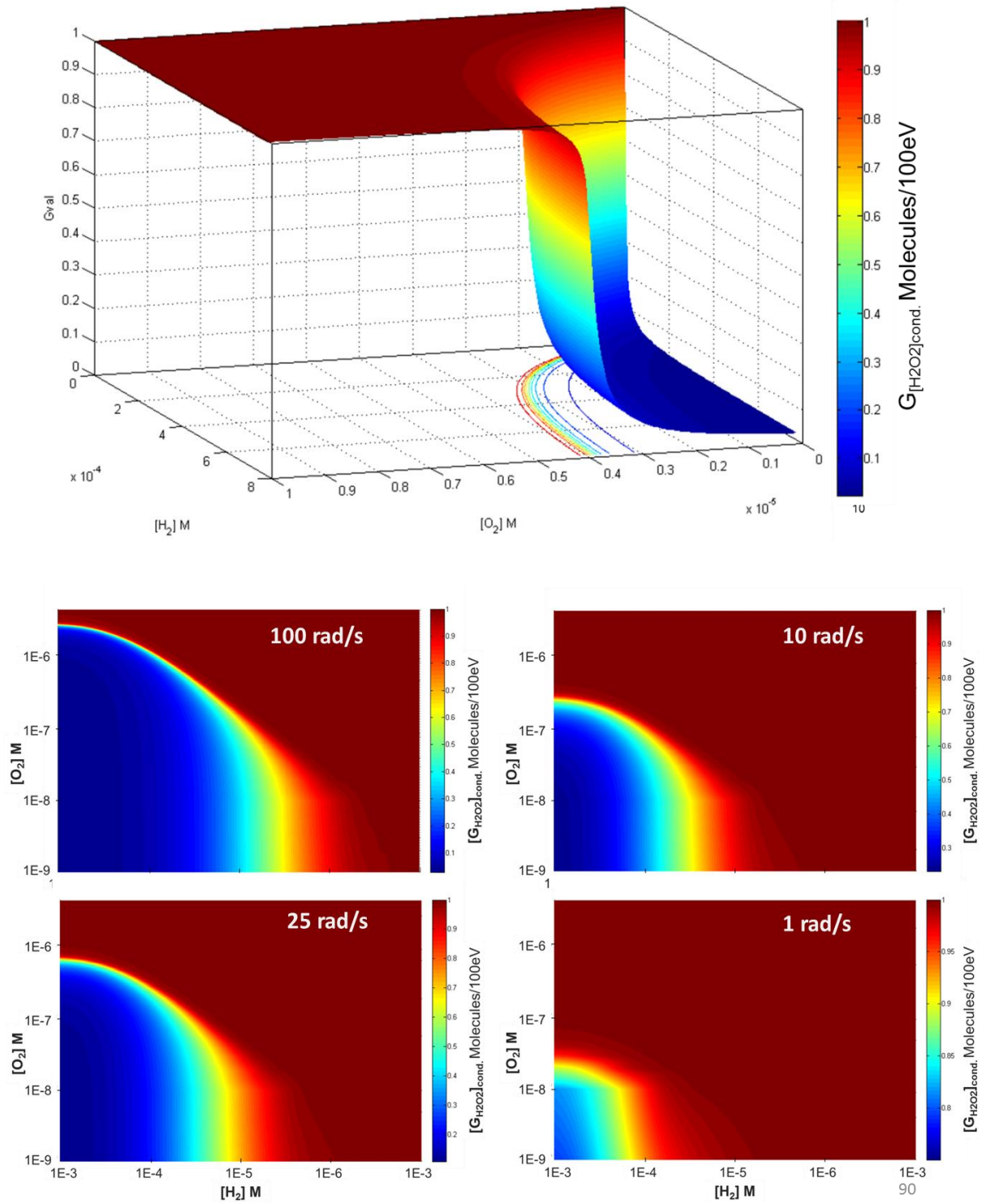


**Figure 9-6.** Topology of the analytical function that comprises the Radiolysis Model subroutine within the MPM V2.

## 9.7 SENSITIVITY RESULTS MIXED POTENTIAL MODEL V2

For anoxic to low oxygen conditions (nano- to micromolar), the fuel dissolution rate predicted by the MPM V2 will depend directly on the concentration of  $\text{H}_2\text{O}_2$  at the fuel surface. A number of competing processes determine this concentration:

- $\text{H}_2\text{O}_2$  is continuously produced within the first 35  $\mu\text{m}$  of the fuel surface. The  $\text{H}_2\text{O}_2$  concentration depends on dose rate and the generation value  $G_{\text{H}_2\text{O}_2}$ , which is determined by the Radiolysis Model subroutine based on local  $[\text{O}_2]$  and  $[\text{H}_2]$  for a given dose rate.
- $\text{H}_2\text{O}_2$  diffuses towards or away from the fuel surface depending on the concentration; the diffusion rates near the surface will be moderated by the corrosion layer.
- $\text{H}_2\text{O}_2$  concentration at environmental boundary (3 mm from fuel) is defined to be zero.
- $\text{H}_2\text{O}_2$  is consumed (dominantly) at the fuel surface by the following coupled half-reactions:



- $\text{H}_2\text{O}_2$  consumption rate at the fuel surface increases significantly when the NMP-catalyzed hydrogen oxidation reaction is taken into account and  $[\text{H}_2] \geq 1.0\text{E-}5$  mole/L (Figure 8):

The increase in the rate of  $\text{H}_2\text{O}_2$  consumption at the fuel surface when NMP-catalyzed hydrogen oxidation is occurring is caused by the kinetic balance of reactions (9-1), (9-2) and (9-3):



Specifically, the large anodic current associated with the hydrogen oxidation reactions increases the rate of the dominant cathodic reaction involving hydrogen peroxide reduction. This process is shown schematically in Figure 9-3c. Therefore, hydrogen peroxide is rapidly depleted when enough hydrogen is present at a fuel surface bearing active NMP sites, thereby decreasing the rate of oxidative dissolution (Equation 9-1). The relative importance of these processes and other chemical and physical effects on the fuel dissolution rate were studied through a series of model sensitivity runs.

Approximately 300 model runs were performed with MPM V2 to determine the relative impacts that different processes, variables and parameters have on the used fuel dissolution rate calculated by the code. Each model run produces an output file consisting of a 100x2000 cell matrix that includes corrosion potentials, reaction current densities, component fluxes, and concentrations of all components at every point in time

at every point in space for the specified conditions. These results have been tabulated and key trends identified.

The detailed model output files are important for understanding interactions between the radiolytic, chemical and physical processes included in the code; however, our ultimate interest (what will be provided to the performance assessment model) is the dissolution rate. Therefore, the output of the MPM V2 sensitivity runs has been synthesized and is represented here in terms of grams of fuel dissolved per surface area per time (Figure 9-7).

Figure 9-7 does not explicitly show the time evolution of the variables; however, the direction of the dose rate and temperature arrows are used to indicate that these variables will be decreasing with time as the fuel decays. The pH and temperature effects on the fuel dissolution rate are of about the same magnitude and are indicated by the same arrow.

It is important to note that there are still relatively large uncertainties in the quantification of how the temperature and pH will affect the fuel dissolution rate. For example, the temperature dependence of most reactions in the parameter database (specifically Table 9-4) is quantified using a reasonable (based on geochemical literature) place holder value of 60,000 J/mole for the activation energy. This, as well as terms accounting for pH dependence and complexation, need to be evaluated experimentally to reduce uncertainties.

Consistent with the experimental literature, the model indicates that decreasing dose rates and temperature decrease the rate of fuel dissolution by almost two orders of magnitude. The main chemical effects included in the model are due to pH and dissolved carbonate, which complexes uranium to increase its dissolved concentration limit. As acidity and carbonate concentrations increase, the fuel dissolution rate increases. The light blue arrows show that fuel dissolution rate decreases with decreasing  $G_{H_2O_2}$  values (due to increasing  $[H_2]$  and decreasing  $[O_2]$ ), increasing schoepite corrosion layer thickness, and increasing concentrations of ferrous iron.

All of these effects, however, are minor relative to the fuel-protecting process that involves the oxidation of  $H_2$  at the fuel surface (dark blue arrow in Figure 9-7). As shown in Figure 9-3,  $H_2$  is included in the MPM V2 in a catalytic reaction occurring on the NMP surfaces. The amount of hydrogen reacted depends on its concentration and the surface area of the NMP. For the sensitivity runs summarized in Figure 9-7, a surface coverage of 1% NMP on the fuel surface was used to quantify the  $H_2$  effect for various  $H_2$  concentrations. Results show that presence of 100 bar  $H_2$ , which may be expected in repositories at 500 meters depth with steel waste package materials, can essentially shut off the oxidative dissolution of the fuel (SKB, 2011). Radiolytic production of  $H_2$  is sufficient to cause a small decrease in the fuel dissolution rate on the same order as the effects of  $G_{H_2O_2}$  and surface layers, but the anodic corrosion of steel can have a much greater effect.

Figure 9-8 shows plots from the MPM V2 sensitivity runs that quantify the  $H_2$  effect at two dose rates. The identical shapes indicate that it is the decrease in the fuel corrosion potential caused by the coupling of the  $H_2$  oxidation to the U(IV)/U(VI) couple that is responsible for the dramatic decrease in the fuel dissolution rate with increasing  $H_2$  concentrations (through the reactions shown conceptually in Figure 9-3). The dissolution rates calculated for  $H_2$  generated from radiolysis and by steel corrosion (values of 1 bar and 10 bars provided to show sensitivity) are indicated in Figure 9-8a. Figure 9-8b shows the corrosion potentials from the electrochemical experiments of Broczkowski et al, 2005 for SIMFUELS made with and without added NMP. Those results suggest that the presence of NMP at the fuel surface is largely responsible for the observed  $H_2$  effect, although the effect does occur to a lesser extent in the absence of NMP. An experimental approach has been designed at ANL to quantify that effect in a future version of the MPM.

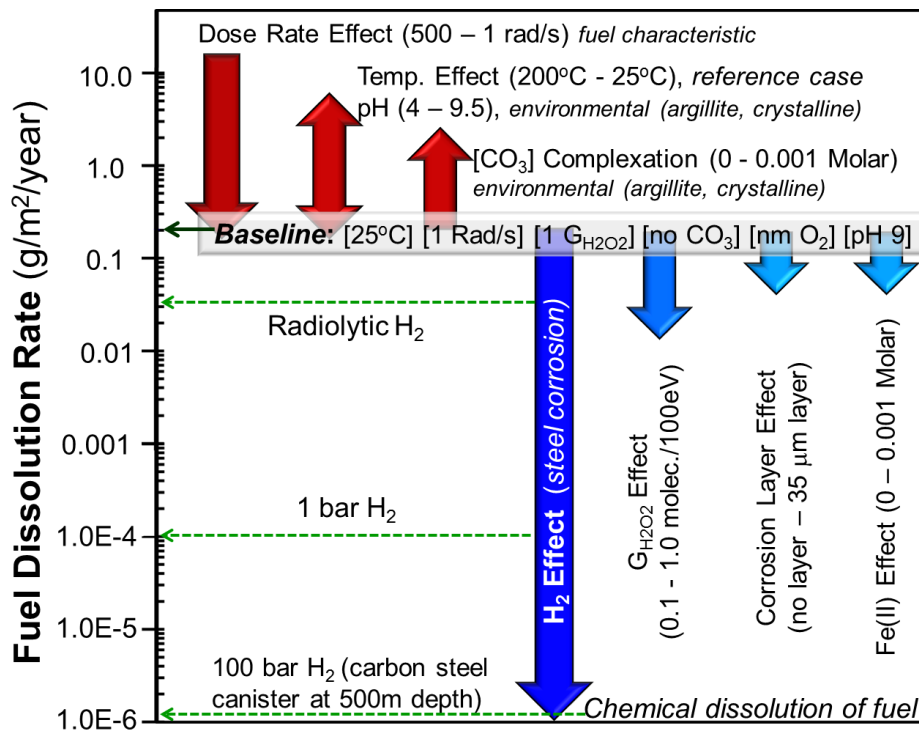


**Figure 9-7.** Summary of compiled results from FY2014 MPM V2 sensitivity runs

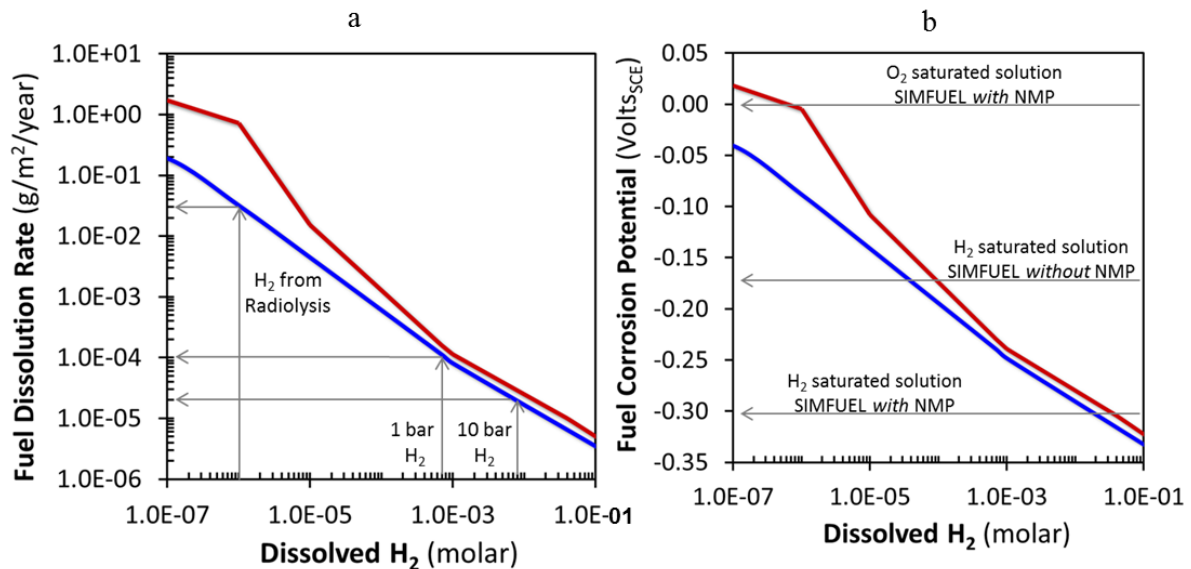


**Figure 9-8.** Details of (a) fuel dissolution rate and (b) corrosion potential calculated using MPM V2 for two dose rates (100 rad/s, red and 25 rad/s, blue).

## 9.8 CONVERSION OF MPM V2 FROM MATLAB TO FORTRAN

The MPM was written in MATLAB to utilize available functions (e.g., to solve ordinary differential equations for mass transport) to facilitate the development of additional process modules, such as including catalytic reactions on NMP and a more detailed radiolysis model. The purpose of the language conversion is to facilitate incorporation of the MPM directly into the performance assessment models for argillite and crystalline rock environments. The initial Fortran version of the Argonne MPM will be issued in early FY2015 to serve as a prototype to develop input and output communication links with PA and other process models. Continued development of the MPM, such as including modules for steel corrosion and the degraded NMP catalysis efficiency due to corrosion and poisoning, will be done using MATLAB to quickly evaluate optional approaches and interactions with the rest of the code. The finalized modules will then be translated to Fortran. This development plan is summarized schematically in Figure 9-1.

The specifics on the conversion are as follows:

- Programming language: Intel(R) Visual Fortran Compiler XE 14
- Additional libraries: LAPACK 3.5.0 Windows 32-bit static library (from <http://icl.cs.utk.edu/lapack-for-windows/lapack/#libraries>)
- Development environment: Visual Studio 2008

To date, a significant amount of the MPM Fortran code has been written and some internal checks (convergence of individual modules) have been done. Initial meetings with personnel developing the PA model have been scheduled for August and November

2014 to discuss the conceptual approach being taken and the interfaces and information exchanges between the Fortran MPM and PA process models. The following provides an annotated list of issues being addressed in the development of the Fortran MPM to support those discussions.

Inputs to MPM:

- There will be two entry points, one for interaction with the PA model and one for a stand-alone run.
- The input to the MPM is the environmental solution chemistry, temperature and dose rate
  - Currently, the environmental solution information that needs to be passed into the MPM includes the pH and concentrations of dissolved oxygen, hydrogen, iron, and carbonate.
  - It is anticipated that reactions with sulfate, chloride and bromide will be added to the MPM in future versions, so the codes are being set up to allow for expanding the number of components (chemical species).
- There are two types of parameters:
  - System parameters that are used in the PA model and other process models
  - MPM parameters that define characteristics of the mixed potential model only.
- The interface is under development, but it is envisioned that the system parameters will be passed into the MPM while an auxiliary function will read the MPM parameters from a data file.

The MPM parameters will be contained in a user-modifiable text file.

Outputs from MPM:

- There will be two exit points, one for interaction with the PA model and one for a stand-alone run.
  - Output to the PA model will be the fuel dissolution rate (mass/surface area/time) and the final concentrations of all components.
  - Output for the stand-alone model will generate a text data file containing the fuel dissolution rate, the concentrations of components, and calculated electrochemical quantities used to determine the fuel dissolution rate, namely, corrosion potential and reaction current densities.

## 9.9 CONCLUSIONS AND FUTURE WORK

The major accomplishments for Argonne's FY2014 work on the Mixed Potential Model (MPM) development project were as follows:

- Added a working noble metal particle (epsilon phase) domain on fuel surface to account for the protective hydrogen effect.
- Incorporated the radiolysis model subroutine in MPM (using an analytical function provided by PNNL)

- Performed systematic sensitivity runs that identify and quantify the processes that affect the fuel dissolution rate.
- Compared sensitivity results with available experimental data (ongoing)
- Developed a research priority list based on results from sensitivity study and comparison with experimental results

The key observation to come out of the MPM sensitivity studies was that the set of coupled electrochemical reactions that comprise the model can be used to quantify the effectiveness of hydrogen within a breached canister to effectively shut down the radiolytic oxidative dissolution of the fuel. At sufficiently high hydrogen concentrations, fuel dissolution will only occur through the much slower chemical dissolution mechanism. This is consistent with experimental results from a number of repository programs (e.g., Shoesmith, 2008; Grambow and others, 2010) and with results from initial electrochemical tests performed in FY2013 as part of this study. The capacity to quantify the hydrogen effect in the used fuel degradation model will provide more realistic radionuclide source terms for use in PA.

The relative effects of temperature, dose rate (burnup), radiolysis, pH, carbonate complexation, ferrous iron and corrosion layer formation were also evaluated in the FY2014 sensitivity runs. All of these variables will influence the fuel degradation rate in distinct ways within argillite and crystalline rock, and other potential disposal environments. However, our sensitivity runs show that the hydrogen effect could be by far (up to four orders of magnitude greater, depending on the hydrogen concentration) the most dominant.

The MPM is uniquely suited to quantify the hydrogen effect on used fuel degradation because it explicitly accounts for all relevant interfacial redox reaction kinetics using fundamental electrochemical principles. This includes the impacts of phases present in the fuel, such as the catalytic effects of noble metal particles and the fuel surface itself, and other materials present in the disposal system that supply reactants or affect key redox reactions. The anoxic corrosion of steels present in the waste package is the main source of hydrogen in the waste package. The MPM was developed with the initial focus on reactions at the fuel surface, and the dissolved hydrogen concentration is currently a user-input value. To account for the hydrogen effect in long-term model runs, corrosion kinetics of steel components leading to hydrogen generation needs to be incorporated into the model and coupled with fuel dissolution kinetics through the dissolved hydrogen concentration.

The current version of the MPM has proven effective for quantifying key processes affecting the rate of used fuel degradation; however, the implementation of MPM within a performance assessment model requires further model development and focused experimental work to provide data and quantify uncertainties in the existing database used to determine model parameter values representing disposal environments of interest. In order to take advantage of the work that has been done so far on the MPM, a number of needs have been identified:

- Incorporate the kinetics for hydrogen generation during the anoxic corrosion of steels into MPM as the source term for hydrogen.

- Perform focused electrochemical experiments with noble metal particle and lanthanide-doped  $\text{UO}_2$  electrodes to determine parameter values needed to accurately model the effects of hydrogen, potential catalytic poisons such as bromide, and the pH and reaction temperature dependencies of fuel dissolution.
- Convert the MPM from MATLAB to Fortran to facilitate integration with PA codes (PFLOTRAN) (ongoing)
- Complete sensitivity runs to identify and assess inputs and outputs for integrating Fortran MPM into PA

## 9.10 REFERENCES

- Broczkowski, M. E., Noël, J. J., Shoesmith, D. W., (2005). The inhibiting effects of hydrogen on the corrosion of uranium dioxide under nuclear waste disposal conditions. *Journal of Nuclear Materials* 346, 16-.
- Buck E., Jerden, J., Ebert, W., Wittman, R., (2013). Coupling the Mixed Potential and Radiolysis Models for Used Fuel Degradation. FCRD-UFD-2013-000290.
- Christensen, H., Sunder, S. (1996). An evaluation of water layer thickness effective in oxidation of  $\text{UO}_2$  fuel due to radiolysis of water. *Journal of Nuclear Materials*, 238, 70-77.
- Ebert, W. L., Cruse, T. A., and Jerden J., (2012). Electrochemical Experiments Supporting Oxide Fuel Corrosion Model. FCRD-UFD-2012-000201.
- R.J. Finch, R.C. Ewing (1992) The corrosion of uraninite under oxidizing conditions. *Journal of Nuclear Materials*, 190, 133-156.
- B. Grambow, J. Bruno, L. Duro, J. Merino, A. Tamayo, C. Martin, G. Pepin, S. Schumacher, O. Smidt, C. Ferry, C. Jegou, J. Quiñones, E. Iglesias, N. Rodriguez Villagra, J. M. Nieto, A. Martínez-Esparza, A. Loida, V. Metz, B. Kienzler, G. Bracke, D. Pellegrini, G. Mathieu, V. Wasselin-Trupin, C. Serres, D. Wegen, M. Jonsson, L. Johnson, K. Lemmens, J. Liu, K. Spahiu, E. Ekeröth, I. Casas, J. de Pablo, C. Watson, P. Robinson, D. Hodgkinson, (2010). Model Uncertainty for the Mechanism of Dissolution of Spent Fuel in Nuclear Waste Repository, 2010 Euratom EUR 24597 EN EUROPEAN COMMISSION, Final Report for MICADO project.
- E.C. Gaucher, C. Tournassat, F.J. Pearson, P. Blanc, C. Crouzet, C. Lerouge, S. Altmann, 2009, A Robust Model for Pore-water Chemistry of Clayrock. *Geochimica et Cosmochimica Acta*, 73 6470–6487
- Guimerà, J., Duro, L., Delos, A. (2006). Changes in Groundwater Composition as a Consequence of Deglaciation Implications for performance Assessment, R-06-105, Swedish Nuclear Fuel and Waste Management Co, SKB, November 2006.
- Jerden, J., Frey, K., Cruse, T., and Ebert, W. (2012). Waste Form Degradation Model Status Report: ANL Mixed Potential Model, Version 1. Archive. FCRD-UFD-2013-000057.
- Jerden, J., Frey, K., Cruse, T., and Ebert, W. (2013). ANL Mixed Potential Model with Experimental Results: Implementation of Noble Metal Particle Catalysis Module. FCRD-UFD-2013-000305.

- Kerisit, S., Liu, C. (2010). Molecular simulation of the Diffusion of Uranyl Carbonate Species in Aqueous Solution. *Geochimica et Cosmochimica Acta*, 74, 4937-4952.
- King, F. and Kolar, M. (1999) Mathematical Implementation of the Mixed-Potential Model of Fuel Dissolution Model Version MPM-V1.0, Ontario Hydro, Nuclear Waste Management Division Report No. 06819-REP-01200-10005 R00.
- King, F. and Kolar, M. (2002). Validation of the Mixed-Potential Model for Used Fuel Dissolution Against Experimental Data., Ontario Hydro, Nuclear Waste Management Division Report No. 06819-REP-01200-10077-R00.
- King, F. and Kolar, M. (2003). The Mixed-Potential Model for UO<sub>2</sub> Dissolution MPM Versions V1.3 and V1.4., Ontario Hydro, Nuclear Waste Management Division Report No. 06819-REP-01200-10104 R00.
- Macpherson, J.V., and Unwin, P.R. (1997). Determination of the Diffusion Coefficient of Hydrogen in Aqueous Solution Using Single and Double Potential Step Chronoamperometry at a Disk Ultramicroelectrode. *Analytical Chemistry*, 69, 2063-2069.
- Murphy, W.M. and Codell, R.C. (1999). *Sci. Basis Nuclear Waste Mgt. XXII*, Materials Research Society, 551-558.
- Nielsen and Jonsson, (2006). Geometrical Alpha- and Beta-dose Distributions and Production Rates of Radiolysis Products in Water in Contact with Spent Nuclear Fuel. *Journal of Nuclear Materials*, 359, 1-7.
- Pastina, B. and LaVerne, J. A. (2001). Effect of Molecular Hydrogen on Hydrogen Peroxide in Water Radiolysis. *Journal of Physical Chemistry A* 105, 9316-9322.
- Radulescu, (2011), LETTER REPORT, Reactor and Nuclear Systems Division, Repository Science/Criticality Analysis FTOR11UF0334, August, 2011
- Shoosmith, D.W., M. Kolar, and F. King (2003). A Mixed-Potential Model to Predict Fuel (Uranium Dioxide) Corrosion Within a Failed Nuclear Waste Container Corrosion, 59, 802-816.
- Shoosmith, D. W. (2008). The Role of Dissolved Hydrogen on the Corrosion/Dissolution of Spent Nuclear Fuel, NWMO TR-2008-19, November 2008 Nuclear Waste Management Organization, 22 St. Clair Avenue East, 6<sup>th</sup> Floor, Toronto, Ontario M4T 2S3, Canada
- SKB (Svensk Kärnbränslehantering AB [Swedish Nuclear Fuel and Waste Management Company]) (2011). Long-Term Safety for the Final Repository for Spent Nuclear Fuel at Forsmark, Technical Report TR-11-01. Three volumes. Stockholm, Sweden: Svensk Kärnbränslehantering AB.
- Torrero, M.E., E. Baraj, J. De Pablo, J. Gimenez, and I. Casas (1997). Kinetics of Corrosion and Dissolution of Uranium Dioxide as a Function of pH. *International Journal of Chemical Kinetics*, 29, 261-267.
- Trummer, M., Roth, O., and M. Jonsson, M. (2009). H<sub>2</sub> Inhibition of Radiation Induced Dissolution of Spent Nuclear Fuel. *Journal of Nuclear Materials*, 383, 226-230
- Tsai, H. (2003). NRC Review of ANL High-Burnup Cladding Performance Program, July 16, (2003).
- Uchida, H., Izumi, K., Aoki, K., Watanabe, M., (2009). Temperature-Dependence of Hydrogen Oxidation Reaction Rates and CO-Tolerance at Carbon-Supported Pt, Pt-Co, and Pt-Ru Catalysts. *Phys. Chem. Chem. Phys.*, 11, 1771-1779

Vinsot A., Mettler S. and Wechner S. (2008). In situ characterization of the Callovo-Oxfordian pore water composition. *Phys.Chem. Earth*, 33, S75–S86.

## 10. SUMMARY

Significant progress has been made in FY14 in both experimental and modeling arenas in evaluation of used fuel disposal in crystalline rocks. The work covers a wide range of research topics identified in the R&D plan. The major accomplishments are summarized below:

- A R&D plan was developed for used fuel disposal in crystalline rocks. A total of 31 research topics (9 for system level and 22 for processes level) have been identified. The technical approach to addressing each of these topics is formulated.
- A generic reference case for crystalline disposal media has been established. The reference case specifies the emplacement concept, waste inventory, waste form, waste package, backfill/buffer properties, EBS failure scenarios, host rock properties, and biosphere. This is an important step in developing a baseline for total system model development. Three emplacement concepts were specified: waste packages containing 4 PWR assemblies emplaced in boreholes in the floors of tunnels (KBS-3 concept), a 12-assembly waste package emplaced in tunnels, and a 32-assembly dual purpose canister emplaced in tunnels.
- We have developed and applied THMC models to the analysis of coupled EBS processes in bentonite-backfilled repositories. We based this development on the extension of the Barcelona Basic Model (BBM) to a dual-structure model for expansive clay, such as bentonite. The dual-structure model has been found to give results that are in better agreement with observations, in particular the rate of buffer re-saturation, by representing identifiable physical mechanisms not treated by the original BBM model. Therefore, this model improvement reduces the modeling uncertainty for THM processes in a bentonite buffer.
- We have examined the consistency of macroscopic measurements, electrical double layer (EDL)-based models, and molecular-scale simulations of clay media for adsorption and diffusion of trace levels of calcium ( $\text{Ca}^{2+}$ ), bromide ( $\text{Br}^-$ ), and tritiated water (HTO) in a loosely compacted, water-saturated Namontmorillonite. Molecular dynamics (MD) simulations were also conducted and used to aid the interpretation of adsorption and diffusion processes in individual clay interlayer nanopores. The MD simulations allow a critical test of various transport/pore models by carefully evaluating the physical meaning of their related fitting parameters on a single set of data. These results highlight the difficulty in constraining current theories of the properties of clay barriers using transport modeling alone.
- DFN generation, parallel flow solutions, and particle tracking were demonstrated at application-relevant scales using fracture parameters from a well-characterized site. We also developed and demonstrated the capability to simulate intrafracture variability within a full-scale DFN network. The ability to produce high-quality computational DFN meshes suitable for state-of-the-art parallel subsurface flow codes is a unique capability that will allow large DFNs to be considered in

applications. The ability to reliably track particles on DFN control volume grids is also a unique capability.

- Refinement and extension of the DFN modeling capability was undertaken to enable representation of the tetrahedral mesh within the DFN mesh. The two realizations of the DFN with boreholes in place is an important demonstration of an advanced modeling capability combining volume and DFN meshes, and incorporating complex geometries. These simulations used the FEHM code to merge the volume and DFN meshes. FEHM has unique capability to use define redundant computational nodes, which greatly facilitated the merging of the meshes. Comparison of simulated and measured saturation values in the BRIE borehole is underway.
- We have made significant progress in effectively demonstrating a method of interrogating and taking defensible credit for slow desorption rates to improve reactive transport predictions over long time and distance scales. We chose uranium in Grimsel Test Site granodiorite as a study case, but the method could be applied to any moderately sorbing radionuclide in any hydrogeologic system. Column transport data allow us interrogate slow desorption sites, while batch sorption data are not able to interrogate these slow sites. The approach we developed will help to reduce conservatism in large-scale predictions. From a practical standpoint, the three-site kinetic model developed from uranium column transport data is easy to implement in performance assessment models with little additional computational burden over a simple linear partition coefficient ( $K_d$ ) model.
- We have made significant progress in understanding colloid-facilitated radionuclide transport in nuclear waste repository environments. We demonstrated a repeat-injection column method for evaluating and parameterizing colloid-facilitated radionuclide transport, using bentonite colloids, Am, and Grimsel Test Site granodiorite FFM as a model system. The method is designed to better interrogate the slower rates (either colloid filtration rates or radionuclide desorption rates from colloids) that have a large impact in performance assessment calculations over long time and distance scales. An increase in colloid recoveries in successive column injections would suggest a fraction of colloids that is relatively susceptible to filtration, and the colloids that remain mobile in later injections will have smaller apparent filtration rate constants that are more relevant for use in large-scale performance assessment calculations.
- A study of the dissolution of intrinsic Pu colloids in the presence of montmorillonite at different temperatures was successfully accomplished using a novel experimental setup containing a dialysis device. This device enables us to separate two solid phases, but let them interact with each other via aqueous Pu ions. Kinetics of a series processes involved in intrinsic Pu colloid dissolution was modeled using 1<sup>st</sup> order reactions to compare the rate constant of different processes. We show that the kinetic constants for dissolution were one to two orders of magnitude lower than that of diffusion of aqueous Pu species in the system. Therefore the dissolution processes was the rate-limiting step. Although the presence of clay changes neither the colloids dissolution nor diffusion rates of

Pu, it can stabilize dissolved Pu species and drive intrinsic Pu colloid dissolution and the formation of more stable Pu pseudo-colloids. Temperature enhances dissolution of intrinsic Pu colloids by overcoming a moderate activation energy ( $28 \text{ kJ mol}^{-1}$ ). Our thermodynamic study shows that the sorption of Pu on montmorillonite is endothermic as a positive change in enthalpy for the sorption has been obtained. The affinity of Pu for the clay increases with increasing of temperature resulting higher  $K_d$  at elevated temperature. The negative values of change of Gibbs free energy for Pu-clay sorption confirm that sorption of Pu onto clay occurs spontaneously and Pu pseudo-colloids are thermodynamically quite stable at both temperatures of 25 to 80 °C. Although the fact that intrinsic Pu colloids tend to dissolve in the presence of montmorillonite may limit the migration of intrinsic Pu colloids, the subsequent formation of thermodynamically more stable Pu pseudo-colloids can play important role in Pu transport in the environment over significant temporal and spatial scales.

- We have examined the reactivity of three different types of intrinsic Pu colloids in the presence of montmorillonite at 25 and 80°C under atmospheric conditions. Pu oxides calcined at 300 and 800 °C and intrinsic Pu colloids produced from acidic solution are quite stable under our experimental conditions. Only two out of seven experiments showed signs of intrinsic Pu colloid dissolution after 100 days. Predicted Pu concentrations calculated using dissolution rate constants obtained from intrinsic Pu colloids formed in alkaline solution are much higher than the measured Pu concentrations, suggesting that these three types of intrinsic Pu colloids are more stable, thus less reactive than the ones formed in alkaline solution. The differences in the reactivity among investigated intrinsic Pu colloids are attributed to their morphological features including crystallinity, crystal growth, aggregation and particle shapes and sizes, all of which are greatly influenced by temperatures during formation of these intrinsic Pu colloids. Intrinsic Pu colloids and/or Pu oxides formed at elevated temperatures are more stable and may play an important role in the migration of intrinsic Pu colloids away from nuclear waste repository setting.
- We have made significant progress in the development of a multiple potential model for used fuel degradation. In FY14, we added several new functionalities to the model. We added a working noble metal particle (epsilon phase) domain on fuel surface to account for the protective hydrogen effect. We also incorporated the radiolysis model subroutine into the model. We performed systematic sensitivity runs that identify and quantify the processes that affect the fuel dissolution rate.

Based on the work accomplished in FY14 and the prior years, the future work is recommended to:

- Focus on two key topics related to deep geologic disposal of used fuel in crystalline rocks: (1) better characterization and understanding of fractured media and fluid flow and transport in such media, and (2) designing effective engineered barrier systems (EBS) for waste isolation. Specific attention will be given to the development of scientifically sound thermal limits for various buffer materials.

- Explore various disposal concepts, for example, borehole disposal vs. drift emplacement, regular waste packages vs. dual purpose canisters (DPCs). Especially, the work will explore potential advantages of crystalline media for the disposal of DPCs, given the high mechanical strength of the rocks.
- Move more towards model demonstrations and applications using data obtained from international collaborations.
- Continue international collaborations, especially with Korea Atomic Research Institute (KAERI), Sweden Underground Research Lab and Czech Bedrichov Tunnel Test Facility.
- Closely coordinate with the deep borehole disposal control account. The data obtained and the tools developed in this control account may be transferable to the deep borehole disposal, or vice versa.
- Continue to work with the generic disposal system analysis control account to refine the reference case for crystalline media and help to develop a performance assessment model for the reference case.



## APPENDIX A

### RESEARCH & DEVELOPMENT (R&D) PLAN FOR USED FUEL DISPOSAL IN CRYSTALLINE ROCKS

**Note: This R&D plan is a revision of an early developed R&D plan for natural system evaluation and tool development (Wang, 2013). In this revision, the newly added research topics are indicated in red. The topics that are no longer applicable to crystalline rocks are indicated in gray.**

#### A1.0 Objectives

The U.S. Department of Energy Office of Nuclear Energy, Office of Fuel Cycle Technology established the Used Fuel Disposition Campaign (UFDC) in fiscal year 2010 (FY10) to conduct the research and development (R&D) activities related to storage, transportation and disposal of used nuclear fuel and high level nuclear waste. The Mission of the UFDC is

*To identify alternatives and conduct scientific research and technology development to enable storage, transportation and disposal of used nuclear fuel and wastes generated by existing and future nuclear fuel cycles.*

The work package of Crystalline Disposal R&D directly supports the following UFDC objectives:

- Develop a fundamental understanding of disposal system performance in a range of environments for potential wastes that could arise from future nuclear fuel cycle alternatives through theory, simulation, testing, and experimentation.
- Develop a computational modeling capability for the performance of storage and disposal options for a range of fuel cycle alternatives, evolving from generic models to more robust models of performance assessment.

A disposal system generally consists of a natural barrier system and an engineered barrier system. The natural barrier system is an integral part of a geologic nuclear waste repository. Spatially, it extends from the disturbed rock zone (DRZ) around a disposal room, created by mechanical, thermal and chemical perturbations due to underground excavation or waste emplacement, to the surrounding geologic media, and continues all the way to a specified repository boundary. The work on natural system evaluation supports all four stages of geologic repository development: site screening, site selection, site characterization, and site suitability study. The information collected in the related activities will play a pivotal role in site screening and site selection. In a crystalline disposal system, the engineered barrier system is an important component for waste isolation. Because of its high mechanical strength and relatively high thermal conductivity, crystalline rocks have certain advantages for emplacement and disposal of large size waste packages such as dual purpose canister (DPC). Large waste packages

can be transported to the disposal drifts through an access ramp. The high mechanical strength of the host rock will also prevent a mechanical damage of waste packages as it occurs due to room closure in in a salt or a shale repository, thus allowing fully take credit for the engineered barrier system.

From the well accepted multiple barrier concept for waste repository safety, each barrier is supposed to be utilized for its safety function independently to the optimal extent. In this sense the natural barrier needs to be evaluated and necessary research conducted to ensure its optimal safety function. From a repository design point of view, an appropriate balance must be maintained between the natural system and the engineered barrier system (EBS) in the contribution to the total system performance. In practice, there is a risk to place too much reliance on the engineered barrier while not fully taking credits for the natural system. Such practice often results in an overly conservative, very expensive EBS design. Thus, it is important that sufficient research will be conducted to fully exploit the credits that can be taken for the natural system barrier.

Given the generic nature of this work, the R&D activities formulated in this planning document will focus on general tool development, generic data collection, and enhanced understanding of geologic media and processes involved in waste disposal through integrated modeling, laboratory and field work. Models and methods for improved understanding can be developed without site-specific data from an actual site considered for disposal in the U.S. Data from representative geologic environments obtained through international collaboration and literature searches can potentially be used for the generic R&D, to ensure that the models and methods work for the desired purpose.

Two major radionuclide release scenarios are generally considered in the performance assessment of a specific geologic repository: undisturbed and disturbed cases. A repository may be disturbed by an inadvertent human intrusion or a natural disruptive event. The nature of a disturbed scenario is site-specific and regulation driven. Given its generic nature, the work planned formulated in this plan will be focused on features, events and processes (FEPs) that are directly related to undisturbed scenarios. Some work is however also planned for disturbed scenarios. Such work will be performed for highly stylized, hypothetical cases, with an objective to inform future repository regulators on developing scientifically sound compliance standards for disturbed scenarios. The work will be focused on

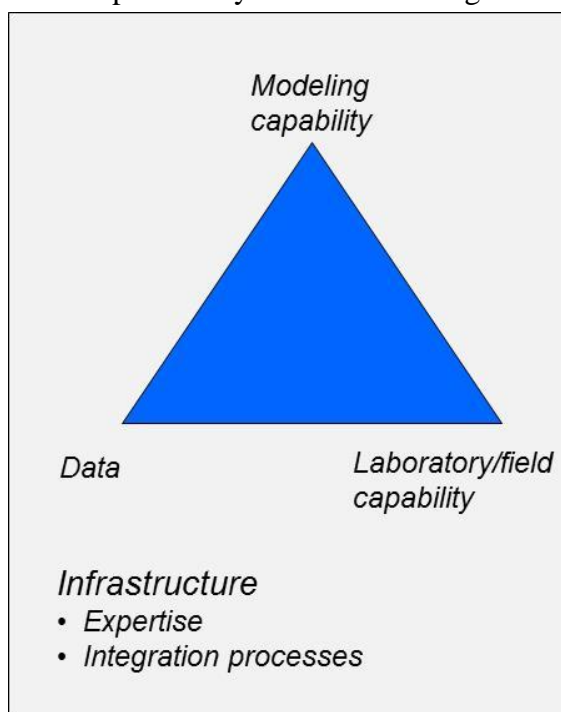


**Figure 1.** Key components of UFDC natural system evaluation and tool development work package.

identifying what types of FEPs may occur in these environments and then develop the needed scientific understanding and quantification of potentially important disruptive events for a given natural environment.

The tools to be developed in this plan will include (1) numerical models and modeling tools, (2) experimental techniques and field testing capabilities that can be used for validating the models, and (3) technical data that are needed to support simulations. In a more general sense, this effort will also include the development of necessary infrastructure (e.g. maintaining appropriate technical expertise and developing appropriate system integration processes among different UFDC work packages) to support actual site screening, site selection, site characterization and eventually repository license application in the future (Figure A1). For model development, it should be noted that multiple-fidelity models will be needed for different applications, ranging from support of simple FEP screening calculations to an ultimate comprehensive license application. The modeling tools to be developed should be able to accommodate this need.

The objective of this plan is to lay out major R&D activities and approaches related to the used fuel disposition in crystalline rocks (mainly granite and high-grade metamorphic rocks). The plan will serve as guidance for the effective integration of the related activities and for the close coordination with other UFDC work packages. It should be kept in mind that the UFDC R&D is a mission oriented program. The activities related to the natural system evaluation and tool development will directly support future site screening, site selection, site characterization and site suitability study. This plan will ensure that all related work will be conducted towards this goal.

This R&D plan is developed based on the report of “Used Fuel Disposition Campaign Disposal Research and Development Roadmap (FCR&D-USED-2011-000065 REV0)” (DOE, 2011) as well as the following documents:

- Research & Development for Used Fuel Disposition Campaign (UFDC) Natural System Evaluation and Tool Development (Rev. 1) (Wang, 2013)
- Natural System Evaluation and Tool Development – FY10 Progress Report (Wang, 2010)
- Deep Borehole Disposal of High-Level Radioactive Waste (Brady et al., 2009)
- Shale Disposal of U.S. High-Level Radioactive Waste (Hansen et al., 2010)
- Salt Disposal of Heat-Generating Nuclear Waste (Hansen and Leigh, 2011)
- Used Fuel Disposition Campaign Features, Events, and Processes (Freeze et al., 2010)

The UFDC Disposal R&D Roadmap serves as upper-tier guidance for this research plan. The roadmap identified high-level research issues and prioritized these activities according to their importance to the waste isolation and containment capabilities of geologic repositories and to the decision making of different stages of repository development. The identified research issues and the related prioritization results are summarized in Section A2.0 of this plan. In this plan, the high-level research issues are

broken into specific research topics, as described in Section A3. Appropriate technical approaches and the required resources for addressing these topics are provided in Section A4. A summary of the R&D plan and the mapping of on-going activities to the plan are provided in Section A5.0.

## **A2.0 Overview of UFDC Disposal R&D Roadmap**

As documented in its roadmap (DOE, 2011; Nutt, 2012), the UFDC applied a system engineering approach to developing its R&D portfolio related to nuclear waste disposal. The R&D portfolio was developed in the following steps:

1. Identify potential R&D issues (information needs and knowledge gaps);
2. Characterize and evaluate R&D issues to support prioritization;
3. Identify overall UFDC issue priorities based on the evaluation.

The potential R&D issues were identified by systematically examining information needs and knowledge gaps related to each Feature, Event, and Process (FEP). The list of FEPs relevant to natural system evaluation and tool development is provided in Appendix A of this plan. In addition, the UFDC also identified a number of cross-cutting issues that are relevant to both the natural system and the engineered barrier system.

Given its generic nature, the UFDC considers, in the evaluation of R&D issues, the following general requirements for a disposal system (IAEA, 2003):

- **Containment:** Provide a high probability of substantially complete containment of short lived radionuclides for some hundreds or thousands of years, perhaps largely within the engineered barriers of the repository.
- **Limited releases:** Delay and limit the rate and the consequent concentrations in which radionuclides will be released from the immediate environment in which the waste was emplaced into the surrounding geologic environment and eventually transported to the biosphere.
- **Dispersion and dilution:** The flux of long lived radionuclides through the geologic barriers involves three-dimensional dispersion, and may take place in widely different groundwater environments.
- **Defense in depth ensured by performance of a geological disposal system dependent on multiple barriers having different safety functions.**

The key information collected for prioritizing the R&D issues is the importance to the safety case. A safety case is the synthesis of evidence, analyses and arguments that quantify and substantiate a claim that the repository will be safe after closure and beyond the time when active control of the facility will be maintained (NEA, 2004). The safety case becomes more comprehensive and rigorous as a program progresses, and is a key input to decision making at several steps in the repository planning and implementation process. A key function of the safety case is to provide a platform for informed discussion whereby interested parties can assess their own levels of confidence in a project, determine any reservations they may have about the project at a given planning

and development stage, and identify the issues that may be a cause for concern or on which further work may be required (NEA, 2004).

The UFDC R&D will support the implementation of a geologic disposal system as they progress through different decision points. Different R&D issues may have variable importance or priority for different decision points. The decision points under consideration for repository development include site screening (broad siting and site down selection), site selection (environmental feasibility, concept feasibility, and site designation), site characterization and disposal system design, and site suitability (licensing).

In the UFDC R&D roadmap, the identified R&D issues were evaluated based on the following principles (DOE, 2011; Nutt, 2012):

- The overall priority of an issue is a function of the importance of the issue to the safety case, the importance of the issue to each decision point, and the adequacy and state of the art of current information.
- The importance of an issue to the safety case is relevant at all decision points; the relative contribution of the three components to overall importance to the safety case may differ over time and at different decision points.
- Issues that are important for nearer-term decisions such as site screening are of higher priority than those that are not important for near term decisions but important for later decisions, all other things being equal.
- Issues for which the current state of the art is well understood, and/or where currently available information is fully adequate to support a particular decision point are of low priority, at least with respect to that decision point.
- For issues evaluated differently for different media, media-specific priorities should be considered.

The results of prioritization of the high-level UFDC R&D issues are summarized in Tables A1 through A4 (DOE, 2011; Nutt, 2012). Design concept development and disposal system modeling are ranked high among 8 cross-cutting issues. For the natural system, the ranking of the issues are illustrated for repositories in crystalline, salt, and shale or clay media and as well for borehole disposal. While it is likely that borehole disposal would be in crystalline media, the issues are different enough from a crystalline medium repository to warrant separate treatment. The highest ranked issues are flow and transport pathways in crystalline media repositories, the excavation disturbed zone for borehole disposal and shale media repositories, hydrologic processes for salt media repositories, chemical processes for shale media repositories, and thermal processes for shale media repositories. The detailed ranking of individual FEPs for natural systems are provided at the end of this appendix. For the engineered barrier systems, the highest ranked issues are waste form, waste container, and radionuclide speciation/solubility. The prioritization results documented in the UFDC R&D roadmap provide overall guidance for the development of the detailed R&D plan developed here.

**Table A1.** Prioritization of Cross-Cutting R&D Issues (DOE, 2011; Nutt, 2012)

Design concept development	High
Disposal system modeling	High
Operations-related research and technology development	Low
Knowledge management	Medium
Site screening and selection tools	Medium
Experimental and analytic techniques for site characterization	Medium
Underground research laboratories	Medium
Research and development capabilities evaluation	Medium

**Table A2.** Prioritization of Natural System R&D Issues (DOE, 2011; Nutt, 2012)

Disposal Environment	Crystalline	Borehole	Salt	Shale
1.2.01. Long-term processes (tectonic activity)	Low	Low	Low	Low
1.2.03. Seismic activity	High Low	High Low	High Low	High Low
- Effects on EBS				
- Effects on NS				
1.3.01. Climatic processes and effects	Low	Low	Low	Low
2.2.01. Disturbed rock zone (DRZ)	Medium	High	Medium	High
2.2.02 Host rock (properties)	High	High	High	High
2.2.03 Other geologic units (properties)	Medium	Medium	Medium	Medium
2.2.05. Flow and transport pathways	Medium	Medium	Low	Medium
2.2.07. Mechanical processes	Low	Low	Medium	Medium
2.2.08. Hydrologic processes	Low	Medium	High	Medium
2.2.09. Chemical processes - chemistry	Low	Medium - High	Low - Medium	Medium - High
2.2.09. Chemical processes - transport	Medium	Medium - High	Medium - High	Medium
2.2.10. Biological processes	Low	Low	Low	Low
2.2.11. Thermal processes	Low	Medium	Low	Medium
2.2.12. Gas sources and effects	Low	Low	Low	Low
2.2.14. Nuclear criticality	Low	Low	Low	Low

Notes:

1. Shading for an entry indicates that research in that area has been undertaken in other geologic disposal programs
2. FEP number lists includes all FEPs beneath the third level

**Table A3. Prioritization of Natural System R&D Issues: Waste Form and Waste Package (DOE, 2011; Nutt, 2012)**

<b>WASTE MATERIALS → SNF, Glass, Ceramic, Metal</b>	
2.1.01.01, .03, .04: INVENTORY	Low
2.1.02.01, .06, .03, .05: WASTE FORM	High
<b>WASTE PACKAGE MATERIALS → Steel, Copper, Other Alloys, Novel Materials</b>	
2.1.03.01, .02, .03, .04, .05, .08: WASTE CONTAINER	High
2.1.07.03, .05, .06, .09: MECHANICAL PROCESSES	Medium
2.1.08.02, .07, .08: HYDROLOGIC PROCESSES	Low
2.1.09.01, .02, .09, .13: CHEMICAL PROCESSES - CHEMISTRY	Medium
- Radionuclide speciation/solubility	High
2.1.09.51, .52, .53, .54, .55, .56, .57, .58, .59: CHEMICAL PROCESSES - TRANSPORT	Low
- Advection, diffusion, and sorption	Medium
2.1.10.x: BIOLOGICAL PROCESSES (no FEPs were scored in this category)	Low
2.1.11.01, .02, .04: THERMAL PROCESSES	Medium
2.1.12.01: GAS SOURCES AND EFFECTS	Low
2.1.13.02: RADIATION EFFECTS	Low
2.1.14.01: NUCLEAR CRITICALITY	Low
<b>BUFFER / BACKFILL MATERIALS → Cementitious, bituminous, mixed materials: clay, salt, crystalline environments</b>	
2.1.04.01: BUFFER/BACKFILL	High
2.1.07.02, .03, .04, .09: MECHANICAL PROCESSES	Medium
2.1.08.03, .07, .08: HYDROLOGIC PROCESSES	Medium
2.1.09.01, .03, .07, .09, .13: CHEMICAL PROCESSES - CHEMISTRY	Medium
- Radionuclide speciation/solubility	High
2.1.09.51, .52, .53, .54, .55, .56, .57, .58, .59, .61: CHEMICAL PROCESSES – TRANSPORT	Medium
- Colloid facilitated transport	Low
2.1.10.x: BIOLOGICAL PROCESSES (no FEPs were scored in this category)	Low
2.1.11.04: THERMAL PROCESSES	Medium
2.1.12.01, .02, .03: GAS SOURCES AND EFFECTS	Medium
2.1.13.02: RADIATION EFFECTS	Low
2.1.14.02: NUCLEAR CRITICALITY	Low

Notes:

1. Shading for an entry indicates that research in that area has been undertaken in other geologic disposal programs
2. FEP number lists includes all FEPs beneath the third level

**Table A4.** Prioritization of Natural System R&D Issues: Seals and Other Materials Package (DOE, 2011; Nutt, 2012)

<b>SEAL / LINER MATERIALS → Cementitious, Asphalt, Metal, Polymers</b>	
2.1.05.01: SEALS	Medium
2.1.06.01: OTHER EBS MATERIALS	Medium
2.1.07.02, .08, .09: MECHANICAL PROCESSES	Medium
2.1.08.04, .05, .07, .08, .09: HYDROLOGIC PROCESSES	Low
- Flow through seals	Medium
2.1.09.01, .04, .07, .09, .13: CHEMICAL PROCESSES – CHEMISTRY	Medium
- Radionuclide speciation/solubility	High
2.1.09.51, .52, .53, .54, .55, .56, .57, .58, .59: CHEMICAL PROCESSES - TRANSPORT	Low
- Advection, diffusion, and sorption	Medium
2.1.10.x: BIOLOGICAL PROCESSES (no FEPs were scored in this category)	Low
2.1.11.04: THERMAL PROCESSES	Medium
2.1.12.02, .03: GAS SOURCES AND EFFECTS	Low
2.1.13.02: RADIATION EFFECTS	Low
2.1.14.02: NUCLEAR CRITICALITY	Low
<b>OTHER MATERIALS → Low pH Cements, Salt-Saturated Cements, Geopolymers, Barrier Additives</b>	
2.1.06.01: OTHER EBS MATERIALS	Medium
2.1.07.08, .09: MECHANICAL PROCESSES	Medium
2.1.08.04, .05: HYDROLOGIC PROCESSES	Medium
2.1.09.04, .07, .09, .13: CHEMICAL PROCESSES - CHEMISTRY	Medium
- Radionuclide speciation/solubility	High
2.1.09.51, .52, .53, .54, .55, .56, .57, .58, .59: CHEMICAL PROCESSES – TRANSPORT	Low
- Advection, diffusion, and sorption	Medium
2.1.10.x: BIOLOGICAL PROCESSES (no FEPs were scored in this category)	Low
2.1.11.04 THERMAL PROCESSES	Medium
2.1.12.02, .03: GAS SOURCES AND EFFECTS	Low
2.1.13.02: RADIATION EFFECTS	Low
2.1.14.02: NUCLEAR CRITICALITY	Low

Notes:

1. Shading for an entry indicates that research in that area has been undertaken in other geologic disposal programs
2. FEP number lists delimited by commas show only the change in the fourth field of the FEP

### A3.0 Research Topics for Used Fuel Disposal in Crystalline Rocks

This section formulates specific R&D topics for used fuel disposal in crystalline rocks. The topics are divided into 2 levels: the system level and the process level. The mapping of individual topics to the natural system FEPs is provided in Table A7 at the end of this appendix. All the topics described below will directly address the high-level R&D issues

that were ranked medium to high in prioritization in the UFDC R&D roadmap. One exception is the biological processes, which were ranked low for all four disposal environments. The reason for its inclusion is that these processes may affect some key chemical processes. In other words, the research topics formulated below are all important for developing a sensible repository research program in the U.S., and therefore they all should be pursued once the funding becomes available.

*System level R&D topics:*

**Topic #S1**

**Title:** Evaluation of potential impacts of disposal options on fuel cycles

**Description:** The DOE is now reconsidering its nuclear waste disposal policy and re-evaluating alternative options to the current once-through open fuel cycle. This policy shift creates a unique opportunity for exploring new concepts and ideas that can potentially lead to the development of transformational technologies for an efficient and clean nuclear fuel cycle. The choice of waste disposal environments may potentially impact the development of upstream processes of the fuel cycle. Such impacts have not been fully explored and evaluated. This research topic will focus on new concept development. Specific activities will include:

- Comparative study of different disposal environments
- Identification and evaluation of potential impacts of different disposal environments on waste separation and waste form development.
- **Capability of crystalline rocks for disposal waste packages of multiple sizes, especially for large dual purpose canisters (DPCs)**

**Anticipated results:** New concept development

**Topic #S2**

**Title:** Disposal concept development

**Description:** As explicitly identified in the UFDC R&D roadmap (DOE, 2011), there is a need for developing a range of generic disposal system design concepts. This research topic will support the overall UFDC effort on the development of disposal system design concepts by cataloging possible combinations and geometries of both host rock and far-field media (e.g., mineral and chemical compositions, physical dimensions, hydrologic properties). The task will define a generic set of key parameters (e.g., water chemistry) for other UFDC activities. Specific activities will include:

- Literature review
- Concept development
- **Development of reference cases for crystalline media**

**Anticipated results:** Generic representations of various disposal environments

**Topic #S3**

**Title:** Disposal system modeling

**Description:** Disposal system modeling is crucial for the whole life cycle of repository development. Such modeling tools will be essential for management decisions on project priority and resource allocation. This research will serve two purposes: (1) supporting the development of the Generic Disposal System Analysis (GDSM) models as well as the

development of higher-fidelity performance assessment models, and (2) developing a comprehensive subsystem model for natural system performance evaluation. The subsystem model will include (1) detailed thermal-hydrologic-mechanical-chemical (THMC) process models (with appropriate levels of fidelity) for flow field and radionuclide transport calculations and (2) probabilistic performance assessment capabilities. This subsystem model will be used for integration and prioritization of relevant natural system evaluation activities. Specific activities will include:

- Selection of flow and radionuclide transport codes
- Improvements to the selected codes
- Wrapping the selected process codes with a Monte-Carlo simulation tool
- Performing Monte-Carlo simulations for total system and subsystem evaluation.

**Anticipated results:** Enhanced process understanding; probabilistic performance assessment tools for natural system evaluation, which will allow for taking more credit for natural system performance; laboratory and field data for model validation and parameterization

#### **Topic #S4**

**Title:** Development of a centralized technical database for crystalline disposal system evaluation

**Description:** Given the quantity of data already accumulated through various repository programs and also the data to be collected from the UFDC R&D activities, it is essential for future repository development to archive and categorize these data in an appropriate manner so that they can be easily accessible to UFDC participants and has appropriate quality assurance enforced. This task will focus on the database development for natural system evaluations. The data to be collected will include thermodynamic data for radionuclide speciation and sorption, groundwater chemistry, hydraulic and mechanical property data, mineralogical and compositional data of representative host and far-field media, spatial distributions of potential host formations, etc. To support site screening and selection, there is a need to develop tools for spatial data analysis and visualization (e.g., a geographic information system). Specific activities will include:

- Collection of user requirements
- Database design
- Retrieval of relevant data that was generated by previous DOE research studies on shale, salt, and crystalline basement repository rocks
- Data collection from UFDC experimental activities
- Database population and maintenance.

**Anticipated results:** Database. This database will serve as a knowledge management system for all natural system evaluation activities. It will serve a part of the technical database supporting the parameter database development for total system performance assessments.

#### **Topic #S5**

**Title:** Evaluation of state of the art of site characterization techniques

**Description:** Site characterization techniques evolved and improved both in the U.S. and other nations as geologic repository programs progress. Advances both in the disposal science and other geotechnical fields (e.g., oil and gas industry, mineral mining,

geothermal exploration, and carbon sequestration) may lead to improved site characterization techniques that could be applied to future site characterization efforts. This activity will evaluate and identify potential field survey techniques that may prove useful for site characterization. The effort will be equally divided into four areas: geophysical techniques, geochemical techniques, hydrological testing techniques, and rock mechanics techniques. Specific activities will include:

- Literature review
- Gap analysis
- Recommendations for future technique development

**Anticipated results:** Information needed for planning further development of site characterization techniques.

### **Topic #S6**

**Title:** Development and demonstration of geophysical techniques for site characterization

**Description:** Existing non-invasive geophysical techniques are adequate for characterizing large-scale subsurface features and physical properties, but continued advances could help achieve high-resolution images of time-varying properties and structural changes that may be important during the site selection or characterization stages. For example, high-resolution seismic imaging of subsurface faults under development for oil and gas exploration purposes could advance to the point where sub-meter sized features can be more easily resolved and high-angle (near vertical) reflectors can be directly imaged. Similarly, advances in seismic imaging could allow the direct detection of fluids and their migration through fractures. Laboratory experiments and waveform modeling approaches could be pursued to develop and test new seismic methods for fluid monitoring. Strategies may be needed to integrate multiple geophysical techniques to optimize information gathering in host-rock and geologic environments. This task will focus on the development of new geophysical techniques that can provide unprecedented high spatial resolutions. Specific activities will be formulated based on the results from Topic #S5.

**Anticipated results:** Improved geophysical techniques for site selection and site characterization.

### **Topic #S7**

**Title:** Identification of the needs for using Underground Research Laboratories (URLs)

**Description:** Underground research laboratories (URLs) can be used to conduct experiments designed to address the issues that require field-scale testing and demonstration. Experimental activities conducted in URLs (and operations-related surface facilities) can potentially help improve public confidence through demonstrating fundamental understanding of disposal and operational concepts. If the U.S. foregoes repository siting for an extended period of time, studies in a domestic URL could help maintain repository development expertise. However, there may be reasons (e.g., cost) not to develop URLs in the U.S. unless they are in geologic media where one does not currently exist elsewhere. Domestic R&D needs could potentially be met by gaining access to URLs in other countries working in relevant geologic media through collaborative studies and experiments. This research topic will (1) identify potential areas in which the UFDC can benefit the most from international collaboration on the

URL research and (2) formulate a strategy for domestic URL development. Specific activities will include:

- Identification of the needs for URLs
- Formulating URL development strategy, especially the international collaboration approaches.

**Anticipated results:** Information needed for developing an international collaboration plan. Actual collaboration will be carried out in individual research topic areas.

### **Topic #S8**

**Title:** Natural analogue studies

**Description:** Natural analogues such as uranium deposits preserve information about physical and chemical processes that may be relevant to nuclear waste isolation in a geologic repository. This information could be useful for repository performance assessment model validation and confidence building. Natural analogues are also needed to identify potential effects of geologic processes that may be relevant to waste disposal in a given geologic medium. Identification of such processes is critical for site screening. Current hydrogeologic modeling practices tend to assume that the system will be static other than changes induced by the repository itself. This is an assumption that needs to be investigated and analogues are the best way for testing this assumption. In a study of analogues for argillaceous rock, a variety of geologic processes have been found that can significantly affect flow and transport pathways through otherwise very low permeability materials. Specific activities will include:

- Literature review
- Systematic evaluation of the uses of natural analogue data for repository development
- Data compilation and synthesis

**Anticipated results:** An overview report with compiled data; enhanced process understanding

*Process-level R&D topics:*

### **Topic #P1**

**Title:** Development of discrete fracture network (DFN) model

**Description:** There is a need to develop improved modeling tools to represent fractures or fracture sets as discrete features. Experience in Sweden and Finland suggests that DFN models offer advantages over continuum models for sparsely fractured media such as fractured crystalline basement rock, especially when fracture networks or network statistics are well characterized. There is also a need for DFN studies for argillaceous host rock in the disturbed rock zone (DRZ). DFN modeling capability would provide an alternative to continuum codes and would also be invaluable for numerically determining effective parameters for use in existing continuum codes. This task will develop a DFN code for modeling multiple-scale, three-dimensional fracture networks. The specific activities will include:

- Review of state of the art of DFN model development
- DFN code development
- Code verification and validation

- Code demonstration
- Better understanding of fracture distribution, fracture closure and opening, and fluid flow and transport in individual fractures in subsurface.

**Anticipated results:** Theory, computer code and validation data for modeling sparsely fractured geologic media; enhanced process understanding

### Topic #P2

**Title:** Parameter estimation and uncertainty quantification of field testing

**Description:** Parameters used in the assessment of groundwater flow and radionuclide transport in saturated media are determined from a wide range of laboratory and field-scale testing. Laboratory measurements are generally conducted under controlled conditions and the uncertainty for parameters from these experiments related to instrumental errors is relatively small. In contrast, field testing such as hydraulic testing in fractured media and tracer testing in the subsurface is analyzed with imperfect knowledge of the hydrogeological system at depth. Consequently, there are often issues of nonuniqueness and significant uncertainties in the parameter values derived from this testing. In the past these uncertainties typically have been evaluated using simple statistical analyses or professional judgment for propagation to total system performance assessments. This task will assess the use of advanced methods in parameter estimation and uncertainty analysis in the interpretation of field testing in saturated media. The task will also address the issues related to flow localization and the associated diffusion into immobile water. Specific activities will include:

- Literature review of state of the art in hydrologic parameter estimation
- Formulation of new techniques (e.g. new optimization techniques)
- Demonstration of new techniques.

**Anticipated results:** New methodology and related software for uncertainty quantification of field testing results; enhanced process understanding

### Topic #P3

**Title:** Development of a new theory for preferential flow in unsaturated porous media

**Description:** Groundwater recharge associated with the unsaturated zone is an important factor for characterizing any repository site and for evaluating its performance. In a water-saturated environment, because thermal effects, multiphase-flows (similar to unsaturated flow) may also occur near the drift in the host formation of a given repository. Preferential flow is a common flow mechanism in the unsaturated zone and has been described as one of the most frustrating processes in terms of hampering accurate predictions of flow and transport in the unsaturated zone as a result of its complexity. This work attempts to apply an optimal principle (that water flow resistance is minimized for the entire flow domain) to steady-state unsaturated flow processes. Specific activities will include:

- Formulation of new preferential flow model
- Comparison of model results with laboratory measurements of fingering flow (available in the literature) and the existing models.

**Anticipated results:** New theory and modeling tools with improved capability of modeling near-field flow and transport; enhanced process understanding

**Topic #P4**

**Title:** Investigation of water movement and transport in low permeability media (clay materials)

**Description:** Low permeability geologic formations such as clay formations are considered as effective media for waste isolation. Understanding water movement in such media is crucial for the performance assessment of a waste isolation system. It was recently discovered that water advection and chemical diffusion in low-permeability media may not follow traditional linear laws such as Darcy's law and Fick's law. This task will systematically study water flow regimes and their transport behaviors in clay formations as a function of clay formation texture and pore geometry. New methodologies will be developed for modeling these non-traditional flow and transport behaviors. Specific activities will include:

- Selection and characterization of clay samples
- Experimental testing of flow regimes in clay samples
- Experimental testing of diffusion regimes in clay samples
- Development of modeling capabilities
- Prediction of water movement and chemical species diffusion in clay formations

**Anticipated results:** New formulations for water flow and transport in clay formations, with supporting experimental data; enhanced process understanding

**Topic #P5 (not applicable to crystalline media)**

**Title:** Investigation of water movement and transport in low permeability media (salt formations)

**Description:** Low permeability geologic formations such as salt beds are considered as effective media for waste isolation. Understanding of water movement in such media is crucial for the performance assessment of a waste isolation system. Significant gaps exist in predicting moisture movement along salt grain boundaries under stress and temperature gradient. This task will establish constitutive relationships for moisture movement in the near-field of a salt repository through laboratory analysis, field testing and modeling. Specific activities will include:

- Experimental testing of water movement in consolidated salt
- Experimental testing of chemical species diffusion in salt
- Development of modeling capabilities
- Prediction of water movement and chemical species diffusion in salt formations.

**Anticipated results:** New formulations for water flow and transport in salt formations, with supporting experimental data; enhanced process understanding

**Topic #P6**

**Title:** Investigation of water movement and transport in deep borehole disposal environments

**Description:** In the deep borehole disposal concept, high level nuclear waste will be emplaced in the depth interval of 3 to 4 km below the surface, based on the premise that water movement at that depth would be minimal. Characterization of water flow in such environments is a technical challenge. This task will first collect relevant information of deep ground water movement and formulate a strategy for developing field characterization strategies for deep borehole disposal. The information to be collected

will include those obtained from continental drilling programs. The task will then focus on the development of novel techniques for characterizing deep ground water movement (e.g., using isotopic signatures). Specific activities will include:

- Literature review on water movement in deep subsurface environments
- Development of novel techniques for deep ground water movement
- Extending the existing groundwater flow models to deep subsurface environments.
- Understanding fracture distribution with depth – an important issue for both crystalline disposal and deep borehole disposal concepts.

**Anticipated results:** Novel field survey techniques and modeling capability for characterizing deep ground water movement; enhanced process understanding; relevant field data

#### **Topic #P7**

**Title:** Novel in-situ techniques for groundwater chemistry characterization

**Description:** An understanding of the repository far-field geochemical system is critical to understanding repository performance. Geochemical conditions and the characteristics and composition of the ground water in the repository far field govern the mobility and solubility of radioactive elements. In addition, the chemistry of water flowing from the far field into the near-field environment is an important control on the near-field chemical environment, which, in turn, affects engineered barrier degradation rates. There is a need for developing chemical sampling techniques to characterize initial fluid composition in shale and salt. This activity will explore and develop novel techniques for characterizing groundwater chemistry. The emphasis will be given to the techniques that can provide fast, accurate, in-situ and high spatial resolution measurements (e.g., in boreholes) with minimum human perturbations. The techniques that can characterize flow localization and the associated chemical heterogeneity is particularly of interest. Specific activities will include:

- Literature review
- Development of high resolution in-situ characterization techniques
- Field demonstration of new techniques

**Anticipated results:** A set of demonstrated techniques ready for field demonstration; relevant lab and field data

#### **Topic #P8**

**Title:** Reactive transport modeling of groundwater chemistry evolution and radionuclide transport

**Description:** This task will aim at improving the existing reactive transport modeling tools for simulating groundwater chemistry evolution and radionuclide migration along the flow path from the DRZ, to the far field and ultimately to the boundary of a repository. Radionuclide transport modeling remains a computationally challenging task. Except for the extreme situation of diffusion-dominated conditions, transport models are more sensitive than flow models to numerical grid effects and small-scale heterogeneity. Relatively fine grids are needed to avoid numerical dispersion when traditional finite-difference or finite-element methods are employed. Multiple radionuclides linked through decay chains need to be considered, and the simulation time steps are thus limited by the

most mobile (least retarded) radioelement. In addition, transport modeling to assess geosphere performance typically requires parametric uncertainty to be addressed, which places a premium on fast execution time of modeling codes. This task will focus on the following improvements to the existing reactive transport modeling capability:

- Incorporation of interfacial reactions (e.g., surface complexation), microbially mediated reactions, colloid-facilitated transport, and radionuclide decay and ingrowth
- Improved representation of spatial heterogeneity of chemical and transport properties
- Coupling of radionuclide transport with evolving water chemistry along a transport pathway (e.g. alkaline plumes)
- Robustness of numerical algorithms for coupling chemical reactions with solute transport
- Explicit consideration of structural complexity of the media in the solute transport (e.g. the fracture-matrix system in DRZ or the micro, macro-pores system for host clay rock)

**Anticipated results:** Modeling tools that will go beyond the traditional  $K_d$  approach for modeling radionuclide partitioning between pore water and solid substrates

#### **Topic #P9**

**Title:** Evaluation of the effects of spatial heterogeneity on radionuclide transport

**Description:** Some key parameters that control radionuclide transport in natural system generally vary spatially. Existing repository performance assessments try to capture this variability with model input parameter uncertainty, which inevitably lead to a significant overestimate of total radionuclide release. This task will develop modeling capabilities to capture the effects of the spatial heterogeneity (e.g.,  $K_d$  values) on radionuclide transport in natural systems. The work will include two parts: the modeling capabilities for realistic representation of spatial heterogeneity and the experimental technique for quantification of this heterogeneity. The work will significantly reduce both the predicted total radionuclide release from a repository and the associated uncertainty through improved performance prediction of the natural barrier system. Specific activities will include:

- Representation of spatial heterogeneity in reactive transport models
- Development of characterization techniques for quantification of spatial heterogeneity
- Model validation and demonstration.

**Anticipated results:** New modeling approaches and characterization techniques for capture the effect of spatial heterogeneity on radionuclide transport.

#### **Topic #P10**

**Title:** Better understanding radionuclide interaction with geomeia

**Description:** As they move through the natural system, radionuclides released from the engineered barrier will experience a complex set of physical and chemical interactions with the geologic media. Existing models generally assume that radionuclide retention in the natural system could be described with a linear, equilibrium  $K_d$  approach. The reality

may be much more complex. This task will develop key experimental techniques and modeling tools in the following areas:

- Thermodynamics and kinetics of radionuclide sorption onto or desorption from representative mineral substrates (e.g. different clay minerals)
- Radionuclide behaviors in high rock/water ratio environments, especially in confined environments such as nanopores and interlayers
- Coupling of redox reactions with radionuclide sorption
- Complexation of radionuclides with natural organic matter
- Radionuclide sorption in the presence of competing species, high ionic strength media, or at elevated temperatures
- Extrapolation from simple system measurements to complex systems
- Radionuclide transport in low permeability media (e.g., membrane effect of clay formation).

**Anticipated results:** Key technical data for the development of next generation (more predictive) radionuclide transport models; enhanced process understanding; relevant laboratory data

### **Topic #P11**

**Title:** New perspective of colloid-facilitated radionuclide transport

**Description:** Colloid facilitated transport (CFT) may have been overestimated in previous performance assessments because many aspects of CFT are not well constrained, thus making pessimistic bounding assumptions necessary. CFT is also an important issue for confidence building of a performance assessment model. Important uncertain processes and parameters associated with CFT include: desorption processes and rates, colloid immobilization processes and associated parameters, the degree to which colloids behave as heterogeneous populations in the subsurface, the role of chemical and flow transients in mobilizing and immobilizing colloids, and colloid generation processes. This task will focus on two key aspects of the CFT: (1) colloid particle formation and transport in porous geologic media and (2) radionuclide partitioning among pore water, colloid particles, and stationary substrates. In recent years, much progress has been made in nanoscience and nanotechnology. Such progress allows re-examining CFT in a new perspective, for example, understanding the size dependence of particle surface chemistry and radionuclide sorption capability. This work will involve laboratory measurements, model development, and field testing. Novel in-situ colloid characterization techniques will be explored. Specific activities will include:

- Literature review
- Better understanding colloid-radionuclide-stationary mineral phase interactions
- Development of novel in-situ techniques for characterizing CFT
- Development of modeling capabilities for simulating CFT.

**Anticipated results:** New modeling and experimental tools as well as key technical data for predicting CFT; enhanced process understanding; relevant laboratory and field data; laboratory and field measurement techniques

### **Topic #P12**

**Title:** Upscaling of key hydrological and geochemical parameters

**Description:** It is known that some key parameters (e.g., dispersion coefficient, matrix diffusion coefficient) controlling radionuclide transport in geologic media are scale-dependent. Capture of this scale dependence is crucial for predicting radionuclide transport in a geologic repository environment. This task will systematically evaluate the existing techniques for upscaling key hydrologic and geochemical parameters, identify the gaps in upscaling, and develop new methodologies for bridging the identified gaps. The parameters of interest include matrix diffusion coefficients, sorption coefficient, chemical reaction kinetics, etc. The laboratory and field experiments of various scales will be explored for conceptual model development and validation. Specific will activities include:

- Literature review on hydrological and geochemical upscaling
- Data collection and multiple scale testing
- Model development for hydrological and geochemical upscaling.

**Anticipated results:** Constitutive relationships for predicting radionuclide transport in natural systems; enhanced process understanding; relevant field data

### Topic #P13

**Title:** Evaluation of biological processes

**Description:** Transport of dissolved radionuclides in the host rock and other geologic units is affected by microbial activity in the host rock and other geologic units (non-host-rock). The effects of biological processes include the formation of complexants, the formation of microbial colloids, the biodegradation of organic compounds, and the bioaccumulation of radionuclides. Similar to purely inorganic complexants, there is a potential for enhanced transport of radionuclides associated with organic complexants. There are fundamental gaps in the methods of characterizing biological processes and their effects on the repository system, and fundamental gaps in available data. This activity will develop better techniques for quantifying microbial activity in a subsurface environment and improve the existing methodology for evaluating microbial impacts on water chemistry and radionuclide transport. Specific activities will include:

- Literature review
- Development of new techniques for characterization of microbial activity in subsurface environments
- Upgrading the existing biogeochemical modeling capability for evaluating microbial activity and its impact on radionuclide transport.

**Anticipated results:** New techniques for characterizing microbial population; an improved methodology for evaluating microbial impacts on radionuclide transport in natural system; enhanced process understanding

### Topic #P14

**Title:** Technical basis for thermal loading limits

**Description:** The repository thermal loading limits are of concern for thermal-mechanical effects on engineered materials and host rocks. Thermal expansion, tensile and compressive stresses, and altered properties of fractures, faults, and the rock matrix are possible. There can also be thermal-chemical alteration of the materials, including, mineral precipitation, dissolution, alteration of minerals with attendant volume changes, and altered properties of fractures, faults, the rock matrix, and the formation of near-field

chemically altered zones (rind). This task will systematically examine the technical basis for the thermal limits of various disposal media (i.e., the maximum wall temperature allowed). Specific activities will include:

- Literature review
- Examination of technical basis for thermal limits of various disposal media, including certain thermal-hydrologic-mechanical-chemical calculations.

**Anticipated results:** Technical basis for the thermal limits of various disposal media

**Topic #P15 (probably applicable to clay buffer materials in the EBS)**

**Title:** Modeling of disturbed rock zone (DRZ) evolution (clay repository)

**Description:** There is a need for improved understanding and representation of the evolution of disturbed rock zone characteristics as a result of thermal-mechanical-hydrological-chemical changes in clay environments, including the coupled evolution of near-field host rock and any backfill/buffer materials that would be used in the design of the repository. This task will address the following specific issues associated with the DRZ:

- Improved methods for representing the complex coupling of processes (physical, chemical, thermal, mechanical), including the coupling of the engineered and natural systems
- Improved methods for representing near- and far-field interface chemistry (perturbation & transient phenomena, repository operation, thermal effect)
- Quantifying gas generation and representing potential impacts (gas displacement and leakage)
- Evaluating the effects of excavation and ventilation-induced fracturing in clay/shale environments
- Better understanding of fracture initiation and healing (re-compaction as a function of environment)
- Improved understanding of heterogeneity and anisotropic properties in the DRZ and their impacts
- Evaluating the potential for the development of fast transport pathways that could bypass the natural or engineered system and associated impacts
- Development of model tools for capturing these processes/issues mentioned above.

**Anticipated results:** Constitutive relationships and computer codes for modeling thermal-mechanical-hydrological-chemical coupling in the near field of a clay repository; enhanced process understanding; relevant laboratory and field data

**Topic #P16 (not applicable to crystalline media)**

**Title:** Modeling of DRZ evolution (salt repository)

**Description:** Evolution of the DRZ in salt is very sensitive to the stress state and exhibits steep transient deformation behavior that evolves into steady-state deformation. This behavior can be understood in terms of plastic dislocation mechanisms in salt crystals. Hence, creep closure of underground openings in salt at ambient temperature can be understood at a mechanistic level. Based on studies at WIPP, the nature of the DRZ can be adequately described for engineering and analysis purposes in terms of stress invariants, which is conducive to finite element calculations. Long-term behavior

including healing can be assessed by tracking the stress state within the structural calculation. For the long-term disposal of high level wastes, a better understanding of rock salt creeping and fracture sealing around the DRZ at elevated temperatures and in the presence of moisture is required. This work will develop the needed tools for testing and simulating salt repository room closure, salt creeping and fracture healing in the presence of moisture at elevated temperatures. Specific activities will include:

- Literature review
- Laboratory and field testing on salt creeping and fracture healing
- Model simulation and data integration.

**Anticipated results:** Constitutive relationships and computer codes for modeling thermal-mechanical-hydrological-chemical coupling in the near field of a salt repository; enhanced process understanding; relevant laboratory and field data

**Interface:** International collaboration, EBS work packages, WIPP R&D, UFDC SDI

**Priority:** Medium

**Resource required:** \$450 K/year for 5 year

**Self-assessment:** The related work was transferred to the SDI work package.

### **Topic #P17**

**Title:** Modeling of DRZ evolution (deep borehole disposal)

**Description:** For deep borehole disposal, simulation of multi-borehole arrays should be undertaken for a system consisting of 10 to 100 individual boreholes. Such investigations could evaluate the potential for communication between boreholes, thermal or hydrologic interactions, and large-scale responses to borehole arrays. Performance assessments are needed to establish a better sense of the potential performance variability that might be expected in multiple implementations of borehole disposal fields. This activity will simulate the coupled thermal-hydrological-mechanical-chemical processes around a single borehole and multiple boreholes as well. Specific activities will include:

- Literature and data collection
- Thermal-hydrological-mechanical-chemical calculations.

**Anticipated results:** Constitutive relationships and computer codes for modeling thermal-mechanical-hydrological-chemical coupling in a deep borehole disposal environment; enhanced process understanding; relevant laboratory and field data

### **Topic #P18**

**Title:** In-situ testing of DRZ development

**Description:** In situ testing could prove quite valuable for proof-of-principle testing. A field test provides an opportunity to observe anticipated phenomenology, validate modeling capabilities, and fine tune design options. This task will focus on full-scale heating testing for the DRZ evolution. In situ testing will confirm the predictive ability of repository models and provides a range of expected parameters and rock mass response. Full-scale heater tests will determine:

- Extent and properties of the disturbed zone
- Fracture healing characteristics
- Changes in permeability and porosity
- Thermomechanical response of compacted backfill
- Water migration and influx rates (where applicable)

- Moisture behavior (e.g., partial vapor pressure)
- Compositional changes; all for heated conditions representative of repository conditions.

**Anticipated results:** Experimental data for model validation

### **Topic #P19**

**Title:** Development of waste form degradation model

**Description:** Currently, in a performance assessment calculation, waste form degradation is modeled with fractional degradation rates. Such models are not able to predict waste form degradation for a wide range of physical/chemical conditions. In this effort, we propose to develop a new generation waste form degradation model that is able to account for complex physical/chemical processes involved in waste form degradation under wide range of disposal conditions. This model will explicitly incorporate potential impacts of radiolysis. The work includes:

- Extensive literature search and data collection
- Formulation of a complex chemical reaction model
- Implementation of the model in a performance assessment calculation.

**Anticipated results:** New model for performance assessments

### **Topic #P20**

**Title:** Development of new waste package concepts and models for evaluation of waste package performance for long-term disposal

**Description:** Waste packages are an important layer of an engineered system for waste isolation, especially for a repository in fractured crystalline rocks. This effort will include two parts: (1) new materials and new concepts for waste package design and (2) improved models for predicting the long-term performance of waste packages in a crystalline repository. One aspect to be examined is the potential interactions of waste packages with buffer materials in the EBS.

**Anticipated results:** New models and experimental data for model parameterization and validation

### **Topic #P21**

**Title:** Backfill and seal materials design

**Description:** This effort will focus on designing new buffer/backfill and seal materials for effective isolation of waste in a repository. The new design will fully take into account the capabilities of the materials as a hydrologic barrier (low permeability to a fluid flow) and a reactive barrier (high radionuclide sorption capacity). It will also consider the availability of the materials and their compatibility with repository environments.

**Anticipated results:** Experimental data and new design concepts

### **Topic #P22**

**Title:** Modeling radionuclide transport in engineered barrier system

**Description:** This effort will focus on the development of a reactive transport model for radionuclide transport with an engineered barrier system. The model consider (1) radionuclide speciation, precipitation and dissolution in an evolving near-field

physical/chemical conditions and (2) radionuclide transport from degraded waste form, to buffer/backfill materials, and to the disturbed rock zone.

**Anticipated results:** Experimental data, new models

#### A4.0 Strategies for Reaching R&D Goals

*System point of view:* As pointed out above, reconsideration of nuclear policy and waste disposal options provides a unique opportunity for evaluating the potential impacts of the choice of waste disposal option on the overall fuel cycle. This work package will support the development of a total system performance (TSPA) model and provide the needed data for simulations. Once matured, a TSPA model can then be used to help prioritize R&D activities for crystalline disposal R&D work package from a system performance point of view.

*Tools & multiple applications:* The tools and capabilities to be developed in this work package will include four integral components: technical data, modeling tools, laboratory techniques, and field observation techniques. An appropriate balance among the four components must be carefully determined in terms of allocation of resources. Given the generic nature of this research, all activities described in section A3.0 will focus on general tool development and non-site specific data collection. For the model development, as mentioned early, models with multiple levels of fidelity may be needed for various applications, ranging from support of a simple FEP screening to an ultimate comprehensive license application. The modeling tools to be developed should be able to meet this need.

*Data management & quality assurance (QA):* During the last few decades, a large quantity of technical data has been accumulated through various repository programs or other programs. It is important to ensure that each proposed R&D activity to fully leverage the existing data. The development of a centralized technical database is a key component for knowledge management.

To ensure that key technical data collected in this work package are usable or recoverable for various future applications, it is imperative that each research activity formulated above must enforce an appropriate level of quality assurance (QA). For example, materials and solutions (e.g., clays) used for testing at different laboratories should be standardized for testing result comparisons.

*International collaboration:* International collaboration is essential for success of many of the research activities proposed in Section A3.0. Table A5 lists the relevant repository programs in other countries, which can potentially be leveraged by the UFDC program. Actual international collaboration will be carried out in individual research topic areas, and the funding levels may need to be adjusted as needed.

*Reporting & publication:* Given the R&D nature of the proposed work, in addition to regular project reports, it is encouraged that the results of the related activities be

published in peer-reviewed journals or presented at national or international conferences. The publication and dissemination of research results are one of the key components to build the credibility of the UFDC program.

*Iterative nature of R&D:* It is important to realize that this R&D plan is a living document, which will be revised as needed as the work progresses. The work scope and the priority may change as a result of future modification to the UFDC R&D Roadmap. Such changes may also be triggered by any change to the upstream processes and designs. For example, an introduction of a new material into the EBS may require evaluation of the transport of new colloid species in the natural system.

## **A5.0 Summary**

The crystalline disposal R&D work package supports all four stages of geologic repository development: site screening, site selection, site characterization, and site suitability studies. This work plan will ensure that sufficient research will be conducted to fully exploit the ability of each barrier for high level waste isolation. Given the generic nature of this work, the R&D activities formulated in this document will focus on general tool development, generic data collection, and enhanced understanding of geologic media and processes involved in waste disposal through integrated modeling, laboratory and field work. A total of 31 research topics (9 for system level and 22 for processes level) have been identified (Table A6), based on the UFDC R&D roadmap (DOE, 2011). The technical approach to addressing each of these topics is formulated and the required resource is estimated. This work plan is a living document, and it will be revised as needed as the work progresses or as the UFDC R&D Roadmap is modified.

**Table A5.** Summary of National Waste Management Programs (DOE, 2011)

Country	Material to be Disposed	Centralized Storage	Geologic Environments	URL	Site-Selection	Anticipated Start of Repository Operations
<b>Finland</b>	SNF		Granite, Gneiss, Grandiorite, Migmatite	ONKALO (Granite)	Site at Olkiluoto Selected	2020
<b>Sweden</b>	SNF	CLAB - Oskarshamn	Granite	Aspo (Granite)	Site at Osthrammar Selected	2023
<b>France</b>	HLW and ILW		Argillite and Granite	Bure (Argillite)	Site near Bure Selected	2025
<b>Belgium</b>	HLW		Clay/Shale	Mol (clay)	Not Initiated	~2040
<b>China</b>	HLW		Granite		Preliminary Investigations Underway - Beishan in Gobi Desert	~2050
<b>Switzerland</b>	HLW	Wulenlingen (ZWILAG)	Clay and Granite	Mont Terri (Clay) Grimsel (Granite)	Initiated	No sooner than 2040
<b>Japan</b>	HLW		Granite and Sedimentary	Mizunami (Granite) Hornonobe (Sedimentary)	Initiated	No Decision Made
<b>Canada</b>	SNF		Granite and Sedimentary	Pinawa (Granite) - being decommissioned	Initiated	No Decision Made
<b>United Kingdom</b>	HLW and ILW		Undecided		Initiated	No Decision Made
<b>Germany</b>	HLW, SNF, heat generating ILW	Gorleben and Ahaus	Salt	Gorleben (Salt)	On Hold	No Decision Made
<b>Republic of Korea</b>	SNF	Envisioned	Granite	Korea Underground Research Tunnel (Granite, Shallow)	Not Initiated	No Decision Made
<b>Spain</b>	No Decision Made	Siting Process Initiated	Granite, Clay, Salt		Not Initiated	No Decision Made

Shaded rows indicate the programs that have on-going UFD collaborations.

**Table A6.** Summary of Research Topics for Crystalline Disposal R&D Work Package

R&D topic	Decision point supported					Nature of R&D	Priority
	Overall fuel cycle	Site screening	Site Selection	Site characterization	Site suitability		
S1: Evaluation of potential impacts of disposal options on fuel cycles	X	X				Concept development	High
S2: Disposal concept development	X	X	X	X	X	Concept development	High
S3: Disposal system modeling	X	X	X	X	X	Modeling (developing integration & decision tools); data collection; process understanding	High
S4: Development of a centralized technical database for natural system evaluation	X	X	X	X	X	Data collection & archive (knowledge management)	High
S5: Evaluation of state of the art of site characterization techniques			X	X	X	Review	High
S6: Development and demonstration of geophysical techniques for site characterization			X	X	X	Field technique development & demonstration	Medium
S7: Identification of the needs for using Underground Research Laboratories (URLs)			X	X	X	Review	High

S8: Natural analog studies		X	X	X	X (Confidence building)	Data collection	Medium
S9: Testing and modeling to support evaluation of direct salt disposal option for electrorefiner salt	X	X	X	X	X	Laboratory testing, data collection, modeling	High
P1: Development of discrete fracture network (DFN) model			X	X	X	Modeling; data collection; field testing	High
P2: Parameter estimation and uncertainty quantification of field testing			X	X (Reducing uncertainty)	X (Reducing uncertainty)	Modeling, field testing	High
P3: Development of a new theory for preferential flow in unsaturated porous media			X	X	X	Modeling; data collection	Medium
P4: Investigation of water movement and transport in low permeability media (clay formations)			X	X	X	Modeling, lab experiments	High
P5: Investigation of water movement and transport in low permeability media (salt formations)			X	X	X	Modeling, lab & field testing	Medium
P6: Investigation of water and transport movement in deep borehole disposal environments		X	X	X	X	Modeling, data collection, field technique development	High
P7: Novel in-situ			X	X	X	Technique development;	Medium

**R&D Plan for UFDC Natural System Evaluation and Tool Development**

May 25, 2011

techniques for groundwater chemistry characterization						process understanding	
P8: Reactive transport modeling of groundwater chemistry evolution and radionuclide transport			X	X (Reducing uncertainty)	X (Reducing uncertainty)	Modeling, data collection; process understanding	High
P9: Evaluation of the effects of spatial heterogeneity on radionuclide transport			X	X (Reducing uncertainty & total dose)	X (Reducing uncertainty & total dose)	Modeling, characterization technique development; process understanding	High
P10: Better understanding radionuclide interaction with geomeia		X	X	X (Reducing uncertainty & total dose)	X (Reducing uncertainty & total dose)	Lab experiments, modeling, process understanding	High
P11: New perspective of colloid-facilitated radionuclide transport		X	X	X (Confidence building)	X (Confidence building)	Modeling, lab experiments, field testing, process understanding	High
P12: Upscaling of key hydrological and geochemical parameters				X	X	Modeling, lab & field testing, process understanding	Medium
P13: Evaluation of biological processes			X	X	X	Technique development, modeling, process understanding	Low
P14: Technical basis for thermal loading	X	X	X	X	X	Modeling, data collection, process understanding	High
P15: Modeling of disturbed rock zone (DRZ) evolution (clay repository)			X	X	X	Modeling, data collection, process understanding	High

P16: Modeling of DRZ evolution (salt repository)			X	X	X	Modeling, data collection, process understanding	Medium
P17: Modeling of DRZ evolution (deep borehole disposal)			X	X	X	Modeling, data collection, process understanding	Medium
P18: In-situ testing of DRZ development			X	X	X	Field testing, data collection	High
P19: Title: Development of waste form degradation model					X	Modeling, data collection	High
P20: Development of new waste package concepts and models for evaluation of waste package performance for long-term disposal					X	Modeling, data collection	High
P21: Backfill and seal materials design					X	Testing, modeling	High
P22: Modeling radionuclide transport in engineered barrier system					X	Modeling, testing	High

Lightly shaded rows indicate R&D topics that have been initiated or for which some progress has been made; heavily shaded rows indicates R&D topics for which significant progress has been made.

## A6.0 References

- Brady, P.V., B.W. Arnold, G.A. Freeze, P.N. Swift, S.J. Bauer, J.L. Kanney, R.P. Rechar, and J.S. Stein, 2009. Deep Borehole Disposal of High-Level Radioactive Waste, SAND2009-4401, August 2009.
- DOE, 2011. Used Fuel Disposition Campaign Disposal Research and Development Roadmap, FCR&D-USED-2011-000065, Rev 0.
- Freeze, G.A., P. Mariner, J.E. Houseworth, J.C. Cunnane, 2010. Used Fuel Disposition Campaign Features, Events, and Processes (FEPs): FY10 Progress Report,” SAND2010-5902, September 2010.
- Hansen, F.D., E.L. Hardin, R.P. Rechar, G.A. Freeze, D.C. Sassani, P.V. Brady, C.M. Stone, M.J. Martinez, J.F. Holland, T. Dewers, K.N. Gaither, S.R. Sobolik, and R.T. Cygan, 2010. Shale Disposal of U.S. High-Level Radioactive Waste, SAND2010-2843, May 2010.
- Hansen, F.D. and C.D. Leigh, Salt Disposal of Heat-Generating Nuclear Waste, SAND2011-0161, January 2011.
- International Atomic Energy Agency (IAEA), 2003, Scientific and Technical Basis for Geological Disposal of Radioactive Wastes, Technical Reports Series No. 413.
- Nuclear Energy Agency (NEA), 2004, “Post-Closure Safety Case for Geological Repositories, Nature and Purpose,” OECD Nuclear Energy Agency, 2004.
- Nutt, M. (2012) Used Fuel Disposition Campaign Disposal Research and Development Roadmap, FCR&D-USED-2011-000065, Rev 1.
- Wang, Y. (editor), 2010. Natural System Evaluation and Tool Development – FY10 Progress Report,” August 2010.
- Wang, Y., M. Simpson, J. Rath, F. Hansen, J. H. Lee, C. Jove-Colon<sup>1</sup>, K. McMahon<sup>1</sup> and P. Swift, 2011, Closing the nuclear fuel cycle with salt, Proceedings of the 13<sup>th</sup> International High-Level Radioactive Waste Management Conference, Albuquerque, NM, April 10-14, 2011.
- Wang, Y., 2013, Research & Development for Used Fuel Disposition Campaign (UFDC) Natural System Evaluation and Tool Development (Rev. 1), FCRD-UFD-2013-000144.

**Table A7.** Ranking of Individual Natural System FEPs

<b>FEP ID and Title</b>	<b>Priority</b>	<b>Related Research Topics</b>
2.2.01.01 - Evolution of EDZ - Clay/Shale	7.83	P15, P4
2.2.08.01 - Flow Through the Host Rock - Salt	7.58	P5
2.2.08.02 - Flow Through the Other Geologic Units - Confining units - Aquifers - Salt	7.58	P2, P3, P1, P12
2.2.08.06 - Flow Through EDZ - Salt	7.58	P16, P5
2.2.08.04 - Effects of Repository Excavation on Flow Through the Host Rock - Salt	6.96	P16
2.2.08.07 - Mineralogic Dehydration - Salt	6.33	P16
2.2.01.01 - Evolution of EDZ - Deep Boreholes	6.00	P17
2.2.09.01 - Chemical Characteristics of Groundwater in Host Rock - Deep Boreholes	5.75	P6
2.2.09.02 - Chemical Characteristics of Groundwater in Other Geologic Units (Non-Host-Rock) - Confining units - Aquifers - Deep Boreholes	5.75	P7, P8, P13
2.2.09.05 - Radionuclide Speciation and Solubility in Host Rock - Deep Boreholes	5.75	P7, P8, P13
2.2.09.06 - Radionuclide Speciation and Solubility in Other Geologic Units (Non-Host-Rock) - Deep Boreholes	5.75	P7, P8, P13
2.2.09.03 - Chemical Interactions and Evolution of Groundwater in Host Rock - Deep Boreholes	5.30	P7, P8, P13
2.2.09.04 - Chemical Interactions and Evolution of Groundwater in Other Geologic Units (Non-Host-Rock) - Confining units - Aquifers - Deep Boreholes	5.30	P7, P8, P13
1.2.03.01 - Seismic Activity Impacts EBS and/or EBS Components -	4.84	
2.2.07.01 - Mechanical Effects on Host Rock - Clay/Shale	3.74	P15
2.2.07.01 - Mechanical Effects on Host Rock - Salt	3.74	P16
2.2.02.01 - Stratigraphy and Properties of Host Rock - Clay/Shale	3.67	S2
2.2.02.01 - Stratigraphy and Properties of Host Rock - Deep Boreholes	3.67	S2
2.2.02.01 - Stratigraphy and Properties of Host Rock - Granite/Crystalline	3.67	S2

2.2.02.01 - Stratigraphy and Properties of Host Rock - Salt	3.67	S2
2.2.09.51 - Advection of Dissolved Radionuclides in Host Rock - Clay/Shale	3.67	P4, P8, P9
2.2.09.51 - Advection of Dissolved Radionuclides in Host Rock - Granite/Crystalline	3.67	P1, P8, P9
2.2.05.01 - Fractures - Host Rock - Other Geologic Units - Clay/Shale	3.58	P1, P15
2.2.05.01 - Fractures - Host Rock - Other Geologic Units - Deep Boreholes	3.58	P6, P1
2.2.05.01 - Fractures - Host Rock - Other Geologic Units - Granite/Crystalline	3.58	P1
2.2.05.01 - Fractures - Host Rock - Other Geologic Units - Salt	3.58	P5, P16
2.2.08.01 - Flow Through the Host Rock - Clay/Shale	3.58	P4
2.2.08.01 - Flow Through the Host Rock - Deep Boreholes	3.58	P6
2.2.08.02 - Flow Through the Other Geologic Units - Confining units - Aquifers - Clay/Shale	3.58	P1, P2, P4
2.2.08.02 - Flow Through the Other Geologic Units - Confining units - Aquifers - Deep Boreholes	3.58	P1, P2, P6
2.2.08.06 - Flow Through EDZ - Clay/Shale	3.58	P4, P15
2.2.08.06 - Flow Through EDZ - Deep Boreholes	3.58	P6, P17
2.2.09.01 - Chemical Characteristics of Groundwater in Host Rock - Clay/Shale	3.50	S2, P8, P7
2.2.09.02 - Chemical Characteristics of Groundwater in Other Geologic Units (Non-Host-Rock) - Confining units - Aquifers - Clay/Shale	3.50	S2, P8, P7
2.2.09.05 - Radionuclide Speciation and Solubility in Host Rock - Clay/Shale	3.50	P8, P10
2.2.09.06 - Radionuclide Speciation and Solubility in Other Geologic Units (Non-Host-Rock) - Clay/Shale	3.50	P8, P10
2.2.09.52 - Advection of Dissolved Radionuclides in Other Geologic Units (Non-Host-Rock) - Confining units - Aquifers - Clay/Shale	3.50	P8, P10

2.2.09.52 - Advection of Dissolved Radionuclides in Other Geologic Units (Non-Host-Rock) - Confining units - Aquifers - Granite/Crystalline	3.50	P8, P10
2.2.09.53 - Diffusion of Dissolved Radionuclides in Host Rock - Clay/Shale	3.50	P8, P10, P9, P12
2.2.09.53 - Diffusion of Dissolved Radionuclides in Host Rock - Granite/Crystalline	3.50	P8, P10, P9, P12
2.2.09.54 - Diffusion of Dissolved Radionuclides in Other Geologic Units (Non-Host-Rock) - Confining units - Aquifers - Clay/Shale	3.50	P8, P10, P9, P12
2.2.09.54 - Diffusion of Dissolved Radionuclides in Other Geologic Units (Non-Host-Rock) - Confining units - Aquifers - Granite/Crystalline	3.50	P8, P10, P9, P12
2.2.09.55 - Sorption of Dissolved Radionuclides in Host Rock - Clay/Shale	3.50	P8, P10, P9, P12
2.2.09.55 - Sorption of Dissolved Radionuclides in Host Rock - Granite/Crystalline	3.50	P8, P10, P9, P12
2.2.09.56 - Sorption of Dissolved Radionuclides in Other Geologic Units (Non-Host-Rock) - Confining units - Aquifers - Clay/Shale	3.50	P8, P10, P9, P12
2.2.09.56 - Sorption of Dissolved Radionuclides in Other Geologic Units (Non-Host-Rock) - Confining units - Aquifers - Granite/Crystalline	3.50	P8, P10, P9, P12
2.2.09.57 - Complexation in Host Rock - Clay/Shale	3.50	P8, P10, P13, S4
2.2.09.57 - Complexation in Host Rock - Granite/Crystalline	3.50	P8, P10, P13, S4
2.2.09.58 - Complexation in Other Geologic Units (Non-Host-Rock) - Clay/Shale	3.50	P8, P10, P13, S4
2.2.09.58 - Complexation in Other Geologic Units (Non-Host-Rock) - Granite/Crystalline	3.50	P8, P10, P13, S4
2.2.09.61 - Radionuclide Transport Through EDZ - Clay/Shale	3.50	P8, P10, P9, P12
2.2.09.61 - Radionuclide Transport Through EDZ - Granite/Crystalline	3.50	P8, P10, P9, P12
2.2.09.64 - Radionuclide Release from Host Rock - Dissolved - Colloidal - Gas Phase - Clay/Shale	3.50	P8, P10, P9, P12, P11

2.2.09.64 - Radionuclide Release from Host Rock - Dissolved - Colloidal - Gas Phase - Granite/Crystalline	3.50	P8, P10, P9, P12, P11
2.2.09.65 - Radionuclide Release from Other Geologic Units - Dissolved - Colloidal - Gas Phase - Clay/Shale	3.50	P8, P10, P9, P12, P11
2.2.09.65 - Radionuclide Release from Other Geologic Units - Dissolved - Colloidal - Gas Phase - Granite/Crystalline	3.50	P8, P10, P9, P12, P11
2.2.11.04 - Thermal Effects on Chemistry and Microbial Activity in Geosphere - Clay/Shale	3.50	P15, P13
2.2.11.04 - Thermal Effects on Chemistry and Microbial Activity in Geosphere - Deep Boreholes	3.50	P17
2.2.11.06 - Thermal-Mechanical Effects on Geosphere - Clay/Shale	3.34	P15, P18
2.2.11.06 - Thermal-Mechanical Effects on Geosphere - Deep Boreholes	3.34	P17
2.2.11.07 - Thermal-Chemical Alteration of Geosphere - Clay/Shale	3.34	P8
2.2.11.07 - Thermal-Chemical Alteration of Geosphere - Deep Boreholes	3.34	P8, P17
2.2.09.59 - Colloidal Transport in Host Rock - Clay/Shale	3.24	P11, P8, P10
2.2.09.59 - Colloidal Transport in Host Rock - Granite/Crystalline	3.24	P11, P8, P10
2.2.09.60 - Colloidal Transport in Other Geologic Units (Non-Host-Rock) - Confining units - Aquifers - Clay/Shale	3.24	P11, P8, P10
2.2.09.60 - Colloidal Transport in Other Geologic Units (Non-Host-Rock) - Confining units - Aquifers - Granite/Crystalline	3.24	P11, P8, P10
2.2.08.04 - Effects of Repository Excavation on Flow Through the Host Rock - Clay/Shale	3.17	P15
2.2.08.04 - Effects of Repository Excavation on Flow Through the Host Rock - Deep Boreholes	3.17	P17

2.2.07.02 - Mechanical Effects on Other Geologic Units - Clay/Shale	3.05	P18, P15
2.2.07.02 - Mechanical Effects on Other Geologic Units - Salt	3.05	P18, P16
2.2.09.03 - Chemical Interactions and Evolution of Groundwater in Host Rock - Clay/Shale	3.05	P8, P12, P7
2.2.09.04 - Chemical Interactions and Evolution of Groundwater in Other Geologic Units (Non-Host-Rock) - Confining units - Aquifers - Clay/Shale	3.05	P8, P12, P7
2.2.09.62 - Dilution of Radionuclides in Groundwater - Host Rock - Other Geologic Units - Clay/Shale	3.05	P8
2.2.09.62 - Dilution of Radionuclides in Groundwater - Host Rock - Other Geologic Units - Granite/Crystalline	3.05	P8
2.2.09.63 - Dilution of Radionuclides with Stable Isotopes - Host Rock - Other Geologic Units - Clay/Shale	3.05	P8
2.2.09.63 - Dilution of Radionuclides with Stable Isotopes - Host Rock - Other Geologic Units - Granite/Crystalline	3.05	P8
2.2.11.01 - Thermal Effects on Flow in Geosphere - Repository-Induced - Natural Geothermal - Clay/Shale	3.05	P4, P18, P15
2.2.11.01 - Thermal Effects on Flow in Geosphere - Repository-Induced - Natural Geothermal - Deep Boreholes	3.05	P6, P17
2.2.11.02 - Thermally-Driven Flow (Convection) in Geosphere - Clay/Shale	3.05	P15
2.2.11.02 - Thermally-Driven Flow (Convection) in Geosphere - Deep Boreholes	3.05	P17
2.2.08.07 - Mineralogic Dehydration - Clay/Shale	2.75	P8, P18
2.2.08.07 - Mineralogic Dehydration - Deep Boreholes	2.75	P8, P17
2.2.01.01 - Evolution of EDZ - Granite/Crystalline	2.53	P1
2.2.01.01 - Evolution of EDZ - Salt	2.53	P16, P18
2.2.09.51 - Advection of Dissolved Radionuclides in Host Rock - Deep Boreholes	2.47	P8, P6, P10

2.2.09.51 - Advection of Dissolved Radionuclides in Host Rock - Salt	2.47	P8, P5, P10
2.2.05.03 - Alteration and Evolution of Geosphere Flow Pathways - Host Rock - Other Geologic Units - Clay/Shale	2.42	P8
2.2.05.03 - Alteration and Evolution of Geosphere Flow Pathways - Host Rock - Other Geologic Units - Deep Boreholes	2.42	P8
2.2.05.03 - Alteration and Evolution of Geosphere Flow Pathways - Host Rock - Other Geologic Units - Granite/Crystalline	2.42	P8
2.2.05.03 - Alteration and Evolution of Geosphere Flow Pathways - Host Rock - Other Geologic Units - Salt	2.42	P8
2.2.11.03 - Thermally-Driven Buoyant Flow / Heat Pipes in Geosphere - Clay/Shale	2.42	P4
2.2.11.03 - Thermally-Driven Buoyant Flow / Heat Pipes in Geosphere - Deep Boreholes	2.42	P6
2.2.03.01 - Stratigraphy and Properties of Other Geologic Units (Non-Host-Rock) - Clay/Shale	2.42	S2
2.2.03.01 - Stratigraphy and Properties of Other Geologic Units (Non-Host-Rock) - Deep Boreholes	2.42	S2
2.2.03.01 - Stratigraphy and Properties of Other Geologic Units (Non-Host-Rock) - Granite/Crystalline	2.42	S2
2.2.03.01 - Stratigraphy and Properties of Other Geologic Units (Non-Host-Rock) - Salt	2.42	S2
2.2.09.01 - Chemical Characteristics of Groundwater in Host Rock - Salt	2.36	S2, P8, P7, P13
2.2.09.02 - Chemical Characteristics of Groundwater in Other Geologic Units (Non-Host-Rock) - Confining units - Aquifers - Salt	2.36	S2, P8, P7, P13
2.2.09.05 - Radionuclide Speciation and Solubility in Host Rock - Salt	2.36	P8, P10
2.2.09.06 - Radionuclide Speciation and Solubility in Other Geologic Units (Non-Host-Rock) - Salt	2.36	P8, P10

2.2.09.52 - Advection of Dissolved Radionuclides in Other Geologic Units (Non-Host-Rock) - Confining units - Aquifers - Deep Boreholes	2.36	P8
2.2.09.52 - Advection of Dissolved Radionuclides in Other Geologic Units (Non-Host-Rock) - Confining units - Aquifers - Salt	2.36	P8
2.2.09.53 - Diffusion of Dissolved Radionuclides in Host Rock - Deep Boreholes	2.36	P8, P10, P12
2.2.09.53 - Diffusion of Dissolved Radionuclides in Host Rock - Salt	2.36	P8, P10, P12
2.2.09.54 - Diffusion of Dissolved Radionuclides in Other Geologic Units (Non-Host-Rock) - Confining units - Aquifers - Deep Boreholes	2.36	P8, P10, P12
2.2.09.54 - Diffusion of Dissolved Radionuclides in Other Geologic Units (Non-Host-Rock) - Confining units - Aquifers - Salt	2.36	P8, P10, P12
2.2.09.55 - Sorption of Dissolved Radionuclides in Host Rock - Deep Boreholes	2.36	P9, P8, P10, P12
2.2.09.55 - Sorption of Dissolved Radionuclides in Host Rock - Salt	2.36	P9, P8, P10, P12
2.2.09.56 - Sorption of Dissolved Radionuclides in Other Geologic Units (Non-Host-Rock) - Confining units - Aquifers - Deep Boreholes	2.36	P9, P8, P10, P12
2.2.09.56 - Sorption of Dissolved Radionuclides in Other Geologic Units (Non-Host-Rock) - Confining units - Aquifers - Salt	2.36	P9, P8, P10, P12
2.2.09.57 - Complexation in Host Rock - Deep Boreholes	2.36	P8, P10
2.2.09.57 - Complexation in Host Rock - Salt	2.36	P8, P10
2.2.09.58 - Complexation in Other Geologic Units (Non-Host-Rock) - Deep Boreholes	2.36	P8, P10
2.2.09.58 - Complexation in Other Geologic Units (Non-Host-Rock) - Salt	2.36	P8, P10
2.2.09.61 - Radionuclide Transport Through EDZ - Deep Boreholes	2.36	P9, P8, P10, P12
2.2.09.61 - Radionuclide Transport Through EDZ - Salt	2.36	P9, P8, P10, P12

2.2.09.64 - Radionuclide Release from Host Rock - Dissolved - Colloidal - Gas Phase - Deep Boreholes	2.36	P9, P8, P10, P12, P11
2.2.09.64 - Radionuclide Release from Host Rock - Dissolved - Colloidal - Gas Phase - Salt	2.36	P9, P8, P10, P12, P11
2.2.09.65 - Radionuclide Release from Other Geologic Units - Dissolved - Colloidal - Gas Phase - Deep Boreholes	2.36	P9, P8, P10, P12, P11
2.2.09.65 - Radionuclide Release from Other Geologic Units - Dissolved - Colloidal - Gas Phase - Salt	2.36	P9, P8, P10, P12, P11
2.2.11.04 - Thermal Effects on Chemistry and Microbial Activity in Geosphere - Granite/Crystalline	2.36	P8, P13
2.2.11.04 - Thermal Effects on Chemistry and Microbial Activity in Geosphere - Salt	2.36	P8, P13
1.2.03.02 - Seismic Activity Impacts Geosphere - Host Rock - Other Geologic Units -	2.32	
2.2.11.06 - Thermal-Mechanical Effects on Geosphere - Granite/Crystalline	2.26	
2.2.11.06 - Thermal-Mechanical Effects on Geosphere - Salt	2.26	P18, P16
2.2.11.07 - Thermal-Chemical Alteration of Geosphere - Granite/Crystalline	2.26	
2.2.11.07 - Thermal-Chemical Alteration of Geosphere - Salt	2.26	P16, P8, P18
2.2.09.59 - Colloidal Transport in Host Rock - Deep Boreholes	2.19	P17, P8
2.2.09.59 - Colloidal Transport in Host Rock - Salt	2.19	P11, P10, P8
2.2.09.60 - Colloidal Transport in Other Geologic Units (Non-Host-Rock) - Confining units - Aquifers - Deep Boreholes	2.19	P11, P10, P8

2.2.09.60 - Colloidal Transport in Other Geologic Units (Non-Host-Rock) - Confining units - Aquifers - Salt	2.19	P11, P10, P8
0.1.03.01 - Spatial Domain of Concern -	2.09	S2
2.2.09.03 - Chemical Interactions and Evolution of Groundwater in Host Rock - Salt	2.06	P8, P16
2.2.09.04 - Chemical Interactions and Evolution of Groundwater in Other Geologic Units (Non-Host-Rock) - Confining units - Aquifers - Salt	2.06	P8
2.2.09.62 - Dilution of Radionuclides in Groundwater - Host Rock - Other Geologic Units - Deep Boreholes	2.06	P8
2.2.09.62 - Dilution of Radionuclides in Groundwater - Host Rock - Other Geologic Units - Salt	2.06	P8
2.2.09.63 - Dilution of Radionuclides with Stable Isotopes - Host Rock - Other Geologic Units - Deep Boreholes	2.06	P8
2.2.09.63 - Dilution of Radionuclides with Stable Isotopes - Host Rock - Other Geologic Units - Salt	2.06	P8
2.2.11.01 - Thermal Effects on Flow in Geosphere - Repository-Induced - Natural Geothermal - Granite/Crystalline	2.06	P1
2.2.11.01 - Thermal Effects on Flow in Geosphere - Repository-Induced - Natural Geothermal - Salt	2.06	P5
2.2.11.02 - Thermally-Driven Flow (Convection) in Geosphere - Granite/Crystalline	2.06	P1
2.2.11.02 - Thermally-Driven Flow (Convection) in Geosphere - Salt	2.06	P5
1.3.01.01 - Climate Change - Natural - Anthropogenic -	1.83	S2
1.3.04.01 - Periglacial Effects -	1.83	
1.3.05.01 - Glacial and Ice Sheet Effects -	1.83	
2.2.11.03 - Thermally-Driven Buoyant Flow / Heat Pipes in Geosphere - Granite/Crystalline	1.64	P1

2.2.11.03 - Thermally-Driven Buoyant Flow / Heat Pipes in Geosphere - Salt	1.64	P5
2.2.07.01 - Mechanical Effects on Host Rock - Deep Boreholes	1.59	P17
2.2.07.01 - Mechanical Effects on Host Rock - Granite/Crystalline	1.59	
2.3.08.02 - Surface Runoff and Evapotranspiration -	1.59	
2.3.08.03 - Infiltration and Recharge -	1.59	P3
1.2.01.01 - Tectonic Activity – Large Scale -	1.46	S4
1.2.08.01 - Diagenesis - Clay/shale	1.46	
1.2.09.01 - Diapirism - Salt	1.46	
2.2.07.02 - Mechanical Effects on Other Geologic Units - Deep Boreholes	1.30	
2.2.07.02 - Mechanical Effects on Other Geologic Units - Granite/Crystalline	1.30	
2.2.10.01 - Microbial Activity in Host Rock - Clay/Shale	1.30	P13
2.2.10.01 - Microbial Activity in Host Rock - Deep Boreholes	1.30	P13
2.2.10.01 - Microbial Activity in Host Rock - Granite/Crystalline	1.30	P13
2.2.10.01 - Microbial Activity in Host Rock - Salt	1.30	P13
2.2.10.02 - Microbial Activity in Other Geologic Units (Non-Host-Rock) - Clay/Shale	1.30	P13
2.2.10.02 - Microbial Activity in Other Geologic Units (Non-Host-Rock) - Deep Boreholes	1.30	P13
2.2.10.02 - Microbial Activity in Other Geologic Units (Non-Host-Rock) - Granite/Crystalline	1.30	P13
2.2.10.02 - Microbial Activity in Other Geologic Units (Non-Host-Rock) - Salt	1.30	P13
2.2.12.02 - Effects of Gas on Flow Through the Geosphere - Clay/Shale	0.95	
2.2.12.02 - Effects of Gas on Flow Through the Geosphere - Deep Boreholes	0.95	
2.2.12.02 - Effects of Gas on Flow Through the Geosphere - Granite/Crystalline	0.95	
2.2.12.02 - Effects of Gas on Flow Through the Geosphere - Salt	0.95	
2.3.09.52 - Surface Water Transport Through Biosphere -	0.85	
2.3.09.53 - Soil and Sediment Transport Through Biosphere -	0.85	
2.3.09.54 - Radionuclide Accumulation in Soils -	0.85	

2.2.12.03 - Gas Transport in Geosphere - Clay/Shale	0.73	
2.2.12.03 - Gas Transport in Geosphere - Deep Boreholes	0.73	
2.2.12.03 - Gas Transport in Geosphere - Granite/Crystalline	0.73	
2.2.12.03 - Gas Transport in Geosphere - Salt	0.73	
2.3.09.51 - Atmospheric Transport Through Biosphere -	0.73	
2.3.09.55 - Recycling of Accumulated Radionuclides from Soils to Groundwater -	0.73	
3.3.04.01 - Ingestion -	0.54	
3.3.04.02 - Inhalation -	0.54	
3.3.04.03 - External Exposure -	0.54	
0.1.02.01 - Timescales of Concern -	0.00	
0.1.09.01 - Regulatory Requirements and Exclusions -	0.00	
0.1.10.01 - Model Issues -	0.00	
0.1.10.02 - Data Issues -	0.00	
1.1.01.01 - Open Boreholes -	0.00	
1.1.02.01 - Chemical Effects from Preclosure Operations -	0.00	
1.1.02.02 - Chemical Effects from Preclosure Operations - In EBS - In EDZ - In Host Rock -	0.00	
1.1.02.03 - Mechanical Effects from Preclosure Operations - In EBS - In EDZ - In Host Rock -	0.00	
1.1.08.01 - Deviations from Design and Inadequate Quality Control -	0.00	
1.1.10.01 - Control of Repository Site -	0.00	
1.1.13.01 - Retrievability -	0.00	
1.2.02.01 - Subsidence -	0.00	
1.2.03.03 - Seismic Activity Impacts Biosphere - Surface Environment - Human Behavior -	0.00	
1.2.04.01 - Igneous Activity Impacts EBS and/or EBS Components -	0.00	

1.2.04.02 - Igneous Activity Impacts Geosphere - Host Rock - Other Geologic Units -	0.00	
1.2.04.03 - Igneous Activity Impacts Biosphere - Surface Environment - Human Behavior -	0.00	
1.2.05.01 - Metamorphism -	0.00	
1.2.09.02 - Large-Scale Dissolution -	0.00	
1.4.01.01 - Human Influences on Climate - Intentional - Accidental -	0.00	
1.4.02.01 - Human Intrusion - Deliberate - Inadvertent -	0.00	
1.4.11.01 - Explosions and Crashes from Human Activities -	0.00	
1.5.01.01 - Meteorite Impact -	0.00	
1.5.01.02 - Extraterrestrial Events -	0.00	
1.5.03.01 - Earth Planetary Changes -	0.00	
2.2.08.01 - Flow Through the Host Rock - Granite/Crystalline	0.00	
2.2.08.02 - Flow Through the Other Geologic Units - Confining units - Aquifers - Granite/Crystalline	0.00	
2.2.08.03 - Effects of Recharge on Geosphere Flow - Host Rock - Other Geologic Units - 0	0.00	
2.2.08.03 - Effects of Recharge on Geosphere Flow - Host Rock - Other Geologic Units - 0	0.00	
2.2.08.03 - Effects of Recharge on Geosphere Flow - Host Rock - Other Geologic Units - 0	0.00	
2.2.08.03 - Effects of Recharge on Geosphere Flow - Host Rock - Other Geologic Units - 0	0.00	
2.2.08.04 - Effects of Repository Excavation on Flow Through the Host Rock - Granite/Crystalline	0.00	
2.2.08.05 - Condensation Forms in Host Rock - 0	0.00	
2.2.08.05 - Condensation Forms in Host Rock - 0	0.00	
2.2.08.05 - Condensation Forms in Host Rock - 0	0.00	
2.2.08.05 - Condensation Forms in Host Rock - 0	0.00	
2.2.08.06 - Flow Through EDZ - Granite/Crystalline	0.00	P1

2.2.08.07 - Mineralogic Dehydration - Granite/Crystalline	0.00	
2.2.08.08 - Groundwater Discharge to Biosphere Boundary - 0	0.00	
2.2.08.08 - Groundwater Discharge to Biosphere Boundary - 0	0.00	
2.2.08.08 - Groundwater Discharge to Biosphere Boundary - 0	0.00	
2.2.08.08 - Groundwater Discharge to Biosphere Boundary - 0	0.00	
2.2.08.09 - Groundwater Discharge to Well - 0	0.00	
2.2.08.09 - Groundwater Discharge to Well - 0	0.00	
2.2.08.09 - Groundwater Discharge to Well - 0	0.00	
2.2.08.09 - Groundwater Discharge to Well - 0	0.00	
2.2.09.01 - Chemical Characteristics of Groundwater in Host Rock - Granite/Crystalline	0.00	P8, P1
2.2.09.02 - Chemical Characteristics of Groundwater in Other Geologic Units (Non-Host-Rock) - Confining units - Aquifers - Granite/Crystalline	0.00	P8, p1
2.2.09.03 - Chemical Interactions and Evolution of Groundwater in Host Rock - Granite/Crystalline	0.00	P8, P1
2.2.09.04 - Chemical Interactions and Evolution of Groundwater in Other Geologic Units (Non-Host-Rock) - Confining units - Aquifers - Granite/Crystalline	0.00	P8, P1
2.2.09.05 - Radionuclide Speciation and Solubility in Host Rock - Granite/Crystalline	0.00	P8, P10
2.2.09.06 - Radionuclide Speciation and Solubility in Other Geologic Units (Non-Host-Rock) - Granite/Crystalline	0.00	P8, P10
2.2.11.05 - Thermal Effects on Transport in Geosphere - Clay/Shale	0.00	
2.2.11.05 - Thermal Effects on Transport in Geosphere - Deep Boreholes	0.00	
2.2.11.05 - Thermal Effects on Transport in Geosphere - Granite/Crystalline	0.00	
2.2.11.05 - Thermal Effects on Transport in Geosphere - Salt	0.00	
2.2.12.01 - Gas Generation in Geosphere - Clay/Shale	0.00	

2.2.12.01 - Gas Generation in Geosphere - Deep Boreholes	0.00	
2.2.12.01 - Gas Generation in Geosphere - Granite/Crystalline	0.00	
2.2.12.01 - Gas Generation in Geosphere - Salt	0.00	
2.2.14.01 - Criticality in Geosphere -	0.00	
2.3.01.01 - Topography and Surface Morphology -	0.00	
2.3.02.01 - Surficial Soil Type -	0.00	
2.3.04.01 - Surface Water -	0.00	
2.3.05.01 - Biosphere Characteristics -	0.00	
2.3.07.01 - Erosion -	0.00	
2.3.07.02 - Deposition -	0.00	
2.3.07.03 - Animal Intrusion into Repository -	0.00	
2.3.08.01 - Precipitation -	0.00	
2.3.09.01 - Chemical Characteristics of Soil and Surface Water -	0.00	
2.3.09.02 - Radionuclide Speciation and Solubility in Biosphere -	0.00	
2.3.09.03 - Radionuclide Alteration in Biosphere -	0.00	
2.3.10.01 - Microbial Activity in Biosphere -	0.00	
2.3.11.01 - Effects of Repository Heat on Biosphere -	0.00	
2.4.01.01 - Human Characteristics -	0.00	
2.4.01.02 - Human Evolution -	0.00	
2.4.04.01 - Human Lifestyle -	0.00	
2.4.08.01 - Land and Water Use -	0.00	
2.4.08.02 - Evolution of Land and Water Use -	0.00	
3.3.01.01 - Radionuclides in Biosphere Media -	0.00	
3.3.01.02 - Radionuclides in Food Products -	0.00	
3.3.01.03 - Radionuclides in Non-Food Products -	0.00	
3.3.06.01 - Radiation Doses -	0.00	
3.3.06.02 - Radiological Toxicity and Effects -	0.00	

---

3.3.06.03 - Non-Radiological Toxicity and Effects -	0.00	
---	------	--